CLIMATE IMPACTS ON GLACIERS AND BIOSPHERE IN FUEGO-PATAGONIA

EDITED BY: Christoph Schneider, Matthias Holger Braun, Marius Schaefer, Jussi Grießinger and Gino Casassa

PUBLISHED IN: Frontiers in Earth Science and Frontiers in Ecology and Evolution

frontiers Research Topics

ISSN 1664-8714
ISBN 978-2-88963-758-4
DOI 10.3389/978-2-88963-758-4

About Frontiers

Frontiers is more than just an open-access publisher of scholarly articles: it is a pioneering approach to the world of academia, radically improving the way scholarly research is managed. The grand vision of Frontiers is a world where all people have an equal opportunity to seek, share and generate knowledge. Frontiers provides immediate and permanent online open access to all its publications, but this alone is not enough to realize our grand goals.

Frontiers Journal Series

The Frontiers Journal Series is a multi-tier and interdisciplinary set of open-access, online journals, promising a paradigm shift from the current review, selection and dissemination processes in academic publishing. All Frontiers journals are driven by researchers for researchers; therefore, they constitute a service to the scholarly community. At the same time, the Frontiers Journal Series operates on a revolutionary invention, the tiered publishing system, initially addressing specific communities of scholars, and gradually climbing up to broader public understanding, thus serving the interests of the lay society, too.

Dedication to Quality

Each Frontiers article is a landmark of the highest quality, thanks to genuinely collaborative interactions between authors and review editors, who include some of the world's best academicians. Research must be certified by peers before entering a stream of knowledge that may eventually reach the public - and shape society; therefore, Frontiers only applies the most rigorous and unbiased reviews.
Frontiers revolutionizes research publishing by freely delivering the most outstanding research, evaluated with no bias from both the academic and social point of view. By applying the most advanced information technologies, Frontiers is catapulting scholarly publishing into a new generation.

What are Frontiers Research Topics?

Frontiers Research Topics are very popular trademarks of the Frontiers Journals Series: they are collections of at least ten articles, all centered on a particular subject. With their unique mix of varied contributions from Original Research to Review Articles, Frontiers Research Topics unify the most influential researchers, the latest key findings and historical advances in a hot research area! Find out more on how to host your own Frontiers Research Topic or contribute to one as an author by contacting the Frontiers Editorial Office: researchtopics@frontiersin.org

CLIMATE IMPACTS ON GLACIERS AND BIOSPHERE IN FUEGO-PATAGONIA

Topic Editors:
Christoph Schneider, Humboldt-Universität zu Berlin, Germany
Matthias Holger Braun, Friedrich-Alexander-University of Erlangen-Nuremberg, Germany
Marius Schaefer, Austral University of Chile, Chile
Jussi Grießinger, Friedrich-Alexander-University of Erlangen-Nuremberg, Germany
Gino Casassa, Universidad de Magallanes, Punta Arenas, and General Directorate of Water (DGA), Chile

Citation: Schneider, C., Braun, M. H., Schaefer, M., Grießinger, J., Casassa, G., eds. (2020). Climate Impacts on Glaciers and Biosphere in Fuego-Patagonia. Lausanne: Frontiers Media SA. doi: 10.3389/978-2-88963-758-4

Table of Contents

frontiers in Earth Science

EDITORIAL
published: 09 April 2020
doi: 10.3389/feart.2020.00091

Editorial: Climate Impacts on Glaciers and Biosphere in Fuego-Patagonia

Christoph Schneider[1], Matthias Holger Braun[2], Marius Schaefer[3], Jussi Grießinger[2] and Gino Casassa[4]*

[1] Geography Department, Humboldt-Universität zu Berlin, Berlin, Germany, [2] Institute of Geography, Friedrich-Alexander-University Erlangen-Nuremberg, Erlangen, Germany, [3] Institute of Physics and Mathematics, Austral University of Chile, Valdivia, Chile, [4] Centro de Investigación GAIA Antártica, Universidad de Magallanes, Punta Arenas, Chile

Keywords: Patagonia, Tierra del Fuego, cryosphere, biosphere, climate variability, climate change

Editorial on the Research Topic

Climate Impacts on Glaciers and Biosphere in Fuego-Patagonia

Southernmost South America including Tierra del Fuego and its adjacent islands form the only significant land masses within the mid-latitude Westerlies of the Southern Hemisphere. Since climate variability in the Southern Hemisphere and its impacts are still insufficiently understood, it is essential to improve our understanding of climate impacts and resulting ecological and glacier responses in the region. The Conference and Workshop "Climate Impacts on Glaciers and Biosphere in Fuego-Patagonia[1]" in Berlin, Germany, 14–19 July 2017, explored these topics and resulted in the current Frontiers Research Topic. The activities were initiated and linked to the joint research project "Responses of Glaciers, Biosphere and Hydrology to Climate Variability and Climate Change across the Southern Andes" (GABY-VASA) by University of Magallanes and the Instituto Antártico Chileno, both in Punta Arenas, Chile, and the Humboldt-Universität zu Berlin, the Friedrich-Alexander-University Erlangen-Nuremberg and RWTH Aachen University in Germany on dendroclimatology, climatology and glaciology in Southern Patagonia and the Cordillera Darwin, jointly funded by the Chilean Comisión Nacional de Investigación Científica y Tecnológica and the German Federal Ministry of Research and Education.

The regional climate in Southernmost South America is heavily influenced by the proximity to the oceans. This generates rather weak seasonal cycles with cool to cold summers and moderate to cold winters, especially on the western Pacific side. Slightly more pronounced, continental seasonal cycles are observed in the East of the Andes. While annual mean air temperatures across the region are decreasing from North to South precipitation patterns show very pronounced east-west gradients. The distinctive gradients in precipitation are caused by the north-south striking mountain ranges of the Patagonian Andes, and the northwest-southeast stretching mountain chains of the Cordillera Darwin. Both mountain ranges enforce heavy precipitation on the west and southwest exposed flanks by uplift and dry foehn-like conditions on the leesides (e.g., Holmlund and Fuenzalida, 1995; Schneider et al., 2003; Rasmussen et al., 2007) which produces extremely high drying ratios (Escobar et al., 1992; Carrasco et al., 2002; Smith and Evans, 2007). At inter-annual to decadal time scales atmospheric teleconnections such as the El Niño Southern Oscillation (ENSO) (Schneider and Gies, 2004), Southern Annular Mode (SAM), and Pacific Decadal Oscillation (PDO) are influencing spatial and temporal patterns of both, precipitation and air temperature. For example, positive SAM modes (Garreaud, 2009; Weidemann, Sauter, Kilian et al.) and the PDO (Villalba et al., 2003) are associated with higher air temperatures. Langhamer et al. show that the source of precipitation in the Southern Andes also depends on these teleconnections.

[1]https://www.geographie.hu-berlin.de/en/professorships/climate_geography/patagonia_workshop

Edited and reviewed by:
Regine Hock, University of Alaska Fairbanks, United States

****Correspondence:***
Christoph Schneider
christoph.schneider@geo.hu-berlin.de

Specialty section:
This article was submitted to Cryospheric Sciences, a section of the journal Frontiers in Earth Science

Received: *26 February 2020*
Accepted: *16 March 2020*
Published: *09 April 2020*

Citation:
Schneider C, Braun MH, Schaefer M, Grießinger J and Casassa G (2020) Editorial: Climate Impacts on Glaciers and Biosphere in Fuego-Patagonia. Front. Earth Sci. 8:91. doi: 10.3389/feart.2020.00091

An important aspect is that Patagonia and Tierra del Fuego, together with the sub-Antarctic islands are the only regions where direct proximity between Antarctica and land masses north of the Southern Ocean is given. Such linkages are for example explored with investigations by Hebel et al. on the biosphere and Oppedal et al. for the regional glacier history.

The Humboldt or Peru Current transports cold waters along the Pacific coast of South America and the strong Westerlies cause reduced air temperatures combined with heavy precipitation in Southern South America. This setting induces both, unique eco-systems comprised by extensive bogs, evergreen and broadleaf *Nothofagus* (rain) forests, as well as characteristical elements of the cryosphere including extensive seasonal snow cover (Aguirre et al.). The mountain ranges host major ice bodies such as the Northern and Southern Patagonia Icefields and the Icefield of the Cordillera Darwin all of them with outlet glaciers reaching down as far as sea level. In addition, a multitude of smaller ice caps and glaciers are wide-spread.

On the eastern side of the Andes, the small ocean basins along the Strait of Magallan, the glacially formed gulfs of Seno Skyring and Seno Otway and large glacial lakes such as Lago Argentino and Lago Viedma provide evidence of extended glaciation until the Last Glacial Maximum (e.g., Rabassa et al., 2011). In recent centuries glacier re-advances cumulated in Little Ice Age maximum glacier extents and associated trimlines and moraines mostly dating from the second half of the nineteenth century as for example explored in Meier et al.. The underlying changes in climate can be evidenced by analyzing dendroclimatological records as pinpointed for example for *N. pumilio* in this Research Topic by Srur et al. and Grießinger et al..

Due to the temperate nature of glaciers associated with its high mass turnover, ice bodies in Patagonia and Tierra del Fuego tend to respond quickly and highly sensitive to atmospheric forcing as shown by analyzing the energy and climatic mass balance in details in Weidemann, Sauter, Malz et al.. There is overall consensus that anthropogenically induced global climate warming has a major impact on the cryosphere in Fuego-Patagonia. Nonetheless, it is still under debate how precisely recent glacier retreat and glacier thinning (e.g., Braun et al., 2019; Dussaillant et al.) can be explained by the combination of recent climate warming and glacier adjustment to late nineteenth century to twentieth century climate variability. Since there are no direct measurements on the icefields, accumulation can only be deduced from firn cores and numerical modeling providing a wide range of 7–34 m per year (Aristarain and Delmas, 1993; Shiraiwa et al., 2002; Schwikowski et al., 2013; Lenaerts et al., 2014; Schaefer et al., 2015). It is disputable if—despite the high drying ratios—such high accumulation rates are feasible by atmospheric moisture transport. An effort toward solving this issue is undertaken by Langhamer et al. by analyzing sources of precipitation.

AUTHOR CONTRIBUTIONS

CS drafted the editorial. MB, JG, MS, and GC subsequently contributed to the text of the editorial. This contents of the editorial was jointly discussed by all authors.

FUNDING

The workshop on Climate Impacts on Glaciers and Biosphere in Fuego-Patagonia on which this Research Topic builds was funded by the CONICYT-BMBF project GABY-VASA under Grant Nos. 01DN15007 and 01DN15020. Further support for the workshop by Geo.X, the Research Network for Geosciences in Berlin and Potsdam, Germany and the Embassy of Chile in Berlin, Germany are gladly acknowledged.

REFERENCES

Aristarain, A., and Delmas, R. (1993). Firn-core study from the Southern Patagonia Ice Cap, South America. *J. Glaciol.* 39, 249–254. doi: 10.1017/S0022143000015914

Braun, M. H., Malz, P., Sommer, C., Farías-Barahona, D., Sauter, T., Casassa, G., Soruco, A., et al. (2019). Constraining glacier elevation and mass changes in South America. *Nat. Clim. Change* 9, 130–136. doi: 10.1038/s41558-018-0375-7

Carrasco, J., Casassa, G., and Rivera, A. (2002). "Meteorological and climatological aspects of the Southern Patagonia Icefield," *The Patagonian Icefields. A Unique Natural Laboratory for Environmental and Climate Change Studies. Series of the Centro De Estudios Científicos,* eds G. Casassa, F. V. Sepúlveda, and R. M. Sinclair (Boston, MA: Springer), 29–41. doi: 10.1007/978-1-4615-0645-4_4

Escobar, F., Vidal, F., Garin, C., and Naruse, R. (1992). "Water balance in the Patagonia Icefield," *Glaciological Researches in Patagonia 1990*, eds R. Naruse and M. Anyia (Nagoya: Japanese Society of Snow and Ice), 109–119.

Garreaud, R. D. (2009): The Andes climate and weather. *Adv. Geosci.* 7, 1–9. doi: 10.5194/adgeo-22-3-2009

Holmlund, P., and Fuenzalida, H. (1995). Anomalous glacier responses to 20th century climatic changes in the Darwin Cordillera, Southern Chile. *J. Glaciol.* 41, 465–473. doi: 10.1017/S0022143000034808

Lenaerts, J. T. M., van den Broeke, M. R., van Wessem, J. M., van de Berg, W. J., van Meijgaard, E., van Ulft Lambertus, H., et al. (2014). Extreme precipitation and climate gradients in Patagonia revealed by high-resolution regional atmospheric climate modeling. *J. Clim.* 27, 4607–4621. doi: 10.1175/JCLI-D-13-00579.1

Rabassa, J., Coronato, A., and Martínez, O. (2011). Late Cenozoic glaciations in Patagonia and Tierra delFuego: an updated review. *Biol. J. Linnean Soc.* 103, 316–335. doi: 10.1111/j.1095-8312.2011.01681.x

Rasmussen, L., Conway, H., and Raymond, C. (2007). Influence of upper air conditions on the Patagonia icefields. *Glob. Planetary Change* 59, 203–216. doi: 10.1016/j.gloplacha.2006.11.025

Schaefer, M., Machguth, H., Falvey, M., Casassa, G., and Rignot, E. (2015). Quantifying mass balance processes on the Southern Patagonia Icefield. *Cryosphere* 9, 25–35. doi: 10.5194/tc-9-25-2015

Schneider, C., and Gies, D. (2004). Effects of El Niño-southern oscillation on southernmost South America precipitation at 53°S revealed from NCEP-NCAR reanalysis and weather station data. *Int. J. Clim.* 24, 1057–1076. doi: 10.1002/joc.1057

Schneider, C., Glaser, M., Kilian, R., Santana, A., Butorovic, N., and Casassa, G. (2003). Weather observations across the Southern Andes at 53°S. *Phys. Geogr.* 24, 97–119. doi: 10.2747/0272-3646.24.2.97

Schwikowski, M., Schläppi, M., Santibañez, P., Rivera, A., and Casassa, G. (2013). Net accumulation rates derived from ice core stable isotope records of Pío XI glacier, Southern Patagonia Icefield. *Cryosphere* 7, 1635–1644. doi: 10.5194/tc-7-1635-2013

Shiraiwa, T., Kohshima, S., Uemura, R., Yoshida, N., Matoba, S., Uetake, J., and Godoi, M. (2002). High net accumulation rates at Campo de Hielo Patagonico Sur, South America, revealed by analysis of a 45.97 m long ice core. *Ann. Glaciol.* 35, 84–90. doi: 10.3189/172756402781816942

Smith, R. B., and Evans, J. P. (2007). Orographic precipitation and water vapor fractionation over the southern Andes. *J. Hydrometeor.* 8, 3–19. doi: 10.1175/JHM555.1

Villalba, R., Lara, A., Boninsegna, J. A., Masiokas, M., Delgado, S., Aravena, J. C., et al. (2003). Large-scale temperature changes across the southern Andes: 20th-century variations in the context of the past 400 years. *Clim. Change* 59, 177–232. doi: 10.1023/A:1024452701153

Conflict of Interest: The authors declare that the research was conducted in the absence of any commercial or financial relationships that could be construed as a potential conflict of interest.

frontiers in Earth Science

ORIGINAL RESEARCH
published: 12 February 2018
doi: 10.3389/feart.2018.00008

Geodetic Mass Balance of the Northern Patagonian Icefield from 2000 to 2012 Using Two Independent Methods

Inés Dussaillant[1,2]*, *Etienne Berthier*[1] *and Fanny Brun*[1,2]

[1] LEGOS/OMP, Université de Toulouse, CNES, Centre National de la Recherche Scientifique, IRD, UPS, Toulouse, France,
[2] IGE, Université Grenoble Alpes, Centre National de la Recherche Scientifique, IRD, Grenoble, France

We compare two independent estimates of the rate of elevation change and geodetic mass balance of the Northern Patagonian Icefield (NPI) between 2000 (3,856 km^2) and 2012 (3,740 km^2) from space-borne data. The first is obtained by differencing the Shuttle Radar Topography Mission (SRTM) digital elevation model (DEM) from February 2000 and a Satellite pour l'Observation de la Terre 5 (SPOT5) DEM from March 2012. The second is deduced by fitting pixel-based linear elevation trends over 118 DEMs calculated from Advanced Spaceborne Thermal Emission and Reflection Radiometer (ASTER) stereo images acquired between 2000 and 2012. Both methods lead to similar and strongly negative icefield-wide mass balance rates of -1.02 ± 0.21 and -1.06 ± 0.14 m w.e. yr^{-1} respectively, which is in agreement with earlier studies. Contrasting glacier responses are observed, with individual glacier mass balance rates ranging from -0.15 to -2.30 m w.e. yr^{-1} (standard deviation = 0.49 m w.e. yr^{-1}; $N = 38$). For individual glaciers, the two methods agree within error bars, except for small glaciers poorly sampled in the SPOT5 DEM due to clouds. Importantly, our study confirms the lack of penetration of the C-band SRTM radar signal into the NPI snow and firn except for a region above 2,900 m a.s.l. covering <1% of the total area. Ignoring penetration would bias the mass balance by only 0.005 m w.e. yr^{-1}. A strong advantage of the ASTER method is that it relies only on freely available data and can thus be extended to other glacierized areas.

Keywords: glacier mass balance, geodetic method, North Patagonian Icefield, radar penetration, Patagonia

OPEN ACCESS

Edited by:
Matthias Holger Braun, University of Erlangen-Nuremberg, Germany

Reviewed by:
Marco Möller, University of Bremen, Germany
Ninglian Wang, Cold and Arid Regions Environmental and Engineering Research Institute, Chinese Academy of Sciences, China

***Correspondence:**
Inés Dussaillant
ines.dussaillant@legos.obs-mip.fr

Specialty section:
This article was submitted to Cryospheric Sciences, a section of the journal Frontiers in Earth Science

Received: *19 September 2017*
Accepted: *22 January 2018*
Published: *12 February 2018*

Citation:
Dussaillant I, Berthier E and Brun F (2018) Geodetic Mass Balance of the Northern Patagonian Icefield from 2000 to 2012 Using Two Independent Methods. Front. Earth Sci. 6:8. doi: 10.3389/feart.2018.00008

INTRODUCTION

Patagonian glaciers and icefields, including the Northern Patagonian Icefield (NPI), are essential indicators of climate change in the southern hemisphere and also stand as one of the major contributors to recent sea level rise (Gardner et al., 2013; Mernild and Wilson, 2016). Direct glaciological observations in this remote region are still scarce, mainly due to the region's inaccessibility and its harsh climate (Buttstädt et al., 2009; Mernild et al., 2015; Schaefer et al., 2015). In recent decades, remote sensing techniques have enabled the spatial coverage of glaciological observations to be extended. They are particularly useful in remote and inaccessible areas like the NPI, making it possible to observe and measure glacier variations and to estimate mass balance rate at regional scales (Rignot et al., 2003; Rivera et al., 2007; Lopez et al., 2010; Davies and Glasser, 2012; Willis et al., 2012a,b; Dixon and Ambinakudige, 2015; Jaber et al., 2016). Among those studies,

mass balance rate estimates are often based on the geodetic method, which allows calculation of glacier volume changes by differentiation of two or more multi-temporal digital elevation models (DEMs) (e.g., Paul et al., 2015; Marzeion et al., 2017). In particular for the NPI, Willis et al. (2012a) measured mass balance using the Shuttle Radar Topography Mission (SRTM) DEM and a collection of freely available Advanced Spaceborne Thermal Emission and Reflection Radiometer (ASTER) DEMs from 2001 to 2011. Jaber et al. (2016) also provided a mass balance estimate for 2000–2014 by comparing two interferometric DEMs, SRTM, and TanDEM-X.

The goal of our study is to produce two new and independent geodetic estimates of the NPI mass balance rate for the time period 2000–2012 using, on one hand, SRTM and SPOT5 and, on the other hand, ASTER DEMs. Although the NPI mass balance rate during this time period has already been estimated in two previous studies (Willis et al., 2012a; Jaber et al., 2016) our contribution is justified by:

(i) The use of ASTER DEMs calculated using the Ames Stereo Pipeline (ASP) (Shean et al., 2016). As shown in the supplement of our study, these DEMs have less artifacts than the 14DMO DEM available from LP-DAAC and used in many earlier studies including the one of Willis et al. (2012a) over the NPI.

(ii) The need to verify the lack of penetration of the February 2000 SRTM radar signal. Until now the effect of radar wave penetration into snow and ice has been assumed to be negligible in Patagonia due to the likely wet condition at the glacier surface in summer, favoring surface scattering of the signal (Willis et al., 2012a; Jaber et al., 2013, 2016). However, this assumption has not been verified yet.

(iii) The need to account for changes in ice-covered areas when calculating the glacier mass balance. None of the earlier studies considered these area changes, known to be large in Patagonia (Davies and Glasser, 2012).

STUDY AREA: NORTHERN PATAGONIAN ICEFIELD, CHILE

The NPI is the second largest temperate ice mass in the southern hemisphere, after the Southern Patagonian Icefield. Located in Chile, it extends from 46°30′S to 47°30′S, stretching for almost 125 km north–south (**Figure 1**). It covers an area of ∼3,740 km^2 (measured in this study for year 2012) extending from sea level to altitudes higher than 4000 m a.s.l. at the summit of Mount San Valentin. It is composed of 38 glaciers larger than 0.5 km^2. San Quintin is the largest glacier, covering 790 km^2. San Rafael (714 km^2) is the only tidewater calving glacier of the icefield and the lowest-latitude tidewater glacier as well as one of the fastest-flowing glaciers in the world (Rignot et al., 1996). The largest proportion of glaciers present fresh-water calving fronts (66% of the total area), whilst a smaller proportion (16%) correspond to land-terminating fronts (Rivera et al., 2007).

The climate of the Northern Patagonian region is dominated by the southern hemisphere westerlies that bring moisture from the Pacific, and the equatorial Pacific sea surface temperature that regulates the El Niño Southern Oscillation (ENSO) and the Pacific Decadal Oscillation (Aravena and Luckman, 2009). This later two large scale modes of natural climate variability, together with the southern annular mode (SAM), are key modulators of temperature and precipitation in the southern Andes at inter-annual and inter-decadal timescales (Gillett et al., 2006; Garreaud et al., 2009). The north–south orientation and high altitude of the Andes chain at this latitude acts as a geographical barrier for the moisture, generating a föhn effect that creates a strong west-to-east gradient of precipitation, with considerably dryer conditions and higher temperatures on the eastern side of the icefield (Fujiyoshi et al., 1987). The average annual precipitation between 1975 and 2011 is 8.03 ± 0.37 m (Schaefer et al., 2013) with little seasonal variability. The 0°C isotherm altitude is at about 2,000 m a.s.l. during the summer, dropping to 900 m a.s.l. during winter (Barcaza et al., 2009).

DATA

DEMs and Satellite Stereo Images

SRTM DEM

The SRTM acquired elevation data between 11 and 22 February 2000 using an interferometric aperture radar sensor (SAR) (Farr et al., 2007). We used the SRTM DEM processed by NASA from the raw C-band radar signal at 1 arcsecond resolution (about 30 m). Due to radar layover or loss of coherence over vegetation and steep terrain, the SRTM DEM may contain data voids that are sometimes filled by interpolation or using an external DEM. For the purposes of DEM comparison, we use the non-void-filled version in which data voids cover 13% of the total NPI glaciated area. By specific elevation bands the percentage of data voids is 3% below 1,000 m a.s.l (total area 1,163 km^2), 22% between 1,000 and 2,000 m a.s.l. (2,323 km^2) and 13% above 2,000 m a.s.l. (370 km^2). A second, void-filled SRTM DEM (version 4, 3 arcsec resolution) produced by the CGIAR-CSI (http://srtm.csi.cgiar.org) is also used to obtain a complete hypsometry of the icefield, necessary for the mass balance calculation.

SPOT5-HRS DEM

The SPIRIT project produced DEMs over glaciated zones from stereo-pairs acquired by the SPOT5 high-resolution stereoscopic (HRS) sensor (Korona et al., 2009). A 40 m DEM, acquired on 18 March 2012, provides a complete coverage of the NPI (**Supplementary Figure S1**). The DEM is delivered with a reliability mask and one ortho-image generated from the rear HRS image. Reliability mask values range from 0 to 255, with 0 indicating the least reliable elevations that are thus masked out in the SPOT5 DEM. Data voids cover 16% of the total NPI glaciated area. By specific elevation bands the percentage of data voids is 7% below 1,000 m a.s.l, 22% between 1,000 and 2,000 m a.s.l. and 13% above 2,000 m a.s.l.

TERRA–ASTER Stereo Images

Raw stereo images obtained by the ASTER sensor on board the TERRA satellite were ordered free of charge from the

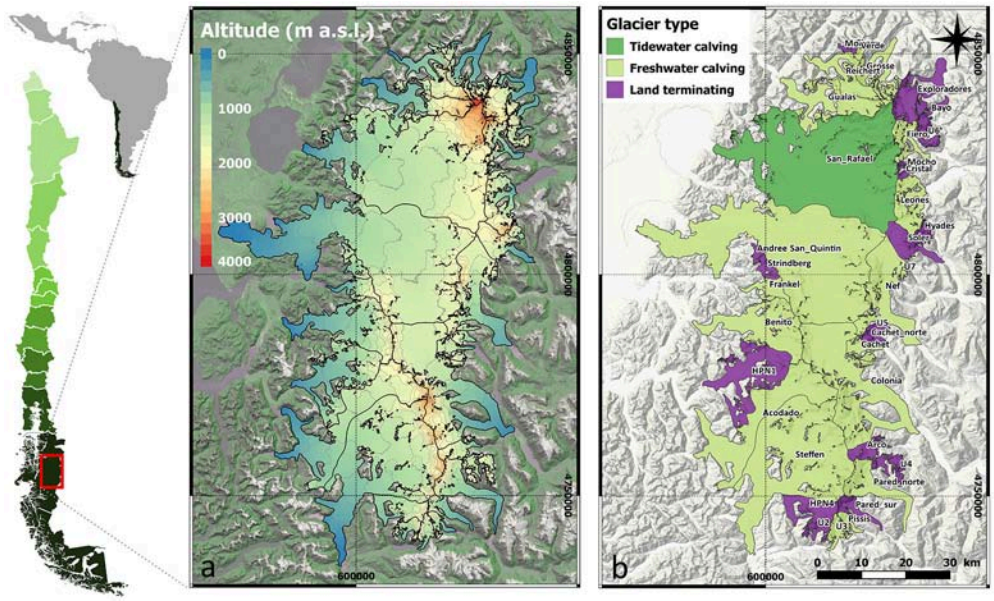

FIGURE 1 | Location of the Northern Patagonian Icefield in Chile. **(a)** Elevation map of the NPI from the SRTM (void-filled version) on top of a cloud-free Landsat image acquired on 11 March 2001. Glacier outline corresponds to ice extents of year 2000. **(b)** 38 glaciers of the NPI are represented using the outline of year 2012 and ice divides from Mouginot and Rignot (2015) with the shaded relief from the SRTM void-filled DEM as background. Colors correspond to different glacier types: dark green is for the single tidewater calving glacier (San Rafael), light green for freshwater calving (i.e., lake-terminating) glaciers and purple for land-terminating glaciers as defined by Rivera et al. (2007).

ECHO/REVERB website (REVERB)[1] from April 2000 to April 2012. After excluding all images with cloud cover fraction larger than 80%, a total of 118 ASTER Level 1A stereo images intersecting the NPI were selected. For the sake of concision, the list of ASTER images used in this study were not provided but is available upon request to the corresponding author.

LANDSAT Images

Four late-summer nearly cloud-free LANDSAT L7 ETM+ orthoimages at 30 m spatial resolution acquired from the USGS Earth Explorer were used to improve glacier and water outlines for years 2000 and 2012 (8 March 2000 and 21 January, 22 February, 26 April 2012).

Glacier Outlines, Water Bodies, and Ice Divides

Initial outlines for glacier limits and water bodies over the NPI area were obtained from online datasets. The Global Land Ice Measurements from Space (GLIMS) database and the Randolph Glacier Inventory version 5.0 (RGI 5.0) offer access to glacier outlines from previous studies and inventories over the Southern Andes region (Rivera et al., 2007; Davies and Glasser, 2012; Pfeffer et al., 2014; Mouginot and Rignot, 2015). Following visual assessment, RGI5.0 was selected as the best existing outline, corresponding to the ice extent of year 2001 (RGI6.0 was not available at the time of our study). RGI5.0 was not used "as is" but was improved as explained in section Improvement of the Glacier Outlines. Water body outlines were acquired from the USGS Earth Explorer SRTM water body data (earthexplorer.usgs.gov), and the ice divides derived from velocity fields (Mouginot and Rignot, 2015) were used to split the icefield into individual glaciers.

[1]REVERB. Available online at: https://reverb.echo.nasa.gov/#utf8=%E2%9C%93&spatial_map=satellite&spatial_type=rectangle

METHODOLOGY

Improvement of the Glacier Outlines

The RGI 5.0 glacier outline was corrected manually using late-summer and cloud-free LANDSAT, ASTER, and SPOT5-HRS images as references to adjust the position of the ice for the years 2000 and 2012. RGI 5.0 ice divides were replaced by the ice divides from Mouginot and Rignot (2015). A visual comparison between our final outlines and best existing previous ones can be observed in **Supplementary Figure S2**. Significant errors and gaps were found in the SRTM water body data, so manual corrections were also performed. Furthermore, a cloud mask was drawn manually to exclude the cloudy pixels over the SPOT5-HRS DEM. No cloud mask was created for ASTER DEMs because the lack of correlation over the clouds leads directly to data voids in the DEMs.

Glacier Volume Change and Mass Balance

As explained above, two different methods were applied to derive the map of the rate of elevation changes over the NPI: SRTM and SPOT5 DEM differencing (*SPOT-SRTM* hereafter) and

linear trend analysis of multiple ASTER DEMs (*ASTER_trend* hereafter).

Generation of ASTER DEMs

ASP is a NASA open source pipeline that allows for the mass production of DEMs out of high-resolution stereo images (Shean et al., 2016). We generated 118 ASTER-ASP DEMs with a grid spacing of 30 m from the raw ASTER L1A stereo images. ASP processing parameters are available upon request to the authors. Each ASTER DEM has a different footprint and, given the 60 km swath of ASTER, does not cover the entire NPI. The result is a spatially-varying number of ASTER DEMs available over the NPI (**Supplementary Figure S1**).

Adjustments of the DEMs

Horizontal adjustment of the DEMs

The DEMs used in this study are produced independently using different methods and without ground control points such that a horizontal shift is expected to exist between them. 2D coregistration (i.e., horizontal adjustment) should be performed on stable terrain and in regions where DEMs are most reliable (Paul et al., 2015). Stable terrain corresponds to all pixels with valid elevation values after excluding ice, snow, water bodies, and clouds.

The SRTM DEM was used as reference, and all other DEMs (SPOT5 and ASTER) were adjusted to it. For *SPOT-SRTM*, the horizontal shift is determined by an iterative minimization of the standard deviation of the elevation difference (*dh*) on stable terrain (Berthier et al., 2007). For *ASTER_trend*, an approach based on terrain slope and aspect was used to calculate the horizontal shift (Kääb, 2005; Nuth and Kääb, 2011). Both coregistration methods lead to similar results. The Nuth and Kääb method is preferred to coregister ASTER DEMs as it is numerically faster and thus more suitable for managing large amounts of data (Paul et al., 2015).

Vertical adjustment of the DEMs

Three different types of vertical biases are quantified on stable terrain and corrected in SPOT5 and ASTER DEMs. We first correct for a simple vertical shift, then biases along and across the satellite tracks and finally we account for elevation difference due to different DEM resolution.

For SPOT5 and ASTER DEMs, the median of the altitude difference with the SRTM DEM over stable terrain is first substracted. To avoid anomalous values that are usually found over steep terrain, only pixels where the slope is $<30^{\circ}$ are considered to estimate this median vertical shift (Berthier et al., 2016). We recognize that this limit is somewhat arbitrary but further justified by the fact that over 90% of the NPI surface has a slope lower than 30°.

For SPOT5 and ASTER DEMs, all derived from stereo imagery, the satellite acquisition geometry and its particular trajectory may induce biases in the DEMs along and across the satellite track direction (Berthier et al., 2007; Scherler et al., 2008; Nuth and Kääb, 2011). We rotate the original coordinate system of the SPOT5 and ASTER DEMs tracks to match their specific trajectory (Nuth and Kääb, 2011). The elevation difference (*dh*) is then computed over stable terrain along and across the satellite track, and corrected using a fifth-order polynomial fit.

We applied a curvature-dependent correction to the SPOT5 and ASTER DEMs. This correction is calculated on the stable terrain by fitting a fifth-order polynomial to the elevation difference with the SRTM DEM plotted as a function of terrain maximum curvature (Gardelle et al., 2012).

After all adjustments, pixels from the SPOT5 and ASTER DEMs which have an absolute elevation difference with SRTM greater than 150 m are considered as outliers and excluded from all subsequent analysis.

Rate of Elevation Change and Mass Balance Rate Calculation

The maps of elevation change rates (dh/dt) are obtained differently for the two methods. For *SPOT-SRTM*, a simple DEM difference is computed and divided by their time separation (12.1 yr) to calculate $dh/dt_{SPOT-SRTM}$. In the case of *ASTER_trend*, for each pixel, a first linear trend is fit through all the available elevation values (from all ASTER DEMs and the SRTM DEM) during 2000–2012. The final dh/dt_{ASTER_trend} is calculated from a second fit considering only the ASTER DEMs within the 95% confidence interval of the first regression line and excluding the SRTM DEM to avoid possible bias due to signal penetration. For the majority of the NPI area, the first valid elevation measurements used in this second linear fit come from a DEM acquired in April 2000, and the last measurements from two DEMs acquired in March 2012 and April 2012 (**Supplementary Figure S3**). We did not observe any obvious temporal concentration of ASTER DEMs. Thus, the time-stamp of the dh/dt maps from the two methods is similar, i.e., 2000–2012.

In the conversion from dh/dt to mass balance, only reliable pixels from glaciated terrain are considered. For *ASTER_trend*, we further exclude all pixels for which the uncertainty of the second linear fit is larger than 3 m yr^{-1} (at the 95% confidence level).

NPI individual glaciers have shown different volume change rates during recent years, with differential responses within glaciers and a strong contrast between the eastern and western margins (Rivera et al., 2007; Willis et al., 2012a). To take into account these local effects, separate calculations were made for each glacier, and then the overall volume change rate and mass balance rate of the NPI were calculated as the area-weighted sum of every glacier. Each individual glacier is divided into 50 m altitude bands using the void-filled version of the SRTM DEM. For each altitude band, we compute the mean dh/dt after excluding all values lying outside of ± 3*NMAD (normalized median absolute deviation).This is an efficient way to exclude outliers (Berthier et al., 2004; Gardelle et al., 2013). The band average dh/dt is then weighted by its area to calculate the glacier-wide average dh/dt. In the rare cases where no measurement is available for an altitude band, the rate of elevation change is assumed to be 0.

Following Fischer et al. (2015), we considered the varying areas of each individual glacier between 2000 and 2012 to convert

volume change rate to mass balance rate. We use a value of 850 $\pm$ 60 kg m^{-3} as the volume-to-mass conversion factor, which is reasonable regarding the duration of our study (>5 years) (Huss, 2013).

Penetration of the SRTM C-Band Radar Signal Over Snow

The *ASTER_trend* method allows rough estimation of the SRTM penetration depth (Wang and Kääb, 2015; Berthier et al., 2016). By extrapolating *dh*/*dt* to the date of acquisition of the SRTM DEM, a reconstructed SRTM DEM (called hereafter $SRTM_{rec}$) can be obtained. The differencing of $SRTM_{rec}$-SRTM maps the penetration depth of the C-band radar signal.

Error Assessment

Formal uncertainties for mass balance estimates were calculated taking into account six main sources of error: errors on *dh*/*dt*, errors in glacier area, error on the density conversion factor, errors due to data voids, errors due to seasonal cycle sampling irregularities and departure from a linear trend.

Uncertainty in Rate of Elevation Change $\left(\sigma_{\frac{dh}{dt}}\right)$

The uncertainty on the elevation change of a pixel is mainly given by the uncertainty inherent in the original DEMs, including the random and systematic errors produced during their coregistration. To assess this error we split the stable terrain *dh*/*dt* maps into 3 × 3 tiles as in Berthier et al. (2016). For each tile the median of *dh*/*dt* on stable ground is computed to visualize the spatial pattern of biases in dh/dt_{ASTER} and $dh/dt_{SPOT-SRTM}$maps (**Figure 2**). We then compute the error in *dh*/*dt* as the mean of the absolute difference of the median *dh*/*dt* for these 9 tiles (**Figure 2**). We obtained an error $\left(\sigma_{\frac{dh}{dt}}\right)$ of 0.07 m yr^{-1} for *SPOT-SRTM* and 0.06 m yr^{-1} for *ASTER_trend*.

Uncertainty in Area (σ_A)

Glacier outlines were improved manually and contain an error that is inherent to the individual that performed the work. The error in glacier area was assessed by drawing buffers around the glacier outline (Granshaw and Fountain, 2006). A one-pixel buffer is a reasonable error level for glacier outlines produced manually, except for debris-covered glaciers (Paul et al., 2015). As the NPI debris coverage is limited, a one-pixel buffer was applied to the NPI outline, leading to an error of about 5% of the measured area. This value is consistent with Paul et al. (2015) and Pfeffer et al. (2014).

Uncertainty in Density Factor ($\sigma_{f\rho}$)

For density the error of $\pm$60 kg m^{-3} is obtained from Huss (2013).

Uncertainty in Data Gaps (g)

A conservative multiplicative factor of 5 is used for the uncertainties in the unsurveyed areas (Berthier et al., 2014).

Uncertainties due to the Uneven Sampling of the Seasonal Cycle

Systematic errors in the *dh*/*dt* from *ASTER_trend* could come from an irregular sampling of the seasonal elevation change cycle as the ASTER DEMs were acquired at different times of the year. For example, a large systematic error (i.e., too negative mass balance) could occur if ASTER DEMs were acquired mostly in winter at the beginning of the study period and mostly in summer toward the end of the study period. To quantify the magnitude of this potential error, we sample a hypothetical seasonal cycle at the time of acquisition of the ASTER DEMs. The amplitude of the seasonal cycle is poorly known for Patagonia and must be spatially variable, so we prefer to use a normalized value of 1 m, with a minimum at the end of April and a maximum at the end of October. As shown in **Figure 3**, the ASTER temporal sampling is sufficiently random that the regression slope is only -0.0013 m yr^{-1}. Even if the seasonal elevation change cycle was as large as 10 m (a high value but not unrealistic for the maritime NPI), the resulting systematic error would be 0.013 m yr^{-1}, well below other sources of uncertainties. This source of error is thus neglected.

Uncertainties Due to Departure from a Linear Trend

The assumption of linearity is one of the weaknesses of our ASTER-based method, as in principle glacier elevation change do not follow a linear behavior. To detect potential changes of the ASTER trends (and mass balances) over time, we divided 2000–2012 into two sub-periods: 2000 to March 2007 (2007.3) and 2007 to May 2012 (2012.5). We did not split the 12-year study period in two sub-periods of equal duration because there was no DEM for year 2006. Conversely, several useful ASTER DEMs were acquired in 2007 (late summer, no clouds, and good spatial coverage of the NPI), thus we decided to cut the period at 2007 and include summer 2007 DEMs in both trends. The NPI-wide mass balance from 2000 to 2007.3 was -1.06 ± 0.20 m w.e. yr^{-1}, and -0.99 ± 0.20 m w.e. yr^{-1} from 2007 to 2012.5. Given error bars, mass balance rates for both sub-periods are not different and agree with the estimate for the whole period 2000–2012 (-1.06 ± 0.15 m w.e. yr^{-1}). This result justifies the assumption of linearity and demonstrates that, within the error bars of our method, we are not able to detect a temporal change in the NPI mass balance.

We then consider all the significant sources of error to calculate our formal uncertainties on mass balance. First, the uncertainty in glacier rate of volume change $\left(\sigma_{\frac{dV}{dt}}\right)$, assuming that the uncertainty on area is independent of the uncertainty on rate of elevation change, was calculated as:

$$\sigma_{\frac{dV}{dt}} = \sqrt{\left(\sigma_A \cdot \overline{\frac{dh}{dt}}\right)^2 + \left(\sigma_{\overline{\frac{dh}{dt}}} \cdot \left(5g + \left(1-g\right)\right) A\right)^2} \quad (1)$$

where $\overline{\frac{dh}{dt}}$ is the mean rate of elevation change, $\sigma_A = \frac{5}{100}A$, and g is the proportion of data gaps from the total area.

Assuming that the uncertainty in rate of volume change is independent of the uncertainty of the density conversion

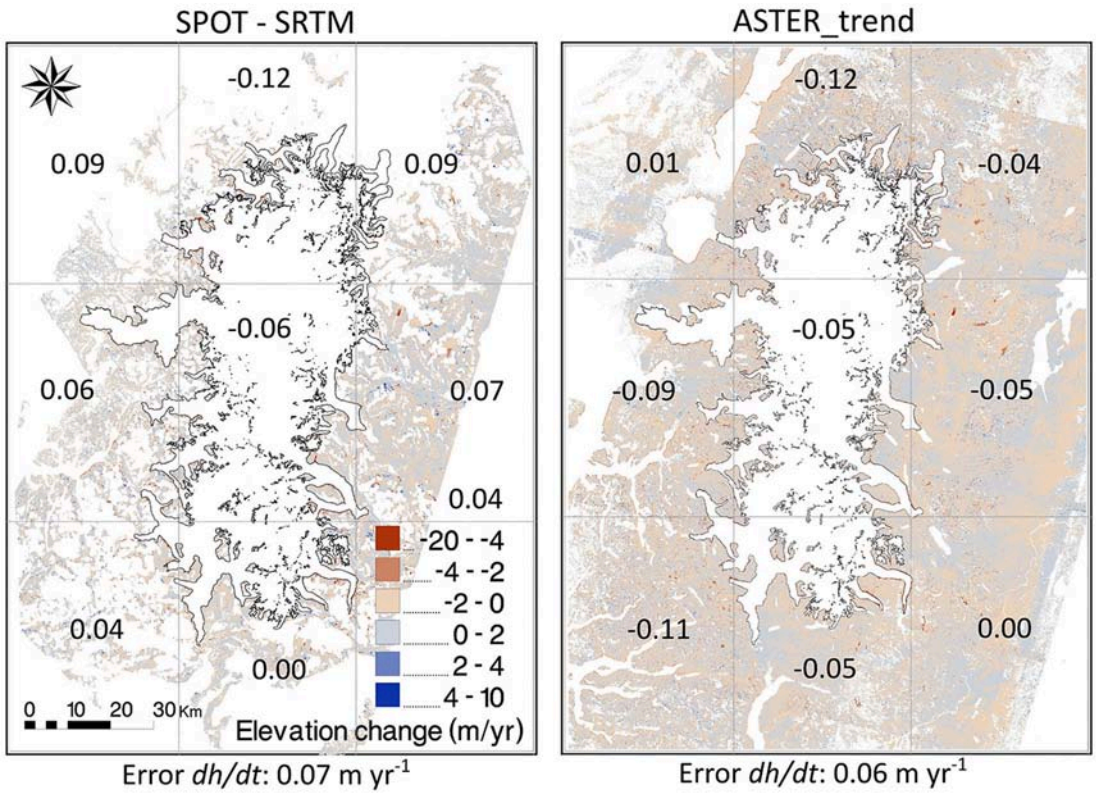

FIGURE 2 | Rate of elevation change over stable terrain in the NPI region during 2000–2012, calculated by the SPOT-SRTM (left) and ASTER_trend (right) methods. The study region is divided into 3 × 3 tiles. The values correspond to the median *dh/dt* on stable ground in each tile. For comparison, the color scale is the same as for the maps of *dh/dt* over glaciers in **Figure 4**.

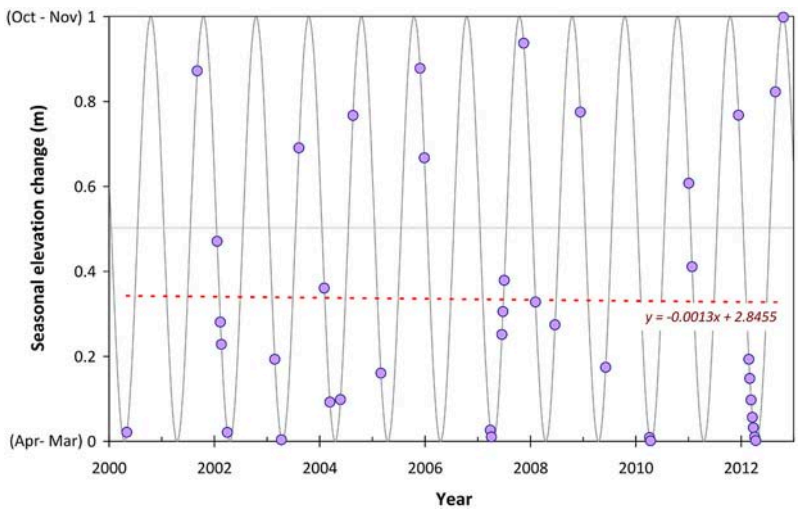

FIGURE 3 | Temporal sampling of the 118 ASTER DEMs used in the ASTER_trend method. The amplitude of the seasonal cycle is normalized to 1 m. Dots correspond to theoretical elevations at the time of acquisition of the ASTER DEM; the red line shows the linear fit to the elevation time series, with a slope of −0.0013 m yr^{-1}.

factor, the uncertainty on geodetic mass balance rate $(\sigma_{\dot{M}})$, was calculated as:

$$\sigma_{\dot{M}} = \sqrt{\left(\sigma_{\frac{dV}{dt}} \cdot f_\rho\right)^2 + \left(\sigma_{f_\rho} \cdot \frac{dV}{dt}\right)^2} \quad (2)$$

where $f_\rho = 850\ kg\ m^{-3}$ is the density conversion factor and $\sigma_{f_\rho} = 60\ kg\ m^{-3}$ is the uncertainty on the density conversion factor (Huss, 2013).

RESULTS

Area Changes

The NPI had a total glacierized area of 3,856 ± 211 km^2 in 2000, and 3,740 ± 200 km^2 in 2012. The total area loss for the period 2000–2012 is 116 km^2 (3%), at a rate of −9.7 km^2 yr^{-1}.

Areal changes are heterogeneous and do not follow any obvious spatial pattern. Largest areal changes are observed on glaciers U4 (19%) located in the south-east, and glaciers Circo (12%) and Grosse (10%) located in the north of the NPI. The largest frontal retreats were observed in the tongues of two glaciers in the south-west, Steffens (3.3 km frontal retreat) and HPN1 (2.5 km retreat over its main tongue and even 3.1 km retreat over one of its tributaries), and San Quintin in the north-west (2.5 km frontal retreat). Glaciers Gualas, Grosse and Reicher in the north and glacier Acodado in the south also showed significant frontal retreats of the order of 1 and 2 km between 2000 and 2012.

Elevation Change Rates and Glacier Mass Balance Rates

Entire NPI

Both methods (*SPOT-SRTM* and *ASTER_trend*) resulted in a similar spatial distribution of *dh*/*dt* over the NPI (**Figure 4**), with maximum thinning rates localized at low elevations over the glacier tongues. Icefield-wide mass balances rates during 2000–2012 are also in excellent agreement: −1.02 ± 0.21 m w.e. yr^{-1} for *SPOT-SRTM* and −1.06 ± 0.15 m w.e. yr^{-1} for *ASTER_trend* (**Table 1**).

Strongest thinning rates are observed over the outlet glaciers of the western margins of the icefield, with *dh*/*dt* rates as negative as −10 m yr^{-1} for the terminating tongues of Frankel, Benito, HPN1 and Acodado glaciers. The largest differences between the two *dh*/*dt* maps are observed over San Rafael glacier, where thinning rates are more negative for *SPOT-SRTM*, and over the north-east margins. Looking closely at the *dh*/*dt* vs. altitude curves for the two methods, a strong thickening is observed above 2,900 m a.s.l. for *SPOT-SRTM*, whereas a slight thinning is measured by *ASTER_trend* (**Figure 4C**). The anomalously positive values in SPOT-SRTM *dh*/*dt* curves at high altitude will be discussed in section Penetration of SRTM Signal Over NPI.

Spatial coverage of valid *dh*/*dt* rates is different for the two methods, with 68% of the total NPI area covered in *SPOT-SRTM*, and a better coverage of 82% in *ASTER_trend*. Almost complete coverage was achieved below 1,000 m a.s.l. in both cases. Higher concentrations of data gaps exist in the accumulation zone (>1,000 m a.s.l.) with 35% gaps for *SPOT-SRTM* vs. 22% for *ASTER_trend*. Both the SPOT5 reliability mask and the ASTER error grid produced during the linear fit suggest larger errors in this region. The lack of image texture over the flat and homogeneous snow surface makes correlation of the stereo images either impossible or erroneous. Higher altitudes are better represented in *ASTER_trend*, with only 10% of data gaps above 2,000 m a.s.l. vs. 49% for *SPOT-SRTM*; the latter is mainly due to voids in the SRTM DEM.

Individual Glaciers

The coverage of individual glaciers with valid *dh*/*dt* measurements is much better for *ASTER_trend*, where all glaciers show two-thirds (66%) of their total area with valid data. In the case of *SPOT-SRTM*, coverage is not as good. Fourteen out of thirty-eight glaciers, corresponding to 77% of the total NPI area, show between one- and two-thirds of their area with valid measurements, while 11 glaciers (6% of the NPI area) show less than one-third (**Figure 5A**).

Individual glacier mass balance rates ($\dot{M}$) for the period 2000–2012 are shown in **Figure 5** and **Supplementary Table S1** for both methods. All glaciers show negative $\dot{M}_{ASTER\_trend}$. Contrarily, $\dot{M}_{SPOT-SRTM}$ for glaciers Grosse, Exploradores, Bayo, and Leones in the north-east part of the NPI and glacier Pissis in the south are slightly positive. However, these five glaciers were poorly sampled due to gaps in the SPOT5 DEM. Both methods agree on highly negative mass balances rates for south-west glaciers. The most negative $\dot{M}$ coincide in glacier HPN1 with values of −2.38 ± 0.32 and −2.30 ± 0.24 m w.e. yr^{-1} for *ASTER_trend* and *SPOT-SRTM* respectively. The $\dot{M}$ for the three largest glaciers of the icefield, San Quintin, San Rafael and Steffens, accounting together for 51% of the total area, are strongly negative and in good agreement between methods.

For all glaciers larger than 100 km^2, $\dot{M}$ from both methods agree within error bars, and their absolute difference is smaller than 0.3 m w.e. yr^{-1} (**Figure 6**). Conversely, smaller glaciers tend to show larger disagreement between methods, with $\dot{M}$ differences up to 1.6 m w.e. yr^{-1}. The largest differences are observed for glaciers poorly sampled in *SPOT-SRTM* (green and orange dots).

TABLE 1 | NPI-wide volume change rate, thinning rate, and mass balance rate estimates for the 2000–2012 time period for the two methods.

Method	*dV*/*dt* (km^3 yr^{-1})	*dh*/*dt* (m yr^{-1})	Mass balance (m w.e. yr^{-1})
SPOT-SRTM	−4.55 ± 0.41	−1.20 ± 0.11	−1.02 ± 0.21
ASTER_trend	−4.72 ± 0.34	−1.25 ± 0.09	−1.06 ± 0.15

DISCUSSION

Area Changes

Our area estimate for 2000 is in good agreement with previous studies, especially with Jaber et al. (2016), suggesting that our error bars are conservative (**Table 2**). Davies and Glasser (2012) obtained a slightly larger value for the NPI area in 2001 because they considered some of the rock nunataks as part of the icefield

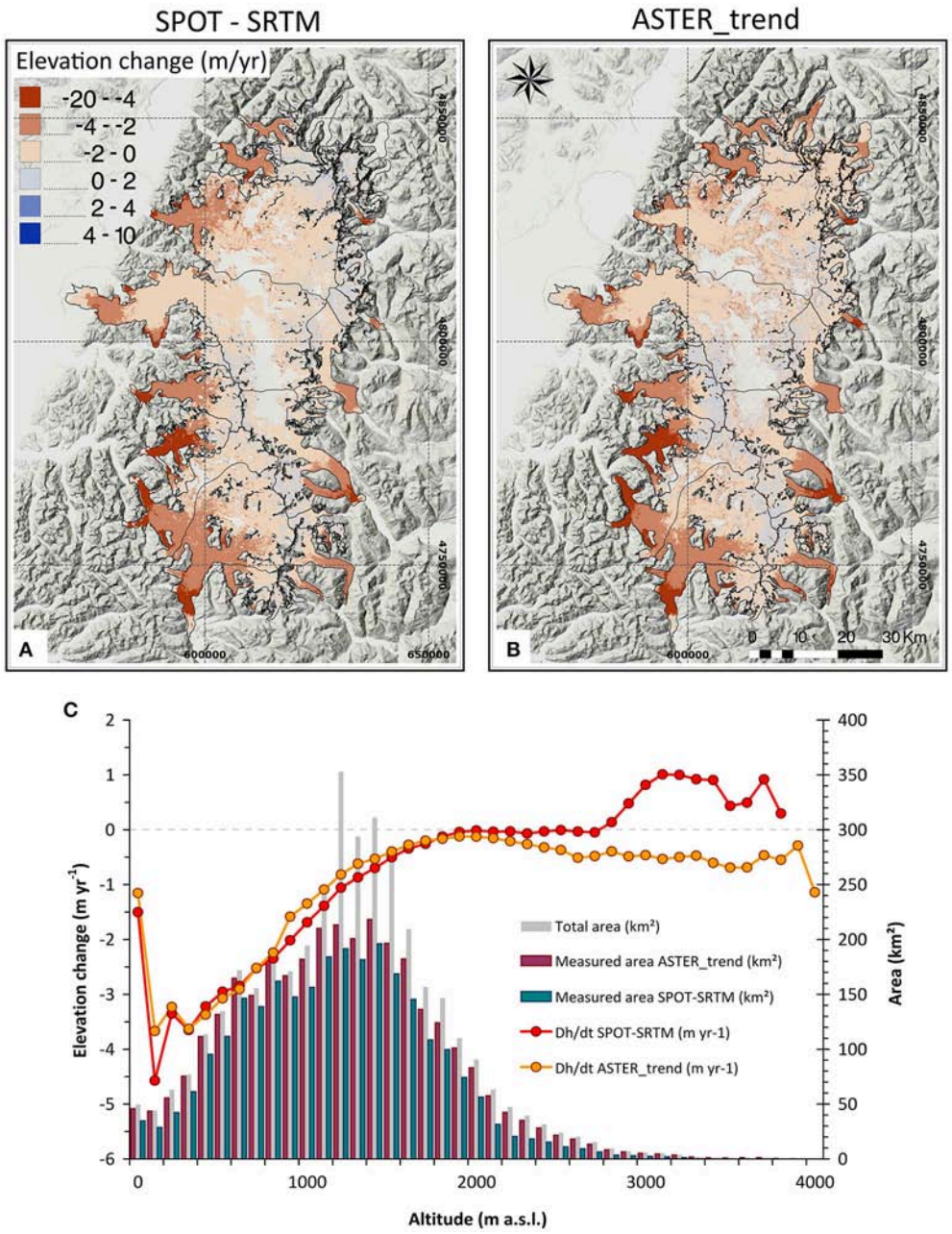

FIGURE 4 | Rate of elevation change (m yr^{-1}) over the NPI for the time period 2000–2012. **(A)** Rate of elevation change from SPOT-SRTM; white blank corresponds to data gaps. **(B)** Rate of elevation change from ASTER_trend; white blank corresponds to data gaps. **(C)** Distribution of the rate of elevation changes as function of altitude; red dots represent SPOT-SRTM and orange dots represent ASTER_trend. The histograms show the hypsometry of the NPI by 100 m elevation bands (gray bars), and the corresponding measured area from SPOT-SRTM (blue bars) and ASTER_trend (purple bars). (Note that hypsometry is shown here every 100 m bands. This is to help visualization although the entire processing was made using 50 m bands).

area. Similarly, Rivera et al. (2007) included adjacent small icy areas as part of the icefield. To our knowledge, we provide the first estimate of NPI area for 2012.

Glacier areal changes are not homogeneous through the NPI. In general the largest frontal retreats were observed for glacier tongues situated in the south-west of the icefield (glaciers Steffens and HPN1), also in agreement with previous studies (Rivera et al., 2007; Lopez et al., 2010; Davies and Glasser, 2012; Willis et al., 2012a). No convincing relationship was observed between glacier-specific area loss and mass balance. This conclusion is in agreement with earlier findings for Alaskan glaciers (Arendt et al., 2002).

We accounted for these area changes in our mass balance rate estimates. At the scale of the entire icefield, the effect is minor as

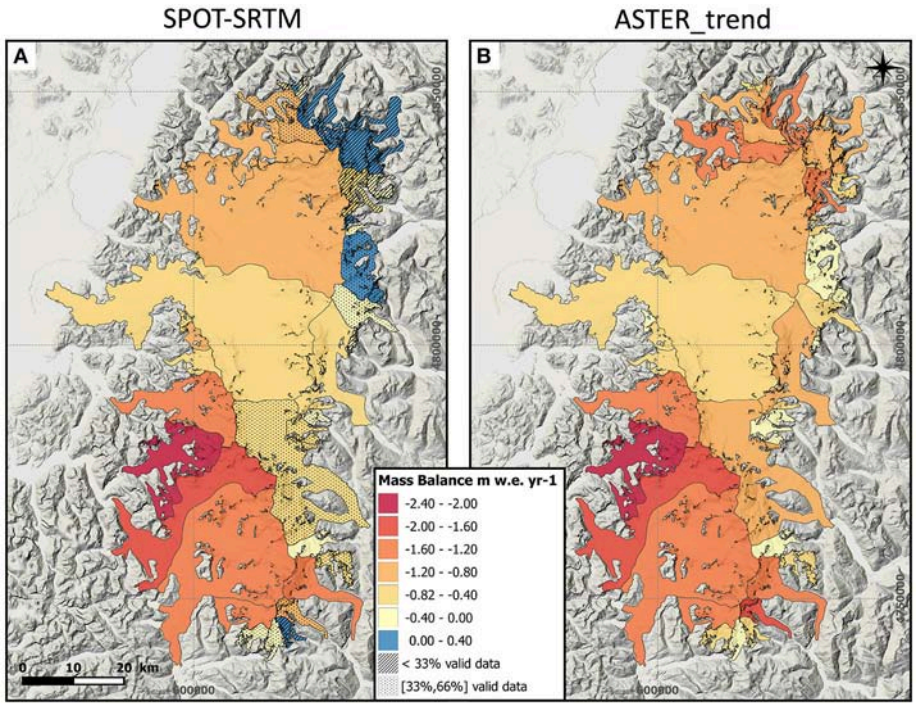

FIGURE 5 | Mass balance rate of NPI individual glaciers from 2000 to 2012. **(A)** Mass balance rate obtained from method SPOT-SRTM. Hatched glaciers have <33% data coverage whereas pointed glaciers have between 33 and 66% coverage. **(B)** Mass balance rate obtained from method ASTER_trend. All glaciers present more than 66% of their area with valid *dh/dt* values.

the NPI mass balance rate is changed by 0.01 m w.e. yr^{-1} if only the 2000 inventory is available. Yet, the mass balance rate can vary by up to 10% for the fastest retreating glaciers.

Penetration of SRTM Signal Over NPI

Some positive *dh* values were found above 2,900 m a.s.l. with the *SPOT-SRTM* method. These positive values are anomalous as, to our knowledge, no study documented thickening in the upper part of the NPI since 2000. **Figure 7** shows the distribution with altitude of our estimate of the SRTM penetration depth (SRTMrec-SRTM), a side product of the *ASTER_trend* method. Positive values are observed above 2,900 m a.s.l. This is consistent with the apparent thickening observed above 2,900 m a.s.l. in the *SPOT-SRTM dh/dt* and thus suggest possible penetration of the SRTM C-band signal on the NPI snow located above 2,900 m a.s.l.

The $SRTM_{rec}$-SRTM and the SPOT-SRTM curves in **Figure 7** do not match perfectly over this high-altitude zone. Likewise, the $SRTM_{rec}$-SRTM curve shows positive values between 1,000 and 2,900 m a.s.l. However, these differences remain within the uncertainties of the SRTM penetration depth, assumed to be roughly ±3.1 m in Berthier et al. (2016), and cannot be further interpreted. We further confirmed that this ±3.1 m is conservative by extrapolating dh/dt_{ASTER_trend} to reconstruct two DEMs at the dates of acquisition of the SPOT5 2012 DEM and of an additional SPOT5 DEM acquired 18 May 2005 (not used in the study for measuring elevation changes but with similar specifications as the SPOT5 DEM 2012). Differencing between $SPOT5_{rec\_2012}$-$SPOT5_{2012}$ and $SPOT5_{rec\_2005}$-$SPOT5_{2005}$ yielded mean *dh* on the NPI of 1.03 m and 0.14 m, respectively, both values well below the 3.1 m assumed error.

If we consider the region above 2,900 m a.s.l., the mean penetration depth is 10 m, a value similar to the 10 m C-band penetration depth found on the dry and cold firn of Greenland and Alaska (Rignot et al., 2001). Averaged over the whole icefield, the mean penetration depth is negligible (0.02 m), in agreement with a recent study in New Zealand (also in the southern hemisphere), where no penetration was found (Wang and Kääb, 2015).

Up to now, SRTM penetration depth has been considered negligible in Patagonia due to almost constant wet conditions at the glacier surface in February 2000 (Jaber et al., 2013). Here we show that penetration is actually occurring at the highest elevations, where temperatures are lower and firn is probably dry even in summer. Nevertheless, only 0.75% of the NPI area (29 km^2) is found above 2,900 m a.s.l., a fraction small enough not to affect the overall mass balance rate of the icefield (the corresponding bias is <0.01 m w.e. yr^{-1}). Therefore, SRTM penetration can be assumed negligible over the NPI. Still, future geodetic mass balance studies in Patagonia using SRTM C-band DEM, should carefully consider the penetration depth, especially when a significant fraction of the glacier lies at high elevations.

The lack of SRTM penetration, except at the highest elevations, is in line with a backscattering analysis using the SRTM swath image data (SRTM-IMGR) in Jaber et al. (2016). They found low backscattering values over the plateau,

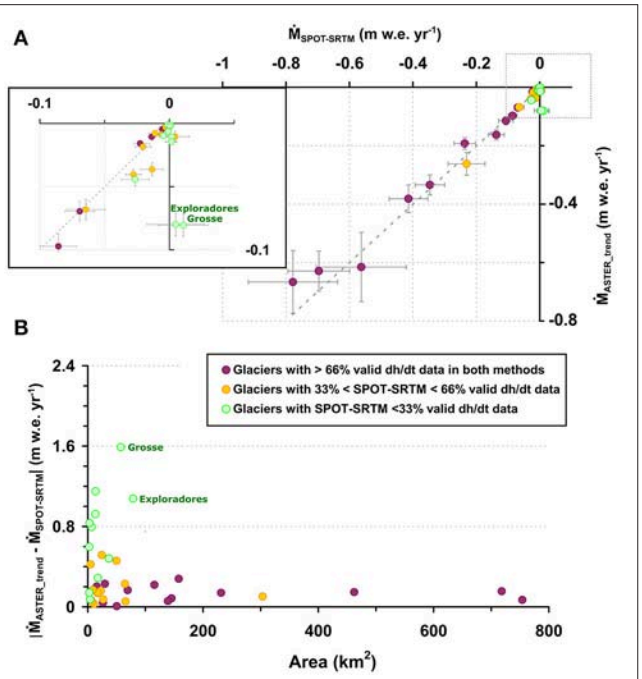

FIGURE 6 | Comparison of individual glacier mass balances from the two methods. **(A)** Mass balance rates obtained from method SPOT-SRTM as function of mass balance rates obtained from method SPOT-SRTM. The dashed line corresponds to the 1:1 line. **(B)** Absolute difference of $\dot{M}$ (m w.e. yr^{-1}) between the two methods as a function of glacier area.

indicating the presence of wet snow and consequent insignificant penetration depth. Less negative backscattering values are also observed over the highest zones, suggesting dryer snow where the C-band signal can penetrate.

Comparison of the Two Geodetic Methods

Both methods led to similar estimates of the NPI mass balance rate for the 2000–2012 period (**Table 3**).

The *SPOT-SRTM* method has already been used in the southern Andes (Falaschi et al., 2016) but this method is all the more relevant now that we have verified the negligible penetration of the SRTM C-band signal at this latitude.

Even though individual ASTER DEMs have a higher noise level than the SPOT5 DEM when subtracted from the SRTM DEM (mean standard deviation of the residual for ASTER DEMs: 14 vs. 8 m for SPOT5 DEMs), their larger number led to final errors on stable ground very similar to those obtained with the *SPOT-STRM* method.

Icefield-wide mass balance error differs slightly between methods (±0.21 m w.e. yr^{-1} for *SPOT-SRTM* and ±0.15 m w.e yr^{-1} for *ASTER_trend*). This difference is mainly related to the amount of data gaps, higher in *SPOT-SRTM*. The distribution of data gaps coincides over the NPI plateau (∼1,200–1,700 m a.s.l.) for both methods. Yet, over some glaciers in the north-east margins of the NPI, specifically Grosse, Bayo, and Exploradores glaciers, less than one-third of their area is covered with the *SPOT-SRTM* method due to clouds in the SPOT5 images. Coverage is also restricted on small steep glaciers like glacier Pissis in the south, where a high percentage of data gaps exists over the SRTM DEM. These latter glaciers are those for which the mass balance rate differs most between the two methods. The redundancy of the acquisitions used in the *ASTER_trend* method overcomes this issue.

TABLE 2 | Comparison of the NPI total area in this and previous studies.

Reference	Year	Area (km^2)
This study	2000	3,856 ± 211
This study	2012	3,740 ± 200
Jaber et al., 2016	2000	3867
Davies and Glasser, 2012	2001	4070
Rivera et al., 2007	2001	3953

The 2000–2012 $\dot{M}$ are in agreement within error bars between the two methods for all glaciers with coverage larger than 66%. Specific cases where $\dot{M}$ do not agree within error bars correspond to glaciers poorly sampled in the *SPOT-SRTM* method due to clouds or SRTM data gaps. The three largest glaciers of the icefield (51% of the total area) present $\dot{M}$ differences smaller than 0.2 m w.e. yr^{-1}.

Availability of the data is also important to consider when comparing the two methods. A strong advantage of the *ASTER_trend* method is that it is based on freely and nearly globally available ASTER L1A stereo images. SPOT5 stereo images were only acquired over specific areas and are not yet freely available. Thus, the *ASTER_trend* has the potential to be extended to wider areas.

Comparison with Previous Estimates

Many studies already estimated the geodetic mass balance rates of the NPI for diverse time periods (Rignot et al., 2003; Aniya, 2007; Rivera et al., 2007; Glasser et al., 2011; Willis et al., 2012a; Jaber et al., 2016). However, only two of these studies examined the same time period as us and can therefore be directly compared with our results (**Table 3**). NPI-wide surface mass balances have also been estimated from atmospheric models (Schaefer et al., 2013; Mernild and Wilson, 2016), but these numbers cannot be compared with ours as they do not account for the mass loss by calving which is an important component of the mass loss for the NPI.

Generally, good agreement is found between our two estimates and previous geodetic estimates (**Table 3**). Although they used ASTER stereo images like us, Willis et al. (2012a) found a smaller mass loss. The difference may result either from the use of different ASTER DEMs, different coregistration methods, the amount of DEMs considered to extract *dh*/*dt* (55 in Willis et al., 2012a, 118 in our study) or the slight difference between time periods. We generated our own ASTER DEM using ASP, and they exhibit less artifacts than the DEMs from the 14DMO product used in Willis et al. (2012a) (**Supplementary Figure S4**).

Our mass loss estimates agree with Jaber et al. (2016) who compared the SRTM DEM with a TanDEM-X DEM mosaic. These two DEMs, derived from radar interferometry,

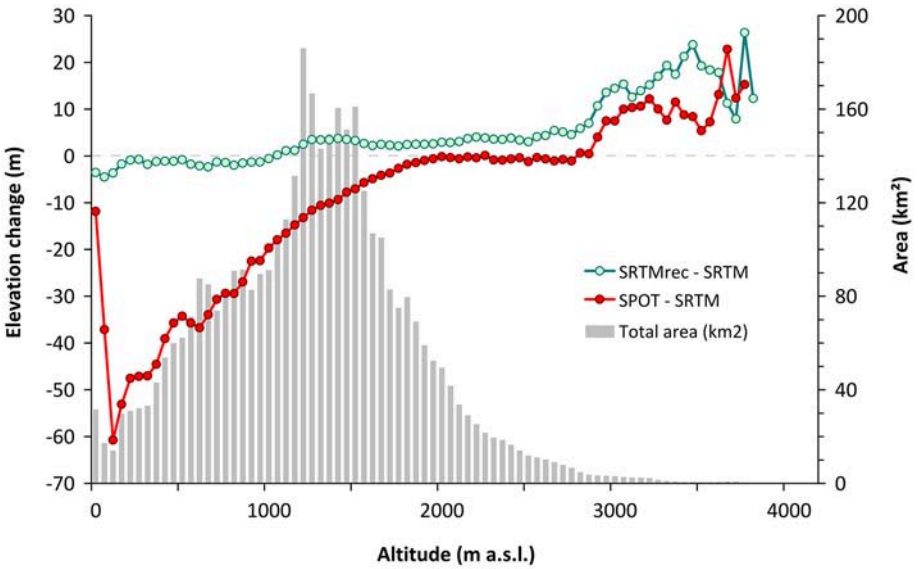

FIGURE 7 | Penetration of the SRTM C-band radar signal as a function of altitude. Curves represent the total elevation difference from SPOT-SRTM (red curve) and $SRTM_{rec}$-SRTM (green curve). Positive values in $SRTM_{rec}$-SRTM represent penetration. The histogram shows the area/altitude distribution.

TABLE 3 | Global volume change rates estimates for the NPI from this and previous studies during similar time periods.

Source	Time period	dV/dt ($km^3\ yr^{-1}$)
This study (*SPOT-SRTM*)	2000–2012	−4.55 ± 0.41
This study (*ASTER_trend*)	2000–2012	−4.72 ± 0.34
Jaber et al., 2016	2000–2014	−4.40 ± 0.13
Willis et al., 2012a	2001–2011	−4.06 ± 0.11

are not affected by clouds and provide good coverage of the accumulation zone. Nevertheless, their coverage of the icefield was not complete, as northernmost NPI glaciers were not covered by TanDEM-X DEMs.

Error estimates in Jaber et al. (2016) and Willis et al. (2012a) are three to four times smaller than ours. One reason for our larger errors could be the factor of five that we conservatively allocated to errors over data gaps. However, mass balance differences of typically 0.2 m w.e. yr^{-1} between our two methods for well-sampled glaciers (**Figure 6**, **Supplementary Table S1**) suggest that our error bars are reasonable and not too conservative.

CONCLUSIONS

We compared two geodetic methods to obtain the region-wide and glacier-wide mass balance rates of the NPI. The first is based on the standard differencing of two DEMs (SRTM and SPOT5) whereas the second method extracts the rate of surface elevation change by fitting a linear trend to over 118 DEMs derived from ASTER stereo images.

For the entire NPI (about 3,800 km^2), excellent agreement is found between the two methods. Following previous studies, our analysis confirms the strong mass loss, with an icefield-wide mass balance rate of -1.06 ± 0.15 m w.e. yr^{-1} (*ASTER_trend*). The thinning rate reaches up to 10 m yr^{-1} for some low-elevation glacier tongues. Importantly, we also verify the lack of significant penetration of the SRTM C-band radar signal in the wet and temperate firn of the icefield except for the highest altitudes where dry snow was present in February 2000 (>2,900 m a.s.l.; <1% of the icefield).

For individual glaciers, larger differences exist between the two methods, especially when the data coverage is more limited. By definition the *SPOT5-SRTM* estimate does not cover the area where clouds are present in the SPOT5 stereo images. The *ASTER_trend* method is less prone to this effect because it relies on numerous (>100) ASTER DEMs. Both methods exhibit data gaps in the upper accumulation areas due to the lack of texture in the optical stereo images. This issue could be solved in the future by using images with higher spatial resolution and better radiometric depth.

Here we have provided insight into the effectiveness, advantages and disadvantages of two methods for estimating the geodetic mass balance rates of Patagonian glaciers and icefields. Both methods lead to coherent and satisfying results, though the free availability of the extensive archive of ASTER stereo images is a strong advantage.

AUTHOR CONTRIBUTIONS

ID: performed all the DEM analysis with inputs from EB and FB. ID: Led the writing of the paper and all other co-authors contributed to it.

ACKNOWLEDGMENTS

ID acknowledges a Ph.D. fellowship from the France Space Agency (CNES) and the Région Occitanie. Etienne Berthier acknowledges support from the CNES and the Programme National de Télédétection Spatiale (PNTS, http://www.insu.cnrs.fr/pnts), grant PNTS-2016-01. ASTER images are courtesy of NASA/METI/AIST/Japan Space systems and U.S./Japan ASTER Science Team. SPOT5 images and DEMs were provided by the SPIRIT project (Korona et al., 2009), funded by CNES. This work could not have been performed without the GLIMS project that allowed populating a vast archive of freely available ASTER stereo images over glaciers. We also acknowledge the Ames Stereo Pipeline developer teams for their help and Vincent Favier for his comments on an earlier version of this manuscript. We are grateful to Ken Moxham for reviewing the English. We thank the editor, Matthias Braun, and two reviewers for their very useful comments on our manuscript.

SUPPLEMENTARY MATERIAL

The Supplementary Material for this article can be found online at: https://www.frontiersin.org/articles/10.3389/feart.2018.00008/full#supplementary-material

Supplementary Figure S1 | Spatial footprint of the SPOT5-HRS DEM for year 2012 (red line). The color code corresponds to the number of ASTER elevation measurements available for every pixel from year 2000 to 2012 (after excluding elevation values outside the following accepted elevation range: within 150 m from the median of all DEMs on ice, and within 100 m off ice).

Supplementary Figure S2 | Comparison of three NPI glacier inventories. **(a)** The Blue line corresponds to the inventory created and used in this study for year 2000 (see section Glacier Outlines, Water Bodies, and Ice Divides), ice divides are obtained from Mouginot and Rignot (2015). The red and green lines correspond to the RGI 5.0 and Rivera et al. (2007) inventories for year 2001 (recently incorporated in RGI 6.0), respectively. Named glaciers are those showing the largest area differences between inventories. **(b)** Zoom over the Cachet glacier area where inventories largely disagree on ice divides. Landsat Image for the 8 of mars 2000 as background. **(c)** Table shows the differences in glacier area between the inventories from Rivera et al. (2007) and the RGI 5.0 compared to the one used in this study, for the 7 glaciers that showed the largest differences. Note that the three largest glaciers of the NPI, San Quintin, San Rafael and Steffens, covering together 51% of the NPI area are included in this table.

Supplementary Figure S3 | Spatial distribution of the minimum **(a)** and maximum **(b)** dates of ASTER DEMs used in our study. White gaps correspond to water bodies and locations where the uncertainty of $dh/dt_{\text{ASTER\_trend}}$ is larger than 3 m yr^{-1} (at the 95% confidence level).

Supplementary Figure S4 | Comparison of SRTM, ASTER-14DMO and ASTER-ASP DEMs along a transverse profile of San Quintin glacier. **(a)** Location of the profile including glacier and stable terrain; transitions are presented as blue lines. **(b)** Elevation profiles extracted from the SRTM (February 2000) ASTER-14DMO and ASTER-ASP (18 March 2012) DEMs. Both ASTER DEMs are derived from the same Level 1A stereo pair. The ASTER-14DMO DEM (used in Willis et al., 2012a) was downloaded from LPDAAC. This profile illustrates the occurrence of numerous artifacts over the glacier surface in the ASTER-14DMO DEM. Conversely, the ASTER-ASP DEM is smoother and follows nicely the undulations of the SRTM DEM with an offset due to glacier thinning between 2000 and 2012. Hence, ASTER-ASP DEMs are more precise and should be preferred to ASTER-DMO DEMs to study glacier elevation changes.

Supplementary Table S1 | Mass balance of NPI individual glaciers from 2000 to 2012 and percentage area measured for SPOT-SRTM and ASTER_trend methods.

REFERENCES

Aniya, M. (2007). Glacier variations of Hielo patagónico Norte, Chile, for 1944/45-2004/05. *Bull. Glaciol. Res*. 24, 59–70.

Aravena, J.-C., and Luckman, B. H. (2009). Spatio-temporal rainfall patterns in Southern South America. *Int. J. Climatol*. 29, 2106–2120. doi: 10.1002/joc.1761

Arendt, A. A., Echelmeyer, K. A., Harrison, W. D., Lingle, C. S., and Valentine, V. B. (2002). Rapid wastage of Alaska glaciers and Their contribution to rising sea level. *Science* 297, 382–386. doi: 10.1126/science.1072497

Barcaza, G., Aniya, M., Matsumoto, T., and Aoki, T. (2009). Satellite-derived equilibrium lines in Northern Patagonia icefield, Chile, and their implications to glacier variations. *Arct. Antarct. Alp. Res*. 41, 174–182. doi: 10.1657/1938-4246-41.2.174

Berthier, E., Arnaud, Y., Baratoux, D., Vincent, C., and Rémy, F. (2004). Recent rapid thinning of the "Mer de Glace" glacier derived from satellite optical images. *Geophys. Res. Lett*. 31:L17401. doi: 10.1029/2004GL020706

Berthier, E., Arnaud, Y., Kumar, R., Ahmad, S., Wagnon, P., and Chevallier, P. (2007). Remote sensing estimates of glacier mass balances in the Himachal Pradesh (Western Himalaya, India). *Remote Sens. Environ*. 108, 327–338. doi: 10.1016/j.rse.2006.11.017

Berthier, E., Cabot, V., Vincent, C., and Six, D. (2016). Decadal region-wide and glacier-wide mass balances derived from multi-temporal ASTER satellite digital elevation models. Validation over the Mont-Blanc area. *Cryospheric Sci*. 4:63. doi: 10.3389/feart.2016.00063

Berthier, E., Vincent, C., Magnússon, E., Gunnlaugsson, Á. Þ*., Pitte, P., Le Meur, E., et al. (2014). Glacier topography and elevation changes derived from pléiades sub-meter stereo images. *Cryosphere* 8, 2275–2291. doi: 10.5194/tc-8-2275-2014

Buttstädt, M., Möller, M., Iturraspe, R., and Schneider, C. (2009). Mass balance evolution of martial Este Glacier, Tierra del Fuego (Argentina) for the period 1960–2099. *Adv. Geosci*. 22, 117–124. doi: 10.5194/adgeo-22-117-2009

Davies, B. J., and Glasser, N. F. (2012). Accelerating shrinkage of Patagonian glaciers from the little ice Age (∼AD 1870) to 2011. *J. Glaciol*. 58, 1063–1084. doi: 10.3189/2012JoG12J026

Dixon, L., and Ambinakudige, S. (2015). Remote sensing study of glacial change in the Northern Patagonian icefield. *Adv. Remote Sens*. 4, 270–279. doi: 10.4236/ars.2015.44022

Falaschi, D., Bolch, T., Rastner, P., Lenzano, M. G., Lenzano, L., Vecchio, A. L., et al. (2016). Mass changes of alpine glaciers at the eastern margin of the Northern and Southern Patagonian icefields between 2000 and 2012. *J. Glaciol.* 63, 258–272. doi: 10.1017/jog.2016.136

Farr, T. G., Rosen, P. A., Caro, E., Crippen, R., Duren, R., Hensley, S., et al. (2007). The shuttle radar topography mission. *Rev. Geophys.* 45:RG2004. doi: 10.1029/2005RG000183

Fischer, M., Huss, M., and Hoelzle, M. (2015). Surface elevation and mass changes of all Swiss glaciers 1980–2010. *Cryosphere* 9, 525–540. doi: 10.5194/tc-9-525-2015

Fujiyoshi, Y., Kondo, H., Inoue, J., and Yamada, T. (1987). Characteristics of precipitation and vertical structure of air temperature in the northern Patagonia. *Bull. Glacier Res*. 4, 15–23.

Gardelle, J., Berthier, E., and Arnaud, Y. (2012). Impact of resolution and radar penetration on glacier elevation changes computed from DEM differencing. *J. Glaciol*. 58, 419–422. doi: 10.3189/2012JoG11J175

Gardelle, J., Berthier, E., Arnaud, Y., and Kääb, A. (2013). Region-wide glacier mass balances over the Pamir-Karakoram-Himalaya during 1999–2011. *Cryosphere* 7, 1263–1286. doi: 10.5194/tc-7-1263-2013

Gardner, A. S., Moholdt, G., Cogley, J. G., Wouters, B., Arendt, A. A., Wahr, J., et al. (2013). A reconciled estimate of glacier contributions to sea level rise: 2003 to 2009. *Science* 340, 852–857. doi: 10.1126/science.1234532

Garreaud, R. D., Vuille, M., Compagnucci, R., and Marengo, J. (2009). Present-day South American climate. *Palaeogeogr. Palaeoclimatol. Palaeoecol.* 281, 180–195. doi: 10.1016/j.palaeo.2007.10.032

Gillett, N. P., Kell, T. D., and Jones, P. D. (2006). Regional climate impacts of the Southern annular mode. *Geophys. Res. Lett.* 33:L23704. doi: 10.1029/2006GL027721

Glasser, N. F., Harrison, S., Jansson, K. N., Anderson, K., and Cowley, A. (2011). Global sea-level contribution from the Patagonian icefields since the little ice age maximum. *Nat. Geosci.* 4, 303–307. doi: 10.1038/ngeo1122

Granshaw, F. D., and Fountain, A. G. (2006). Glacier change (1958–1998) in the north cascades national park complex, Washington, USA. *J. Glaciol.* 52, 251–256. doi: 10.3189/172756506781828782

Huss, M. (2013). Density assumptions for converting geodetic glacier volume change to mass change. *Cryosphere* 7, 877–887. doi: 10.5194/tc-7-877-2013

Jaber, W. A., Floricioiu, D., and Rott, H. (2016). "Geodetic mass balance of the Patagonian icefields derived from SRTM and TanDEM-X data," in *2016 IEEE International Geoscience and Remote Sensing Symposium (IGARSS)* (Bijing), 342–345.

Jaber, W. A., Floricioiu, D., Rott, H., and Eineder, M. (2013). "Surface elevation changes of glaciers derived from SRTM and TanDEM-X DEM differences," in *2013 IEEE International Geoscience and Remote Sensing Symposium - IGARSS* (Melbourne), 1893–1896.

Kääb, A. (2005). Combination of SRTM3 and repeat ASTER data for deriving alpine glacier flow velocities in the Bhutan Himalaya. *Remote Sens. Environ.* 94, 463–474. doi: 10.1016/j.rse.2004.11.003

Korona, J., Berthier, E., Bernard, M., Rémy, F., and Thouvenot, E. (2009). SPIRIT. SPOT 5 stereoscopic survey of polar ice: reference images and topographies during the fourth international polar year (2007–2009). *ISPRS J. Photogramm. Remote Sens.* 64, 204–212. doi: 10.1016/j.isprsjprs.2008.10.005

Lopez, P., Chevallier, P., Favier, V., Pouyaud, B., Ordenes, F., and Oerlemans, J. (2010). A regional view of fluctuations in glacier length in southern South America. *Glob. Planet. Change* 71, 85–108. doi: 10.1016/j.gloplacha.2009.12.009

Marzeion, B., Champollion, N., Haeberli, W., Langley, K., Leclercq, P., and Paul, F. (2017). Observation-based estimates of global glacier mass change and its contribution to sea-level change. *Surv. Geophys.* 38, 105–130. doi: 10.1007/s10712-016-9394-y

Mernild, S. H., Beckerman, A. P., Yde, J. C., Hanna, E., Malmros, J. K., Wilson, R., et al. (2015). Mass loss and imbalance of glaciers along the Andes Cordillera to the sub-Antarctic islands. *Glob. Planet. Change* 133, 109–119. doi: 10.1016/j.gloplacha.2015.08.009

Mernild, S., and Wilson, R. (2016). The Andes Cordillera. Part III: glacier surface mass balance and contribution to sea level rise (1979–2014). *Int. J. Climatol.* 37, 3154–3174. doi: 10.1002/joc.4907

Mouginot, J., and Rignot, E. (2015). Ice motion of the Patagonian icefields of South America: 1984–2014. *Geophys. Res. Lett.* 42, 1441–1449. doi: 10.1002/2014GL062661

Nuth, C., and Kääb, A. (2011). Co-registration and bias corrections of satellite elevation data sets for quantifying glacier thickness change. *Cryosphere* 5, 271–290. doi: 10.5194/tc-5-271-2011

Paul, F., Bolch, T., Kääb, A., Nagler, T., Nuth, C., Scharrer, K., et al. (2015). The glaciers climate change initiative: methods for creating glacier area, elevation change and velocity products. *Remote Sens. Environ.* 162, 408–426. doi: 10.1016/j.rse.2013.07.043

Pfeffer, W. T., Arendt, A. A., Bliss, A., Bolch, T., Cogley, J. G., Gardner, A. S., et al. (2014). The Randolph glacier inventory: a globally complete inventory of glaciers. *J. Glaciol.* 60, 537–552. doi: 10.3189/2014JoG13J176

Rignot, E., Echelmeyer, K., and Krabill, W. (2001). Penetration depth of interferometric synthetic-aperture radar signal in snow and ice. *Geophys. Res. Lett.* 28, 3501–3504. doi: 10.1029/2000GL012484

Rignot, E., Forster, R., and Isacks, B. (1996). Mapping of glacial motion and surface topography of Hielo Patagónico Norte, Chile, using satellite SAR L-band interferometry data. *Ann. Glaciol.* 23, 209–216. doi: 10.1017/S026030550001346X

Rignot, E., Rivera, A., and Casassa, G. (2003). Contribution of the Patagonia icefields of South America to sea level rise. *Science* 302, 434–437. doi: 10.1126/science.1087393

Rivera, A., Benham, T., Casassa, G., Bamber, J., and Dowdeswell, J. A. (2007). Ice elevation and areal changes of glaciers from the Northern Patagonia icefield, Chile. *Glob. Planet. Change* 59, 126–137. doi: 10.1016/j.gloplacha.2006.11.037

Schaefer, M., MacHguth, H., Falvey, M., and Casassa, G. (2013). Modeling past and future surface mass balance of the Northern Patagonia icefield. *J. Geophys. Res. Earth Surf.* 118, 571–588. doi: 10.1002/jgrf.20038

Schaefer, M., MacHguth, H., Falvey, M., Casassa, G., and Rignot, E. (2015). Quantifying mass balance processes on the Southern Patagonia icefield. *Cryosphere* 9, 25–35. doi: 10.5194/tc-9-25-2015

Scherler, D., Leprince, S., and Strecker, M. R. (2008). Glacier-surface velocities in alpine terrain from optical satellite imagery—accuracy improvement and quality assessment. *Remote Sens. Environ.* 112, 3806–3819. doi: 10.1016/j.rse.2008.05.018

Shean, D. E., Alexandrov, O., Moratto, Z. M., Smith, B. E., Joughin, I. R., Porter, C., et al. (2016). An automated, open-source pipeline for mass production of digital elevation models (DEMs) from very-high-resolution commercial stereo satellite imagery. *ISPRS J. Photogramm. Remote Sens.* 116, 101–117. doi: 10.1016/j.isprsjprs.2016.03.012

Wang, D., and Kääb, A. (2015). Modeling glacier elevation change from DEM time series. *Remote Sens.* 7, 10117–10142. doi: 10.3390/rs70810117

Willis, M. J., Melkonian, A. K., Pritchard, M. E., and Ramage, J. M. (2012a). Ice loss rates at the Northern Patagonian icefield derived using a decade of satellite remote sensing. *Remote Sens. Environ.* 117, 184–198. doi: 10.1016/j.rse.2011.09.017

Willis, M. J., Melkonian, A. K., Pritchard, M. E., and Rivera, A. (2012b). Ice loss from the Southern Patagonian ice field, South America, between 2000 and 2012. *Geophys. Res. Lett.* 39:L17501. doi: 10.1029/2012GL053136

Conflict of Interest Statement: The authors declare that the research was conducted in the absence of any commercial or financial relationships that could be construed as a potential conflict of interest.

frontiers in Earth Science

ORIGINAL RESEARCH
published: 13 February 2018
doi: 10.3389/feart.2018.00002

Cirque Glacier on South Georgia Shows Centennial Variability over the Last 7000 Years

Lea T. Oppedal[1,2]*, *Jostein Bakke*[1,2], *Øyvind Paasche*[2], *Johannes P. Werner*[1,2] and *Willem G. M. van der Bilt*[1,2]

[1] Department of Earth Science, University of Bergen, Bergen, Norway, [2] Bjerknes Centre for Climate Research, Bergen, Norway

A 7000 year-long cirque glacier reconstruction from South Georgia, based on detailed analysis of fine-grained sediments deposited downstream in a bog and a lake, suggests continued presence during most of the Holocene. Glacier activity is inferred from various sedimentary properties including magnetic susceptibility (MS), dry bulk density (DBD), loss-on-ignition (LOI) and geochemical elements (XRF), and tallied to a set of terminal moraines. The two independently dated sediment records document concurring events of enhanced glacigenic sediment influx to the bog and lake, whereas the upstream moraines afford the opportunity to calculate past Equilibrium Line Altitudes (ELA) which has varied in the order of 70 m altitude. Combined, the records provide new evidence of cirque glacier fluctuations on South Georgia. Based on the onset of peat formation, the study site was deglaciated prior to 9900 ± 250 years ago when Neumayer tidewater glacier retreated up-fjord. Changes in the lake and bog sediment properties indicate that the cirque glacier was close to its maximum Holocene extent between 7200 ± 400 and 4800 ± 200 cal BP, 2700 ± 150 and 2000 ± 200 cal BP, 500 ± 150–300 ± 100 cal BP, and in the Twentieth century (likely 1930s). The glacier fluctuations are largely in-phase with reconstructed Patagonian glaciers, implying that they respond to centennial climate variability possibly connected to corresponding modulations of the Southern Westerly Winds.

Keywords: glacier, distal glacier-fed lake, distal glacier-fed bog, glacial sediments, holocene, neoglacial, Southern Ocean, sub-Antarctica

OPEN ACCESS

Edited by:
Matthias Holger Braun, University of Erlangen-Nuremberg, Germany

Reviewed by:
Bethan Joan Davies, Royal Holloway, University of London, United Kingdom
Olga Nikolaevna Solomina, Institute of Geography (RAS), Russia

***Correspondence:**
Lea T. Oppedal
lea.oppedal@gmail.com

Specialty section:
This article was submitted to Quaternary Science, Geomorphology and Paleoenvironment, a section of the journal Frontiers in Earth Science

Received: *29 September 2017*
Accepted: *11 January 2018*
Published: *13 February 2018*

Citation:
Oppedal LT, Bakke J, Paasche Ø, Werner JP and van der Bilt WGM (2018) Cirque Glacier on South Georgia Shows Centennial Variability over the Last 7000 Years. Front. Earth Sci. 6:2. doi: 10.3389/feart.2018.00002

INTRODUCTION

The accelerated melting of glaciers in the Southern Ocean (Cook et al., 2010; Scambos et al., 2014; Koppes et al., 2015) manifests rapid climate change over the last decades (Gille, 2002, 2008; Vaughan et al., 2003; Böning et al., 2008). Although anthropogenic forcing probably explains parts of this regional-scaled glacier retreat, strong regional feedback mechanisms still predominate (Thompson et al., 2011; Wang and Cai, 2013). Many of these mechanisms can be traced back to the Southern Westerly Winds, which are closely linked to the Southern Ocean's uptake of CO_2 through their effect on upwelling of carbon-rich deep water, and therefore have the potential to affect climate globally (Lenton and Matear, 2007; Le Quéré et al., 2007; Hodgson and Sime, 2010; Sigman et al., 2010). At present, the strength and position of the westerlies are rapidly shifting, but the processes behind these changes remain poorly understood, due to scarcity and of

instrumental time series and paleoclimatic reconstructions (Hodgson and Sime, 2010), including glacier records which can help map out temporal and spatial changes during the Holocene.

Glaciers are established proxies of climate change (e.g., Oerlemans, 2005) and ubiquitous on Southern Ocean islands, but few reconstructions currently exists. Moreover, most work on Holocene glacier variability in the Southern Ocean is restricted to moraine chronologies (Solomina et al., 2015 and references therein). Mapping and dating of moraines provide valuable information of a glacier's extent, size, and position at points in time. However, moraine chronologies do not capture retreat phases or length of events, and cannot exclude the possibility that moraines have been erased by subsequent glacier advances of equal or larger magnitude (Balco, 2009).

The study of sediments deposited in distal glacier-fed lakes provide the opportunity to continuously reconstruct up-valley glacier variability, although not without caveats. This approach (Karlén, 1976; Bakke et al., 2010) is based on quantification of the sediment delivery by glacial erosion beneath temperate glaciers and its relationship to glacier size (Herman et al., 2015), and assumes that para- and extra-glacial material can either be ignored or identified and removed from the final glacier reconstruction, which is not always the case. Either way, larger glaciers produce more erosional products available for downstream transport by meltwater. These fine-grained glacigenic sediments settle out of suspension in downstream lakes and thus builds unremitting archives of variations in glacier size. Here we take advantage of this lake approach in an effort to produce a new and reliable glacier reconstruction from South Georgia.

The Late Pleistocene-Holocene glacier history of South Georgia has previously been reconstructed in some detail (e.g., Clapperton et al., 1989a; Gordon and Timmis, 1992; Bentley et al., 2007; Roberts et al., 2010) suggesting large Neoglacial advances. At present, only two continuous reconstructions of past glacier change exist: Rosqvist and Schuber (2003) provides a sediment record from Block lake (Husvik, **Figure 1**) based on gray-scale density, loss-on-ignition and grain-size spanning from 7400 to 1000 cal BP (**Figure 9C**), while Van Der Bilt et al. (2017) reconstruct the last 1250 years with a record from the Middle Hamberg lake (south of Grytviken, **Figure 1**) based on titanium counts validated against sediment density and grain size (**Figure 9B**). Both studies suggest centennial-scaled variability, although we do not know whether these records are representative for South Georgia. In order to enhance our understanding of Holocene glacier fluctuations on the island, we need to test if these records can be replicated.

In this study, we present a continuous reconstruction of Diamond glacier (unofficially named) on north-central South Georgia (**Figure 1**) covering the last 7200 years. Our glacier reconstruction is based upon measurements of physical, geochemical, and magnetic properties (cf. Bakke et al., 2010) of sediments deposited in the distal glacier-fed Diamond lake as well as the adjacent Diamond bog (both unofficially named). Mapped marginal moraines in front of Diamond glacier provide an independent framework for the past glacier fluctuations, although the timing of these moraines remains unresolved. Together, the lake-, bog- and moraine records demonstrate a consistent Holocene glacial history of Diamond glacier, which compares well with reconstructed glaciers on South Georgia and in Patagonia.

SETTING

The sub-Antarctic island of South Georgia is about 170 km long and up to 40 km wide, with extensive glacier cover and an axial, alpine mountain range where mountains rise to nearly 3,000 m (**Figure 1**). Regional climate is influenced by the position and intensity of the westerlies, the position of the Polar Front Zone, and the Antarctic winter sea ice limit, which together mediate the temperature and moisture supply to the island (Pendlebury and Barnes-Keoghan, 2007; **Figure 1**). An instrumental temperature record exists for King Edward Point (KEP, c. 2 m altitude), Grytviken (**Figure 2A**). For the period 1905–1982, mean annual temperature was 2.0°C and mean summer (December–Feburary) temperature was 4.9°C. Mean annual precipitation was c. 1,500 mm and mean winter precipitation was 144 mm over the same time interval.

Due to a significant leeside effect on the island, glaciation on the northeast coast is restricted to small cirque and plateau glaciers, while tidewater and calving valley and outlet glaciers occupy the valleys and fjords (**Figure 1**; Gordon et al., 2008). According to observations, temperature is the dominant driver of glacier mass balance (Gordon and Timmis, 1992). Cirque and small valley glaciers respond most sensitively to shifts in climate, and have been receding in response to regional warming since the 1950s (Gordon and Timmis, 1992). With a delayed response, the larger valley and tidewater glaciers followed suit after the early 1970s (Gordon and Timmis, 1992), and now more than 97 % of the glaciers on South Georgia are retreating (Cook et al., 2010).

Olsen Valley in Cumberland West Bay, (**Figure 2**; Supplementary Figure 1) offers a favorable setting for reconstructing past cirque glacier variability using sediments deposited in distal glacier-fed Diamond lake and Diamond bog in combination with a sequence of mapped marginal moraines in front of Diamond glacier. Diamond glacier is located in a cirque southwest of the summit Diamond Peak (∼510 m altitude) between c. 360 and 500 m altitude (2011) (54.20°S 36.64°W). A sequence of marginal moraines are deposited in front of the glacier, marking former glacier front positions. In the lower valley, marginal moraines mark the former glacier front positions of Neumayer tidewater glacier when it advanced into the valley from the west (cf. Bentley et al., 2007).

In the upper reaches of the valley, sediment-laden meltwater, originating from Diamond glacier, is funneled through a well-defined channel before feeding into the gently sloping valley below. The meltwater follows a course of about six kilometers down Olsen Valley before entering Cumberland West Bay (**Figure 2B**). The stream is intersected by an alluvial fan in the central part of the valley, containing both fresh sediments and sediments covered by vegetation, indicating deposition of glacial sediments both today and in the past. The meltwater has cut deep meanders (up to 4 m) into the bog covering the valley floor in the

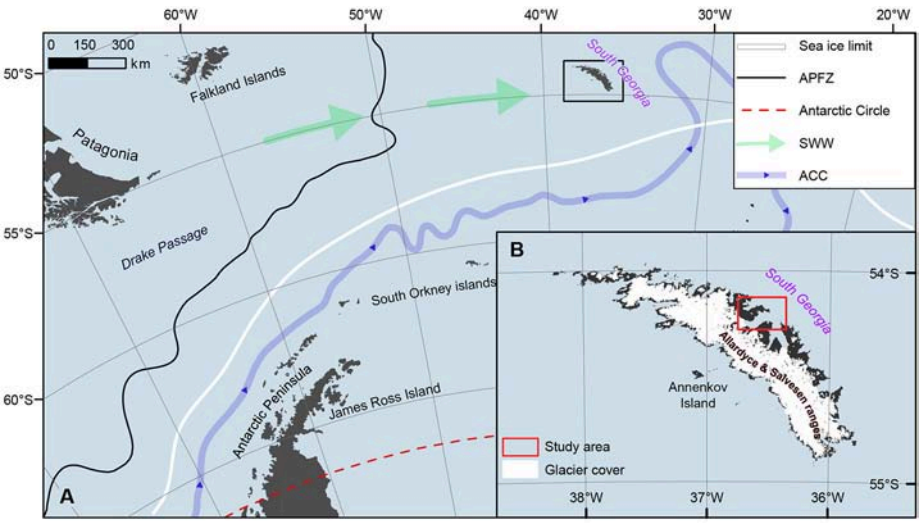

FIGURE 1 | (A) Overview map showing South Georgia in the Southern Ocean with major circulation patterns such as the Antarctic Polar Front Zone (APFZ), the Southern Westerly Winds (SWW), and the Antarctic Circumpolar Current (ACC), as well as the Antarctic Circle and winter sea ice limit after Scar (2015) and Orsi et al. (1995). **(B)** Inset of South Georgia showing the current glacier extent after SGGIS (2017) and our study area.

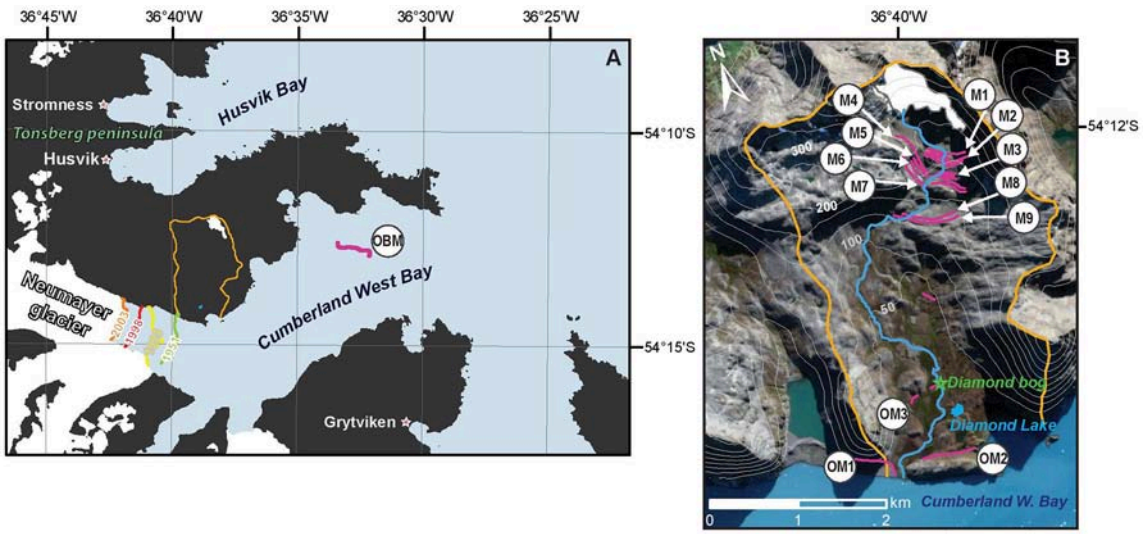

FIGURE 2 | (A) Overview map of the Cumberland West Bay and Husvik Bay area indicating the studied catchment (orange), Diamond glacier (white), and Diamond lake (blue), as well as the Neumayer Glacier with four historical glacier front positions after SGGIS (2017), and the Antarctic Cold Reversal moraine (magenta) after Hodgson et al. (2014); Graham et al. (2017). **(B)** Simplified geomorphological map of Olsen Valley showing the cirque glacier (white), lake (blue), and bog (green) as well as the DB2 coring location (green star), mapped marginal moraines (pink) and the main stream (blue).

lower valley. Sediment sections along the river show alternating layers of peat and fine-grained sediments in the upper meter, indicating deposition of glacially derived sediments when the river floods its plains (Matthews et al., 2005).

Further downstream, the stream enters another alluvial fan separated from Diamond Lake by a marsh. The meltwater drains into the alluvial fan, which during times of moderate to high runoff has standing water. If the water level increases above c. 0.5 m, water overflows the marsh and drains into Diamond Lake. We find it likely that this occurs every year during the ablation season. The lake (54.24°S 36.65°W, 16 m altitude) covers around 10,000 m^2 and is ∼3 m deep. Its catchment covers c.11 km^2, with 3% of that surface currently occupied by the Diamond glacier. Bedrock, consisting of andesitic volcaniclastic greywackes (Tanner, 1981 in Quilty, 2007), is exposed in the steeper part of the valley, which is free of vegetation, and unprotected paraglacial sediments are present in an area of c. 2 km^2 downstream of the glacier. The gentle slopes of the lower valley, below c. 150 m altitude, are covered by vegetation which protects the lake from mass-wasting processes. The grass *Festuca contracta*

covers the slightly raised areas in the valley, while vegetation on the bog is dominated by the moss *Tortula robusta,* with grass and flowering plants present such as *Acaena magellanica* and *Rostkovia magellanica.* Following the classification of peat on South Georgia by Smith (1981), Diamond Bog is a soligenous eutrophic mire. It is developed on the floor of a broad valley and traversed by drainage channels which increases runoff and lowers the nutrient levels of the peat. At the coring site, Diamond Bog is 220 cm.

MATERIALS AND METHODS

Our reconstruction of glacier fluctuations at the Diamond cirque glacier is based on a multi-proxy approach (Bakke et al., 2010), integrating geomorphological field mapping, and physical, magnetic and geochemical analyses on sediments deposited in the distal glacier-fed lake and bog.

Geomorphological Mapping

We mapped the geomorphology of the Diamond catchment (**Figure 2B**) based on ESA Sentinal satellite imagery (Google, n.d.)[1] combined with field surveys during January 2008 and December 2011. Our main goal was to identify marginal moraines marking former glacier coverage, and to determine past and present pathways of glacial meltwater. The topographic maps of South Georgia were, at the time of our field work, not of a resolution suitable for detailed mapping and positioning; we therefore used a hand-held GPS device (Garmin CSX60) for sites and sampling locations. The average off-set on the positions are in the order of 2–10 m.

Lake Survey and Sediment Coring

We mapped the bathymetry of Diamond lake (**Figure 3**) using a Garmin Fishfinder 160x echo sounder combined with a GPS and retrieved the sediment cores from the deepest and most central part of the lake (**Figure 3**, **Table 1**). For the longer piston cores (LDP1, 75 cm and LDP2, 246 cm) we used a modified piston corer able to capture up to six meters of sediments. The surface sediments at each of the two coring sites (LDS1, 34 cm and LDS2, 46 cm), we extracted using a gravity corer (Renberg and Hansson, 2008). In addition, we retrieved three sediment cores from a section of Diamond bog, upstream of the lake, by hammering PVC tubes into the bog (**Figure 2B**, **Table 1**).

Sample Treatment and Laboratory Analyses

Prior to sub-sampling, we visually logged the lithological characteristics of the sediment cores, and used an ITRAX X-ray fluorescence (XRF) core scanner to map out the sediment geochemistry (c.f. Kylander et al., 2011). Together with the geochemical mapping at 200-μm resolution, we obtained optical and radiographic images at the same time (**Figure 6**). The XRF analyses were made using a molybdenum tube with power settings of 30 kV and 35 mA, employing a counting time of 10 s

[1]Google (n.d.). *Google Map of South Georgia [Online]*. Available online at: https://goo.gl/Dr1pYP (Accessed 2008).

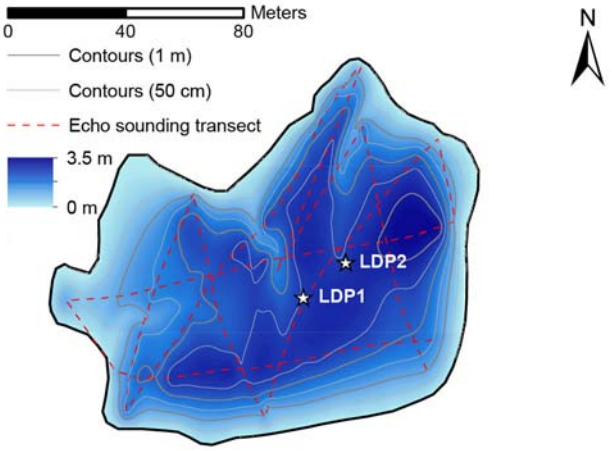

FIGURE 3 | Bathymetry of Diamond lake indicating the echo sounding transects (red stippled lines) and coring locations for piston cores LDP1 and LDP2 in the deepest part of the lake. Gravity cores LDS1 and LDS2 were taken at the same two locations.

TABLE 1 | Overview of sediment cores.

Core	Location	Length	Depth	Equipment
LDS1	54° 14′ 08.39″S 36° 38′ 51.49″W	34 cm	2.6 m	Gravity corer
LDP1	54° 14′ 08.39″S 36° 38′ 51.49″W	75 cm	2.6 m	Piston corer
LDS2	54° 14′ 07.97″S 36° 38′ 50.68″W	46 cm	2.5 m	Gravity corer
LDP2	54° 14′ 07.97″S 36° 38′ 50.68″W	246 cm	2.5 m	Piston corer
DB1	54° 14′ 03.13″S 36° 39′ 01.34″W	138 cm	N/A	PVC tube
DB2	54° 13′ 58.65″S 36° 38′ 57.81″W	204 cm	N/A	PVC tube
DB3	54° 13′ 55.24″S 36° 38′ 56.93″W	67 cm	N/A	PVC tube

(N_{LDP1} = 3179, N_{LDP2} = 12280, N_{DB1} = 6771, N_{DB2} = 10201, N_{DB3} = 3551).

We scanned the cores for surface Magnetic Susceptibility (MS) at 0.5 cm intervals on a Bartington MS2 point sensor (range = 0.1) (N_{LDP1} = 132, N_{LDP2} = 492, N_{DB1} = 277, N_{DB2} = 297, N_{DB3} = 135). Since the gravity cores (LDS1 and LDS2) had already been sub-sampled in the field (every 0.25 cm and 0.5 cm, respectively), we measured the bulk magnetic susceptibility of these samples on a MFK1-FA (sensitivity: 2×10^{-8} SI). We use the MS data to tentatively correlate the four cores from Diamond lake (**Figure 5**). Being the two longest cores from, respectively, the lake and the bog, we selected core LDP2 and core DB2 for further and more detailed analyses.

We followed the protocol for Loss-On-Ignition (LOI) after Dean (1974) and dry-bulk density (DBD) after Bakke et al. (2005) of 1 cm^3 dry sub-samples every 0.5 cm (N_{LDP2} = 492, N_{DB2} = 408). Using an MFK1-FA (sensitivity: 2×10^{-8} SI), we analyzed the mass specific magnetic susceptibility (χbulk)

(Thompson and Oldfield, 1986) of discrete samples (6.8 cm^3) at 1 cm intervals ($n_{LDP2} = 238$, $n_{DB2} = 204$). Prior to measurements, we freeze-dried the samples to remove the water and thereby reduce chances of post-sampling diagenesis. With the aim of distinguishing between para- and ferromagnetic sediments, we conducted the measurements at both room temperature (293 K) and 77 K (liquid nitrogen), and calculated the paramagnetic ratio ($\chi bulk_{77K}/\chi bulk_{293K}$) for each sample (Lanci and Lowrie, 1997).

The grain size distribution of 20 samples from LDP2 and 5 samples from DB2 were analyzed using a Mastersizer 3000 with an LV dispersion unit. All samples were pre-treated for c. 24 h with 35% hydrogen peroxide to remove the organic material (Vasskog et al., 2016) and sonicated with ultrasound for 60 s. prior to measurement. Bulk sample sizes were adjusted to have an obscuration rate of 10–20%, and measured for 10 s (blue laser) and 20 s (red laser) using refraction index of 2.5, absorption index of 0.01, and stirring rate of 2,500 rpm.

Age-depth relationships were established for the lake- and bog cores with the help of 24 individual samples of terrestrial macrofossils collected from LDP2 and DB2. Samples were submitted to Poznan Radiocarbon Laboratory for AMS radiocarbon dating (**Table 2**). Based on these dates, we constructed age-depth models for each core with the software package Clam 2.2 (Blaauw, 2010). We applied statistical cross-matching techniques to further constrain the age models, and to demonstrate correspondence between the three sediment cores (section Age-Depth Modeling).

TABLE 2 | Radiocarbon dates obtained for LDP2 and DB2.

Core	Depth	Lab. no	^{14}C date (BP)
LDP2	12.5 cm	Poz-52654	1120 ± 30
LDP2	37.5 cm	Poz-52656	1450 ± 30
LDP2	62.5 cm	Poz-52657	2215 ± 35
LDP2	87.5 cm	Poz-52658	2450 ± 30
LDP2	112.5 cm	Poz-52659	3585 ± 35
LDP2	137.5 cm	Poz-52660	2875 ± 30
LDP2	162.5 cm	Poz-52699[a]	3340 ± 40
LDP2	183.5 cm	Poz-52662	4435 ± 35
LDP2	205.5 cm	Poz-52663[b]	5180 ± 50
LDP2	221.5 cm	Poz-74625[c]	4915 ± 35
LDP2	223.0 cm	Poz-5266[d]	8370 ± 50
LDP2	243.0 cm	Poz-52666[d]	8860 ± 50
DB2	13.0 cm	Poz-52671	−224 ± 27
DB2	26.0 cm	Poz-52672	185 ± 30
DB2	49.0 cm	Poz-52673[e]	1320 ± 70
DB2	64.0 cm	Poz-52674	1265 ± 30
DB2	81.5 cm	Poz-52676	1765 ± 30
DB2	95.5 cm	Beta-464014	2620 ± 30
DB2	105.5 cm	Poz-52677	2775 ± 30
DB2	113 cm	Poz-74626	2915 ± 30
DB2	130 cm	Poz-52678	3300 ± 90
DB2	159.5 cm	Poz-52679	3560 ± 35
DB2	179.5 cm	Poz-52680	3665 ± 35
DB2	203.5 cm	Poz-52681	3850 ± 40

Radiocarbon dates obtained for the Lake Diamond Piston core (LDP2) and Diamond Bog core (DB2).

Equilibrium Line Altitude Calculations

We constrained former glacier extents combining satellite imagery (present) with fairly intact moraines, which were mapped during the two fieldwork seasons (2008 and 2011). We used ArcMap v. 10.4 as the platform to apply the cartographic method (e.g., Ballantyne, 1989) for reconstruction of past glacier extents and surface areas. Based on this, we estimated the present and past Equilibrium Line Altitudes (ELA) of Diamond glacier (**Figure 2B**) using the Accumulation Area Ratio method (AAR) (Porter, 1975) with an accumulation area of 0.6 ± 0.05, which is the standard AAR value used for cirque glaciers. In addition, we used the Area x Altitude method and the Area x Altitude Balance-Ratio method (AABR) (Osmaston, 2005) with a range of balance ratios (BR) (1.5, 1.9, and 2.5) since little is known about the balance ratio in this region. The ELA reported for each moraine is the mean value of the different estimates.

RESULTS

Moraines

We mapped nine terminal moraine ridges (M1-M9) in front of Diamond glacier (**Figure 2B**), which we use to reconstruct former glacier extent and calculate the corresponding ELAs (**Figure 4**; Supplementary Table 1). The moraines are free of vegetation, and none of them is ice-cored. We group them into four clusters described in the following.

The outermost moraine cluster (M9-M8) consists of two distinct free-standing continuous ridges (c. 2–3 m high and 300 m) located, c. 40 m apart, at a shelf (c. 170 m altitude) right before the valley drops steeply into the gently sloping lower Olsen Valley. The ridges are located at both sides of the present-day meltwater stream emerging from Diamond glacier. They consist of diamictic sediments, ranging from clay to gravel. Scattered boulders (10–30 cm in diameter) are partly embedded within or resting on the ridge surfaces. Cross sections of the moraines show an asymmetric profile with a steeper distal slope (c. 30°) and a low-angle proximal slope (c. 10°). The area distal to the ridges has exposed bedrock on both sides of the meltwater stream, which cuts through the moraines in a south westerly direction. Both ridges have undulating long profiles, which indicates partial erosion by meltwater, implying that the drainage pattern was more directly oriented toward the south when the ice front was closer to the terminal moraines. We cannot ascertain the processes of moraine formation, as no exposure in the ridge was present. At the time of moraine formation, we estimate that the ELAs were 64 ± 13 and 70 ± 12 m lower than in 2011, respectively for M8 and M9 (**Figure 4**; Supplementary Table 1).

The intermediate moraine cluster consists of two freestanding ridges (M7-M6), varying from 1 to 3 m in height, that continue for more than 600 m and are only cut by the river from Diamond glacier confined to a canyon (with a depth between 3 and 10 m) distal from the moraine, which funnels the meltwater toward the lower valley. Proximal to the two ridges is another partly preserved ridge (M5) that continue for approximately 550 m. Like the outermost moraines, ridges M7-M5 are composed of

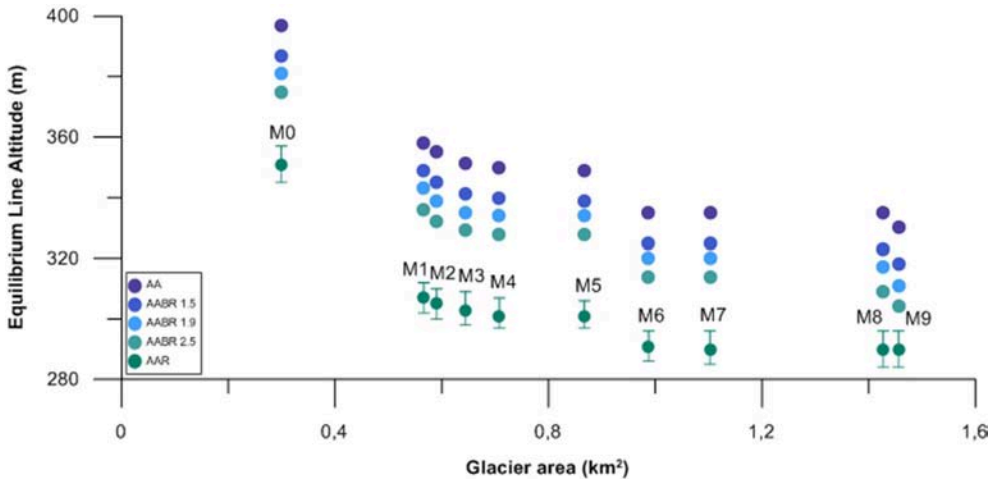

FIGURE 4 | Reconstructed ELA for glacier stages M0 (2011) to M9 using the Accumulation Area Ratio method (AAR) (Porter, 1975), with an accumulation area of 0.6 ± 0.05, the Area x Altitude method (AA) and the Area x Altitude Balance-Ratio method (AABR) (Osmaston, 2005) with balance ratios of 1.5, 1.9, and 2.5. The ELAs are plotted against the present (2011) and reconstructed glacier areas based on glacier outlines by moraines (M1–M9).

diamictic sediments with grain sizes ranging from clay to gravel, but with fewer boulders embedded and on the ridge surfaces. The cross profile of the ridges shows a steep distal side (c. 36°) and a more gently sloping proximal side (c. 15°). The similarities with the outermost moraine system is striking. At the time M7 and M6 were formed, ELA was 61 ± 13 m lower than in 2011, while the corresponding ELA for M5 is 47 ± 14 m (**Figure 4**; Supplementary Table 1).

The inner moraine cluster is located less than 50 meters proximal to ridge M5. However, the geomorphology of this moraine system is different with numerous small ridges located very close to each other. One of the ridges (M4) is freestanding and slightly higher than the others (4 m high). It can be followed over a distance of 700 m, only crosscut by the present-day meltwater stream. On the north side of M4 more than 15 small (<1 m high) saw-tooth shaped ridges can be mapped over a distance of less than 50 meters (M3). The diamicton in the moraines consists of fine sand, gravel and boulders up to 1 m in diameter. The lack of clay and fine silt indicate presence of water during deposition. Our interpretation is that the moraine cluster nested to M4, including the many smaller moraine ridges, represent an oscillatory glacier front with moraines deposited rapidly by a shrinking glacier. At the time of moraine formation, ELA was 46–47 ± 14 m lower than in 2011 (**Figure 4**; Supplementary Table 1).

The *innermost moraine cluster* consists of more than 30 individual moraine ridges deposited in a 200-meter-wide area around 320 m altitude. The two most pronounced ridges are marked M2 and M1 on the map. The ridges are between 0.5 and 1.5 meters high and are strongly asymmetrical, with a much steeper (35°) distal face and gentler (20°) proximal face. The geomorphology of the moraines is very similar to what Lukas (2012) describes as annual moraines formed when the glacier advances and acts as a bulldozer on the sediments in front. Such moraines are observed in front of several mountain glaciers on the peninsulas of north eastern South Georgia, documenting glacier retreat during the past century (Gordon et al., 2008). During the time of moraine formation, ELA was 42 ± 15 and 38 ± 15 m lower than in 2011 (**Figure 4**; Supplementary Table 1).

Based on GPS measurements of the glacier front during our two field campaigns, the glacier front retreated approximately 150 m between January 2008 and December 2011. This suggests that Diamond glacier follows the same pattern of rapid glacier retreat observed on South Georgia, in the sub-Antarctic, in Patagonia and indeed, globally (e.g., Cook et al., 2010; Koppes et al., 2015; Zemp et al., 2015).

In the lower valley, we mapped three moraines, covered by grasses and herbs, which outline past glacier front positions of Neumayer tidewater glacier, which advanced into the valley from the west. Parallel to Cumberland West Bay, a prominent lateral moraine (OM3), 1–4 m in height, sloping from 60 to 45 m altitude is deposited superimposed on a 100 m-high and 1 km long bedrock ridge. About 1 km further north, several cones consisting of diamict material rising above the bog likely represent remnants of a marginal moraine system (OM2). A pronounced ridge along the mountainside between Olsen Valley and the next tributary valley to the west marks a younger glacier advance (OM1). This ridge is between 2 and 6 m high and the material in the ridge is a diamicton of fine sand and boulders up to 40 cm in diameter.

Lake Sediments

Based on the correlation of the MS stratigraphy of the sediment cores from Diamond lake, (**Figure 5**), we argue that core LDP2 is representative for the lake. Piston core equipment sometimes fails to capture the sediment-water interface, and correlation between LDP2 and the gravity core LDS2 (taken from the same location) suggests that this is the case for LDP2. Possible overlaps between LDP2 and LDS2 were tested using a Bayesian cross matching algorithm by Werner and Tingley (2015) (Supplementary Material; Section Age-Depth Modeling), which suggests that 10 cm of the topmost sediments of LDP2 were likely lost during coring. We sub-divide LDP2 into six

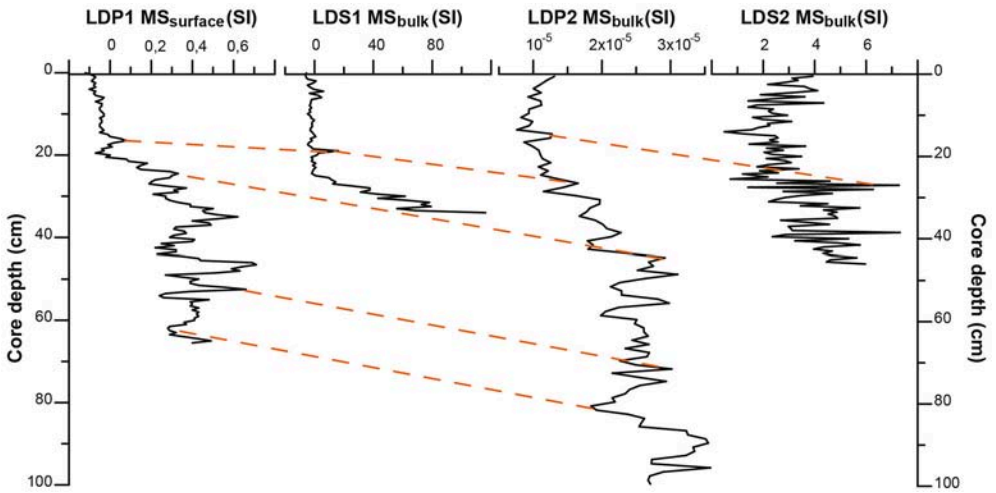

FIGURE 5 | Intrabasin correlation based on the magnetic susceptibility (MS) stratigraphy of the piston cores (LDP1 and upper 100 cm of LDP2) and gravity cores (LDS1 and LDS2) retrieved from Diamond Lake. The stippled orange lines show the implied correlation between the cores.

units (A–F) based on visual logging of the core (**Figure 6A**), and further divides unit F into five sub units (F1–F5) based on visual logging, grain size measurements and χbulk. Below, we give a description of each unit along with the sediment parameters LOI, DBD, χbulk, and Ti XRF count rate which we use to detect changes in the minerogenic vs. organic content in the core. The ratio of χbulk measured at 77 K and 293 K ($\chi bulk_{77K}/\chi bulk_{293K}$) is close to 3.8 throughout the core (**Figure 6A**), indicating that paramagnetic minerals dominate the samples (Lanci and Lowrie, 1997). Most values are in fact higher than 3.8, which is theoretically impossible, but can be explained. We ascribe these high values to the fact that actual temperatures of the samples when measured deviated from either 77 or 293 K, as the room might have been too cold. Samples of weak magnetic susceptibility are more prone to this error.

Unit A

Unit A (243.5–246 cm) is a matrix-supported diamict, consisting of sub-angular clasts with no apparent orientation embedded in a well consolidated very dark gray matrix of clay to very fine sand (**Figure 9**). The clasts range in size from c. 2–20 mm and include one cobble at the bottom of the unit, measuring c. 80 mm across. The unit is characterized by high DBD, χbulk and Ti values [medians of 0.5 g/cm^3, 9.0 × 10^{-8} m^3 kg^{-1} and 1,030 counts per second (cps)], reflecting its high minerogenic content. Based on the poor sorting and the sub-angular clasts, we interpret unit A as glacial till deposited during the last glacier retreat from the coring site.

Unit B

Unit A grades into unit B (223–243.5 cm), a dense, structureless and highly decomposed very dark brown peat with one laminae of sandy silt at 230 cm. The high organic content of the unit is reflected by high LOI values (median of 80 %) corresponding with low values of DBD, χbulk, and Ti (medians of 0.1 g/cm^3, 2.8 × 10^{-8} m^3 kg^{-1} and 80 cps). We interpret unit A to represent a peat bog environment with little (glacio-) fluvial influence.

Unit C

A sharp erosive bedding plane separates unit B from unit C (221.5–223 cm), a very thin bed of dark gray moderately sorted sand, with sub-rounded grains ranging from c. 1–5 mm, and containing one wood fragment (10 mm long, 5 mm in diameter). The unit is best resolved in the high-resolution XRF counts, with high Ti counts around 1,000 cps, reflecting the minerogenic nature of the sediments. Based on the sediment texture and wood fragment, we interpret the unit to represent a flooding event, causing erosion into unit B. According to our age-depth model (**Figure 7**), the resulting unconformity represents a hiatus of ∼2000 years.

Unit D

Unit C has a sharp bedding contact with Unit D (194–221.5 cm), which consists of a dark grayish brown organic-rich silt with grain sizes ranging from clay to medium sand (**Figure 9**). The sediments are well consolidated (median DBD of 0.6 g/cm^3), and small plant fragments are dispersed throughout the unit (median LOI of 11 %). The high minerogenic content is reflected by high median values of DBD, χbulk (7.9 × 10^{-8} m^3 kg^{-1}) and Ti (930 cps) (**Figure 5**). We interpret unit C to represent glacial flour (clay and silt) and reworked sediments (sand) deposited in a lake.

Unit E

A sharp undulating non-erosive bedding contact separates unit D from unit E (185.5–194 cm), which is composed of a poorly sorted very coarse dark gray loosely consolidated sand containing sub-angular pebbles up to 30 mm across and no silt or clay particles. The high minerogenic content is reflected by low LOI values (median of 2%) and high values of DBD (median of 1.1 g/cm^3), Ti (median of 960 cps) and χbulk (one bulk

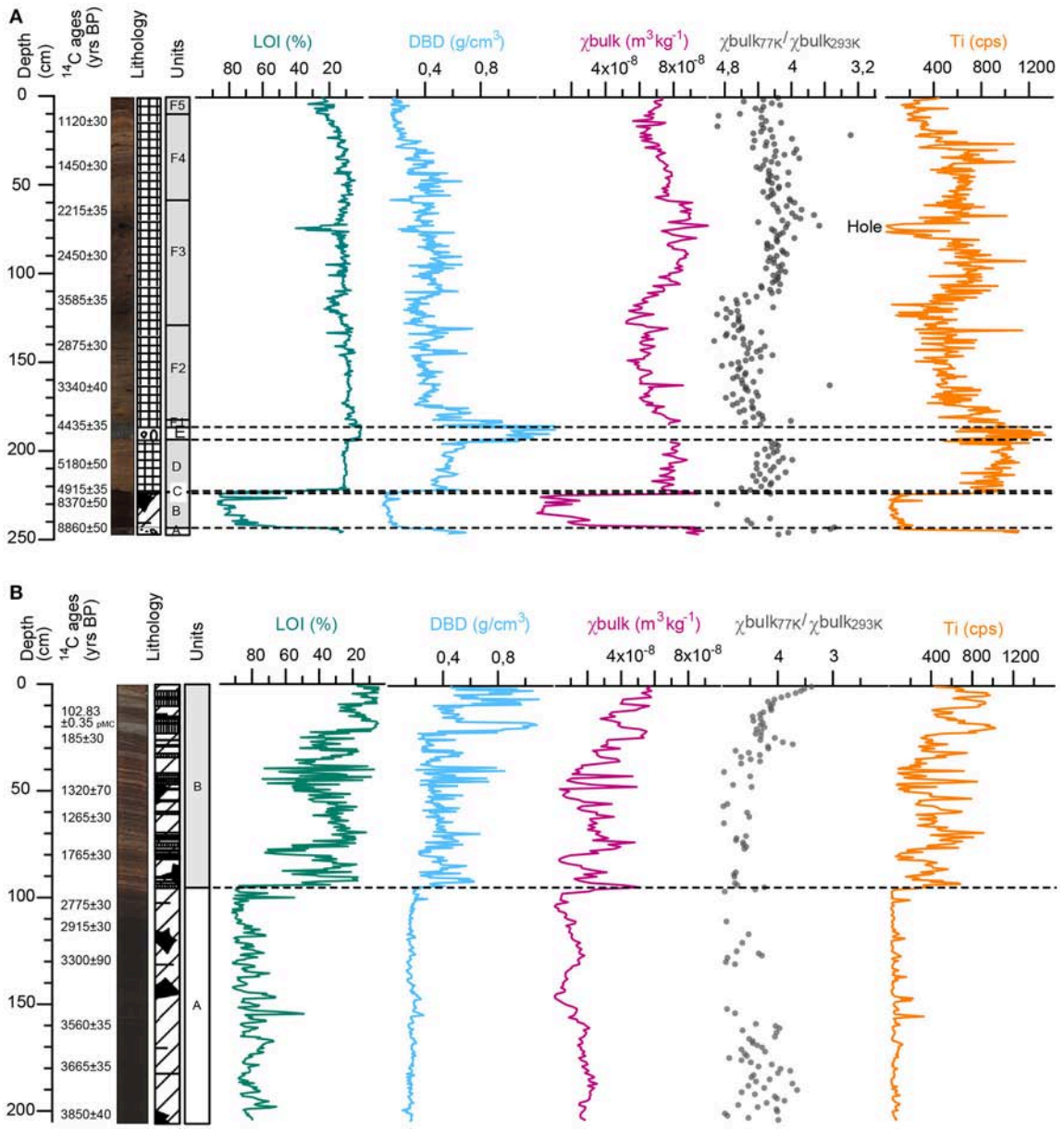

FIGURE 6 | Selected sediment variables from **(A)** LDP2 (Diamond lake) and **(B)** DB2 (Diamond bog). Radiocarbon ages, line-scan images, sedimentary log, lithostratigraphic units, loss-on-ignition (LOI), dry bulk denisty (DBD), mass specific magnetic susceptibility (χbulk), paramagnetic ratio ($\chi bulk_{77K}/\chi bulk_{293K}$) and XRF titanium counts (cps).

measurement of 4.0×10^{-7} m^3 kg^{-1}) (**Figure 5**). We interpret unit E as a slump, formed by mass wasting of sediments from a moraine.

Unit F

Unit F (0–185.5 cm) consists of dark brown to dark grayish brown organic-rich sediments with dominant grain sizes ranging from clay to fine sand. We interpret unit F to represent a lake similar as today, into which the meltwater stream carried glacially eroded silt and clay directly from the glacier, but also remobilized coarser grain fractions as well as terrestrial plants in the catchment during times of high runoff. We argue that the input of minerogenic sediments to the lake is positively correlated with glacier size (Section Reconstructing the Glacier). Based on variations in color, minerogenic content, χbulk, grain size distribution, and organic content, we divide unit F into five sub units (F1–F5).

Unit F1 (185.5–182 cm) is a dark grayish brown organic-rich silty sand displaying similar characteristics as unit D, but is dominated by sand, rather than silt. It was likely deposited under similar environmental conditions as unit D, but also affected by the preceding mass wasting event (Unit E). One grain size

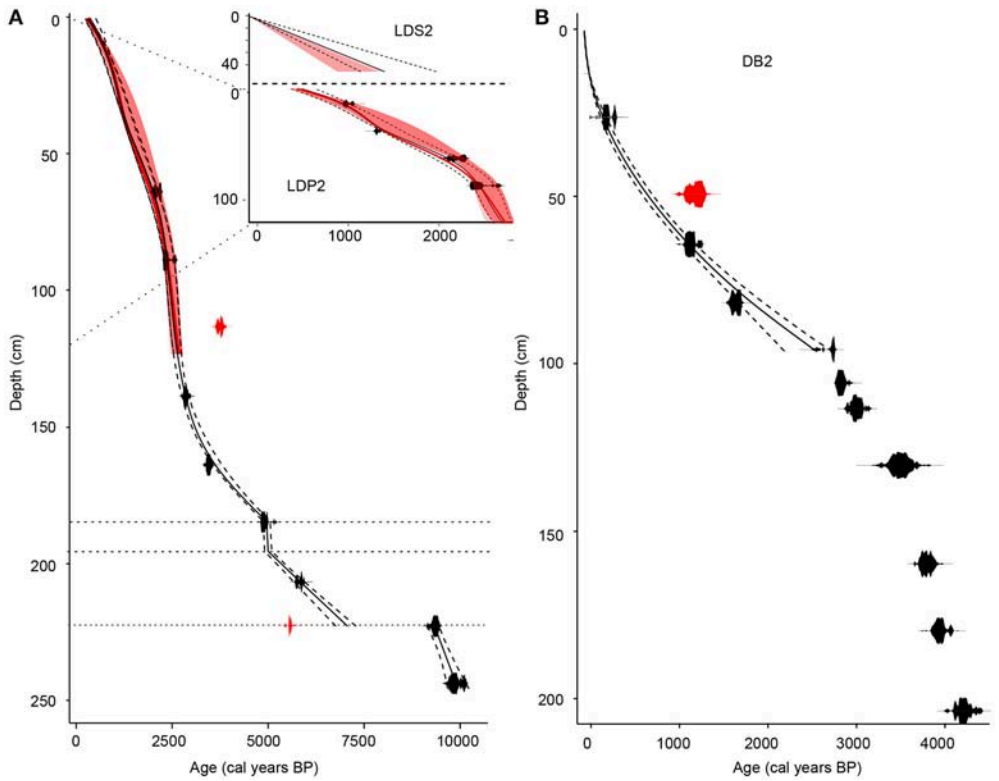

FIGURE 7 | Age-depth models for **(A)** LDP2 and LDS2 (lake), and **(B)** DB2 (bog). Each calibrated ^{14}C age range is shown in black. Outliers are displayed in red. The Clam models are represented by solid black lines, with broken black lines marking the 95% confidence bands. Horizontal stippled black lines mark the slump between 185 and 195 cm, as well as the hiatus at 223 cm in LDP2. The dark red lines mark the best fitting age models for LDS2 and the upper 95 cm of LDP2, which were constrained using Bayesian statistics. Bands in a lighter red and pink shade marks the 50 and 95% confidence intervals, respectively.

measurement at 182 cm shows that very fine sand dominates, and median χbulk is 8.1×10^{-8} m^3 kg^{-1}.

Unit F2 (182–128 cm) consists of consolidated organic-rich sandy silt with a dark grayish brown color, interspersed by lamination of well sorted very fine sand at 181, 153, 148, 146, 137, and 134 cm. Grain size measurements reveal a bimodal distribution with peaks around very fine sand and medium silt (**Figure 9**). The finer fractions indicate input of glacial sediments while the sand is likely remobilized paraglacial sediments from the fan next to the lake. Throughout the unit, χbulk generally decreases. Values are low (median of 6.4×10^{-8} m^3 kg^{-1}), but increases over the sand layers (**Figure 6A**).

Unit F3 (128–58 cm) is a dark brown organic-rich silty sand with high content of moderately decomposed plant fragments. The grain size distribution of four samples (118, 88, 70, and 65 cm) peaks around very fine sand, but silt is also present. χbulk generally increases through the unit (median of 8.0 x 10^{-8} m^3 kg^{-1}). Between 71 and 75 cm, large terrestrial plant fragments (likely the herb *Aceana magellanica/tenera)* are found at the center of the core, probably representing a flooding event, with the high organic content of the layer reflected in a drop in the DBD and χbulk values (**Figure 6A**). Part of this organic material fell out when splitting the core into two half tubes. The resulting hole caused very low XRF counts (190 cps) as the detector was not close enough to the sediment surface (**Figure 6A**). Terrestrial plant fragments are found at several depths in the unit (e.g., 86, 97, 110, and 120 cm). The terrestrial plant remains and coarse grain sizes indicate a high energy system causing remobilization of sediments and terrestrial organic material in the catchment, and subsequent deposition into the lake. While sand settles in the lake, the finer fractions are transported all the way into Cumberland West Bay.

Unit F4 (58–10 cm) is dark grayish brown organic-rich silt. Grain size measurements at 55, 33, 24 and 14 cm show dominating clay and silt fractions. At 44 and 48 cm, fine sand dominates but the finer fractions are also present. In the lower 24 cm χbulk values are comparable to unit D and F1, but starts to decrease from 5.6×10^{-8}40 cm, reaching around 13 cm with χbulk (5.6×10^{-8} m^3 kg^{-1}). We interpret this unit to represent lower energy conditions than in unit F3. The presence of clay and silt indicate input of glacial sediments. According to χbulk glacial input is high, comparable to that of unit D, between c. 58 and 38 cm, but decreases through the rest of the unit. Deposition of remobilized sand occurs at some intervals, indicating events or short periods of higher run-off.

Unit F5 (10–0 cm), consists of dark brown organic-rich silty sand (**Figure 10**) with a high content of woody plant fragments,

increasing toward the top. The grain size distribution of one sample at 3 cm peaks around very fine sand, similar to unit F3, but the silt (and clay) content is a little higher. χbulk increases through the unit from 5.6×10^{-8} to 7.3×10^{-8} m^3 kg^{-1}. We interpret unit F5 to represent a system of increasingly high run-off, where both clay and silt from the glacier as well as remobilized sediments and terrestrial organic material from the catchment are deposited in the lake.

Bog Sediments

During the coring of the DB2, we measured compaction due to the friction in the corer to be ∼16 cm, but since we know little about how the compaction was distributed through the core, we do not attempt to correct for it. We sub-divide DB2 into two units (A and B) based on visual inspection of the core (**Figure 6B**).

Unit A

Unit A (95–204 cm) is composed of dense, highly decomposed black peat with laminations of clayey silt at 100 and 155 cm. The high organic content is reflected in the high median value of LOI (87 %) and low median values of DBD, χbulk and Ti (0.2 g/cm^3, 1.0×10^{-8} m^3 kg^{-1} and 90 cps) (**Figure 6B**). We interpret unit A to represent a peat bog environment with little influence of glacial meltwater.

Unit B

Unit A grades into unit B (0–95 cm), which consists of very dark brown clayey peat interbedded with gray to grayish brown layers of fine minerogenic material and fragments of moss and rootlets. Bedding planes are indistinct, and bed thicknesses vary from <1 mm to 5 cm, with three 3–5 cm thick layers in the upper 25 cm of the unit. Using the XRF count ratio Fe/Ti, we identified 33 minerogenic layers in unit B, which we confirmed by inspection of the sediments. The grain size distribution of four minerogenic layers at 3–5, 6.5–10, 18.5–23, and 73–74 cm, reveal a domination by silt and clay. At the bottom of the unit (94 cm) grain sizes are dominated by very fine to fine sand in addition to a high content of silt and clay. The organic content of the unit is moderately to poorly decomposed, with the degree of decomposition decreasing toward the top of the core which preserves the topsoil. Compared to unit A, the measured sediment parameters show higher variability in Unit B, reflecting the variable content of minerogenic vs. organic material. LOI varies between 4 and 88%, DBD varies between 0.2 g/cm^3 and 1.1 g/cm^3, χbulk varies between 3.0×10^{-9} m^3 kg^{-1} and 5.8×10^{-8} m^3 kg^{-1}, and Ti varies between 210 cps and 1460 cps. The paramagnetic ratio is close to 3.8 throughout the unit (**Figures 6B**, **10**), indicating one main sediment source (Section Lake Sediments). This, together with the grain size distribution of the minerogenic layers and the transport of glacial meltwater through the bog in a deep channel, suggests that the minerogenic layers in the bog are composed of glacial sediments. We interpret unit B as a peat bog environment such as today, where glacially eroded sediments are deposited onto the bog when the river overflows its banks. The high content of sand in the bottom of the unit concurs in time with the increased sand input to the lake (Section Reconstructing the Glacier) and infers higher energy in the system.

Age-Depth Modeling

We established age-depth relationships for LDP2, LDS2, and DB2 (**Figure 7**) in the following steps (for more details on the approach see Supplementary Material):

1) Based on the 24 radiocarbon ages (**Table 2**; **Figure 6**) we constructed independent age-depth models for LDP2 and DB2 using the software Clam 2.2 (Blaauw, 2010), with the SHCal13 calibration curve (Hogg et al., 2013) and post-bomb curve 4 for zones 1–2 (Hua et al., 2013), generating 2000 iterations for each core. Owing to stratigraphically inverted ages, we excluded radiocarbon samples Poz-52659 (LDP2), Poz-74625 (LDP2), and Poz-52673 (DB2) from the age models (**Table 2**). Poz-52659 and Poz-52673 were excluded based on their improbable old ages and the small sample size of Poz-52673. We chose to exclude Poz-74625 rather than Poz-52664 because we deem the resulting sedimentation rate to be more likely as visual inspection of the sediments reveal no major changes in this interval. We interpret and treat unit E (185.5–194 cm) in LDP2 as a slump (section Lake Sediments) because of its gravel content and erosional contact with unit D. Based on the sudden jump in age, we infer an unconformity between unit B and C. We therefore made one set of age models for units D-F (upper 221 cm), and one for unit B. To obtain the best goodness-of-fit, we applied a smooth spline interpolation for the upper 221 cm (**Figure 7A**). With only two ages in unit B, we were left with the option of linear interpolation between them. We constrained the DB2 age model by an assumed surface age of −61 year. BP (2011 AD), the year of coring. Owing to the low concentration of minerogenic sediments in unit A, we only use unit B in step 2 and 3 below. We therefore applied a smooth spline interpolation between the ages for unit B only (**Figure 7B**).
2) Assuming that both cores are now on correct age scales, they likely record the same minerogenic events. We used the ratio of Fe/Ti to identify 33 minerogenic layers in the upper 95 cm of DB2 (Supplementary Figure 2), and compared them to sediments in LDP2 representing the same age intervals. In **Figure 8**, we show the Fe/Ti ratios of the minerogenic layers in DB2 vs. the Fe/Ti ratios for the corresponding layers in LDP2. Based on the good correspondence between the two records, we argue that we can use the age model of DB2 to further constrain the last 2700 years of the age model of LDP2.
3) We used a modified version of the algorithm by Werner and Tingley (2015), to statistically cross-match LDP2 and DB2, and further constrain the uncertainties of the LDP2 age model. The motivation behind the algorithm is that the variables of the records should respond to the same environmental driver—in this case glacier fluctuations—and that thus the common variability expressed in the used variable can be used to cross-match the cores within the allowed uncertainties of the age-depth models. The result of the cross-matching is shown in Supplementary Figure 3.

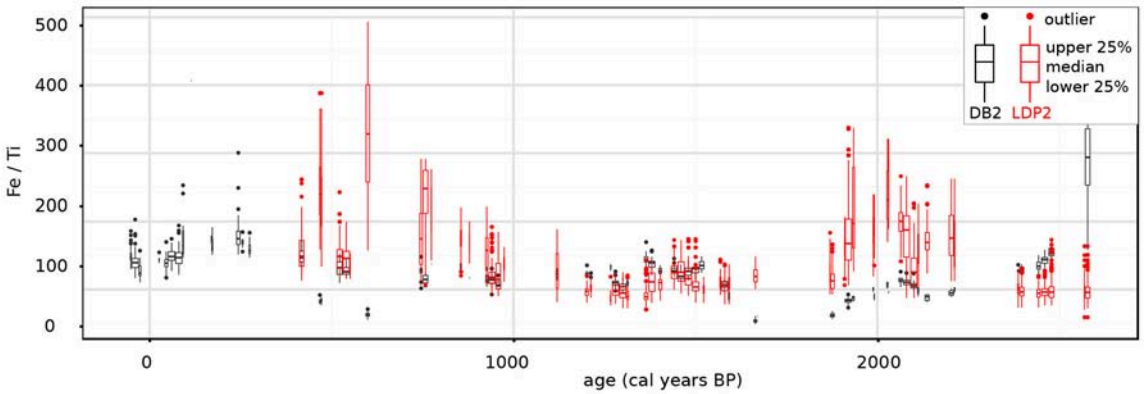

FIGURE 8 | Comparison of layers with high minerogenic content in DB2 (black) with sediments corresponding to the same time intervals in LDP2 (red), covering the past 2700 years. We used high-resolution XRF counts (0.02 cm) to be able to resolve the layers, which are here represented by Fe/Ti. The box plots indicate the range of Fe/Ti values within each layer. The width of the box plots indicate the thickness of each layer. DB2 extends beyond LDP2 due to the missing topmost sediments of LDP2.

4) From cross-matching LDP2 and LDS2 by eye (**Figure 5**), we argue that the top sediments of LDP2 are missing. In order to extend LDP2 to the present, we constructed an age model for the undated core LDS2 based solely on the sedimentation rates inferred for LDP2. Using the aforementioned algorithm, we tried to reconcile the possible age models for LDP2/LDS2 (Supplementary Figures 5, 6).

DISCUSSION

Reconstructing the Glacier

There is a long tradition for utilizing downstream basins as sedimentary archives for reconstructing glaciers dating back to pioneering work by Karlén (1981). Since these early studies, progress have been made regarding the methodological tool-kit invoked in order to track past glacier activity (e.g., Bakke et al., 2010) as well as tools for precise modeling of the age-depth relationship based on ^{14}C dates, ^{210}Pb dates and tephra (Blaauw, 2010) ensuring robust chronologies. One of the challenges with lake-based glacier reconstructions is the necessity of recognizing various catchment processes that potentially can impact downstream sedimentary records (Rubensdotter and Rosqvist, 2005; Bakke and Paasche, 2011). To disentangle the different processes acting on the archives, it is increasingly common to employ multiple proxies (e.g., Bakke et al., 2010; Vasskog et al., 2012). Sediment variables, commonly reflecting the glacial signal include elements such as Si, K, Ca, Ti, Fe, Rb, and Zr (Davies et al., 2015), variations in bulk organic matter as given by loss-on-ignition (e.g., Karlén, 1976), DBD (e.g., Bakke et al., 2005) and grain size (e.g., Matthews and Karlén, 1992), as well as a range of magnetic properties (e.g., Paasche et al., 2007). In this study, we use mass specific magnetic susceptibility (χbulk) as an indicator of change in the suspended glacigenic input to the bog and lake. Magnetic susceptibility is a measure of the magnetic minerals in a sample which is closely related to the concentration of minerogenic material (Thompson et al., 1975; Thompson and Oldfield, 1986). The approach of using χbulk as a proxy for glacier variations is validated by the positive correlation of χbulk with DBD, surface magnetic susceptibility and common detrital elements such as K, Ca, Ti, V, Mn, Fe, and Sr (Supplementary Table 2).

Olsen Valley represents a relative simple system where a single river drains a small upstream cirque glacier, feeding meltwater through the lower valley from a point source. Given the high ablation season temperatures (mean $T_{Oct-Apr} = 3.6^{\circ}C$) we assume that the glacier is temperate and also remained temperate during the period covered by our sediment record (last 7200 years). We neither find geomorphological evidence, such as ice-cored moraines, that the glacier was cold based or polythermal during this period, nor are such previously reported from the island. For the sake of comparison, polytemperate glaciers in Scandinavia and Greenland typically have mean ablation temperatures around 1°C or colder (Østrem et al., 1988; Weidick, 1992). Such a decrease in temperature is highly unlikely for the Holocene on South Georgia, as indicated by the GDGT temperature record by Foster et al. (2016) and the δD temperature record from the Antarctic Peninsula by Mulvaney et al. (2012). The size variations of temperate glaciers are typically positively correlated to the production and evacuation of glacial sediments (Herman et al., 2015).

We regard the minor minerogenic content in the bog during the late Holocene climate optimum (4800 ± 200 to 2700 ± 150 cal BP, section Glacier retreat: 4800 ± 200 to 2700 ± 150 cal BP), when the glacier is inferred to be very small, as evidence that the glacier is the main driver of the sediment variability in the bog (Matthews et al., 2005). The sediment influx to the bog and lake is predominantly associated with the ablation season (summer) when increased runoff causes the river to transport and subsequently deposit glacial flour in the bog and lake. Based on the low mean summer precipitation (mean $P_{JJA} = 105$ mm), we argue that the additional extra-glacial sedimentary delivery from the other parts of the catchment is small compared to that which stems from glacial meltwater. There exsists no record of extreme precipitaiton events from South Georgia, however such events

can cause inwash of inorganic sedimentation to our sites and is a possible error source for our interpretations. Sitting in a gently sloping valley covered by vegetation, we consider mass wasting processes not likely to affect the bog and lake.

While the gently sloping part of the valley is covered by peatland, thereby limiting the possibility of reworking of older sediments (paraglacial activity), glacigenic deposits closer to the glacier, as well as in three fans deposited in the lower valley, are potentially available for erosion and thus re-mobilization (Ballantyne, 2002). This could potentially be a source of error when using the sediments to reconstruct the up-valley glacier. Still, since sedimentation into the bog and lake happens mainly during the ablation season, we argue that re-deposition of paraglacial sediments would only reinforce the glacier signal rather than distort it. The presence of fine sand in the lake (**Figure 9**) indicates that there is indeed a paraglacial component present. These sediments are likely remobilized from the alluvial fan to the west of the lake during periods of high runoff. This is supported by the domination of clay and silt in the bog, which is located up valley from the fan, suggesting low paraglacial input. Sand in the bog is limited to an interval between 93 and 95 cm (c. 2700–2400 cal BP). This interval concurs in time with increased sand input to unit F3 (2700 ± 150–2000 ± 200), suggesting that both lake and bog received paraglacial sediments from up valley sources (likely the alluvial fans) between 2700 ± 150 and 2000 ± 200 cal BP when runoff was at its highest in the last 7200 years.

Seeing as both the bog and lake receive input of glacigenic material during periods of high river discharge, we claim that the two records should co-vary in phase over time. This assumption is confirmed in **Figure 8**, which shows increased χbulk in LDP2 corresponding in time with the 33 silt layers identified in DB2. This relationship serves to validate the lake record and demonstrates the potential in using distal-glacier fed bogs as archives of glacier variability. Other lines of evidence also suggest that the lake and bog capture the same glacial history. The paramagnetic ratios ($\chi bulk_{77K}/\chi bulk_{293K}$) of LDP2 and DB2 indicate that both records are dominated by paramagnetic minerals (Lanci and Lowrie, 1997) (**Figure 11**; section Lake Sediments) and that this doesn't change during the period in question. This shows that the minerogenic material deposited in the lake and bog derives predominantly from one source only, unless one assumes that the signal is the same for the entire catchment, which is unlikely considering the geological processes involved. Further supporting evidence is the overlapping grain size distributions of the bog and lake. Characteristic of glacial flour, we argue that the source of the minerogenic and fine-grained sediments is erosion by the Diamond glacier, which, drawing from moraine evidence, was present in the catchment during the Holocene.

The mapped moraines in front of Diamond glacier provide spatial constraints for the glacier fluctuations reconstructed from the sediments, as we arguably detect the documented glacier advances of the LIA and in the 1930s both in the sediment records and in the moraine sequence. Based on previous studies from South Georgia, we argue that M1 was deposited during the 1930s while M2 was deposited during the Little Ice Age (LIA). An extensive glacier advance during the LIA (seventeenth to ninetieth centuries) is well-documented on the peninsulas of northeastern South Georgia (Gordon and Timmis, 1992). Clapperton et al. (1989b) estimate an average ELA depression of c. 50 m during this period, corresponding with a cooling of 0.5°C. Within the uncertainty range, this is comparable to the ELA of M2. Proximal to the LIA moraine it is common to find a moraine deposited during the twentieth century (Gordon and Timmis, 1992). This advance was documented by historical evidence (Hayward, 1983), showing that many glaciers advanced in the twentieth century. Cirque and valley glaciers were at its most advanced position in the 1930s, while larger valley and tidewater glaciers reached their maximum glacier extent in the 1970s. Such a glacier advance is also documented for the Hamberg glacier by Van Der Bilt et al. (2017). Furthermore, during the recession phase after the twentieth century advance, many cirque glaciers deposited annual moraines (Gordon and Timmis, 1992), such as the ones observed in the innermost moraine cluster. Thus, Diamond glacier followed a similar pattern to that observed for small glaciers (0.1–4.0 km^2) on South Georgia during the late Holocene, with a Little Ice Age advance, a period of recession, a twentieth century advance and a recent recession (Gordon and Timmis, 1992). Based on the lake sediments, we argue that M8 and M9 were deposited prior to lake formation 7200 ± 400 years ago. We assume that the glacier would produce a distinctly higher χbulk in the lake at this time (being 30% larger than the glacier which deposited M7). The lake record, however, indicates that the glacier repeatedly reached close to its maximum Holocene position (**Figure 11**).

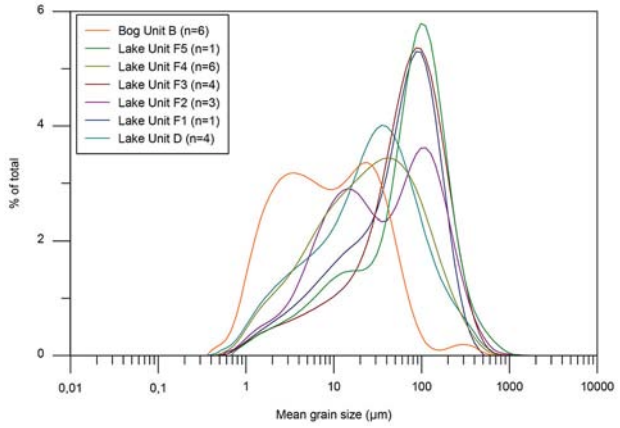

FIGURE 9 | Distribution of mean grain-size values of the analyzed samples (n) in unit D and F1–F5 of Diamond lake as well as Unit B of Diamond bog.

Holocene Glacier Variability in Olsen Valley

In the following we present the reconstructed Holocene glacier variability in Olsen Valley as interpreted from the lake and bog sediment records and linked to the moraine sequence based on previous studies of glacier front positions on South Georgia (section Reconstructing the Glacier). We use χbulk as a proxy for glacier size, except in the topmost part of the lake record where we use κbulk (see section Sample Treatment and

Laboratory Analyses). Since we combine two different measures of magnetic susceptibility in the lake, we standardize the χbulk and κbulk results (**Figure 11A**). To account for glacier response time, we apply 30-year bins in the presentation of the glacier reconstruction following Van Der Bilt et al. (2017).

Deglaciation of Lower Olsen Valley: <9900 ± 250 cal BP

Based on the onset of peat accumulation in Diamond lake, lower Olsen valley was ice free prior to 9900 ± 250 cal BP. We argue that the diamicton found in Unit A (LDP2) was deposited by the Neumayer Glacier, as moraines OM2 and OM3 outline a glacier advance from the west (**Figure 2B**) (Bentley et al., 2007). This is supported by the slightly lower values of $\chi bulk_{77K}/\chi bulk_{293K}$ in Unit A compared to the rest of the record (**Figure 6A**), indicating a different sediment source. A retreat of Neumayer Glacier from Olsen Valley before 9900 ± 250 cal BP agrees with radiocarbon dates of peat and lake bases in the Cumberland Bay and Stromness Bay area (cf. Van Der Putten and Verbruggen, 2005) suggesting that the lower zone (<50 m a.s.l.) was deglaciated in in the first centuries of the Holocene.

Marine evidence connects OM1 and OM2 to the glacier retreat following the Antarctic Cold Reversal on South Georgia (15 170–13 340 cal BP). Hodgson et al. (2014) document a partially preserved moraine in the outer basin of Cumberland West Bay (**Figure 2A**). This moraine is associated to the Antarctic Cold Reversal advance on South Georgia by Graham et al. (2017) who dated the transition from subglacial to ice-proximal sediments in a core taken through the equivalent moraine in Cumberland East Bay to 13,340 cal BP. Another date from the same sediment core suggests nearby glacier sources at the outer basin moraine until c. 10,600 cal BP (Graham et al., 2017). Based on the above dates, we suggest that OM2 and OM3 were deposited between c. 10,600 and 9900 ± 250 cal BP.

Glacier Advance: 7200 ± 400 to 4800 ± 200 cal BP

We have evidence of continuous peat formation and dry land conditions until 9350 cal BP, but the unconformity between unit C and D makes it difficult to establish when the lake formed, as we have no account of what happened between 9350 and 7200 ± 400 cal BP. The period between 7200 ± 400 and 4800 ± 200 cal BP (unit D) is characterized by high input of clay and silt (**Figure 9**). Characteristic of glacial flour, these fine-grained sediments were transported in suspension by glacial meltwater directly from the glacier. We interpret the high χbulk values to represent a glacier close to its maximum Holocene position (**Figure 11A**). In line with our findings, evidence from bryophytes and seeds on nearby Tønsberg Peninsula (**Figure 2A**; Van Der Putten et al., 2004) suggests cold and wet conditions between 7000 and 4000 years BP, which would favor glacier a during this period.

Glacier Retreat: 4800 ± 200 to 2700 ± 150 cal BP

From 4800 ± 200 cal BP χbulk decreases and remains low until 2700 ± 150 cal BP (Unit F2, **Figure 6A**, **Figure 11A**). In Diamond Bog median LOI is close to 90% (**Figure 6B**), suggesting that the bog was isolated from meltwater input (**Figure 10**). However, the presence of clay and silt in Diamond Lake (**Figure 9**) suggests that the glacier was present in the catchment, and had not completely melted away. Evidence for a contemporaneous Late Holocene climate optimum on South Georgia has been found in several studies, reporting reduced glacier activity (Rosqvist and Schuber, 2003) higher temperatures (Clapperton et al., 1989a; Strother et al., 2015; Foster et al., 2016) and a drier climate (Van Der Putten et al., 2004, 2009). Paleoclimatic records from other sub-Antarctic locations such as the Antarctic Peninsula (Sterken et al., 2012), Livingstone Island (Björck et al., 1991), South Shetland Islands (Björck et al., 1993), and James Ross Island (Mulvaney et al., 2012) demonstrate consistent climate change over a wide region.

Glacier Advance: 2700 ± 150 to 2000 ± 200 cal BP

From 2700 ± 150 cal BP we see a sudden shift in the sedimentary regime of both the bog and the lake. Large amounts of sand and silt suddenly starts to wash into the bog (**Figure 6B**). Sand, silt and terrestrial plants are deposited in the lake (Unit F3, **Figure 6A**), and modeled sedimentation rates increase in both records (**Figure 7**). We interpret this shift to mark a sudden transition from warm and dry climate conditions with restricted glaciation to a wetter and colder period favoring glacier advance. The energy in the hydrological system of the valley is high, as indicated by the coarser grain fractions and the input of terrestrial organic material, and the contribution of precipitation vs. glacier advance to the increased χbulk values are difficult to disentangle. However, based on the sensitive response of present cirque glaciers on South Georgia (Van Der Bilt et al., 2017), we find it likely that Diamond glacier advanced within short time after 2700 ± 150 cal BP. The change in the sediment records coincides with a shift in climatic conditions, which is recorded in various proxy records from South Georgia. Clapperton et al. (1989a) dated moraines on north-central South Georgia to around 2000 cal BP. Rosqvist and Schuber (2003) document cirque glacier advance at the same time in Husvik (**Figure 2A**), while evidence from changes in pollen and macrofossils from Tønsberg Peninsula (**Figure 2A**; Van Der Putten et al., 2004, 2009) and Annenkov Island (**Figure 1**; Strother et al., 2015) mark a sudden change in vegetation in response to cooler and wetter conditions from around 2700 cal BP, and Foster et al. (2016) infer cooling on Annenkov Island based on glycerol dialkyl glycerol tetraethers (GDGTs) (**Figure 11E**). The shift to a cool and wet climate around 2700 cal BP also falls in line with evidence of a major glacier advance prior to 2600 cal BP in the south-central Andes (Grosjean et al., 1998). On James Ross Island, temperatures starts to decrease after 3000 cal BP (Mulvaney et al., 2012; **Figure 11F**), while evidence of peat growth initiation since 2800 cal BP suggests warmer summers in the western Antarctic Peninsula (Yu et al., 2016), demonstrating the Antarctic dipole (Yuan, 2004).

Glacier Retreat: 2000 ± 200 to 1000 ± 200 cal BP

Clay and silt dominate the sediments deposited in Diamond bog and Diamond lake between 2000 ± 200 cal BP and 1000 ± 200 cal BP clay (Unit F4, **Figures 6A**, **Figure 11A**). The decrease in relative sand content indicates lower runoff, and a gradual decrease in χbulk suggests glacier retreat back to

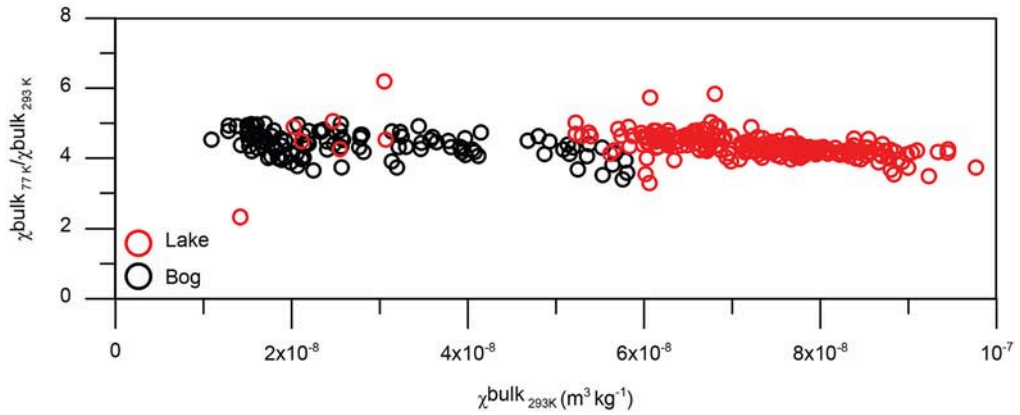

FIGURE 10 | The mass specific magnetic susceptibility ($\chi bulk_{293\,K}$) plotted against the paramagnetic ratio ($\chi bulk_{77\,K}/\chi bulk_{293\,K}$) for the lake (red) and bog (black) sediments show that both records are dominated by paramagnetic minerals, indicating one main sediment source.

mid-Holocene conditions (**Figure 11A**). This coincides with cirque glacier retreat in neighboring Husvik (**Figure 2A**), as demonstrated by Rosqvist and Schuber (2003) (**Figure 11C**) and higher temperatures at the western Antarctic Peninsula inferred from changes in peat growth (Yu et al., 2016).

Glacier Advance: 1000 ± 200 to 300 ± 100 cal BP

From 1000 ± 200 to 600 ± 100 cal BP there is a gradual increase in χbulk (**Figure 11A**), which we interpret as glacier advance based on the dominating clay and silt fractions in this interval. Between 500 ± 150 and 300 ± 100 cal BP, a sharp rise in χbulk and a higher concentration of sand and terrestrial plant fragments, suggests higher runoff. Peaking around 400 ± 150 cal BP, we interpret the increase in χbulk to represent the LIA. This glacier advance is also evident from the bog record, where a 4.5 cm thick silt layer with high χbulk values was deposited at 450 ± 200 cal BP. The LIA is also captured by Van Der Bilt et al. (2017) at 300 cal BP (**Figures 11A,B**) and widely documented on the island (e.g., Clapperton et al., 1978, 1989a,b; Gordon and Timmis, 1992; Roberts et al., 2010). Clapperton et al. (1989b) estimated an average ELA depression of 50 m during the LIA on the northeast coast of South Georgia. If applied to our site, the LIA moraine of Diamond glacier is likely represented by moraine M2 (Section Reconstructing the Glacier; **Figure 2B**). Coinciding with the LIA advance, Foster et al. (2016) document rapid cooling from c. 400 cal BP on Annenkov Island, and a millennial-scale cooling trend on James Ross Island culminates at c. 400 cal BP (Mulvaney et al., 2012) (**Figures 11E,F**).

Twentieth Century Glacier Advance

Increased χbulk suggests a recent glacier advance during the twentieth century. In the lake record, χbulk increases from AD 1920 ± 10 years, while a silt layer in the bog is dated to AD 1950 ± 10 years. Being a cirque glacier, we argue that Diamond glacier likely advanced in the 1930s, which is the case for cirque and small valley glaciers across the northeastern coast of South Georgia (Hayward, 1983; Gordon and Timmis, 1992; Gordon et al., 2008). The advance concurs with a drop in temperature to 3.3°C (AD 1931) at Grytviken compared to the mean summer temperature (Dec-Feb) of 4.9 ± 0.8°C (1905–2016), and is also recorded in Middle Hamberg lake (Van Der Bilt et al., 2017). According to Landsat imagery, Neumayer Glacier retreated 5600 m between 1999 and 2016 (Pelto, 2016), and we know from our field measurements that Diamond glacier front retreated approximately 150 m between 2008 and 2012. The glacier retreat is reflected in the lake sediments by decreasing χbulk (**Figure 11A**) in the topmost sediments, although not as clearly as in Van Der Bilt et al. (2017)'s record from Middle Hamberg lake (**Figure 11C**). Remobilization of paraglacial sediments in front of the rapidly retreating Diamond glacier, might mask the glacial signal in the lake and bog sediments during the paraglacial period, which typically lasts 10–50 years after a glacier retreat (Bakke et al., 2009). The ongoing glacier recession on South Georgia is well documented by observational data (Gordon et al., 2008; Cook et al., 2010) and follows a pattern of warming and glacier retreat observed from Patagonia to the Antarctic Peninsula (Koppes et al., 2015) as well as the rests of the world (Zemp et al., 2015).

Glacier Variability on South Georgia vs. Patagonia

The glacier reconstruction from Olsen Valley suggests that Diamond glacier was close to its maximum Holocene extent between 7200 ± 400 and 4800 ± 200 cal BP, 2700 ± 150 and 2000 ± 200 cal BP, 500 ± 150–300 ± 100 cal BP, and in the 1930s. Bertrand et al. (2012) provide a continuous glacier reconstruction from the Northern Patagonian Icefield based on a multiproxy analysis of a fjord sediment core, revealing repeated episodes of centennial scaled glacier advance over the past 5000 years (**Figure 11D**). The two records thus vary on a similar frequency and both show increased glacier activity during the last millennia. The glacier fluctuations documented by Bertrand et al. (2012) seem to be alternately in- and out of phase with those of Diamond glacier, although we find it too early to conclude about timing due to differing glacier response times and dating uncertainties. In general, the two records correspond best during periods of

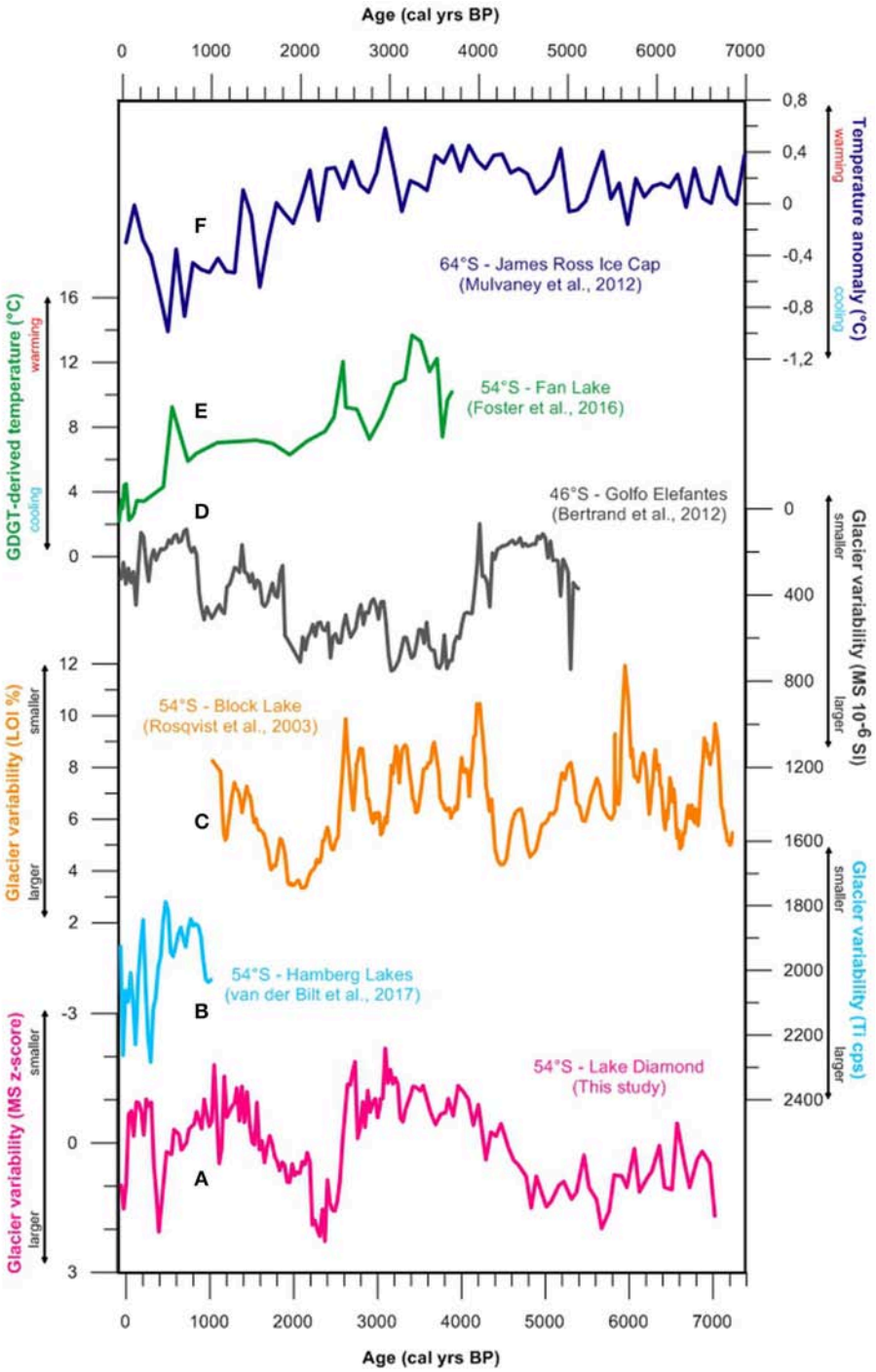

FIGURE 11 | Comparison between our glacier reconstruction for Diamond glacier **(A)** and records of glacier variability on South Georgia from Block lake (Rosqvist and Schuber, 2003) **(B)** and Middle Hamberg lake (Van Der Bilt et al., 2017) **(C)**, and Golfo Elefantes in Northern Patagonia **(D)** (Bertrand et al., 2012), a GDGT-derived temperature curve from Fan lake, Annenkov Island, South Georgia **(E)** (Foster et al., 2016), and δD-derived temperature anomalies relative to the 1961-1990 mean from James Ross Ice Cap, Antarctic Peninsula **(F)** (Mulvaney et al., 2012).

major glacier advance such as prior to 2000 cal BP, the LIA and the twentieth century advance, while they are out of phase on a millennial time scale during the mid-Holocene (**Figures 11A,D**). We speculate that the latitudinal expansion of the westerlies during cold phases causes both sites to be influenced by the same wind circulation system (Lamy et al., 2010), improving

the correspondence of the glacier records during these periods. There are also other records from Patagonia to compare with. It turns out that the timing of South Georgia glacier advances concur with several of the Holocene glaciations of the Patagonian Icefield suggested by Anyia (2013) and Strelin et al. (2014), particularly since c. 2700 cal BP. Anyia (2013) proposes five Neoglacial episodes: at 4500–4000 cal BP, 3600–3300 cal BP, 2700–2000 cal BP, 1600–900 cal BP and in the seventeenth to nineteenth centuries century. Based on surface exposure dating, Strelin et al. (2014) suggest six Holocene glacier advances of the Southern Patagonian Icefield at 7700–7200 cal BP, 6000–5000 cal BP, 2500–2000 cal BP, 1500–1100 cal BP >400 cal BP and <300 cal BP. The covariance between South Georgia and Patagonian glacier fluctuations on centennial time scales points to shared regional climate forcing, possibly related to persistent changes in the Southern Hemisphere westerlies which arguably can have a large impact on local variations in precipitation and temperature (cf. Moreno et al., 2014).

CONCLUSIONS

A 7000-year long continuous cirque glacier reconstruction, based on analyses of glacier-fed lake and bog sediments from the same catchment, suggest that glaciers on South Georgia have varied on centennial time scales for the time interval in question. Evidence for this pattern of variability is obtained by employing the same combination of magnetic, physical, and geochemical sedimentary analyses on the two independently dated sediment archives from the bog and lake, which in sum have enabled us to reproduce the history of the cirque glacier and precisely constrain the timing of the glacier fluctuations. A set of marginal moraines in the catchment outline the past extent of the Neumayer tidewater glacier, which probably filled the lower valley during the Late-Pleistocene, and subsequently advanced to a position just west of Olsen Valley several times, including the past century. In front of the cirque glacier, a mapped moraine sequence provide spatial constraints to the continuous glacier reconstruction. Reconstructed ELAs demonstrate that the recent glacier retreat stands out in a Holocene context although changes are within 100 m altitude. Based on the combination of two different glacial sedimentary archives, a consistent picture emerges of the Holocene glacier evolution in the studied catchment; characterized by deglaciation some time prior to 9900 ± 250 cal BP, and glacier advance close to its maximum Holocene extent between 7200 ± 400 and 4800 ± 200 cal BP, 2700 ± 150 and 2000 ± 200 cal BP, 500 ± 150–300 ± 100 cal BP, and in the 1930s. Changes in glacier size is constrained by a sequence of moraines in front of the cirque glacier. The reconstructed glacier fluctuations agrees with existing moraine chronologies, two previous continuous glacier reconstructions and various paleoclimate records on South Georgia, highlighting the ability of these sedimentary records to capture concordant shifts. Moreover, the centennial scaled glacier variability documented here are largely in-phase with patterns of retreat and advance of Patagonian glaciers, especially during the past three millennia, although caution is warrant due to chronological uncertainties. This, nevertheless, points to large-scale climate shifts potentially linked to the Southern Hemisphere Westerlies, although this is something that requires further studies before any solid conclusions can be drawn.

AUTHOR CONTRIBUTIONS

JB, ØP, and LO were responsible for the conceptual design of the work. JB and ØP mapped and the study area in 2008, and JB and colleagues further mapped the catchment and cored the lake and bog in 2012. LO performed the laboratory analyses, and lead the writing and compilation of figures and tables. All authors have given substantial contributions to the interpretations of the data and the writing of the article. In cooperation with LO and JW performed the age-depth modeling and statistical cross-matching (**Figures 7**–**8**), and WvdB designed the maps (**Figures 1**–**3**). All authors approve of the submitted version of the manuscript and thereby agree to be accountable for all aspects of the work, ensuring that questions related to the accuracy or integrity of any part of the work are appropriately investigated and resolved.

ACKNOWLEDGMENTS

This is a contribution from the project "Shifting Climate States of the Polar Regions," funded by the Norwegian Research Council (Grant 210004). We would like to thank Anne Bjune, Bjørn Christian Kvisvik, Åsmund Bakke, Sunniva Solheim Vatle, and Thom Whitfield for their effort during fieldwork, and British Antarctic Survey for their field support. We would also like to thank Sven Lukas and Gunhild Rosqvist for contributing to the manuscript, and Lubna S. J. Al-Saadi and Eivind W. N. Støren for help with grain size measurements. Finally, thank you to reviewers Olga N. Solomina and Bethan J. Davies, whose comments helped improve and clearify the manuscript.

SUPPLEMENTARY MATERIAL

The Supplementary Material for this article can be found online at: https://www.frontiersin.org/articles/10.3389/feart.2018.00002/full#supplementary-material

REFERENCES

Anyia, M. (2013). Holocene glaciations of Hielo Patagónico (Patagonian Icefield), South America: a brief review. *Geochem. J.* 47, 98–105. doi: 10.2343/geochemj.1.0171

Bakke, J., Dahl, S. O., Paasche, Ø., Simonsen, J. R., Kvisvik, B., Bakke, K., et al. (2010). A complete record of Holocene glacier variability at Austre Okstindbreen, northern Norway: an integrated approach. *Quat. Sci. Rev.* 29, 1246–1262. doi: 10.1016/j.quascirev.2010.02.012

Bakke, J., Lie, Ø., Heegaard, E., Dokken, T., Haug, G. H., Birks, H. J. B., et al. (2009). Rapid oceanic and atmospheric changes during the Younger Dryas cold period. *Nat. Geosci.* 2, 202–205. doi: 10.1038/ngeo439

Bakke, J., Lie, Ø., Nesje, A., Dahl, S. O., and Paasche, Ø. (2005). Utilizing physical sediment variability in glacier-fed lakes for continuous glacier reconstructions

during the Holocene, northern Folgefonna, western Norway *Holocene* 15, 161–176. doi: /10.1191/0959683605hl797rp

Bakke, J., and Paasche, Ø. (2011). "Sediment core and glacial environment reconstruction," in *Encyclopedia of Snow, Ice and Glaciers*, eds V. P. Singh, P. Singh, and U. K. Haritashya (Dordrecht: Springer).

Balco, G. (2009). The geographic footprint of glacier change. *Science* 324, 599–600. doi: 10.1126/science.1172468

Ballantyne, C. K. (1989). The loch lomond readvance on the isle of skye, scotland: glacier reconstruction and paleoclimatic implications. *J. Quatern. Sci.* 4, 9–108. doi: 10.1002/jqs.3390040201

Ballantyne, C. K. (2002). Paraglacial geomorphology. *Quat. Sci. Rev.* 21, 1935–2017. doi: 10.1016/S0277-3791(02)00005-7

Bentley, M. J., Evans, D. J. A., Fogwill, C. J., Hansom, J. D., Sugden, D. E., and Kubik, P. W. (2007). Glacial geomorphology and chronology of deglaciation, South Georgia, sub-Antarctic. *Quat. Sci. Rev.* 26, 644–677. doi: 10.1016/j.quascirev.2006.11.019

Bertrand, S., Hughen, K. A., Lamy, F., Stuut, J.-B. W., Torrejón, F., and Lange, C. B. (2012). Precipitation as the main driver of Neoglacial fluctuations of Gualas glacier, Northern Patagonian Icefield. *Clim. Past* 8, 1–16. doi: 10.5194/cp-8-1-2012

Björck, S., Håkansson, H., Olsson, S., Barnekow, L., and Janssens, J. (1993). Paleoclimatic studies in South Shetland Islands, Antarctica, based on numerous stratigraphic variables in lake sediments. *J. Paleolimnol.* 8, 233–272. doi: 10.1007/BF00177858

Björck, S., Håkansson, H., Zale, R., Karlén, W., and Jönsson, B. L. (1991). A late Holocene lake sediment sequence from Livingstone Island, South Shetland Islands, with paleoclimatic implications. *Antarct. Sci.* 3, 61–72. doi: 10.1017/S095410209100010X

Blaauw, M. (2010). Methods and code for "classical" age-modelling of radiocarbon sequences. *Quat. Geochronol.* 5, 512–518. doi: 10.1016/j.quageo.2010.01.002

Böning, C. W., Dispert, A., Visbeck, M., Rintoul, S. R., and Schwarzkopf, F. U. (2008). The response of the Antarctic Circumpolar Current to recent climate change. *Nat. Geosci.* 1, 864–869. doi: 10.1038/ngeo362

Clapperton, C. M., Sugden, D. E., Birnie, J., and Wilson, M. (1989a). Late-glacial and Holocene glacier fluctuations and environmental change on South Georgia, Southern Ocean. *Quatern. Res.* 31, 210–228. doi: 10.1016/0033-5894(89)90006-9

Clapperton, C. M., Sugden, D. E., Birnie, R. V., Hanson, J. D., and Thom, G. (1978). "Glacier fluctuations in South Georgia and comparison with other island groups in the Scotia Sea," in *Antarctic Glacial History and World Palaeoenvironments*, ed E. M. Van Zinderen Bakker (Rotterdam: A. A. Balkema), 99–104.

Clapperton, C. M., Sugden, D. E., and Pelto, M. (1989b). "Relationship of land terminating and fjord glaciers to Holocene climatic change, South Georgia, Antarctica," in *Glacier Fluctuations and Climatic Change*, ed J. Oerlemans (Dordrecht: Kluwer Academic Publishers), 57–75.

Cook, A. J., Poincet, S., Cooper, A. P. R., Herbert, D. J., and Christie, D. (2010). Glacier retreat on South Georgia and implications for the spread of rats. *Antarct. Sci.* 22, 255–263. doi: 10.1017/S0954102010000064

Davies, S., Lamb, H., and Roberts, S. (2015). "Micro-XRF core scanner in palaeolimnology: recent developments," in *Micro-XRF Studies of Sediment Cores. Developments in Paleoenvironmental Research,* eds I. Croudace and R. Rothwell. (Dordrecht: Springer), 189–226.

Dean, W. E. Jr. (1974). Determination of carbonate and organic matter in calcareous sediments and sedimentary rocks by loss on ignition: comparison with other methods. *J. Sediment. Petrol.* 44, 242–248.

Foster, L. C., Pearson, E. J., Juggins, S., Hodgson, D., Saunders, K. M., Verleyen, E., et al. (2016). Development of a regional glycerol dialkyl tetraether (GDGT)-temperature calibration for Antarctic and sub-Antarctic lakes. *Earth Planet. Sci. Lett.* 433, 370–379. doi: 10.1016/j.epsl.2015.11.018

Gille, S. T. (2002). Warming of the Southern Ocean since the 1950s. *Science* 295, 1275–1277. doi: 10.1126/science.1065863

Gille, S. T. (2008). Decadal-scale temperature trends in the Southern Hemisphere Ocean. *J. Clim.* 21, 4749–4765. doi: 10.1175/2008JCLI2131.1

Gordon, J. E., Haynes, V. M., and Hubbard, A. (2008). Recent glacier changes and climate trends on South Georgia. *Glob. Planet Change* 60, 72–84. doi: 10.1016/j.gloplacha.2006.07.037

Gordon, J. E., and Timmis, R. J. (1992). Glacier fluctuations on South Georgia during the 1970s and early 1980s. *Antarct. Sci.* 4, 215–226. doi: 10.1017/S0954102092000336

Graham, A. G., Kuhn, G., Meisel, O., Hillenbrand, C.-D., Hodgson, D. A., Ehrmann, W., et al. (2017). Major advance of South Georgia glaciers during the Antarctic Cold Reversal following extensive sub-Antarctic glaciation. *Nat. Commun.* 8:14798. doi: 10.1038/ncomms14798

Grosjean, M., Geyh, M. A., Messerli, B., Schreier, H., and Veit, H. (1998). A late-Holocene (<2600 BP) glacial advance in the south-central Andes (29°), northern Chile. *Holocene* 8, 473–479. doi: 10.1191/095968398677627864

Hayward, R. J. C. (1983). Glacier fluctuations in South Georgia, 1883-1974. *Br. Antarct. Surv. Bull.* 52, 47–61.

Herman, F., Beyssac, O., Brughelli, M., Lane, S. N., Leprince, S., Adatte, T., et al. (2015). Erosion by an Alpine glacier. *Science* 350, 193–195. doi: 10.1126/science.aab2386

Hodgson, D. A., Graham, A. G. C., Griffiths, H. J., Roberts, S. J., Cofaigh, C. Ó., Bentley, M. J., et al. (2014). Glacial history of sub-Antarctic South Georgia based on the submarine geomorphology of its fjord. *Quat. Sci. Rev.* 89, 129–147. doi: 10.1016/j.quascirev.2013.12.005

Hodgson, D. A., and Sime, L. S. (2010). Southern westerlies and CO_2. *Nat. Geosci.* 3, 666–667. doi: 10.1038/ngeo970

Hogg, A. G., Hua, Q., Blackwell, P. G., Niu, M., Buck, C. E., Guilderson, T. P., et al. (2013). SHCal13 southern hemisphere calibration, 0-55,000 years cal BP. *Radiocarbon* 55, 1889–1903. doi: 10.2458/azu_js_rc.55.16783

Hua, Q., Barbetti, M., and Rakowski, A. Z. (2013). Atmospheric radiocarbon for the period 1950-2010. *Radiocarbon* 55, 2059–2072. doi: 10.2458/azu_js_rc.v55i2.16177

Karlén, W. (1976). Lacustrine sediments and tree-limit variations as indicators of holocene climatic fluctuations in lappland, Northern Sweden. *Geogr. Ann. Ser. A* 58, 1–34. doi: 10.2307/520740

Karlén, W. (1981). Lacustrine sediment studies. A technique to obtain a continuous record of Holocene glacier variations. *Geogr. Ann. Ser. A* 63, 273–281. doi: 10.2307/520840

Koppes, M., Hallet, B., Rignot, E., Mouginot, J., Wellner, J. S., and Boldt, K. (2015). Observed latitudinal variations in erosion as a function of glacier dynamics. *Nature* 526, 100–103. doi: 10.1038/nature15385

Kylander, M. E., Ampel, L., Wohlfarth, B., and Veres, D. (2011). High-resolution X-ray fluorescence core scanning analysis of Les Echets (France) sedimentary sequence: new insights from chemical proxies. *J. Quatern. Sci.* 26, 109–117. doi: 10.1002/jqs.1438

Lamy, F., Killian, R., Arz, H. W., Francois, J. P., Kaiser, J., Prange, M., et al. (2010). Holocene changes in the position and intensity of the southern westerly wind belt. *Nat. Geosci.* 3, 695–699. doi: 10.1038/ngeo959

Lanci, L., and Lowrie, W. (1997). Magnetostratigraphic evidencethat "tiny wiggles" in the oceanic magnetic anomaly record represent geomagnetic paleointensity variations. *Earth Planet. Sci. Lett.* 148, 581–592. doi: 10.1016/S0012-821X(97)00055-1

Lenton, A., and Matear, R. J. (2007). Role of the Southern Annular Mode (SAM) in Southern Ocean CO_2 uptake. *Glob. Biogeochem. Cycles* 21, 1–17. doi: 10.1029/2006GB002714

Le Quéré, C., Rödenbeck, C., Buitenhuis, E. T., Conway, T. J., Langenfelds, R., Gomez, A., et al. (2007). Saturation of the Southern Ocean CO_2 sink due to recent climate change. *Science* 316, 1735–1738. doi: 10.1126/science.1136188

Lukas, S. (2012). Processes of annual moraine formation at a temperate alpine valley glacier: insights into glacier dynamics and climatic controls. *Boreas* 41, 463–480. doi: 10.1111/j.1502-3885.2011.00241.x

Matthews, J. A., Berrisford, M. S., Dresser, P. Q., Nesje, A., Dahl, S. O., Bjune, A. E., et al. (2005). Holocene glacier history of Bjørnbreen and climatic reconstruction in central Jotunheimen, Norway, based on proximal glaciofluvial stream-bank mires. *Quat. Sci. Rev.* 24, 67–90. doi: 10.1016/j.quascirev.2004.07.003

Matthews, J. A., and Karlén, W. (1992). Asynchronous neoglaciation and Holocene climatic change reconstructed from Norwegian glaciolacustrine sedimentary sequences. *Geology* 20, 991–994. doi: 10.1130/0091-7613(1992)020<0991:ANAHCC>2.3.CO2

Moreno, P. I., Vilanova, I., Villa-Martínez, R., Garreaud, R. D., Rojas, M., and De Pol-Holz, R. (2014). Southern Annular Mode-like changes in southwestern Patagonia at centennial timescales over the last three millennia. *Nat. Commun.* 5:4375. doi: 10.1038/ncomms5375

Mulvaney, R., Abram, N. J., Hindmarsh, R. C., Arrowsmith, C., Fleet, L. and Triest, J. (2012). Recent Antarctic peninsula warming relative to Holocene climate and ice-shelf history. *Nature* 489, 141–144. doi: 10.1038/nature11391

Oerlemans, J. (2005). Extracting a climate signal from 169 Glacier records. *Science* 308, 675–677. doi: 10.1126/science.1107046

Orsi, A. H., Whitworth, T., and Nowlin, W. D. (1995). On the meridional extent and fronts of the Antarctic Circumpolar Current. *Deep Sea Res. Part I* 42, 641–673. doi: 10.1016/0967-0637(95)00021-W

Osmaston, H. (2005). Estimates of glacier equilibrium line altitudes by the Area x Altitude, the Area x Altitude Balance Ratio and the Area x Altitude Balance Index methods and their validation. *Quatern. Int.* 138–139, 22–31. doi: 10.1016/j.quaint.2005.02.004

Østrem, G., Dale Selvig, K., and Tandberg, K. (1988). *Atlas of Glaciers in South Norway*. Oslo: Noregs vassdrags- og energidirektorat.

Paasche, Ø., Dahl, S. O., Bakke, J., Løvlie, R., and Nesje, A. (2007). Cirque glacier activity in arctic Norway during the last deglaciation. *Quatern. Res.* 68, 387–399. doi: 10.1016/j.yqres.2007.07.006

Pelto, M. (2016). *Neumayer Glacier, South Georgia, 5.6 km retreat 1999-2016 [Online]. From a Glacier's perspective.* Available online at: https://goo.gl/rRuYBb (Accessed September 8, 2017).

Pendlebury, S. F., and Barnes-Keoghan, I. P. (2007). Climate and climate change in the sub-Antarctic. *Pap. Proc. R. Soc. Tasmania* 141, 67–81.

Porter, S. (1975). Equilibrium-line altitudes of late Quaternary glaciers in the Southern Alps, New Zealand. *Quatern. Res.* 5, 27–47. doi: 10.1016/0033-5894(75)90047-2

Quilty, P. G. (2007). Origin and evolution of the sub-Antarctic islands: the foundation. *Pap. Proc. R. Soc. Tasmania* 141, 35–58.

Renberg, I., and Hansson, H. (2008). The HTH sediment corer. *J. Paleolimnol.* 40, 655–659 doi: 10.1007/s10933-007-9188-9

Roberts, S. J., Hodgson, D. A., Shelley, S., Royles, J., Griffiths, H. J., Deen, T. J., et al. (2010). Establishing lichonometric ages for nineteenth- and twentieth-century glacier fluctuations on South Georgia (South Atlantic). *Geogr. Ann. Ser. A* 92, 125–139. doi: 10.1111/j.1468-0459.2010.00382.x

Rosqvist, G. C., and Schuber, P. (2003). Millennial-scale climate changes on South Georgia, Southern Ocean. *Quatern. Res.* 59, 470–475. doi: 10.1016/S0033-5894(03)00036-X

Rubensdotter, L., and Rosqvist, G. (2005). Influcence of geomorphological setting, fluvial-, glaciofluvial- and mass-movement processes on sedimentation in alpine lakes. *Holocene* 19, 665–678. doi: 10.1177/0959683609104042

Scambos, T. A., Berthier, E., Haran, T., Schuman, C. A., Cook, A. J., Ligtenberg, S., et al. (2014). Detailed ice loss pattern in the northen Antarctic Peninsula: widespread decline driven by ice front retreats. *Cryosphere* 8, 2135–2145. doi: 10.5194/tc-8-2135-2014

Scar (2015). *Antarctic Digital Database, Version 6.0. Database, Manual and Bibliography [Online].* Available online at: http://www.add.scar.org/ (Accessed 2017).

SGGIS (2017). *South Georgia Geographic Information Systems [Online]*. Available online at: http://sggis.gov.gs/ (Accessed 2017).

Sigman, D. M., Hain, M. P., and Haug, G. H. (2010). The polar ocean and glacial cycles in atmospheric CO_2 concentration. *Nature* 466, 47–55. doi: 10.1038/nature09149

Smith, R. I. L. (1981). Types of peat and peat-forming vegetation on South Georgia. *Br. Antarct. Survey Bull.* 53, 119–139.

Solomina, O. N., Bradley, R. S., Hodgson, D. A., Ivy-Ochs, S., Jomelli, V., Mackintosh, A. N., et al. (2015). Holocene glacier fluctuations. *Quat. Sci. Rev.* 111, 9–34. doi: 10.1016/j.quascirev.2014.11.018

Sterken, M., Roberts, S., Hodgson, D. A., Vyverman, W., Balbo, A. L., Sabbe, K., et al. (2012). Holocene glacial and climate history of Prince Gustav Channel, northeastern Antarctic Peninsula. *Quat. Sci. Rev.* 31, 93–111. doi: 10.1016/j.quascirev.2011.10.017

Strelin, J. A., Kaplan, M. R., Vandergoes, M. J., Denton, G. H., and Schaefer, J. M. (2014). Holocene glacier history of the Lago Argentino basin, Southern Patagonian Icefield. *Quat. Sci. Rev.* 101, 124–145. doi: 10.1016/j.quascirev.2014.06.026

Strother, S. L., Salzmann, U., Roberts, S. J., Hodgson, D. A., Woodward, J., Van Nieuwenhuyze, W., et al. (2015). Changes in Holocene climate and the intensity of Southern Hemisphere Westerly Winds based on a high-resolution palynological record from sub-Antarctic South Georgia. *Holocene* 25, 263–279. doi: 10.1177/0959683614557576

Tanner, P. W. G. (1981). "Turbidite sequences on South Georgia, South Atlantic: their structural relationship and provencance," in *Geological Evolution of Antarctica*, eds M. R. A. Thomson, L. A. Crame, and J. W. Thomson (Cambridge: Cambridge University Press), 353–359.

Thompson, R., Batterbee, R. W., O'sullivan, P. E., and Oldfield, F. (1975). Magnetic susceptibility of lake sediments. *Limnol. Oceanogr.* 20, 687–698. doi: 10.4319/lo.1975.20.5.0687

Thompson, R., and Oldfield, F. (1986). *Environmental Magnetism*. London: Allen and Unwin.

Thompson, D. W. J., Solomon, S., Kushner, P. J., England, M. H., Grise, K. M., and Karoly, D. J. (2011). Signatures of the Antarctic ozone hole in Southern Hemisphere surface climate change. *Nat. Geosci.* 4, 741–749. doi: 10.1038/ngeo1296

Van Der Bilt, W. G. M., Bakke, J., Werner, J. P., Paasche, Ø., Rosqvist, G., and Vatle, S. S. (2017). Late Holocene glacier reconstruction reveals retreat behind present limits and two-stage Little Ice Age on subantarctic South Georgia. *J. Quatern. Sci.* 32, 888–901. doi: 10.1002/jqs.2937

Van Der Putten, N., Stieperaere, H., Verbruggen, C., and Ochyra, R. (2004). Holocene paleoecology and climate history of South Georgia (sub-Antarctica) based on macrofossil record of bryophytes and seeds. *Holocene* 14, 382–392. doi: 10.1191/0959683604hl714rp

Van Der Putten, N., and Verbruggen, C. (2005). The onset of deglaciation of Cumberland Bay and Stromness Bay, South Georgia. *Antarct. Sci.* 17, 29–32. doi: 10.1017/S0954102005002397

Van Der Putten, N., Verbruggen, C., Ochyra, R., Spassov, S., De Beaulieu, J.-L., De Dapper, M., et al. (2009). Peat bank growth, Holocene paleoecology climate history of South Georgia (sub-Antarctica), based on a botanical macrofossil record. *Quat. Sci. Rev.* 28, 65–79. doi: 10.1016/j.quascirev.2008.09.023

Vasskog, K., Kvisvik, B. C., and Paasche, Ø. (2016). Effects of hydrogen peroxide treatment on measurements of lake sediment grain-size distribution. *J. Paleolimnol.* 56, 365–381. doi: 10.1007/s10933-016-9924-0

Vasskog, K., Paasche, Ø., Nesje, A., Boyle, J. F., and Birks, H. J. B. (2012). A new approach for reconstructing glacier variability based on lake sediments recording input from more than one glacier. *Quatern. Res.* 77, 192–204. doi: 10.1016/j.yqres.2011.10.001

Vaughan, D. G., Marshall, G. J., Connelley, W. M., Parkinson, C., Mulvaney, R., Hodgson, D. A., et al. (2003). Recent rapid regional climate warming on the Antarctic Peninsula. *Clim. Change* 60, 243–274. doi: 10.1023/A:1026021217991

Wang, G., and Cai, W. (2013). Climate-change impact on the 20th-century relationship between the Southern Annular Mode and global mean temperature. *Sci. Rep.* 3, 1–6. doi: 10.1038/srep02039

Weidick, A. (1992). *Glacier Inventory and Atlas of West Greenland*. Copenhagen: Gronland Geologiske Undersøgelse.

Werner, J. P., and Tingley, M. P. (2015). Technical note: probabilistically constraining proxy age-depth models within a Bayesian hierarchical reconstruction model. *Clim. Past* 11, 533–545. doi: 10.5194/cp-11-533-2015

Yu, Z., Beilman, D. W., and Loisel, J. (2016). Transformations of landscape and peat-forming ecosystems in response to late Holocene climate change in the western Antarctic Peninsula. *Geophys. Res. Lett.* 43, 7186–7195. doi: 10.1002/2016GL069380

Yuan, X. J. (2004). ENSO-related impacts on Antarctic sea ice: a synthesis of phenomenon and mechanisms. *Antarct. Sci.* 16, 415–425. doi: 10.1017/S0954102004002238

Zemp, M., Frey, H., Gärtner-Roer, I., Nussbaumer, S. U., Hoelzle, M., Frank, P., et al. (2015). Historically unprecedented global glacier decline in the early 21st century. *J. Glaciol.* 61, 745–762. doi: 10.3189/2015JoG15J017

Conflict of Interest Statement: The authors declare that the research was conducted in the absence of any commercial or financial relationships that could be construed as a potential conflict of interest.

frontiers in Earth Science

ORIGINAL RESEARCH
published: 03 April 2018
doi: 10.3389/feart.2018.00027

Imprints of Climate Signals in a 204 Year $\delta^{18}O$ Tree-Ring Record of *Nothofagus pumilio* From Perito Moreno Glacier, Southern Patagonia (50°S)

Jussi Grießinger[1], Lukas Langhamer[2], Christoph Schneider[3], Björn-Lukas Saß[1], David Steger[3], Pedro Skvarca[4], Matthias H. Braun[1], Wolfgang J.-H. Meier[1], Ana M. Srur[5] and Philipp Hochreuther[1]*

[1] Institute of Geography, Friedrich-Alexander-Universität Erlangen-Nürnberg, Erlangen, Germany, [2] Institute of Atmospheric and Cryospheric Sciences, University of Innsbruck, Innsbruck, Austria, [3] Geography Department, Humboldt Universität zu Berlin, Berlin, Germany, [4] Glaciarium Centro de Interpretación de Glaciares, El Calafate, Argentina, [5] Instituto Argentino de Nivología, Glaciología y Ciencias Ambientales, CONICET, Mendoza, Argentina

OPEN ACCESS

Edited by:
Davide Tiranti, Agenzia Regionale per la Protezione Ambientale (ARPA), Italy

Reviewed by:
Bao Yang, Cold and Arid Regions Environmental and Engineering Research Institute (CAS), China
Li Wu, Anhui Normal University, China

***Correspondence:**
Jussi Grießinger
jussi.griessinger@fau.de

Specialty section:
This article was submitted to Quaternary Science, Geomorphology and Paleoenvironment, a section of the journal Frontiers in Earth Science

Received: *29 January 2018*
Accepted: *14 March 2018*
Published: *03 April 2018*

Citation:
Grießinger J, Langhamer L, Schneider C, Saß B-L, Steger D, Skvarca P, Braun MH, Meier WJ-H, Srur AM and Hochreuther P (2018) Imprints of Climate Signals in a 204 Year $\delta^{18}O$ Tree-Ring Record of Nothofagus pumilio From Perito Moreno Glacier, Southern Patagonia (50°S). Front. Earth Sci. 6:27. doi: 10.3389/feart.2018.00027

A 204 year-long record of $\delta^{18}O$ in tree-ring cellulose of southern beech (*Nothofagus pumilio*) from a site near Perito Moreno Glacier (50°S) in Southern Patagonia was established to assess its potential for a climate reconstruction. The annually resolved oxygen isotope chronology is built out of seven individual tree-ring $\delta^{18}O$ series with a significant mean inter-series correlation ($r = 0.61$) and is the first of its kind located in Southern America south of 50°S. Over a common period from 1960 to 2013 of available stationary and high-resolution gridded CRU TS v. 4.01 data, the $\delta^{18}O$ chronology exhibits a strong sensitivity toward hydroclimatic as well as temperature parameters as revealed by correlation analyses. Among these, positive correlations with maximum temperature in the first part of the summer season (CRU $r_{ONDJ} = 0.51$, $p < 0.01$) and negative correlations with precipitation in the latter half of the vegetation period (CRU $r_{ONDJ} = -0.54$, $p < 0.01$) show the highest sensitivities. A strong supra-regional influence of the Southern Annular Mode (SAM) is clearly recorded in this chronology as indicated by significant positive correlations during the vegetation period ($r_{ONDJ} = 0.62$, $p < 0.01$). This indicates that the presented $\delta^{18}O$-chronology shows great promise to reconstruct the influence and variability of the SAM within the last two centuries in southern South America. The modulation of positive and negative anomalies within this series can be interlinked to changes in moisture source origin as revealed by backward trajectory modeling. Additionally, these anomalies can be directly associated to positive or negative phases of the Antarctic Oscillation Index (AAOI) and therefore the strength of the Westerlies. Aligned by the analysis on the influence of different main weather types on the $\delta^{18}O$ chronology it is shown that such time-series hold the potential to additionally capture their respective influence and change during the last centuries.

Keywords: tree-ring $\delta^{18}O$, *Nothofagus pumilio*, Southern Patagonia, Perito Moreno Glacier, Southern Annular Mode (SAM), backward trajectory modeling, main weather types

INTRODUCTION

The climate of southern South America (40–55°S) is mainly determined by its location within the belt of the Southern Hemisphere Westerlies. As a consequence of only minor annual changes within the dominant pressure systems, strong westerly winds are prevailing throughout the year clearly influencing the seasonal distribution of temperature and rainfall in this area (Villalba et al., 2003). The mainly N-S directed mountain ridges of the southern Andes form one of the sharpest zonal transitions of climate in the world (Schneider et al., 2003). The latitudinal arranged high-mountain orography close to the Pacific coastline leads to a large-scale uplift of moist air masses, resulting in strong orographic precipitation on the windward western fringes of the Andes (Garreaud et al., 2009, 2013). In contrast, the east-facing side of the Andean crests is characterized by typical orographically induced lee-effects resulting in a steep gradient of decreasing precipitation from West to East with increasing distance from the Andean crest line (Garreaud et al., 2013). As a consequence, the evolution of the zonal vegetation has adapted to this gradient resulting in a transition from deciduous forests accompanying the humid Andean ridges toward the steppe vegetation of the semi-arid south-eastern part of Patagonia (Paruelo et al., 1998).

Since the 1930's, the southern part of South America was subject to a substantial increase in near-surface air temperatures (Rosenblüth et al., 1997; Carrasco et al., 2002; Villalba et al., 2003). For the recent decades, a general increase in temperature cannot be clearly verified for the southern Andean region and is therefore under debate (Vuille et al., 2015). Likely coupled to general changes within large-scale circulation patterns, a profound glacier retreat and surface lowering for the Northern (NPI) and Southern Patagonian ice fields (SPI) is reported for the same period (Willis et al., 2012; Malz et al., 2018), mainly leading to substantial changes in the hydrosphere (Vuille et al., 2015). Hence, especially the core areas and surroundings of both, NPI and SPI are stated as key regions for analyzing the course, extent and effects of climate change on the Southern Hemisphere (Rignot et al., 2003). Unfortunately, a general challenge for a verifiable quantification of climate change in the region between 45 and 55°S is the still underrepresented existence of long-term high-resolution climate datasets. Since the available station network is sparsely distributed and contains mainly short time-series with prevalent data gaps, a substantial analysis on the spatiotemporal magnitude and impact of this change is hampered and yet challenging. In contrast, reliable data for understanding processes on the dynamics and responses of the glaciers of the SPI are urgently needed (Casassa et al., 2002; Stuefer et al., 2007).

The use of diverse proxy archives recording environmental conditions on different time-scales can help to attenuate the assessment of climate change. Especially tree-rings with their annual resolution contain a high potential to interlink recent changes with conditions in the past. Studies on the use of oxygen isotope ratios in tree rings have proven the importance of this proxy as a valuable tool for palaeoclimatic research. In a *sensu stricto* palaeoclimatic context, they have been successfully applied globally for the reconstruction of different atmospheric parameters like precipitation (Danis et al., 2006; Treydte et al., 2006, 2007; Reynolds-Henne et al., 2007; Grießinger et al., 2011), temperature (Edwards et al., 2008; Lavergne et al., 2016), relative air humidity (Edwards et al., 2008; Grießinger et al., 2017), cloud cover (Liu et al., 2012, 2014), extreme weather events or droughts (Miller et al., 2006; Berkelhammer and Stott, 2008; Sano et al., 2017) as well as supra-regional atmospheric circulation patterns (Welker et al., 2005; Brienen et al., 2012; Saurer et al., 2012; Hochreuther et al., 2016). Such diversity of reconstructible parameters highlights the complexity of oxygen isotope signals in tree rings and underline the difficulty for an evident identification of a single climate parameter triggering the respective $\delta^{18}O_{tree-ring}$ signal (McCarroll and Loader, 2004). Nevertheless, the main advantage of $\delta^{18}O$ as the target within the variety of existing tree-ring parameters lies within its ability to interlink different natural archives and geospheres via the water cycle.

Nothofagus pumilio is a widely distributed, dominant broadleaved tree-species forming pure or mixed forests in the mountainous areas in South America. Its natural distribution reaches from the coastal-near lowlands on the western margins of the Chilean Andes up to the sub-alpine vegetation belt on the western as well as eastern flanks of the Andean crests (Mathiasen and Premoli, 2010). Due to its wide geographical distribution, several studies on *Nothofagus pumilio* have been previously carried out clearly indicating the high potential of tree-ring width to reconstruct past climate variability (e.g., Villalba et al., 2003; Lara et al., 2005). In comparison to other geographical areas, accompanying studies on stable isotopes in tree-rings in southern South America are still scarce. Recently, the works by Lavergne et al. (2016, 2017a,b) revealed the high potential of such studies on tree-ring $\delta^{18}O$ and therein reflected informations on (past) climate variability in northern Patagonia. However, research on $\delta^{18}O$ in tree-rings from the areas in Patagonia south of 50°S are up to now not existing for comparable research.

Within this study, we aim at evaluating the general potential of $\delta^{18}O$ in tree-ring cellulose of *Nothofagus pumilio* for the use as a climate proxy at a glacier-near site close to the Perito Moreno Glacier as part of the SPI (50°S). In doing so, we want (i) to evaluate to which extent our annually resolved tree-ring oxygen isotope time series is sensitive to local climate conditions, (ii) to decipher the possible influence of supra-regional phenomena influencing southern South America like the Southern Annular Mode (SAM) or ENSO on variations of tree-ring $\delta^{18}O$, and (iii) analyse the influence of differing moisture origins and changing frequencies in the appearance of main weather types on $\delta^{18}O$ variations in *Nothofagus pumilio* during years of noticeable positive or negative deviations from the long-term mean.

MATERIALS AND METHODS

Study Site and Sampling

As part of the Southern Patagonian Ice Field, the Perito Moreno Glacier (PMG) is a typical calving glacier on the eastern margin of the Southern Patagonian Icefield (**Figure 1**). In contrast to other surrounding glaciers, its extent within the last decades

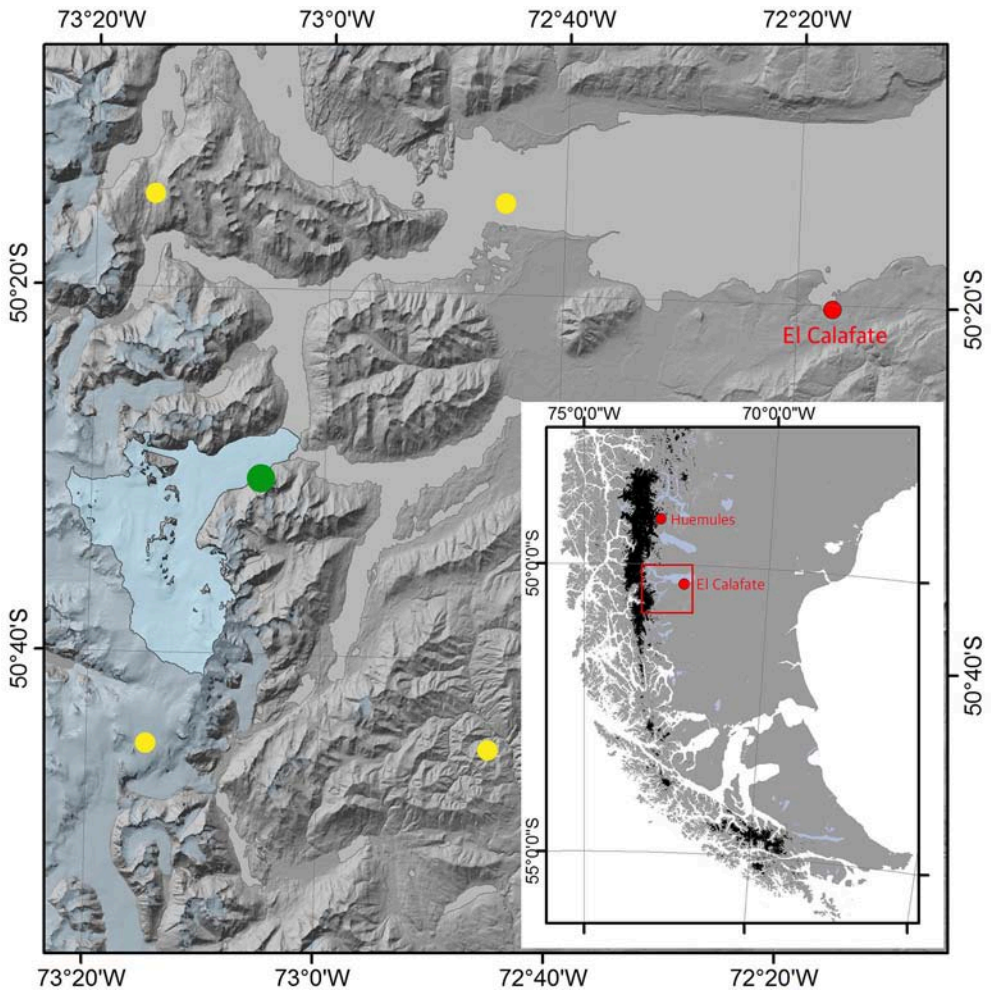

FIGURE 1 | Digital Elevation Model (SRTM) of Southern Patagonia overviewing the investigation area of this study. Bright blue area: Extent and catchment of the Perito Moreno Glacier. Green Circle: location of tree-ring sampling site. The yellow circles represent the four nearest 0.5° grid points of the CRU TS v. 4.01 dataset. Inlay: Blackened areas in the Inlay mark locations of glaciated areas in South America. Dark blue area: Actual extent of glaciated areas of the Southern Patagonia Ice Field (SPI). Red dots: location of the nearest meteorological stations in El Calafate and Los Huemules (Inlay).

is characterized by only minor fluctuations of the glacier front (Stuefer et al., 2007). Assumable general minor variations in the absolute glacier extent during the last century led to the establishment of *Nothofagus* forests in the former glaciated areas and along the elder lateral and terminal moraines (Aniya and Skvarca, 2012) (**Figure 2**).

Local climate as reflected by the closest meteorological station in El Calafate (198 masl) is characterized by an annual precipitation of 200 mm and a mean annual temperature of 7.5 °C being characteristic for a steppe climate (**Figure 2**). Relatively cold winters (T_{JJA} = 1.4°C, $Precip_{JJA}$ = 45 mm) alternate with warm and dry summers (December to February; T_{DJF} = 13.0°C, $Precip_{DJF}$ = 27 mm). Months with a maximum amount of rainfall are April (18 mm) and May (20 mm). As stated by Garreaud et al. (2009), the region is characterized by a steep gradient in decreasing precipitation. Therefore, we additionally used a 10 year dataset from a climate station at Estancia Los Huemules (49.1°S/7.6°W), located 140 km north of our sampling site at an elevation of approx. 460 masl. The obtained values indicate similar results for temperature (T_{Year} = 7.4°C; T_{DJF} = 12.9°C, T_{JJA} = 1.9°C) but are displaying substantial differences in the respective amount in annual and seasonal precipitation ($Precip_{Year}$ = 931 mm, $Precip_{DJF}$ = 230 mm, $Precip_{JJA}$ = 212 mm). Although the time-series from Los Huemules is too short for a substantial and statistically sound analysis of climate-proxy relationships, we consider especially the apparent differences in precipitation obviously caused by elevational and distance effects as relevant for a latter discussion.

Tree-ring samples of southern Beech (*Nothofagus pumilio*) were collected during a field campaign at Parque Nacional Perito Moreno in the austral spring (November 2014). Sampling was performed on the southern lateral moraine of Perito Moreno Glacier at elevations between 500 and 600 masl (**Figures 1**, **2**). The sampling design focused on mainly undisturbed and mature

FIGURE 2 | Panoramic overview on the location of the sampled forest site on the Perito Moreno Glacier lateral moraine. Picture taken by B.L. Saß.

trees with a distinct distance from depressions. In addition, well drained slope stands with inclinations higher than 30° were preferred to minimize the influence of stagnant or ground water on our sampled trees. In total, 96 (paired) cores from 48 tree individuals were extracted using a 5 mm diameter MORA increment borer.

Dating and Evaluation of $\delta^{18}O_{TRC}$

Ring widths of the collected samples were measured using a Lintab 6 system (Rinntech, Heidelberg, Germany) with an accuracy of 0.01 mm to exactly date each increment core. Regarding the convention by Schulman (1956) the calendar year overlap of the austral vegetation period (September of the actual year to May of the following year) has to be taken into account for the termination of the exact end-date of our tree-ring series. In this case, the last completely formed tree-ring is of 2013 (with the respective vegetation period from September 2012 to May 2013), while the ring of 2014 was not completely formed when sampling took place, yet. Although in parts visible and measurable, the year 2014 was therefore truncated off our series to avoid a bias in our annual values. Following standard methods by Cook and Kairiukstis (1990) and Fritts (1976), after the visual and statistical cross-dating all individual ring-width series were averaged into a mean tree-ring width chronology spanning the period 1809–2013 using the TSAP-Win Software (RINNTECH).

For the analysis of the ratio of oxygen isotopes in tree-ring cellulose (thereafter expressed as $\delta^{18}O_{TRC}$), we selected seven cores from different tree individuals out of the sample pool, exceeding the usually accepted minimum sample depth of four to five cores per investigation site to ensure a representative and reliable oxygen isotope chronology (Leavitt, 2010). In comparison to other studies, the individual tree analysis of $\delta^{18}O_{TRC}$ was not only assigned to the years of available stationary climate date (usually the last 50–60 years), but was moreover applied for the complete available period from 1809 to 2013 (204 years). Hence, pooling of samples was avoided to preserve occurring (high-)frequency variabilities within the individual $\delta^{18}O_{TRC}$-series. All cores chosen for the oxygen isotope analyses met the criteria of: (1) a similar maximum tree age of at least 170 years to avoid possible signal-biasing juvenile effects within the last decades, (2) no missing rings or plateaus of depressed growth with extremely narrow rings (< 0.3 mm) to ensure sufficient material for the isotope analysis (3) similar growth trends for the selected individual trees.

As the initial step for the $\delta^{18}O$ tree-ring analysis, dated growth rings were cutted under a binocular using a razor blade. Afterwards, following the method described by Wieloch et al. (2011), α-cellulose was extracted for all seven trees to avoid a signal biasing contamination with resins and lignin. The resultant α-cellulose samples were homogenized using an ultrasonic sound system described by Laumer et al. (2009) and subsequently freeze-dried in a lyophilization unit (M. Christ Ltd.). Individual cellulose samples of ∼200 μg were weighted and packed into silver capsules and stored prior the isotope measurement for minimum 48 h in a vacuum oven to avoid a possible hygroscopically caused exchange with ambient air. The final analysis of the cellulose $^{18}O/^{16}O$ ratio (expressed as $\delta^{18}O$) was determined using a continuous flow Delta V Advantage Isotope Ratio Mass Spectrometer (Thermo Fisher Scientific Inc.) coupled to a HEKATech pyrolysis reactor. Measurements were calibrated to periodically interposed internal and international laboratory standards resulting in an analytical precision better than 0.2‰.

Climate Data and Examination of Proxy-Climate Relationships

For a profound and statistically as well as climatologically reproducible quantitative analysis of climate-proxy relationships, a survey of available representative (regional) climate datasets is required. Especially in high mountain areas and/or remote areas like Patagonia, this is a critical step since meteorological datasets by rain gauges are frequently not representative compared to the

climate at the sampling sites due to larger distance and differing altitudes of the climate stations. To quantify the proxy-climate relationships of our $\delta^{18}O_{TRC}$ series, we first performed Pearson's correlations with temperature and precipitation data from the nearest climate station in El Calafate with the longest available measuring period in the region (**Figure 1**).

For the period from 1960 to 2013, common data for temperature (T_{mean}, T_{min}, T_{max}) and precipitation is available. Since the general availability of meteorological stations on the eastern margins of the Andes south of 45°S that (i) comprise records spanning more than 30 years, (ii) show a continuously recording with no data gaps, and (iii) provide a sufficient spatial density to gain the possibility to build regional means is scarce, we additionally applied analyses with gridded datasets from the four nearest 0.5° CRU TS 4.01 gridpoints (Harris and Jones, 2017, data from https://crudata.uea.ac.uk/cru/data/hrg/cru_ts_4.01/, cf. **Figure 1** overview map). The respective CRU time-series cover a maximum period from 1901 to 2016 and have the advantage to contain a wide range of (hydro)climatic variables including data on cloud cover, diurnal temperature range, frost day frequency, potential evapotranspiration, precipitation, T_{mean}, T_{min}, T_{max}, vapor pressure and wet day frequency (rain days per month).

To evaluate possible influence of supra-regional climate phenomena influencing our time-series, we additionally performed statistical analyses with datasets of the Southern Annular Mode (SAM, or Antarctic Oscillation AAO) and the Oceanic Nino Index (ONI). The SAM describes the pattern of climate variability in the southern Hemisphere and reflects in southern South America the latitudinal distribution on the strength and distribution of rainfall, demonstrably even throughout the last Millennium (Abram et al., 2013). For areas in Patagonia south of 40°S, it is reported for the determination of long-term climate variability by triggering surface air temperatures (Garreaud et al., 2009). Hence, it is expected to be of great relevance for tree-growth in Patagonia (Villalba et al., 2012). The recently developed ONI-Index from the NOAA is a novel ENSO indicator for monitoring the contrasting patterns of El Niño and La Niña phases responsible for substantial changes in weather patterns over South America. Therefore both, the SAM (https://climatedataguide.ucar.edu/climate-data/marshall-southern-annular-mode-sam-index-station-based) and the ONI Indices (http://origin.cpc.ncep.noaa.gov) were chosen for testing their respective influences on our $\delta^{18}O_{TRC}$ series.

Moisture Source Detection by Backward Trajectory Modeling

As stated, the $\delta^{18}O$ in natural archives is known as an applicable parameter for the reconstruction of moisture history, variability, and hydroclimate in general. However, recent studies demonstrated the importance of including analyses on the moisture transport history for a thorough interpretation of $\delta^{18}O$ signals in trees especially on sites affected by surrounding high mountain belts or seasonally distinctive differing moisture sources (Berkelhammer and Stott, 2008; Brienen et al., 2012; Wernicke et al., 2017). Demonstrably, the alteration of the $\delta^{18}O$ signal in precipitation during its transportation across the southern Andes is triggered by isotope fractionation effects like an amount, distance and altitude effect (Vogel et al., 1975; Stern and Blisniuk, 2002). As stated by Stern and Blisniuk (2002), precipitation in this region is predominantly derived of moisture sources originating from the Pacific Ocean.

In general, the $\delta^{18}O$ content of tree-ring cellulose is stated to be controlled by (i) the isotopic composition of the source water, (ii) an evaporative enrichment of ^{18}O on leaf level during gas exchange, and (iii) a plant-internal alteration through fractionation effects during cellulose synthesis (Barbour, 2007; Gessler et al., 2014; Treydte et al., 2014). Since substantial changes in the moisture origin of precipitation will lead to changes in the $\delta^{18}O$ source water signal (Dansgaard, 1964), differences in the annual origin of air masses are expected to also alter our respective $\delta^{18}O_{TRC}$ value as reported by other studies (Johnson and Ingram, 2004; Dayem et al., 2010; Wernicke et al., 2017). By taking into account possible influences of these effects on our $\delta^{18}O_{TRC}$ time series, the analysis of backward trajectory modeling for selected years seems to be an appropriate approach to disentangle the influence of differing moisture signal of differing atmospheric water pools on our time series.

The use of trajectories enables to visualize movement patterns of air parcels in the free atmosphere. In doing so, backward trajectory calculations provide insights into the analysis on the origin of air parcels. By neglecting possible mixture effects with neighboring air parcels and cloud condensation effects, the modification of specific humidity along a trajectory within a certain time step is the result of moisture uptake (evaporation) or moisture loss (precipitation) (Stohl and James, 2004). A verified method to determine moisture origins using backward trajectories was developed by Sodemann et al. (2008). Therein, once a trajectory absorbs moisture within the mixed and turbulent planetary boundary layer, a moisture source is detected. Those moisture sources are then corrected to their respective proportion to the precipitation in the target area, including rain-out effects during the transportation pathway of the air parcels. The starting points of the respective backward trajectories are located on the intersections of a latitudinal/longitudinal 0.75° × 0.75° grid. The starting points of the respective backward trajectories expands between 74.25° to 72.75°W and 48.0° to 51.75°S framing the target region. In the vertical the grid is separated into 11 equidistant levels starting from the surface to the 500 hPa level. This leads to a total amount of 198 starting points. Their location is chosen as such to detect the complete range of the potential rainfall in the surroundings of the SPI. Calculations of trajectories were carried out using the Lagrangian Analysis Tool LAGRANTO (Wernli and Davies, 1997) applied to ERA-Interim data (www.ecmwf.int; Dee et al., 2011). Every 6 h on each starting point an individual 18 day backward trajectory calculation starts. At any time, a trajectory hits land surface, it is artificially lifted by 10 hPa. Subsequently, the resulting moisture sources were projected on earth surface with a 1.5° resolution.

In a first approach, we tested a possible recording of moisture source origins in the $\delta^{18}O_{TRC}$ by focusing on the analysis of selected years during the common period of available

proxy and ERA-Interim data from 1979 to 2013. In addition to the information gained by the analyses on proxy-climate-relationship, we tried to disentangle and quantify possible influences of a changing source water/precipitation ^{18}O signal on our $\delta^{18}O_{TRC}$ chronology. Hence, we selected for further analyses in each case for 2 years, that are characterized by a markedly positive (1999, 2008) or negative deviation (2000, 2002) from the long-term $\delta^{18}O_{TRC}$ mean.

Weather Type Classification

While analyzing differences monthly precipitation data, changing or dominant influences of Mesoscale Weather Types (Grosswetterlagen/GWL) can be one driving factor for diverging monthly or even seasonal amounts of annual precipitation at the same location. On annual as well as decadal scale, shifts in the individual frequency of occurrence of a given GWL may therefore lead to substantial influences on regional ecosystems e.g., through an improvement or deterioration of plant available water during the vegetation period. To additionally test this influence of mesoscale climate effects on our $\delta^{18}O_{TRC}$ during recent decades, we investigated possible effects of weather types for the period 1979–2013.

The presented GWL classifications are calculated for a period of common data spanning from 1979-2013 using daily mean sea level pressure (MSLP) reanalysis data from the ERA-Interim dataset (www.ecmwf.int; Dee et al., 2011) with the same spatial resolution of $0.75^\circ \times 0.75^\circ$ as used for the backward trajectory modeling. The temporal resolution is 12 h (0 a.m., 12 p.m. UTC). Applied for the area 10° to 80°S and 40° to 110°W, the data frame covers most of South America and the Antarctic Peninsula. The choice of the area as well as MSLP as weather classification variable are selected with reference to weather type classifications used by Frank (2002), Schneider et al. (2003) and Weidemann et al. (under review). We applied the cost733class-1.2 software (http://cost733.geo.uni-augsburg.de/cost733class-1.2) originally designed to classify circulation type patterns in Europe (Philipp et al., 2014b). The optimal number of classes is obtained by a k-means cluster algorithmic evaluation focusing on explained cluster variance (ECV) with increasing cluster numbers. The number of ten weather types was found to be optimal as there was no significant increase in ECV with higher cluster numbers. This is in accordance to the weather type classification by Frank (2002), used by Schneider et al. (2003) and both, earlier synoptic weather interpretation by Endlicher (1991) and the weather type classification based on empirical orthogonal functions presented by Compagnucci and Salles (1997). We applied the automated classification map-pattern scheme by Lund (1963) based on MSLP which makes use of so-called leader patterns. It constitutes a low computational cost predecessor of later cluster algorithms (Hartigan, 1975; Murtagh, 1985). Within the LUND-algorithm, in a first run a leader is identified as the one observation showing most matching cases (observations) of correlations that succeed a pre-defined threshold with all other observations (Lund, 1963; Philipp et al., 2014a). After removing the generated leader class, e.g., all Pearson correlation coefficient threshold succeeding correlations including the leader itself, the remaining class leaders are called in similar iterative processes (Lund, 1963; Philipp et al., 2014a). Following the assignment of all leaders, weather types are determined by returning all daily observations to the data pool and assigning each one to the nearest leader based on linear correlation (Lund, 1963; Philipp et al., 2014a). The threshold used in this study is set to a Pearson correlation coefficient of 0.85. Advantage of the Lund classification scheme is based on the fact, that it underlines the prevalence of weather types with westerly air flow. Subsequently, further significantly different but scarce weather types are detected. In contrast, k-mean leader algorithms tend to define balanced classes by equalizing the centroid size (Philipp et al., 2014b) resulting in a principally unilateral representation of similar weather types of westerly airflow. As a result, ten main weather types were acquired by our classification scheme.

RESULTS AND DISCUSSION

Characteristics of the $\delta^{18}O_{TRC}$ Time-Series

With a mean inter-tree correlation coefficient of $r = 0.61$, the seven individual *Nothofagus pumilio* $\delta^{18}O_{TRC}$ time series were significantly correlated between each other. This supports our use of the mean site $\delta^{18}O_{TRC}$ chronology for all subsequent analyses. The resulting oxygen isotope series covers the period from 1809 until 2013 (204 years) and represents one of the longest available, annually resolved tree-ring oxygen isotope time series in southern South America. In particular, the chronology thus covers the climatically interesting final phase of the Little Ice Age, allowing future comparisons with past regional glacier fluctuations. As given in **Table 1**, the $\delta^{18}O_{TRC}$ time-series is characterized by a low autocorrelation (AC1 = 0.23) and a high signal-to-nose-ratio (SNR = 5.512). The standard deviation is quite low ($SD = 0.51$), with a maximum range of 2.6‰ between the minimum in 1976 (25.27‰) and the maximum in 1961 (27.89‰), respectively. Reflected by the Expressed Population Signal (EPS) threshold of EPS > 0.85 in **Figure 3**, the chronology can be considered as being reliable and representative starting from the year 1833.

However, the year-to-year variability within our time-series is noticeably high, expressed by years with remarkable positive and negative deviation from the long-term mean. Especially within the recent decades, the number of such (mainly positive)

TABLE 1 | General site characteristics and $\delta^{18}O_{Tree-ring}$-chronology statistics of the Perito Moreno Glacier sampling site.

Sample site	Tree species	Coordinates	Alt. (masl)	Age span	Mean $\delta^{18}O$	SD	SNR	AC1
Perito Moreno lateral moraine	*Nothofagus pumilio*	50°31′ S/73°07′ W	500–580	1809–2013 (204a)	26.67‰	0.51	5.512	0.23

SD, standard deviation; SNR, signal-to-noise ratio; AC1, first order autocorrelation.

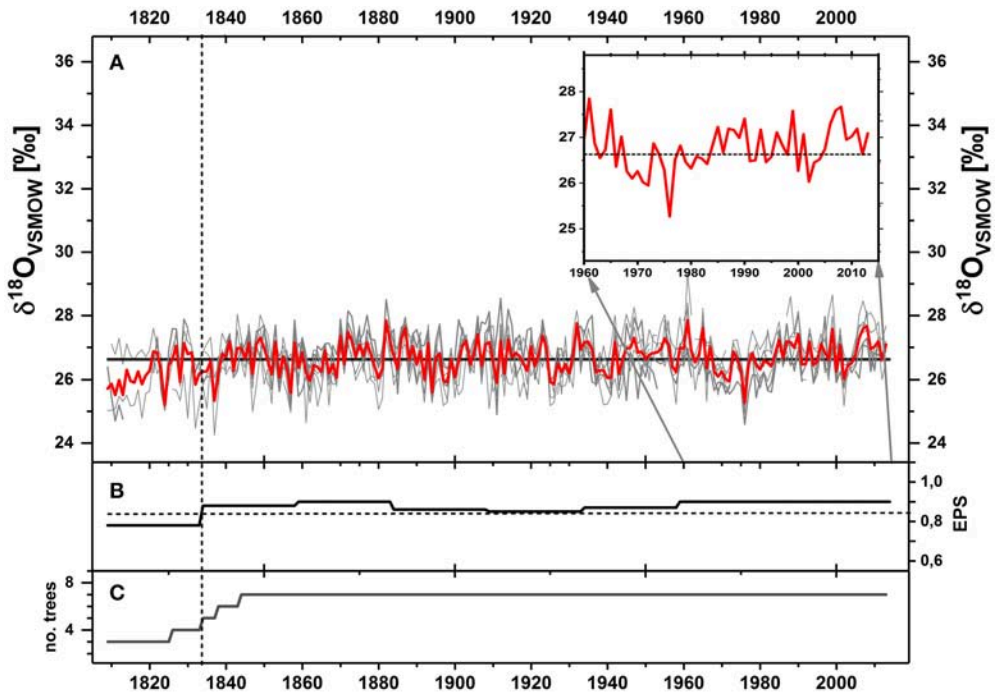

FIGURE 3 | (A) 204 year $\delta^{18}O_{Tree-ring}$ chronology (1809–2013) of *Nothofagus pumilio* trees from the Perito Moreno Glacier. Gray curves reflect the seven individual $\delta^{18}O_{TRC}$ time-series, bold red line the respective annual $\delta^{18}O_{TRC}$ mean of all trees. Bold horizontal black line: long-term mean of averaged time series. Vertical dotted line indicates the year, when threshold of EPS > 0.85 is reached (1833). Inlay shows $\delta^{18}O_{TRC}$ chronology (red curve) and long-term mean (horizontal line) for the period 1960–2013. **(B)** Expressed Population signal (EPS) calculated for a 50 year window with an 25 year overlap. Dotted horizontal line indicates 0.85 threshold. **(C)** Sample depth indicating the number of trees during the respective period.

extreme values with a deviation of more than 1.5 *SD* (σ) seems to increase (**Figure 3**). Compared to the mean time-series value of 26.68‰, decadal phases of lowered oxygen isotope values are apparent for the periods 1920–1930 and 1960–1980. Periods of comparably higher isotope values can be observed during 1900 to 1920 and from 1940 to 1965. Since the beginning of the 1980's, a general increasing trend in $\delta^{18}O_{TRC}$ of +0.8‰ can be detected, only intermitted by a few years with more negative values. We assume that this reflects a general tendency to warmer and drier local climate conditions as reported by Garreaud et al. (2009) leading to a higher amount of heavier ^{18}O isotopes stored in the tree-rings of *Nothofagus pumilio*.

Imprints of Climate Signals in $\delta^{18}O_{TRC}$ From Perito Moreno

Figure 4 displays results of correlations between our mean series and values of the climate station in El Calafate during the period 1960–2013. It is apparent, that the $\delta^{18}O_{TRC}$ variations are mostly sensitive to parameters reflecting hydroclimate within the vegetation period. Unfortunately, in the year 2001 the location of the meteorological station in El Calafate was moved several kilometers eastwards to the new local airport. This resulted in a necessary analytical split-up to account for possible coupled distance effects. Since this mainly influences the precipitation values, we separately analyzed (i) Period 1 from 1960 to 2000 and (ii) Period 2 from 2001 to 2013 (both not illustrated). However, to test the transferability of mean values for a possibly resultant climate reconstruction, we additionally checked correlations with the overall period spanning the years 1960–2013 (**Figure 4**). At first view, the resulting analysis of proxy-climate relationships reveal similar results. In both of the splitted time periods, a consistent (negative) influence of summer precipitation is apparent. The most significant influences on our $\delta^{18}O_{TRC}$ series result with the summer season mean from December to February (period 1: $r_{DJF} = -0.48$, $p < 0.01$; period 2: $r_{DJF} = -0.48$, $p < 0.05$) and for the main part of the vegetation period (period 1: $r_{ONDJF} = -0.42$, $p < 0.01$; period 2: $r_{ONDJF} = -0.42$, $p < 0.05$). Interestingly, for the overall period from 1960 to 2013 this relationship is shown to be dampened ($r = -0.38$, $p < 0.05$, **Figure 4**). Calculations with temperature data reveal a strong and significant positive influence on maximum temperature of March ($r_{March} = 0.43$, $p < 0.05$ for period 1 and $r_{March} = 0.54$, $p < 0.5$ for period 2). Even for the common period from 1960 to 2013, this positive relationship is consistent, but also slightly lowered as seen for the precipitation data ($r_{March} = 0.47$, $p < 0.01$).

Since the station of El Calafate is located 80 km east of our study site (**Figure 1**) and an obvious change in vegetation from *Nothofagus* forests at Perito Moreno moraine and steppe vegetation in El Calafate exists, we expect a substantial bias for calculations with this precipitation dataset. We assume that especially the available rainfall datasets from El Calafate station

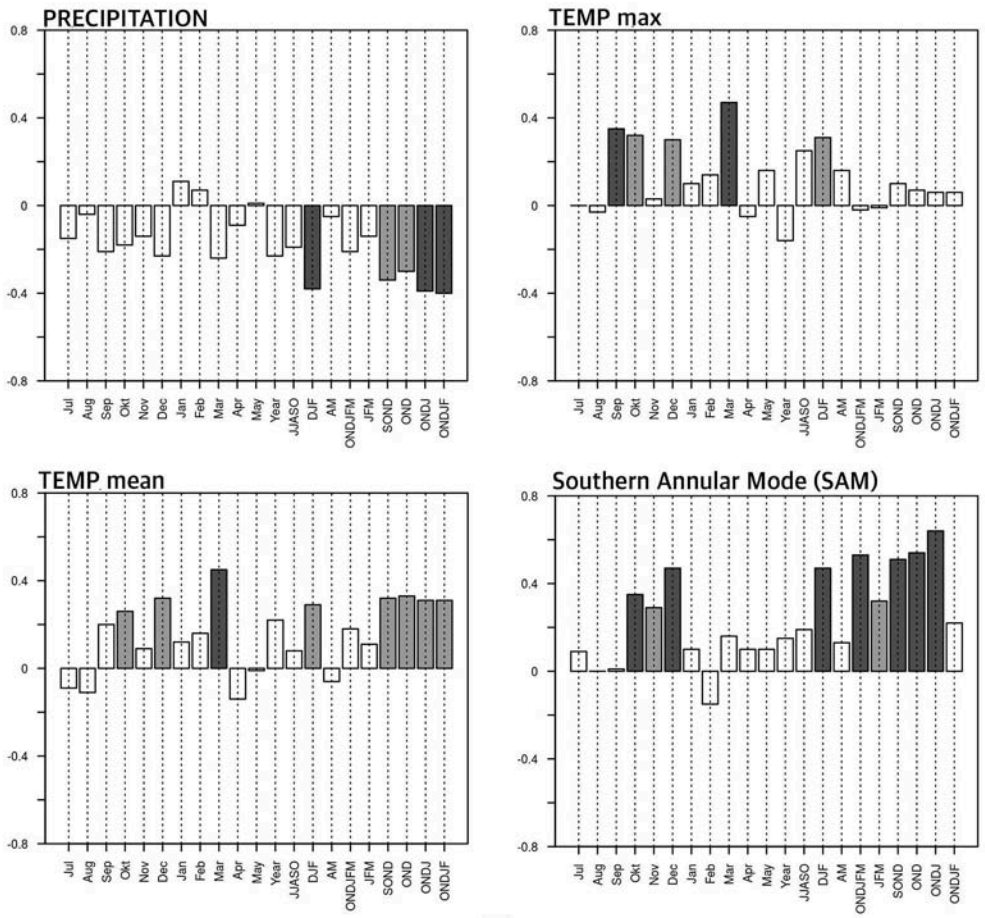

FIGURE 4 | Climate-Proxy-Relationships between the $\delta^{18}O_{TRC}$ time series and selected climate parameters of the climate station in El Calafate. In addition, results of calculations with the Southern Annular Mode (SAM) are shown. Light gray bars indicate correlations reaching the $p < 0.05$ level of significance, dark gray bars correlations exceeding the $p < 0.01$ level of significance.

have to be considered not to be representative for our study site. In this context, the fundamental discrepancy of more than 700 mm between the yearly sum of rainfall measured in El Calafate compared to Los Huemules is an additional indicator of this assumed lack of representativeness (**Figure 5**). In the context of a general decrease in precipitation with increasing distance from the main Andean crests as reported by Garreaud et al. (2013), precipitation values recorded at stations like Los Huemules in terms of geographical location and elevation seem to be more appropriate for reflecting actual local climate conditions (**Figure 5**). This assumption is underlined by the results of a test with the corresponding temperature and precipitation datasets (figure not shown). Although due to the short overlap between the proxy and climate station series of only 7 years, significances of the results have to be regarded with caution. Despite, in parts substantial contrasting results are apparent. This applies without exception to the correlations between proxy and precipitation values, which consistently show in contrast to El Calafate positive correlations between the different autumn and summer seasonal means and the respective $\delta^{18}O_{TRC}$ (e.g., $r_{MAR-APR} = 0.71$, $p < 0.05$; $r_{JAN-APR} = 0.69$, $p < 0.05$).

Therefore, additional analyses with CRU TS 4.01 data for a corresponding period from 1960 to 2013 were performed to test their respective representativeness for our study site (**Figure 6**). Best results were obtained by building a regional mean of the nearest four grid points (cf. **Figure 1**). Mentionable, individual examination of climate-proxy relationships for all grid points constantly reveal almost identical responses. Like the calculations with the data from El Calafate, the obtained results indicate a strong (negative) influence of precipitation during the vegetation period from October to January ($r_{ONDJ} = -0.54, p < 0.01$) on our time-series. The sensitivity to precipitation is further underlined by significant negative correlations within the frequency in wet days during the vegetation period ($r_{SOND} = -0.55$, $p < 0.01$; $r_{OND} = -0.55$, $p < 0.01$). Supporting the results with station data from El Calafate, relationships between $\delta^{18}O_{TRC}$ values and different temperature parameters (T_{mean}, T_{max}, T_{min}) stay either consistent or were significantly stronger. Most significant positive correlations prevail with maximum temperatures during

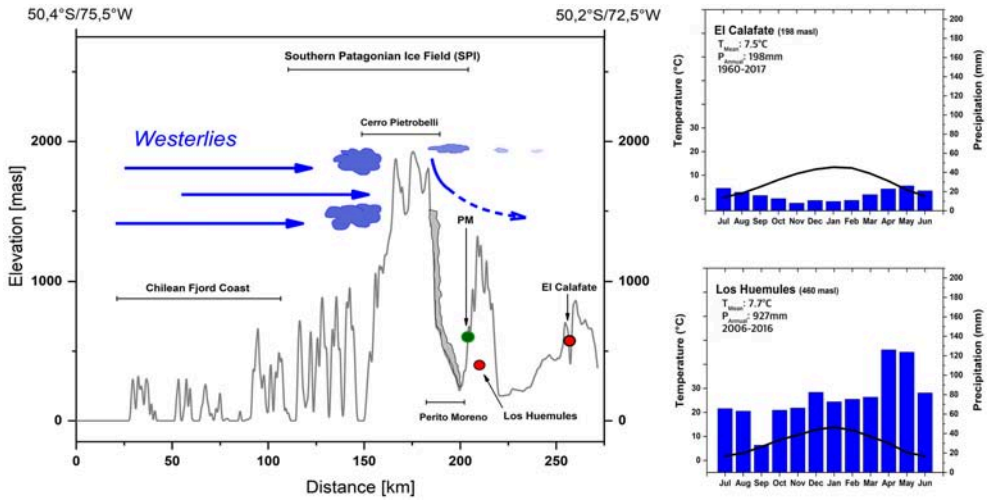

FIGURE 5 | (Left) Elevation profile from the Pacific Ocean across the Andes and the Southern Patagonian Ice Field to El Calafate. Green circle indicates geographical setting of the sampling site at Perito Moreno Glacier southern lateral moraine (PM). Red circles indicate location of the AWS in El Calafate and the comparable geographical location (elevation, distance from main Andean ridge) of the AWS in Los Huemules. **(Right)** Climate diagrams of meteorological stations in El Calafate and Estancia Los Huemules.

selected seasonal means of the vegetation period ($r_{ONDJ} = 0.51$, $p < 0.01$ and $r_{SOND} = 0.49$, $p < 0.01$). Almost no significant relationships were found for the parameters number of frost days, minimum temperature, cloud cover or vapor pressure (not displayed). By combining these findings, phases with warmer and drier conditions and therefore higher evapotranspiration within the vegetation period should lead to the implementation of heavier ^{18}O isotopes in the tree-ring cellulose of *Nothofagus pumilio*. This may be caused by the effect of enhanced leaf-water fractionation in favor of the implementation of heavier ^{18}O isotopes during such phases (Barbour, 2007).

Our analyses with the station-based Marshall Southern Annular Mode Index (SAM) led to even better results indicating a strong influence of seasonal modulations of the SAM on our $\delta^{18}O_{TRC}$ -variations (**Figure 4**). Highly significant positive values are apparent for the whole or parts of the vegetation period, indicating a consistent signal of the SAM. Best results with highest positive correlations can be obtained for a seasonal mean combining spring and summer months ($r_{ONDJ} = 0.62$, $p < 0.01$) or early summer ($r_{OND} = 0.56$; $p < 0.01$), respectively. Additional correlations with the ENSO-related ONI-Index also reveal a positive influence on the $\delta^{18}O_{TRC}$ during the beginning of the vegetation period, however with a lower significance ($r_{ASO} = 0.41$, $p < 0.05$).

In summary, calculations with the regional mean of a CRU TS 4.01 dataset imply, that the seasonal amount of rainfall as well as the maximum temperature during the vegetation period have the largest influence on our $\delta^{18}O_{TRC}$ time-series. The consistent and significant relationships between local temperature and selected seasonal precipitation values for both, instrumental as well as CRU TS 4.01 data are encouraging. This tendency of positive correlations with temperature and negative correlations with precipitation were also reported by Lavergne et al. (2016), who studied the usability of δ^{18}O in *Nothofagus* and *Fitzroya* species in northern Patagonia. The detected strong SAM signals in our $\delta^{18}O_{TRC}$ chronology are in good accordance to existing studies on a spatially consistent influence of the SAM on tree growth in southern South America (Villalba et al., 2012). It is therefore obvious, that our oxygen isotope time series contains valuable amounts of this supra-regional signal. Demonstrably, it can serve as a valuable proxy for SAM variability and therefore regional climate variability within the last two centuries.

Atmospheric Moisture Sources and $\delta^{18}O_{TRC}$

Analysis of moisture source detection was applied for the seasons with highest significant correlations as revealed by proxy-climate relationships. Since our $\delta^{18}O_{TRC}$ values have an annual scale time-resolution, we focused on the analysis of moisture sources during the whole or parts of the vegetation period. **Figure 7** shows the resulting maps of moisture sources during the period September–March for the years 1999 and 2000 (positive anomalies), as well as 2000 and 2002 (negative anomalies). In all 4 years, the maximum of moisture uptake is located in a spatially small region just off the Pacific coast line of the Southern Patagonian Icefield. Moisture sources, which contributed more than 1 mm/month, extend to the subtropics and highlight the role of subtropical moist air injections for the SPI region. Small recognizable differences in moisture sources for the chosen positive or negative years during the extremes are apparent.

Differences between the selected years and the average conditions of the selected time period from 1979 to 2017 are given as an anomaly plot in **Figure 8**. It is apparent, that a higher amount of moisture originates from an area around 90°W and 40°S. In the selected positive extreme years of 1999 and 2008, more moisture comes from subtropical regions. For the vegetation period in the year 2008, our dataset indicated enhanced Westerlies in the mid latitude section. We assume,

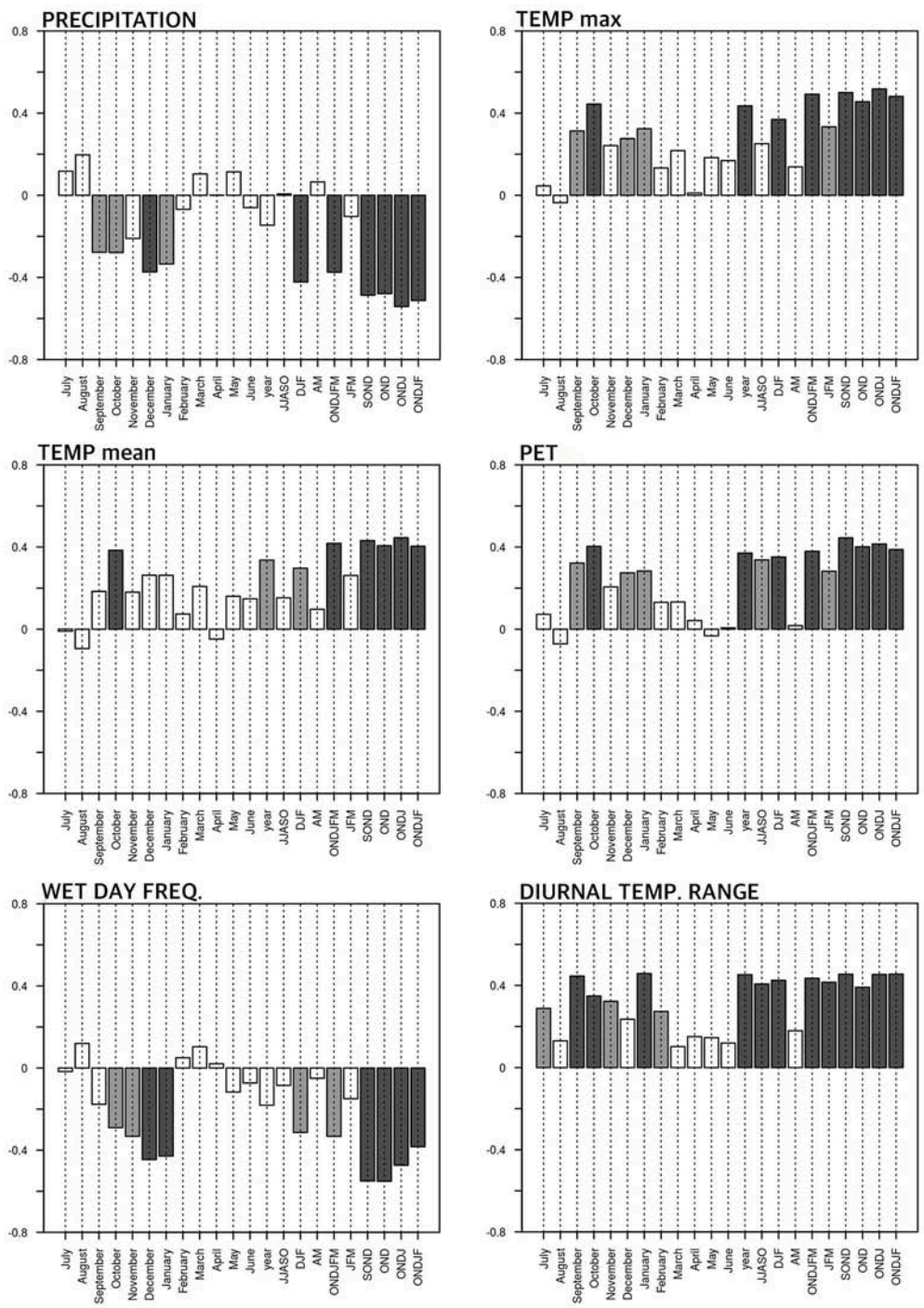

FIGURE 6 | Climate-proxy-relationship between our $\delta^{18}O_{TRC}$ time series and the six most sensitive climate parameters of the calculated regional mean CRU 4.02 data. Light gray bars indicate correlations reaching the $p < 0.05$ level of significance, dark gray bars correlations exceeding the $p < 0.01$ level of significance.

that this could have resulted in a shorter and probably faster moisture transport to the target area, associated with lowered fractionation effects leading to more positive $\delta^{18}O_{TRC}$ values. In contrast, the negative extreme year of 2000 showed an enhanced moisture uptake in the subpolar region. Positive geopotential height anomalies around Antarctica weakened the influence of the westerly wind belt. As a result, cold and dry descending air masses (katabatic winds) from Antarctica triggered the convection over the ice free pacific planetary boundary layer and led to an increase in moisture uptake from 45°S polewards

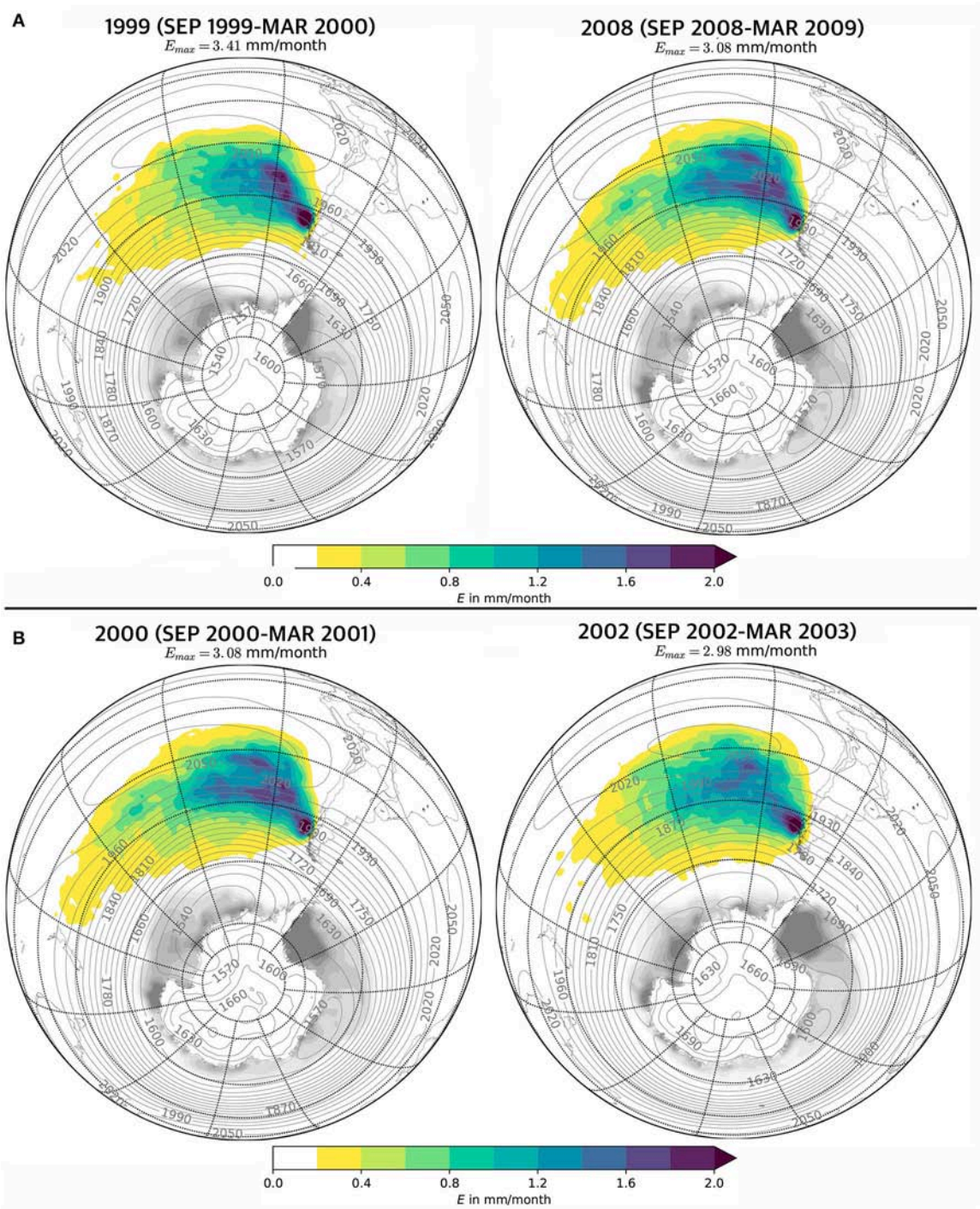

FIGURE 7 | Mean moisture sources (colored area, in mm/month) of the Southern Patagonia Icefield for the chosen **(A)** positive and **(B)** negative extreme years. The individual maximum moisture source exceeding the colorbar legend (E_{max}) is indicated for orientation. Gray lines indicate the average 800 hPa geopotential height and the gray shaded area the average sea ice cover during the respective time period. Interval of the Meridians is 30°, of the Parallels 15°.

(Drüe and Heinemann, 2001). A reduction in the moisture contribution off the Pacific coastline is also apparent in both, the vegetation period 2000 and 2002, although the general anomaly patterns show only little similarities. For instance, the vegetation period 2002 is characterized by an enhanced moisture uptake also in the subtropical region, with up to 0.15 mm/month more moisture originating from the South American continent (**Figure 7**). The associated moisture source recycling could then

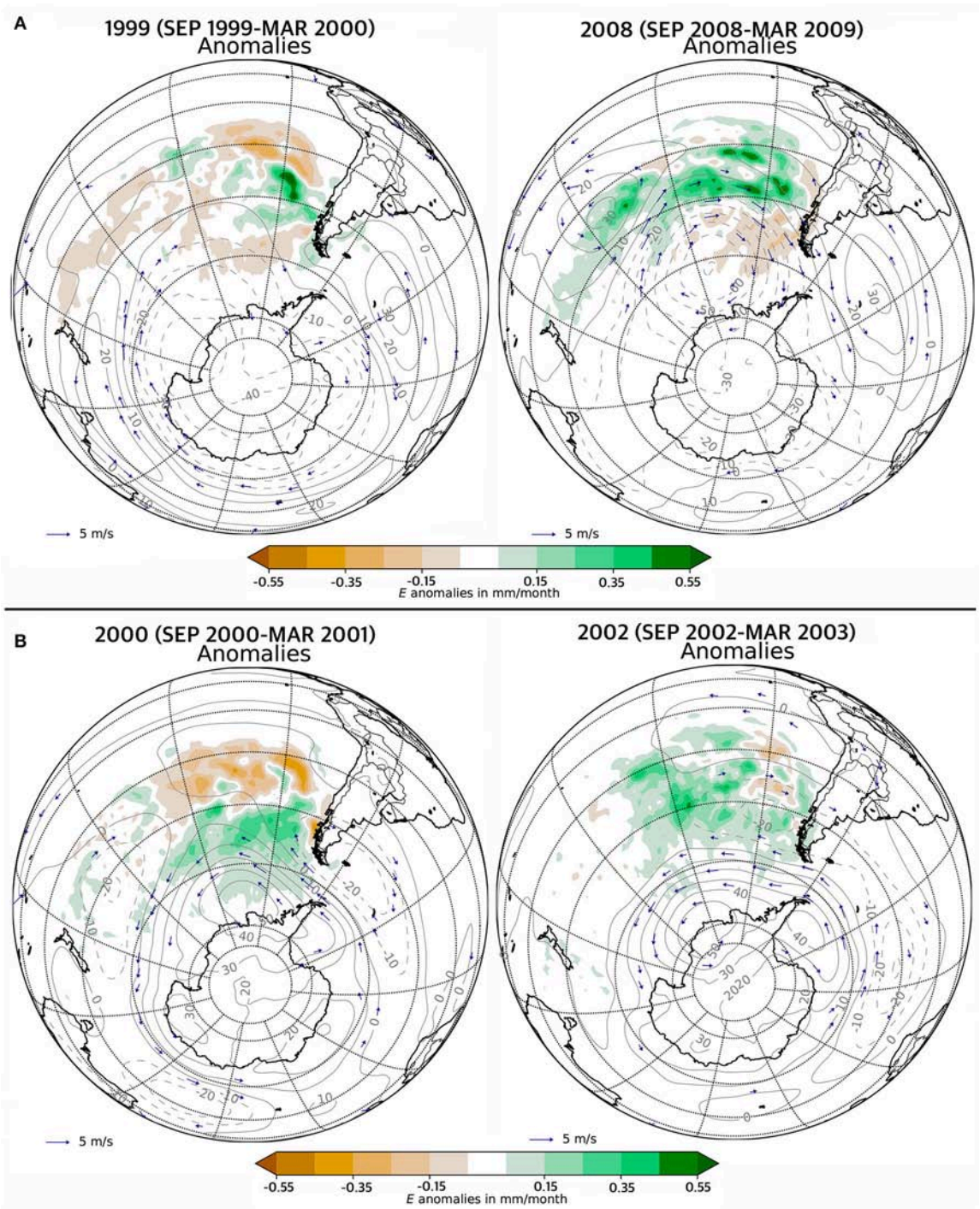

FIGURE 8 | Mean moisture source anomalies in mm/month for the chosen **(A)** positive and **(B)** negative extreme years. Orange areas highlight a moisture source deficit and green areas a surplus during the respective period. The anomalies of the 800 hPa geopotential height and wind field anomalies exceeding 1.5 m/s are depicted as well. Interval of the Meridians are 30°, of the Parallels 15°.

alter the respective $\delta^{18}O_{TRC}$ value and might result in a more negative $\delta^{18}O_{TRC}$.

As described, the negative extreme years can be linked to weaker westerlies around 60°S. Thereby motivated, we tried to disentangle a possible linkage between our extreme years and calculated means for the Antarctic Oscillation Index (AAOI) derived from the NOAA. Interestingly, the negative amplitudes in our two chosen years 2000 and 2003 can be associated to a

negative Antarctic oscillation Index (AAOI; $AAOI_{2000} = -0.45$; $AAOI_{2002} = -0.49$), whereas on the contrary a positive AOI is reported during the positive extremes in 1999 and 2008 ($AAOI_{1999} = 0.91$; $AAOI_{2008} = 0.74$). Despite the up to now insufficient data assignment, we nevertheless assume a stored AAOI signal within our $\delta^{18}O_{TRC}$ which underlines the importance of such time series for a retrospective analysis of extremes or the identification of tipping points on a spatially and/or temporally changing influence of the AOI in South America (Gong and Wang, 1999).

Since we only selected 4 years for our analyses, we are aware that the obtained results at this point certainly cannot be regarded as significant and certainly have to be regarded as provisional. For example, an additional cross-validation with measured precipitation values is necessary, but remains at this point difficult since substantial comparisons are heavily biased due to the assumed problematic precipitation values from the existing meteorological stations. In addition, our results would benefit from a further comparison and cross-validation with data from the Global Network of Isotopes in Precipitation (GNIP). However, this is unfortunately not possible and prevented (i) by generally very sparse, short and incomplete datasets in the area of southern South America or (ii) due to their non-representative location and/or highly faulty and missing data. Notably in an upcoming study, especially regional moisture dynamics caused by the influence of typical lee-effects at orographic barriers have to be therefore accounted (Jiang, 2003; Mölg et al., 2009). However, we can state in accordance to existing studies

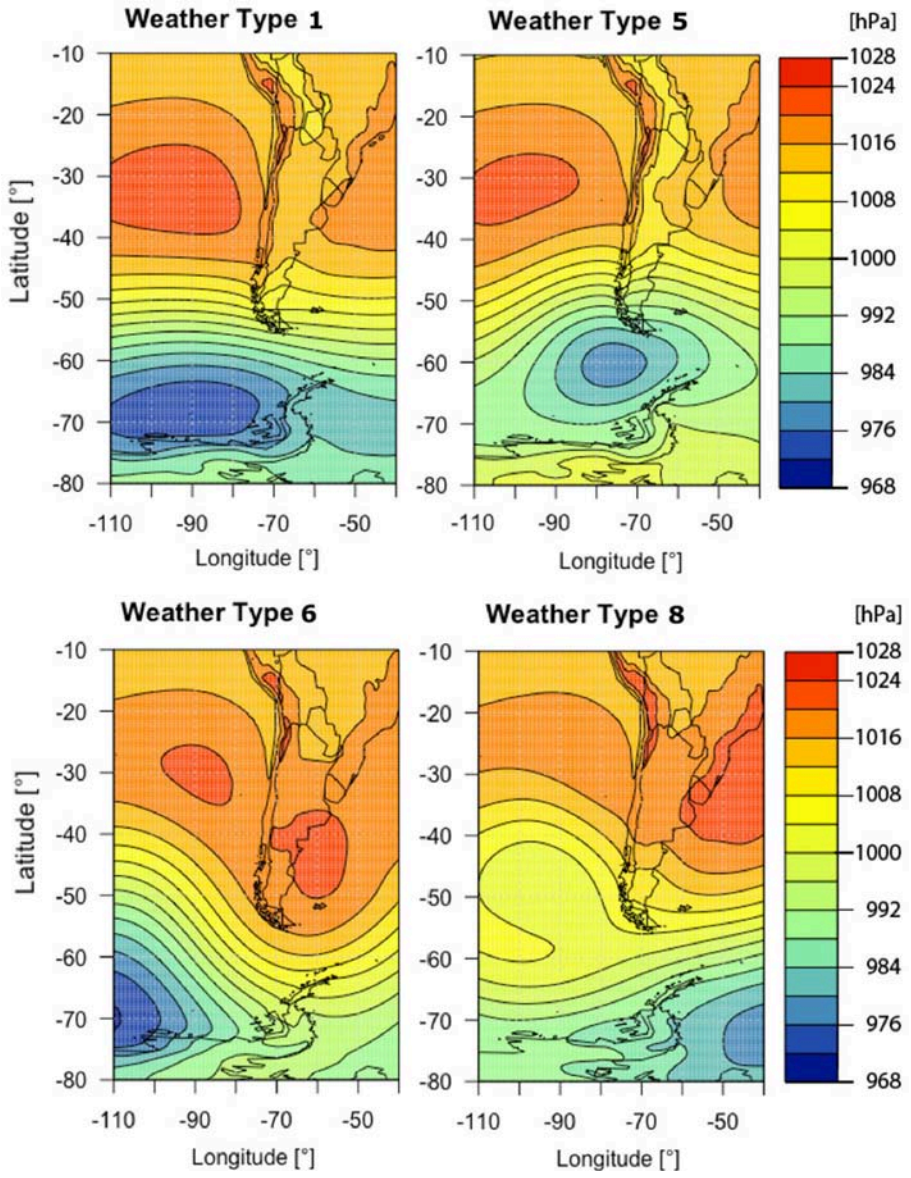

FIGURE 9 | Most relevant main weather types (GWL's) for this study as defined by Weidemann et al. (under review) for South America.

(Wernicke et al., 2017), that the influence of differing moisture pools might have a high impact on our tree-ring $\delta^{18}O$.

Main Weather Types and $\delta^{18}O_{TRC}$

By comparing the seasonal variations in the respective frequencies of all ten weather types with our time series during the period 1979–2013, four types were identified to have the highest influence on our chronology (**Figure 9**). Most promising results were obtained with the influence of main weather type 8 (GWL 8, **Table 2**). For the effect of GWL 8 on our site, we assume comparatively more warm but moist influx from the North and a less pronounced Foehn-effect compared to the regular and typical westerly patterns of GWL 1–3. Highest (negative) correlations between the $\delta^{18}O_{TRC}$ and GWL 8 are apparent for late autumn (March to April, $r_{MAR-APR} = -0.52$, $p < 0.01$), the latter half of the vegetation period from January to April ($r_{JFMA} = -0.43$, $p < 0.05$) and the vegetation period ($r_{SEP-APR}$, $r = -0.42$, $p < 0.05$) (**Table 2**). Calculations with a combination of GWL 6 and 8 (both with similar inflow conditions) also reveal for the same periods a general similar and consistently negative relationships. The combined influence of the combined GWL 6+8 indicate their highest correlation also for late autumn ($r_{MAR-APR} = -0.46$, $p < 0.01$). These findings are in general consistent with the analysis of weather station and SAM data since they reveal that GWL's which do not trigger the typical Foehn-type situations (GWL 6 and GWL 8) tend to either increase precipitation or decrease air temperature (or both in parallel) at our sampling site. The sampling site appears to be situated well-sheltered to the east of the mountain range, and to be low enough to substantially profit from Foehn-effects during regular westerly air flow (approx. on 54% of all days; cf. Weidemann et al., under review). This is also indicated by prevailing positive, but weak correlations between $\delta^{18}O_{TRC}$ and GWL 1 (not shown here).

Results on the analysis of main weather type 5 (GWL 5) on our time-series also reveal continuous negative correlations, which in parts reach the $p < 0.05$ threshold of significance (e.g., December to February, $r_{DEC-FEB} = -0.40$, $p < 0.05$; **Table 2**). In general, an influence of GWL 5 points to southwesterly inflow under rather cyclonic conditions. The flow might be channelized into a more southerly flow along the Andes and therefore should result in overall colder and (possibly due to a reduced Foehn effect) more moist conditions at our sampling site. Negative correlations with the frequency occurrence of GWL 5 would in this respect be consistent with the findings in regard to the results of a strong SAM influence and derived moisture source origins.

It has to be stated, that prevailing influences of the weather type GWL 8 and a combination of GWL6 and GWL 8 with synoptically similar effects on our site are clearly recognizable in our time series. Especially in the latter half of the vegetation period, these weather types and their resulting conditions at our sampling site obviously trigger the regional climate and therefore the $\delta^{18}O_{TRC}$ values. For a substantial spatial analysis about the extent and/or a quantification of regional effects or even general trends of such GWL's in Southern Patagonia, more sites and longer datasets for comparisons are needed. Additional combined analyses on moisture sources associated to the most influencing GWL's could also be of great benefit for disentangling individual extreme events or even past variations in the occurrence of weather types. As mentioned, main challenges for a substantial interpretation are posed by the location of our study site close to the Perito Moreno Glacier and associated local-scale effects like the influence of katabatic winds possibly biasing supra-regional signals.

TABLE 2 | Correlation coefficients (r) between $\delta^{18}O_{TRC}$ and selected main weather types (Grosswetterlagen, GWL).

	GWL 1	GWL 5	GWL 8	GWL 6+8
Sep-May	0.33	−0.37	−0.38	−0.23
Sep-Apr	0.35	−0.39	**−0.42**	−0.23
Jan-Apr	0.22	−0.13	**−0.43**	−0.33
Dec-Feb	0.28	**−0.40**	0.16	0.09
Mar-Apr	0.13	−0.08	**−0.52**	**−0.46**

Bold values indicate r-values being significant on the $p < 0.05$ level.

CONCLUSIONS

Within this study we established an annually resolved record of tree-ring $\delta^{18}O_{TRC}$ from *Nothofagus pumilio* trees at Perito Moreno Glacier. The resulting time-series covers the period 1809–2013 and is the first of its kind in Southern Patagonia south of 50°S. Within the scope of this study, we carried out multiple analyses on proxy-climate relationships to disentangle the imprints of regional to supra-regional climate signals on our $\delta^{18}O_{TRC}$. Results from the proxy-climate calibration indicate a highly significant sensitivity of our time-series on the variability of the Southern Annular Mode (SAM) during the summer season. This signal in its absolute correlation value is much higher than any correlations with climate parameters from local station data or interpolated climate data from the CRU is TS 4.01 datasets. Hence, our calibration study demonstrates, that the obtained $\delta^{18}O_{TRC}$ series is a suitable proxy for the reconstruction of the SAM influence in this region.

Correlations with local station data as well as CRU v. 4.01datasets show a clear and stable relationship with temperature and precipitation for selected seasonal means during the vegetation period. Among these, particularly positive correlations with late autumn temperature in March (station data), maximum temperatures in the early vegetation period (October to January, CRU data) and negative correlations with precipitation data for different parts of the vegetation period (e.g., December to February, CRU data) were apparent. Despite the characteristically steep gradient in precipitation from West to East and coupled changes in vegetation from *Nothofagus* forests at our sample site to the steppe vegetation in El Calafate, we assume that the strong relationships between our proxy and the CRU datasets display a common long-term trend which possibly can be further quantified in an upcoming climate reconstruction. Obviously, the interpolated and gridded CRU-datasets are a more suitable record better displaying climate conditions at our sample

site whereas station data from El Calafate tends to especially underestimates actual precipitation conditions.

A promising approach to disentangle the influence of changing source water pools in precipitation lies in the use of backward trajectories for the determination of moisture sources. In doing so, we were able to interlink years with prominent deviations from the long-term mean in our time-series to varying moisture pools in the Pacific Ocean. Additionally, these years can be directly linked to positive or negative AAOI-phases. An extension of such analyses to the period before 1979 by the use of other ERA datasets with possibly similar spatial resolution would be of great interest to further evaluate this relationship back in time.

Demonstrably, the influence of selected main weather types on our sample site is recorded in our $\delta^{18}O_{TRC}$ series. In general, the analysis on changing frequencies of mean weather types can help to identify and explain causes for extremes or abrupt shifts in the absolute values of a multi-century $\delta^{18}O_{TRC}$ time series. If these shifts can be coupled to changes in synoptic regimes primarily during a reasonable period when the respective proxy is directly recording environmental changes (e.g., during the vegetation period), such time-series can help to understand and decipher phases of stable and/or changing climate conditions in the past.

A main advantage on the choice of glacier-near sites for investigations on $\delta^{18}O_{TRC}$ lies within a possible linkage between different archives linked through the hydrological cycle. Such coupled information derived from the biosphere and observed responses in the cryosphere could lead to a better understanding of interactions and connections within the hydrosphere or atmosphere. Specifically, a possible outcome in further studies could be the comparison of mass balance time-series with local $\delta^{18}O_{TRC}$ series.

AUTHOR CONTRIBUTIONS

JG: Performed the statistical analyses and drafted the manuscript; JG, PS, B-LS, and MB: Contributed to the conception and design of the study; WM, PH, LL, CS, and DS: Performed individual data analyses. All authors jointly contributed to submitted version of the manuscript.

FUNDING

This study was funded by the joint CONYCET-BMBF research project GABY-VASA (grant no. 01DN15020).

ACKNOWLEDGMENTS

We thank I. Burchardt, A. Beyer, and R. Höfner-Stich (University of Erlangen-Nuremberg) for their support during sample preparation and oxygen isotope analyses.

REFERENCES

Abram, N. J., Mulvaney, R., Vimeux, F., Phipps, S. J., Turner, J., and England, M. H. (2013). Evolution of the Southern Annular Mode during the past millennium. *Nat. Clim. Change* 4, 564–569. doi: 10.1038/nclimate2235

Aniya, M., and Skvarca, P. (2012). Little Ice Age advances of Glaciar Perito Moreno, Hielo Patagónico Sur, South American. *Bull. Glaciol. Res.* 30, 1–8. doi: 10.5331/bgr.30.1

Barbour, M. M. (2007). Stable oxygen composition in plant tissue: a review. *Funct. Plant Biol.* 34, 83–94. doi: 10.1071/FP06228

Berkelhammer, M., and Stott, L. (2008). Recent and dramatic changes in Pacific storm trajectories recorded in $\delta^{18}O$ from Bristlecone Pine tree ring cellulose. *Geochem. Geophys. Geosyst.* 9, 1525–2027. doi: 10.1029/2007GC001803

Brienen, R. J., Helle, G., Pons, T. L., Guyot, J. L., and Gloora, M. (2012). Oxygen isotopes in tree rings are a good proxy for Amazon precipitation and El Nino-Southern Oscillation variability. *Proc. Natl. Acad. Sci.* 109, 16957–16962. doi: 10.1073/pnas.1205977109.

Carrasco, J., Casassa, G., and Rivera, A. (2002). "Meteorological and climatological aspect of the Southern Patagonia Icefield," in *The Patagonia Icefields*, eds G. Casassa, F. Sepulveda and M. Sincler (New York, NY: Kluwer-Plenum), 29–41.

Casassa, G., Rivera, A., Aniya, M., and Naruse R. (2002). "Current knowledge of the Southern Patagonia Icefield," in *The Patagonian Ice Fields: A Unique Natural Laboratory for Environmental and Climate Change Studies,* eds G. Casassa, F. V. Sepúlveda and R. Sinclair (New York, NY: Kluwer Academic/Plenum Publishers), 67–83.

Compagnucci, R. H., and Salles, M. A. (1997). Surface pressure patterns during the year over southern South America. *Int. J. Climatol.* 17, 635–653.

Cook, E., and Kairiukstis, L. (1990). *Methods of Dendrochronology, 1st Edn*. Dordrecht; Boston; London: Springer.

Danis, P. A., Masson-Delmotte, V., Stievenard, M., Guillemin, M. T., Daux, V., Naveau, P., et al. (2006). Reconstruction of past precipitation $\delta^{18}O$ using tree-ring cellulose $\delta^{18}O$ and $\delta^{13}C$: A calibration study near Lac d'Annecy, France. *Earth Planet. Sci. Lett.* 243, 439–448. doi: 10.1016/j.epsl.2006.01.023

Dansgaard, W. (1964). Stable isotopes in precipitation. *Tellus* 16, 436–468.

Dayem, K. E., Molnar, P., Battisti, D. S., and Roe, G. H. (2010). Lessons learned from oxygen isotopes in modern precipitation applied to interpretation of speleothem records of paleoclimate from eastern Asia. *Earth Planet. Sci. Lett.* 295, 219–230. doi: 10.1016/j.epsl.2010.04.003

Dee, D. P., Uppala, S. M., Simmons, A. J., Berrisford, P., Poli, P., Kobayashi, S., et al. (2011). The ERA-Interim reanalysis: configuration and performance of the data assimilation system. *Q. J. R. Meteorol. Soc.* 137, 553–597. doi: 10.1002/qj.828

Drüe, C., and Heinemann, G. (2001). Airborne investigation of arctic boundary-layer fronts over the marginal ice zone of the Davis Strait. *Bound-Layer Meteorol.* 101, 261–292. doi: 10.1023/A:1019223513815

Edwards, T. W. D., Birks, S. J., Luckman, B. H., and MacDonald, G. M. (2008). Climatic and hydrologic variability during the past millennium in the eastern Rocky Mountains and Northern Great Plains of western Canada. *Q. Res.* 70, 188–197. doi: 10.1016/j.yqres.2008.04.013

Endlicher, W. (1991). *Zur Klimageographie und Klimaökologie von Südpatagonien. 100 Jahre Klimatologische Messungen in Punta Arenas [Climate-Geography and Climate-Ecology of Southern Patagonia. Hundred Years of Climate Measurements in Punta Arenas].* Vol 32. Freiburg: Univ. Freiburg; Department of Physical Geography, Freiburger Geographische Hefte, 181–211.

Frank, A. (2002). *Semi-Objektive Klassifikation und Statistische Auswertung von Wetterlagen Südpatagoniens [Semi-Objective Classification and Statistical Analysis of Weather Types of South Patagonia],* Master Thesis, Univ. Freiburg.

Fritts, H. (1976). *Tree Rings and Climate.* London, UK; San Francisco, CA; New York, NY: Academic Press Inc.; Elsevier Inc.

Garreaud, R. D., Vuille, M., Compagnucci, R., and Marengo, J. (2009). Present-day south American climate. *Palaeogeogr. Palaeoclimatol. Palaeoecol.* 281, 180–195. doi: 10.1016/j.palaeo.2007.10.032

Garreaud, R., Lopez, P., Minvielle, M., and Rojas, M. (2013). Large-scale control on the Patagonian climate. *J. Clim.* 26, 215–230. doi: 10.1175/JCLI-D-12-00001.1

Gessler, A., Ferrio, J. P., Hommel, R., Treydte, K., Werner, R. A., and Monson, R. K. (2014). Stable isotopes in tree rings: towards a mechanistic understanding of

isotope fractionation and mixing processes from the leaves to the wood. *Tree Physiol.* 34, 796–818. doi: 10.1093/treephys/tpu040.

Gong, D., and Wang, S. (1999). Definition of Antarctic oscillation index. *Geophys. Res. Lett.* 26, 459–462. doi: 10.1029/1999GL900003

Grießinger, J., Bräuning, A., Helle, G., Thomas, A., and Schleser, G. (2011). Late Holocene Asian summer monsoon variability reflected by δ18O in tree-rings from Tibetan junipers. *Geophys. Res. Lett.* 38:L03701. doi: 10.1029/2010GL045988

Grießinger, J., Helle, G., Hochreuther, P., Schleser, G. H., and Bräuning, A. (2017). Late Holocene relative humidity history on the southeastern Tibetan plateau inferred from a tree-ring δ^{18}O record: recent decrease and conditions during the last 1,500 years. *Q. Int.* 430, 52–59. doi: 10.1016/j.quaint.2016.02.011

Harris, I. C., and Jones, P. D. (2017). CRU TS4.01: Climatic Research Unit (CRU) Time-Series (TS) version 4.01 of high-resolution gridded data of month-by-month variation in climate (Jan. 1901- Dec. 2016). *Centre Environ. Data Anal.*

Hartigan, J. (1975). *Clustering Algorithms*. Wiley Series in Probability and Mathematical Statistics. John Wiley & Sons.

Hochreuther, P., Wernicke, J., Grießinger, J., Mölg, T., Zhu, H., Wang, L., et al. (2016). Influence of the Indian Ocean Dipole on tree-ring δ^{18}O of monsoonal Southeast Tibet. *Clim. Change* 137, 217–230. doi: 10.1007/s10584-016-1663-8

Jiang, Q. (2003). Moist dynamics and orographic precipitation. *Tellus* 55a, 301–316. doi: 10.1034/j.1600-0870.2003.00025.x

Johnson, K., and Ingram, B. (2004). Spatial and temporal variability in the stable isotope systematics of modern precipitation in China: implications for paleoclimate reconstructions. *Earth Planet. Sci. Lett.* 220, 365–377. doi: 10.1016/S0012-821X(04)00036-6

Lara, A., Villalba, R., Wolodarsky-Franke, A., Aravena, J. C., Luckman, B. H., and Cuq, E. (2005). Spatial and temporal variation in *Nothofagus pumilio* growth at tree line along its latitudinal range (35°40'-55°S) in the Chilean Andes. *J. Biogeogr.* 32, 879–893. doi: 10.1111/j.1365-2699.2005.01191.x

Laumer, W., Andreu, L., Helle, G., Schleser, G. H., Wieloch, T., and Wissel, H. (2009). A novel approach for the homogenization of cellulose to use micro-amounts for stable isotope analyses. *Rapid Commun. Mass Spectromet.* 23, 1934–1940. doi: 10.1002/rcm.4105.

Lavergne, A., Daux, V., Villalba, R., Pierre, M., Stievenard, M., and Srur, A. M. (2017a). Improvement of isotope-based climate reconstructions in Patagonia through a better understanding of climate influences on isotopic fractionation in tree rings. *Earth Planet. Sci. Lett.* 459, 372–380. doi: 10.1016/j.epsl.2016.11.045

Lavergne, A., Daux, V., Villalba, R., Pierre, M., Stievenard, M., Vimeux, F., et al. (2016). Are the oxygen isotopic composition of *Fitzroya cupressoides* and *Nothofagus pumilio* cellulose promising proxies for climate reconstructions in northern Patagonia? *J. Geophys. Res.* 121, 767–776. doi: 10.1002/2015JG003260

Lavergne, A., Gennaretti, F., Risi, C., Daux, V., Boucher, E., Savard, M. M., et al. (2017b). Modelling tree ring cellulose δ^{18}O variations in two temperature-sensitive tree species from North and South America. *Clim. Past* 13, 1515–1526. doi: 10.5194/cp-13-1515-2017

Leavitt, S. (2010). Tree-ring C-H-O isotope variability and sampling. *Sci. Total Environ.* 408, 5244–5253. doi: 10.1016/j.scitotenv.2010.07.057

Liu, X., An, W., Treydte, K., Shao, X., Leavitt, S., Hou, S., et al. (2012). Tree-ring δ^{18}O in southwestern China linked to variations in regional cloud cover and tropical sea surface temperature. *Chem. Geol.* 291, 104–115. doi: 10.1016/j.chemgeo.2011.10.001

Liu, X., Xu, G., Grießinger, J., An, W., Wang, W., Zeng, X., et al. (2014). A shift in cloud cover over the southeasternTibetan plateau since 1600: evidence from regional tree-ring δ18O and its linkages to tropical oceans. *Quat. Sci. Rev.* 88, 55–68. doi: 10.1016/j.quascirev.2014.01.009

Lund, I. (1963). Map-pattern classification by statistical methods. *J. Appl. Meteorol.* 2, 56–65. doi: 10.1175/1520-0450(1963)002<0056:MPCBSM>2.0.CO;2

Malz, P., Meier, W., Casassa, G., Jana, R., Skvarca, P., and Braun, M. H. (2018). Elevation and mass changes of the Southern Patagonia Icefield derived from TanDEM-X and SRTM Data. *J. Remote Sens.* 10:188. doi: 10.3390/rs10020188

Mathiasen, P., and Premoli, A. C. (2010). Out in the cold: genetic variation of *Nothofagus pumilio* (Nothofagaceae) provides evidence for latitudinally distinct evolutionary histories in austral South America. *Mol. Ecol.* 19, 371–385. doi: 10.1111/j.1365-294X.2009.04456.x.

McCarroll, D., and Loader, N. J. (2004). Stable isotopes in tree rings. *Quat. Sci. Rev.* 23, 771–801. doi: 10.1016/j.quascirev.2003.06.017

Miller, D. L., Mora, C. I., Grissino-Mayer, H. D., Mock, C. J., Uhle, M. E., and Sharp, Z. (2006). Tree-ring isotope records of tropical cyclone activity. *Proc. Natl. Acad. Sci. U.S.A.* 103, 14294–14297. doi: 10.1073/pnas.0606549103

Mölg, T., Chiang, J. C. H., Gohm, A., and Cullen, N. J. (2009). Temporal precipitation variability versus altitude on a tropical high mountain: Observations and mesoscale atmospheric modelling. *Q. J. R. Meteorol. Soc.* 135, 1439–1455. doi: 10.1002/qj.461

Murtagh, F. (1985). *Multidimensional Clustering Algorithms. COMPSTAT Lectures 4.*

Paruelo, J., Beltran, A., Jobbagy, E., Sala, O., and Golluscio, R. (1998). The climate of Patagonia: general patterns and controls on biotic processes. *Ecologia Austral.* 8, 85–101

Philipp, A., Beck, C., Esteban, P., Kreienkamp, F., Krennert, T., Lochbihler, K., et al. (2014a). *cost733class-1.2 - User Guide.* Available online at: http://cost733.geo.uni-augsburg.de/cost733class-1.2

Philipp, A., Beck, C., Huth, R., and Jacobeit, J. (2014b). Development and comparison of circulation type classifications using the cost 733 dataset and software. *Int. J. Climatol.* 36, 2673–2691. doi: 10.1002/joc.3920

Reynolds-Henne, C. E., Siegwolf, R. T. W., Treydte, K., Esper, J., Henne, S., and Saurer, M. (2007). Temporal stability of climate-isotope relationships in tree rings of oak and pine (Ticino, Switzerland). *Glob. Biochem. Cycles* 21:GB4009. doi: 10.1029/2007GB002945

Rignot, E., Rivera, A., and Casassa, G. (2003). Contribution of the Patagonia Icefields of South America to Sea Level Rise. *Science* 302, 434–437. doi: 10.1126/science.1087393

Rosenblüth, B., Fuenzalida, H. A., and Aceituno, P. (1997). Recent temperature variations in southern South America. *Int. J. Climatol.* 17, 67–85.

Sano, M., Dimri, A. P., Ramesh, R., Xu, C., Li, Z., and Nakatsuka, T. (2017). Moisture source signals preserved in a 242-year tree-ring δ^{18}O chronology in the western Himalaya. *Glob. Planet. Change* 157, 73–82. doi: 10.1016/j.gloplacha.2017.08.009

Saurer, M., Kress, A., Leuenberger, M., Rinne, K. T., Treydte, K. S., and Siegwolf, R. T. W. (2012). Influence of atmospheric circulation patterns on the oxygen isotope ratio of tree rings in the Alpine region. *J. Geophys. Res.* 117:D05118. doi: 10.1029/2011JD016861

Schneider, C., Glaser, M., Kilian, R., Santana, A., Butorovic, N., and Casassa, G. (2003). Weather observations across the Southern Andes at 53°S. *Phys. Geogr.* 24, 97–119. doi: 10.2747/0272-3646.24.2.97

Schulman, E. (1956). *Dendroclimatic Change in Semiarid America*. Tucson, AZ: University of Arizona Press.

Sodemann, H., Schwierz, C., and Wernli, H. (2008). Interannual variability of Greenland winter precipitation sources: Lagrangian moisture diagnostic and North Atlantic Oscillation influence. *J. Geophys. Res. Atmos.* 113:D03107. doi: 10.1029/2007JD008503

Stern, L. A., and Blisniuk, P. M. (2002). Stable isotope composition of precipitation across the southern Patagonian Andes. *J. Geophys. Res.* 107, ACL 3-1–ACL 3-14. doi: 10.1029/2002JD002509

Stohl, A., and James, P (2004). A Lagrangian analysis of the atmospheric branch of the global water cycle: Part 1: method description, validation, and demonstration for the August 2002 flooding in central Europe. *J. Hydrometeorol.* 5, 656–678. doi: 10.1175/1525-7541(2004)005<0656:ALAOTA>2.0.CO;2

Stuefer, M., Rott, H., and Skvarca, P. (2007). Glaciar Perito Moreno, Patagonia: climate sensitivities and glacier characteristics preceding the 2003/04 and 2005/06 damming events. *J. Glaciol.* 53, 3–16. doi: 10.3189/172756507781833848

Treydte, K., Boda, S., Graf Pannatier, E., Fonti, P., Frank, D., Ullrich, B., et al. (2014). Seasonal transfer of oxygen isotopes from precipitation and soil to the tree ring: source water versus needle water enrichment. *New Phytol.* 202, 772–783. doi: 10.1111/nph.12741.

Treydte, K., Frank, D., Esper, J., Andreu, L., Bednarz, Z., Berninger, F., et al. (2007). Signal strength and climate calibration of a European tree-ring isotope network. *Geophys. Res. Lett.* 34:L24302. doi: 10.1029/2007GL031106

Treydte, K., Schleser, G. H., Helle, G., Esper, J., Frank, D. C., Winiger, M., et al. (2006). The twentieth century was the wettest period in northern Pakistan over the past Millennium. *Nature* 440, 1179–1182. doi: 10.1038/nature04743

Villalba, R., Lara, A., Boninsegna, J. A., Masiokas, M., Delgado, S., Aravena, J. C., et al. (2003). Large-scale temperature changes across the southern Andes: 20th-century variations in the context of the past 400 years. *Clim. Change* 59, 177–232. doi: 10.1023/A:1024452701153

Villalba, R., Lara, A., Masiokas, M. H., Urrutia, R., Luckman, B. H., Marshall, G. J., et al. (2012). Unusual Southern Hemisphere tree growth patterns induced by changes in the Southern Annular Mode. *Nat. Geosci.* 5, 793–798. doi: 10.1038/ngeo1613

Vogel, J. C., Lerman, J. C., and Mook, W. G. (1975). Natural isotopes in surface and groundwater from Argentina. *Hydrological Science Bulletin* 20, 203–220.

Vuille, M., Franquist, E., Garreaud, R., Lavado, W., and Caceres, B. (2015). Impact of the global warming hiatus on Andean temperature. *J. Geophys. Res.* 120, 3745–3757. doi: 10.1002/2015JD023126

Welker, J. M., Rayback, S., and Henry, G. H. R. (2005). Arctic and North Atlantic Oscillation phase changes are recorded in the isotopes (δ^{18}O and δ^{13}C) of *Cassiope tetragona* plants. *Glob. Change Biol.* 11, 997–1002. doi: 10.1111/j.1365-2486.2005.00961.x

Wernicke, J., Hochreuther, P., Grießinger, J., Zhu, H., Wang, L., and Bräuning, A. (2017). Air mass signals in δ^{18}O of tree-ring cellulose revealed by back-trajectory modeling at the monsoonal Tibetan plateau. *Int. J. Biometeorol.* 61, 1109–1124. doi: 10.1007/s00484-016-1292-y

Wernli, H., and Davies, H. C. (1997). A Lagrangian-based analysis of extratropical cyclones. I: the method and some applications. *Q. J. R. Meteorol. Soc.* 123, 467–489.

Wieloch, T., Helle, G., Heinrich, I., Voigt, M., and Schyma, P. (2011). A novel device for batch-wise isolation of α-cellulose from small amount wholewood samples. *Dendrochronologia* 29, 115–117. doi: 10.1016/j.dendro.2010.08.008

Willis, J. M., Melkonian, A. K., Pritchard, M. E., and Rivera, A. (2012). Ice loss from the Southern Patagonian Ice Field, South America, between 2000 and 2012. *Geophys. Res. Lett.* 39:L17501. doi: 10.1029/2012GL053136

Conflict of Interest Statement: The authors declare that the research was conducted in the absence of any commercial or financial relationships that could be construed as a potential conflict of interest.

frontiers in Earth Science

ORIGINAL RESEARCH
published: 08 May 2018
doi: 10.3389/feart.2018.00053

A 17-year Record of Meteorological Observations Across the Gran Campo Nevado Ice Cap in Southern Patagonia, Chile, Related to Synoptic Weather Types and Climate Modes

Stephanie S. Weidemann[1,2]*, *Tobias Sauter*[3], *Rolf Kilian*[4,5], *David Steger*[1], *Nicolas Butorovic*[6] and *Christoph Schneider*[1]

[1] Geography Department, Humboldt University, Berlin, Germany, [2] Department of Geography, RWTH Aachen University, Aachen, Germany, [3] Department of Geography, Friedrich-Alexander University, Erlangen, Germany, [4] Department of Geology, University of Trier, Trier, Germany, [5] Departamento de Biologia Marina, Universidad de Magallanes, Punta Arenas, Chile, [6] Laboratorio de Climatologia, Instituto de la Patagonia, Universidad de Magallanes, Punta Arenas, Chile

OPEN ACCESS

Edited by:
John F. Burkhart,
University of Oslo, Norway

Reviewed by:
Zoe Courville,
US Army Corps of Engineers Cold Regions Research and Engineering Laboratory, United States
Guillermo Pablo Podesta,
University of Miami, United States
Joseph Michael Shea,
University of Northern British Columbia, Canada

***Correspondence:**
Stephanie S. Weidemann
s.weidemann@geo.rwth-aachen.de

Specialty section:
This article was submitted to Interdisciplinary Climate Studies, a section of the journal Frontiers in Earth Science

Received: 01 January 2018
Accepted: 18 April 2018
Published: 08 May 2018

Citation:
Weidemann SS, Sauter T, Kilian R, Steger D, Butorovic N and Schneider C (2018) A 17-year Record of Meteorological Observations Across the Gran Campo Nevado Ice Cap in Southern Patagonia, Chile, Related to Synoptic Weather Types and Climate Modes. Front. Earth Sci. 6:53. doi: 10.3389/feart.2018.00053

The network of long-term meteorological observations in Southernmost Patagonia is still sparse but crucial to improve our understanding of climatic variability, in particular in the more elevated and partially glaciated Southernmost Andes. Here we present a unique 17-year meteorological record (2000–2016) of four automatic weather stations (AWS) across the Gran Campo Nevado Ice Cap (53°S) in the Southernmost Andes (Chile) and the conventional weather station Jorge Schythe of the Instituto de la Patagonia in Punta Arenas for comparison. We revisit the relationship between *in situ* observations and large-scale climate models as well as mesoscale weather patterns. For this purpose, a 37-year record of ERA Interim Reanalysis data has been used to compute a weather type classification based on a hierarchical correlation-based leader algorithm. The orographic perturbation on the predominantly westerly airflow determines the hydroclimatic response across the mountain range, leading to significant west-east gradients of precipitation, air temperature and humidity. Annual precipitation sums heavily drop within only tens of kilometers from ~7,500 mm a^{-1} to less than 800 mm a^{-1}. The occurrence of high precipitation events of up to 620 mm in 5 days and wet spells of up to 61 consecutive days underscore the year-around wet conditions in the Southernmost Andes. Given the strong link between large-scale circulation and orographically controlled precipitation, the synoptic-scale weather conditions largely determine the precipitation and temperature variability on all time scales. Major synoptic weather types with distinct low-pressure cells in the Weddell Sea or Bellingshausen Sea, causing a prevailing southwesterly, northwesterly or westerly airflow, determine the weather conditions in Southernmost Patagonia during 68% of the year. At Gran Campo Nevado, more than 80% of extreme precipitation events occur during the persistence of these weather types. The evolution of the El Niño Southern Oscillation and Antarctic Oscillation

impose intra- and inter-annual precipitation and temperature variations. Positive Antarctic Oscillation phases on average are linked to an intensified westerly airflow and warmer conditions in Southernmost Patagonia. Circulation patterns with high-pressure influence leading to colder and dryer conditions in Southernmost Patagonia are more frequent during negative Antarctic Oscillation phases.

Keywords: Southern Patagonia, Chile, meteorological observations, Gran Campo Nevado Ice Cap, weather type classification, ENSO, Mann-Kendall trend test

1. INTRODUCTION

The climate of Southernmost Patagonia is dominated by impinging westerlies coming from the Pacific Ocean, which are strongly perturbed by the north-south striking Southern Andes. The strong orographic induced uplift results in hyperhumid conditions at the windward side of the Southernmost Andes while downslope subsidence leads to strong arid conditions within a belt of a few hundred kilometers on the eastern side (Carrasco et al., 2002; Schneider et al., 2003; Garreaud et al., 2013). Due to the prevailing westerlies and the vicinity of the Pacific Ocean, temperatures are moderate in Southernmost Patagonia with low daily and seasonal temperature amplitudes (Paruelo et al., 1998; Schneider et al., 2003; Villalba et al., 2003).

Moderate summer temperatures and high accumulation amounts constrain the equilibrium altitude line (ELA) at around 700 m elevation and thus enabled the formation of glaciated areas south of the Southern Patagonian Icefield. One of these is the Gran Campo Nevado (GCN) Ice Cap which extends to about 200 km^2 in the south of the Muñoz Gamero peninsula at about 53°S (**Figure 1**) (Schneider et al., 2007). The GCN Ice Cap is made up of the main glacier plateau with highest elevations of ~1,630 m a.s.l. and several individual outlet glaciers, some reaching sea level. The predominant westerlies cause overall strong winds and sharp local west-east gradients in precipitation and air temperature. Schneider et al. (2003) estimated the maximal annual precipitation amount of up to 10,000 mm a^{-1} at the highest elevations causing a high mass turnover with steep specific mass-balance gradients of the GCN outlet glaciers (Möller et al., 2007; Weidemann et al., 2013).

Large-scale modes of climate variability like the El Niño Southern Oscillation (ENSO) and Antarctic Oscillation (AAO), also known as the Southern Hemisphere Annular Mode (SAM), significantly influence precipitation and air temperature in southern South America (e.g., Thompson and Solomon, 2002; Marshall, 2003; Schneider and Gies, 2004; Fogt and Bromwich, 2006; Gillett et al., 2006). ENSO influences the interannual climate variations in the subtropical parts of South America, and weakens toward the southern tip of South America (Aceituno, 1988; Schneider and Gies, 2004; Gillett et al., 2006; Aravena and Luckman, 2009; Garreaud et al., 2009). Intensified positive AAO phases lead to a strong temperature and precipitation response (Gillett et al., 2006; Aravena and Luckman, 2009; Garreaud et al., 2009).

Climate variability in Southern Patagonia is the key driver of local changes in the cryosphere (e.g., Möller et al., 2007; Davies and Glasser, 2012). A variety of environmental paleorecords offer the possibility to study climate changes and short term climate variability (e.g., storm events) in Southern Patagonia from the late Holocene to the Last Glacial Maximum and beyond (e.g., Villalba et al., 2003; Lamy et al., 2010; Kilian and Lamy, 2012). However, the network of long-term meteorological observations which is needed to calibrate paleoclimate proxies for example from dendro-climatology (Aravena et al., 2002), sediment (Kilian et al., 2007) or peat cores (Kilian et al., 2003, 2007) as well as recent (Schneider et al., 2007) and Holocene (Koch and Kilian, 2005; Kilian et al., 2013) glacier fluctuations in the Southern Andes is still sparse in Southernmost Patagonia. The mass balance modeling study of Möller and Schneider (2008) indicate a pronounced mass-balance sensitivity of the GCN Ice Cap to temperature. The presented meteorological time series provide the opportunity to study the climate forcing on recent changes of the ice cap. The quality of future surface mass balance modeling studies benefits significantly from such unique long-term time series.

Here, we revise and extend former climate studies at the GCN Ice Cap (Schneider et al., 2003; Schneider and Gies, 2004) by analyzing the main climate features and their variability. Meteorological observations since 2000 provide more robust estimates of the observed annual and seasonal means, anomalies, extremes and trends. The characteristics are related to mesoscale weather patterns, classified by a hierarchical correlation-based leader algorithm. Annual and seasonal trends in air temperature are investigated by applying the non-parametric Mann-Kendall and Sen slope estimator trend test (Mann, 1945; Kendall, 1975; Yue et al., 2002). Furthermore, we focus on how ENSO and AAO impact the regional climate.

2. DATA

2.1. Observations

We analyze meteorological time series of four AWS located close to the GCN Ice Cap and one conventional weather station (WS) at Punta Arenas in Chile (**Figure 1**). An overview of the pertinent data is given in **Table 1**. Detailed information about the geographical setting of AWS Paso Galería (PG), AWS Puerto Bahamondes (BH) and AWS Estancia Skyring (SR) is given in Schneider et al. (2003). In addition, a fourth AWS named Arévalo (AR) has operated since September 2007 and is located at the northwestern side of the ice cap at about 58 m a.s.l..

The AWS are manufactured by Campbell Scientific Ltd. (United Kingdom). The similarly designed stations are equipped

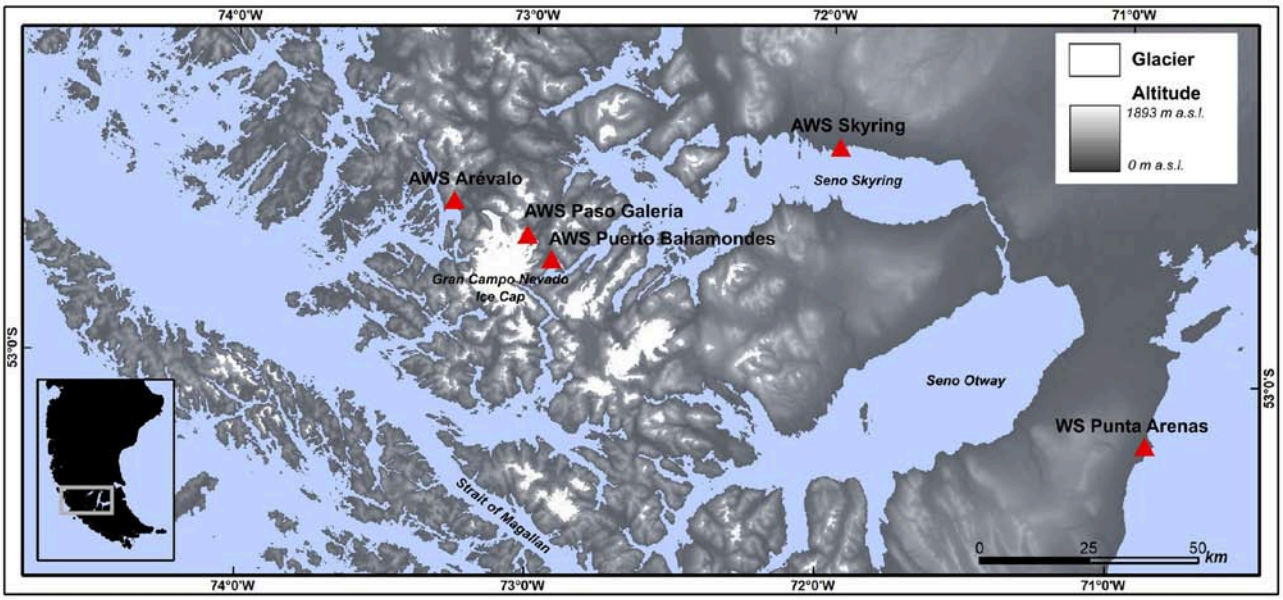

FIGURE 1 | Location of automatic weather stations (AWS) at the Gran Campo Nevado Ice Cap and the weather station (WS) at Punta Arenas. Glacier outlines are based on the Randolph Glacier Inventory 6.0.

TABLE 1 | Pertinent data to the weather station and automatic weather stations used in this study.

Name	Acronym	Latitude/Longitude	Altitude	Operating since	Variable
Arévalo	AR	52°41'S/73°16'W	58 m	September 2007	T, rH, P, SW, v, dir
Paso Galería	PG	52°45'S/73°01'W	383 m	October 1999	T, rH, P, SW, v, dir
Puerto Bahamondes	BH	52°48'S/72°56'W	26 m	October 1999	T, rH, P, SW, v, dir, sp
Skyring	SR	52°33'S/71°58'W	8 m	March 2001	T, rH, P, SW, v, dir
Punta Arenas (J.S.)	PA	53°08'S/70°53'W	6 m	Approx. 1970	T, rH, P, v, dir

Meteorological variables are air temperature (T), relative humidity (rH), precipitation (P), incoming shortwave radiation (SW), wind speed (v), wind direction (dir) and surface pressure (sp).

with sensors of air temperature, air humidity, precipitation, solar radiation, wind speed and wind direction (**Table 2**, Figure S1). All meteorological variables but precipitation are measured at 2 m above the surface. Precipitation is measured at 1 m above the ground using unshielded tipping-bucket rain gauges. This type of measurement underestimates precipitation by up to 30% at wind speeds of 1.5 m s^{-1} and even up to 50% at wind speeds of 3.0 m s^{-1} (Rasmussen et al., 2012; Buisán et al., 2017). Wind-speed induced deviations increase during snowfall due to an intensified drifting of snow (Rasmussen et al., 2012; Buisán et al., 2017). Substantial deviations are further suspected during high precipitation events, since strong precipitation events are often accompanied with strong wind gusts. During periods with very strong winds, the tipping bucket tends to shake which leads to an overestimation of precipitation. Correction factors for this kind of inaccuracy are not available. According to Schneider et al. (2003), the precision of the precipitation measurement at AWS BH and AWS PG is estimated to be about ±20%. We used this number as estimate of uncertainty for all AWS in this study. Wind-speed induced deviations have been minimized due to an additional fixation of the rain gauges in 2010 at AWS PG and in 2016 at AWS BH to avoid the shaking of the tipping bucket. Overall, precipitation data must be interpreted with care bearing in mind that these data are subject to considerable uncertainty in the order of potentially several tens of percent. Meteorological observations at the conventional WS Punta Arenas (PA) hold the longest and most complete time series. These observations (2000-2016) are measured according to the World Meteorological Organization standards. Data are provided by the Laboratory of Climatology, Instituto de la Patagonia, Universidad de Magallanes. Yearly records are published in Anales del Instituto de la Patagonia, Chile (e.g., Butorovic, 2016).

The quality of the time series is assured by performing some basic quality integrity and outlier checks (Durre et al., 2010). In case of unrealistic values, such as relative humidity larger than 100%, identical values for maximum and minimum air temperature, or a repetition of data records within a month, data are excluded. Furthermore, records are checked for daily outliers (Durre et al., 2010) and missing values within a month. Months with missing values of daily observations are not further considered. In case of precipitation, this leads to an exclusion of daily precipitation observations at AWS BH in 2000/01 and

TABLE 2 | Instrumentation at AWS Paso Galería, AWS Puerto Bahamondes, AWS Arévalo, and AWS Skyring as used in this study.

Variable	Sensor	Type	Nominal accuracy
Air temperature	Thermistor	Campbell HMP-35-AC, Campbell CS215	< 0.1 K, ±0.9°C (−40° to 70°C)
Relative humidity	Capacitor	Campbell HMP-35-AC, Campbell CS215	±3%, ±4% (0 to 100%)
Precipitation	Unheated tipping bucket rain gauges	Campbell AGR100, Young RM52203	±20% (assumption)
Wind direction	Wind vane, combined wind monitor	Campbell W200P, Young 05103	±2°, ±3°
Wind speed	Anemometer	Campbell A100R, Young 05103	1% ±0.1 m s^{-1}, 1% ±0.3 m s^{-1}
Incoming shortwave radiation	Silicon pyranometer	Campbell SP1110, Campbell CS300	±3%,±5% (daily totals)

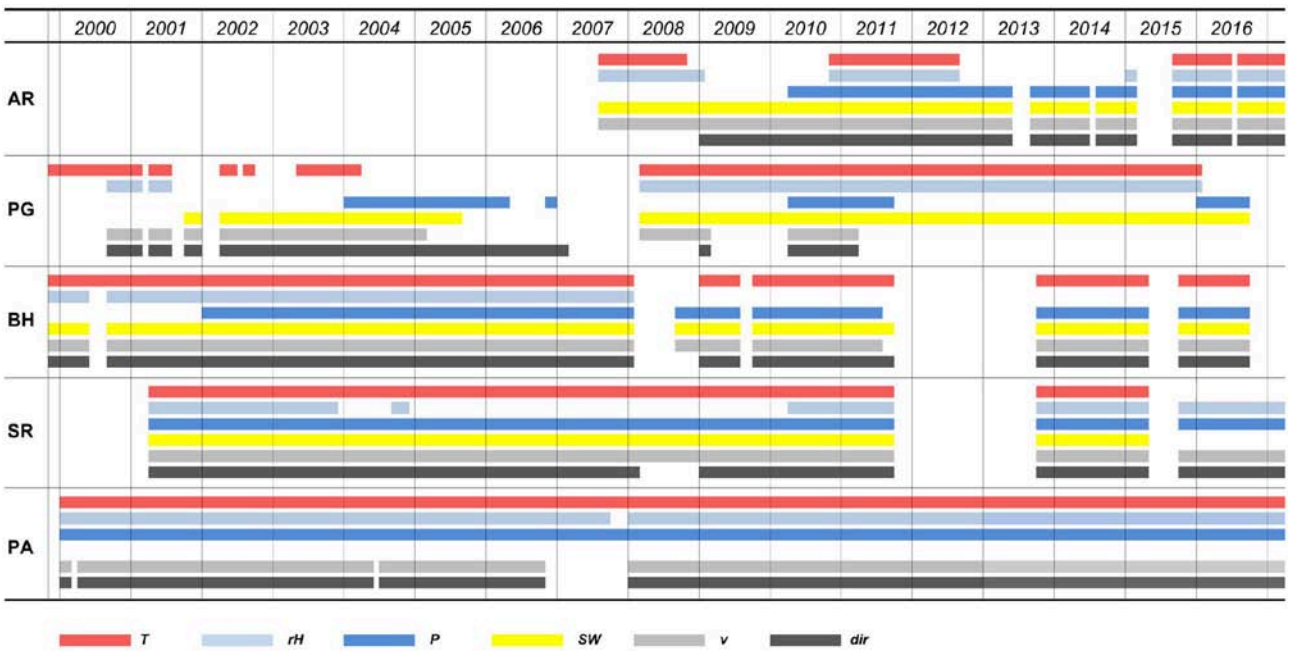

FIGURE 2 | Available observation periods at AWS Arévalo (AR), AWS Paso Galería (PG), AWS Puerto Bahamondes (BH), AWS Skyring (SR), and WS Punta Arenas (PA). Shown are measurement periods of air temperature (T), relative humidity (rH), precipitation (P), incoming shortwave radiation (SW), wind speed (v), and direction (dir).

at AWS PG in 2008/09. In addition, failures of power supply or sensors due to harsh weather conditions cause substantial data gaps in addition. **Figure 2** shows the available observation periods for each station on a monthly basis as used in this study.

2.2. Reanalysis Data

For mesoscale weather type classification, daily mean sea level pressure (MSLP) reanalysis data are obtained from the ERA-Interim dataset provided by the European Centre for Medium-Range Weather Forecasts (ECMWF) (Dee et al., 2011). The data sets are downloaded with a spatial resolution of 0.75° × 0.75° grids and 12-hourly temporal resolution (0 a.m., 12 p.m. UTC) between 1979 and 2016 for the area 10°S −80°S and 40°W −110°W covering most of South America and the Antarctic Peninsula. The selected area as well as the choice of MSLP as weather classification variable followed the weather type classification as used by Frank (2002) and Schneider et al. (2003).

2.3. Indices of Large-Scale Modes of Climate Variability

To reveal the impact of ENSO and the AAO on climate variability in Southernmost Patagonia, we compare the monthly anomalies of observations with the Oceanic Niño Index (ONI) and the Antarctic Oscillation Index (AAOI). Both indices are provided by the U.S. National Oceanic and Atmospheric Administration (NOAA) - Climate Prediction Center.

ONI identifies El Niño and La Niña events in the tropical Pacific by using a 3-month running mean of ERSST.v5 sea surface temperature anomalies in the Niño 3.4 region (5°N-5°S, 120°-170°W) (Barnston et al., 1997; Huang et al., 2017). Events are defined as five consecutive overlapping 3-month periods with anomalies ≥+0.5°C for El Niño and ≤-0.5°C for La Niña events. Data is available from http://www.cpc.ncep.noaa.gov/data/indices/oni.ascii.txt.

The monthly AAOI is constructed by projecting the monthly mean 700 hPa height anomalies poleward of 20°S onto the first

empirical orthogonal function mode of monthly mean height anomalies at 700 hPa (Thompson and Solomon, 2002). Positive phases are characterized by a strengthening and poleward shift of the westerlies with decreased surface pressure and geopotential height over the fringe of Antarctica. During negative phases, opposite conditions prevail. Monthly data of AAOI can be obtained from http://www.cpc.ncep.noaa.gov/products/precip/CWlink/daily_ao_index/aao/aao_index.html.

3. METHODS

3.1. Indices of Climate Extremes

Climate extremes of air temperature and precipitation (**Table 3**) are described using selected indices of extremes (Tank et al., 2009). In case of air temperatures extremes, time series of maximum (TX) and minimum (TN) air temperature are analyzed regarding the number of days with ice ($TX \leq 0°C$) (ID) and frost ($TN \leq 0°C$) (FD). Percentiles are calculated based on the available observations period (**Figure 2**) to define the number of days with TX < 10th percentile (P1TX), TN < 10th percentile (P1TN), TX > 90th percentile (P9TX) and TN > 90th percentile (P9TN). Furthermore, we are interested in the maximum length of a cold spell (CS) with consecutive days of TN < 10th percentile, and the maximum length of a warm spell (TWS) with consecutive days of TX > 90th percentile per year.

Precipitation extremes are described by the absolute maximum of 1-Day (PDX) and 5-Day (P5DX) precipitation (mm) as well as the annual amount of daily precipitation larger than the 95th percentile (P95P) and the 99th percentile (P99P). The maximum number of days with daily precipitation higher than 20 mm (HP) and below 1 mm (DD), and the maximum length of wet spells (PWS) and dry spells (DS) per year are also examined.

3.2. Weather Type Classification

Weather types are classified by applying the automated classification map-pattern scheme by Lund (1963) based on MSLP. The LUND-algorithm is based on so-called leader patterns. It constitutes a low computational cost predecessor of other cluster algorithms (Hartigan, 1975; Murtagh, 1985). Within the LUND-algorithm, in a first run a leader is defined as the one observation showing most similar cases (observations) of correlations higher than a given threshold with all other observations (Lund, 1963; Philipp et al., 2014a). After removal of the leader and its matching cases, e.g., all observations that correlate with the identified leader above the set threshold Pearson correlation coefficient, the remaining class leaders are called in similar iterative processes (Lund, 1963; Philipp et al., 2014a). After the determination of all leaders, single days are assigned to a specific weather type by returning all observations to the data pool and assigning each one to the nearest leader based on linear correlation (Lund, 1963; Philipp et al., 2014a). The threshold Pearson correlation coefficient for finding leader weather types in this study is set to 0.85. The Lund classification scheme accentuates the dominance of few weather types with westerly air flow. Subsequently, it finds further weather types that occur only rarely but are important and significantly different patterns. In contrast, k-mean leader algorithms tend to locate centroids in such that all classes become equally large (Philipp et al., 2014b). The latter would have resulted in many undesirably similar weather types of principally westerly airflow.

Weather type classifications are calculated from the ERA-Interim MSLP reanalysis data for the period 1979–2016.

TABLE 3 | Indices of air temperature extremes based on daily maximum (TX) and minimum (TN) air temperatures.

	AR		PG		BH		SR		PA	
	Value	**Year**	**Value**	**Year**	**Value**	**Year**	**Value**	**Year**	**Value**	**Year**
Max TX	23.6	2008	20.4	2004	24.5	2008	25.8	2004	29	2013
Max TN	−5.4	2011	−8.9	2002	−8.1	2005	−11.3	2001	−5.1	2002
Max range	15.1	2008	15.3	2002	16.1	2005	21.0	2006	19.2	2004
Max ID	8	2012	39	2012	6	2005	7	2014	4	2002
Max FD	49	2011	130	2009	66	2001/02	112	2005	100	2002
Max P1TX	69	2012	58	2012	63	2014	64	2014	58	2002
Max P1TN	61	2011	50	2003	60	2002	61	2002	68	2002
Max P9TX	56	2008	54	2001	58	2004	61	2008	53	2008
Max P9TN	51	2016	83	2013	75	2015	70	2014	50	2004
Max CS	16	2012	11	2012	19	2005	16	2001/14	13	2001
Max TWS	9	2008	14	2004	13	2005/08	13	2005	12	2008
Mean TX	7.4	07–16	5.1	00-16	8.9	00–16	9.7	01-16	10.2	00-16
Mean TN	4.5	07–16	2.3	00-16	4.0	00–16	3.2	01–16	2.6	00–16
Mean range	2.8	07–16	2.8	00-16	4.9	00-16	6.5	01–16	7.6	00–16

*Listed are the absolute maximum of daily TX and TN, of daily air temperature range, of days with ice (TX<0°C) (ID) and with frost (TN<0°C) (FD), maximum of days with TX< 10th percentile (P1TX), TN < 10th percentile (P1TN), TX> 90th percentile (P9TX) and TN> 90th percentile (P9TN), maximum length of a cold spell (CS) with consecutive days of TN < 10th percentile, and the maximum length of a warm spell (TWS) with consecutive days of TX > 90th percentile. Percentiles are calculated based on the observations period of each station (**Figure 2**).*

We apply the cost733class-1.2 software (http://cost733.geo.uni-augsburg.de/cost733class-1.2) originally designed for circulation type classifications in Europe (Philipp et al., 2014b). We checked for the optimal number of classes using a k-means leader algorithm by evaluating the increase of explained cluster variance with increasing numbers of cluster. The number of 10 weather types was found to be optimal which is in accordance with the weather type classification of Frank (2002), used by Schneider et al. (2003). Earlier weather type classifications document only six weather types (Endlicher, 1991; Compagnucci and Salles, 1997). **Figure 7** shows the resulting 10 MSLP centroids obtained from the classification procedure after Lund (1963) as used in this study.

3.3. Trend Detection

Annual and seasonal trends in air temperature based on the 17-year record of AWS PG, AWS BH, AWS SR, and WS PA are analyzed. Air temperature changes over the given time period can further be related to observed recent changes of the GCN Ice Cap outlet glaciers.

Trends are detected using the non-parametric Mann-Kendall (MK) and Sen slope estimator (SSE) trend test. The combined MK and SSE test has been frequently used to quantify the significance and magnitude of trends in climatological and hydrological time series (e.g., Hamed, 2008; Gocic and Trajkovic, 2013; Kisi and Ay, 2014; Onyutha et al., 2016). The MK test is a non-parametric test to identify linear and non-linear trends in time series (Mann, 1945; Kendall, 1975). The test does not require normally-distributed input data and has a low sensitivity to abrupt breaks due to inhomogeneous time series. The magnitude of the trend in terms of slope is the robust estimate of the median following the approach by Sen (1968) and Theil (1950).

The elimination of autocorrelation in time series analysis is essential because otherwise autocorrelation increases the chances of detecting a significant trend even in case trends are absent. Therefore, Yue et al. (2002) proposed the Trend-Free Pre-Whitening (TP) method in case both trend and lag-1 autocorrelation exist in the data record.

To detect trends in the time series we followed the described steps below:

- testing the significance of the lag-1 autocorrelation (AC) in each time series (step 1)
- in case of significant AC, TP is applied (step 2) and the MK and SSE tests are applied subsequently
- in case of insignificant AC, the MK and SSE tests are performed directly on the original time series (step 3)

The Trend-Free Pre-Whitening procedure (step 2) includes the following steps. First, the apparent linear trend of the time series X_i is removed. Afterward, the lag-1 correlation coefficient r_{ac} of the detrended time series $X_{DE,i}$ is determined. The lag-1 AC is then eliminated from $X_{DE,i}$ by:

$$X_{DE,A,i} = X_{DE,i} - r_{ac} \cdot X_{DE,i-1}. \quad (1)$$

The removed linear trend is then added to $X_{DE,A,i}$ to obtain the final blended time series to which the MK and SSE trend detection test is applied.

4. RESULTS AND DISCUSSION

4.1. Time Series and Extremes

Time series of air temperature, relative humidity, precipitation, wind speed and wind direction are analyzed regarding their daily, monthly and annual means, and anomalies. Mean annual and monthly values of the meteorological variables for each station are listed in Table S1 in the supplement. Annual means are averaged based on monthly mean values. The study period of each time series relates to the available observation period shown in **Figure 2**.

4.1.1. Air Temperature

Mean annual air temperatures for the individual measurement period of each station (**Figure 2**) along the west-east transect are 5.8°C at AWS AR, 3.8°C at AWS PG, 6.0°C at AWS BH, 6.6°C at AWS SR, and 6.6°C at WS PA.

The air temperature distribution in mountain areas with strong orographic effects can also be detected in the spatial distribution of mean daily maximum and minimum air temperature and air temperature range (**Table 3**). The absolute extremes of daily air temperatures range from −8.9°C and +20.4°C at AWS PG, from −8.1°C and +24.5°C at AWS BH, and −11.3°C and +25.8°C at AWS SR during the observation period 2000 to 2016.

The coldest temperature regime with the lowest mean of daily maximum temperature of +5.1°C and minimum temperature of 2.3°C is found at AWS PG. The numbers of frost and ice days are larger than at the other stations due to the altitude and contiguity to the ice cap (**Table 3**). In 2009, minimum temperature dropped below 0°C in 36% of the days. The lower amplitudes of the annual temperature cycle of AWS AR and AWS BH are a result of more maritime conditions compared to

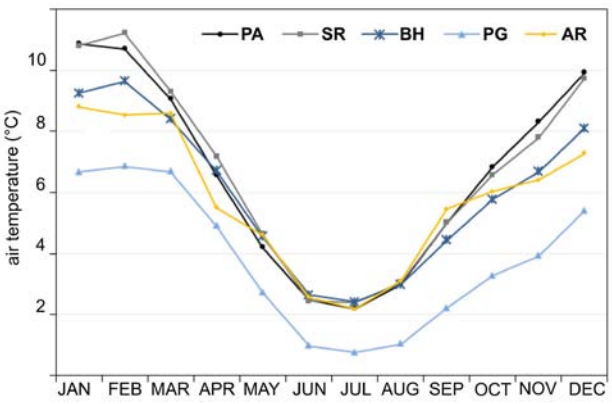

FIGURE 3 | Mean monthly air temperature at AWS Arévalo (AR), AWS Paso Galería (PG), AWS Puerto Bahamondes (BH), AWS Skyring (SR), and WS Punta Arenas (PA) averaged over the individual observation period (**Figure 2**).

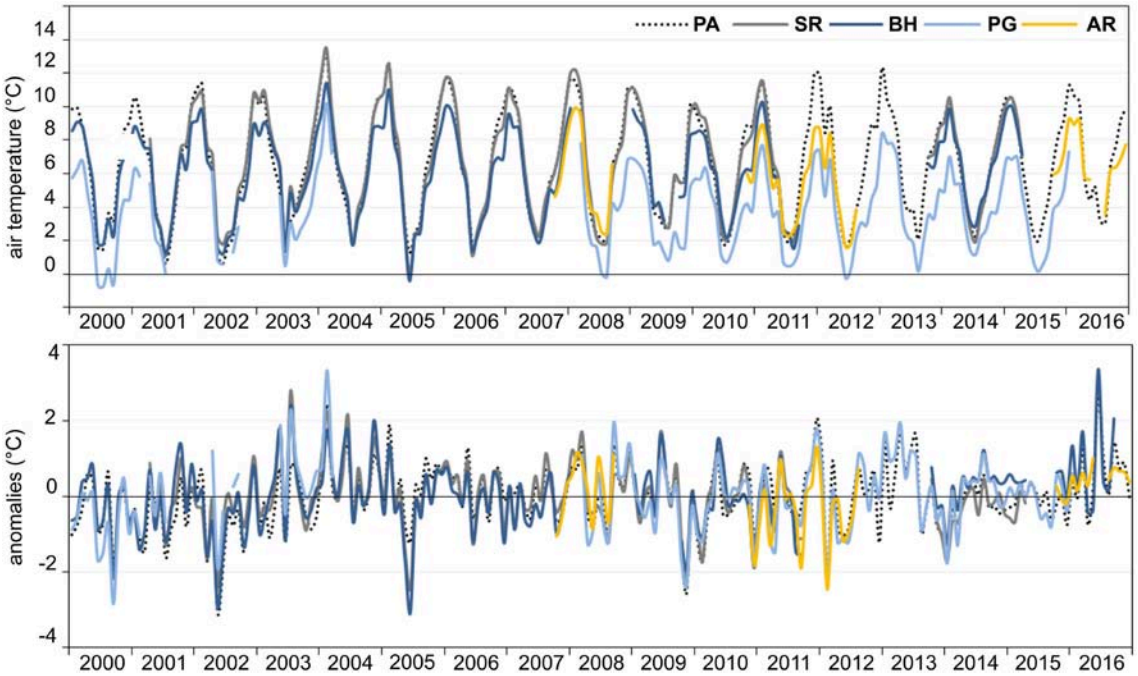

FIGURE 4 | Monthly air temperature and monthly anomalies at AWS Arévalo (AR), AWS Paso Galería (PG), AWS Puerto Bahamondes (BH), AWS Skyring (SR), and WS Punta Arenas (PA) from 2000 to 2016.

AWS SR and WS PA (**Figure 3**, Table S1). The influence of the Pacific Ocean also leads to less days with frost and ice. Toward the east the mean annual temperatures and the number of days with daily maximum air temperature exceeding the 90th percentile and daily minimum air temperature dropping below the 10th percentile increase.

Figure 4 illustrates the monthly means of air temperature and anomalies since 2000, showing a high correlation of $r = 0.94–0.99$ in temperature variability between all stations. Above average cold months were observed in spring 2000, winter 2002 and 2005, spring 2009 and summer 2011/12 at all stations. The longest cold spell and the largest numbers of days where the maximum temperature drops below the 10th percentile for AWS AR and AWS PG are found in 2012 (**Table 3**). Positive anomalies occurred during winter 2003, the summer months 2003/04 and during winter 2016.

The annual anomalies of mean, maximum and minimum temperatures suggest in general milder climate conditions with less extremes since 2012 at GCN (Tables S2, S3). This observation is supported by lower annual means of daily temperature ranges and a decreasing number of days with frost per year at all stations. Furthermore, the percentage of days per year with extreme warm (P9X) or cold conditions (P1N) are decreasing as well (Table S3). Annual changes in the duration of cold or warm spells, however, are not significant. We hypothesize that the warmer conditions are caused by the strengthening of the westerlies during the enhanced positive AAO in recent years (Marshall, 2003).

4.1.2. Wind Speed and Direction

The prevailing westerlies dominate the wind patterns year-around at GCN with mean annual wind speeds ranging from 3.1 m s^{-1} (AWS BH) to 5.1 m s^{-1} (AWS PG) (**Figure 5**). The highest mean of daily mean and maximum wind speeds of 5.1 m s^{-1} and 13.4 m s^{-1} are observed at AWS PG along with prevailing north-west winds. Mean wind speeds of 3.1 m s^{-1} at AWS BH are lower than at AWS SR and WS PA with values of 3.7 m s^{-1} and 4.5 m s^{-1}, respectively. The mean maximum wind speed of 9.7 m s^{-1} at AWS BH, however, is higher than at AWS SR (8.0 m s^{-1}). Schneider et al. (2003) pointed out that this underscores the occurrence of strong gusty winds in morphologically structured landscapes. In general, mean and maximum wind speeds decrease during the winter months at all stations but AWS AR. The characteristic southerly winds at AWS AR are caused by the topographic situation channeling the airflow.

4.1.3. Precipitation

A sharp gradient of precipitation can be found across the GCN Ice Cap within only tens of kilometers. Mean annual precipitation (2008–2016) increases from ~3,800 mm at the west side of GCN at AWS AR to ~6,100 mm at AWS PG while it decreases again on the lee-side to ~4,000 mm at AWS BH. Within a distance of about 80 km, precipitation sharply drops to ~790 mm at AWS SR. Mean annual amounts of 570 mm are observed at WS PA for the same study period. Considering the observations at AWS PG since 2002, the annual mean accounts for ~7,500 mm with the highest annual

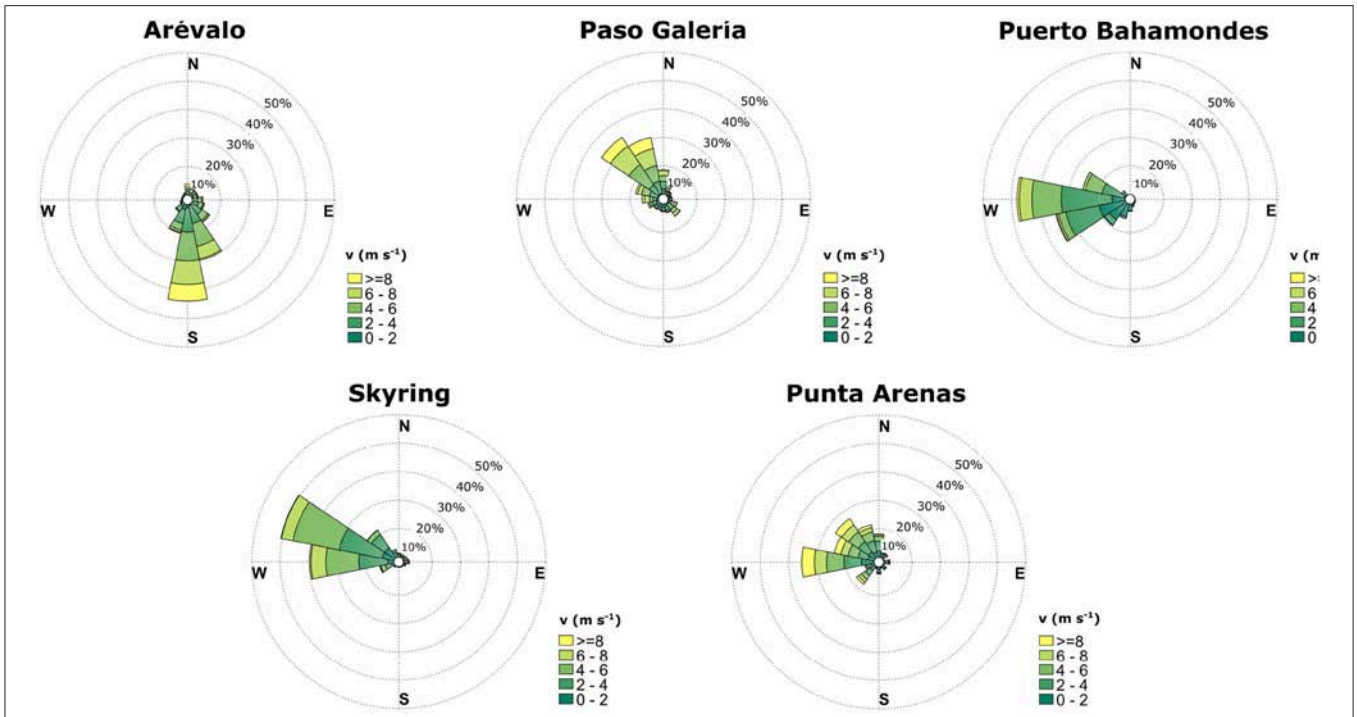

FIGURE 5 | Frequency of wind direction and wind speed (v) at AWS Arévalo, AWS Paso Galería, AWS Puerto Bahamondes, AWS Skyring, and WS Punta Arenas. The available observation period for each station can be found in **Figure 2**.

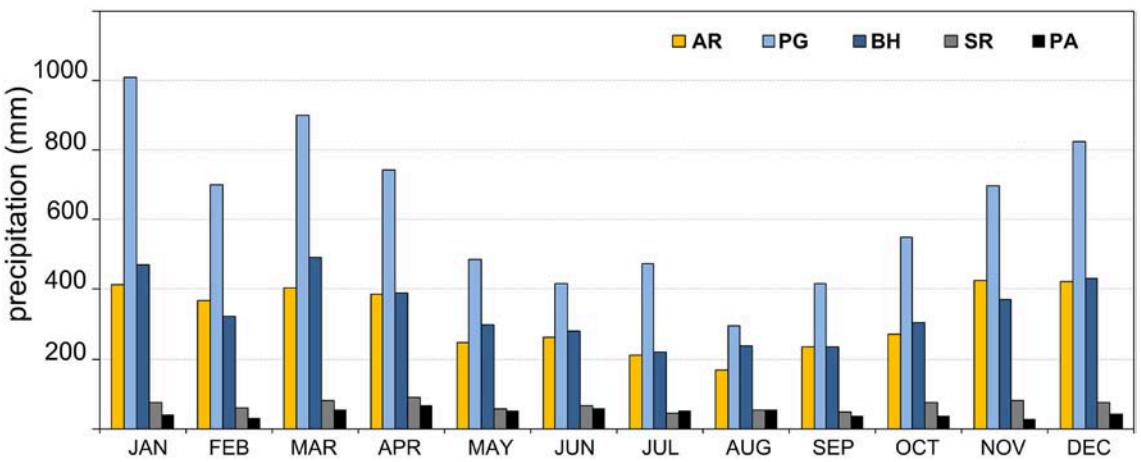

FIGURE 6 | Mean monthly precipitation AWS Arévalo (AR) (2008-2016), AWS Paso Galería (PG), AWS Puerto Bahamondes (BH), AWS Skyring (SR), and WS Punta Arenas (PA). Values were averaged from 2000 to 2016.

amount of ~9,500 mm measured in 2003. Higher measurement inaccuracies in the first years of precipitation observations must be assumed due to the less firm installation of the rain gauge. Therefore, the estimated mean annual values of AWS PG (10,900 mm ±20%) and AWS BH (6,600 mm ±20%) as provided by Schneider et al. (2003) are resulting from measurement errors during episodes of strong winds, leading to an overestimation of annual precipitation sums between 2000 and 2003.

The intra-annual variability of precipitation at AWS AR, AWS PG, and AWS BH correlates well with the highest amounts occuring during the austral summer. The drop in monthly precipitation in February is revealed at all three stations (**Figure 6**). The annual course at AWS SR is more similar to the ones at GCN, but with much lower precipitation, while the intra-annual variability at WS PA is opposite. Precipitation during the winter is slightly higher than during the austral summer. Inter-annual variations of precipitation between AWS SR and AWS

PA show opposite patterns. In years with positive precipitation anomalies at AWS SR, precipitation mostly decreases at AWS PA (Table S2). In principal, the same holds true for AWS BH and AWS PA for the few full years of available precipitation data.

The occurrence of high precipitation events of up to 620 mm in 5-days in 2004 and wet spells of up to 61 days in 2006 underscore the year-around wet conditions at GCN (**Table 4**). Individual events of extreme precipitation (P5DX, P95P, P99P) are most frequent at AWS PG. Between 2002 and 2006, 26% of the annual amount of precipitation fell during days where the daily precipitation exceeds the 95th percentile (Table S4). This ratio changes to a mean of 8% in 2010, 2011, 2016. The amounts of precipitation during extreme precipitation events and days with daily precipitation larger than 20 mm (HP) are similar between the western (AWS AR) and eastern side (AWS BH) of GCN with a high year-to-year variability between 2011 and 2016. The percentage of HP is negligible for AWS SR and WS PA. Nevertheless, daily extreme events of up to 124 mm can occur at AWS SR as observed in 2010. The lengths of wet spells are subsequently smaller while the lengths of dry spells are much larger compared to the three stations at GCN (**Table 4**).

4.2. Trends

Annual and seasonal trends in mean (T), minimum (TN) and maximum (TX) air temperature are analyzed for AWS PG, AWS BH, AWS SR, and WS PA as described in section 3.3. Significant lag-1 autocorrelation was only detected for TN of AWS BH which was corrected following the TP procedure before trend detection. An overview of the trend analysis results is given in **Table 5**.

Trends in annual mean air temperature for AWS PG and AWS PA are significant at the 90% level with a trend magnitude (Sen Slope) of $+0.05^{\circ}C\ a^{-1}$ and $+0.02^{\circ}C\ a^{-1}$. An increasing

TABLE 4 | Indices of precipitation extremes.

	AR		PG		BH		SR		PA	
	Value	**Year**	**Value**	**Year**	**Value**	**Year**	**Value**	**Year**	**Value**	**Year**
Max 1-Day	125	2011	284	2004	213	2006	124	2010	51	2012
Max 5-Day	256	2011	620	2004	341	2004	201	2001	94	2012
Max P95P	1258	2014	2693	2003	1517	2007	524	2001	254	2015
Max P99P	441	2012	979	2006	620	2007	370	2001	85	2012
Max HP	79	2012	159	2003	80	2007	9	2001	7	2015
Max DD	90	2016	83	2005	128	2002	259	2006	284	2016
Max PWS	47	2016	61	2006	45	2010	15	2001	12	2006
Max DS	9	2012	14	2005	21	2006/16	50	2006	33	2005

*Listed are the absolute maximum of 1-Day and 5-Day precipitation (mm), of the total annual amount of daily precipitation larger than the 95th percentile (P95P), of the total annual amount of daily precipitation larger than the 99th percentile (P99P), the maximum number of days with daily precipitation higher than 20 mm (HP), the maximum number of days with daily precipitation below 1 mm (DD), and the maximum length of wet spells (PWS) and dry spells (DS). Percentiles are calculated based on the observations period of each station (**Figure 2**).*

TABLE 5 | Statistical results of the trend analysis for annual and seasonal mean (T), maximum (TX), and minimum (TN) air temperature in $^{\circ}C\ a^{-1}$ for AWS Paso Galería (PG), AWS Puerto Bahamondes (BH), AWS Skyring (SR), and WS Punta Arenas (PA).

		PG			BH			SR			PA		
		T	**TX**	**TN**	**T**	**TX**	**TN**	**T**	**TX**	**TN**	**T**	**TX**	**TN**
Annual	Sen Slope	0.05	−0.15	0.31	0.03	−0.08	0.09	−0.02	−0.05	0.11	0.03	0.03	0.03
	p-value	**0.04**	0.48	**<0.01**	0.46	**0.06**	0.31	0.74	0.55	0.25	**0.04**	0.23	0.30
DJF	Sen slope	0.01	-0.24	0.16	0.01	−0.15	0.11	-0.11	-0.22	0.14	-0.01	−0.01	−0.02
	p-value	1.00	**0.02**	0.11	1.00	**0.02***	**0.04***	**0.06**	**0.03**	0.38	0.65	0.90	0.65
MAM	Sen slope	0.04	-0.03	0.22	0.04	-0.07	0.14	0.09	0.01	0.24	0.02	0.03	0.02
	p-value	0.51	0.84	**0.01**	0.45	0.44	**0.03**	0.25	0.95	**<0.01**	0.13	0.30	0.65
JJA	Sen slope	0.04	−0.12	0.15	0.09	-0.03	0.14	0.02	−0.05	0.10	0.05	0.04	0.03
	p-value	0.46	**0.04**	**0.01***	**0.08**	0.64	0.09	0.84	0.64	0.20	**0.08**	0.11	0.23
SON	Sen slope	0.02	-0.08	0.19	0.05	-0.11	0.18	0.00	−0.17	0.10	0.04	0.03	0.06
	p-value	0.65	**0.01**	**0.01**	0.14	0.08	**0.02**	0.95	0.16	0.25	0.17	0.48	0.11

*Significant values at the 90% level are shown in bold. Trends significant at the 95% level are bold and underlined. P-values denoted with * are obtained after TP procedure from time series with significant lag-1 autocorrelation. In case of annual trend calculation, years with less than 250 days per year with data were not considered.*

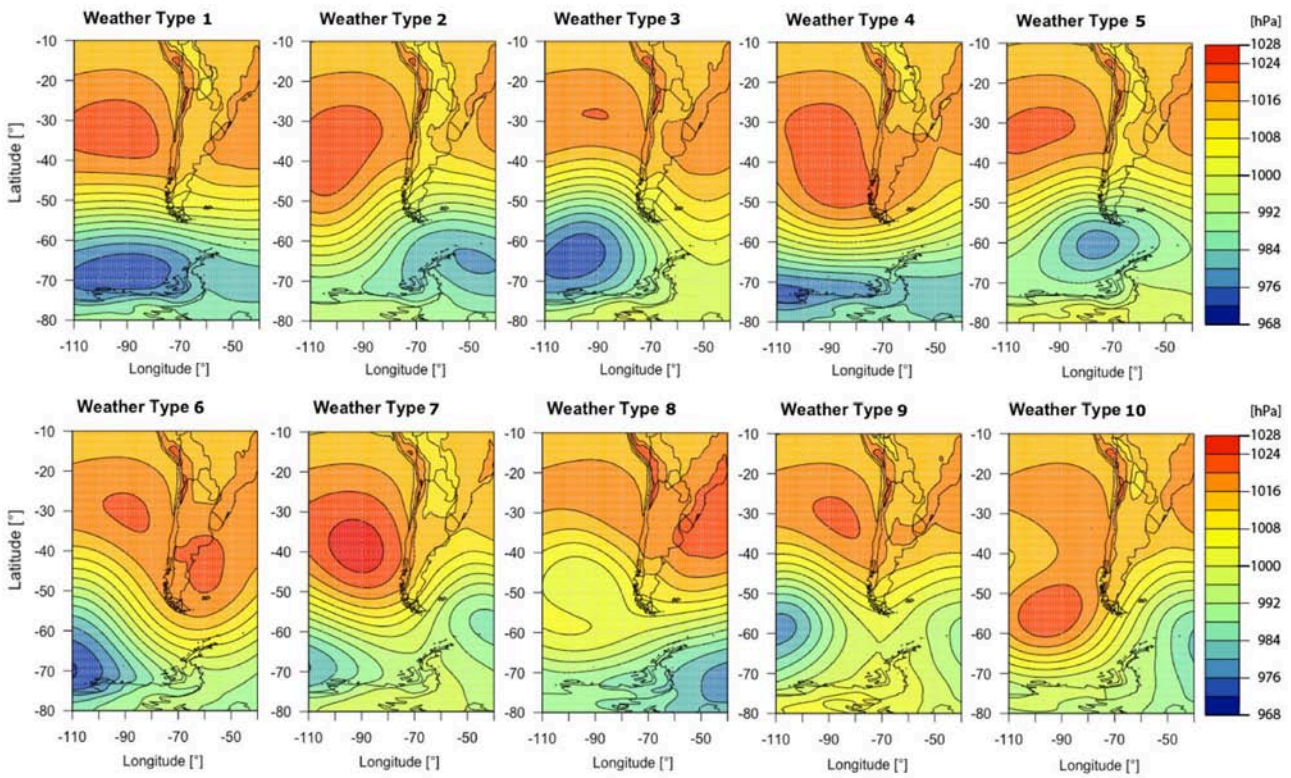

FIGURE 7 | Ten major weather types classified by means of ERA-Interim MSLP reanalysis data for the period 1979 to 2016.

trend of seasonal mean air temperature is only apparent during winter (JJA) at AWS BH and WS PA. A significant upward trend is detected in the annual TN at AWS PG of +0.31°C a^{-1} between 2000 and 2016. This upward trend is also reflected in different seasons as well. TN increases significantly during spring (SON), winter and fall (MAM) at AWS PG, and during summer (DJF), spring and fall at AWS BH. Three of four stations show upwards trends of TN during spring and fall. In contrast, significant downward trends of TX during the summer season are determined for AWS PG, AWS BH and AWS SR. The largest trend of −0.24°C a^{-1} (2000 and 2016) was found at AWS PG. No significant trend has been detected in annual and seasonal TX time series for WS PA.

4.3. Types of Synoptic Weather Patterns

Ten major types of synoptic weather patterns have been classified for Southernmost Patagonia (**Figure 7**). Weather type 1 is characterized by a strong north-south pressure gradient resulting from a distinct high-pressure cell over the Pacific and low-pressure trough over the Bellingshausen Sea, which leads to intensified westerlies. During weather type 2, the high-pressure cell is weaker and shifted toward the south, while the low-pressure cell is located south of Tierra del Fuego in the Weddell Sea. Cold and humid air masses from the south-west are advected to Southernmost Patagonia (Frank, 2002). A similar circulation pattern to type 2, but with a distinct low-pressure cell located south of Tierra del Fuego in the Drake Passage occurs during weather type 5. A north-westerly advection of humid and warm air occurs when both, the Pacific anticyclone and the low-pressure cell, are shifted toward the north-west of southern South America compared to type 1. Pressure gradients become weaker during weather type 9 while the principal synoptic configuration is mostly the same.

The atmospheric circulation of weather type 4 is dominated by an intensified high-pressure cell in the southern Pacific reaching far toward the eastern side of the Southern Andes. The persistence of this situation leads to warmer and dryer conditions. A southward shift of the Pacific anticyclone with the advection of colder air masses from south-west, is present during weather type 7. A strong high-pressure cell in the southern Atlantic accompanied with low pressure in the southern Pacific is present during weather type 6. The Atlantic anticyclone is stronger and shifted toward the north in case of type 8. Both weather patterns imply a northerly or westerly airflow with increased air temperatures. The circulation pattern of weather type 10 is dominated by a strong high-pressure cell located far toward the south in the Pacific leading to a cold and humid airflow from the south over Southernmost Patagonia.

Major synoptic weather types with distinct low-pressure cells in the Weddell Sea (types 2 and 5) or Bellingshausen Sea (types 1, 3, and 9), causing a prevailing southwesterly, northwesterly or westerly airflow, account for 68% of all days in Southernmost Patagonia. In 32% of all situations, high pressure cells over the southern Pacific (types 4, 7, and 10) and southern Atlantic (types

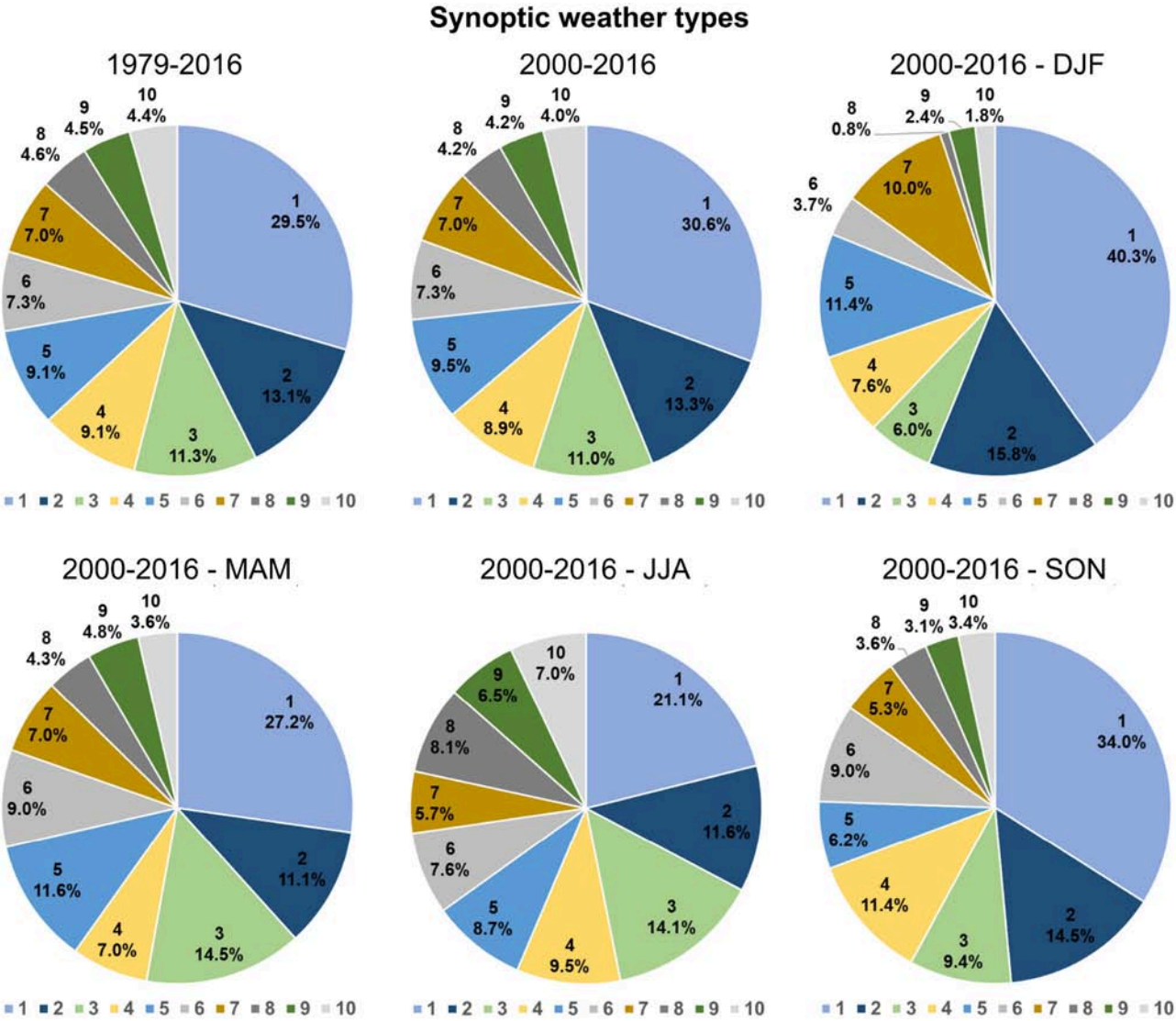

FIGURE 8 | Frequencies of synoptic weather types averaged between 1979 and 2016, 2000 and 2016 and for summer (DJF), fall (MAM), winter (JJA) and spring (SON) between 2000 and 2016.

6 and 8) determine the weather of Southernmost Patagonia. Circulation pattern type 1 with a strong zonal westerly air flow is the most common type of all weather patterns, occurring 30% of the year (**Figure 8**, **Table 6**). During the austral summer the frequency of weather patterns with westerly air flow increases to 76% compared to high-pressure influenced weather types (24%). During the austral winter anticyclonic circulation patterns account for 40% of all situations, while low-pressure weather types occur less. This is in accordance with the generally lower wind speeds found in winter at all weather stations in this study.

Anomalies of observed air temperature, precipitation, wind speed, solar radiation, and relative humidity are analyzed according to the major synoptic types of weather patterns for all five stations (**Figure 9**). Similar types of weather patterns are grouped into classes as listed in **Table 6**. Large positive air temperature anomalies are accompanied with strong westerlies (class 1) at all five stations. Air temperature anomalies at AWS BH, AWS AR, and AWS PG however are smaller compared to AWS SR and WS PA due to the influence of the nearby GCN Ice Cap and proximity to the Pacific Ocean. The impact of strong westerlies on air temperature anomalies is largest in the austral fall. On days with southwesterly airflow (class 2 and 5), air temperatures slightly drop at the stations located close to GCN Ice Cap, while air temperatures tend to rise during northwesterly airflow (class 3 and 9). The advection of colder air masses from the southwest (class 2 and 5) largely determines the air temperature variability during the summer and fall season.

The impact of circulation patterns with intensified high-pressure cells in southern Pacific and Atlantic (classes 4 and 7, 6 and 8 and 10) on air temperature variability is in general low, but

TABLE 6 | Frequency of synoptic weather types and classes (%) between 1979 and 2016 and 2000 and 2016.

	Frequency of synoptic types (%)										Frequency of synoptic classes (%)					
1979-2016	**1**	**2**	**3**	**4**	**5**	**6**	**7**	**8**	**9**	**10**	**1**	**2 and 5**	**3 and 9**	**4 and 7**	**6 and 8**	**10**
Mean	30	13	11	9	9	7	7	5	4	4	30	22	16	16	12	4
DJF	38	15	8	7	11	3	10	1	4	2	38	26	12	17	4	2
MAM	26	12	14	7	10	9	7	5	6	5	26	22	19	14	14	5
JJA	20	12	13	10	9	8	5	9	5	8	20	21	19	15	17	8
SON	34	14	10	12	6	9	6	4	3	3	34	20	13	18	12	3
2000-2016	**1**	**2**	**3**	**4**	**5**	**6**	**7**	**8**	**9**	**10**	**1**	**2 and 5**	**3 and 9**	**4 and 7**	**6 and 8**	**10**
Mean	31	13	11	9	9	7	7	4	4	4	31	23	15	16	12	4
DJF	40	16	6	8	11	4	10	1	2	2	40	27	8	18	5	2
MAM	27	11	15	7	12	9	7	4	5	4	27	23	19	14	13	4
JJA	21	12	14	10	9	8	6	8	6	7	21	20	21	15	16	7
SON	34	15	9	11	6	9	5	4	3	3	34	21	12	17	13	3

Frequencies are given as annual means and seasonal means for summer (DJF), fall (MAM), winter (JJA) and spring (SON).

highest for AWS SR and WS PA. The advection of air masses from the north and northwest under high-pressure influence (class 6 and 8) cause warmer conditions at all stations in SON and DJF, while temperatures decrease during the austral winter except for AWS AR which is the only station located clearly west of the Cordillera. The advection of cold air masses from the south (class 10) causes a significant decrease of daily air temperature at all stations with the largest negative anomalies for WS PA and AWS SR. During fall and spring, air temperatures drop significantly below the specific means (class 10).

Circulation patterns highly impact the precipitation variability at the GCN Ice Cap during all seasons. The orographic induced uplift of the humid air masses from west and southwest (classes 1 and 2 and 5) comes along with year-around positive precipitation anomalies at the GCN Ice Cap. Precipitation amounts decrease significantly during high-pressure influences, in case of classes 6 and 8 and 10. The stations located at GCN (AWS AR, AWS BH, AWS PG) obtain more than 80% of daily precipitation during westerly airflow. East of the GCN Ice Cap at AWS SR and WS PA, mean daily precipitation amounts are similar during all weather types. Precipitation increases slightly on days with southwesterly air flow at AWS SR, while at WS PA daily precipitation increases on days with north to northwesterly wind directions (classes 3 and 9 and 6 and 8). The annual precipitation amounts at AWS SR and WS PA are still mainly determined by the airflow from west (class 1) and south west (class 2 and 5) despite the fact that these stations are clearly located on the leeward of the Cordillera during westerly air flow but extreme precipitation rates are rare. Of all daily precipitation extremes (higher than the 90th percentile) 80% can be associated with classes 1 and 2 and 5 at the GCN stations, while the percentage decreases to 70% at AWS SR and 51% at WS PA. High precipitation events at WS PA are also present during the class 3 and 8 with 20 and 13% of the days, respectively. This finding indicates that precipitable water in the air column is carried across the Cordillera by strong upper air westerly winds. During classes 1 and 2 and 5, both stations experience often foehn-type weather conditions with cloud dispersal due to the subsidence of air masses on the lee-side of the Cordillera. High incoming solar radiation can therefore be observed at AWS SR during these types of weather patterns. Since the westerly air flow is also accompanied by higher air temperatures, relative humidity decreases at all stations, but strongest at AWS SR and WS PA.

Wind speed is highest during westerly (class 1) and southwesterly (class 2 and 5) airflow for all stations. AWS AR shows negative wind speed anomalies on days with strong westerlies which are caused by the location of the AWS and local effects due to the surrounding topography as described in section 4.1.2. Wind from north-northwest (classes 3 and 9 and 6 and 8) is in general weaker on days with high-pressure influence (class 6 and 8).

4.4. Teleconnection to El Nino-Southern Oscillation and Antarctic Oscillation

4.4.1. Time Series

Most of the monthly anomaly records show significant lag-1 autocorrelations at the 95% level which were eliminated before removing the trend as described in section 3.3. Time series are then correlated to ONI and AAOI also considering time lags of up to +3 months. Correlations between monthly anomalies of mean (T), maximum (TX), and minimum (TN) air temperature, rel. humidity (rH), precipitation (P) and wind speed (v), and monthly ONI and AAOI are listed in **Table 7**.

Correlations between monthly anomalies and ONI are weak (**Table 7**, **Figure 10**), which is consistent with previous studies (Schneider and Gies, 2004; Garreaud et al., 2009). Since 2000 seven cold (ONI≤-0.5) and five warm (ONI≥ +0.5) periods have been observed. A significant negative correlation of −0.26 can be identified for precipitation anomalies at AWS BH. Monthly precipitation decreases by −9% (−32 mm) during El Niño events (ONI≥ +0.5) at AWS BH compared to the monthly mean (2000-2016) while it increases by +9% during La Nina events

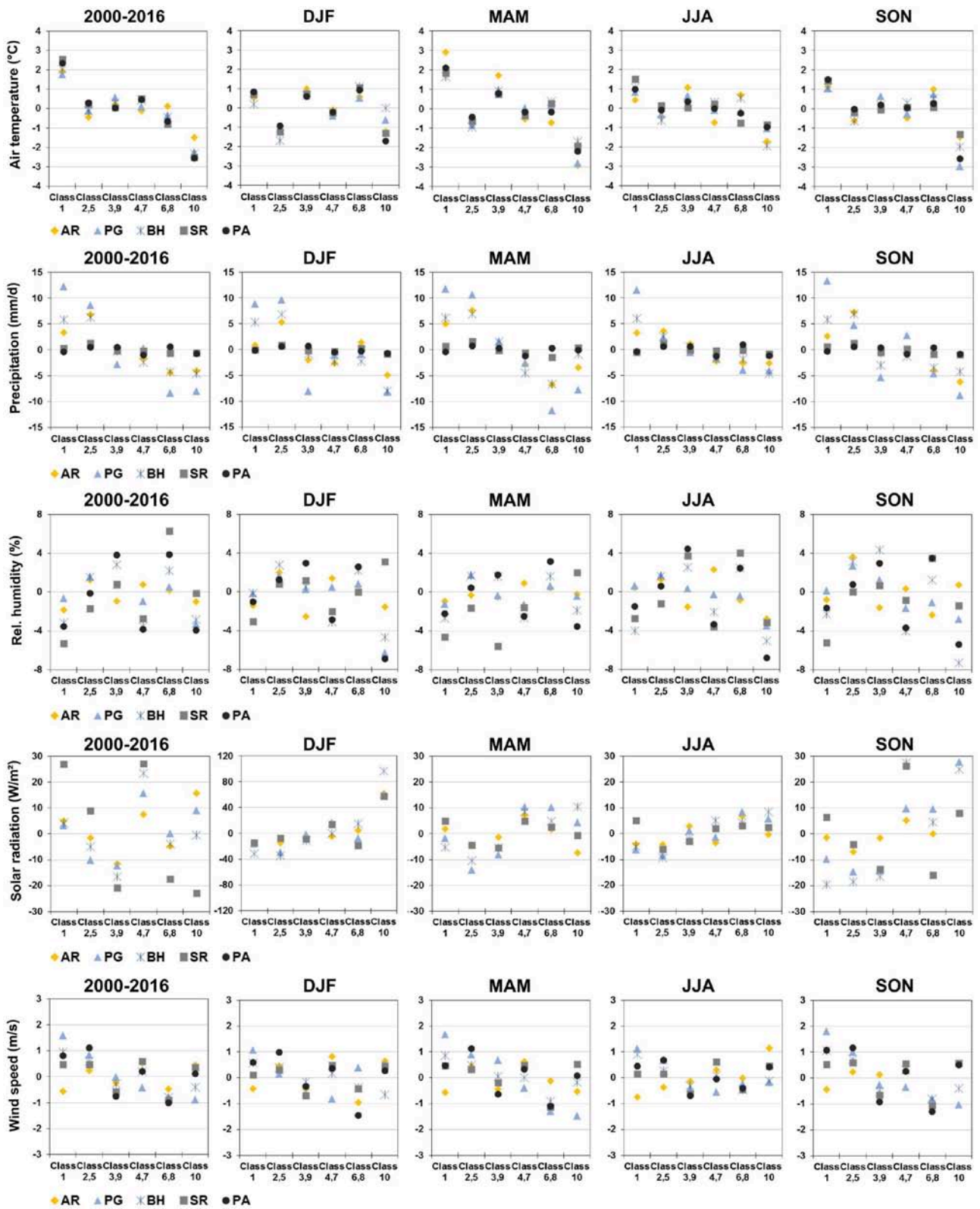

FIGURE 9 | Daily anomalies of air temperature, precipitation, relative humidity, solar radiation, and wind speed for each class of synoptic weather patterns between 2000 and 2016 and for summer (DJF), fall (MAM), winter (JJA), and spring (SON) between 2000 and 2016.

TABLE 7 | Correlation between ONI and AAOI and monthly anomalies of mean (T), maximum (TX), and minimum (TN) air temperature, relative humidity (rH), precipitation (P) and wind speed (v) at AWS Paso Galería (PG), AWS Puerto Bahamondes (BH), AWS Skyring (SR), and WS Punta Arenas (PA) for different time lags (T0 to T+3 months).

		ONI				AAOI			
		PG	**BH**	**SR**	**PA**	**PG**	**BH**	**SR**	**PA**
T	*T0*	−0.01	0.03	−0.13	**−0.12**	**0.34**	**0.49**	**0.36**	**0.42**
	T+1	0.05	0.03	−0.13	−0.10	−0.12	0.04	−0.07	−0.03
	T+2	0.05	0.05	−0.10	−0.08	−0.10	0.02	−0.04	−0.03
	T+3	0.11	0.09	−0.06	−0.04	0.05	0.07	−0.04	**0.12**
TX	*T0*	−0.02	−0.12	**−0.14**	−0.08	**0.38**	**0.39**	**0.38**	**0.43**
	T+1	0.03	−0.10	−0.11	−0.05	−0.08	−0.11	**−0.15**	−0.01
	T+2	0.03	−0.06	−0.08	−0.02	−0.04	−0.01	−0.03	−0.06
	T+3	0.09	−0.02	−0.04	0.02	**0.23**	0.12	0.13	0.11
TN	*T0*	−0.05	0.12	0.05	−0.11	**0.27**	**0.39**	**0.22**	**0.32**
	T+1	−0.01	0.10	0.01	−0.11	**−0.21**	**-0.14**	**−0.18**	−0.06
	T+2	−0.02	0.12	0.03	**−0.12**	−0.13	−0.02	−0.02	−0.03
	T+3	0.02	**0.17**	0.05	−0.10	0.01	−0.02	−0.07	0.09
rH	*T0*	**−0.29**	0.05	**0.21**	0.05	−0.06	**−0.21**	**−0.18**	−0.02
	T+1	**−0.29**	0.01	0.17	0.08	−0.06	−0.12	**0.25**	−0.07
	T+2	**−0.32**	−0.04	**0.18**	0.08	−0.10	−0.14	0.10	−0.11
	T+3	**−0.33**	−0.06	**0.19**	0.05	−0.01	0.02	0.09	0.06
P	*T0*	−0.03	**−0.26**	−0.11	0.02	**0.22**	**0.19**	0.11	−0.05
	T+1	0.01	**−0.23**	−0.10	0.00	−0.10	−0.07	0.07	−0.06
	T+2	−0.05	**−0.22**	−0.09	−0.03	0.10	0.10	0.09	0.00
	T+3	−0.08	**−0.19**	−0.10	−0.05	−0.11	0.03	0.02	−0.08
v	*T0*	0.08	**−0.17**	**−0.14**	0.01	**0.20**	**0.31**	0.05	0.12
	T+1	0.08	**−0.14**	**−0.19**	−0.02	−0.13	−0.02	−0.06	0.12
	T+2	0.00	**−0.14**	**−0.20**	−0.07	0.05	0.12	0.07	**0.17**
	T+3	0.01	**−0.15**	**−0.21**	−0.06	−0.11	−0.09	**−0.18**	−0.09

Significant values at the 90% level are shown in bold, correlations significant at 95% are bold and underlined. Times series were tested for lag-1 autocorrelation and apparent linear trends were removed before correlation analysis.

(ONI≤-0.5) (**Table 8**). The influence of ENSO on precipitation variability diminishes further to the east of the Southernmost Andes (**Table 7**). These findings are similar to Schneider and Gies (2004). However, only for AWS BH there is an indication that ENSO events may influence precipitation at GCN in the way as it is argued by Schneider and Gies (2004). Significant correlations between precipitation and ONI for any other AWS at GCN are not evident.

The link between AAO and the climate conditions at GCN and Punta Arenas is evident (**Table 7**, **Figure 10**). Positive correlations are significant for T, TX, TN at time-lag T0 for all four stations. Correlations range from +0.34 to +0.49 for T, +0.38 to +0.43 for TX and +0.22 to +0.39 for TN. Highest correlation values are found at AWS BH and WS PA. Anomalies of relative humidity ($r = -0.21$), wind speed ($r = +0.31$) and precipitation ($r = +0.19$) of AWS BH are also linked to AAO.

It is known that positive phases of AAO are associated with dryer and warmer conditions in southern South America (Gillett et al., 2006) which becomes evident in this study as well. The strengthening of the westerlies during positive AAO phases come along with an increase of mean monthly air temperatures by +20% (+0.6°C) at AWS PG, +16% (+1.1°C) at AWS BH, +14% (+1.0°C) at AWS SR and 13% (+0.9°C) at WS PA compared to the monthly average (2000-2016) (**Table 8**). Colder conditions with up to 23% (−1.0°C) below the average (AWS PG) occur during negative phases of AAO in Southernmost Patagonia. Deviations of TN between the monthly mean during negative and positive AAO phases compared to the overall mean varies between −45% (−1.2°C) to +33% (+0.6°C) at AWS PG, −26% (−1.0°C) to +22% (+0.9°C) at AWS BH, -26% (−0.8°C) to +26% (+0.8°C) at AWS SR, and −20% (−0.6°C) to +21% (+0.6°C) at WS PA. Air temperature increase during positive AAO phases is accompanied by positive precipitation and wind speed anomalies at the GCN stations. Deviations in monthly precipitation between negative and positive AAOI and the overall mean range from −16% (−96 mm) to 8% (+48 mm) at AWS PG, −9% (−32 mm) to +10% (+34 mm) at AWS BH and −6% (−4 mm) to +10% (+7 mm) at AWS SR (**Table 8**).

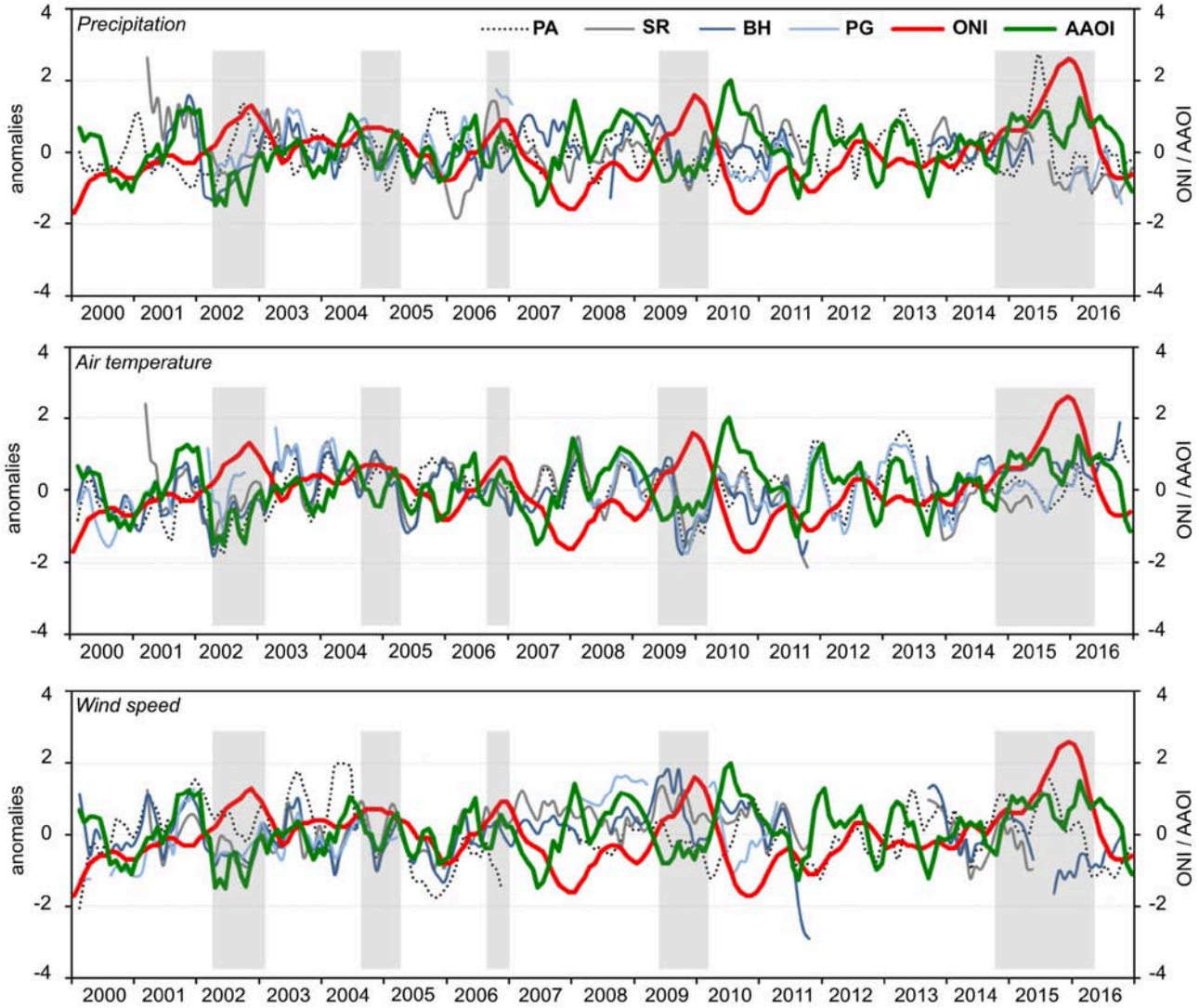

FIGURE 10 | Standardized monthly anomalies of precipitation, mean air temperature and wind speed at AWS Paso Galería (PG), AWS Puerto Bahamondes (BH), AWS Skyring (SR), and WS Punta Arenas (PA) and monthly ONI and AAOI values. El Niño events based on a threshold of +0.5°C for ONI are highlighted by the gray shading. Standardized monthly anomalies of climate variables are illustrated as a 3-month running mean.

4.4.2. Types of Synoptic Weather Patterns

We further analyze how the frequency of the major types of synoptic weather patterns changes during positive and negative phases of AAO and ENSO between 2000 and 2016 (**Table 9**). The impact of AAO on the synoptic situation in Southernmost Patagonia is largest for the synoptic classes 1, 2 and 5 and 10 since the AAO implies a weakening or strengthening of the westerly air flow. In case of negative AAO phases, days with strong westerly airflow (class 1) decrease by about one third compared to the average, while southwesterly air flow (class 2 and 5) increases by about 41% compared to average (2000–2016). On contrary, during positive AAO phases the westerly airflow dominates the climate at GCN. The high-pressure influence accompanied by cold winds from the south (class 10) is intensified during negative AAO and weakened during positive AAO. This is in good agreement with the observation of air temperature increase in Southernmost Patagonia during positive AAO phases.

During La Niña events, north-westerly advection of humid air masses (class 3 and 9) is more frequent, while the frequency for circulation patterns with high-pressure influence decreases (classes 6 and 8 and 10). During El Niño events, the frequency of north-westerly airflow decreases while weather classes with high-pressure influence are more present (classes 4 and 7 and 10). Strong La Niña events (ONI≤ -1.0°C) can be associated with enhanced westerlies (+27%) (**Table 9**), which is consistent with higher precipitation sums at AWS BH (Schneider and Gies, 2004). An intensified low-pressure cell over the Weddell Sea causing southwesterly air flow (class 2 and 5) is enhanced during stronger El Niño events (ONI$\geq +1.0$°C), while northwesterly

TABLE 8 | Deviations (%) of monthly mean (T), maximum (TX), and minimum (TN) air temperature, relative humidity (rH), precipitation (P) and wind speed (v) from the monthly means (2000-2016) during positive and negative ENSO and AAO phases.

		PG		BH		SR		PA		PG		BH		SR		PA	
		O+	O-	O+	O-	O+	O-	O+	O-	A+	A-	A+	A-	A+	A-	A+	A-
T	*T0*	−4	8	12	2	10	11	7	13	20	−23	16	−17	14	−13	13	−10
	T+1	4	6	20	5	21	12	14	13	6	10	7	−2	9	−1	5	2
	T+2	5	1	22	5	26	9	15	9	3	15	4	1	7	1	1	9
	T+3	4	−6	18	−1	24	1	11	3	−1	13	3	3	3	2	−2	10
TX	*T0*	−5	20	6	8	7	12	6	9	11	−11	8	−9	11	−10	9	−7
	T+1	1	19	12	11	16	12	11	9	2	12	3	0	7	−1	4	2
	T+2	3	14	13	11	20	9	12	6	0	14	2	3	5	0	1	6
	T+3	1	9	10	6	19	3	9	1	0	11	1	3	3	1	−2	7
TN	*T0*	7	1	21	0	20	12	9	22	33	−45	22	−26	26	−26	21	−20
	T+1	18	2	33	7	37	16	21	24	11	3	12	−5	16	−3	8	3
	T+2	18	−4	34	6	46	11	24	19	6	16	8	0	13	−1	3	15
	T+3	12	−12	29	−2	40	−3	17	9	1	17	7	2	4	2	−3	17
rH	*T0*	−1	−2	0	0	5	0	−2	−1	−1	0	−4	2	−2	3	−1	0
	T+1	−1	−1	−1	0	6	−2	−2	−1	0	−1	−3	2	0	0	−1	−1
	T+2	−2	−1	−2	0	8	−3	−2	0	0	0	−3	3	2	−2	−1	−1
	T+3	−2	−1	−1	2	9	−4	−1	1	0	0	−1	2	2	−3	1	−2
P	*T0*	7	−13	−9	9	−6	−10	−4	−9	8	−16	10	−9	10	−6	−8	1
	T+1	11	−5	−5	15	−4	−11	−4	−9	−7	18	−1	8	0	0	−2	−7
	T+2	14	0	1	21	−2	4	−2	2	−6	3	9	0	9	−4	5	−11
	T+3	8	−1	1	14	0	6	8	1	−22	14	−4	−5	−1	−3	−2	−8
v	*T0*	−3	0	2	3	4	4	7	−5	11	−13	11	−10	3	−1	3	−1
	T+1	0	0	3	4	4	6	5	−3	6	−1	4	−3	1	2	5	2
	T+2	3	1	3	5	4	6	3	−2	9	−7	3	−1	2	−1	5	5
	T+3	2	0	1	4	1	4	1	−4	3	−2	−2	3	−2	3	2	7

Results are listed for ONI ≥-0.5 (O+), ONI ≤-0.5 (O-), AAOI ≥0.5 (A+), and AAOI ≤-0.5 (A-) at different time lags (T0 to T+3 months) for AWS Paso Galería (PG), AWS Puerto Bahamondes (BH), AWS Skyring (SR), and WS Punta Arenas (PA).

TABLE 9 | Relative changes (%) of synoptic types and classes during positive and negative AAO and ENSO events between 2000 and 2016.

	Relative changes of synoptic types (%)										Relative changes of synoptic classes (%)					
	1	2	3	4	5	6	7	8	9	10	1	2 and 5	3 and 9	4 and 7	6 and 8	10
AAOI −0.5	−37	30	−19	−39	74	−36	51	1	96	64	−37	41	11	0	−29	64
AAOI +0.5	36	−27	−2	20	−40	21	−16	−21	−63	−43	36	−35	−19	4	−3	−43
ONI −0.5	4	−9	17	−6	3	8	8	−39	11	−18	4	−9	16	0	−16	−18
ONI +0.5	1	23	−23	12	−6	−13	2	35	−34	12	1	7	−26	8	−4	12
ONI −1.0	27	−22	18	4	−13	23	−10	−73	−33	−61	27	−22	4	−2	−19	−61
ONI +1.0	−5	49	−32	20	10	−51	5	60	−37	−18	−5	27	−33	13	−18	−18

airflow (class 3 and 9) occurs less frequently. The frequencies of high-pressure weather classes (classes 6 and 8 and 10) are below the average during both strong El Niño and La Niña events. The impact of ENSO on the variability of synoptic weather patterns generally is rather weak as already identified with respect to the meteorological observations other than precipitation at AWS BH.

5. CONCLUSION

We analyzed the main features of climate and climate variability in Southernmost Patagonia using a unique 17-year meteorological record (2000–2016) of four AWS in the vicinity of the GCN Ice Cap (53°S). Special attention was given to the link between observed mean, extremes and trends of the AWS records

as well as the impact of synoptic weather types and leading modes of global atmospheric variability (ENSO and AAO).

Annual and seasonal trends in air temperature were investigated by applying the non-parametric Mann-Kendall and Sen slope estimator trend test. A weather type classification based on the hierarchical correlations-based leader LUND-algorithm was computed using a 37-year record of ERA Interim Reanalysis data. Major synoptic weather types with distinct low-pressure cells in the Weddell Sea or Bellingshausen Sea causing a prevailing southwesterly, northwesterly or westerly airflow, determine the weather conditions in Southernmost Patagonia during 68% of the time. Circulation patterns with high-pressure cells over the Southern Pacific and Atlantic are present on 32% of all days between 2000 and 2016. The predominance of weather types with humid westerly airflow leads to significant west-east gradients of precipitation and relative humidity across the GCN Ice Cap. Mean annual precipitation (2008 to 2016) increases from ~3,800 mm at the west side of GCN at AWS AR to ~6,100 mm at AWS PG while it decreases again on the lee-side to ~4,000 mm at AWS BH. Within a distance of tens of kilometers precipitation sharply drops to below 800 mm further to the east. More than 80% of extreme precipitation events (>90th percentile) at GCN appears during synoptic types with strong westerly air flow. The occurrence of high precipitation events of up to 620 mm in 5 days and wet spells of up to 61 consecutive days underscore the year-around wet conditions at GCN. High precipitation events and long wet spells become less frequent toward the east of GCN.

We further identify extremes of daily maximum and minimum air temperatures of up to +25.8°C and -11.3°C along with the largest daily temperature range being located on the east side of GCN. Days with daily maximum temperatures exceeding the 90th percentile and days with daily minimum temperature falling below 0°C are less frequent since 2012 indicating a stronger maritime influence in the study region in recent years which might be attributable to increased positive AAO in recent years (Marshall, 2003). Mean annual air temperature increases by +0.05°C a^{-1} at GCN and +0.02°C a^{-1} at AWS Punta Arenas during the study period (2000–2016).

The influence of ENSO on intra-annual precipitation and temperature variations is not evident for all investigated stations. At AWS BH precipitation decreases by -9% compared to the monthly mean (2000-2016) during El Niño events while it increases by +9% during La Niña events. The evolution of the AAO determines the synoptic weather types along with air temperature and precipitation variations. Positive AAO phases on average are linked to an intensified westerly airflow (type 1) and warmer conditions in Southernmost Patagonia. Circulation patterns with high-pressure influence leading to colder and dryer conditions in Southernmost Patagonia are more frequent during negative AAO phases.

AUTHOR CONTRIBUTIONS

SW processed and analyzed the data and drafted the manuscript. DS prepared the synoptic weather type classification. TS, RK, CS designed, installed and maintain the measurement network at GCN. All authors discussed the results and jointly worked on the manuscript.

FUNDING

This study was funded by the CONYCET-BMBF project GABY-VASA, grant No. 01DN15007, by the German Research Foundation project Gran Campo Nevado, grant No. SCHN 680/1-1 and by the German Research Foundation project MANAU, grant No. SA 2339/3-1.

ACKNOWLEDGMENTS

We thank Marcelo Arévalo, Marco Möller, Paul Bumeder, Michael Glaser, Johannes Koch, Michael Moritz, Markus Stickling and many others for their help in the field at Gran Campo Nevado Ice Cap during the past 17 years. We are grateful for technical support and advice regarding the weather type classification by Andreas Philipp, University of Augsburg. We thank all reviewers and the editor for their input which helped improving the manuscript considerably.

SUPPLEMENTARY MATERIAL

The Supplementary Material for this article can be found online at: https://www.frontiersin.org/articles/10.3389/feart.2018.00053/full#supplementary-material

REFERENCES

Aceituno, P. (1988). On the functioning of the southern oscillation in the south american sector. part I: surface climate. *Monthly Weather Rev.* 116, 505–524.

Aravena, J., Lara, A., Wolodarsky-Franke, A., Villalba, R., and Cuq, E. (2002). Tree-ring growth patterns and temperature reconstruction from nothofagus pumilio (fagaceae) forests at the upper tree line of southern chilean patagonia. *Rev. Chil. Hist. Nat.* 75, 361–376. doi: 10.4067/S0716-078X2002000200008

Aravena, J.-C., and Luckman, B. H. (2009). Spatio-temporal rainfall patterns in southern south america. *Int. J. Climatol.* 29, 2106–2120. doi: 10.1002/joc.1761

Barnston, A., Chelliah, M., and Goldenberg, S. (1997). Documentation of a highly enso-related sst region in the equatorial pacific. *Atmosphere-Ocean* 35, 367–383. doi: 10.1080/07055900.1997.9649597

Buisán, S., Earle, M., Collado, J., Kochendorfer, J., Alastrué, J., Wolff, M., et al. (2017). Assessment of snowfall accumulation underestimation by tipping bucket gauges in the spanish operational network. *Atmos. Meas. Tech.* 10:1079. doi: 10.5194/amt-10-1079-2017

Butorovic, N. (2016). Resumen meteorológico año 2015. estación jorge schythe. *Anal. Inst. Patag.* 44, 102–110. doi: 10.4067/S0718-686X2016000100009

Carrasco, J., Casassa, G., and Rivera, A. (2002). "Meteorological and climatological aspect of the southern patagonia icefield," in *The Patagonia Icefields*, eds G. Casassa, F. Sepulveda, and R. Sinclair (New York, NY: Kluwer-Plenum), 29–41.

Compagnucci, R. H., and Salles, M. A. (1997). Surface pressure patterns during the year over southern south america. *Int. J. Climatol.* 17, 635–653.

Davies, B., and Glasser, N. (2012). Accelerating shrinkage of patagonian glaciers from the little ice age (ad 1870) to 2011. *J. Glaciol.* 58, 1063–1084. doi: 10.3189/2012JoG12J026

Dee, D., Uppala, S., Simmons, A., Berrisford, P., Poli, P., Kobayashi, S., et al. (2011). The era-interim reanalysis: configuration and performance of the

data assimilation system. *Q. J. R. Meteorol. Soc.* 137, 553–597. doi: 10.1002/qj.828

Durre, I., Menne, M. J., Gleason, B. E., Houston, T. G., and Vose, R. S. (2010). Comprehensive automated quality assurance of daily surface observations. *J. Appli. Meteorol. Climatol.* 49, 1615–1633. doi: 10.1175/2010JAMC2375.1

Endlicher, W. (1991). Zur klimageographie und klimaökologie von südpatagonien. 100 jahre klimatologische messungen in punta arenas. *Freiburger Geographische Hefte* 32, 181–211.

Fogt, R. L., and Bromwich, D. H. (2006). Decadal variability of the enso teleconnection to the high-latitude south pacific governed by coupling with the southern annular mode. *J. Clim.* 19, 979–997. doi: 10.1175/JCLI3671.1

Frank, A. (2002). *Semi-objektive klassifikation und statistische auswertung von wetterlagen südpatagoniens [semi-Objective Classification and Statistical Analysis of Weather Types of South Patagonia]*. Master thesis, Univ. Freiburg, Germany .

Garreaud, R., Lopez, P., Minvielle, M., and Rojas, M. (2013). Large-scale control on the patagonian climate. *J. Clim.* 26, 215–230. doi: 10.1175/JCLI-D-12-00001.1

Garreaud, R. D., Vuille, M., Compagnucci, R., and Marengo, J. (2009). Present-day south american climate. *Palaeogeogr. Palaeoclimatol. Palaeoecol.* 281, 180–195. doi: 10.1016/j.palaeo.2007.10.032

Gillett, N. P., Kell, T. D., and Jones, P. D. (2006). Regional climate impacts of the southern annular mode. *Geophys. Res. Lett* 33:L23704. doi: 10.1029/2006GL027721

Gocic, M., and Trajkovic, S. (2013). Analysis of changes in meteorological variables using mann-kendall and sen's slope estimator statistical tests in serbia. *Global Planet. Change* 100(Suppl. C), 172–182. doi: 10.1016/j.gloplacha.2012.10.014

Hamed, K. H. (2008). Trend detection in hydrologic data: the mann–kendall trend test under the scaling hypothesis. *J. Hydrol.* 349, 350–363. doi: 10.1016/j.jhydrol.2007.11.009

Hartigan, J. (1975). *Clustering Algorithms*. Wiley Series in Probability and Mathematical Statistics. New York, NY: John Wiley & Sons.

Huang, B., Thorne, P. W., Banzon, V. F., Boyer, T., Chepurin, G., Lawrimore, J. H., et al. (2017). Extended reconstructed sea surface temperature, version 5 (ersstv5): Upgrades, validations, and intercomparisons. *J. Clim.* 30, 8179–8205. doi: 10.1175/JCLI-D-16-0836.1

Kendall, M. (1975). *Rank Correlation Methods*. London: Griffin.

Kilian, R., Baeza, O., Breuer, S., Ríos, F., Arz, H., Lamy, L., et al. (2013). Late glacial and holocene paleogeopgraphical and paleoecological evolution of the seno skyring and otway fjord systems in the magellanes region. *Anal. Inst. Patag.* 41, 7–21. doi: 10.4067/S0718-686X2013000200001

Kilian, R., Hohner, H., Biester, H., Wallrabe-Adams, C., and Stern, C. (2003). Holocene peat and lake sediment tephra record from the southernmost andes (53-55°s). *Rev. Geol. Chile* 30. 47–64. doi: 10.4067/S0716-02082003000100002

Kilian, R., and Lamy, F. (2012). A review of glacial and holocene paleoclimate records from southernmost patagonia (49–55°s). *Q. Sci. Rev.* 53, 1–23. doi: 10.1016/j.quascirev.2012.07.017

Kilian, R., Schneider, C., Koch, J., Fesq-Martin, M., Biester, H., Casassa, C., et al. (2007). Palaeoecological constraints on late glacial and holocene ice retreat in the southern andes (53°s). *Global Planet. Change* 59, 49–66. doi: 10.1016/j.gloplacha.2006.11.034

Kisi, O., and Ay, M. (2014). Comparison of mann–kendall and innovative trend method for water quality parameters of the kizilirmak river, turkey. *J. Hydrol.* 513(Suppl. C), 362–375. doi: 10.1016/j.jhydrol.2014.03.005

Koch, J., and Kilian, R. (2005). 'little ice age' glacier fluctuations, gran campo nevado, southernmost chile. *Holocene* 15, 20–28. doi: 10.1191/0959683605hl780rp

Lamy, F., Kilian, R., Arz, H., Francois, J.-P., Kaiser, J., Prange, M., et al. (2010). Holocene changes in the position and intensity of the southern westerly wind belt. *Nat. Geosci.* 3, 695–699. doi: 10.1038/ngeo959

Lund, I. (1963). Map-pattern classification by statistical methods. *J. Appl. Meteorol.* 2, 56–65.

Mann, H. (1945). Nonparametric tests against trend. *Econometrica* 13, 245–259. doi: 10.2307/1907187

Marshall, G. J. (2003). Trends in the southern annular mode from observations and reanalyses. *J. Clim.* 16, 4134–4143. doi: 10.1175/1520-0442(2003)016<4134:TITSAM>2.0.CO;2

Möller, M., and Schneider, C. (2008). Climate sensitivity and mass-balance evolution of gran campo nevado ice cap, southwest patagonia. *Ann. Glaciol.* 48, 32–42. doi: 10.3189/172756408784700626

Möller, M., Schneider, C., and Kilian, R. (2007). Glacier change and climate forcing in recent decades at gran campo nevado, southernmost patagonia. *Ann. Glaciol.* 46, 136–144. doi: 10.3189/172756407782871530

Murtagh, F. (1985). "Multidimensional clustering algorithms," in *COMPSTAT Lectures 4*, eds J. M. Chambers, J. Gordesch, A. Klas, L. Lebart, and P. P. Sint (Wien-Würzburg: Physica Verlag), 1–131.

Onyutha, C., Tabari, H., Taye, M. T., Nyandwaro, G. N., and Willems, P. (2016). Analyses of rainfall trends in the nile river basin. *J. Hydroenviron. Res.* 13(Suppl. C), 36–51. doi: 10.1016/j.jher.2015.09.002

Paruelo, J., Beltran, A., Jobbagy, E., Sala, O., and Golluscio, R. (1998). The climate of patagonia: general patterns and controls on biotic processes. *Ecol. Aust.* 8, 85–101.

Philipp, A., Beck, C., Esteban, P., Kreienkamp, F., Krennert, T., Lochbihler, K., et al. (2014a). *cost733class-1.2 - User Guide*. Available online at: http://cost733.geo.uni-augsburg.de/cost733class-1.2.

Philipp, A., Beck, C., Huth, R., and Jacobeit, J. (2014b). Development and comparison of circulation type classifications using the cost 733 dataset and software. *Int. J. Climatol.* 36, 2673–2691. doi: 10.1002/joc.3920

Rasmussen, R., Baker, B., Kochendorfer, J., Meyers, T., Landolt, S., Fischer, A. P., et al. (2012). How well are we measuring snow: the noaa/faa/ncar winter precipitation test bed. *Bull. Am. Meteorol. Soc.* 93, 811–829. doi: 10.1175/BAMS-D-11-00052.1

Schneider, C., and Gies, D. (2004). Effects of el niño–southern oscillation on southernmost south america precipitation at 53°s revealed from ncep–ncar reanalyses and weather station data. *Int. J. Climatol.* 24, 1057–1076. doi: 10.1002/joc.1057

Schneider, C., Glaser, M., Kilian, R., Santana, A., Butorovic, N., and Casassa, G. (2003). Weather observations across the southern andes at 53°s. *Phys. Geogr.* 24, 97–119. doi: 10.2747/0272-3646.24.2.97

Schneider, C., Schnirch, M., Acuña, C., Casassa, G., and Kilian, R. (2007). Glacier inventory of the gran campo nevado ice cap in the southern andes and glacier changes observed during recent decades. *Glob. Plan. Change* 59, 87–100. doi: 10.1016/j.gloplacha.2006.11.023

Sen, P. (1968). Estimates of the regression coefficient based on kendall's tau.. *J. Am. Stat. Assoc.* 63, 1379–1389.

Tank, A. K., Zwiers, F., and Zhang, X. (2009). Guidelines on analysis of extremes in a changing climate in support of informed decisions for adaption. *Clim. Data Monit.* 72, 1–55.

Theil, H. (1950). A rank-invariant method of linear and polynomial regression analysis. *Proc. K. Ned. Akad. Wet.*, A53, 386–392.

Thompson, D. W. J., and Solomon, S. (2002). Interpretation of recent southern hemisphere climate change. *Science* 296, 895–899. doi: 10.1126/science.1069270

Villalba, R., Lara, A., Boninsegna, J. A., Masiokas, M., Delgado, S., Aravena, J. C., et al. (2003). "Large-scale temperature changes across the southern andes: 20th-century variations in the context of the past 400 years," in *Climate Variability and Change in High Elevation Regions: Past, Present & Future*, ed H. F. Diaz (Dordrecht: Springer), 177–232.

Weidemann, S., Sauter, T., Schneider, L., and Schneider, C. (2013). Impact of two conceptual precipitation downscaling schemes on mass-balance modeling of gran campo nevado ice cap, patagonia. *J. Glaciol.* 59, 1106–1116. doi: 10.3189/2013JoG13J046

Yue, S., Pilon, P., Phinney, B., and Cavadias, G. (2002). The influence of autocorrelation on the ability to detect trend in hydrological series. *Hydrol. Process.* 16, 245–259. doi: 10.1002/hyp.1095

Conflict of Interest Statement: The authors declare that the research was conducted in the absence of any commercial or financial relationships that could be construed as a potential conflict of interest.

frontiers in Earth Science

ORIGINAL RESEARCH
published: 29 May 2018
doi: 10.3389/feart.2018.00057

Climate and *Nothofagus pumilio* Establishment at Upper Treelines in the Patagonian Andes

Ana M. Srur[1]*, *Ricardo Villalba*[1], *Milagros Rodríguez-Catón*[1], *Mariano M. Amoroso*[2,3] and *Eugenia Marcotti*[1,4]

[1] Instituto Argentino de Nivología, Glaciología y Ciencias Ambientales, CCT CONICET Mendoza, Mendoza, Argentina, [2] Instituto de Investigaciones en Recursos Naturales, Agroecología y Desarrollo Rural, Sede Andina, Universidad Nacional de Río Negro, Bariloche, Argentina, [3] CCT CONICET Patagonia Norte, Bariloche, Argentina, [4] Instituto de Ecorregiones Andinas CONICET-UNJu, Universidade Nacional de Jujuy, San Salvador de Jujuy, Argentina

The upper treeline provides a unique opportunity for documenting changes in forest dynamics in the context of current environmental fluctuations. Documenting the response of forests to present environmental changes will be very useful in developing and validating vegetation models that predict plant responses to global changes resulting from human activities. It is generally suggested that the expansion of the upper treeline is limited by cold temperatures, so warmer conditions are expected to induce an advance of forests into alpine vegetation. Significant changes in temperature and precipitation have already been documented in regional studies along the Patagonian Andes during the last decades. Across Patagonia, there are strong relationships between changes in climate and variations in the Southern Annular Mode (SAM). The atmospheric circulation indexes, act as climate packages summarizing climatic information since they combine changes in environmental variables. In order to complement previous studies in the northern Patagonia treeline, we have conducted a this study in the southern Patagonian Andes to: (1) characterize the patterns of *Nothofagus pumilio* establishment in the upper treeline along a precipitation gradient, (2) to establish the relationship between variations in regional climate and tree establishment and (3) to determine the influence of continental and hemispheric-scale climatic forcing on tree establishment at regional scale. Our studies suggest that the location of the upper treeline of the *N. pumilio* forest in the Patagonian Andes is sensitive to changes in climate variations. The temperature increment has facilitated the tree recruitment, however, the rate of seedling establishment appears to be more strongly modulated by the interaction between temperature increase and variations in precipitation. The expansion of the upper treeline has been limited to 5–10 m from the abrupt treeline. This comparatively reduced advance of the forest in the alpine grassland is regulated by other biotic and abiotic factors rather than the temperature increase. While the recent expansion of the upper treeline in northern Patagonia was regulated by temperature and precipitation variations associated with the different phases of the Pacific Decadal Oscillation, the establishment above the upper treeline in the southern Patagonian Andes was facilitated by climatic variations induced by the positive trend of the SAM during the last decades.

Keywords: establishment, upper treeline, treeline dynamics, Southern Annular Mode, Pacifical Decadal Oscillation, temperature, precipitation

OPEN ACCESS

Edited by:
Marius Schaefer,
Universidad Austral de Chile, Chile

Reviewed by:
Zoltan Kern,
MTA Research Centre for Astronomy and Earth Sciences, Hungary
Olga Nikolaevna Solomina,
Institute of Geography (RAS), Russia

***Correspondence:**
Ana M. Srur
asrur@mendoza-conicet.gob.ar

Specialty section:
This article was submitted to Cryospheric Sciences, a section of the journal Frontiers in Earth Science

Received: *22 January 2018*
Accepted: *07 May 2018*
Published: *29 May 2018*

Citation:
Srur AM, Villalba R, Rodríguez-Catón M, Amoroso MM and Marcotti E (2018) Climate and Nothofagus pumilio Establishment at Upper Treelines in the Patagonian Andes. Front. Earth Sci. 6:57. doi: 10.3389/feart.2018.00057

INTRODUCTION

The upper altitudinal limit of the forest is exposed to extreme environmental conditions. Small fluctuations in this environment determine changes in the patterns of tree establishment and mortality, which in turn alter forest distribution. Therefore, the upper treeline provides a unique opportunity for documenting changes in forest dynamics in the context of current environmental fluctuations. Indeed, the advance of new trees within and even above the upper treeline, as well as the increase in growth of trees, can be considered as reliable indicators of the forest's responses to changes in environmental conditions (Holtmeier and Broll, 2005). Documenting the response of forests to present environmental changes will be very useful in developing and validating vegetation models that predict plant responses to global changes resulting from human activities.

Several studies suggest that the expansion of the upper treeline is limited by cold temperatures, so warmer conditions are expected to induce an advance of forests into alpine vegetation (Tranquilini, 1979; Jobbagy and Jackson, 2000; Grace et al., 2002; Camarero and Gutiérrez, 2004; Körner and Paulsen, 2004; among others). Daubenmire's pioneering studies (Daubenmire, 1954) indicated that the forest's altitudinal limit coincided with the isotherm of 10°C during the warmest month of the year. More recently, Körner (1998) proposed a thermal threshold of 5.5–7.5°C during the growing season for the growth and development of plant tissues of tree species living in the upper boundary of the forest. Although temperature appear to be the main factor controlling the upper elevational limit of the forest, not all treelines reacts similarly to variations in temperature. On a global scale, warmer temperatures are not always associated with treeline advances (Harsch et al., 2009). Differences in treeline responses to global temperature increase may reflect distinct rates of temperature increases between regions (Trenberth et al., 2014) or treeline responses to different seasonal (spring vs. summer) temperature variations (Körner and Paulsen, 2004; Harsch et al., 2009). In addition, treeline responses can be asynchronous with temperature changes, either due to delays in physiological processes or growth activation after overpassing heating thresholds (Rupp et al., 2001; Renwick and Rocca, 2015).

In a global review, Harsch et al. (2009) reported that treelines have advanced in 52% of the studied sites and remaining stable or unchanged in the rest, with the exception of one site in recession. Differences in responses would indicate that besides temperature, other environmental factors control treeline location. For example, interspecific interactions play an important role in controlling treeline dynamics (Spasojevic et al., 2013; Tingstad et al., 2015; Liang et al., 2016; Saccone et al., 2017; among others). Warming in the Tibetan Plateau has increased shrub density, which in turn slowed tree establishment above the treeline (Liang et al., 2016). Studies of tree colonization on recent moraines in southern Patagonia, show that *Nothofagus pumilio* mostly established in sectors covered by biological soil crust and/or creeping shrubs dominated by *Empetrum rubrum* (Pissolito, 2016). Other authors argued that factors such as wind and blowing ice modulate the carbon balance of individuals, and consequently the production of woody tissues (Stevens and Fox, 1991). The cold-induced photoinhibition appears also to regulate the germination and survival of new individuals (Danby and Hik, 2007). These interactions would act by masking or weakening the relationship between temperature increments and treeline rises.

According to Holtmeier and Broll (2005) the importance of different factors in regulating forest line dynamics depends on the spatial scale of the study and the speed of response of individuals to environmental changes to which they are exposed. These authors propose that on a global scale, the factors controlling treeline are macro-climatic factors, such as temperature and/or precipitation. However, at regional scale, inter-annual or seasonal climatic variability are more important (Holtmeier and Broll, 2005). At the site scale, microclimatic relationships such as wind exposure, duration of snow cover, soil type, human impact among others, are the dominant factors (Holtmeier and Broll, 2005).

In recent years have significantly increased the number of studies documenting the progress and retreat of treelines in the ecotones between forest and alpine vegetation or tundra (Kirdyanov et al., 2012; Elliott and Cowell, 2015; Franke et al., 2017; Jochner et al., 2017; among others). Most treelines are characterized by gradual transitions between the forest and the alpine vegetation. This transition is characterized by forest patches that increase the heterogeneity of the site and favor the establishment of new individuals (Spasojevic et al., 2013, 2014). The upper limit of the forest in the Patagonian Andes is dominated by species of *Nothofagus* trees displaying an abrupt limit between the forest and the grasslands, without a gradual transition of patches or isolated individuals toward the high Andean vegetation (**Figure 1**; Cuevas, 2000; Daniels and Veblen, 2003; Harsch et al., 2012; Srur et al., 2016). Therefore, it is very likely that the establishment and survival of new individuals will be more difficult in abrupt rather than transitional ecotones between the forest and the upper Andean vegetation.

Significant changes in temperature and precipitation have already been documented in regional studies along the Patagonian Andes during the last decades (Masiokas et al., 2008, 2009; Falvey and Garreaud, 2009). According with the last IPCC report, a precipitation decrease concurrent with a temperature increase of 0.1°C per decade has been recorded since 1960 in southern Chile and adjacent Argentina (Magrin et al., 2014). Across Patagonia, there are strong relationships between changes in climate (temperature and precipitation) and variations in the Southern Annular Mode (SAM or Antarctic Oscillation; Garreaud, 2009; Garreaud et al., 2009; Moreno et al., 2014). SAM is the main mode of variability of tropospheric circulation in the extra-tropical region of South America, characterized by pressure anomalies of opposite sign in the sub-Antarctic region (60–65°S) and in the temperate band at ∼40–50°S (Garreaud et al., 2009). Positive correlations between SAM and temperature throughout Patagonia (40°-54°S) and negative correlations with zonal wind intensity and precipitation north of 50°S during summer have been documented from climate analyses (Marshall, 2003; Villalba et al., 2012; Moreno et al., 2014).

The atmospheric circulation indexes such as SAM, act as climate packages summarizing climatic information since

FIGURE 1 | Abrupt treeline in the El Chaltén. Picture taken by Ricardo Villalba in the 2016–2017 summer.

they combine changes in precipitation, temperature, wind, evaporation, among other environmental variables. The use of these indices allows us to reduce the spatial and temporal complexity of climate variables and to determine relationships with biotic processes in areas where climate data are scarce (Stenseth et al., 2003). Although changes in the atmospheric circulation indexes do not directly affect treeline dynamics, variations in SAM, or other circulation indexes, are related to anomalies in the temperature or/and precipitation, which in turn affect treeline advances or retreats (Woodward et al., 1995; Daniels and Veblen, 2003; Wang et al., 2006; Astudillo-Sánchez et al., 2017). Indeed, a recent study in the Northern Andes of Patagonia indicates that the establishment of *Nothofagus* in the upper treeline is markedly regulated by regional climatic variations associated with phase changes in the Pacific Decadal Oscillation (Srur et al., 2016).

There are larger uncertainty about future climate changes in southern Patagonia, however, the registered increase in temperature concomitant with the dominant glacier retreat are expected to continue or even intensified during the twenty-first century (Magrin et al., 2014). Changes in environmental conditions can lead to loss of biodiversity, changes in the demography and distribution of species, and consequently alter the structure and composition of communities (Hansen et al., 2001; Bellard et al., 2012; Mainali et al., 2015). Therefore, studying forest dynamics in the areas exposed to climate change, such as treeline, is relevant to understanding how future climate will affect the functioning of ecosystems and the services that they provide to humans.

In order to complement previous studies documenting the climatic influences on tree establishment in the northern Patagonia treeline, we have conducted a similar study in the southern Patagonian Andes to: (1) characterize the patterns of *N. pumilio* establishment in the upper treeline along a precipitation gradient, (2) to establish the relationship between variations in regional climate and tree establishment, and (3) to determine the influence of continental and hemispheric-scale climatic forcing on tree establishment at regional scale. Finally, the results from this study in the southern Patagonian Andes will be compared with those from the northern Patagonia to establish differences and similarities in the patterns of tree establishment at the upper treeline and their relationships with climate.

MATERIALS AND METHODS

Study Area

The study area is situated along the Río de las Vueltas basin in the Santa Cruz province, Argentina, from El Chaltén village to Lago del Desierto (**Figure 2**). The whole region is under the strong influence of the persistent Westerlies throughout the year (Villalba et al., 2003; Garreaud et al., 2009, 2013). The Andes acts as a barrier to the humid air masses coming from the Pacific inducing an important west-east precipitation gradient (Villalba et al., 2003). The temperature of the region is influenced by both latitude and altitude, the average temperature described for the area is 6°C (Villalba et al., 2003).

Forests in the area belong to the sub-Antarctic phytogeographic province, Deciduous Forest District and are dominated by *N. pumilio* (Cabrera, 1976). From the lower part of the forest and up to 800–950 m, well-developed and erect *N. pumilio* individuals vary between 10 and 20 m in height (Boelcke et al., 1985). On the contrary, individuals are smaller in the highest parts of the forest and become stunted near the upper boundary. As the snow load increases with elevation, typical 6–8 m L-shaped individuals give way to multi stem krummholz at the upper edge of the forest.

At El Chaltén (400 m a.s.l.), located in the forest-steppe ecotone, the total annual precipitation is ∼550 mm, evenly distributed throughout the year. Mean annual temperature at this locality is close to 7°C (data provided by Los Glaciares National Park, period 1992–2001). At 1,100 m a.s.l. in the upper treeline, the period covered by snow is of ∼140 days per year,

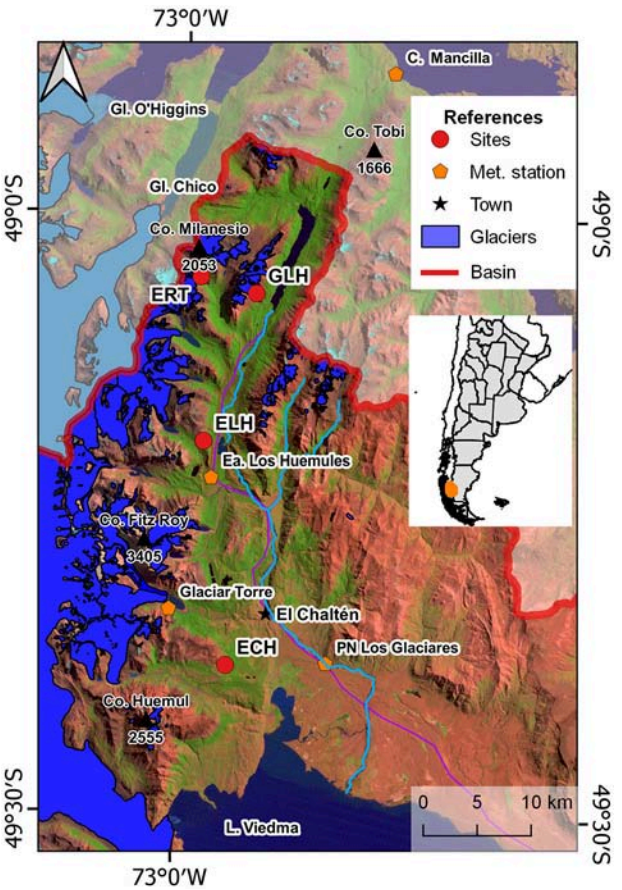

FIGURE 2 | Location of the sample sites along the precipitation gradient. For more details regarding the sampling sites, refer to **Table 1**.

TABLE 1 | Geographic location and characteristics of sample sites.

	El Chaltén	Estancia Los Huemules	Glaciar Huemul	Estancia Río Toro
Code	ECH	ELH	GLH	ERT
Latitude °S	49.38	49.20	49.07	49.06
Longitude °W	72.94	72.99	72.91	72.98
Elevation m asl	1,073	1,053	993	1,027
Slope (°)	9.6	23	26	35
Aspect	E-SE	SE	S-SE	E
Soil type	Molisols	Molisols	Molisols	Molisols
Characteristic	Dry treeline	Mesic treeline	Wet treeline	Wet treeline
Density (ind/ha)	41.96	18.49	153.05	8.86
Height (mm)	83.7	79.0	98.6	143.3
Basal diameter (mm)	11.6	2.5	6.8	9.8
Mean age (years)	12.18 (1.64) a	14.53 (1.29) a	12.79 (0.89) a	9.8 (1.78) a
Mean distance to treeline (m)	5.88 (0.37) a	11.84 (0.40) b	3.14 (0.11) c	4.8 (0.33) a

For mean age and distance to treeline, the standard errors are displayed in parentheses. Different letters show statistically significant differences at $p \leq 0.05$.

extending from the beginning of June to middle November (period 2004–2013, data from IANIGLA). At the mesic sector in the Estancia Los Huemules, 17 km in northwest direction from from El Chaltén, the total annual precipitation is above 1,000 mm and the mean annual temperature reaches 6°C (period 2007–2012). At the wet sector of the precipitation gradient, total annual rainfalls are above 2,000 mm. Although our record for Estancia Río Toro is short (less than a year), total annual precipitation at the close meteorological station of Cerro Mansilla (309 m) is around 2,400 m. Cerro Mansilla is located 52 km to the north of El Chaltén and just 27 km from our sites at the wet extreme of the precipitation gradient.

Four study sites were established along the southeast-northwest precipitation gradient in the Río de las Vueltas basin (**Table 1**; **Figure 2**). At the driest treeline site on Pliegue Tumbado, slopes are gentle with E-SE orientation. The density of seedling above treeline exceeds 40 individuals per hectare with mean height and basal diameter of 8 and 1.1 cm, respectively (**Table 1**, **Figure 3A**). On the mesic sector, the upper treeline is located on gentle to middle slopes facing the SE. Here, the density is larger than 18 individuals per hectare. This site recorded the smallest individuals both in height and diameter (**Table 1**, **Figure 3B**). Finally, at the wettest treelines (**Figures 3C,D**), seedling density is extremely variable between sites (**Table 1**). At the Estancia Río Toro treeline, individuals are taller and growing on steep slopes (**Table 1**; **Figure 3D**).

Fieldwork and Laboratory Methods

Four study sites were established along the precipitation gradient from the relative dry forest-steppe ecotone in El Chaltén to the humid Laguna del Desierto in the upper sector of the Río de las Vueltas basin. Sampling was conducted during the austral summers from 2004–2005 to 2010–2011. Two to four rectangular plots were established at each of four sites, extending from the local treeline up to the alpine grasses (**Table 1**, **Figure 3**). In each plot, we measured the distance between the new individuals and the continuous treeline. In order to determine the year of tree establishment, increment cores were taken as close to the root collar as possible using increment borers. Individuals with a basal diameter <3 cm were cut at the root collar, and their cross-sections sliced in the laboratory using a sliding microtome. At El Chaltén (ECH), Glacial Huemul (GLH), and Estancia Río Toro (ERT) sites, 187, 62 and 51 individuals were sampled, respectively. In Estancia Los Huemules (ELH), the site showing the highest tree density, we randomly sampled 1 of each 4 individuals from a total of 122 samples. Increment borer samples were mounted on wooden mounts and subsequently polished. All samples were processed and dated following the standard dendrochronology technique proposed by Stokes and Smiley (1968). For cores that did not reach the pith, the missing rings were estimated following Villalba and Veblen (1997).

Analysis

The establishment patterns in the treeline were analyzed taking into account the age of the individuals and the distance

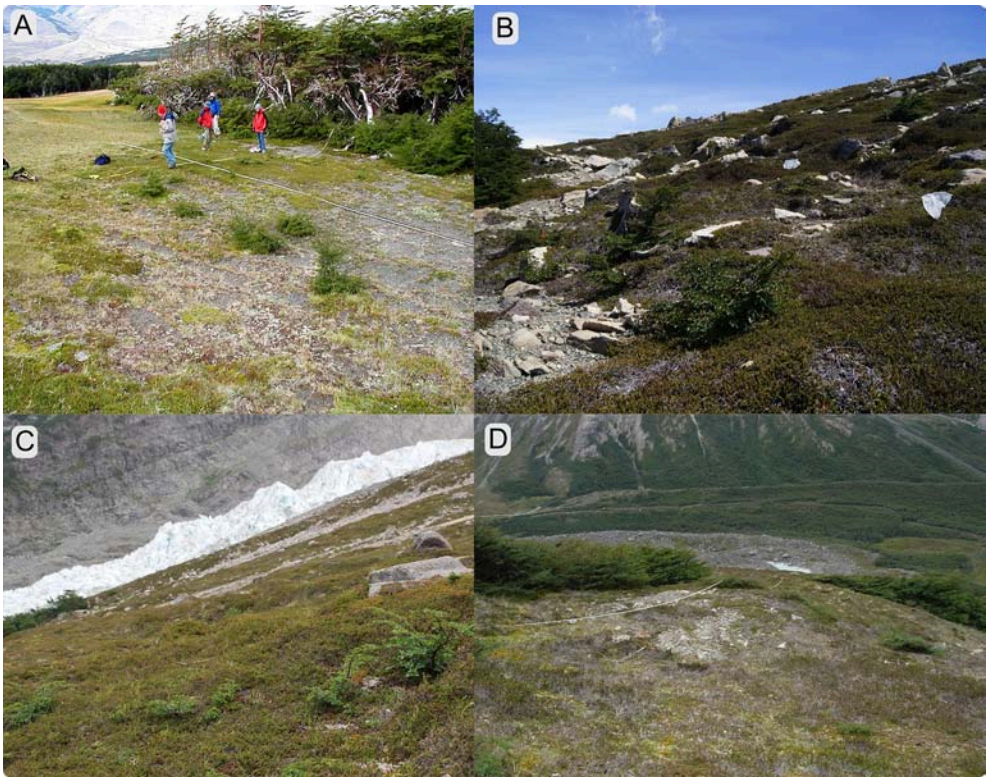

FIGURE 3 | Tree establishment above the *Nothofagus* abrupt treelines at the sampling sites. **(A)** El Chalten, **(B)** Estancia Los Huemules, **(C)** Glaciar Huemul, and **(D)** Estancia Rio Toro.

of the seedling to the treeline. Differences in the distance between individuals and treelines between sites were evaluated using the non-parametric *U*-test of Mann–Whitney (Zar, 1999).

Temperature and precipitation records in the Río de las Vueltas basin are short and fragmentary. Therefore, we used in the comparisons between climate and tree establishment the records from Punta Arenas, representing the most extent and complete series of temperature and precipitation for the region. The climate data was downloaded from the website of the Chilean Meteorological Directorate (http://www.meteochile.gob.cl/PortalDMC-web/index.xhtml).

The Niño 3.4, PDO and SAM Marshal indexes were obtained, respectively, from:

http://www.cgd.ucar.edu/cas/catalog/climind/TNI_N34/index.html (access date 8 September 2016)

http://research.jisao.washington.edu/pdo/PDO.latest (access date 20 June 2016)

http://www.nerc-bas.ac.uk/public/icd/gjma/newsam.1957.2007.txt (access date 03 March 2017)

Using the ffcsaps function of the dplR package (Bunn et al., 2016), interannual variations in establishment, temperature and precipitation were smoothed using spline funtions.

RESULTS

Mean ages from the individuals established above upper treeline showed no significant differences between sites (dry, mesic, and humid) along the precipitation gradient from El Chaltén to Laguna del Desierto (**Table 1**). However, the mean distance from the edge of the forest at which new individuals are established, showed significant differences between sites (**Table 1**). Whereas the ELH and GLH sites showed the largest and smallest distance from the continuous forest line, respectively, the sites at the extremes of the gradient (ECH and ERT) showed intermediate values and not significant differences between them (**Table 1**).

The rate of *N. pumilio* establishment over time followed similar patterns at the different sites along the precipitation gradient (**Figure 4**). In general, the establishment patterns presented a bimodal distribution characterized by a gradual increase in the number of individuals since the mid-1970s, peaking in the late 1980s—early 1990s and again around the year 2000. This particular pattern is reinforced when tree establishment is evaluated at regional level (**Figure 4**). However, it should be noted some temporary differential response in tree establishment between wet and dry sites. Whereas at the wettest site (ERT) the maximum establishment peak took place in the most recent period, at the driest sites (ECH and ELH) the establishment was more abundant in the earliest period.

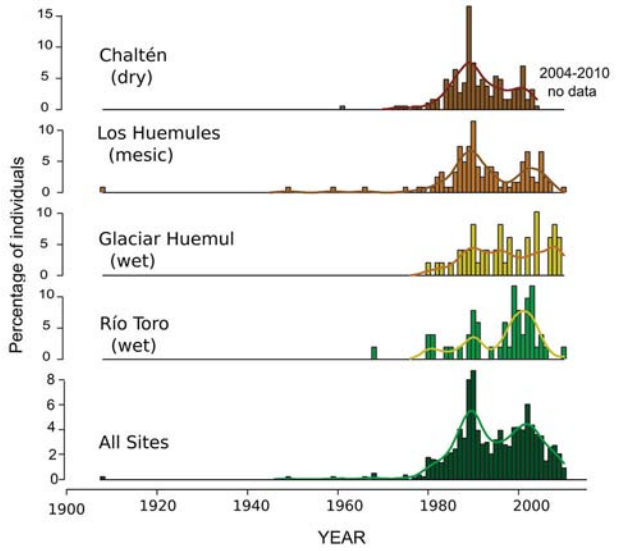

FIGURE 4 | Frequency distribution of individuals established at the upper-treeline sites. Sampling sites ordered from the driest (top) to the wettest (bottom) along El Chalten-Laguna del Desierto precipitation gradient. The regional establishment is shown at the bottom. Smoothed versions of the establishment temporal distributions estimated using a 10-year cubic spline function are also shown.

The temporal pattern of *Nothofagus* establishment in the treeline appear to be influenced by climatic variability (**Figure 5**). Both peaks in the temporal distribution of the establishment are related to summer temperature increases, while the decrease in recent years is concurrent with a marked reduction in summer precipitation (**Figure 5**).

DISCUSSION

The upper treeline from *N. pumilio* in the southern Patagonian Andes is sensitive to variations in climate. The increment in summer temperatures recorded between the cold interval 1966–1977 (mean = 9.6°C) to the prevailing warmer period from 1978 to present (mean = 10.34°C) has favored the establishment and survival of new individuals above the upper treeline. Old photographs from the region indicate that the upper treeline has remained quite stable at least for seven decades since the beginning of the twentieth century to the mid-1970s. Along the El Chaltén-Lago del Desierto precipitation gradient, all selected sites showed seedling establishment above treeline. However, it is important to note that local site conditions, such as steep slopes and/or lack of herbaceous cover, strongly inhibit the *Nothofagus* seedling establishment on the upper treeline. Our results are consistent with previous studies documenting a treeline advance during the past decades related to temperature increases since the mid-1970s in many sites along the Patagonian Andes (Daniels and Veblen, 2004; Srur et al., 2004, 2016).

The *Nothofagus* recruitment above the upper treeline started at mid-1970 and continues until today, albeit with differences in the patterns of establishment rates. At the dry-mesic sectors in the transect, the tree establishment that started in the mid-1970 following the temperature increment, peaked in the late 1980s, coincident with abundant summer precipitations from 1988 to 1994. The temporal changes in establishment rates at these sites indicated that tree establishment and survival at dry-mesic treelines is also modulated by amount of soil water available for growth. On the contrary, above-average precipitation in the wet treelines prolongs the snow cover duration and significantly reduce the extent of the growing season. A more attenuated peak in tree establishment occurred at the end of the 1980's in the wet sectors in comparison with that recorded at the drier sites along the precipitation transect. At the wet Estancia Río Toro site, the largest rate of recruitment were centered around the year 2000, concurrent with warmer summers recording normal precipitation (**Figure 4**). In consequence, our observations reveal important interactions between temperature and establishment modulated by precipitation. The establishment of new individuals in the dry upper treelines requires warmer temperatures accompanied by abundant precipitations to ensure the survival of the recent established plants. In humid environments, the higher temperatures that act reducing the permanence of snow, increase the duration of the growing season, and consequently, facilitate the establishment of new individuals in the upper treeline.

The dynamics of the *Nothofagus* treeline has also been investigated in New Zealand (Harsch et al., 2012). With morphological characteristics similar to the *Nothofagus* forests in Patagonia, forest expansion in the New Zealand upper treeline appears to be limited mainly by the scarcity of suitable microsites for seedling establishment. Therefore, the authors suggest that treelines in New Zealand appears to be less sensitive to recent global warming, and consequently, unlikely to show substantial upward movement under the current low demographic rates recorded at high elevations. Our results for Patagonia show, on the contrary, that treelines dominated by *N. pumilio* are sensitive to temperature changes, but other abiotic changes such as precipitation appears to play a key role in tree establishment. Poor-developed soils with extremely low water capacity, provides extremely adverse conditions to seedling colonization in southern Patagonia (Pissolito, 2016). Whereas warmer temperatures could lead to increases in tree establishment, abundant precipitation would contribute to the survival of seedling, particularly in the dry and mesic environments of the Patagonian upper treeline (Daniels and Veblen, 2004; Srur et al., 2016).

At the wet treelines in the rainy Chilean sector, Piper et al. (2013) also noted that warming has favored the establishment of *N. pumilio* seedlings in the southern Andes, however, they highlighted the importance of site-specific conditions in modulating the response of tree dynamics to climate change. They argued that heat-induced water deficits do not cancel out the benefits of higher temperatures for *Nothofagus* seedling survival and growth. Comparatively, the results from Piper et al. (2013) are consistent with those recorded at our wetter sites, since the increase in temperature in the early 2000's, concurrent with normal precipitation, favored establishment at the wet but

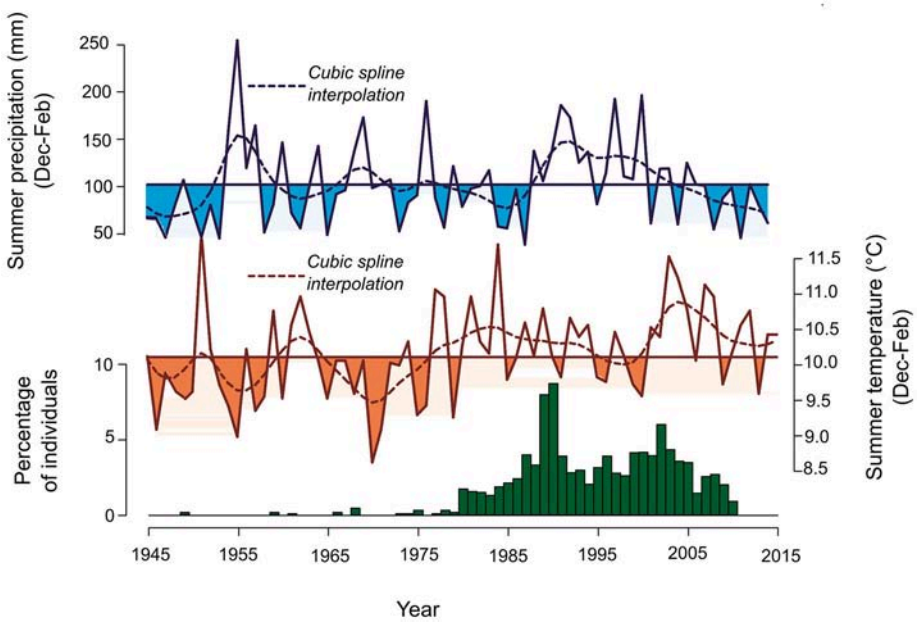

FIGURE 5 | Temporal variations in regional seedling establishment at the upper treelines in southern Patagonia and in Punta Arenas summer (December to February) temperature and precipitation. Straight lines represent the summer temperature and precipitation means. Smoothed versions of establishment and climatic variations using a cubic spline function of 10 years are also shown (dashed line).

not at the dry treelines. At the rainy treelines, precipitation is enough to compensate the increase in evapotranspiration due to higher temperatures. However, the long-term negative trend in precipitation since 2000 seems to have affected establishment in both wet and dry upper forests along the Río de las Vueltas basin (**Figure 5**). The scarce recruitment recorded in the last decade is in line with studies reporting the negative effects of warming on *N. pumilio* establishment due to the more severe water deficits recently recorded in the dry Patagonian Andes from Argentina (Heinemann et al., 2000; Daniels and Veblen, 2003; Srur et al., 2016).

In the Patagonian Andes, as well as in New Zealand, tree dynamics at the upper treeline has also been related to *Nothofagus* seed production and dispersal. Indeed, masting events have been reported for *N. pumilio* in Tierra del Fuego (Cuevas, 2000, 2002). Although two recruitment peaks are recorded at regional scale, they are not observed at most individual sites (**Figure 4**). Unfortunately, our records of seed production and seedling survival for the region are short, and therefore, not able of reliably detecting masting events. Therefore, the importance of long-term studies to properly answer relevant dynamics process in the treeline are evident. For the Chilean rainy treelines, Piper et al. (2013) reported an increase in seed production but not peaks in tree establishment, suggesting that an increase in *Nothofagus* seed production not necessarily reflect higher recruitment rates. For the *Nothofagus* treelines in New Zealand, Richardson et al. (2005) documented an increment in seed production over the past 30 years but not a concomitant recruitment increase over the same period (Harsch et al., 2012).

Another topic of discussion in relation to forest expansion deals with the distance between new establishment and the location of the current treeline. Most studies agree that the distance between new seedlings and the treeline depend on forest location and intensity of prevailing winds. Wind protected sites by tree barriers, windward slopes or large outcrops facilitate the establishment of seedlings through the creation of safe sites (Holtmeier and Broll, 2007; McIntire et al., 2016). Upper treelines in Patagonia are affected by the strong westerly winds all year round (Villalba et al., 2003; Garreaud et al., 2009), which certainly influence the dispersal of *N. pumilio* seeds. The longest distance recorded between new individuals and the continuous treeline was of 11.84 m at the forest leeward in Estancia Los Huemules. Therefore, and in accordance with other authors, not only the temperature increase modulates the treeline progression but also other abiotic factors existing at the site. Recent studies suggest that *N. pumilio* seed is comparatively heavy in the context of wind dispersed trees, being particularly the heaviest of all seeds within the genus *Nothofagus* in South America (Urretavizcaya et al., 2016). The *N. pumilio* seed is 9 times heavier than *N. dombeyi*'s and 11 times than *N. antartica*' s (Urretavizcaya et al., 2016). This characteristics of *N. pumilio* seed may also explain why tree establishment always occurs nearby the forest (Rusch, 1993). In general, the establishment is limited to 5 m from the tree line, even when appropriate microsites may be available at greater distances. Similarly, Harsch et al. (2012) noted that *Nothofagus* recruitment in New Zealand is mostly limited to the proximity to the forest. Therefore, the rate of *Nothofagus* treeline expansion is not only modulated by changes in temperature. Biotic and abiotic factors other than temperature

also modulate the rhythm of treeline progression into upper alpine vegetation.

Variations in temperature and precipitation at the southern end of South America are largely modulated by changes in the phases of the South Annular Mode (SAM; Falvey and Garreaud, 2009; Garreaud et al., 2009). The positive phase of SAM, characterized by anomalies of high atmospheric pressure in medium latitudes, is related to elevated temperatures and reduced precipitation in the Patagonian Andes (Marshall, 2003; Garreaud et al., 2009; Villalba et al., 2012). In particular, the positive trend in the SAM since the late 1950s is consistent with the rise in temperatures in the region. For the period 1957–2015 (59 years) the variations in the average annual temperature of Punta Arenas are significantly related to SAM ($r = 0.46$, $p < 0.001$; **Figure 6**). Consequently, the process of treeline expansion in our region in response to rising temperatures is finally a response to the positive trend observed in the SAM since the early 1960s (**Figure 6**). Relationships between SAM and precipitation in the Southern Patagonian Andes are more difficult to assess given the complexity of precipitation patterns introduced by the Andes Mountains and the lack of long and reliable meteorological records. The relationship between the annual precipitation of Punta Arenas and SAM is not statistically significant over the common period 1957–2015, but it is during the last 30 years. For the period 1986–2015, the positive trend in the SAM has contributed to the decrease in total annual precipitation in Punta Arenas since the early 1990s ($r = -0.52$; $p < 0.003$). As noted above, the increase in temperature since the mid-1970s has facilitated the establishment of new individuals in the upper treeline. However, the temporary rhythm of establishment has been partly modulated by variations in precipitation, particularly summer rainfall in the drier treelines. The steady decline in precipitation over the last few decades would be responsible for the slower rhythm of establishment in recent years. This situation would be affecting the establishment and/or survival of seedlings in both dry and wet sites along the precipitation gradient of Río Las Vueltas basin.

Similar to what has been documented in this paper, the increase in spring-summer temperature of 0.5°C in northern Patagonia facilitated the establishment of new individuals over the upper limit of the forest (Srur et al., 2016). However, this increase in temperature that occurred in the 1976/77 climate jump was associated with the documented phase change, from negative to positive, of the Pacific Decadal Oscillation (PDO). In its return to the negative phase of PDO at the beginning of the twenty-first century (Trenberth et al., 2014; Vuille et al., 2015), the climate in northern Patagonia became more variable, with spring-summer temperatures similar to those recorded in the negative phase of PDO prior to

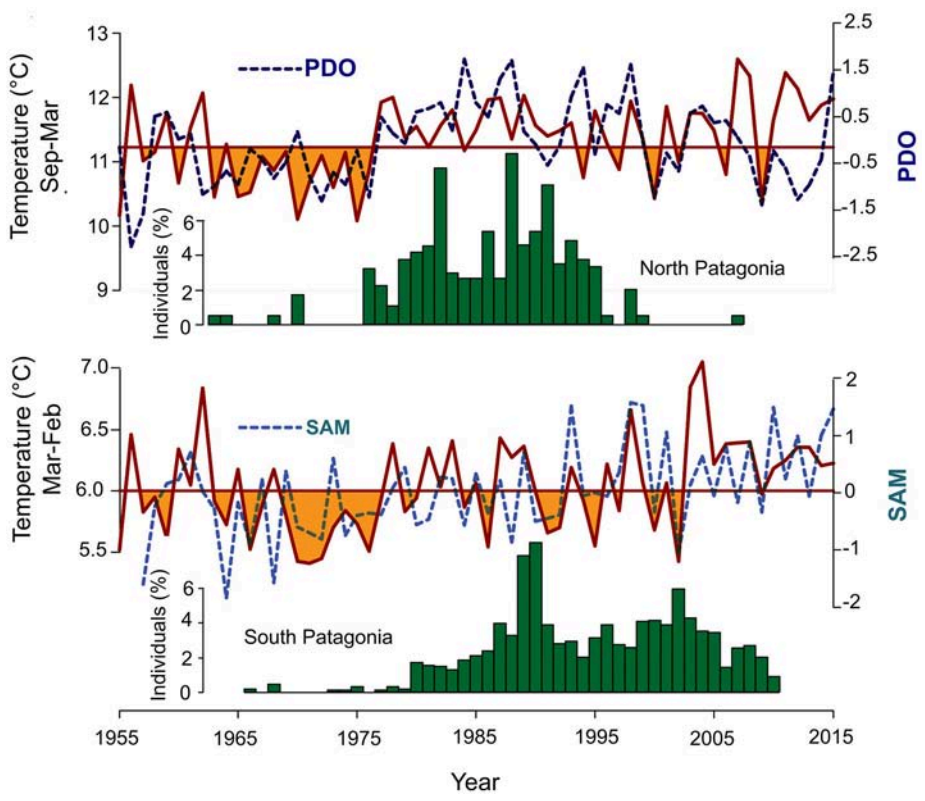

FIGURE 6 | Comparison between tree establishment above upper treelines in northern and southern Patagonia and their relationships with temperature and the associated atmospheric circulation indices. Temperature plotted with continuous line, PDO and SAM represented with dashed line.

1976. In particular, the establishment on the treeline in northern Patagonia follows more closely the variations in the PDO phases than in temperature changes (**Figure 6**). Indeed, Stenseth et al. (2003) argue that atmospheric circulation indices integrate a set of environmental variables beyond those that could be reflected in a single climatic variable such as temperature. The negative PDO phase is associated with lower temperatures, but also with lower precipitation in northern Patagonia (Srur et al., 2016). It is probably the combined occurrence of colder spring-summer and lower precipitation that has reduced or silenced the establishment of *Nothofagus* specimens on the abrupt treeline in northern Patagonia.

Similarly, the establishment of *Nothofagus* on treeline in the Southern Patagonian Andes seems to be more strongly regulated by SAM's influence on temperature and precipitation regimes. The sustained increase in temperature associated with the persistence of the positive phase of SAM since the mid-1970's has facilitated establishment over treeline, but variations in establishment rates seem to be associated with variations in regional precipitation also influenced by SAM. In particular, the lack of establishment over the last few years in the Southern Patagonian Andes would be a response to the reduction in regional precipitation, as temperatures have remained at levels similar to those recorded since the mid-1970s.

CONCLUSIONS

Our studies suggest that the location of the upper treeline of the *N. pumilio* forest in the Patagonian Andes is sensitive to changes in climate variations. The recorded increments in regional temperature have facilitated the establishment and therefore the ascent of the upper treeline. However, the regional expansion of the treeline is extremely variable when it is evaluated at local scale. Site topography, exposure and soil development, among other factors, markedly influence *N. pumilio* tree establishment at local scale in the upper treeline. The temperature increment has facilitated the tree recruitment in both the dry-mesic and wet treelines along the precipitation gradient in Río de las Vueltas basin. However, the rate of seedling establishment appears to be more strongly modulated by the interaction between temperature increase and variations in precipitation. In the dry to mesic sites of the upper treeline, the survival of the seedlings depends on the occurrence of wet periods, whereas wet periods prolong the snowpack cover in the wet treelines limiting tree establishment. Finally, prolong droughts affect tree establishment at both dry and humid treelines on the Argentinean slopes of the southern Andes.

The expansion of the upper treeline in the Patagonian Andes has been limited to 5–10 m from the abrupt treeline. This comparatively reduced advance of the forest in the alpine grassland is regulated by other biotic and abiotic factors rather than the temperature increase. The location of the sites in relation to prevailing winds, microsite conditions, and the comparatively heavy seeds of *N. pumilio* (up to 9–11 times the seed weight of other *Nothofagus* seeds) affects the spatial advance of the upper treeline.

While the recent expansion of treeline in northern Patagonia was regulated by temperature and precipitation variations associated with the different phases of PDO, the climatic variations induced by the persistently positive trend of SAM during the last decades were what facilitated the establishment in the Southern Patagonian Andes. In both cases, the rhythm of establishment in the upper treeline responded to interactions between temperature and precipitation rather than to variations in only one of these meteorological variables. The scarce precipitation associated with the negative phase of PDO in the north and with the positive phase of SAM in the southern Patagonian Andes seems to have reduced establishment in recent years. Conversely, temperature increases in response to the positive phases of both PDO and SAM from the 1970s onwards triggered the establishment process at the upper boundary of the forest.

Despite the high value of retrospective studies such as the one presented here, the need for long-term monitoring of forest dynamics in treeline areas is evident. These studies would allow us to clarify basic aspects of the population dynamics of the species in these climate change-sensitive sites, such as variability in seed production or seedling mortality rates, providing us with more information about the effects that such change may have on the future distribution of forests and the ecosystem services they provide.

AUTHOR CONTRIBUTIONS

AS and RV participated in the development of all the paper (field work, data analysis and writing). MR-C participated in fieldwork, data analysis and paper review. MA participated in the fieldwork and review of the paper. EM analyzed some of the data and reviewed the work.

ACKNOWLEDGMENTS

This study was partially supported by CONICET, Argentina. The authors would like to thank Alberto Ripalta, Claudia Guerrido, Mariano Masiokas, and Silvia Delgado for field work assistance. The authors would also like to thank the owners and administrators of Estancia Río Toro (José María Barale and Ricardo Sanchez) and of Estancia Los Huemules (Federico Reese). On the other hand, we would also like to thank you for the permits granted by the administration of national parks, especially Los Glaciares section. Lidia Ferri and Pierre Pitte provided useful comments on the manuscript.

REFERENCES

Astudillo-Sánchez, C. C., Villanueva-Díaz, J., Endara-Agramont, A. R., Nava-Bernal, G. E., and Gómez-Albores, M. A. (2017). Climatic variability at the treeline of Monte Tlaloc, Mexico: a dendrochronological approach. *Trees* 31, 441–453. doi: 10.1007/s00468-016-1460-z

Bellard, C., Bertelsmeier, C., Leadley, P., Thuiller, W., and Courchamp, F. (2012). Impacts of climate change on the future of biodiversity. *Ecol. Lett.* 15, 365–377. doi: 10.1111/j.1461-0248.2011.01736.x

Boelcke, O., Moore, D. M., and Roig, F. A. (1985). *Transecta Botánica de la Patagonia Austral*. Buenos Aires: Consejo Nacional de Investigaciones Cientificas y Tecnicas.

Bunn, A., Korpela, M., Biondi, F., Campelo, F., Mérian, P., Qeadan, F., et al. (2016). *dplR: Dendrochronology Program Library in R*. Available online at: http://CRAN.R-project.org/package=dplR

Cabrera, A. L. (1976). *Regiones Fitogeográficas Argentinas. Enciclopedia Argentina de Agricultura y Jardinería*. Buenos Aires: Acme.

Camarero, J. J., and Gutiérrez, E. (2004). Pace and pattern of recent treeline dynamics: response of ecotones to climatic variability in the Spanish Pyrenees. *Clim. Change* 63, 181–200. doi: 10.1023/B:CLIM.0000018507.71343.46

Cuevas, J. G. (2000). Tree recruitment at the *Nothofagus pumilio* alpine timberline in Tierra del Fuego, Chile. *J. Ecol.* 88, 840–855. doi: 10.1046/j.1365-2745.2000.00497.x

Cuevas, J. G. (2002). Episodic regeneration at the *Nothofagus pumilio* alpine timberline in Tierra del Fuego, Chile. *J. Ecol.* 90, 52–60. doi: 10.1046/j.0022-0477.2001.00636.x

Danby, R. K., and Hik, D. S. (2007). Evidence of recent treeline dynamics in southwest Yukon from aerial photographs. *Arctic* 60, 411–420.

Daniels, L. D., and Veblen, T. T. (2003). Altitudinal treelines of the southern Andes near 40°S. *For. Chron.* 79, 237–241. doi: 10.5558/tfc79237-2

Daniels, L. D., and Veblen, T. T. (2004). Spatiotemporal influences of climate on altitudinal treeline in northern Patagonia. *Ecology* 85, 1284–1296. doi: 10.1890/03-0092

Daubenmire, R. (1954). Alpine timberlines in the Americas and their interpretation. *Butl. Univ. Bot. Stud.* 11, 119–136.

Elliott, G. P., and Cowell, C. M. (2015). Slope aspect mediates fine-scale tree establishment patterns at upper treeline during wet and dry periods of the 20th century. *Arct. Antarct. Alp. Res.* 47, 681–692. doi: 10.1657/AAAR0014-025

Falvey, M., and Garreaud, R. D. (2009). Regional cooling in a warming world: recent temperature trends in the southeast Pacific and along the west coast of subtropical South America (1979–2006). *J. Geophys. Res.* 114, 1–16. doi: 10.1029/2008JD010519

Franke, A. K., Bräuning, A., Timonen, M., and Rautio, P. (2017). Growth response of Scots pines in polar-alpine tree-line to a warming climate. *For. Ecol. Manag.* 399, 94–107. doi: 10.1016/j.foreco.2017.05.027

Garreaud, R. D. (2009). The Andes climate and weather. *Adv. Geosci.* 22, 3–11. doi: 10.5194/adgeo-22-3-2009

Garreaud, R. D., Vuille, M., Compagnucci, R., and Marengo, J. (2009). Present-day South American climate. *Palaeogeogr. Palaeoclimatol. Palaeoecol.* 281, 180–195. doi: 10.1016/j.palaeo.2007.10.032

Garreaud, R., Lopez, P., Minvielle, M., and Rojas, M. (2013). Large-scale control on the Patagonian climate. *J. Clim.* 26, 215–230. doi: 10.1175/JCLI-D-12-00001.1

Grace, J., Berninger, F., and Nagy, L. (2002). Impacts of climate change on the tree line. *Ann. Bot.* 90, 537–544. doi: 10.1093/aob/mcf222

Hansen, A. J., Neilson, R. P., Dale, V. H., Flather, C. H., Iverson, L. R., Currie, D. J., et al. (2001). Global change in forests: responses of species, communities, and biomesinteractions between climate change and land use are projected to cause large shifts in biodiversity. *Bioscience* 51, 765–779. doi: 10.1641/0006-3568(2001)051[0765:GCIFRO]2.0.CO;2

Harsch, M. A., Buxton, R., Duncan, R. P., Hulme, P. E., Wardle, P., and Wilmshurst, J. (2012). Causes of tree line stability: stem growth, recruitment and mortality rates over 15 years at New Zealand *Nothofagus* tree lines. *J. Biogeogr.* 39, 2061–2071. doi: 10.1111/j.1365-2699.2012.02763.x

Harsch, M. A., Hulme, P. E., McGlone, M. S., and Duncan, R. P. (2009). Are treelines advancing? A global meta-analysis of treeline response to climate warming. *Ecol. Lett.* 12, 1040–1049. doi: 10.1111/j.1461-0248.2009.01355.x

Heinemann, K., Kitzberger, T., and Veblen, T. T. (2000). Influences of gap microheterogeneity on the regeneration of *Nothofagus pumilio* in a xeric old-growth forest of northwestern Patagonia, Argentina. *Can. J. For. Res.* 30, 25–31. doi: 10.1139/x99-181

Holtmeier, F.-K., and Broll, G. (2005). Sensitivity and response of northern hemisphere altitudinal and polar treelines to environmental change at landscape and local scales. *Glob. Ecol. Biogeogr.* 14, 395–410. doi: 10.1111/j.1466-822X.2005.00168.x

Holtmeier, F.-K., and Broll, G. (2007). Treeline advance - driving processes and adverse factors. *Landsc. Online* 1, 1–33. doi: 10.3097/LO.200701

Jobbagy, E. G., and Jackson, R. B. (2000). Global controls of forest line elevation in the northern and southern hemispheres. *Glob. Ecol. Biogeogr.* 9, 253–268. doi: 10.1046/j.1365-2699.2000.00162.x

Jochner, M., Bugmann, H., Nötzli, M., and Bigler, C. (2017). Among-tree variability and feedback effects result in different growth responses to climate change at the upper treeline in the Swiss Alps. *Ecol. Evol.* 7, 7937–7953. doi: 10.1002/ece3.3290

Kirdyanov, A. V., Hagedorn, F., Knorre, A. A., Fedotova, E. V., Vaganov, E. A., Naurzbaev, M. M., et al. (2012). 20th century tree-line advance and vegetation changes along an altitudinal transect in the Putorana Mountains, northern Siberia: 20th century tree-line advance, N Siberia. *Boreas* 41, 56–67. doi: 10.1111/j.1502-3885.2011.00214.x

Körner, C. (1998). Re-assessment of high elevation treeline positions and their explanation. *Oecologia* 115, 445–459. doi: 10.1007/s004420050540

Körner, C., and Paulsen, J. (2004). A world-wide study of high altitude treeline temperatures. *J. Biogeogr.* 31, 713–732. doi: 10.1111/j.1365-2699.2003.01043.x

Liang, E., Wang, Y., Piao, S., Lu, X., Camarero, J. J., Zhu, H., et al. (2016). Species interactions slow warming-induced upward shifts of treelines on the Tibetan Plateau. *Proc. Natl. Acad. Sci. U.S.A.* 113, 4380–4385. doi: 10.1073/pnas.1520582113

Magrin, G. O., Marengo, J. A., Boulanger, J. P., Buckeridge, M. S., Castellanos, E., Poveda, G., et al. (2014). "Central and South America," in *Climate Change 2014: Impacts, Adaptation, and Vulnerability. Part B: Regional Aspects. Contribution of Working Group II to the Fifth Assessment Report of the Intergovernmental Panel on Climate Change* (Cambridge, UK; New York, NY: Cambridge University Press), 1499–1566.

Mainali, K. P., Warren, D. L., Dhileepan, K., McConnachie, A., Strathie, L., Hassan, G., et al. (2015). Projecting future expansion of invasive species: comparing and improving methodologies for species distribution modeling. *Glob. Change Biol.* 21, 4464–4480. doi: 10.1111/gcb.13038

Marshall, G. J. (2003). Trends in the Southern Annular Mode from observations and reanalyses. *J. Clim.* 16, 4134–4143. doi: 10.1175/1520-0442(2003)016<4134:TITSAM>2.0.CO;2

Masiokas, M. H., Luckman, B. H., Villalba, R., Delgado, S., Skvarca, P., and Ripalta, A. (2009). Little ice age fluctuations of small glaciers in the Monte Fitz Roy and Lago del Desierto areas, South Patagonian Andes, Argentina. *Palaeogeogr. Palaeoclimatol. Palaeoecol.* 281, 351–362. doi: 10.1016/j.palaeo.2007.10.031

Masiokas, M. H., Villalba, R., Luckman, B. H., Lascano, M. E., Delgado, S., and Stepanek, P. (2008). 20th-century glacier recession and regional hydroclimatic changes in northwestern Patagonia. *Glob. Planet. Change* 60, 85–100. doi: 10.1016/j.gloplacha.2006.07.031

McIntire, E. J. B., Piper, F. I., and Fajardo, A. (2016). Wind exposure and light exposure, more than elevation-related temperature, limit tree line seedling abundance on three continents. *J. Ecol.* 104, 1379–1390. doi: 10.1111/1365-2745.12599

Moreno, P. I., Vilanova, I., Villa-Martínez, R., Garreaud, R. D., Rojas, M., and De Pol-Holz, R. (2014). Southern annular mode-like changes in southwestern Patagonia at centennial timescales over the last three millennia. *Nat. Commun.* 5: 4375. doi: 10.1038/ncomms5375

Piper, F. I., Fajardo, A., and Cavieres, L. A. (2013). Simulated warming does not impair seedling survival and growth of *Nothofagus pumilio* in the southern Andes. *Perspect. Plant Ecol. Evol. Syst.* 15, 97–105. doi: 10.1016/j.ppees.2013.02.003

Pissolito, C. (2016). *Sucesión Primaria de la Vegetación en Bosques de Nothofagus spp. en los Andes Patagónicos: Patrones Espacio-Temporales de Establecimiento de Plantas e Implicancias Para la Restauración*. Ph.D. Dissertation, Universidad Nacional de Cuyo, Mendoza.

Renwick, K. M., and Rocca, M. E. (2015). Temporal context affects the observed rate of climate-driven range shifts in tree species: importance of temporal context in tree range shifts. *Glob. Ecol. Biogeogr.* 24, 44–51. doi: 10.1111/geb.12240

Richardson, S. J., Allen, R. B., Whitehead, D., Carswell, F. E., Ruscoe, W. A., and Platt, K. H. (2005). Climate and net carbon availability determine temporal patterns of seed production by *Nothofagus*. *Ecology* 86, 972–981. doi: 10.1890/04-0863

Rupp, T. S., Chapin, F. S., and Starfield, A. M. (2001). Modeling the influence of topographic barriers on treeline advance at the forest-tundra ecotone in northwestern Alaska. *Clim. Change* 48, 399–416. doi: 10.1023/A:1010738502596

Rusch, V. E. (1993). Altitudinal variation in the phenology of *Nothofagus pumilio* in Argentina. *Rev. Chil. Hist. Nat.* 66, 131–141.

Saccone, P., Hoikka, K., and Virtanen, R. (2017). What if plant functional types conceal species-specific responses to environment? Study on arctic shrub communities. *Ecology* 98, 1600–1612. doi: 10.1002/ecy.1817

Spasojevic, M. J., Bowman, W. D., Humphries, H. C., Seastedt, T. R., and Suding, K. N. (2013). Changes in alpine vegetation over 21 years: are patterns across a heterogeneous landscape consistent with predictions? *Ecosphere* 4, 1–18. doi: 10.1890/ES13-00133.1

Spasojevic, M. J., Harrison, S., Day, H. W., and Southard, R. J. (2014). Above- and belowground biotic interactions facilitate relocation of plants into cooler environments. *Ecol. Lett.* 17, 700–709. doi: 10.1111/ele.12272

Srur, A. M., Villalba, R., Rodríguez-Catón, M., Amoroso, M. M., and Marcotti, E. (2016). Establishment of *Nothofagus pumilio* at upper treelines across a precipitation gradient in the Northern Patagonian Andes. *Arct. Antarct. Alp. Res.* 48, 755–766. doi: 10.1657/AAAR0016-015

Srur, A. M., Villalba, R., Villagra, P. E., Morales, M. S., and Lana, N. B. (2004). "Estructura y dinámica del bosque de Nothofagus pumilio a lo largo de un gradiente altitudinal en El Chaltén, Santa Cruz," in *II Reunión Binacional de Ecología. XI Reunión de la Sociedad de Ecología de Chile y XXI Reunión Argentina de Ecología* (Mendoza).

Stenseth, N. C., Ottersen, G., Hurrell, J. W., Mysterud, A., Lima, M., Chan, K. S., et al. (2003). Studying climate effects on ecology through the use of climate indices: the North Atlantic oscillation, El Nino Southern oscillation and beyond. *Proc. R. Soc. Lond. B. Biol. Sci.* 270, 2087–2096. doi: 10.1098/rspb.2003.2415

Stevens, G. C., and Fox, J. F. (1991). The causes of treeline. *Annu. Rev. Ecol. Syst.* 22, 177–191. doi: 10.1146/annurev.es.22.110191.001141

Stokes, M. A., and Smiley, T. L. (1968). *An Introduction to Tree-Ring Dating*. Chicago, IL; London: University of Chicago Press.

Tingstad, L., Olsen, S. L., Klanderud, K., Vandvik, V., and Ohlson, M. (2015). Temperature, precipitation and biotic interactions as determinants of tree seedling recruitment across the tree line ecotone. *Oecologia* 179, 599–608. doi: 10.1007/s00442-015-3360-0

Tranquilini, W. (1979). "General features of the upper timberline," in *Physiological Ecology of the Alpine Timberline* (Berlin; Heidelberg: Springer), 1–4.

Trenberth, K. E., Fasullo, J. T., Branstator, G., and Phillips, A. S. (2014). Seasonal aspects of the recent pause in surface warming. *Nat. Clim. Change* 4, 911–916. doi: 10.1038/nclimate2341

Urretavizcaya, M. F., Contardi, L. T., Oyharçabal, M. F., and Pasquini, M. (2016). Calidad de semillas de especies nativas del bosque andino patagónico de la provincia de Chubut y su importancia para la producción de plantines. *Rev. Fac. Agron. Plata* 115, 9–18. Available online at: http://hdl.handle.net/10915/54164

Villalba, R., Lara, A., Boninsegna, J. A., Masiokas, M., Delgado, S., Aravena, J. C., et al. (2003). Large-scale temperature changes across the southern Andes: 20th-century variations in the context of the past 400 years. *Clim. Change* 59, 177–232. doi: 10.1023/A:1024452701153

Villalba, R., Lara, A., Masiokas, M. H., Urrutia, R., Luckman, B. H., Marshall, G. J., et al. (2012). Unusual Southern Hemisphere tree growth patterns induced by changes in the Southern Annular Mode. *Nat. Geosci.* 5, 793–798. doi: 10.1038/ngeo1613

Villalba, R., and Veblen, T. T. (1997). Regional patterns of tree population age structures in Northern Patagonia: climatic and disturbance influences. *J. Ecol.* 85, 113–124. doi: 10.2307/2960643

Vuille, M., Franquist, E., Garreaud, R., Lavado Casimiro, W. S., and Cáceres, B. (2015). Impact of the global warming hiatus on Andean temperature. *J. Geophys. Res. Atmospheres* 120, 3745–3757. doi: 10.1002/2015JD023126

Wang, T., Zhang, Q.-B., and Ma, K. (2006). Treeline dynamics in relation to climatic variability in the central Tianshan Mountains, Northwestern China. *Glob. Ecol. Biogeogr.* 15, 406–415. doi: 10.1111/j.1466-822X.2006.00233.x

Woodward, A., Schreiner, E. G., and Silsbee, D. G. (1995). Climate, geography, and tree establishment in Subalpine Meadows of the Olympic Mountains, Washington, U.S.A. *Arct. Alp. Res.* 27, 217–225. doi: 10.2307/1551952

Zar, J. (1999). *Biostatistical Analysis*. Upper Saddle River, NJ: The University of Chicago Press.

Conflict of Interest Statement: The authors declare that the research was conducted in the absence of any commercial or financial relationships that could be construed as a potential conflict of interest.

frontiers in Earth Science

ORIGINAL RESEARCH
published: 29 May 2018
doi: 10.3389/feart.2018.00062

An Updated Multi-Temporal Glacier Inventory for the Patagonian Andes With Changes Between the Little Ice Age and 2016

Wolfgang J.-H. Meier, Jussi Grießinger, Philipp Hochreuther and Matthias H. Braun*

Institute of Geography, Friedrich-Alexander-Universität Erlangen-Nürnberg, Erlangen, Germany

We present a satellite-derived glacier inventory for the whole Patagonian Andes south of 45. 5°S and Tierra del Fuego including recent changes. Landsat TM/ETM+ and OLI satellite scenes were used to detect changes in the glacierized area between 1986, 2005 and 2016 for all of the 11,209 inventoried glaciers using a semi-automated procedure. Additionally we used geomorphological evidence, such as moraines and trimlines to determine the glacierized area during the Little Ice Age for almost 90% of the total glacierized area. Within the last ~150 years the glacierized area was reduced from 28,091 ± 890 km^2 to 22,636 ± 905 km^2, marking an absolute area loss of 5,455 ± 1,269 km^2 (19.4 ± 4.5%). For the whole study region, the annual area decrease was moderate until 1986 with 0.10 ± 0.04% a^{-1}. Afterwards the area reduction increased, reaching annual values of 0.33 ± 0.28% a^{-1} and 0.25 ± 0.50% a^{-1} for the periods of 1986–2005 and 2005–2016, respectively. There is a high variability of change rates throughout the Patagonian Andes. Small glaciers, especially in the north of the Northern Patagonian Icefield (NPI) and between the latter and the Southern Patagonian Icefield (SPI) had over all periods the highest rates of shrinkage, exceeding 0.92 ± 1.22% a^{-1} during 2005–2016. In the mountain range of the Cordillera Darwin (CD), and also accounting for small ice fields south of 52°S, highest rates of shrinkage occurred during 1986–2005, reaching values up to 0.45 ± 0.23% a^{-1}, but decreased during the 2005–2016 period. Across the Andean main crest, the eastern parts of the NPI, SPI and adjoined glaciers had in absolute values the highest area reduction exceeding 2,145 ± 486 km^2 since the LIA. Large calving glaciers show a smaller relative decrease rate compared to land-terminating glaciers but account for the most absolute area loss. In general, glacier shrinkage is dependent on latitude, the initial glacier area, the environment of the glacial tongue (calving or non-calving glaciers) and in parts by glacial aspect.

Keywords: Glacier change, Little Ice Age, South America, remote sensing, glacier mapping

OPEN ACCESS

Edited by:
Alun Hubbard,
UiT The Arctic University of Norway, Norway

Reviewed by:
Bethan Joan Davies,
Royal Holloway, University of London, United Kingdom
Jonathan Ryan,
Brown University, United States
Antoine Rabatel,
Université Grenoble Alpes, France

****Correspondence:***
Wolfgang J.-H. Meier
Wolfgang.jh.meier@fau.de

Specialty section:
This article was submitted to Cryospheric Sciences, a section of the journal Frontiers in Earth Science

Received: *31 January 2018*
Accepted: *09 May 2018*
Published: *29 May 2018*

Citation:
Meier WJ-H, Grießinger J, Hochreuther P and Braun MH (2018) An Updated Multi-Temporal Glacier Inventory for the Patagonian Andes With Changes Between the Little Ice Age and 2016. Front. Earth Sci. 6:62. doi: 10.3389/feart.2018.00062

INTRODUCTION

The climate of southwest Patagonia is heavily influenced by the straight zonal band of Westerlies from the Pacific Ocean (Garreaud et al., 2013; Lenaerts et al., 2014). The mountains of the southern Andes form an orographic obstacle perpendicular to the prevalent atmospheric flow. This generates an uplift of humid air masses which results in extreme amounts of precipitation at the windward

side of the orogen (Schneider et al., 2003; Smith and Evans, 2007). Accordingly, precipitation on the western side can exceed up to 10,000 mm a^{-1} (Carrasco et al., 2000; Schneider et al., 2003), whereas the amount rapidly decreases within a distance of ∼50–150 km eastwards to <500 mm a^{-1}, thus forming a steep west-east gradient (Carrasco et al., 2002) (**Figure 1**). The vicinity of the Pacific Ocean causes moderate temperatures, yet the vast precipitation rate nourishes many glaciers, constituting the largest temperate ice bodies in the Southern Hemisphere outside the Polar Regions (Aniya, 2013). The main ice bodies of South America, the Northern Patagonian Icefield (NPI) and the Southern Patagonian Icefield (SPI), cover an area of about 4,200 and 13,000 km^2, respectively (Aniya, 1988; Aniya et al., 1992). For both ice fields a continuous retreat has been reported in several studies, except for some unusual advances e.g., by glacier Pío XI (Rivera et al., 1997, 2007; Masiokas et al., 2009b and references therein; Lopez et al., 2010). The 76 major outlet glaciers of the NPI and the SPI typically descent to sea level and are frequently calving into fjords in the west and into lakes to the east, with extraordinary flow velocities up to several km a^{-1} (Sakakibara and Sugiyama, 2014). The tidewater—and lacustrine-calving outlet glaciers are frequently used as indicators of climate change, although they are subject to the influence of more complex glacial—and geomorphologic features leading to an asynchronous behavior (Lopez et al., 2010; Sakakibara and Sugiyama, 2014).

The Federal initiatives of Argentina and Chile document the need for a detailed glacier inventory on a national and/or regional scale that does not only focus on the already well-epresented major ice fields. Glaciers of NPI and SPI solely make up 20% of the total number of 9,429 glaciers (Randolph Glacier Inventory: RGI 6.0) south of 45.5°S (Pfeffer et al., 2014; Randolph Glacier Inventory Consortium, 2017). As the NPI and SPI cover almost 65% of the total glacierized area of southern South America, their contribution to sea level rise is one of the most substantial outside the ice sheets of Greenland and Antarctica (Rignot et al.,

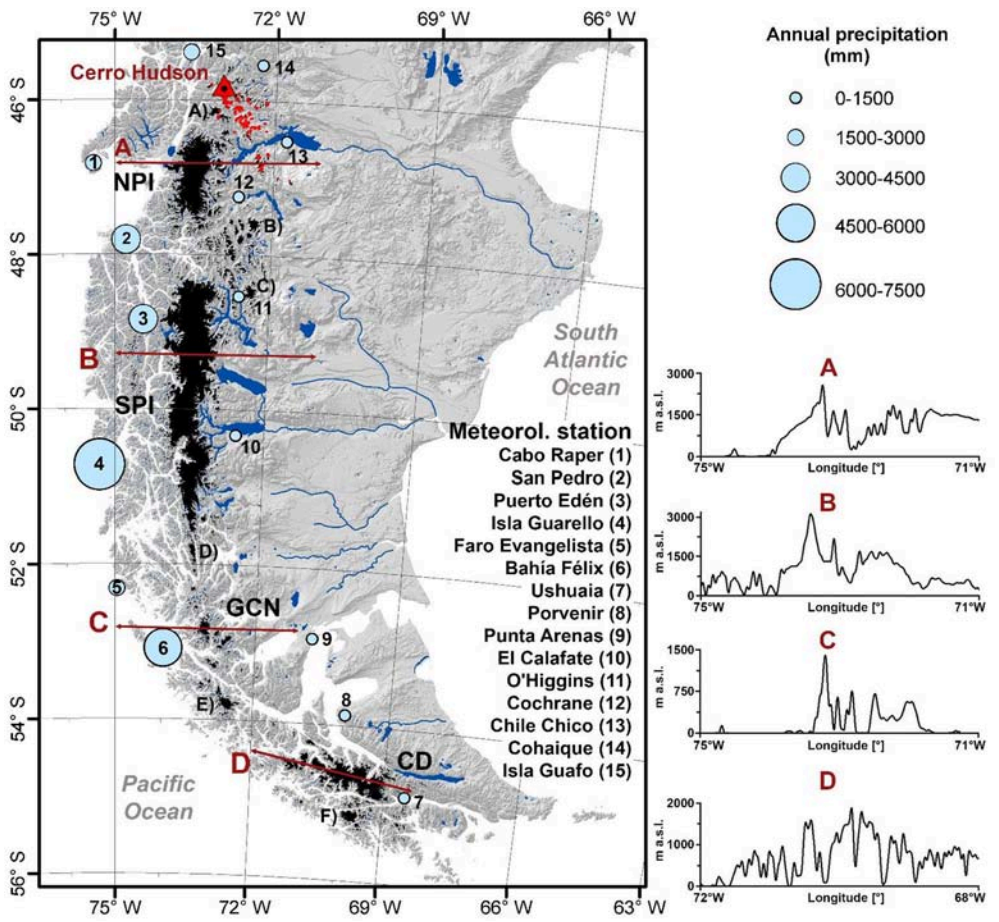

FIGURE 1 | Location of the investigated glacierized area of the Patagonian Andes and Tierra del Fuego with its main ice bodies: Northern Patagonian Icefield (NPI), Southern Patagonian Icefield (SPI), Gran Campo Nevado (GCN), the Cordillera Darwin (CD), and smaller ice bodies: (A) Cerro Erasmo (CE) (B) Monte San Lorenzo (MSL) (C) Sierre de Sangra (SD) (D) Cordillera Sarmiento (CS) (E) Isla Santa Inés (ISI) (F) Isla Hostle (IH). Many glaciers are covered with volcanic deposits due to the eruption of Cerro Hudson in 1991 (red). The high relief energy, displayed by the height transects **(A–D)** transverse to the Andean range and alongside the Cordillera Darwin, leads to high precipitation amounts on the windward side. Eastward of the main ridge, precipitation is rapidly decreasing (Meteorol. data from the Argentinian and Chilean Meteorological Services, lakes from Messager et al., 2016).

2003; Glasser et al., 2011; Malz et al., 2018). Recently, Malz et al. (2018) reported that the SPI solely contributes to the global sea level rise between 2000 and 2015/16 with a mass loss rate equivalent to 0.033 ± 0.006 mm a^{-1}. Geodetic mass balance calculations, as performed by Dussaillant et al. (2018) for the NPI and Malz et al. (2018) for the SPI, require a precise knowledge of the glacial extent. Though the Randolph Glacier Inventory (Pfeffer et al., 2014; Randolph Glacier Inventory Consortium, 2017) is the globally most complete glacier dataset, its accuracy is highly variable and small ice bodies are underrepresented (e.g., Masiokas et al., 2015). Also for larger glaciers (>10 km^2), the glacier outlines and ice divides incorporated in the RGI were not sufficient e.g., for the study of Malz et al. (2018). For this purpose, Dussaillant et al. (2018) had to correct the glacier outlines (taken from the RGI) and ice divides manually, whereas Malz et al. (2018) used an automated mapping approach and also generated new ice divides. Paul and Mölg (2014) named a problematic bias that appears for glacial delineation in the Northern Patagonian Andes from e.g., large amounts of seasonal snow due to the maritime climate and the steep terrain causing widespread cast shadow. Hence, a spatially well-replicated high-resolution dataset of glaciers for the accurate assessment of the regional glacial change in the Southern Andes is still missing.

While studies of individual ice caps (e.g., Rivera and Casassa, 2004; Falaschi et al., 2013) and –fields (Rivera et al., 2007; Schneider et al., 2007; Masiokas et al., 2015) provide a high level of detail, their results are largely incomparable, as they document the state of the local cryosphere at specific points in time, and employ a wealth of methods differing by sensor, approach or thresholds. For example, newly established glacier inventories for the Chilean Andes (Barcaza et al., 2017) performed a glacial change analysis on a small amount of 100 glaciers along a 4,000 km transect for the period 2000–2015 using Landsat TM/ETM+, while Masiokas et al. (2015) report changes of the northeast SPI between 1979 and 2005 using ASTER and ETM+ data for 250 glaciers.

The study of Davies and Glasser (2012) intends to overcome this issue by extrapolating glacier change from the extent during the Little Ice Age (LIA, ~1870 AD) to the actual extent in 2011, covering the area between 41 and 56°S. Based on a sample depth of 640 manually digitized glaciers, a total area loss of 4,131 km^2 since the LIA was calculated. With 60% of the studied glaciers being outlet glaciers of the major ice fields, the study focuses on the area change of the large glaciers, whereas observed change rates of medium—to small glaciers may be subject to a considerable uncertainty. Additionally, smaller glaciers (<0.1 km^2) were not investigated by Davies and Glasser (2012) and change analysis for 20% of the total glacier number (RGI 6.0) was performed. Consequently, their derived LIA extents are also based on a pixel resolution of 30 m, which justifies the focus on the larger ice bodies. Based on multiple digitization of six glaciers of the NPI an area uncertainty of ± 2% (Davies and Glasser, 2012) was estimated and used for the whole dataset and the whole studied period. This uncertainty value might be questionable, as the relative area error increases strongly with decreasing glacier area (Fischer et al., 2014). In summary, a comprehensive and unbiased glacier inventory, based upon a uniform set of methods, sensor resolution and investigation periods is still lacking for Patagonia. In order to overcome the existing incomparability of local inventories and covering the whole glacierized area of the Southern Andes, we revised and extended the existing glacier inventories for the Patagonian Andes south of 45.5°S including the Tierra del Fuego (**Figure 1**). Based on multi-spectral remote sensing techniques glacier outlines were derived in a semi—automated process from Landsat-5 TM, and Landsat-8 OLI. To assess the regional glacier change, the glacier outlines were inferred for almost all glaciers between the periods 1985/1986, 2005/2006, and 2016/2017. For the LIA, the extents of over 2,500 glaciers were compiled by manual digitization using the Landsat data and additionally Sentinel-2 data from the European Space Agency (ESA). This approach provides a better pixel resolution of 10 m compared to the Landsat data with 30 m. We provide a robust error assessment based on a representative sample of the LIA glacier extents, considering the area class specific area uncertainty. Our LIA glacial extents involve almost 90% of the total glacierized area of 1985/86 thus reveling a change rate assessment during the last 150 years for nearly the whole studied area.

METHODS

Glacier Inventory 1986/87, 2005/2006, and 2016/17

Different techniques for an automated glacier delineation using optical satellite imagery have been successfully applied in various glacierized regions (Andreassen et al., 2008; Bolch et al., 2010a,b). These automated methods provide precise, reproducible and consistent results (Paul et al., 2013) and are well-suited for the examination of larger geographical areas. Since glacier mapping requires as a prerequisite a low surface coverage with seasonal snow and optical sensors are restricted by cloud cover, the availability of suitable satellite scenes from the end of the ablation period is limited. In addition, a small solar altitude angle or inconvenient azimuth angle combined with steep terrain resulting in cast shadows hamper an automated mapping approach. Hence, multiple Landsat satellite scenes for the same periods served as a baseline for our semi-automatic multi-temporal mapping between the periods 1986/87, 2005/2006, and 2016/2017. We used both, Landsat-5 TM and Landsat-8 OLI scenes from the United States Geological Survey (level 1T) for the semi-automated mapping. Due to the failure of the scan line corrector (SLC) the Landsat-7 ETM+ data were not used for the automated approach but serve frequently as well as the Sentinal-2 images as auxiliary data for manual improvement of the outlines, e.g., in shadowed regions (**Figure 2c**) and for seasonal snow.

Since the period of southern hemispheric summer is overlapping parts of two calendar years, we set the respective time span to the starting date of the summer, thus defining the three periods as 1986, 2005, and 2016. In contrast to the recommended GLIMS threshold of 0.01 km^2 as the minimum glacier area (Raup and Khalsa, 2007) we adjusted the minimum threshold in our inventory to ice bodies larger than 0.025 km^2 due to (i)

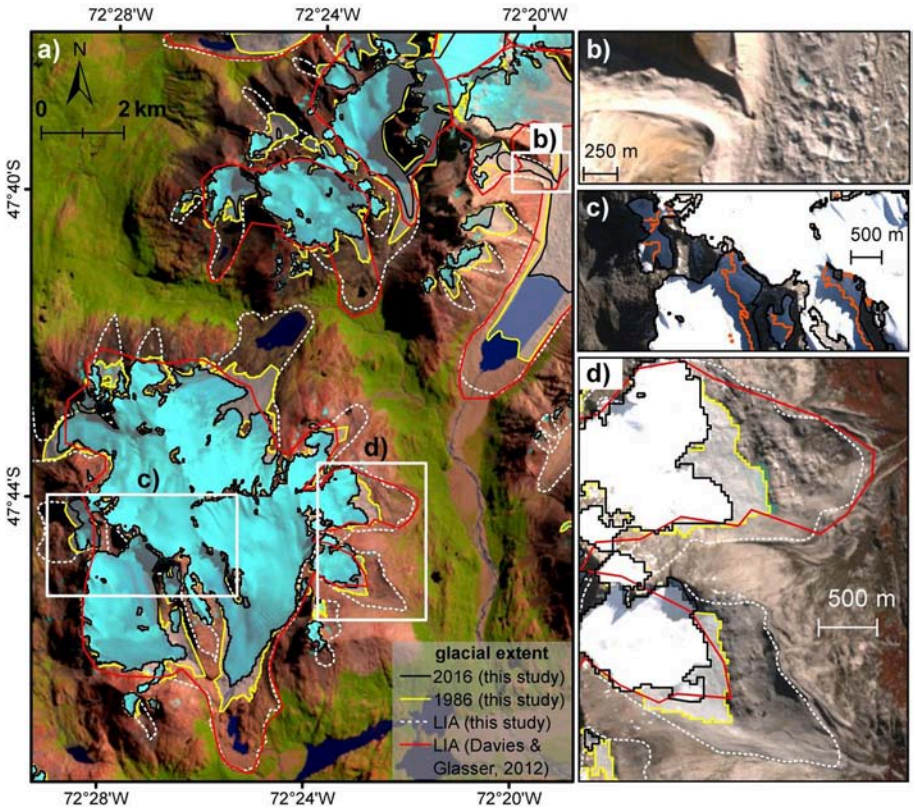

FIGURE 2 | (a) Landsat-8 OLI false color composite (Bands 6,5,4; acquired 05-03-2016) showing the southern part of the Monte San Lorenzo massive (see **Figure 1**) in the north east (Peak of MSL at 47°36'S). Vegetation trimlines are clearly visible for larger valley glaciers. Images (b–d) show magnified sub-regions with Sentinel-2 True Color Image (Bands 2,3,4; acquired 16-04-2017). Black lines represent the manually improved glacier outlines derived from the semi-automated glacier delineation of 2016 (threshold of the TM4/TM6 = 1.8). Ice below a debris cover is visible by ice flow pattern and thermocarst processes **(b)**. The semi-automated mapping reveals good results except for shadowed regions. For the latter **(c)** the original derived outlines (orange) were manually improved. The higher resolution datasets enable the delimitation of several frontal moraine systems **(d)**. In some cases the derived LIA extents from Davies and Glasser (2012) and from this study are very well aligned. But by using better resolved satellite images more LIA glacial extent could be precisely digitized.

the available image resolutions; (ii) a probable misclassification of snow patches; and (iii) a necessary minimum area to detect consistent area changes over the analyzed period.

After re-projecting all scenes to the local UTM zone (18S/19S) for each scene the quality of the orthorectification was checked. Ratio images were calculated by dividing the raw digital numbers for the bands TM3/TM5 (Landsat-5 TM) and TM4/TM6 (Landsat-8 OLI), respectively. The ratio images were converted to a binary image using different threshold values. Starting with a threshold value of 1.0, the value was stepwise increased by 0.1 intervals, ending at a maximum threshold of 3.0. The chosen interval is reasonable since only a few pixel in the outlines change by modifying the threshold by 0.1 (Paul and Hendriks, 2010; Paul et al., 2015). Afterwards, the resulting binary raster was vectorized to generate the glacier polygons without applying any filter. The glacier polygons were compared to a false color composite of the mid-infrared, near infrared and red channels (5-4-3 and 6-5-4, respectively) to obtain the most suitable threshold, mostly ranging between values of 1.7 and 2.2 (**Figure 2a**). The used threshold values and utilized Landsat scene (acquisition date, path/row) are stored within the attributes of the derived respective glacier outline. We created a mask within the already obtained glacier outlines to apply larger thresholds for the band ratio to enhance the assessment of slightly snow-covered rock outcrops. Though water bodies are mistakenly classified as glacier and snow, ratioing the red and mid-infrared channel provided the advantage that glaciers situated in cast shadows could be better delineated than by ratioing of near-infrared and mid-infrared (Paul and Andreassen, 2009). Despite a DEM-derived mask to exclude sea surface in fjords and water bodies >0.1 km^2 from the HydroLAKES database (Messager et al., 2016), a manual correction of the outlines was necessary for nearly every glacier. Additionally, we mapped the shape and area of every lake that was formed between the LIA maximum and 2016 by using the Normalized Difference Water Index (NDWI, threshold value 0.015) and manual mapping.

Suitable scenes since the beginning of the Landsat-5 TM mission, i.e., with only sparse cloud cover and seasonal snow (acquisition date: summer and autumn) were used for a temporal consistency test to distinguish between seasonal snow and small glaciers. Moreover, the use of multi-temporal scenes permitted the manual correction for debris-covered glaciers,

as some glaciological structures, i.e., expanding melting ponds, collapse structures or flow patterns were visible (**Figure 2b**). The glacier outlines were subdivided into individual catchments by extracting the ridgelines and glacier basins using a UTM-projected void-filled DEM with a resolution of 1 arc second (SRTM, LP DACC NASA Version 3). Frequently, the ice bodies reached over the crest of the mountains but are separated by the hydrological basin into distinct individual glaciers. Only if the subsequent ice body exceeds the used threshold value for the glacierized area of 0.025 km^2 we treated them as individual glaciers. At times, drainage basins are ambiguous, hence a few parts of the ice fields are more or less plain in higher elevations and no information about the actual ice flow can be attained by the hydrological basin analysis. Additionally, some large outlet glaciers of the NPI and SPI were subdivided into single glaciers although they share the same hydrological basin. In those cases we used the recently proposed suggestions for glacier divides based on ice flow directions by Mouginot and Rignot (2015).

Due to glacier retreat and the separation and disconnection of former connected glaciers into single basins, our glacier Inventory for 2016 possesses the most subdivides of all periods. For the change analysis, those separated parts were considered as parts of the prior glacier. The Global Land Ice Measurements from Space (GLIMS) identification system based on the latitude/longitude position of a glacier (Raup and Khalsa, 2007) was used and we maintained existing GLIMS IDs were appropriate. The dataset includes all important glacier parameters recommended by Paul et al. (2009). Glacier delineation is aggravated in the northern region of our study area due to the eruption of Cerro Hudson 1991. This event was the second largest Andean volcanic eruption in the twentieth century, causing with an eruptive volume of 8 km^3 heavy ashfall toward the southeast of Patagonia (Scasso et al., 1994; Tilling, 2009). Every single glacier in the studied region was finally inspected visually for errors in misclassification of the band ratio. Additionally, for the year 1986 the automatic glacier delineation in parts of the Gran Campo Nevado and Cordillera Darwin was biased by a high seasonal snow cover and cirrus clouds. The latter still allows a visual identification and distinction of the glacier outlines but is misclassified by an automated mapping. Therefore, in those regions a higher amount of manual mapping and corrections had to be performed.

Determination of the LIA Extent

The Little Ice Age glacial extent was digitized manually, proceeding from the 1986 glacial extent, based on clear visible morphological evidence, e.g., vegetation trimlines or lateral— and terminal moraine systems (**Figures 2a,d**). To avoid an overestimation of the LIA extent, larger rock outcrops (as included in the scenes from 1986) were preserved. Due to its higher resolution compared to Landsat 8 OLI (30 m), data from Sentinel-2 (10 m) were also used for the mapping (**Figures 2b–d**). As proposed by Paul et al. (2013) we also crosschecked our retained glacial extents with high-resolution data from DigitalGlobe. In contrast to other locations like in South Eastern Tibet (Bräuning, 2006; Hochreuther et al., 2015), the ecesis time and thus the vegetation cover on the moraines in the Andes display a higher variation. For example, on the western side of the NPI and SPI, the noted ecesis time varies between 6 and 25 and up to 70 years, respectively (Heusser, 1964; Mercer, 1970; Winchester and Harrison, 1996). In contrast, on the eastern side succession needs between 22 and up to 92 years for the NPI (Winchester and Harrison, 2000; Winchester et al., 2001) and 40 up to 100 years for the SPI, respectively (Pisano, 1978; Dollenz, 1991). In the southernmost regions of Patagonia like Gran Campo Nevado and Cordillera Darwin, the colonization of a recently exposed moraine took <15 and 20 years (Holmlund and Fuenzalida, 1995; Koch and Kilian, 2005). Therefore, we included for the determination of the final LIA glacial extent both completely and partly forest covered terminal moraines.

As the end and also the maximum extent of the LIA is probably variable over the whole study region and local climate conditions as well as different glacial response times can create a bias we define the end of the LIA as 1870 AD for the change calculation. This is consistent with tree ring records for the northern and southern Patagonia, indicating a shift toward warmer temperatures at 1875 (Villalba et al., 2003) and cotemporaneous for the ice retreat and dated moraines (Moy et al., 2009 and references within).

In cases when glaciers formed multiple moraine ridges and trimlines, morphological features were used being closest situated to the recent appropriate glacier (**Figure 2d**). This approach avoids a possible bias caused by an overestimation of the LIA extent. The resulting glacier extent therefore can be considered as a minimum estimation. Finally, our resulting inventory was compared to already published LIA positions (Aniya, 1995, 1996; Holmlund and Fuenzalida, 1995; Kuylenstierna et al., 1996; Harrison and Winchester, 1998, 2000; Winchester and Harrison, 2000; Koch and Kilian, 2005; Araneda et al., 2007; Aravena, 2007; Harrison et al., 2007, 2008, 2012; Strelin and Iturraspe, 2007; Strelin et al., 2008; Masiokas et al., 2009a,b; Glasser et al., 2011; Aniya and Skvarca, 2012; Davies and Glasser, 2012; Rivera et al., 2012).

Uncertainty Assessment

Manual Delineation of the LIA Extent

The LIA glacier outlines were delineated manually and are subject to uncertainties caused by a subjective interpretation and generalization (Paul et al., 2003). Following the guidelines for quality assessment of a glacier area determination (Paul et al., 2017), we estimated the analysts precision by multiple digitization of 360 representative glaciers ranging from 0.04 to 1,100 km^2 with different challenges, e.g., debris cover, floating termini, and cast shadowed regions. The relative digitization inaccuracy commonly increases with decreasing glacier area (Paul et al., 2013; Fischer et al., 2014; Pfeffer et al., 2014). To account for the glacier area distribution of the glaciers in our inventory, we selected the glaciers for the triple digitization in a manner that 85% of them belong to an area-class smaller than 5 km^2. The resulting area-class specific relative mean deviation is much larger for smaller glaciers, resulting in an area uncertainty of $\pm$ 8.4% for glaciers smaller than 0.01 km^2, dropping below $\pm$ 5% when glacier area exceeds 2 km^2 (**Figure 3**). In comparison,

glaciers larger than 5 km^2 only exhibit a mean uncertainty of ± 2.1%.

A second uncertainty factor results from the mapping approach of the LIA maximum extent itself. The moraines and vegetation trimlines that were used for the glacial delineation probably represent the maximum extent of the LIA that does not imperatively reflect the end of the LIA (∼1870 AD). In their review papers Aniya (2013) and Masiokas et al. (2009b) emphasized that the LIA Maximum extent and the end of the LIA occurred contemporaneously for the NPI and nearby glaciers but differ highly for the SPI. For the latter the last LIA maximum was reached until 1800 AD but with a high variability within the 28 studied glaciers to more than 200 years (Masiokas et al., 2009b). For the Magallanes-Tierra del Fuego region the LIA maximum was also reached approximately in 1780 AD but the glaciers stayed still close to the LIA extent until the end of the nineteenth century (Strelin and Iturraspe, 2007; Strelin et al., 2008). A numeric uncertainty estimation of this error is not possible. We tried to keep the error as low as possible by mapping those morphological features closest to the glacier margins (see **Figure 2d**).

Semi-automatic Mapping

Since no appropriate high-resolution reference data is available for the complete dataset and the whole time-span of the investigation period, we determined the precision of our manually improved, semi-automatically derived inventory by applying a positive and negative buffer to the glacier outlines (Granshaw and Fountain, 2006; Bolch et al., 2010a,b). The buffer method accounts for the length of the glacier perimeter, resulting in a higher relative error toward smaller glaciers since those have relatively more edge pixels than larger glaciers (Bolch et al., 2010a; Guo et al., 2015)

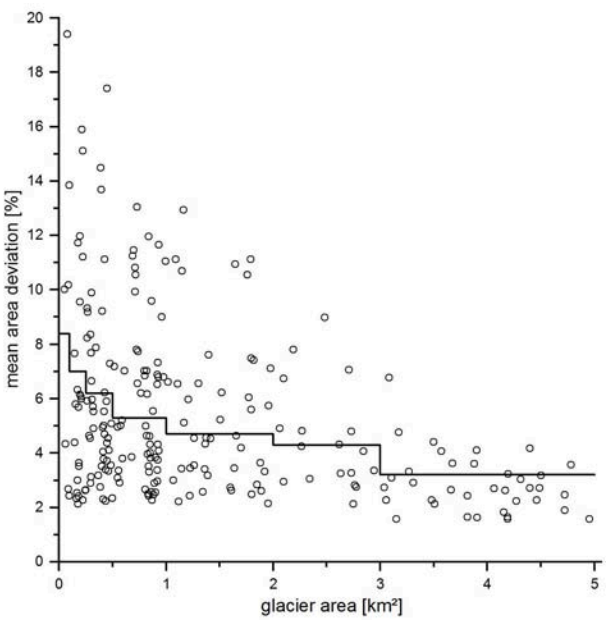

FIGURE 3 | Mean area deviation of 335 multiple digitized glaciers of the LIA extent. Solid line indicates the area class specific uncertainty resulted from fitting a power law by least squares.

The buffer size is dependent on an uncertainly value and is applied to the ice bodies before the intersection with the drainage basins. Consequently, this method will not provide any uncertainty estimations where glaciers adjoin (Paul et al., 2017). Nevertheless, for the ice divides and drainage basins there is probably a small uncertainty, as the former was partly derived from ice flow measurements (Mouginot and Rignot, 2015) and the latter relies on the quality of the DEM, which is susceptible to small errors (Smith and Sandwell, 2003). Omitting these errors at interior ice divides is legitimated since we used the same divides for all investigated time periods. Thus, the total derived area and change rates are not influenced (Pfeffer et al., 2014; Guo et al., 2015; Paul et al., 2017).

The frequently used buffer sizes are ± 0.5 to ± 1 pixel, e.g., ± 15 to ± 30 m (Rivera et al., 2007; Bolch et al., 2010b; Wang et al., 2011). Guo et al. (2015) compared automatically derived and manually improved glacier outlines based on Landsat data to DGPS measurements and revealed an accuracy of ± 18 and ± 11 m, respectively. Following Paul et al. (2013) we compared 15 of our Landsat derived and manually improved glacier outlines to manually delineated glacier outlines from Google Maps™, both from 2016. Every 15 m we calculated the offset between the Landsat and manually derived glacier outlines and obtained a mean offset of 14 m for clean ice bodies. Furthermore, following the same routine as for clean ice bodies, we compared the manually improved glacier outlines for 15 debris covered glaciers, revealing a mean offset of 32 m. Consequently, the use of ± 15 m as buffer size for clean ice and ± 30 m for debris—and ash-covered glaciers is reasonable for our study.

Moreover, the outline accuracy is influenced by the geolocation (i) and the scene quality (ii) of the used satellite data (Paul et al., 2017; Rabatel et al., 2018). To reduce the positional error (i) we align the used Landsat scenes with distinct landforms like moraine ridges, prominent mountain peaks or shorelines revealing an almost perfect matching. Insufficient scene quality (ii) i.e., cloud cover, cast shadow due to low solar angle, and seasonal snow can hamper the automatic measurements and have a huge variability. We minimized those errors by carefully selecting the used Landsat scenes, representing the annual snow minima. Cast shadows and perturbation due to cloud cover were manually edited by the use of different satellite scenes from the same year and the comparison to different sensors like the Sentinel-2 data (**Figure 2c**). In the maritime south western region in rare cases seasonal snow hamper the automated delineation but still allow manual digitization. For those cases, following Bolch et al. (2010a), we applied an additional error of ± 3% to each scene with seasonal snow.

The areal uncertainty for all compiled glaciers of 2016 was ± 4.0%, corresponding to ± 905 km^2, with clean ice bodies having a smaller mean uncertainty than debris covered glaciers with ± 3.6% and ± 5.8%, respectively. Those values are in good agreement with other previous published inventories (Andreassen et al., 2008; Paul and Mölg, 2014). Uncertainty increases toward the smallest and elongated glaciers reaching

values up to ± 70% of the glacier's area. Consequently, the obtained results of the multi-temporal comparison of the Landsat derived glacier outlines must be treated with caution especially for very small glaciers (Paul et al., 2003), fostering our chosen threshold for glacier area larger than 0.025 km^2.

RESULTS

Overview of the Glacier Inventory 2016

In total, our inventory comprises for the year 2016 an amount of 11,209 glaciers (compared to the RGI 6.0: 9,429 individual glaciers) covering a total area of 22,636 ± 905 km^2. The glacierized area is dominated by the major outlet glaciers of the SPI and NPI. In doing so, glaciers larger than 5 km^2 are responsible for 80.7 ± 2.2% of the area, while representing only 3.2% of the total glacier number (**Table 1**, **Figure 4A**). The 30 largest outlet glaciers constitute ∼50% of the total glacierized surface. Here, the largest glacier Pío XI (WGI ID: SPI-137) covers 1,255 ± 5 km^2 (5.5% of the total area). A classification of the inventory by area (**Table 1**) demonstrates, that almost 63% of all obtained glaciers are associated to area classes smaller than 0.25 km^2, representing merely 3 ± 1% of the total glacier area. A further 34% of the glacier number (implies an area of 16.5 ± 2.5%) belongs to the three classes ranging from 0.25 to 5 km^2. The relationship between the number of glaciers per area class and the respective glacierized area is almost perfectly inverted (**Figure 4A**), which additionally supports the significance of the large glaciers for the South American cryosphere. The overall majority of the glaciers and the glacierized area range between 500 and 1,500 m a.s.l., while the average maximum altitude increases with glacier area (**Figures 4B,C**). The average glacier elevation for glaciers north of the Strait of Magallanes is 1,350 m a.s.l.

TABLE 1 | Area classification of the glaciers used in the inventory and the associated summed areas.

Area class [km^2]	Count	Count [%]	Area [km^2]	Area[%]
[0.025; 0.05[	2370	21.1	85 ± 30	0.4
[0.05; 0.1[	2179	19.4	156 ± 31	0.7
[0.1; 0.25[	2472	22.1	402 ± 59	1.7
[0.25; 0.5[	1515	13.5	535 ± 78	2.4
[0.5; 1[	1181	10.5	842 ± 99	3.7
[1; 5[	1134	10.1	2344 ± 189	10.4
[5; 10[	149	1.3	1027 ± 65	4.5
[10; 50[	143	1.3	3038 ± 127	13.4
[50; 100[	29	0.26	1905 ± 58	8.4
[100; 500[	30	0.27	6290 ± 98	27.8
[500; 1000[	6	0.05	4756 ± 71	21.0
≥ 1000	1		1255 ± 5	5.5
Total	11209		22636 ± 905	100

Four hundred fifty-one glaciers are currently calving, of which 93 are of marine (∼20%) and 358 (∼80%) of lacustrine type. We detected 32 dead ice bodies formed due to the disintegration of former glaciers and 17 regenerated glaciers, the latter commonly in steep terrain, with a mean elevation of 545 m a.s.l. far below the average of 1,275 m a.s.l.

Along the longitudinal facing Andean main ridge, over 9,000 glaciers (∼80%) were located within a distance of 1,200 km from north to south (RGI 6.0: 7,447 individual glaciers). The other 20% are situated southeast of the Strait of Magellan within the Cordillera Darwin (CD) and the small icefield of Isla Hostle (IH). On the west side of the Andean crest, the number of glaciers is considerably lower (∼3,200) than in the east (∼5,860). The mean elevation, both for the western and eastern glaciers is decreasing from north to south from a maximum of 1,530 m a.s.l. (Cerro Hudson and Cerro Erasmo) to a minimum with 765 m a.s.l. (Isla Santa Inés). Glaciers toward the west showed a continuous linear descent in their mean elevation ($r^2 = 0.67$) whereas glaciers on the eastern side showed more vertical variability (**Figure 5A**). Conspicuously in the lee of the icefields, the mean elevation displays the highest values whereas, in the fjord-rich area between the NPI and SPI, the mean elevation is decreasing. In the southern part of the SPI (∼51°S) the width of the Andean orogen narrows rapidly from more than 60 to <10 km. At this latitude, a significant decline in the mean elevation for the eastern glaciers is noticeable (**Figure 5A**). In the transitional zone to the Cordillera Sarmiento south of the SPI, the extension of the Andean ridge remains comparatively narrow until 54°S and the mean elevation for western and eastern glaciers only differs slightly.

Two thousand one hundred thirty-five glaciers are located in the Magallanes-Tierra del Fuego (CD, IH) region (RGI 6.0: 1,982 glaciers). The mountain range is predominantly west-east running. As humid air masses originate predominantly from the west and from the south (Holmlund and Fuenzalida, 1995) we divided the study region in a northern part and a southern part of the main mountain ridge. Glaciers north of the main crest have a mean elevation of 900 m a.s.l., 100 m higher than southern glaciers (**Figure 5B**). They also exhibit a weak relationship ($r^2 = 0.37$) of increasing mean elevation with increasing longitude. On the other hand, glaciers that are located south of the range do not show any relationship toward an increasing mean elevation ($r^2 = 0.05$). Nevertheless, the overall elevation for glaciers in the western and eastern parts ($n = 513$ and $n = 300$) reveal an increase from 745 m a.s.l. to 965 m a.s.l. within 250 km.

Glaciers of Southernmost South America

Cerro Hudson and Cerro Erasmo

North of the NPI, larger glaciers are attached to the orographic zones of Cerro Hudson (CH) and Cerro Erasmo (CE). This sub-region is delimited toward the south by a mountain range located north of Rio Exploradores and toward the east by the Lago Buenos Aires. CH is an active volcano characterized by a pronounced caldera with a range of 15 km at 1,900 m a.s.l. The mountain range of Cerro Erasmo is located around 15 km south west of CH with an elevation comparable to CH. A total area of 615 ± 80 km^2 is covered by 1,375 individual glaciers (RGI 6.0: 1,132 glaciers) resulting in a very small mean glacier area of

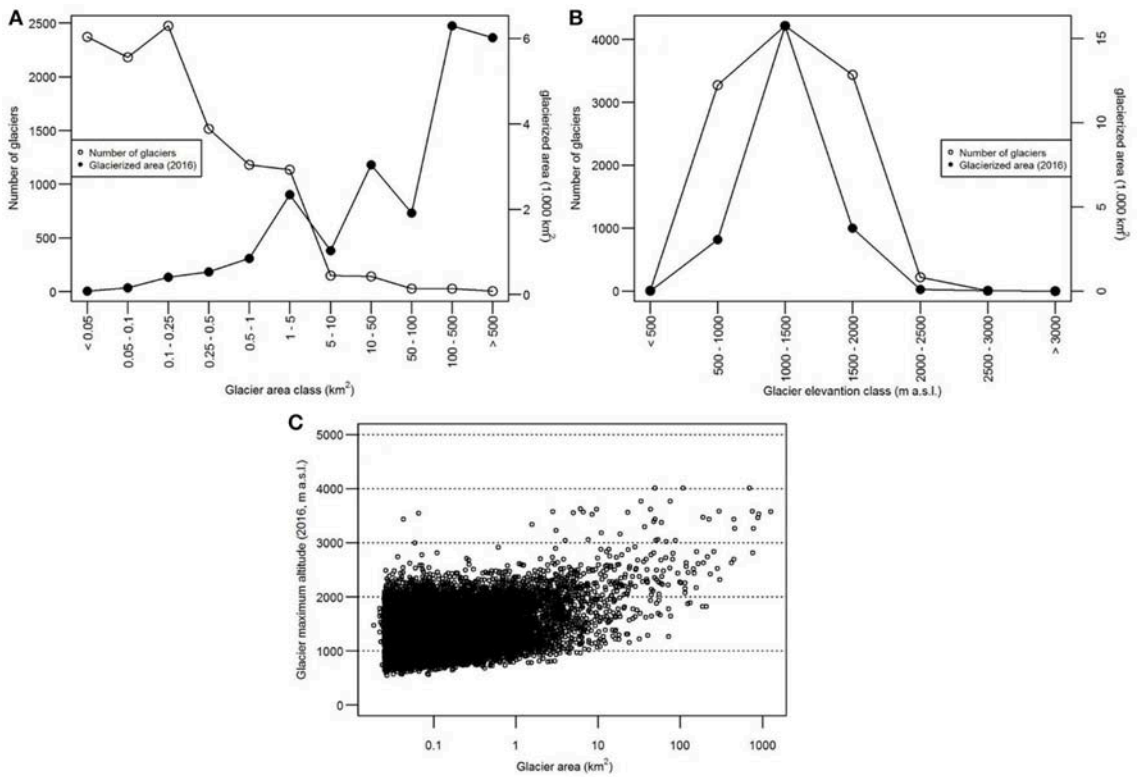

FIGURE 4 | Total glacier number and area with regards to the glacial area class **(A)** and glacier mean elevation class **(B)**. Glacier maximum altitude against glacier area **(C)**.

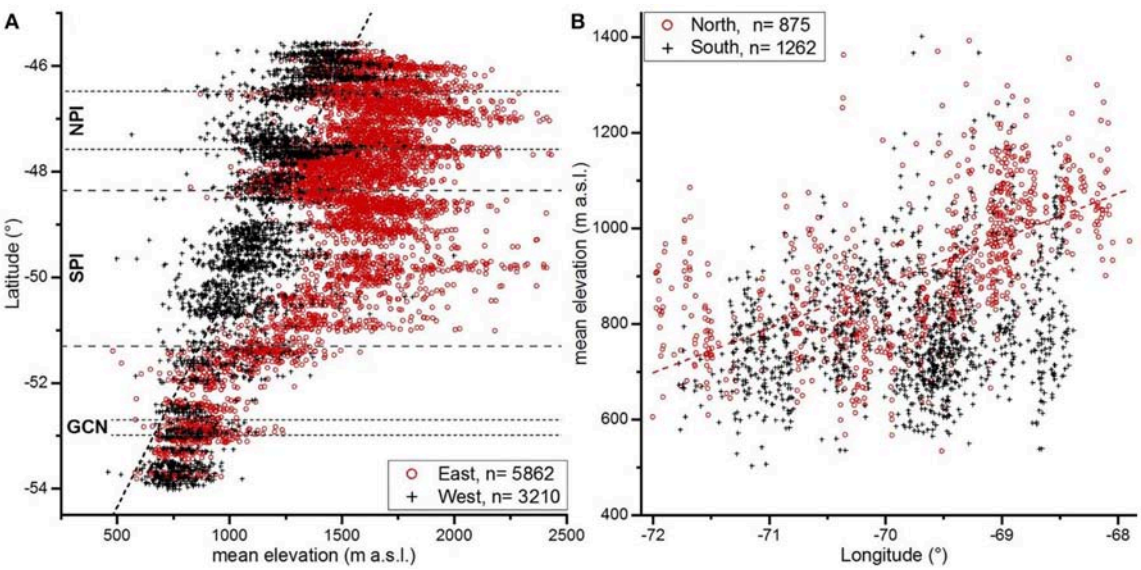

FIGURE 5 | (A) Glacier mean elevation along the north-south running Andean main ridge between 45.5 and 54°S. Glaciers lying west of the main ridge are shown in black, those on the eastern side in red. The dashed/dotted horizontal lines indicate the north-south extent of the main icefields. The regression function explains 67% of the variance distribution for glaciers at the western side of the ice divide. **(B)** Mean elevation of the glaciers along the west east-running mountains of the Cordillera Darwin south of the Magellan Strait (Red and black dots are located north and south of the cordillera, respectively). Dead ice bodies and regenerated glaciers are not included. There is a weak relationship between decreasing longitude and rising glacier mean elevation ($r^2 = 0.37$) for glaciers north of the main ridge.

0.45 km^2. On the one hand the relative high area uncertainty is caused by the overall small glacier area, on the other hand it is the result of volcanic eruption of Cerro Hudson 1991 (Tilling, 2009). Many glaciers toward the southeast are covered with a thick dark layer of tephra (compare **Figure 1**). We could manually identify 150 glaciers which were not or just merely detected by the automated delineation, and mapped them manually and applied afterwards a buffer of ± 30 m. One large outlet glaciers each are descending from the Hudson caldera and from CE toward north western direction. As shown in **Figure 6** (CH, CE) those outlets of CH and CE account for almost 20% of the total glacierized area in this sub-region. Besides those larger glaciers, north-, northwest, and west facing glaciers are lowest in number and area. The majority of all glaciers in terms of total number and area have an aspect between east and south, reaching the local maximum at southeastern exposition (**Figure 6** CH, CE). The glacier mean elevation is 1,570 m a.s.l. reaching the highest values at northeastern and the lowest at southeastern slopes (**Figure 7**). Compared to the NPI and SPI calving glaciers have no major significance in this region, only 30 glaciers were terminating in small lakes.

Northern Patagonian Icefield and Nearby Glaciers

The NPI is the second largest icefield in the Patagonian Andeans covering an area of 3,675 ± 80 km^2. Since the mountain range is north-south striking, most of the glaciers can be assigned to a western or eastern exposition. Glaciers descend from the highest mountain peaks exceeding 4,000 m a.s.l (Monte San Valentin) in the north-eastern part within a short flow length of <50 km to sea level elevation (glacier San Rafael). At the pronounced mountain peak of Cerro Co Arenales (>3,400 m a.s.l) glacier Acodado and glacier Steffen descend toward the southwest. These two glaciers form a large coherent ice body denying an automated

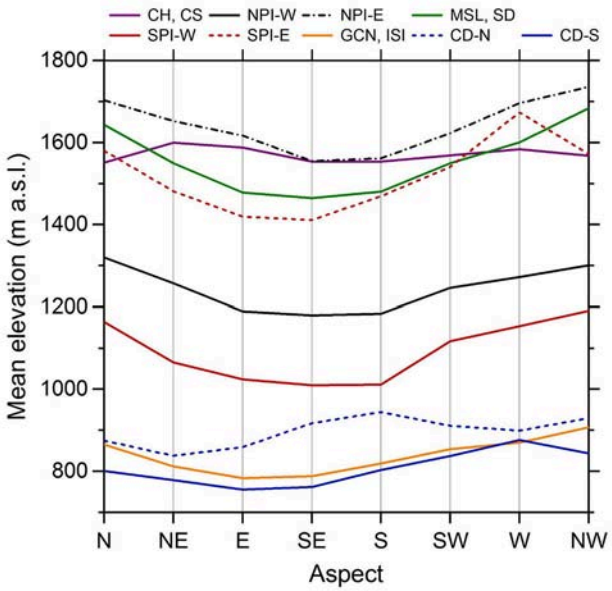

FIGURE 7 | Glacier mean elevation with respect to the glacial aspect for the different sub-regions.

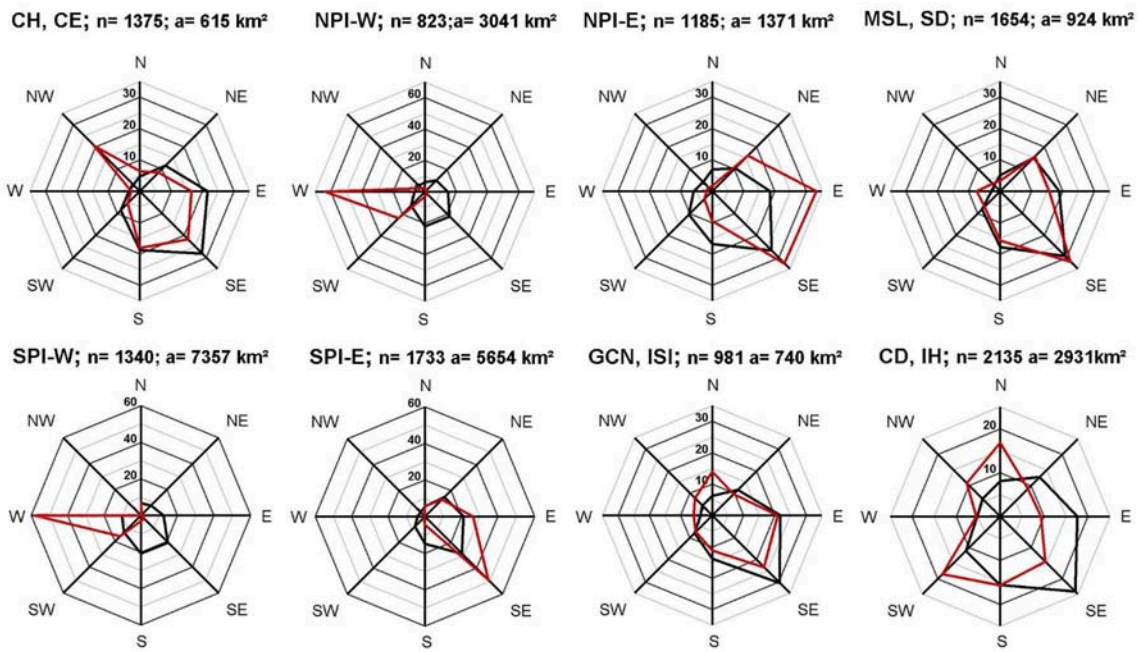

FIGURE 6 | Percentage of glacier number (black) and area (red) for the respective regions in dependence of glacier aspect-class. Number of inventoried glaciers (n) and the total area (a) is given in the respective headline for the different sub-regions. All percentages are based on the particular values of the studied regions (for the used abbreviation refer to **Figure 1**).

watershed delineation and can only be separated by analyzing the ice flow direction (e.g., Rivera et al., 2007; Mouginot and Rignot, 2015). The NPI consists of 171 adjoined (directly connected) glaciers, whereas the 27 major outlet glaciers (>10 km^2) cover 97 ± 1% of the entire icefield. The NPI is surrounded by several 100 of smaller glaciers that are close-by to the icefield but not directly connected. Hence, all adjoined glaciers of the NPI and also nearby located glaciers that are not connected directly to the icefield, were divided in a western and eastern part for further analysis along the Andean crest (**Figure 6**, NPI-W, NPI-E). On the western side, more than 820 glaciers (RGI 6.0: 548 individual glaciers) are nearly equally distributed according their aspect, having a small tendency toward the southeast, but the glacierized area is dominated by the large western outlets (60% of the glacierized area). Across the ice divide, the ∼1,300 glaciers (RGI 6.0: 895 individual glaciers) are prominently facing southeast, but their area is equally distributed with 35% each between the eastern and southeastern aspect. In total 43 glaciers are calving into lakes, the only marine terminating glacier is Glacier San Rafael which is with 758 ± 8 km^2 also the largest of the concerning glaciers. Also 55 debris covered glaciers are predominantly located on the leeward side of the orogen. Glacier mean elevation is lowest for the large outlets toward the western side. On average the mean elevation of glaciers on the windward side is with 1,240 m a.s.l. much lower than the mean elevation for the leeside glaciers with 1,640 m a.s.l. (**Figure 5A**). For both, the western and eastern part, the mean glacier elevation reaches its minimum at east and southeastern exposition with 1,180 and 1,555 m a.s.l, respectively (**Figure 7**).

Southern Patagonian Icefield and Nearby Glaciers

The SPI is the largest of all coherent ice bodies in Patagonia (12,232 ± 201 km^2) with a distance of 350 km north to south, and some summits reaching more than 3,000 m a.s.l. The contiguous ice body of the SPI is composed of 652 individual glaciers that are directly connected. Including also small glaciers that are not directly connected to the SPI but are within the inner perimeter of the icefield as performed by Casassa et al. (2014) reveals a total glacier number of 722 (RGI 6.0: 336 glaciers). Due to the analogous geographical setting of the north-south running Andean mountains, the SPI bears a resemblance of distribution patterns of glacial aspect to area to the NPI and was therefore also divided in a western and eastern part, also including not directly connected mountain glaciers (**Figure 6**, SPI-W; SPI-E). The 150 major outlet glaciers of the SPI and attached valley glaciers have a mainly western or eastern exposition. Around 1,300 glaciers on the western (RGI 6.0: 975 individual glaciers) side are nearly equally distributed according their aspect but the glacierized area is dominated again by the large western outlets (60% of the glacierized area). Across the ice divide, the ∼1,700 glaciers (RGI 6.0: 1,338 individual glaciers) are in number prominently facing southeast and also their area distribution has a similar pattern with 60% of the glacierized area having a southeastern aspect. Those glaciers that have eastern, southeastern and southern aspects indicate the lowest mean elevation (1,440 m a.s.l.) whereas glacier mean elevation increases for western, north-western and northern aspects to 1,625 m a.s.l. A similar distribution for glacier mean elevation is found on the western side of the ice field, though the mean elevation is ∼250 m lower than on the eastern side (**Figure 7**). A small number of debris-covered glaciers could also be identified (n = 65), commonly located on the eastern side.

Monte San Lorenzo and Sierra de Sangra

Between the NPI and SPI the landscape is characterized by large fjord systems and a moderate mean elevation mostly below 1,500 m a.s.l. Toward the Argentinian border, the elevation of the terrain increases, promoting the formation of glaciers. The glacierized area centers around Monte San Lorenzo (MSL) in the north reaching 3,700 m a.s.l. and Sierre de Sangra (SL) in the south with summits up to 2,000 m a.s.l. Both mountain ranges are directly located at the international border between Argentina and Chile. The largest glaciers are found within the two mountain ranges, between them the average glacial area is with 0.5 km^2 comparable small. In total the region between the two major icefields contains 1,654 glaciers (RGI 6.0: 1,393 individual glaciers), covering merely 924 ± 95 km^2 with a preponderantly south-eastern aspect (**Figure 6**, MSL, SD). Glacier mean elevation (**Figure 7**) is lowest (1,450 m a.s.l.) for this aspect class and highest for NW-aspect (1,690 m a.s.l.). Accordingly, the total glacier number is lowest for glaciers with a northwestern aspect (**Figure 6**). 41 of all glaciers are debris-covered, and a further 41 lacustrine-calving.

Minor Icefields (GCN, ISI)

Between the Cordillera Darwin and the southern part of the Cordillera Sarmiento, the average elevation decreases below 2,000 m a.s.l. The whole region is characterized by a high density of fjords and lakes. Toward the south the elevation of the Andean mountain range decreases continuously resulting in mean elevations lower than 1,000 m a.s.l. In contrast to the observed averaged maximum elevation of 1,750 m a.s.l at the SPI, the averaged maximum glacier elevation of 950 m a.s.l is much lower. Despite the comparable low elevation of the Andes there is still a pronounced glacial coverage north and south of the Strait of Magellan. The largest continuous ice body is the Gran Campo Nevado (189 ± 5 km^2) with some outlets calving into the sea, or proglacial lakes. The comparably small ice cap of GCN is surrounded by a large amount of small mountain glaciers. South of the Magellan Strait on Isla Santa Inés (ISI) the second major ice cap (168 ± 5 km^2) of this sub-area is located. In total 981 glaciers were identified for the whole region (RGI 6.0: 1,161 glaciers), which cover a total area of 740 ± 53 km^2. Remarkably, only 25 glaciers account for almost 50% of the total area. 46 glaciers have calving termini (7 marine and 39 lacustrine). Most of the glaciers are classified as clean ice, only 10 glaciers located within the GCN are debris—covered, and five debris-covered glaciers descend from the northern located volcano Monte Burney (S 52.3°, W 73.4°). Within the GCN and ISI, eastern—and southwestern facing glaciers are most frequent (over 50%) and also cover the largest area (**Figure 6**, GCN, ISI). Westerly-exposed glaciers are smallest in terms of number and area. Conversely, they exhibit the highest mean elevation, which drops

from 900 m a.s.l. for west—and northwest exposed glaciers to <780 m a.s.l. for the east—and southeast orientated glaciers (**Figure 7**).

Cordillera Darwin and Isla Hostle

The Cordillera Darwin (CD) is the highest glacierized mountain range in the Tierra del Fuego with several summits reaching more than 2,000 m a.s.l. The CD is frequently seamed by north south running fjords that separate the mountain range in different small parts with steep terrain (see elevation profile in **Figure 1**). The ∼250 km long mountain range is west-east running, hence many of the glaciers have a northern or southern orientation. In total an area of 2,931 ± 155 km^2 is covered by glaciers of which 875 are located at the northern side of main mountain divide and 1,262 south of it (RGI 6.0: 852 and 1,130 individual glaciers, respectively). The largest continuous ice body is located in the center of the mountain range, covering an area of 1,760 ± 51 km^2. Some smaller ice bodies (179 ± 5 km^2), separated by the fjord channels, are located to the west within a short distance to the main ice field. A small icefield (203 ± 6 km^2) is located in the southernmost area of Tierra del Fuego at Isla Hostle (55.1°S). The outlet glaciers of all ice fields frequently descent to sea elevation, and nearly 100 glaciers calve into the numerous fjords. In total, 24 dead ice bodies and regenerated glaciers were identified wherein the largest dead ice body (0.6 km^2) is formed by the disintegration of Glacier Marinelli, the fastest retreating glacier in the CD (Koppes et al., 2009). In total, glaciers facing southeast are most common, but they occupy only a minor area (**Figure 6**. CD, IH). The large outlet glaciers of the longitudinal mountain range typically have a northern or southern aspect; hence they also dominate the area distribution. For glaciers south of the main ridge, the glacial mean elevation is lowest for south and southeastern aspects but reaching a maximum for western expositions.

Glacier Recession Since the Little Ice Age (1870–2016)

The maximum extent of more than 2,600 glaciers during the Little Ice Age was digitized between 45.5 and 55°S. Since many of the former glaciers consist of compound basins and there is no possibility to evaluate the exact date of separation, their initial basins were used for the change detection analysis. The 2,600 LIA maxima contain more than 4,000 of the recent glacier boundaries, which accounts for 35% of the total inventory. This corresponds to 90% of the total glacierized area in 1986. Accordingly, for only 10% of the glacierized area in 1986, no LIA maximum could be detected. In order to provide a minimum estimation of the total LIA extent for all glaciers, we added the glacial extents derived in 1986 for the missing 10% of the glacierized area. From 1986 to 2016, we provide change rates for all glaciers south of 45.5°. Only for few glaciers at the most western locations a multi-temporal comparison was not possible since suitable satellite images were not available. Consequently, the respective 186 glaciers (45 km^2) were excluded from the change analysis.

Nearly 2,200 out of the 2,600 digitized LIA extents are located in the Patagonian Andes, of which 200 completely vanished by 1986 (**Figure 8A**). Out of the sum of 420 recorded LIA maxima within the Cordillera Darwin, only 18 glaciers disappeared. Those were all land-terminating small glaciers in the eastern part of the Cordillera. The 182 glaciers that disappeared north of the Strait of Magellan are all located on the eastern side of the Andean main crest. The total number of glaciers that completely vanished since the LIA increases toward the north, with the majority (141) located north of 48°S. The most frequent glacier aspect for those glaciers is southeast, east and south. Only 41 glaciers had different expositions. **Figure 8A** shows the relative area change for the 2,600 LIA glaciers between 1870 and 2016. Nearly all glaciers (90%) that disappeared had an area smaller 0.5 km^2 and in general larger glaciers exhibit a smaller relative area decrease than smaller ones.

Overall Change Rates

Since the Little Ice Age, the glacier area decreased from 28,091 ± 890 km^2 to 22,636 ± 905 km^2 in 2016. These results display an absolute area loss of 5,455 ± 1,269 km^2 (19.4 ± 4.5%). Following the suggestions by Bolch et al. (2010a) we summarized area changes for the periods 1870–2016, 1870–1986, 1986–2005, and 2005–2016, and 1986–2016 (**Table 2**). The strongest annual area decrease appeared between 1986 and 2005 with an average area loss of 0.33 ± 0.28% a^{-1}. Between 2005 and 2016 glacier recession was comparable high at 0.25 ± 0.50% a^{-1}. Due to the high uncertainty values these two change rates do not differ significantly. Between 1986 and 2016 the glaciers loss in average an area of 0.29 ± 0.17% a^{-1}, whereas between 1870 and 1986 the decrease rate of 0.10 ± 0.04% a^{-1} is slightly smaller.

On average, calving glaciers show the lowest percentage of area reduction in the period between the LIA and 2016. For the 2,600 known LIA extents, land-terminating glaciers had an area reduction of 0.41 ± 0.10% a^{-1}, whereas marine and lacustrine calving glaciers at the same time merely decreased by 0.15 ± 0.08% a^{-1}. However, the calving glaciers are commonly the largest in the study region, consequently the total average area reduction for calving glaciers is with 0.07 ± 0.02 km^2 a^{-1} ten times higher than for the smaller terrestrial ending glaciers. A total of 1,159 newly formed lakes and the enlargement of prior existing LIA lakes was mapped resulting in an increase of the total lake surface area of 889 km^2. There is a strong relationship between glacial shrinkage and the resulting lake area ($r^2 = 0.78$). Over 650 LIA glaciers of area class smaller than 0.5 km^2 had a relative area reduction of more than 75% within the last 150 years. Larger glaciers up to 5 km^2 still suffer of an enormous decrease of more than 50% (**Figure 8A**). With increasing glacier area the relative surface degradation decreases, simultaneously the absolute values for area loss reaches their maximum. A surface loss of more than 1,000 km^2 for only 9 glaciers equals nearly one fifth of the total area degradation of the studied region.

Within the last 30 years, the total glacierized area decreased by 8.8 ± 5.1% from 24,818 ± 912 km^2 to 22,636 ± 905 km^2 (**Table 2**) and a total number of 192 glaciers completely disappeared. **Figure 8B** indicates a higher percentage area loss for smaller glaciers. Most glaciers that have melted down entirely are smaller than 0.1 km^2 and even glaciers up to 0.8 km^2 completely disappeared. On the other hand, plenty of glaciers of area class

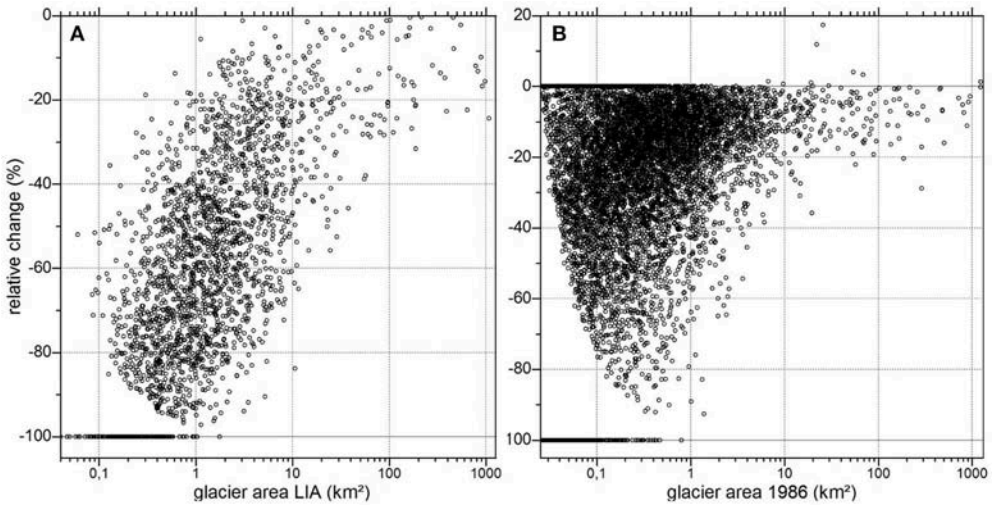

FIGURE 8 | relative area change for the moraine-derived LIA glaciers ($n = 2616$) between 1870 and 2016 depended on the initial glacier area **(A)** and relative area change between 1986 and 2016 in dependence of the initial glacier area in 1986 **(B)**.

TABLE 2 | Decrease in glacier area for the inventoried glaciers between LIA and 2016 for different time periods to derive annual change rates for the studied region.

Year	Area [km^2]	Period	Area change [km^2]	Area change [%]	Annual change [km^2 a^{-1}]	Annual change [% a^{-1}]
1870	28090.8 ± 890.1	1870–2016	−5454.7 ± 1269.3	−19.4 ± 4.5	−37.36 ± 8.69	−0.13 ± 0.03
1986	24817.9 ± 912.3	1870–1986	−3272.4 ± 1274.6	−11.6 ± 5.1	−28.21 ± 10.99	−0.10 ± 0.04
2005	23277.1 ± 907.2	1986–2005	−1540.8 ± 1286.6	−6.2 ± 5.2	−81.10 ± 67.72	−0.33 ± 0.28
2016	22635.6 ± 904.9	2005–2016	−641.5 ± 1281.3	−2.8 ± 5.5	−58.32 ± 116.48	−0.25 ± 0.50
		1986–2016	−2182.3 ± 1284.9	−8.8 ± 5.2	−72.74 ± 42.83	−0.29 ± 0.17

0.25–1 km^2 did not show a noticeable decline over the same period.

Only 13 glaciers showed an advance during the last decades, the rest is either constant or retreating (**Figure 8B**). The majority of the advancing glaciers (10 out of 13) are located in the Cordillera Darwin and all belong to the marine-calving type. Glacier Pío XI and a small tributary south of it account for significant advances at the west side of the SPI. The latter glacier is the only terrestrial terminating glacier that shows a recent advance. Glacier Pío XI is the only known glacier that exceeds its glacier's Neoglacial maximum extent and is under scientific focus since 1830 (Warren et al., 1997 and literature within). Finally, on the eastern side of the SPI, the Perito Moreno glacier shows an advance but solely of small dimension. Across the whole study area, it is apparent that smaller glaciers indicate a greater percentage of loss between 1986 and 2016. Glaciers ranging from 0.1 to 1 km^2 ($n = 5{,}168$) lost on average 20% of their initially glacierized area. Conversely, glaciers larger than 50 km^2 ($n = 66$) decreased by 1,197 ± 164 km^2 in total, corresponding to 8.2% of their original area. Glacier shrinkage is not only restricted to the lower ablation zones but also occurs in high elevation zones due to dry calving of steep hanging glaciers and ice aprons. Also, the expansion of internal rock outcrops over the observation period is frequently seen in the accumulation areas of larger glaciers, indicating a glacial thinning. Small glaciers show the highest variability in relative surface reduction ranging between equilibrium and total decay.

Table 3 and **Figure 9** give an overview of glacier shrinkage since the LIA for the respective studied regions. Glacial recession was highest in the area north of the NPI for the Cerro Hudson und Cerro Erasmo region. The relative area reduction was highest for the sub-regions of CH, CE and MSL, SD, revealing an area reduction of 48 ± 11% and 42 ± 10% since the LIA. For the period between 1870 and 1986 those inventoried regions showed the highest relative change rates of the whole inventory, according to 0.27 ± 0.10% a^{-1} and 0.24 ± 0.09% a^{-1}. In both cases the annual change rate increases from from 3.26 ± 1.24 km^2 a^{-1} and 3.96 ± 1.49 km^2 a^{-1} for 1870–1986 to 6.35 ± 3.38 km^2 a^{-1} and 6.91 ± 4.25 for 1985–2016. Due to the high uncertainty value those accelerated shrink rates are statistically not significant and a more or less constant area reduction since the LIA is also probable. In total the CH, CE and MSL, SD sub-regions lost 1,236 ± 298 km^2 since the end of the LIA (**Table 3**). Especially glacier area classes ranging from 0.1 to 1 km^2 exhibit the largest area loss (30%) within the last 30 years. Glaciers with an eastern—and southeastern exposition suffered the greatest

TABLE 3 | Area changes for the respective studied regions for different time periods (1870, 1986, 2005, 2016).

Year		Area change [km^2]	Area change [%]	Annual change [$km^2 a^{-1}$]	Annual rate [% a^{-1}]		Area change [km^2]	Area change [%]	Annual change [$km^2 a^{-1}$]	Annual rate [% a^{-1}]
LIA-16	CH, CE	−568.5 ± 133.5	−48.0 ± 11.3	−3.89 ± 0.91	−0.33 ± 0.08	NPI -W	−570.7 ± 118.9	−15.8 ± 3.3	−3.91 ± 0.81	−0.11 ± 0.02
LIA-86		−377.9 ± 143.2	−31.9 ± 12.1	−3.26 ± 1.24	−0.27 ± 0.10		−301.5 ± 123.0	−8.3 ± 3.4	−2.60 ± 1.06	−0.07 ± 0.03
86–05		−121.1 ± 105.8	−15.0 ± 15.4	−6.37 ± 5.57	−0.79 ± 0.69		−174.4 ± 103.2	−5.3 ± 3.1	−9.18 ± 5.43	−0.28 ± 0.16
05–16		−69.5 ± 92.1	−10.1 ± 15.0	−6.32 ± 8.38	−0.92 ± 1.22		−94.9 ± 98.3	−3.0 ± 8.6	−8.63 ± 8.94	−0.28 ± 0.28
86–16		−190.6 ± 101.5	−23.6 ± 12.6	−6.35 ± 3.38	−0.79 ± 0.42		−269.2 ± 107.9	−8.1 ± 3.3	−8.97 ± 3.60	−0.27 ± 0.11
LIA-16	NPI -E	−715.1 ± 173.3	−34.3 ± 8.3	−4.90 ± 1.19	−0.23 ± 0.06	MSL, SD	−667.1 ± 165.2	−41.9 ± 10.4	−4.57 ± 1.13	−0.29 ± 0.07
LIA-86		−545.4 ± 181.5	−26.1 ± 8.7	−4.70 ± 1.56	−0.22 ± 0.08		−459.9 ± 173.2	−28.9 ± 10.9	−3.96 ± 1.49	−0.24 ± 0.09
86–05		−92.4 ± 147.0	−6.0 ± 9.5	−4.87 ± 7.74	−0.32 ± 0.50		−148.9 ± 130.9	−13.2 ± 11.6	−7.83 ± 6.89	−0.69 ± 0.61
05–16		−77.3 ± 136.8	−5.3 ± 9.4	−7.02 ± 12.43	−0.48 ± 0.85		−58.3 ± 120.1	−5.9 ± 12.2	−5.31 ± 10.92	−0.54 ± 1.11
85–16		−169.7 ± 142.5	−11 ± 9.2	−5.66 ± 4.75	−0.37 ± 0.31		−207.2 ± 127.5	−18.3 ± 11.3	−6.91 ± 4.25	−0.61 ± 0.38
LIA-16	SPI -W	−791.0 ± 171.2	−9.7 ± 2.1	−5.42 ± 1.17	−0.07 ± 0.02	SPI -E	−1430.0 ± 313.7	−20.2 ± 4.4	−9.79 ± 2.15	−0.14 ± 0.03
LIA-86		−323.3 ± 177.8	−4.0 ± 2.2	−2.79 ± 1.53	−0.03 ± 0.02		−924.5 ± 320.6	−13 ± 4.5	−7.97 ± 2.76	−0.11 ± 0.04
86–05		−334.7 ± 177.2	−4.3 ± 2.3	−17.62 ± 9.32	−0.23 ± 0.12		−382.6 ± 274.8	−6.2 ± 4.5	−20.14 ± 14.46	−0.33 ± 0.24
05–16		−133.0 ± 170.6	−1.8 ± 2.3	−12.09 ± 15.51	−0.16 ± 0.08		−123.0 ± 266.7	−2.1 ± 4.6	−11.17 ± 24.24	−0.19 ± 0.42
85–16		−467.7 ± 176.2	−6.0 ± 2.3	−15.59 ± 5.87	−0.2 ± 0.08		−505.5 ± 279.8	−8.2 ± 4.5	−16.85 ± 9.33	−0.27 ± 0.15
LIA-16	GCN, ISI	−143.3 ± 58.3	−16.2 ± 6.6	−0.98 ± 0.40	−0.11 ± 0.05	CD-N	−315.8 ± 64.2	−18.8 ± 3.8	−2.16 ± 0.44	−0.13 ± 0.03
LIA-86		−59.9 ± 62.3	−6.8 ± 7.1	−0.52 ± 0.54	−0.06 ± 0.06		−159.8 ± 70.0	−9.5 ± 4.2	−1.38 ± 0.61	−0.08 ± 0.04
86–05		−49.1 ± 54.4	−6.0 ± 6.6	−2.59 ± 2.86	−0.31 ± 0.35		−130.7 ± 64.8	−8.6 ± 4.1	−6.88 ± 3.44	−0.45 ± 0.23
05–16		−34.3 ± 49.8	−4.4 ± 6.4	−3.12 ± 4.52	−0.40 ± 0.58		−25.3 ± 57.6	−1.8 ± 4.1	−2.30 ± 5.23	−0.16 ± 0.37
85–16		−83.5 ± 53.9	−10.1 ± 6.5	−2.78 ± 1.80	−0.34 ± 0.37		−156.0 ± 64.0	−10.2 ± 4.2	−5.20 ± 2.13	−0.34 ± 0.14
LIA-16	CD-S	−254.4 ± 60.3	−14.0 ± 3.3	−1.74 ± 0.41	−0.10 ± 0.02					
LIA-86		−123.5 ± 86.9	−6.8 ± 4.8	−1.06 ± 0.75	−0.06 ± 0.04					
86–05		−106.7 ± 80.1	−6.3 ± 4.7	−5.61 ± 4.22	−0.33 ± 0.25					
05–16		−24.3 ± 50.2	−1.5 ± 3.2	−2.21 ± 4.56	−0.14 ± 0.29					
85–16		−131.9 ± 66.3	−7.7 ± 3.9	−4.36 ± 2.21	−0.26 ± 0.13					

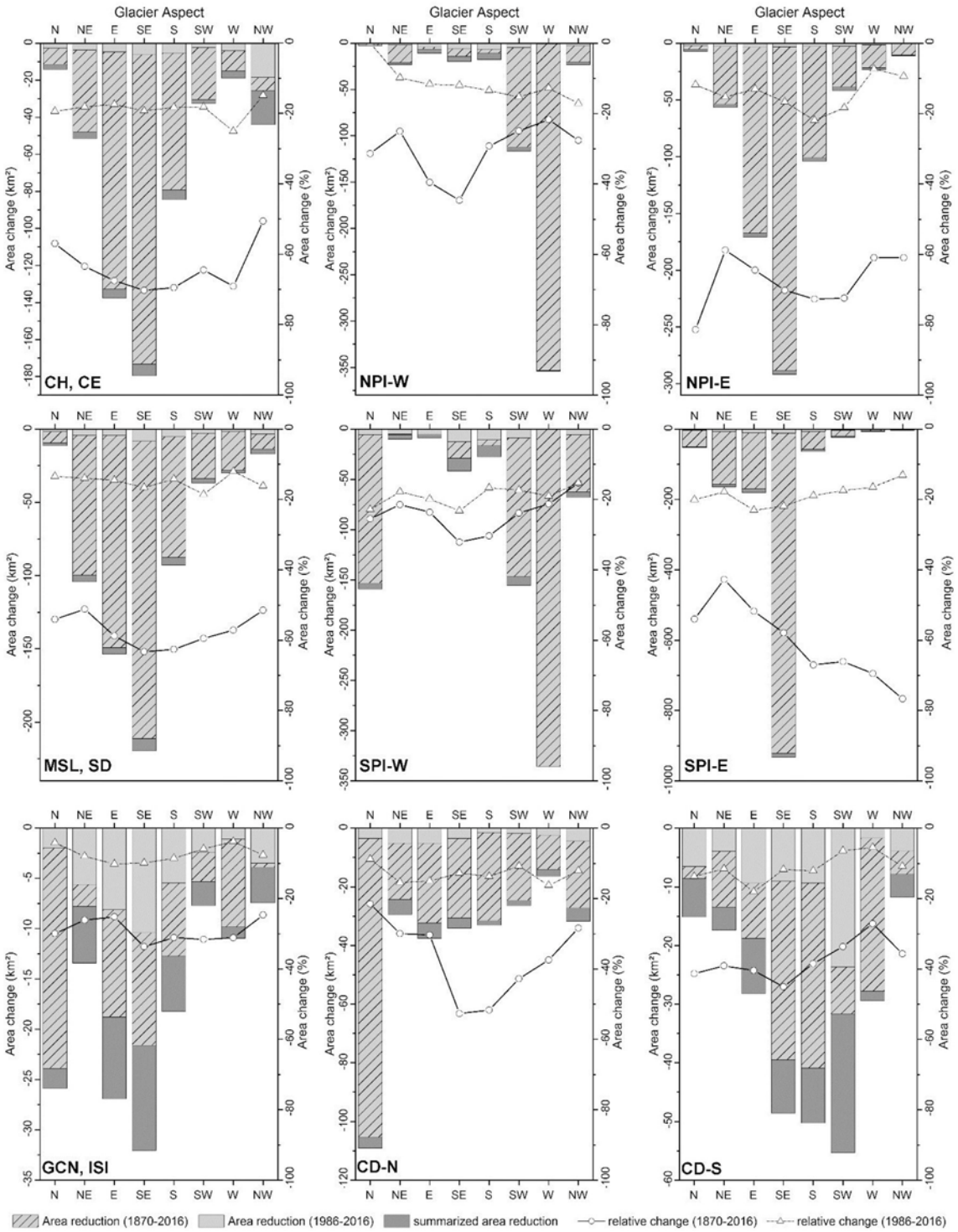

FIGURE 9 | Absolute (bars) and relative (lines) area loss since the LIA, dependent on glacial aspect. Anytime no LIA extent could be digitized, the glacial area of the 1986 derived inventory was used.

loss in terms of total area and relative area (**Figure 9**: CH, CE; MSL, SD). The LIA extents for the majority of all glaciers of those sub-regions were manually digitized, only a few ones had to be interpolated by using the outlines from 1986. But at the volcano Cerro Hudson the LIA outline of the major outlet glacier could not be determined hence the induced lahars due to the eruption in 1991 devastated the moraine systems (**Figure 9**, CH, CE, NW-aspect).

Since the LIA, the western NPI and SPI lost the bulk of their area through western-exposed glaciers, whereas these were the ones with low relative change rates (**Figure 9**: NPI-W, SPI-W). In total, the western parts of the NPI and SPI and adjoined glaciers reveal an area reduction of 1,361 ± 290 km^2 since the LIA, whereas the glacierized area in the eastern parts was reduced by 2,145 ± 487 km^2 (**Table 3**). Until 1986 the area loss since 1870 was moderate for the NPI-W and SPI-W with 2.60 ± 1.06 $km^2\ a^{-1}$ and 2.79 ± 1.53 $km^2\ a^{-1}$, respectively. In both cases the annual area change increased between 1986 and 2016, reaching a maximum of 15.59 ± 5.87 $km^2\ a^{-1}$ at the SPI. The eastern part of the NPI and adjoined mountain glaciers reveal an area loss of 715 ± 173 km^2 since the LIA. Including all uncertainties the annual change rates are more or less constant ranging between 4.70 ± 1.56 $km^2\ a^{-1}$ and 7.02 ± 12.43 $km^2\ a^{-1}$. Annual change rates of the eastern part of the Andean main crest at the SPI are nearly twice as high as for the NPI-E according to 7.97 ± 1.6 $km^2\ a^{-1}$ between 1870 and 1986 and 16.85 ± 9.33 $km^2\ a^{-1}$ for the period of 1986–2016.The total area loss for the eastern part of the SPI accounts for 1,430 km^2 since the LIA and is the largest of the whole investigated region. For both regions the total area loss was highest for southeast and eastern facing glaciers (**Figure 9**, NPI-E and SPI-E). For the entire inventory, the glaciers of the GCN, ISI sub-region shows the lowest total area reduction since the LIA (143 ± 59 km^2). Simultaneously, the area loss rate between the LIA and 1986 was the lowest (0.06 ± 0.06% a^{-1}) of all measured sub-regions (**Table 3**). Yet as shown in **Figure 9** digitizing the LIA extents was frequently not possible due to the glaciers calving into fjords and the lack of moraines. Therefore, many glacial extents of 1986 fill this gap, leading to possible bias. Nevertheless, during the last 30 years the glacial area is also subject to high loss rates reaching values up to 0.40 ± 0.58% a^{-1}. For the northern CD, glaciers with northern aspect are responsible for the highest amount of area loss, while south-/southeast-exposed glaciers have the highest relative loss rates (**Figure 9**, CD-N). On the southern declivity, southeast to southwest expositions dominate the area change, whereas the relative are change reaches its maximum for southeast facing glaciers. The northern as well as the southern part of the CD reveal a low area reduction of 0.08 ± 0.04 and 0.06 ± 0.04% a^{-1} between the LIA and 1986, respectively. Glacier shrinkage accelerates slightly since 1986 to 0.34 ± 0.14 and 0.26 ± 0.13% a^{-1}, respectively.

It is additionally apparent that for smaller glaciers (<10 km^2) the reported relative change is higher than for larger glaciers. In absolute values, however, the large glaciers make a huge contribution to the reduction in surface area. For example, the area loss of 791 ± 171 km^2 for the SPI-W between LIA and 2016 is dominated by only 15 of the 1,300 glaciers that account for over 65% of the area change.

DISCUSSION

Our semi-automated acquisition of all South American glaciers south of 45.5° offers the possibility to compare and verify numerous previous studies that focused on single or multiple glacial settings, or aimed at inferring complete inventories. In total our glacier inventory contains 11,209 individual glaciers in 2016, whereas the RGI 6.0 provides a total of 9,429 glaciers for the same region (Pfeffer et al., 2014; Randolph Glacier Inventory Consortium, 2017). On the one hand we inventoried 867 additional glaciers (∼75 km^2), on the other hand, 2,729 RGI glaciers (corresponding to 308 km^2) are not incorporated in our new inventory. This large difference cannot be explained by the different glacier area thresholds that were used in the both inventories. Only 640 of the 2,729 glaciers (RGI 6.0) are smaller than 0.025 km^2 and are therefore not included in our inventory. The remaining 2,089 glaciers are either misclassified seasonal snowfields which have been rejected by our temporal consistency test, in rare cases wrongly classified water bodies, or glaciers which already disappeared since the turn of the millennium. The glaciers that are included in both inventories also differ in total number due to the small-scaled drainage basin analysis that was performed in our updated inventory. The RGI 6.0 inventoried a total of 6,700 glaciers, whereas we subdivided those glaciers into 10,344 individual entities. The resulting differences in the individual glacier catchment areas and different investigation periods aggravate a direct comparison of the particular glaciers. For our studied region the total area estimation provided by the RGI 6.0 is with 25,452 km^2 even larger than our estimated glacierized area of 24,818 ± 912 km^2 in 1986 (23,277 ± 907 and 22,636 ± 905 km^2 in 2005 and 2016, respectively). Even considering the glacierized area of 308 km^2 that we did not record in our inventory and an additionally mapped area of 168 km^2 of rock outcrops (refers to 1986) than comprised in the RGI 6.0 the difference in the two datasets still can exceed 1,000 km^2 (refers to the glacierized area of 2005). Those differences can only be attributed to our manually improvement of the automatic derived outlines, whereas many glaciers in the RGI were not adequately enhanced. A glacier inventory in 2001 was performed by Rivera et al. (2007) and De Angelis (2014) for the NPI and SPI, respectively. For the NPI 70 glaciers larger than 0.5 km^2 were detected, covering an area of 3,953 km^2 in 2001 (Rivera et al., 2007, **Table 4**). In our study the NPI is assembled of 171 individual glaciers (>0.025 km^2) covering an area of 3,806 ± 80 km^2 in 2005. The number of large outlet glaciers is not modified between the two datsets rather the glacierized area at the outer perimeter of the icefield was subdivided particularly. De Angelis (2014) considered for the SPI 139 glaciers larger than 5 km^2 covering an area of 12,363 km^2 in 2001. In our inventory (2016) the SPI is assembled of 128 glaciers larger than 5 km^2 and over 500 smaller glaciers that were excluded by De Angelis (2014) covering an area of 12,232 ± 201 km^2 (**Table 4**).

Most studies which provide not only an inventoried dataset but also include a change assessment of the glacierized area focus predominantly on the NPI and SPI. **Table 4** lists the results from our study for the NPI, SPI, and two smaller catchments in comparison to previous published results. The small catchments are located at the eastern side of the Andean main crest at MSL and Lakes San Martín (LSM). Dussaillant et al. (2018) calculated the glacierized area of the NPI for 2000 and 2012 with 3,856 ± 211 km^2 and 3,740 ± 200 km^2, respectively. Their calculated area loss of 116 ± 290 km^2 (3 ± 7.5%) is in good agreement with our

TABLE 4 | Comparison of the inventoried glacierized areas and change rates for the NPI, SPI and sub-regions of the MSL (Monte San Lorenzo) and LSM (Lakes San Martín).

	Year	Area [km^2]	Period	Area loss [km^2]	Area loss [%] [%]	Area loss [km^2 a^{-1}]	Area loss [% a^{-1}]	Source
NPI	1870	4457.6 ± 79.2	1870–16	−782.8 ± 112.2	−17.6 ± 2.5	−5.36 ± 0.77	−0.12 ± 0.01	This study
NPI	1986	4004.5 ± 77.6	1870–86	−453.2 ± 110.8	−10.2 ± 2.8	−3.90 ± 0.96	−0.09 ± 0.02	This study
NPI	2005	3806.3 ± 79.7	1986–05	−198.2 ± 111.2	−5.0 ± 2.8	−10.43 ± 5.85	−0.26 ± 0.15	This study
NPI	2016	3674.9 ± 79.5	2005–16	−131.4 ± 112.0	−3.5 ± 3.0	−11.95 ± 10.23	−0.31 ± 0.27	This study
NPI	1870	4635 ± 93	1870–11	−659.7 ± 112.1	−14.2 ± 2.6	−4.68 ± 0.87	−0.10 ± 0.02	Davies and Glasser, 2012
NPI	1986	4142 ± 83	1870–86	−493.4 ± 124.3	−10.6 ± 3.0	−4.25 ± 1.07	−0.09 ± 0.03	Davies and Glasser, 2012
NPI	2001	4070 ± 81	1986–01	−72.1 ± 116.1	−1.7 ± 2.9	−5.15 ± 7.74	−0.12 ± 0.19	Davies and Glasser, 2012
NPI	2011	3976 ± 80	2001–11	−94.1 ± 113.8	−2.3 ± 2.9	−8.55 ± 11.38	−0.23 ± 0.29	Davies and Glasser, 2012
NPI	2000	3856 ± 211	2000–12	−116 ± 290	−3.0 ± 7.5	−9.66 ± 24.16	−0.25 ± 0.63	Dussaillant et al., 2018
NPI	2012	3740 ± 200						Dussaillant et al., 2018
NPI	1979	4093	1979–01	−140 ± 61	−3.4 ± 1.5	−6.36 ± 2.77	−0.15 ± 0.07	Rivera et al., 2007
NPI	2001	3953						Rivera et al., 2007
SPI	1870	14208.0 ± 184.3	1870–16	−1976 ± 272.8	−13.9 ± 1.9	−13.54 ± 1.86	−0.10 ± 0.01	This study
SPI	1986	13043.9 ± 186.9	1870–86	−1164.0 ± 262.5	−8.2 ± 2.0	−10.03 ± 2.27	−0.07 ± 0.02	This study
SPI	2005	12485.6 ± 199.4	1986–05	−558.4 ± 273.3	−4.3 ± 2.1	−29.38 ± 14.38	−0.23 ± 0.11	This study
SPI	2016	12231.7 ± 201.1	2005–16	−253.9 ± 283.3	−2.0 ± 2.3	−23.08 ± 25.75	−0.18 ± 0.21	This study
SPI	1870	14862 ± 122	1870–11	−1644 ± 122	−11.1 ± 0.8	−11.65 ± 0.87	−0.08 ± 0.01	Davies and Glasser, 2012
SPI	1986	13657 ± 124	1870–86	−1205 ± 124	−8.1 ± 0.9	−10.38 ± 1.07	−0.07 ± 0.01	Davies and Glasser, 2012
SPI	2001	13424 ± 116	1986–01	−233 ± 116	−1.7 ± 0.9	−15.53 ± 7.74	−0.11 ± 0.06	Davies and Glasser, 2012
SPI	2011	13218 ± 113	2001–11	−206 ± 206	−1.5 ± 0.9	−18.73 ± 11.38	−0.15 ± 0.09	Davies and Glasser, 2012
SPI	1986	13003 ± 282	1986–00	−489 ± 377	−3.8 ± 2.9	−34.93 ± 26.93	−0.27 ± 0.21	Casassa et al., 2014
SPI	2000	12514 ± 250						Casassa et al., 2014
LSM	1870	246.6 ± 9.1	1870–16	−73.8 ± 12.7	−29.9 ± 5.2	−0.50 ± 0.08	−0.20 ± 0.03	This study
LSM	1986	194.1 ± 8.3	1870–86	−52.5 ± 12.0	−21.3 ± 6.2	−0.45 ± 0.10	−0.18 ± 0.05	This study
LSM	2005	178.0 ± 8.2	1986–05	−16.0 ± 11.3	−8.3 ± 6.3	−0.84 ± 0.59	−0.43 ± 0.33	This study
LSM	2016	172.8 ± 8.1	2005–16	−5.2 ± 12.0	−2.9 ± 7.0	−0.48 ± 1.09	−0.27 ± 0.63	This study
LSM	1870	423.2 ± 8.5	1870–16	−102.9 ± 10.6	−24.3 ± 2.5	−0.73 ± 0.08	−0.17 ± 0.02	Davies and Glasser, 2012
LSM	1986	365.9 ± 7.3	1870–86	−57.2 ± 11.2	−13.5 ± 3.0	−0.49 ± 0.10	−0.12 ± 0.03	Davies and Glasser, 2012
LSM	2001	364.3 ± 7.3	1986–01	−1.6 ± 10.3	−0.4 ± 2.8	−0.11 ± 0.69	−0.03 ± 0.19	Davies and Glasser, 2012
LSM	2011	320.2 ± 6.4	2005–16	−44.1 ± 9.7	−12 ± 3.0	−4.0 ± 0.97	−1.21 ± 0.30	Davies and Glasser, 2012
LSM	1979	220.9 ± 7.4	1979–05	−33.7 ± 9.9	−15.3 ± 4.5	−1.29 ± 0.38	−0.59 ± 0.17	Masiokas et al., 2015
LSM	2005	187.2 ± 7.4						Masiokas et al., 2015
MSL	1870	322.5 ± 10.1	1870–16	−137.0 ± 12.7	−42.5 ± 3.9	−0.93 ± 0.09	−0.29 ± 0.03	This study
MSL	1986	225.3 ± 9.2	1870–86	−97.1 ± 12.0	−30.1 ± 5.3	−0.84 ± 0.10	−0.26 ± 0.04	This study
MSL	2005	199.2 ± 9.1	1986–05	−26.1 ± 11.3	−11.5 ± 5.0	−1.37 ± 0.60	−0.60 ± 0.27	This study
MSL	2016	185.4 ± 10.1	2005–16	−13.8 ± 12.0	−6.9 ± 6.0	−1.26 ± 1.09	−0.63 ± 0.55	This study
MSL	1870	265.3 ± 8.4	1870–11	−83.2 ± 10.6	−31.3 ± 4.0	−0.59 ± 0.08	−0.22 ± 0.03	Davies and Glasser, 2012
MSL	1986	192.5 ± 7.3	1870–86	−73.8 ± 11.2	−27.4 ± 5.8	−0.62 ± 0.1	−0.24 ± 0.05	Davies and Glasser, 2012
MSL	2001	184.7 ± 7.3	1986–01	−7.8 ± 9.7	−4.1 ± 5.6	−0.56 ± 0.69	−0.27 ± 0.30	Davies and Glasser, 2012
MSL	2011	182.1 ± 6.4	2001–11	−2.6 ± 9.7	−1.4 ± 5.3	−0.24 ± 0.97	−0.14 ± 0.53	Davies and Glasser, 2012
MSL	1985	239	1985–08	−44 ± 13	−18.6 ± 5.9	−1.9 ± 0.6	−0.81 ± 0.26	Falaschi et al., 2013
MSL	2000	215	1985–00	−24 ± 13	−9.9 ± 5.3	−1.6 ± 0.8	−0.66 ± 0.35	Falaschi et al., 2013
MSL	2008	195	2000–08	−21 ± 13	−8.7 ± 5.3	−2.6 ± 1.6	−1.09 ± 0.66	Falaschi et al., 2013

derived glacier outlines between 2005 (3,806 ± 80 km^2) and 2016 (3,675 ± 80 km^2), indicating an area loss of 3.5 ± 3.0%. Between 1979 and 2001 Rivera et al. (2007) estimated an area decrease of 3.4 ± 1.5% for the NPI whereas we estimate an area decrease by 5.0 ± 2.9% between 1986 and 2005. The least area reduction was calculated for the periods of 1986–2001 and 2001–2011 by Davies and Glasser (2012) according to 1.7 ± 2.9% and 2.3 ± 2.9%, respectively. As stated, a direct comparison of our study with the previous studies is problematic, since the area of the NPI was measured at different times, the applied methods are diverse, and the uncertainty values differ highly. For 2000/2001 three area estimations of the NPI (**Table 4**) were performed, revealing a mean deviation of ± 107 km^2. This comparable high mean deviation is an important issue concerning the reliability of the calculated area change and change rates that vary in the same magnitude (**Table 4**). Our nearest area estimation of the NPI in terms of time (2005) is with 3,806 ± 80 km^2 around 150 km^2 smaller than the estimated areas of 2000/2001. But also for the same investigation time of 1986 our estimated area is ∼140 km^2 smaller than the derived outlines by Davies and Glasser (2012). We attribute those regional differences that apply to the whole inventory to four factors: first the definition of the respective ice fields or study regions differ. Davies and Glasser (2012) as well as Schneider et al. (2007) for the GCN, include glaciers at the perimeter of the ice fields that were, according to our LIA maxima moraine mapping, not connected to the ice field itself even during this cooler period. In addition, Casassa et al. (2014) also include single glaciers within the inner perimeter of the SPI to the icefield even when they are not directly connected to itself. Our inventory assigns only those glaciers to the respective ice field which were directly connected with it at least during the LIA. Secondly, the newly available, multi-season remote sensing data that were used in our study enable the recognition of small catchments and moraine settings, as well as the differentiation of temporal snow fields, firn basins and small glaciers. We assume, that existing studies might thus have overestimated the truly glacierized area. Thirdly, other regional inventories, e.g., Masiokas et al. (2015) and Barcaza et al. (2017) include in their inventory ice bodies larger 0.01 km^2 whereas our study provides only ice bodies larger 0.025 km^2. Finally, the amount of rock outcrops included in the previous inventories and that were excluded from the glacierized area in our study contributes a substantial spatial difference, as already described by Rivera et al. (2007) for the inventory of Aniya (1988). The rock outcrops could be one of the major error sources between the different inventories. For 2001 rock outcrops for the NPI were estimated as 120 and 175 km^2, respectively (Rivera et al., 2007; Davies and Glasser, 2012). Our inventory contains for the interior rocks in 1986 and 2005 an area of 205 km^2 and 231 km^2, respectively.

For the SPI our results are in good accordance to the area estimation of Casassa et al. (2014) with nearly the same area in 1986 (**Table 4**). Also, the calculated change rates, although not for the same periods are nearly the same, whereas Davies and Glasser (2012) calculated only one half of our estimated area loss within the last 30 years (**Table 4**). Our obtained glacierized area in 1986 and 2005 of the sub-region LSM and MSL, respectively, lie within the uncertainty value provided by the previous inventories (**Table 4**, LSM, MSL). Taking every uncertainty into account, the discrepancies in the glacierized area estimation between the outlines derived by Davies and Glasser (2012) and our study are very high, exceeding a relative difference of 50% for the LSM sub-region (**Table 4**, LSM). In 2005 our estimated area of the LSM sub-region (178 ± 8 km^2) is in good agreement with the previously calculated area of 187 ± 7 km^2 for the same investigation period (Masiokas et al., 2015), whereas Davies and Glasser (2012) measured an area of 364 ± 7 km^2 in 2001 (**Table 4**). Our estimated area loss of 26 ± 11 km^2 between 1986 and 2005 for the MSL sub-region is equivalent to the area reduction of 24 ± 13 km^2 between 1986 and 2001 (Falaschi et al., 2013) and is twice as high as measured by Davies and Glasser (2012) for 1986–2001 (**Table 4**).

Table 4 corroborates also the differences in the LIA extents between the inventories that exceed several hundred km^2. For the same studied region, Davies and Glasser (2012) obtain by the sample-based calculation of the LIA extent a total area of 25,939 ± 518 km^2. In contrast, our detected extent of 28,091 ± 890 km^2 is by 8.3% significantly larger. The LIA extents from the prior study were adapted to our drainage basins to ensure a comparability of the two data sets. The glacial extents represented in both studies differ largely with an area difference exceeding 4000 km^2 for the same glacierized regions. On the one hand we digitized a larger area of 1,280 km^2, on the other hand Davies and Glasser (2012) included 2,750 km^2 that are not contained in our inventory. Those area differences arise from various factors: first, some LIA glacial extents are subject of controversial scientific debate, e.g., LIA extents in the fjords of Bahia Pía, Cordillera (Kuylenstierna et al., 1996; Koch, 2015). As we want to provide a reliable minimum estimation of the LIA extent we used the estimated area provided by Kuylenstierna et al. (1996) for the glaciers in the Bahia Pía which are significant smaller than the outlines by Davies and Glasser (2012). Secondly, we preserved larger rock outcrops (as included in the inventory from 1986) to avoid an overestimation of the glacierized area, leading to an area exceeding 1,300 km^2, whereas Davies and Glasser (2012) estimated 310 km^2 of interior rock outcrops. At last, in some cases we could not find sufficient morphological evidence for the prior derived outlines and did not include them. Alternately existing outlines could be improved by higher resolution data (see **Figure 2d**). For the glaciers larger than 100 km^2 the relative difference between the two studies is with ± 3.8% comparably small but those values rapidly increase with decreasing glacier area leading to a mean relative difference of ± 30% for glaciers ranging between 5 and 10 km^2 and even exceeding up to more than 100% for small glaciers. Our study provides 1760 LIA glacial extents that were not included in previous inventories, covering an area of 2,249 ± 110 km^2. Those newly derived outlines could probably not be mapped by Davies and Glasser (2012) due to the lack of high resolution data, since these glaciers are fairly small: 61% of those new generated LIA extents belong to the glacier area class smaller than 1 km^2 covering an area of 506 ± 30 km^2. For 3,976 glaciers inventoried in the RGI 6.0 study region (corresponds to 42% of the glaciers) we could therefore identify the LIA glacial extent, whereas the study by Davies and Glasser (2012)

determined the LIA extent for 1881 (20%) of the RGI 6.0 glaciers.

The sub-regions of CH, CE, and MSL, SD show the highest relative area loss since the LIA according to a relative area reduction of 48 ± 11 and 42 ± 10%, respectively. At the same time those sub-regions possess the smallest glacial mean area. This is in good agreement with other findings, indicating larger relative area decrease for small glaciers within the last decades (Masiokas et al., 2015). At the same time Masiokas et al. (2015) emphasize the high variability of shrinkage rates (0–100%) for smaller glacier units. We observed this high variation also in our complete studied region, especially for glaciers smaller than 1 km^2 (**Figure 8B**). Frequently those glaciers that reveal a small relative shrinkage are situated in couloirs, at exposed slopes combined with dry calving or in shadowed cirques, favoring their preservation (Falaschi et al., 2013). For the MSL sub-region Falaschi et al. (2013) report an increase in area loss between 1985 and 2000 and 2000 and 2008 according to 1.6 and 2.6 $km^2\ a^{-1}$, respectively. In this study, no absolute area uncertainties are provided, but the authors used the same error estimation as in our inventory, consequently the margin of uncertainty are nearly the same (**Table 4**). In absolute values we confirm those results but given the large error term and the short time period of change assessment the values are not statistically significant. Davies and Glasser (2012) state the increasing shrinkage for the NPI and SPI twice as high in the recent years than between 1870 and 1986 reaching a maximum between 2001 and 2011. It could be problematic to assume a real acceleration within the recent decades since the uncertainty values of ± 2% by Davies and Glasser (2012) or the area loss calculation by Casassa et al. (2014) for the SPI with 489 ± 377 km^2 between 1986 and 2000 reveal that the area reduction rates are within the uncertainty range (**Table 4**). On the other hand, we can support the acceleration in the recent area loss rates compared to the period between the LIA and 1986. However, the derived annual shrinkage rates have to be regarded with caution, as the assumption of a constant shrinkage rate between the LIA maximum and 1986 is fairly unlikely. It is also possible that within the period between LIA and 1986 there were many sub-periods where glacier shrinkage was faster or even much slower. Additionally many calving glaciers are variable due to non-climatic factors and do not show a constant behavior, e.g., several of the glaciers of the Cordillera Darwin reveal an advance since 1986 whereas the surrounding land-terminating glaciers al retreated. Considering all uncertainty values it could be also possible for the whole studied region as one, that the glacier recession is more or less constant since the end of the LIA. On the other hand some morphological features that were used for the LIA mapping could be far older than 1870 as expressed in the uncertainty assessment. Then it is possible that the shrinkage rates are even smaller than our calculated values.

For the other major ice fields like CD, IH, and ISI Bown et al. (2015) derived from ASTER and Landsat ETM+ data between 2001 and 2011 an area of 2,331, 274, and 273 km^2, respectively. In total 1,681 glaciers were identified covering an area of 3,289 km^2. Our study estimates for the same region with 3,169 km^2 in 2005 identifying over 2,400 individual glaciers. Although the differences of both independent derived inventories seem to be small (∼120 km^2), they are very important concerning the change analysis. For example within the last 30 years we measured an area reduction of 287 ± 130 km^2 for the Cordillera Darwin and adjoined glaciers, including IH and ISI, which is only twice as high as the uncertainties between two derived inventories.

With respect to local factors, our data supports the findings of Davies and Glasser (2012) that calving glaciers show the smallest rates of shrinking, and smaller glaciers shrink faster on average. Considering aspect, for the whole inventory, southeast-oriented glaciers showed the highest annual retreat, whereas we could not find a significant west-east gradient in this manner. The latter is in accordance with findings of Davies and Glasser (2012), just as the absolute rate of area loss being highest with glaciers with western aspect. This is especially remarkable, since this not only includes the mainly west-east-oriented, large glaciers of the NPI and SPI, but the whole inventory.

The total area change reflects mainly the differences in the two largest glacier area classes (>100 km^2; 42 glaciers account for 40.2% of the total area change, and in the glaciers between 1 and 5 km^2 in area (20.4%). The former is in accordance with Rivera et al. (2007), who report for the the NPI that e.g., Glaciar San Quintín alone accounted with 33 km^2 for a large part of the total area change of 140 km^2 between 1979 and 2001.

CONCLUSION/ SUMMARY

A large scaled glacier inventory was derived for the whole Patagonian Andes south of 45.5°S and Tierra del Fuego. In 2016 a total 11,209 glaciers, covering an area of 22,636 ± 905 km^2 were inventoried. Compared to other inventories that contain our whole study region, we identified due to our detailed basin analysis a surplus of nearly 2000 glaciers (compared to the RGI 6.0). The SPI and the NPI are the largest temperate ice bodies in South America, covering an area of 12,232 ± 201 and 3,674 ± 80 km^2, respectively. Most of the glaciers have a south-eastern aspect, but larger outlet glaciers depend on the large scale orientation of the mountain ranges. The outlet glaciers are frequently perpendicular orientated to the longside mountain range, resulting in western and eastern aspect for the NPI and SPI and a north and south aspect for the CD. Change analysis for the whole glacierized area was done for 1986, 2005, and 2016 indicating an area loss of 8.6% (2,182 ± 1,276 km^2) within the last 30 years. Additionally, the glacial extent for over 2600 glaciers during the Little Ice Age was derived resulting in a glacial cover of 28,091 ± 890 km^2. Overall glacier shrinkage increased for the periods 1870–1986, 1986–2005, 2005–2016 from 0.10 ± 0.04 to 0.33 ± 0.28% a^{-1} ending at 0.25 ± 0.50% a^{-1}, respectively. The relative area loss was highest for smaller glaciers. In total over 600 glaciers completely disappeared since the Little Ice Age and over 650 glaciers reveal an area reduction of over 70%. Beside the glacier area, glacial retreat is influenced by latitude and terminating environment. Glacier shrinkage was highest in the northern parts of our study region. Also, between the two largest icefields and east of them, relative decrease in area was highest for small glaciers. Glaciers of the Cordillera Darwin were

retreating fastest between 1986 and 2005; afterwards the rate of glacial shrinkage decreased. Land-terminating glaciers showed the highest and most continuous retreat, whereas calving glaciers are more variable due to non-climatic factors, e.g., calving process and bedrock topography.

AUTHOR CONTRIBUTIONS

WM performed the glacial delineation and performed subsequent analysis together with PH and JG. MB initiated and supervised the study and wrote jointly with WM the manuscript.

FUNDING

This study was funded by the joint CONYCET-BMBF research project GABY-VASA: Responses of Glaciers, Biosphere and Hydrology to Climate variability and climate change across the Southern Andes (grant no. 01DN 15020).

REFERENCES

Andreassen, L. M., Paul, F., Kääb, A., and Hausberg, J. E. (2008). Landsat-derived glacier inventory for Jotunheimen, Norway, and deduced glacier changes since the 1930s. *Cryosphere* 2, 131–145. doi: 10.5194/tc-2-13 1-2008

Aniya, M. (1988). Glacier inventory for the northern Patagonia Icefield, Chile, and variations 1944/45 to 1985/86. *Arctic Alp. Res.* 20, 179–187. doi: 10.2307/1551496

Aniya, M. (1995). Holocene glacial chronology in Patagonia: tyndall and upsala glaciers. *Arctic Alp. Res.* 27, 311–322. doi: 10.2307/1552024

Aniya, M. (1996). Holocene variations of Ameghino Glacier, southern Patagonia. *Holocene* 6, 247–252. doi: 10.1177/095968369600600211

Aniya, M. (2013). Holocene glaciations of Hielo Patagónico (Patagonia Icefield), South America: a brief review. *Geochem. J.* 47, 97–105. doi: 10.2343/geochemj.1.0171

Aniya, M., Naruse, R., Shizukuishi, M., Skvarca, P., and Casassa, G. (1992). Monitoring recent glacier variations in the Southern Patagonia Icefield, utilizing remote sensing data. *Int. Arch. Photogramm. Remote Sens.* 29, 87–94.

Aniya, M., and Skvarca, P. (2012). Little ice age advances of glaciar perito moreno, hielo patagónico sur, South America. *Bull. Glaciol. Res.* 30, 1–8. doi: 10.5331/bgr.30.1

Araneda, A., Torrejón, F., Aguayo, M., Torres, L., Crues, F., Cisternas, M., et al. (2007). Historical records of San Rafael glacier advances (North Patagonian Icefield): another clue to 'Little Ice Age' timing in southern Chile? *Holocene* 17, 987–998. doi: 10.1177/0959683607082414

Aravena, J. C. (2007). Reconstruction of climate variability from tree-ring records and glacier fluctuations in the southern Chilean Andes. Ph.D. thesis, University of Western Ontario, London, ON.

Barcaza, G., Nussbaumer, S. U., Tapia, G., Valdès, J., Gacìa, J. L., Videla, Y., et al. (2017). Glacier inventory and recent glacier variations in the Andes of Chile, South America. *Ann. Glaciol.* 58, 1–15. doi: 10.1017/aog.2017.28

Bolch, T., Menounos, B., and Wheate, R. (2010a). Landsat-based inventory of glaciers in western Canada, 1985–2005. *Remote Sens. Environ.* 114, 127–137. doi: 10.1016/j.rse.2009.08.015

Bolch, T., Yao, T., Kang, S., Buchroithner, M. F., Scherer, D., Maussion, F., et al. (2010b). A glacier inventory for the western nyainqentanglha range and the nam co basin, tibet, and glacier changes 1976–2009. *Cryosphere* 4, 419–433. doi: 10.5194/tc-4-419-2010

Bown, F., Rivera, A., Zenteno, P., Bravo, C., and Cawkwell, F. (2015). "First glacier inventory and recent glacier variations on Isla Grande de Tierra del Fuego and adjacent islands in Southern Chile," in *Global Land Ice Measurements From Space,* eds J. S. Kargel, G. J. Leonard, M. P. Bishop, A. Kääb, and B. H. Raup (Heidelberg; Berlin: Springer), 661–673.

Bräuning, A. (2006). Tree-ring evidence of Little Ice Age glacier advances in southern Tibet. *Holocene* 16, 369–380. doi: 10.1191/0959683606hl922rp

Carrasco, J., Casassa, G., and Rivera, A. (2000). "Meteorological *in situ* observation in the southern ice cap, Patagonia," in *Proceedings of the 6th International Conference on Southern Hemisphere Meteorology and Oceanography*. Santiago: American Meteorological Society, 300–301.

Carrasco, J., Casassa, G., and Rivera, A. (2002). "Meteorological and climatological aspect of the Southern Patagonia Icefield," in *The Patagonia Icefields*, eds G. Casassa, F. V. Sepúlveda, and R. M. Sinclair (New York, NY: Kluwer-Plenum). 29–41.

Casassa, G., Rodriguez, J. L., and Loriaux, T. (2014). "A new glacier inventory for the Southern Patagonia icefield and areal changes 1986-2000," in *Global Land Ice Measurements From Space,* eds J. S. Kargel, G. J. Leonard, M. P. Bishop, A. Kääb, and B. H. Raup (Heidelberg; Berlin: Springer), 639–660.

Davies, B. J., and Glasser, N. F. (2012). Accelerating shrinkage of Patagonian glaciers from the "Little Ice Age" (c. AD 1870) to 2011). *J. Glaciol.* 58, 1063–1084. doi: 10.3189/2012JoG12J026

De Angelis, H. (2014). Hypsometry and sensitivity of the mass balance to changes in equilibrium-line altitude: the case of the Southern Patagonia Icefield. *J. Glaciol.* 60, 14–28. doi: 10.3189/2014JoG13J127

Dollenz, O. (1991). Sucesion vegetal en el sistema morrenico del Glaciar Dickson, Magallanes, Chile. *Anales Insituto de la Patagonia Seria Ciencias Naturales* 20, 50–60.

Dussaillant, I., Berthier, E., and Brun, F. (2018). Geodetic mass balance of the Northern Patagonian Icefield from 2000 to 2012 using two independent methods. *Front. Earth Sci.* 6:8. doi: 10.3389/feart.2018.00008

Falaschi, D., Bravo, C., Masiokas, M., Villalba, R., and Rivera, A. (2013). First Glacier inventory and recent changes in glacier area in the monte san lorenzo region (47°S), Southern Patagonian Andes, South America. *Arct. Antarct. Alp. Res.* 45, 19–28. doi: 10.1657/1938-4246-45.1.19

Fischer, M., HussChloé Barboux, M., and Hoelzle, M. (2014). The new swiss glacier inventory SGI2010: relevance of using high-resolution source data in areas dominated by very small glaciers. *Arct. Antarct. Alp. Res.* 46, 933–945. doi: 10.1657/1938-4246-46.4.933

Garreaud, R., Lopez, P.;, Minvielle, M., and Rojas, M. (2013). Large-scale control on the patagonian climate. *J. Clim.* 26, 215–230. doi: 10.1175/JCLI-D-12-00001.1

Glasser, N. F., Harrison, S., Jansson, K. N., Anderson, K., and Cowley, A. (2011). Global sea-level contribution from the Patagonian Icefields since the Little Ice Age maximum. *Nat. Geosci.* 4, 303–307. doi: 10.1038/ngeo1122

Granshaw, F. D., and Fountain, A. G. (2006). Glacier change (1958–1998) in the North Cascades National Park Complex, Washington, USA. *J. Glaciol.* 52, 251–256. doi: 10.3189/172756506781828782

Guo, W., Liu, S., Xu, J., Wu,. L., Shangguan, D., Yao, X., et al. (2015). The second Chinese glacier inventory: data, methods and results. *J. Glaciol.* 61, 357–372. doi: 10.3189/2015JoG14J209

Harrison, S., Glasser, N. F., Duller, G. A. T., and Jansson, K. N. (2012). Early and mid-holocene age for the tempanos moraines, Laguna San Rafael, Patagonian Chile. *Quat. Sci. Rev.* 31, 82–92. doi: 10.1016/j.quascirev.2011.10.015

Harrison, S., Glasser, N. F., Winchester, V., Haresign, E., Warren, C., Duller, G. A. T., et al. (2008). Glaciar León, Chilean Patagonia: late-Holocene chronology and geomorphology. *Holocene* 18, 643–652. doi: 10.1177/0959683607 086771

Harrison, S., and Winchester, V. (1998). Historical fluctuations of the Gualas and Reicher Glaciers, North Patagonian Icefield, Chile. *Holocene* 8, 481–485. doi: 10.1191/095968398672334459

Harrison, S., and Winchester, V. (2000). Nineteenth- and twentieth century glacier fluctuations and climatic implications in the Arco and Colonia Valleys, Hielo Patagónico Norte, Chile. *Arct. Antarct. Alp. Res.* 32, 55–63. doi: 10.2307/1552410

Harrison, S., Winchester, V., and Glasser, N. F. (2007). The timing and nature of recession of outlet glaciers of Hielo Patagónico Norte, Chile, from their Neoglacial IV (Little Ice Age) maximum positions. *Glob. Planet. Change* 59, 67–78. doi: 10.1016/j.gloplacha.2006.11.020

Heusser, C. J. (1964). "Some pollen profiles from Laguna de San Rafael area, Chilem," in *Ancient Pacific Flora; the Pollen Story,* ed L. M. Cranwell (Honolulu: University of Hawaii Press), 95–115.

Hochreuther, P., Loibl, D., Wernicke, J., Zhu, H., Grießinger, J., and Bräuning, A. (2015). Ages of major Little Ice Age glacier fluctuations on the southeast Tibetan plateau derived from tree-ring-based moraine dating. *Palaeogeogr. Palaeoclimatol. Palaeoecol.* 422, 1–10. doi: 10.1016/j.palaeo.2015.01.002

Holmlund, P., and Fuenzalida, H. (1995). Anomalous glacier responses to 20th century climatic changes in Darwin Cordillera, southern Chile. *J. Glaciol.* 41, 465–473. doi: 10.1017/S0022143000034808

Koch, J. (2015). Little Ice Age and recent glacier advances in the Cordillera Darwin, Tierra del Fuego, Chile. *Anal. Instituto Patagonia* 43, 127–136. doi: 10.4067/S0718-686X2015000100011

Koch, J., and Kilian, R. (2005). Little Ice Age glacier fluctuations, Gran Campo Nevado, southernmost Chile. *Holocene* 15, 20–28. doi: 10.1191/0959683605hl780rp

Koppes, M., Hallet, B., and Anderson, J. (2009). Synchronous acceleration of ice loss and glacial erosion, Glaciar Marinelli, Chilean Tierra del Fuego. *J. Glaciol.* 55, 207–220. doi: 10.3189/002214309788608796

Kuylenstierna, J., Rosqvist, G. C., and Holmlund, P. (1996). Late- Holocene glacier variations in the Cordillera Darwin, Tierra del Fuego, Chile. *Holocene* 6, 353–358. doi: 10.1177/095968369600600310

Lenaerts, J. T. M., Van den Broeke, M. R., Van Wessem, J. M., and Van de Berg, W. J. (2014). Extreme precipitation and climate gradients in Patagonia revealed by high-resolution regional atmospheric climate modeling. *J. Clim.* 27, 4607–4621. doi: 10.1175/JCLI-D-13-00579.1

Lopez, P., Chevallier, P., Favier, V., Pouyaud, B., Ordenes, F., and Oerlemans, J. (2010). A regional view of fluctuations in glacier length in southern South America. *Glob. Planet. Change* 71, 85–108. doi: 10.1016/j.gloplacha.2009.12.009

Malz, P., Meier, W., Casassa, G., Jaña, R., Skvarca, P., and Braun, M. H. (2018). Elevation and mass changes of the Southern Patagonia Icefield Derived from TanDEM-X and SRTM Data. *Remote Sens.* 10:188. doi: 10.3390/rs10020188

Masiokas, M. H., Delgado, S., Pitte, P., Berthier, E., Villalba, R., Skvarca, P., et al. (2015). Inventory and recent changes of small glaciers on the northeast margin of the Southern Patagonia Icefield, Argentina. *J. Glaciol.* 61, 511–523. doi: 10.3189/2015JoG14J094

Masiokas, M. H., Luckman, B. H., Villalba, R., Delgado, S., Skvarca, P., and Ripalta, A. (2009a). Little Ice Age fluctuations of small glaciers in the Monte Fitz Roy and Lago del Desierto areas, south Patagonian Andes, Argentina. *Palaeogeogr. Palaeoclimatol. Palaeoecol.* 281, 1351–1362. doi: 10.1016/j.palaeo.2007.10.031

Masiokas, M. H., Rivera, A., Espizua, L. E., Villalba, R., Delgado, S., and Aravena, J. C. (2009b). Glacier fluctuations in extratropical South America during the past 1000 years. *Palaeogeogr. Palaeoclimatol. Palaeoecol.* 281, 242–268. doi: 10.1016/j.palaeo.2009.08.006

Mercer, J. H. (1970). Variations of some Patagonian glaciers since the Late-Glacial; II. *Am. J. Sci.* 269, 1–25. doi: 10.2475/ajs.269.1.1

Messager, M. L., Lehner, B., Grill, G., Nedeva, I., and Schmitt, O. (2016). Estimating the volume and age of water stored in global lakes using a geo-statistical approach. *Nat. Commun.* 7:13603. doi: 10.1038/ncomms13603

Mouginot, J., and Rignot, E. (2015). Ice motion of the Patagonian Icefields of South America. *Geophys. Res. Lett.* 42, 1441–1449. doi: 10.1002/2014GL062661

Moy, C. M., Moreno, P. I., Dunbar, R. B., and Haberzettl, T. (2009). "Past climate variability in South America and surrounding regions: from the Last Glacial Maximum to the Holocene," in *Past Climate Variability in South America and Surrounding Regions: From the Last Glacial Maximum to the Holocen*, eds F. Vimeux, F. Sylvestre, and M. Khodri (New York, NY: Springer), 353–392.

Paul, F., and Andreassen, L. M. (2009). A new glacier inventory for the Svartisen region, Norway, from Landsat ETM+ data: challenges and change assessment. *J. Glaciol.* 55, 607–618. doi: 10.3189/002214309789471003

Paul, F., Barrand, N. E., Berthier, E., Bolch, T., Casey, K., Frey, H., et al. (2013). On the accuracy of glacier outlines derived from remote-sensing data. *Ann. Glaciol.* 54, 171–182. doi: 10.3189/2013AoG63A296

Paul, F., Barry, R. G., Cogley, J. G., Frey, H., Haeberli, W., Ohmura, A., et al. (2009). Recommendations for the compilation of glacier inventory data from digital sources. *Ann. Glaciol.* 50, 119–126. doi: 10.3189/172756410790595778

Paul, F., Bolch, T., Briggs, K., Kääb, A., McMillan, M., McNabb, R., et al. (2017). Error sources and guidelines for quality assessment of glacier area, elevation change, and velocity products derived from satellite data in the Glaciers_cci project. *Remote Sens. Environ.* 2003, 256–275. doi: 10.1016/j.rse.2017.08.038

Paul, F., Bolch, T., Kääb, A., Nagler, T., Nuth, C., Scharrer, K., et al. (2015). The glaciers climate change initiative: methods for creating glacier area, elevation change and velocity products. *Remote Sens. Environ.* 162, 408–426. doi: 10.1016/j.rse.2013.07.043

Paul, F., and Hendriks, J. (2010). "Optical remote sensing of glaciers," in *Remote Sensing of Glaciers - Techniques for Topographic, Spatial and Thematic Mapping of Glaciers,* eds P. Pellikka, and W. G. Rees (Leiden: CRC Press, Taylor and Francis Group), 137–152.

Paul, F., Huggel, C., Kääb, A., Kellenberger, T., and Maisch, M. (2003). "Comparison of TM-derived glacier areas with higher resolution data sets. EARSeL eProceedings 2, 15-21," in *Proceedings of the EARSeL Workshop on Remote Sensing of Land Ice and Snow* (Berne).

Paul, F., and Mölg, N. (2014). Hasty retreat of glaciers in northern Patagonia from 1985 to 2011. *J. Glaciol.* 60, 1033–1043. doi: 10.3189/2014JoG14J104

Pfeffer, T. W., Arendt, A. A., Bliss, A., Bolch, T., Cogley, J. G., Gardner, A. S., et al. (2014). The randolph glacier inventory: a globally complete inventory of glaciers. *J. Glaciol.* 60, 537–552. doi: 10.3189/2014JoG13J176

Pisano, E. (1978). Establecimiento de Nothofagus betuloides (Mirb.) Blume (Coigue de Magallanes) en un valle en proceso de desglaciacion. *Anales del Insituto de la Patagonia* 9, 107–128.

Rabatel, A. J. L., Ceballos, N., Micheletti, E., Jordan, M., and Braitmeier, J., Gonzalez, N. et al. (2018). Toward an imminent extinction of Colombian glaciers? *Geogr. Ann. A Phys. Geogr.* 100, 75–95. doi: 10.1080/04353676.2017.1383015

Raup, B., and Khalsa, S. J. S. (2007). *GLIMS Analysis Tutorial, vers. 22/05/2007 (pp. 15).* Boulder: NSIDC. Available online at: http://glims.org/MapsAndDocs/assets/GLIMS_Analysis_Tutorial_a4.pdf

Randolph Glacier Inventory Consortium (2017). *Randolph Glacier Inventory – A Dataset of Global Glacier Outlines: Version 6.0: Technical Report, Global Land Ice Measurements from Space*, Digital Media.

Rignot, E., Rivera, A., and Casassa, G. (2003). Contribution of the patagonia icefields of south america to sea level rise. *Science* 302, 434–437. doi: 10.1126/science.1087393

Rivera, A., Aravena, J. C., and Casassa, G. (1997). Recent fluctuations of glaciar Pío XI, patagonia: discussion of a glacial surge hypothesis. *Mount. Res. Dev.* 17, 309–322. doi: 10.2307/3674021

Rivera, A., Benham, T., Casassa, G., Bamber, J., and Dowdeswell, J. (2007). Ice elevation and areal changes of glaciers from the Northern Patagonia Icefield, Chile. *Glob. Planet. Change* 59, 126–137. doi: 10.1016/j.gloplacha.2006.11.037

Rivera, A., and Casassa, G. (2004). Ice elevation, areal and frontal changes of glaciers from National Park Torres del Paine, Southern Patagonia Icefield. *Arct. Antarct. Alp. Res.* 36, 379–389. doi: 10.1657/1523-0430(2004)036[0379:IEAAFC]2.0.CO;2

Rivera, A., Koppes, M., Bravo, C., and Aravena, J. C. (2012). Little Ice Age advance and retreat of Glaciar Jorge Montt, Chilean Patagonia, recorded in maps, air photographs and dendrochronology. *Climate Past* 8, 403–414. doi: 10.5194/cp-8-403-2012

Sakakibara, D., and, Sugiyama S. (2014). Ice-front variations and speed changes of calving glaciers in the Southern Patagonia Icefield from 1984 to 2011. *J. Geophys. Res. Earth Surf.* 119, 2541–2554. doi: 10.1002/2014JF003148

Scasso, R. A., Corbella, H., and Tiberi, P. (1994). Sedimentological analysis of the tephra from the 12-15 August 1991 eruption of Hudson volcano. *Bull. Volcanol.* 56, 121–132. doi: 10.1007/BF00304107

Schneider, C., Glaser, M., Kilian, R., Santana, A., Butorovic, N., and Casassa, G. (2003). Weather observations across the southern Andes at 53°S. *Phys. Geogr.* 24, 97–119. doi: 10.2747/0272-3646.24.2.97

Schneider, C., Schnirch, M., Acu-a, C., and Kilian, R. (2007). Glacier inventory of the Gran Campo Nevado Ice Cap in the Southern Andes and glacier changes observed during recent decades. *Glob. Planet. Change* 59, 87–100. doi: 10.1016/j.gloplacha.2006.11.023

Smith, B., and Sandwell, D. (2003). Accuracy and resolution of shuttle radar topography mission data. *Geophys. Res. Lett.* 30, 1–4. doi: 10.1029/2002GL016643

Smith, R. B., and Evans, J. P. (2007). Orographic precipitation and water vapor fractionation over the southern Andes. *J. Hydrometeorol.* 8, 3–19. doi: 10.1175/JHM555.1

Strelin, J., Casassa, G., Rosqvist, G., and Holmlund, P. (2008). Holocene glaciations in the Ema Glacier valley, Monte Sarmiento Massif, Tierra del Fuego. *Palaeogeogr. Palaeoclimatol. Palaeoecol.* 260, 299–314. doi: 10.1016/j.palaeo.2007.12.002

Strelin, J., and Iturraspe, R. (2007). Recent evolution and mass balance of Cordón Martial glaciers, Cordillera Fueguina Oriental. *Glob. Planet. Change* 59, 17–26. doi: 10.1016/j.gloplacha.2006.11.019

Tilling, R. L. (2009). Volcanism and associated hazards: the Andean perspective. *Adv. Geosci.* 22, 125–137. doi: 10.5194/adgeo-22-125-2009

Villalba, R., Lara, A., Boninsegna, J. A., Masiokas, M., Delgado, S., Aravena, J. C., et al. (2003). Large-Scale Temperature Changes across the Southern Andes: 20th-Century Variations in the Context of the Past 400 Years. *Clim. Change* 59, 177–232. doi: 10.1023/A:1024452701153

Wang, W., YOA, T., and Yang, X. (2011). Variations of glacial lakes and glaciers in the Boshula mountain range, southeast Tibet, from the 1970s to 2009. *Ann. Glaciol.* 52, 9–17. doi: 10.3189/172756411797252347

Warren, C. R., Rivera, A., and Post, A. (1997). Greatest Holocene advance of Glaciar Pío XI, Chilean Patagonia: possible causes. *Ann. Glaciol.* 24, 11–15. doi: 10.1017/S026030550001185X

Winchester, V., and Harrison, S. (1996). Recent oscillations of the San Quintin and San Rafael Glaciers, Patagonian Chile. *Geogr. Ann.* 78, 35–49. doi: 10.1080/04353676.1996.11880450

Winchester, V., and Harrison, S. (2000). Dendrochronology and lichenometry: colonization, growth rates and dating of geomorphological events on the east side of the North Patagonian Icefield, Chile. *Geomorphology* 34, 181–194. doi: 10.1016/S0169-555X(00)00006-4

Winchester, V., Harrison, S., and Warren, C. R. (2001). Recent retreat Glacier Nef, Chilean Patagonia, dated by lichenometry and dendrochronology. *Arct. Antarct. Alp. Res.* 33, 266–273. doi: 10.2307/1552233

Conflict of Interest Statement: The authors declare that the research was conducted in the absence of any commercial or financial relationships that could be construed as a potential conflict of interest.

frontiers in Earth Science

ORIGINAL RESEARCH
published: 19 June 2018
doi: 10.3389/feart.2018.00081

Glacier Mass Changes of Lake-Terminating Grey and Tyndall Glaciers at the Southern Patagonia Icefield Derived From Geodetic Observations and Energy and Mass Balance Modeling

Stephanie S. Weidemann[1,2], Tobias Sauter[3], Philipp Malz[3], Ricardo Jaña[4], Jorge Arigony-Neto[5], Gino Casassa[6,7] and Christoph Schneider[1]*

[1] Geography Department, Humboldt University, Berlin, Germany, [2] Department of Geography, RWTH Aachen University, Aachen, Germany, [3] Department of Geography, Friedrich-Alexander University, Erlangen, Germany, [4] Instituto Antártico Chileno, Punta Arenas, Chile, [5] Instituto de Oceanografia, Universidade Federal do Rio Grande, Rio Grande, Brazil, [6] Geoestudios Ltda, San José de Maipo, Chile, [7] Dirección de Programas Antárticos y Subantárticos, Universidad de Magallanes, Punta Arenas, Chile

OPEN ACCESS

Edited by:
Thomas Vikhamar Schuler, University of Oslo, Norway

Reviewed by:
Qiao Liu, Institute of Mountain Hazards and Environment (CAS), China
Daniel Farinotti, ETH Zürich, Switzerland
Alexander H. Jarosch, University of Iceland, Iceland

***Correspondence:**
Stephanie S. Weidemann
s.weidemann@geo.rwth-aachen.de

Specialty section:
This article was submitted to Cryospheric Sciences, a section of the journal Frontiers in Earth Science

Received: *26 November 2017*
Accepted: *29 May 2018*
Published: *19 June 2018*

Citation:
Weidemann SS, Sauter T, Malz P, Jaña R, Arigony-Neto J, Casassa G and Schneider C (2018) Glacier Mass Changes of Lake-Terminating Grey and Tyndall Glaciers at the Southern Patagonia Icefield Derived From Geodetic Observations and Energy and Mass Balance Modeling. Front. Earth Sci. 6:81. doi: 10.3389/feart.2018.00081

In this study we demonstrate how energy and mass fluxes vary in space and time for Grey and Tyndall glaciers at the Southern Patagonia Icefield (SPI). Despite the overall glacier retreat of most Patagonian glaciers, a recent increase in mass loss has been observed, but individual glaciers respond differently in terms of spatial and temporal changes. In this context, the detailed investigation of the effect of mass balance processes on recent glacier response to climate forcing still needs refinement. We therefore quantify surface energy-fluxes and climatic mass balance of the two neighboring glaciers, Grey and Tyndall. The COupled Snow and Ice energy and MAss balance model COSIMA is applied to assess recent surface energy and climatic mass balance variability with a high temporal and spatial resolution for a 16-year period between April 2000 and March 2016. The model is driven by downscaled 6-hourly atmospheric data derived from ERA-Interim reanalysis and MODIS/Terra Snow Cover and validated against ablation measurements made in single years. High resolution precipitation fields are determined by using an analytical orographic precipitation model. Frontal ablation is estimated as residual of climatic mass balance and geodetic mass balance derived from TanDEM-X/SRTM between 2000 and 2014. We simulate a positive glacier-wide mean annual climatic mass balance of $+1.02 \pm 0.52$ m w.e. a^{-1} for Grey Glacier and of $+0.68 \pm 0.54$ m w.e. a^{-1} for Tyndall Glacier between 2000 and 2014. Climatic mass balance results show a high year to year variability. Comparing climatic mass balance results with previous studies underlines the high uncertainty in climatic mass balance modeling with respect to accumulation on the SPI. Due to the lack of observations accumulation estimates differ from previous studies based on the methodological approaches. Mean annual ice loss by frontal ablation is estimated to be 2.07 ± 0.70 m w.e. a^{-1} for Grey Glacier

and 3.26 ± 0.82 m w.e. a^{-1} for Tyndall Glacier between 2000 and 2014. Ice loss by surface ablation exceeds ice loss by frontal ablation for both glaciers. The overall mass balance of Grey and Tyndall glaciers are clearly negative with −1.05 ± 0.18 m w.e. a^{-1} and −2.58 ± 0.28 m w.e. a^{-1} respectively.

Keywords: Patagonia, glacier climatic mass balance, frontal ablation, energy and mass balance model, orographic precipitation model, TanDEM-X

1. INTRODUCTION

1.1. Rationale

Most Patagonian glaciers have been thinning and retreating at high rates during the past decades. Mass loss of the Northern Patagonia Icefield (NPI) and the Southern Patagonia Icefield (SPI) contributed to sea-level rise by 0.042 ± 0.002 mm a^{-1} between 1964/1975 and 2000 (Rignot et al., 2003), increasing to 0.067 ± 0.004 mm a^{-1} between 2000 and 2012 (Willis et al., 2012b). The main driver of the long-term demise of the ice-fields is most likely to be the warming climate (e.g., Rignot et al., 2003; Sakakibara and Sugiyama, 2014). Observed annual air temperatures at surface stations have increased by + 0.04°C to + 1.4°C south of 46°S during the past century (Rosenblüth et al., 1995). No significant trend of precipitation has been observed since 1950, but large inter-annual and decadal variations have been found (Carrasco et al., 2008; Aravena and Luckman, 2009; Lenaerts et al., 2014). Reanalysis data from 1960 to 2000 however show a slight decrease in solid precipitation over the ice-fields as a result of increasing air temperatures (Rasmussen et al., 2007).

Despite the general retreat of the outlet glaciers of the NPI and SPI, the individual responses show spatial and temporal non-uniform patterns (e.g., Aniya et al., 1996; Rivera and Casassa, 1999; Rivera et al., 2007; Lopez et al., 2010; Davies and Glasser, 2012; Sakakibara and Sugiyama, 2014; Minowa et al., 2015; Malz et al., 2018). Recent retreats of calving glaciers, such as Upsala and Jorge Montt glaciers are associated with ice flow acceleration and ice dynamical thinning near the calving front (Naruse and Skvarca, 2000; Rivera et al., 2012; Jaber et al., 2013; Muto and Furuya, 2013; Sakakibara and Sugiyama, 2014; Mouginot and Rignot, 2015). However, only a small number of NPI and SPI outlet glaciers show an extraordinary retreat including a recent ice speed acceleration between 2000 and 2011. The mean ice speed of the NPI and SPI even decreased between 2000 and 2011 compared to the time period of 1984 to 2000 (Sakakibara and Sugiyama, 2014). The recent increase in mass loss of the NPI and SPI therefore still seems to be mainly caused by long-term warming, while fjord geometry and ice dynamic processes are responsible for the rapid frontal retreat of individual calving glaciers, which enhances the mass loss (Casassa et al., 1997; Koppes et al., 2011; Rivera et al., 2012; Willis et al., 2012a,b; Sakakibara and Sugiyama, 2014). Recent surface mass balance modeling studies, however, estimate positive surface mass balance for the NPI and SPI, suggesting a slight increase in precipitation and cooling of the upper-atmospheric temperatures during the last decade as being the main driver (Lenaerts et al., 2014; Schaefer et al., 2015; Mernild et al., 2016). The contrasting pattern of observed glacier retreat and positive surface mass balance are assumed to be a result of increasing ice flow velocities associated with ice loss due to calving. However, ice loss due to increasing ice flow velocities has been observed only for those few tide-water glaciers undergoing a recent rapid glacier change.

In this study we demonstrate how energy and mass fluxes vary in space and time for Grey and Tyndall glaciers at the SPI. We aim to compute high resolution 6-hourly fields of surface energy fluxes and climatic mass balance for two neighboring glacier catchments by applying the COupled Snowpack and Ice surface energy and MAss balance model (COSIMA) (Huintjes et al., 2015) between 2000 and 2016. Different statistical downscaling methods are used to derive atmospheric input datasets. Precipitation fields are generated by applying an orographic precipitation model (OPM hereafter) based on the linear theory of orographic precipitation by Smith and Barstad (2004). The model has also been implemented successfully in several previous glaciological studies (Schuler et al., 2008; Jarosch et al., 2012; Weidemann et al., 2013). Cloudiness patterns are obtained from MODIS satellite data product MOD10A1 to correct for spatial variations of solar radiation. Geodetic mass balance changes are obtained by subtracting high-resolution TanDEM-X and SRTM data between 2000 and 2014 (Malz et al., 2018). We derive frontal ablation from modeled climatic mass balance and geodetic mass balance for each glacier for the same study period. The paper focuses on the validation of the downscaling results of atmospheric input data, and the comparison of modeled surface energy-fluxes, modeled climatic mass balance, and derived frontal ablation between both study sites.

1.2. Study Area

The study sites Grey and Tyndall glaciers are located at the southeastern part of the SPI (50.7°S–51.30°S, 73.5°W–73.1°W) (**Figure 1**). In 2016, glacier areas were 239.0 and 301.4 km^2, respectively (Meier et al., 2018). The Equilibrium Line Altitude (ELA) is estimated to be 970 ± 50 m above sea level (a.s.l.) for Grey Glacier (De Angelis, 2014; Schaefer et al., 2015) and 925 ± 25 m a.s.l. for Tyndall Glacier (Nishida et al., 1995; De Angelis, 2014).

Grey Glacier calves into a proglacial lake divided into three glacier termini which have shown different retreat and thinning rates over the last decades. The highest flow velocities of up to 2.8 m d^{-1} are observed at the central front of the glacier (Schwalbe et al., 2017). The glacier front has remained rather stable over the past two decades. According to Davies and Glasser (2012), both glaciers showed similar annual shrinkage of about −0.1 to −0.15% (1970–2011), with the fastest period of area loss occurring from 1986 to 2001.

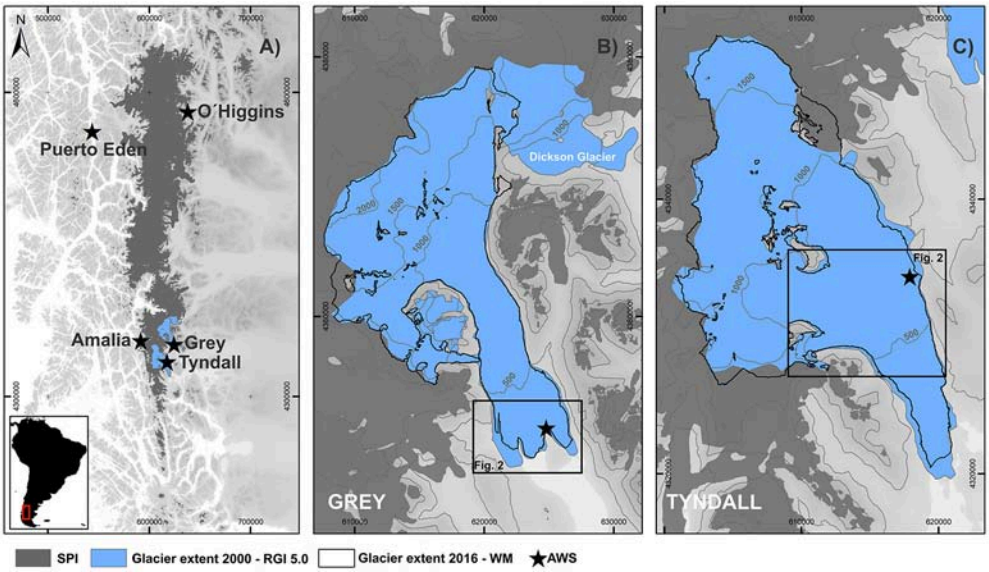

FIGURE 1 | (A) The location of Grey and Tyndall glaciers at the SPI and the location of the weather stations Puerto Eden, O'Higgins, Amalia, Tyndall and Grey, **(B)** Grey Glacier including the location of AWS Grey, **(C)** Tyndall Glacier including the location of AWS Tyndall. Glacier outlines are visualized for 2000 based on the RGI 5.0 and for 2016 based on a new glacier inventory by Meier et al. (2018). The coordinates are in UTM zone 18S in meters.

Information on accumulation amounts on the central part of the SPI are rare and mostly rely on a few firn cores retrieved of shallow to medium depth. The harsh weather conditions and the strong influence of meltwater percolation in the main plateaus are the prime reasons for sparse datasets (Godoi et al., 2002; Casassa et al., 2006). Three drilling sites located on the SPI allow estimation of a mean accumulation of 1.2 m water equivalent (w.e.) a^{-1} at Perito Moreno at 2,000 m a.s.l. in 1980/81-1985/86 (Aristarain and Delmas, 1993), 12.9–14.7 m w.e. a^{-1} at 1,756 m a.s.l. at Tyndall Glacier in 1998/99 with a firn-ice transition at 42.5 m depth (Godoi et al., 2002; Shiraiwa et al., 2002; Kohshima et al., 2007), and 3.4–7.1 m w.e. a^{-1} at 2,600 m a.s.l. at Pio XI Glacier for the period 2000–2006 with a firn-ice transition at 50.6 m depth (Schwikowski et al., 2013). These observations suggest high spatial differences of accumulation in the upper part of the SPI, indicating also that these findings might be strongly influenced by local conditions at the drilling sites.

2. DATA

2.1. Observations

Two automatic weather stations (AWS) are situated at Grey Glacier. AWS Grey has been running since March 2015 and measures hourly incoming solar radiation, wind speed and direction, air temperature, relative humidity at 2 m above the surface, and precipitation. Precipitation is measured at a height of 1 m using an unshielded tipping-bucket rain gauge. AWS Grey is located on rock close to the glacier margin between the eastern and middle front of Grey Glacier (**Figure 1**) at 50.98°S, 73.22°W at 229 m a.s.l. For modeling purpose, we installed an additional basic AWS in the ablation area at 50.97°S, 73.22°W for a period of 6 months from March 2015 to September 2015, measuring solar radiation, air temperature, and relative humidity. High coefficients of determination of 0.95–0.98 have been detected between the hourly datasets of both stations. To account for the cooling effect of the glacier surface we applied a bias-correction of air temperature as described in section 3.1.1.

The Chilean Water Directorate (DGA) provides additional AWS datasets within the study area. The AWS Tyndall is installed at 51.14°S, 73.35°W on the ablation area of Tyndall Glacier at 627 m a.s.l. and has been running since December 2013. This dataset contains hourly data of incoming and outgoing shortwave and longwave radiation, air temperature and humidity, surface pressure, wind speed and wind direction. Precipitation data of the weather stations Puerto Eden, O'Higgins, and Amalia are used for OPM validation. The weather stations Amalia and Puerto Eden are located west of the SPI at 50.95°S, 73.69°W at 60 m a.s.l. and 49.1°S, 74.4°W at 10 m a.s.l., while the weather station O'Higgins is situated at 48.91°S, 73.11°W at 265 m a.s.l. on the eastern margin of the SPI (**Figure 1**). Precipitation at Puerto Eden was measured from 1998 to 2010 although there are several data gaps. Data from the weather station O'Higgins covers the period from 2010 to 2014 while precipitation data from the weather station Amalia is limited to the period from June 2015 to April 2016.

Additionally, ablation stake measurements are available for Grey Glacier and Tyndall Glacier. Observations at Grey Glacier are limited to three time periods from January to March 2015, March to September 2015, and September 2015 to January 2016. Surface elevation changes of up to −8 m during the austral summer 2015/16 caused a complete melt-out of most stakes. Stake measurements were taken along a transect between 550 and 576 m a.s.l. on Tyndall Glacier from November 2012 to May 2013 (Geoestudios, 2013).

2.2. Reanalysis Data

Atmospheric model input datasets for COSIMA and OPM are derived from the latest large-scale ERA-Interim reanalysis product supplied by the European Centre for Medium-Range Weather Forecasts (ECMWF) (Dee et al., 2011).

COSIMA is forced by downscaled 6-hourly surface incoming solar radiation SW_{in} (W m^{-2}) and air temperature T_{2m} (°C), as well as relative humidity rH_{2m} (%), surface pressure p_s (hPa), and wind speed at 2 m u_{2m} (m s^{-1}), derived from the grid point located closest to the study sites (51.0°S, 73.5°W) for the time period from April 1st, 2000 to March 31st, 2016.

Running the OPM to compute liquid P_{liq} and solid precipitation P_{solid} (m) requires the following 6-hourly ERA-Interim atmospheric datasets: horizontal and vertical wind components, temperature, relative humidity, geopotential heights, and large-scale precipitation. The environmental and moist adiabatic lapse rates are calculated using datasets of air temperatures from the 850 and 500 hPa levels. The wind components of the 850 hPa level are used as large-scale prevailing wind conditions. The data of precipitation and relative humidity (850 hPa) are needed to calculate the background precipitation and filter constraints within the OPM routine as described in section 3.1.3. Since the atmospheric input of the OPM should represent upstream conditions, data is averaged over six grid points located west along the SPI (50.0°S–53.0°S, 75°W–73.5°W).

2.3. Cloud Cover

Cloud cover information is required to correct the spatial distribution of incoming solar radiation. Binary cloud cover information is included by default in the daily MODIS (Moderate Resolution Imaging Spectroradiometer) snow cover product MOD10A1 Version 6 (Hall and Riggs, 2016) with a spatial resolution of 500 m. MOD10A1 has also been used successfully in previous studies over snow and ice-covered grounds (e.g., Möller et al., 2011; Spiess et al., 2016).

Daily fractional cloud cover is further derived by averaging the binary cloud cover information of a fixed 5 × 5 grid point window for each central grid point within the COSIMA modeling domain. This method is used to calculate fractional cloud cover in the MODIS product MOD06L2 and has also been customized for the MOD10A1 product by Möller et al. (2011). Fractional cloud cover information serves as COSIMA input for parametrization of the incoming and outgoing longwave radiation.

2.4. Elevation Data And Glacier Outline

The digital elevation model (DEM) generated from the Shuttle Radar Topography Mission (SRTM) (Hoffmann and Walter, 2006; Jarvis et al., 2008) is used as the reference surface elevation in 2000 for COSIMA and OPM runs. COSIMA and OPM runs are carried out with a spatial resolution of 500 and 1,000 m, respectively. Glacier outlines for model runs have been used from the Randolph Glacier Inventory RGI 5.0 for 2000 (Consortium, 2015) to compare COSIMA results with previous surface mass balance studies (Schaefer et al., 2015; Mernild et al., 2016). In the RGI 5.0 the catchment of Grey Glacier also includes the neighboring Dickson Glacier (**Figure 1**).

Mean annual surface height changes between 2000 and 2014 are derived from SRTM and TanDEM-X data (Malz et al., 2018). This data is further needed for geodetic mass balance and frontal ablation estimations. Furthermore, annual surface height changes are considered in the altitude dependent calculation of atmospheric variables, e.g., air temperature in COSIMA.

3. METHODOLOGY

3.1. Surface Energy And Mass Balance

Climatic mass balance changes are estimated using the open source COupled Snowpack and Ice surface energy and MAss balance model (COSIMA) that was designed and validated in detail by Huintjes et al. (2015). COSIMA combines a surface energy balance model with a multi-layer sub-surface snow and ice model to fully resolve energy fluxes and mass balance processes.

The energy balance model combines all energy fluxes F that contribute to the surface energy budget and calculates the energy available for surface melting Q_{melt} (Oerlemans, 2001):

$$F = SW_{in} \cdot (1-\alpha) + LW_{in} + LW_{out} + Q_{sens} + Q_{lat} + Q_g + Q_{liq}. \quad (1)$$

It takes into consideration: the shortwave incoming radiation SW_{in}, the albedo α, the incoming LW_{in} and outgoing longwave radiation LW_{out}, the sensible Q_{sens} and the latent heat flux Q_{lat}, the ground heat flux Q_g, and the heat flux of liquid precipitation Q_{liq}. The latter is normally neglected (Cuffey and Paterson, 2010) but has been included here due to the significant amount of liquid precipitation in the ablation area of Patagonian glaciers.

Ablation occurs due to sublimation, subsurface melt, and surface melt. Q_{melt} requires the surface temperature T_s to be at the melting point (0°C) and a positive energy flux F toward the surface to prevail. In this case, Q_{melt} equals F. If T_s is below the melting point, no melt occurs. The subsurface snow module is structured in layers of 0.2 m thickness with a domain depth of 100 m (**Table 1**). Each layer is characterized by a temperature, density and liquid water content. The densification of the dry-snow pack is calculated using an empirical relation according to Herron and Langway (1980). The initial density profile of the snow pack is calculated by a linear interpolation between 250 and 550 kg m^{-3}. Different values of albedo for snow, firn and ice are considered (**Table 1**). A key variable to link the surface and subsurface modules is T_s since it controls the conductive heat flux between the surface and the two upper subsurface layers as well as defining LW_{out} and providing the lower temperature for calculating sensible and latent heat flux according to the bulk approach. Energy balance and subsurface heat conduction each provide T_s. Both modules are solved iteratively until the convergence of T_s. The initial subsurface temperature T_{sub} profile is linearly scaled from depth to the glacier surface between -1°C and 0°C (**Table 1**). In case modeled T_{sub} or T_s exceeds the melting point, it is set to 0°C and the remaining energy is used for subsurface or surface melt, respectively.

The parametrization of α is calculated as a function of snowfall frequency and snow depth following the scheme of Oerlemans and Knap (1998). The amount of incoming longwave radiation

TABLE 1 | Best-fit COSIMA and OPM parameter settings.

	Parameter	*Value*/ Range	Unit	Fixed/ Calculated	Source
COSIMA	Total domain depth	100	m	F	–
	Model layer thickness	0.1	m	F	–
	Ice albedo	0.3	–	F	Schaefer et al., 2015
	Fresh snow albedo	0.9	–	F	Huintjes et al., 2015
	Firn albedo	0.45	–	F	Schaefer et al., 2015
	Temperature lapse rate	−0.73	°C 100 m^{-1}	F	ERA-Interim
	Surface pressure gradient	−0.105	hPa m^{-1}	F	ERA-Interim
	Snow density for P_{solid}	250	kg m^{-3}	F	Huintjes et al., 2015
	Threshold for P_{solid} to P_{liq}	0–2.0	°C	F	Möller et al., 2007
	Snow pack density profile	250 to 550	kg m–3	C	Huintjes et al., 2015
OPM	Uplift sensitivity factor	0.006*	–	C	Smith and Barstad, 2004
	Water vapor scale height	2466*	m	C	Smith and Barstad, 2004
	Conversion/fallout time scale	1453*	m s^{-1}	C	Jiang and Smith, 2003
	Brunt-Väisälä frequency	0.008*	s^{-1}	C	Smith and Barstad, 2004
	Averaged falling speed	1.3	m s^{-1}	F	Weidemann et al., 2013
	Froude number	0.87*	–	C	Kunz and Kottmeier, 2006
	Threshold Froude number	≥1	–	F	–
	Thresholds relative humidity	90	%	F	Smith and Barstad, 2004

*Values denoted with * are mean values.*

is parametrized from air temperature, water vapor pressure and cloud cover fraction while outgoing longwave radiation is calculated from the surface temperature using the Stefan-Boltzmann law, assuming an emissivity of one.

Turbulent heat fluxes Q_{sens} and Q_{lat}, are calculated through the bulk aerodynamic method according to Oerlemans (2001) between the surface and two meters above ground by means of T_{2m}, rH_{2m} and u_{2m}. Q_g describes the sum of conductive heat flux and the energy flux from penetrating shortwave radiation. Heat flux through liquid precipitation depends on the temperature differences between the surface and a height of 2 m and the amount of liquid precipitation (Maniak, 2010).

Melt water production at the glacier surface serves as input for the snow model to simulate percolation, retention and refreezing of melt water within the snow pack. COSIMA is described in more detail by Huintjes et al. (2015).

3.1.1. Air Temperature

Air temperature is statistically downscaled from ERA-Interim data to AWS Grey and AWS Tyndall by using Quantile Mapping (e.g., Panofsky and Brier, 1968; Gudmundsson et al., 2012). Quantile Mapping is a common technique for statistical bias correction of climate-model outputs by mapping the modeled cumulative distribution function of the variable of interest onto the observed cumulative distribution function that has been derived from empirical percentiles (Gudmundsson et al., 2012).

Bias-corrected air temperature is spatially interpolated using a fixed lapse rate from the AWS locations. The lapse rate is calculated from nine ERA-Interim grid points over the study area using monthly T_{2m}. Furthermore, the surface elevation is updated each mass balance year based on the mean annual surface elevation changes from 2000 to 2014 observed by Malz et al. (2018). Surface elevation changes since 2014 are then kept constant.

3.1.2. Solar Radiation

Incoming shortwave radiation SW_{in} is taken from ERA-Interim and downscaled to AWS data using Quantile Mapping. The spatial distribution of SW_{in} is derived from a modified radiation model according to Kumar et al. (1997) that computes clear-sky direct and diffuse shortwave radiation depending on the geographical position, elevation, albedo and shading by the surrounding terrain, and the slope and aspect of each grid cell. The potential clear-sky radiation $SW_{in,pot,glacier}$ is corrected for cloud cover by downscaled ERA-Interim $SW_{in,AWS}$ at the AWS grid point.

At each time step the ratio $r_{SW,pot,glacier}$ of $SW_{in,pot,AWS}$ at the AWS location and any other pixel $SW_{in,pot,glacier}$ in the glacier domain is calculated. The spatial distribution of $SW_{in,glacier}$ including the effects of cloud cover and terrain shading at each grid point is calculated by:

$$SW_{in,glacier} = r_{SW,pot,glacier} \cdot SW_{in,AWS}. \quad (2)$$

Equation (2) assumes a homogenous cloud cover over the glacier area. Since in reality the cloud cover varies between the AWS location and the upper parts of the glacier, an additional cloud cover correction factor is included. In cases when the cloud cover differs between the AWS location and any other location on the glacier, $SW_{in,glacier}$ is calculated as follows:

$$SW_{in,glacier,cloudy} = r_{SW,pot,glacier} \cdot SW_{in,AWS} \cdot \acute{\eta} \quad (3)$$

$$SW_{in,glacier,clear} = r_{SW,pot,glacier} \cdot \frac{SW_{in,AWS}}{\acute{\eta}} \quad (4)$$

Equation (3) corrects the distribution of incoming solar radiation glacier-wide in case of clear sky conditions at the AWS and cloudy conditions over the glacier, while Equation (4) is used in case of inverse conditions between AWS and the remaining parts of the glacier. $\acute{\eta}$ describes an empirical coefficient being 0.4 at 51°S (Budyko, 1974). The coefficient implies that during fully overcast conditions the clear-sky incoming shortwave radiation is reduced by 60%.

3.1.3. Precipitation

Precipitation distribution is modeled using an analytical orographic precipitation model (OPM) based on the linear steady-state theory of airflow dynamics (Smith and Barstad, 2004; Barstad and Smith, 2005). A more detailed description and validation of the model itself is given by Smith and Barstad (2004) and Barstad and Smith (2005) while the methodical application as used in this study is described in more detail in Weidemann et al. (2013).

The OPM estimates precipitation resulting from forced orographic uplift of air masses over a mountain assuming stable and saturated atmospheric conditions. The model estimates the condensation rate by the terrain-induced vertical air velocity, the horizontal wind speed and advection of water vapor, and includes effects of airflow dynamics and downslope evaporation as well. The main term of the linear model describing the orographic precipitation generation is solved in Fourier space for each Fourier component (k,l) as follows:

$$\hat{P}(k,l) = \frac{C_w \cdot i \cdot \sigma \cdot \hat{h}(k,l)}{(1 - i \cdot m \cdot H_w)(1 + i \cdot \sigma \cdot \tau_c)(1 + i \cdot \sigma \cdot \tau_f)}. \quad (5)$$

Equation (5) includes an uplift sensitivity factor C_w, the water vapor scale height H_w, the complex number i, the intrinsic frequency σ, the Fourier transform of the orography $\hat{h}$, and the vertical wavenumber m and the delay time scales for conversion τ_c and fallout τ_f of hydrometeors. The thermodynamic sensitivity C_w accounts for the effects of saturation water vapor density, the moist adiabatic and environmental lapse rates. H_w mainly depends on the environmental air temperature and lapse rate. Airflow dynamics are represented by the intrinsic frequency, including the vertical and horizontal winds. One of the airflow features included is the decay of vertical velocity with altitude which is described by m. The calculation of m contains the buoyancy frequency in saturated atmosphere and the moist Brunt-Väisälä frequency N_m to consider the effect of moist air masses on the static stability. Additionally, the precipitation generation is shifted downstream from the water source region depending on the wind speed and the cloud time parameter τ_c and τ_f.

The final term of orographic precipitation distribution is obtained by an inverse Fourier Transformation

$$P_{oro}(x,y) = \int\int \hat{P}(k,l) \cdot e^{i\cdot(kx+ly)} \cdot dk \cdot dl. \quad (6)$$

Final total precipitation fields are then generated by considering large-scale precipitation which we hereafter refer to as background precipitation P_{back}. The procedure of final precipitation and P_{back} calculations is described in the following.

The application of the OPM is limited to stable and saturated air masses, not capturing flow blocking effects or being applicable during unstable atmospheric conditions. Time intervals which do not fulfill the model constraints have to be filtered out. To ensure saturated and stable atmospheric conditions, relative humidity rH, N_{m}, and the moist Froude number are suitable as model constraints (e.g., Smith and Barstad, 2004; Schuler et al., 2008; Jarosch et al., 2012; Weidemann et al., 2013). The moist Froude number describes the airflow regime as a dimensionless number and can be associated to specific orographic precipitation patterns (Kunz and Kottmeier, 2006). In this study, it is used as an index to ensure linear airflow without flow blocking.

We need to run the OPM twice to replace the orographic fraction of ERA-Interim precipitation by high resolution orographic precipitation fields (e.g., Schuler et al., 2008; Weidemann et al., 2013). In the first step, the OPM is forced by ERA-Interim atmospheric and elevation data to determine P_{back} under consideration of the model constraints by subtracting the modeled orographic fraction from ERA-Interim precipitation. The second step implies the application of the OPM to the SRTM elevation model at a high spatial resolution of 1 km using the same input parameters to achieve high resolution P_{oro} fields. A threshold is applied to ensure positive values of P_{oro}. Finally, high-resolution total precipitation fields (P) are calculated by means of P_{oro} and P_{back} under consideration of the model constraints. In case model constraints are complied with, P_{oro} is added to P_{back}. Otherwise, only P_{back} is assumed.

The amount of solid precipitation P_{solid} is calculated by:

$$P_{solid} = P \cdot f, \quad (7)$$

$$f = 0.5 \cdot (-tanh((T_{2m} - 1) \cdot 3) + 1). \quad (8)$$

Applying Equation (7), the proportion of solid precipitation to total precipitation f is smoothly scaled between 100% and 0% within a T_{2m} range of 0°C and 2°C (Möller et al., 2007; Weidemann et al., 2013).

3.2. COSIMA-Calibration

As calibration for climatic mass balance results we use ablation stake measurements made at Grey Glacier from 2015/2016. We run COSIMA with varying parameter settings of model domain depth, layer depth, initial temperature profile, and albedo values for ice and snow based on values used in Huintjes et al. (2015) and Schaefer et al. (2015) to achieve the best model fit at the location of stakes for the measurement period. The RMSE between the

best model fit and observed values is ±0.53 m w.e. COSIMA reproduces well the measured ablation amounts in winter and summer, as shown in **Figure 2**. In case of Grey Glacier, COSIMA tends to underestimate ablation. Best fit model parameters are listed in **Table 1**.

Surface mass balance observations based on stake measurements at Tyndall Glacier from November 2012 to May 2013 are in good agreement with modeled climatic mass balance as well, with a RMSE of ±0.64 m w.e. COSIMA overestimates ablation in average by 6.5%.

3.3. COSIMA-Uncertainties

The uncertainties of modeled climatic mass balance are estimated by accounting for uncertainties in the spatial distribution of input datasets of air temperature and solid precipitation due to the lack of observations in the accumulation area. The spatial distribution of air temperature is determined by the chosen lapse rate, while the amount of modeled precipitation is mainly controlled by the OPM filter constraint *rH*. We therefore include varying values of these for the assessment of climatic mass balance uncertainties as described in the following section.

The best fit parameter setting based on our findings is listed in **Table 1** including a calculated air temperature lapse rate of 0.73°C 100 m^{-1} and a threshold for the OPM filter constraint *rH* of 90%. In addition, a second air temperature lapse rate of 0.67°C 100 m^{-1}—as used in earlier mass balance studies (e.g., Fernández and Mark, 2016)—and two *rH* thresholds of 85 and 95% are considered. In total, six runs are carried out for the mass balance year 2015/16 to assess the uncertainty of glacier-wide climatic mass balance and surface height change related to this climatic mass balance. This results in standard deviations of ±0.52 m w.e. and ±0.65 m w.e. for Grey Glacier and ±0.54 and ±0.67 m for Tyndall Glacier.

3.4. Geodetic Mass Balance Derived From TanDEM-X/SRTM

For DEM production, a differential SAR interferometric approach was used to generate a DEM out of bi-static TanDEM-X and TanSAR-X image pairs. Afterwards, the resulting DEM needed refined horizontal and vertical adjustments on the reference DEM (SRTM). Details about the interferometric processing and postprocessing can be found in detail in Malz et al. (2018).

After DEM generation, annual surface elevation changes were computed by differencing the TanDEM-X from the reference SRTM DEM for the time period between both acquisitions with

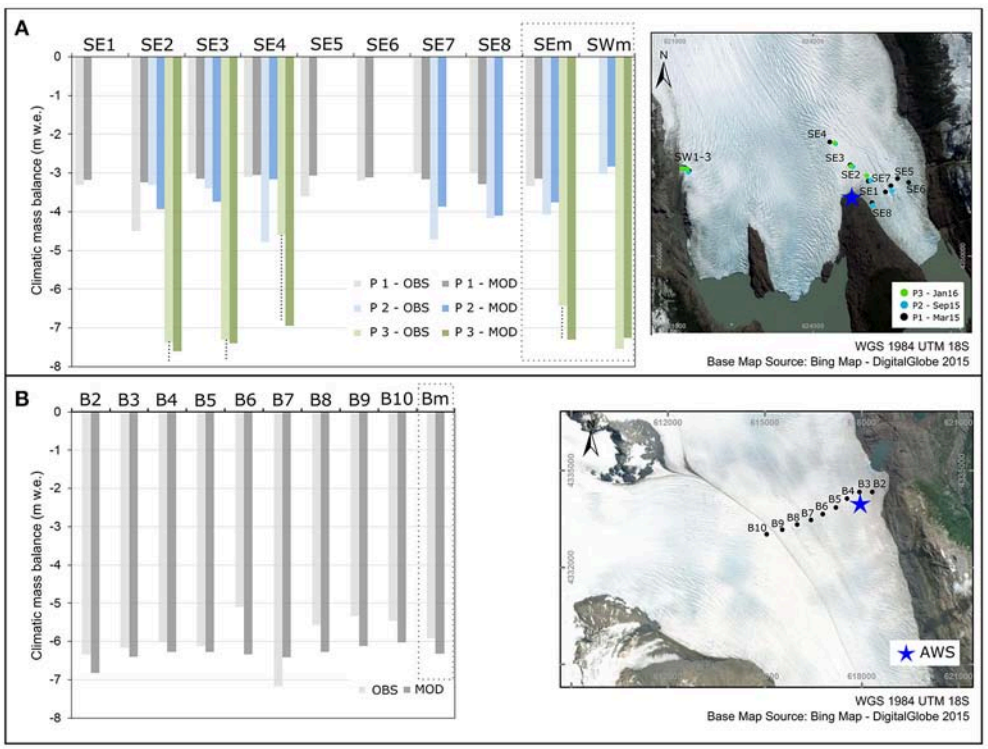

FIGURE 2 | Comparison of modeled and observed climatic mass balance at Grey Glacier and Tyndall Glacier by means of ablation stake data. **(A)** Measurements at Grey Glacier were carried out three times: from January 2015 to March 2015 (P1), March 2015 to September 2015 (P2), and September 2015 to January 2016 (P3). *SWm* is the mean of measured ablation at the western glacier tongue and *SEm* mean values of the ablation at the eastern glacier tongue. The black dashed lines indicate that the observed surface mass balance values represent only minimum values since these stakes melted completely out over the austral summer 2015/16, **(B)** surface mass balance observations at Tyndall Glacier are available along a transect (B2-B10) from November 2012 to May 2013 (Geoestudios, 2013). *Bm* is the mean of measured ablation. The coordinates of the subset maps are in UTM zone 18S in meters.

a spatial resolution of 30 × 30 m. In this study, we further interpolated the final product to a spatial resolution of 500 m × 500 m as used in COSIMA to later derive the amount of frontal ablation. For both glaciers, surface height changes based on TanDEM-X/SRTM are converted to mass balance changes using a constant density of 850 kg m^{-3} (Huss, 2013) and to volume changes by multiplying with the pixel area (500 × 500 m).

We assess the uncertainties of elevation change rate dh/dt and mass balance M using a simplified error propagation of Malz et al. (2018). Mass balance uncertainty (ϵ_M) is estimated using:

$$\epsilon_M = |M| \cdot \sqrt{\left(\frac{\delta_{dh/dt}}{dh/dt}\right) \cdot \left(\frac{\delta_\rho}{\rho}\right)} \quad (9)$$

considering the uncertainty δ of elevation change rate dh/dt and of density ρ for mass conversion. The uncertainty of elevation change rate includes the error of the relative vertical accuracy of SRTM and TanDEM-X DEM, the radar penetration into snow and ice and an inaccuracy resulting from the extrapolation during gap filling Malz et al. (2018). For Grey and Tyndall glaciers, this results in $\delta_{dh/dt}$ of 0.19 and 0.24 m a^{-1} for the study period of 2000–2014. A density uncertainty δ_ρ of 60 kg m^{-3} is taken into account while converting elevation changes to mass balance changes.

4. RESULTS AND DISCUSSION

4.1. Atmospheric Data

The evaluation of COSIMA input based on ERA-Interim, downscaled ERA-Interim and MODIS is summarized in Table S1 for Grey and Tyndall glaciers for each mass balance year (April 1st to March 31). Results of downscaled air temperature, solar radiation and precipitation will be discussed in more detail in the following section. Annual glacier-wide means and standard deviations are given below for the study period of 2000 to 2016.

4.1.1. Air Temperature

Downscaling results of daily ERA-Interim T_{2m} by means of station data are visualized in **Figure 3** for both AWS Grey and AWS Tyndall, respectively. Data from AWS Tyndall is split into a validation [April to October 2015 (yellow)] and calibration period. For the validation period, low temperatures are underestimated while high temperatures are overestimated.

The glacier-wide mean T_{2m} averaged over the whole study period is −2.4 ± 0.6°C for Grey Glacier and −0.7 ± 0.5°C for Tyndall Glacier. Glacier-wide air temperatures are higher than the mean value for the complete study period from 2003/04 to 2008/09 and 2011/12 to 2015/16. Air temperatures are lower than the average by 1.0°C to 1.3°C in 2001/02 and 2002/03. For the mass balance years 2004/05 to 2008/09, Mernild et al. (2016) simulates lower glacier-wide air temperatures of −2.7 ± 0.2°C and −1.0 ± 0.2°C compared to our results of −2.1 ± 0.2°C and −0.4 ± 0.2°C for Grey and Tyndall glaciers, respectively. For the time period of 2009/10 to 2013/14 both studies show slightly colder conditions.

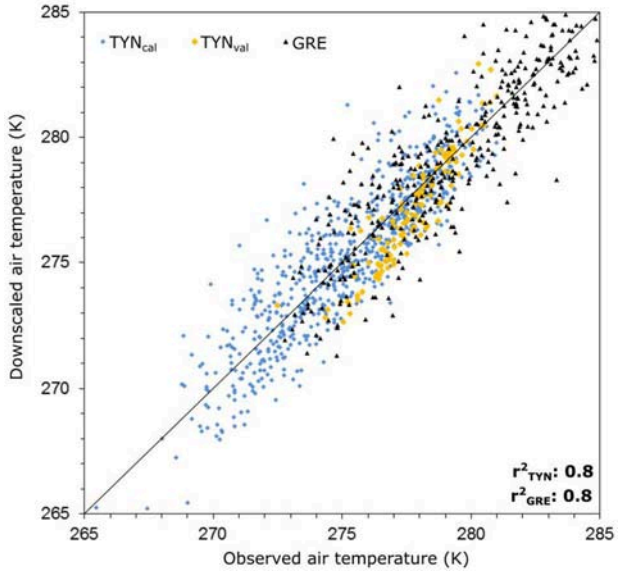

FIGURE 3 | Downscaled ERA-Interim T_{2m} vs. observed data of AWS Grey (GRE) and AWS Tyndall (TYN). Data of AWS Tyndall from April to October 2015 (yellow) is used as validation.

4.1.2. Solar Radiation and Cloud Cover

SW_{in} of ERA-Interim and AWS Tyndall and AWS Grey are in good agreement with each other and achieve high correlation. The bias-correction based on Quantile Mapping as described earlier led to better results regarding the overall sums and maximal values. As shown in **Figure 4** downscaled ERA-Interim data and observed data are in good agreement. The coefficient of determination is 0.8 for both AWS. Spatial fields of SW_{in} corrected by AWS data and MODIS cloud cover show an altitude-dependent pattern. The glacier-wide means of SW_{in} averaged over the study period are 109 ± 4 and 127 ± 5 W m^{-2} for Grey and Tyndall glaciers respectively (Table S1).

Cloud cover patterns by MODIS10A1 show overcast conditions during 90% of the time at the upper parts of both glaciers. Mean cloud cover is less in the lower parts with values ranging from 55 to 80%. The glacier-wide mean is 85 ± 0.1% for Grey Glacier, while overcast conditions at Tyndall Glacier occur 79 ± 0.1 % of the time.

4.1.3. Precipitation

OPM runs have been carried out with varying thresholds of the model constraint rH according to the values used in previous studies (e.g., Crochet et al., 2007; Schuler et al., 2008; Jarosch et al., 2012) to find the best model fit compared to observed data. We chose the measurement period from AWS Grey from April 2015 to March 2016 to be the calibration period and, the available data from AWS Grey and the weather station Amalia to be the calibration data. Best fits have been achieved using the constraint $rH \geq 90$ which has also been applied successfully at the Gran Campo Nevado Ice Cap by Weidemann et al. (2013). For the given constraints, the OPM performs 55% of the time.

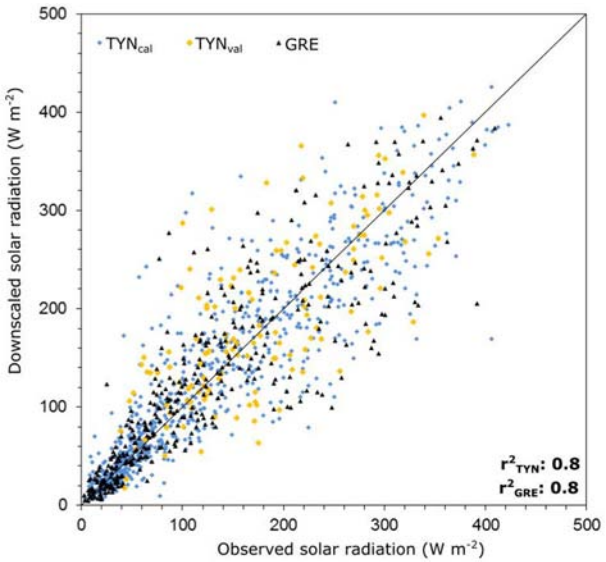

FIGURE 4 | Downscaled ERA-Interim SW_{in} vs. observed data of AWS Grey (GRE) and AWS Tyndall (TYN). Data of AWS Tyndall from April to October 2015 (yellow) is used as validation.

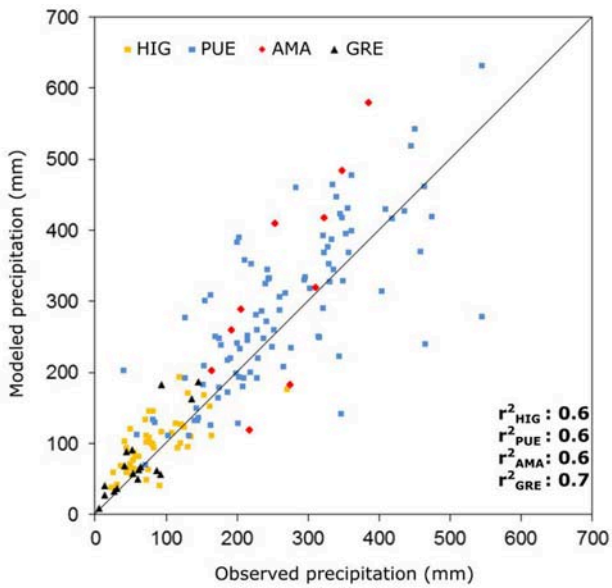

FIGURE 5 | Monthly modeled precipitation (mm) by OPM simulations and observed precipitation of the weather stations Puerto Eden (PUE), O'Higgins (HIG), Amalia (AMA), Tyndall (TYN), and Grey (GRE).

Best-fit OPM results are compared to observed precipitation data from four weather stations as illustrated in **Figure 5**. The explained variance between modeled and observed monthly precipitation data are 64% for the stations Puerto Eden, Amalia, and O'Higgins, and 73% for AWS Grey. The amount of modeled orographic precipitation accounts for 79.7 and 41.2% of the total modeled precipitation amount for the weather station Amalia and the AWS Grey, respectively. The weather stations Puerto Eden and O'Higgins are less influenced by orographic effects (orographic fraction less than 15%) due to the larger distance to the mountain range leading to a small fraction of modeled orographic precipitation. At these locations, modeled precipitation is mainly determined by the modeled background precipitation, which is based on ERA-Interim precipitation. The annual amounts of ERA-Interim precipitation are reduced by up to 15% in the central parts of the mountain range after subtracting the modeled orographic fraction from ERA-Interim precipitation as part of the background precipitation calculation.

Varying the filter constraint rH determines the amount of modeled orographic precipitation which is either reduced or enhanced. Therefore, this affects in particular the modeled precipitation at the locations of the weather station Amalia and the AWS Grey, which are highly influenced by orographic effects. Mean annual modeled precipitation amounts increase by 3–6% using $rH \geq 85$ at the four weather stations, while they decrease by 2–14% using $rH \geq 95$. Maximal annual precipitation amounts are in general shifted slightly to the windward side of the SPI mountain range. Depending on the filter constraints, the maximal annual precipitation amounts differ by around ±15% compared to $rH \geq 90$.

In general, the OPM tends to overestimate precipitation amounts at the weather stations. Despite possible measurement inaccuracies, the results are still in good agreement with observed data. Precipitation measuring equipment, such as installed at Grey Glacier, tends to underestimate precipitation in cases of snowfall or high wind speeds.

The glacier-wide mean annual precipitation amounts are 5.9 ± 1.0 m w.e. a^{-1} at Grey Glacier and 7.1 ± 1.1 m w.e. a^{-1} at Tyndall Glacier, averaged over the study period of 2000–2016. Mernild et al. (2016) simulate glacier-wide annual precipitation amounts of 10.26 ± 0.54 m w.e. a^{-1} for Grey Glacier and 9.19 ± 0.46 m w.e. a^{-1} for Tyndall Glacier between 2004/05 and 2013/14. These values are significantly higher than our findings. For the same period, we simulate glacier-wide mean annual precipitation of 6.27 ± 1.0 m w.e. a^{-1} for Grey Glacier and 7.45 ± 1.1 m w.e. a^{-1} for Tyndall Glacier.

The modeled ratio of solid to overall precipitation accounts for about 84.5 and 69.5% for Grey and Tyndall glaciers, respectively. Mean values for the SPI are estimated between 55% (Mernild et al., 2016) and 59% (Schaefer et al., 2015). Higher ratios of solid to overall precipitation for Grey and Tyndall glaciers compared to the mean value for the SPI seem reasonable since more than about 80% of the total falls in higher elevations as solid precipitation. This is at least partly due to the southern and lee-side location of these glaciers within the SPI.

4.2. Modeled Surface Energy Balance

The glacier-wide mean monthly surface energy balance components for both glaciers averaged between 2000 and 2016 are shown in **Figure 6**. The glacier-wide energy input is dominated year-around by LW_{in} (+ 279 W m^{-2}) and SW_{in} (+ 109 W m^{-2}), followed by Q_{sens} (+ 11 W m^{-2}), Q_g (+ 4 W m^{-2}) and Q_{liq} (+ 1 W m^{-2}). Available energy at the glacier surface is

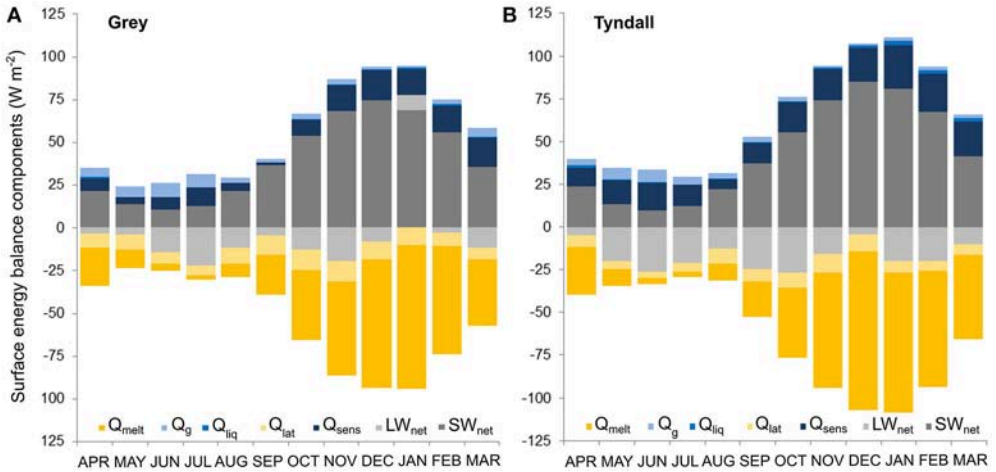

FIGURE 6 | Monthly surface energy balance components averaged between April 2000 and March 2016 for **(A)** Grey Glacier and **(B)** Tyndall Glacier. Abbreviations are explained in Equation 1.

consumed by LW_{out} (-288 W m^{-2}), SW$_{out}$ (−70 W m^{-2}), Q_{lat} (−9 W m^{-2}), and Q_{melt} (−36 W m^{-2}). The main source of melt energy is SW_{net} (+ 39 W m^{-2}).

The highest SW_{net} values are reached during the summer months (October to March) due to higher incoming solar radiation. Albedo values are similar throughout the year with a glacier wide-mean of 0.6. The highest values of Q_{sens} are reached during the austral summer months while Q_g is slightly higher during the winter. LW_{in} exceeds the amount of LW_{out} in January over extensive areas of the glacier and air temperatures are above the melting point and relative humidity is high in January. This atmospheric situation results in a large down-welling long-wave radiation from the atmosphere toward the glacier surface. The glacier and snow emission, however, are restricted to emission at 0°C. Therefore, LW_{out} is limited to 311 W m^{-2}. In consequence, the model calculates positive LW_{net} for the core melt phase in the austral summer.

Q_{liq} is negligible regarding the glacier-wide mean. However, it plays a more prominent role as a source of melt energy in the ablation area. Positive Q_g may result due to the assumption of the ice temperature at the bottom of the model domain section (3.1), which may lead to unrealistic high positive Q_g values especially at higher elevation where the annual air temperature is lower.

The energy budget of a snowpack is also affected by snow drift. Since COSIMA does not integrate snow drift parametrization, sublimation at the glacier surface may be overestimated (Barral et al., 2014; Huintjes et al., 2015). Furthermore, katabatic flow over large glaciers generates turbulences and enhances the turbulent exchange (Q_{lat}, Q_{sens}) (Oerlemans and Grisogono, 2002). Surface melt may therefore be underestimated by neglecting katabatic winds when applying COSIMA.

The surface energy balance components of Tyndall Glacier do not show any significant differences compared to Grey Glacier between 2000 and 2016. The glacier-wide energy input is also dominated by LW_{in} (+ 273 W m^{-2}) and SW_{in} (+ 127 W m^{-2}), followed by Q_{sens} (+ 16 W m^{-2}), Q_g (+ 3 W m^{-2}) and Q_{liq} (+ 1 W m^{-2}). Energy sinks are LW_{out} (-291 W m^{-2}), SW$_{out}$ (-82 W m^{-2}), Q_{lat} (−7 W m^{-2}), and Q_{melt} (-40 W m^{-2}). The modeled radiation terms at the AWS Tyndall pixel are in good agreement with observed data. The overall mean of SW_{in}, SW$_{out}$, LW_{in}, and LW_{out} differ by 5–7% for the mass balance year of 2015/16.

4.3. Modeled Climatic Mass Balance

Modeled glacier-wide mean annual climatic mass balance are positive for Grey Glacier with +0.86 ± 0.52 m w.e. a^{-1} and for Tyndall Glacier with +0.41 ± 0.54 m w.e. a^{-1} for the study period from April 2000 to March 2016 (Table S2).

Negative climatic mass balance years of Grey Glacier are simulated for 2001/02, 2004/05, 2011/12, and 2015/16, while the most negative climatic mass balance is reached in 2015/16 (Table S2). In mass balance years where the climatic mass balance is negative, either less P_{solid}, higher T_{2m}, or higher SW_{in} amounts occurred compared to the average (**Figure 7**). High positive climatic mass balance years are modeled for 2007/08 and 2013/14 caused by above-average P_{solid} amounts and lower SW_{in} values. Very low mean T_{2m} compensate low amounts of P_{solid} and SW_{in} in 2000/01. The glacier-wide mean climatic mass balance for the period 2000–2016 ranges from −11.9 ± 2.1 m w.e. a^{-1} in the lowest areas of the ablation area to + 10.3 ± 1.8 m w.e. a^{-1} in the top parts of the accumulation area (**Figures 8**, **9**).

Modeled mean annual ELA accounts for 960 ± 70 m a.s.l. ranging from 900 to 1,140 m a.s.l. These values are in good agreement with estimated mean ELA of De Angelis (2014) and Schaefer et al. (2015). The highest values for ELA of up to 1,140 m a.s.l. are simulated for the climatic mass balance years 2004/05 and 2015/2016. According to Malz et al. (2018), larger surface lowering have been observed at both outer glacier tongues of Grey Glacier. This pattern can also be distinguished in the modeled climatic mass balance results mainly because of the elevation feedback in air temperature as a consequence of the fact that the lateral glacier tongues have a lower surface elevation than Grey Glacier's middle branch (**Figure 8**).

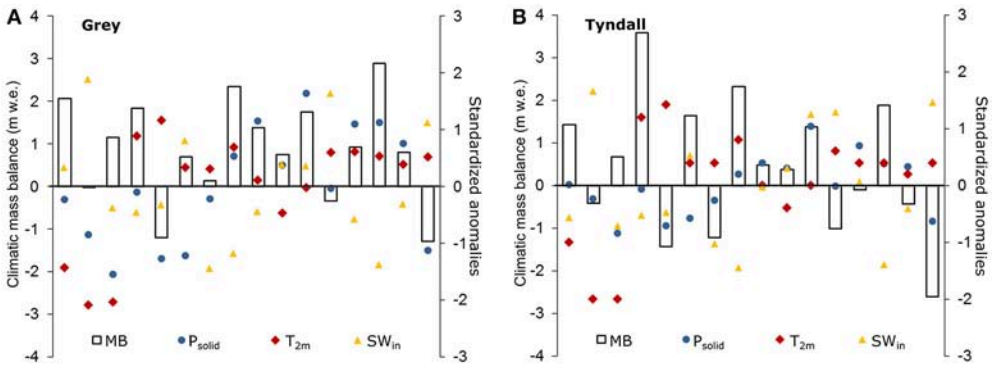

FIGURE 7 | Modeled annual climatic mass balance (MB) based on COSIMA simulations and standardized anomalies of P_{solid}, T_{2m}, SW_{in} from the mean between April 2000 and March 2016 for **(A)** Grey Glacier and **(B)** Tyndall Glacier.

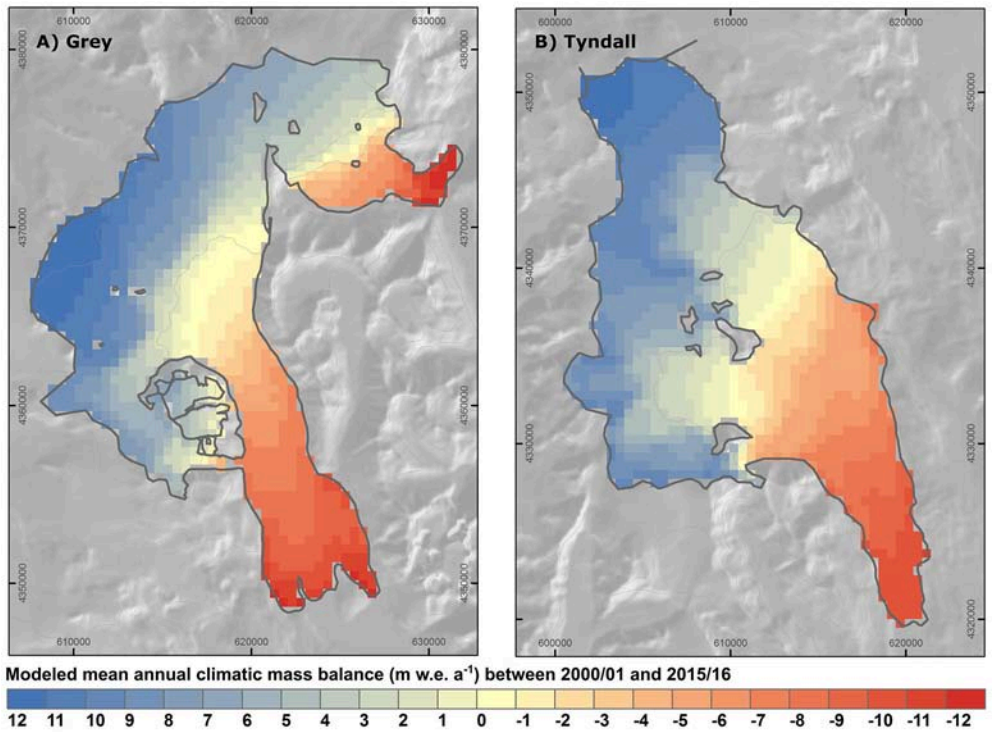

FIGURE 8 | Modeled mean annual climatic mass balance in m w.e. a^{-1} based on COSIMA simulations for the study period April 2000 to March 2016 for **(A)** Grey Glacier and **(B)** Tyndall Glacier. The coordinates are in UTM zone 18S in meters.

For Tyndall Glacier, negative climatic mass balance is simulated in 2001/02, 2004/05, 2006/07, 2011/12, 2012/13, 2014/5, and 2015/16 (Table S2). The inter-annual variations of climatic mass balance are high, ranging from -2.60 ± 0.54 to $+3.60 \pm 0.54$ m w.e. a^{-1}. In positive climatic mass balance years higher P_{solid}, lower T_{2m}, or lower SW_{in} amounts occurred compared to the average of each variable (**Figure 7**). Very high positive climatic mass balance in 2003/2004 is caused by high solid precipitation amounts in the lower altitudes. The combination of high air temperatures, high incoming solar radiation, and low solid precipitation amounts caused the strongly negative mass balance year in 2015/16.

The glacier-wide mean climatic mass balance for the period 2000–2016 ranges from -10.9 ± 3.2 m w.e. a^{-1} in the lowest areas of the ablation area to $+11.4 \pm 1.9$ m w.e. a^{-1} in the top parts of the accumulation area. In some years modeled annual ablation is as negative as -13.5 m w.e. a^{-1} and maximum accumulation reaches up to $+ 14.7$ m w.e. a^{-1} (**Figure 10**). The amount of accumulation in the highest altitudes seems reasonable compared to the study of Kohshima et al. (2007) who estimated

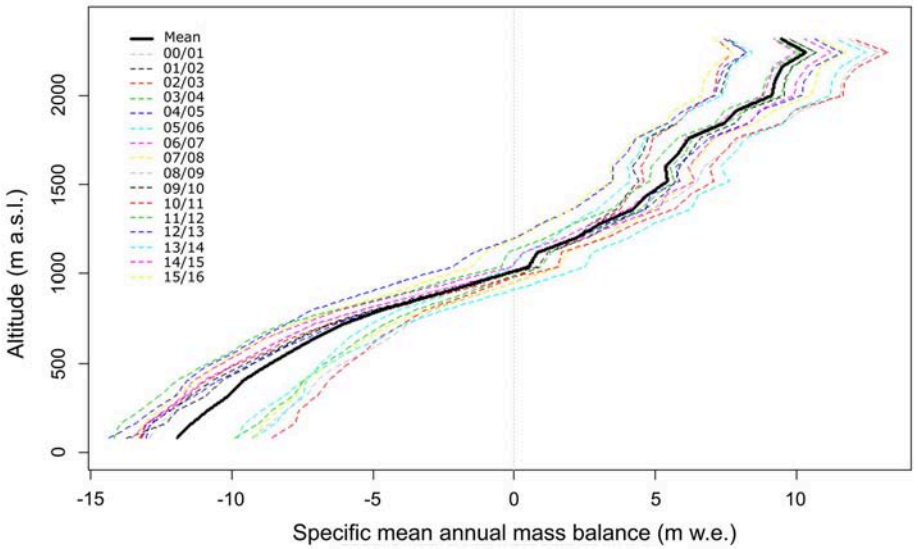

FIGURE 9 | Modeled climatic mass balance profiles for Grey Glacier for each mass balance year from 2000/2001 (00/01) to 2015/2016 (15/16). Climatic mass balance is averaged over 80 m altitude bins.

an annual net accumulation in the period of the austral winter 1998 to the austral winter 1999 of + 12.9 m w.e. at 1,756 m a.s.l. The mean modeled ELA is 920 ± 60 m a.s.l. ranging from 760 m a.s.l. to 1,000 m a.s.l. ELA values are within the range of previous estimates by Nishida et al. (1995), Casassa et al. (2014), and De Angelis (2014).

Comparing modeled climatic mass balance results with previous studies, especially Mernild et al. (2016), we simulate less positive climatic mass balance including high year to year variations. According to Mernild et al. (2016), mean annual surface mass balance was estimated to be about +2.86 ± 0.28 and +0 .71 ± 0.35 m w.e. a^{-1} between 2004/05 to 2008/2009 for Grey and Tyndall glaciers, respectively, with a slight increase in positive surface mass balance for the following period between 2009/10 and 2013/2014. COSIMA climatic mass balance results for the period 2004/05 to 2008/09 are less positive with +0.67 ± 0.52 m w.e. for Grey Glacier and +0.35 ± 0.54 m w.e. a^{-1} for Tyndall Glacier. The increase in positive climatic mass balance for the following period to 2013/14 is also reproduced by COSIMA. The contributions of subsurface melt, sublimation, refreezing, and evaporation are comparatively small (Table S2). The amounts of sublimation and evaporation are similar to values of Mernild et al. (2016).

The main reason for the differences in climatic mass balance is the amount of modeled annual precipitation. Current estimates from Schaefer et al. (2013); Lenaerts et al. (2014); Mernild et al. (2016) based on numerical simulations suggest average accumulation rates of 8-9 m w.e. a^{-1} for the SPI. At isolated locations, extreme precipitation rates of up to 30 m w.e. a^{-1} are suspected. These rather unrealistic amounts may result from an overestimation of modeled water vapor over the SPI. However, the lack of observed accumulation data of the SPI as described in section 1.2 and especially at Grey and Tyndall glaciers does not allow a detailed validation of modeled precipitation amounts.

4.4. Observed Geodetic Balance and Derived Frontal Ablation

Glacier-wide mean annual surface height changes between 2000 and 2014 simulated by COSIMA show an overall increase of +2.34 ± 0.65 m a^{-1} for Grey Glacier and +1.93 ± 0.67 m a^{-1} Tyndall Glacier due to high accumulation amounts. Observed mean annual surface height changes based on TanDEM-X/SRTM data indicate glacier average ice thinning of -1.23 ± 0.19 m a^{-1} and −3.04 ± 0.24 m a^{-1} for Grey and Tyndall glaciers, respectively. **Figure 11** illustrates the spatial differences of surface height changes between COSIMA and TanDEM-X/SRTM, interpolated to 500 m, for both glaciers. TanDEM-X/SRTM observes glacier thinning even in the accumulation areas, while COSIMA estimates a gain of mass in the accumulation area and a loss of mass in the ablation area (**Figure 12**).

The spatial distribution of surface height at the glacier fronts of Grey are non-uniform. Differences between both datasets at the outer tongues are small, especially at the western part, while high differences occur at the middle part of Grey Glacier. The latter is caused by a constant ice flow into this branch over time. Surface height changes and the front position of this middle branch remain constant over the entire study period. The western and eastern branches of the glacier tongue, however, seem to be partially decoupled from the main ice flow causing surface lowering which is mainly driven by climatic mass balance processes. The different ice dynamical effects at the glacier fronts are underlined by observed ice velocities based on LandSat-8 by Schwalbe et al. (2017). The highest velocities are observed at the middle part of the glacier terminus while the ice flow within the outer fronts is smaller. At Tyndall Glacier, we observe a more uniform pattern at the front but also a retreat of the glacier front (**Figure 11**). As expected, the smallest differences of surface height changes between COSIMA and TanDEM-X/SRTM are close to the mean ELA of both glaciers (**Figure 12**).

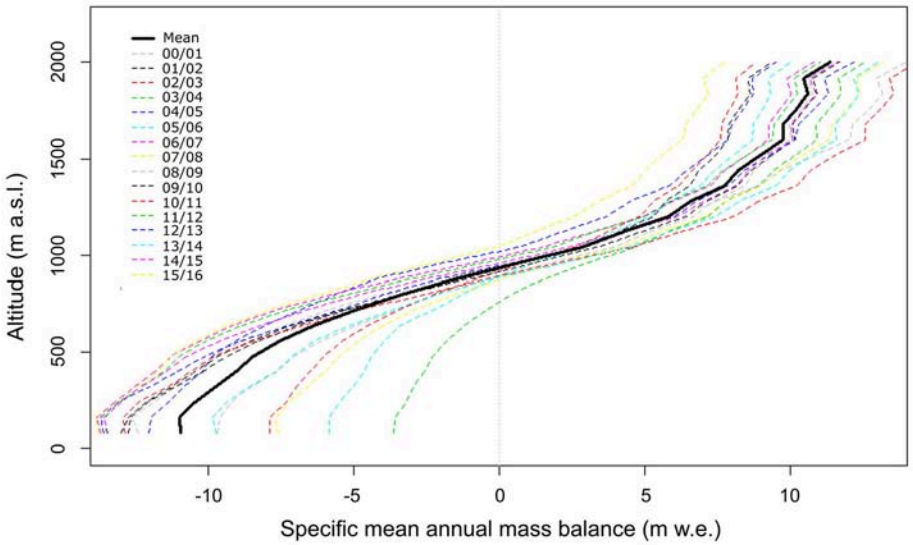

FIGURE 10 | Modeled climatic mass balance profiles for Tyndall Glacier for each mass balance year from 2000/2001 (00/01) to 2015/2016 (15/16). Climatic mass balance is averaged over 80 m altitude bins.

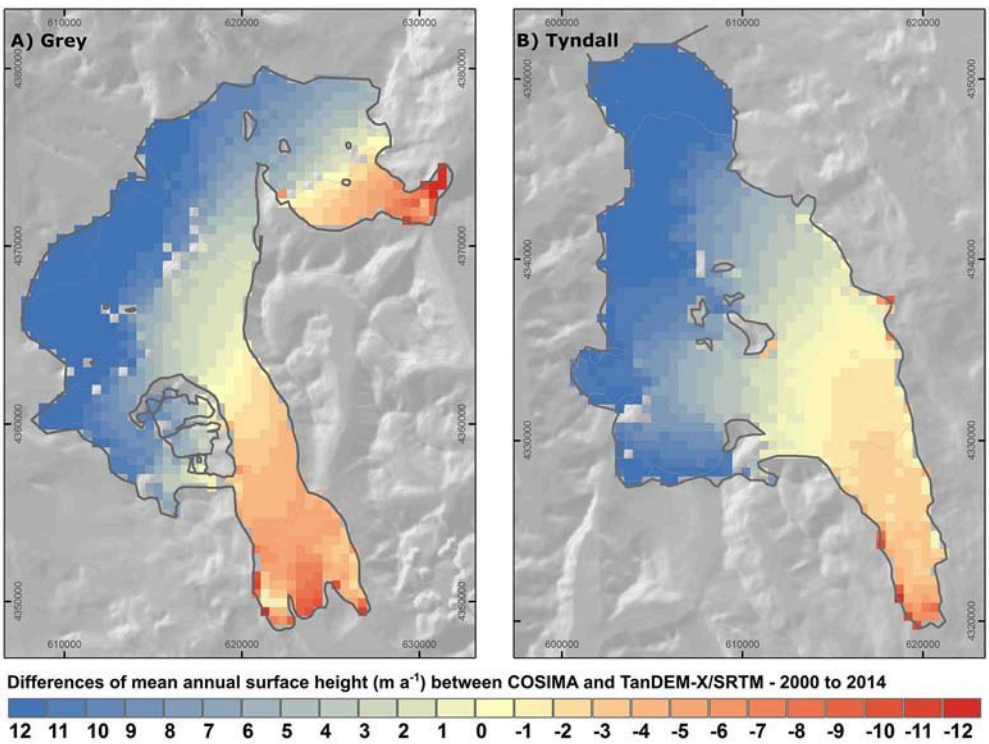

FIGURE 11 | Differences between mean annual surface height changes (m) based on COSIMA as the result of climatic mass balance and mean annual surface height changes (m) based on TanDEM-X/SRTM, interpolated to a spatial resolution of 500 m, between 2000 and 2014 for **(A)** Grey Glacier and **(B)** Tyndall Glacier. The coordinates are in UTM zone 18S in meters.

The glacier-wide mean annual climatic mass balance by COSIMA for the period of 2000–2014 is $+1.02 \pm 0.52$ m w.e.a^{-1} and $+0.68 \pm 0.54$ m w.e.a^{-1} for Grey and Tyndall glaciers, respectively. The positive climatic mass balance is mainly influenced by high accumulation amounts in the upper parts of the glaciers. A significant increase of glacier mass in the

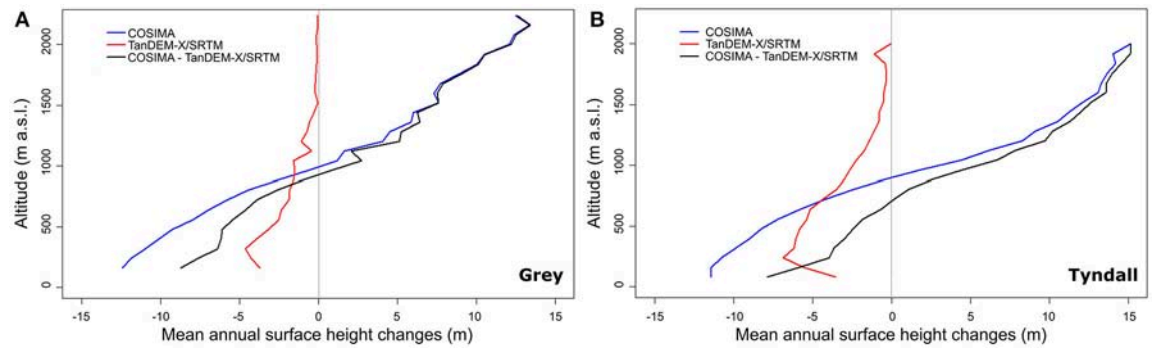

FIGURE 12 | Profiles of differences between mean surface height changes (m) based on COSIMA as the result of climatic mass balance and mean annual surface height changes (m) based on TanDEM-X/SRTM for **(A)** Grey Glacier and **(B)** Tyndall Glacier. Differences are averaged over 80 m altitude bins.

accumulation area has not been observed by TanDEM-X/SRTM (**Figure 12**).

Converting surface height changes by TanDEM-X/SRTM into mass balance changes yields in a mean geodetic mass balance of -1.05 ± 0.18 m w.e.a^{-1} for Grey Glacier and -2.58 ± 0.28 m w.e.a^{-1} for Tyndall Glacier. Since different densities for snow, firn, and ice are used within COSIMA, the mean density for converting surface height changes into climatic mass balance changes is lower within the COSIMA model than the density of 850 kg m^{-3} assumed for converting observed surface height changes by TanDEM-X/SRTM.

The differences between the modeled climatic mass balance and the geodetic mass balance are assumed to equal the amount of ice loss by frontal ablation which accounts for 2.07 ± 0.70 m w.e. a^{-1} for Grey Glacier and 3.26 ± 0.82 m w.e. a^{-1} for Tyndall Glacier. Ice loss by surface melt is larger than by frontal ablation with mean annual amounts of 3.48 m w.e.a^{-1} and 3.71 m w.e.a^{-1}, respectively.

Schaefer et al. (2015) inferred a frontal ablation, that they denoted as calving flux, of 1.51–1.55 ± 0.10 and 1.58-1.69 ± 0.11 km^3 a^{-1} from 2000 to 2011 for Grey and Tyndall glaciers. Integrating the differences of surface height changes between COSIMA and TanDEM-X/SRTM into volume changes results in frontal ablation of 1.09 ± 0.26 and 1.49 ± 0.28 km^3 a^{-1} for Grey and Tyndall glaciers from 2000 to 2014. Our findings underline a significant difference in recent volume loss between both glaciers due to differences in ice dynamical processes.

5. CONCLUSION

Recent climatic mass balance is calculated for 16 years between April 2000 and March 2016 using the surface energy and mass balance model COSIMA. COSIMA is driven by downscaled ERA-Interim data and MODIS cloud cover data. We successfully applied a linear orographic precipitation model to simulate precipitation fields with high spatial and temporal resolution.

We simulate a positive glacier-wide mean annual climatic mass balance of $+1.02 \pm 0.52$ m w.e. a^{-1} for Grey Glacier and of $+0.68 \pm 0.54$ m w.e. a^{-1} for Tyndall Glacier between 2000 and 2014. Climatic mass balance results show a high year to year variability. Main sources of melt energy are incoming solar radiation and the sensible heat flux. Modeled climatic mass balance for both glaciers is mainly controlled by the amount of solid precipitation and surface melt. The contributions of subsurface melt, sublimation, refreezing, and of evaporation are comparatively small. The lack of observed accumulation data causes high uncertainties in climatic mass balance simulations regarding the glacier-wide amount of solid precipitation. Therefore, climatic mass balance results of this study and previous ones differ considerably because of the use of different precipitation modeling scheme and atmospheric input data.

The comparison of surface height changes between COSIMA and TanDEM-X/SRTM data between 2000 and 2014 underlines the strong ice dynamical effects on glacier mass balance at Grey and Tyndall glaciers. Ice losses by frontal ablation are estimated to be 2.07 ± 0.70 m w.e. a^{-1} for Grey Glacier and 3.26 ± 0.82 m w.e. a^{-1} for Tyndall Glacier between 2000 and 2014. However, ice loss by surface ablation still exceeds the ice loss by frontal ablation. Surface height changes and changes of the frontal position differ significantly between the three fronts of Grey Glacier. Ice loss at the lateral branches seem to result mainly from negative climatic mass balance while the calving front of the central branch remains stable over the entire study period due to a sustained influx of ice in this part of the glacier.

Using geodetic and climatic mass balance to derive frontal ablation has been successfully applied in other studies (Nuth et al., 2012; Schaefer et al., 2015). The lack of observation and, in particular, information about the bedrock topography or ice thickness limit the applicability of high resolution ice dynamical models up to now. Nevertheless, the use of ice dynamical models will be a crucial advancement to fully quantify the ice dynamical processes and impact on the overall mass change, in future studies.

The outcomes of this study further confirm that the chosen methodological approaches to assess surface energy-fluxes and climatic mass balance are promising and suitable to be applied to the entire SPI in future investigations.

AUTHOR CONTRIBUTIONS

SW carried out COSIMA simulations, processed and analyzed the data. SW, TS, CS jointly designed the study and prepared the manuscript. PM processed surface height changes based on TanDEM-X/SRTM. RJ, JA-N, GC organized all logistics for the field campaigns. SW, TS, CS, RJ, JA-N, GC contributed to the field work. All authors discussed the results and reviewed the manuscript.

FUNDING

This research was funded by the CONICYT-BMBF project GABY-VASA: 01DN15007, 01DN15020, and BMBF20140052.

ACKNOWLEDGMENTS

We thank the Chilean Weather Service (DMC) and Chilean Water Directorate (DGA) for providing weather station data, and Marius Schaefer for providing stake measurements from Grey Glacier. We thank all participants, and especially Marcelo Arévalo, Guisella Gacitúa, Inti Gonzalez, Roberto Garrido, Matthias Braun, and Wolfgang Meier for their support during the field work at Grey Glacier. CONAF granted access to Torres del Paine National Park and provided support. Bigfoot and Hotel Lago Grey provided navigation support at Grey Lake. We thank all reviewers, the editor Thomas Schuler and the chief editor Regine Hock for their input which markedly helped to improve the manuscript.

SUPPLEMENTARY MATERIAL

The Supplementary Material for this article can be found online at: https://www.frontiersin.org/articles/10.3389/feart.2018.00081/full#supplementary-material

REFERENCES

Aniya, M., Sato, H., Naruse, R., Skvarca, P., and Casassa, G. (1996). The use of satellite and airborne imagery to inventory outlet glaciers of the southern patagonia icefield, south america. *Photogramm. Eng. Remote Sens.* 62, 1361–1369.

Aravena, J.-C., and Luckman, B. H. (2009). Spatio-temporal rainfall patterns in southern south america. *Int. J. Climatol.* 29, 2106–2120. doi: 10.1002/joc.1761

Aristarain, A. J., and Delmas, R. J. (1993). Firn-core study from the southern patagonia ice cap, south. *J. Glaciol.* 39, 249–254. doi: 10.1017/S0022143000015914

Barral, H., Genthon, C., Trouvilliez, A., Brun, C., and Amory, C. (2014). Blowing snow in coastal adelie land, antatrctica: three atmopsheric-moisture issues. *Cryosphere* 8, 1905–1919. doi: 10.5194/tc-8-1905-2014

Barstad, I., and Smith, R. B. (2005). Evaluation of an orographic precipitation model. *J. Hydrometeorol.* 6, 85–99. doi: 10.1175/JHM-404.1

Budyko, M. (1974). *Climate and Life*. New York, NY: Academic Press Inc.

Carrasco, J., Osorio, R., and Casassa, G. (2008). Secular trend of the equilibrium-line altitude on the western side of the southern andes, derived from radiosonde and surface observations. *J. Glaciol.* 54, 538–550. doi: 10.3189/002214308785837002

Casassa, G., Brecher, H., Rivera, A., and Aniya, M. (1997). A century-long recession record of glacier o'higgins, chilean patagonia. *Ann. Glaciol.* 24, 106–110.

Casassa, G., Luis, A. R., and Schwikowski, M. (2006). "Glacier mass balance data for southern south america (30°s-56°s)," in *Glacier Science and Environmental Change*, ed P. Knight (Oxford: Blackwell), 239–241.

Casassa, G., Rodríguez, J. L., and Loriaux, T. (2014). "A new glacier inventory for the southern patagonia icefield and areal changes 1986–2000," in *Global Land Ice Measurements from Space*, eds J. S. Kargel, G. J. Leonard, M. P. Bishop , A. Kääb, and B. H. Raup (Berlin; Heidelberg: Springer), 639–660.

Consortium, R. (2015). "Randolph glacier inventory – a dataset of global glacier outlines: Version 5.0.: Technical report" in *Global Land Ice Measurements from Space* (Colorado, CO Digital Media.)

Crochet, P., Jóhannesson, T., Jónsson, T., Sigurðsson, O., Björnsson, H., Pálsson, F., et al. (2007). Estimating the spatial distribution of precipitation in iceland using a linear model of orographic precipitation. *J. Hydrometeorol.* 8, 1285–1306. doi: 10.1175/2007JHM795.1

Cuffey, K., and Paterson, W. (2010). *The pyhsics of Glaciers, 4th Edn*. Burlington VT; Oxford: Butterworth-Heinemann; Elsevier Inc.

Davies, B., and Glasser, N. (2012). Accelerating shrinkage of patagonian glaciers from the little ice age (ad 1870) to 2011. *J. Glaciol.* 58, 1063–1084. doi: 10.3189/2012JoG12J026

De Angelis, H. (2014). Hypsometry and sensitivity of the mass balance to changes in equilibrium-line altitude: the case of the southern patagonia icefield. *J. Glaciol.* 60, 14–28. doi: 10.3189/2014JoG13J127

Dee, D., Uppala, S., Simmons, A., Berrisford, P., Poli, P., Kobayashi, S., et al. (2011). The era-interim reanalysis: configuration and performance of the data assimilation system. *Q. J. R. Meteorol. Soci.* 137, 553–597. doi: 10.1002/qj.828

Fernández, A., and Mark, B. (2016). Modeling modern glacier response to climate changes along the andes cordillera: a multiscale review. *J. Adv. Model. Earth Syst.* 8, 467–495. doi: 10.1002/2015MS000482

Geoestudios (2013). Implementación nivel 2 estrategia nacional de glaciares: Mediciones glaciológicas terrestres en chile central, zona sur y patagonia. *Report Dirección General de Aguas, Santiago, Chile*, SIT 327, 1–475.

Godoi, M. A., Shiraiwa, T., Kohshima, S., and Kubota, K. (2002). "Firn-core drilling operation at tyndall glacier, southern patagonia icefield," in *The Patagonian Icefields: A Unique Natural Laboratory for Environmental and Climate Change Studies*, eds G. Casassa, F. V. Sepúlveda, and R. M. Sinclair (Boston, MA: Springer US), 149–156.

Gudmundsson, L., Bremnes, J. B., Haugen, J. E., and Engen-Skaugen, T. (2012). Technical note: downscaling rcm precipitation to the station scale using statistical transformations - a comparison of methods. *Hydrol. Earth Syst. Sci.* 16, 3383–3390. doi: 10.5194/hess-16-3383-2012

Hall, D. K., and Riggs, G. A. (2016). *Modis/Terra Snow Cover Daily l3 Global 500m grid v005, 2000 to 2016*. Boulder, CO:. NASA National Snow and Ice Data Center Distributed Active Archive Center.

Herron, M., and Langway, C. (1980). Firn densification: an empirical model. *J. Glaciol.* 25, 373–385. doi: 10.1017/S0022143000015239

Hoffmann, J., and Walter, D. (2006). How complementary are srtm-x and-c band digital elevation models? *Photogramm. Eng. Remote Sens.* 72, 261–268. doi: 10.14358/PERS.72.3.261

Huintjes, E., Sauter, T., Schröter, B., Maussion, F., Yang, W., Kropáček, J., et al. (2015). Evaluation of a coupled snow and energy balance model for zhadang glacier, tibetan plateau, using glaciological measurements and time-lapse photography. *Arctic Antarctic Alpine Res.* 47, 573–590. doi: 10.1657/AAAR0014-073

Huss, M. (2013). Density assumptions for converting geodetic glacier volume change to mass change. *Cryosphere* 7, 877–887. doi: 10.5194/tc-7-877-2013

Jaber, W. A., Floricioiu, D., Rott, H., and Eineder, M. (2013). "Surface elevation changes of glaciers derived from srtm and tandem-x dem differences," in *IGARSS 2013* (IEEE Xplore), 1893–1896.

Jarosch, A. H., Anslow, F. S., and Clarke, G. K. C. (2012). High-resolution precipitation and temperature downscaling for glacier models. *Clim. Dyn.* 38, 391–409. doi: 10.1007/s00382-010-0949-1

Jarvis, A., Reuter, H., Nelson, A., and Guevara, E. (2008). Hole-filled SRTM for the globe Version 4, available from the CGIAR-CSI SRTM 90m Database. Available online at: http://srtm.csi.cgiar.org

Jiang, Q., and Smith, R. B. (2003). Cloud timescales and orographic precipitation. *J. Atmos. Sci.* 60, 1543–1559. doi: 10.1175/2995.1

Kohshima, S., Takeuchi, N., Uetake, J., Shiraiwa, T., Uemura, R., Yoshida, N., et al. (2007). Estimation of net accumulation rate at a patagonian glacier by ice core analyses using snow algae. *Glob. Planet. Change* 59, 236–244. doi: 10.1016/j.gloplacha.2006.11.014

Koppes, M., Conway, H., Rasmussen, L. A., and Chernos, M. (2011). Deriving mass balance and calving variations from reanalysis data and sparse observations, glaciar san rafael, northern patagonia, 1950–2005. *Cryosphere* 5, 791–808. doi: 10.5194/tc-5-791-2011

Kumar, L., Skidmore, A. K., and Knowles, E. (1997). Modelling topographic variation in solar radiation in a gis environment. *Int. J. Geogr. Infor. Sci.* 11, 475–497. doi: 10.1080/136588197242266

Kunz, M., and Kottmeier, C. (2006). Orographic enhancement of precipitation over low mountain ranges. part i: model formulation and idealized simulations. *J. Appl. Meteorol. Clim.* 45, 1025–1040. doi: 10.1175/JAM2389.1

Lenaerts, J. T. M., van den Broeke, M. R., van Wessem, J. M., van de Berg, W. J., van Meijgaard, E., van Ulft, L. H., et al. (2014). Extreme precipitation and climate gradients in patagonia revealed by high-resolution regional atmospheric climate modeling. *J. Clim.* 27, 4607–4621. doi: 10.1175/JCLI-D-13-00579.1

Lopez, P., Chevallier, P., Favier, V., Pouyaud, B., Ordenes, F., and Oerlemans, J. (2010). A regional view of fluctuations in glacier length in southern south america. *Glob. Planet. Change* 71, 85–108. doi: 10.1016/j.gloplacha.2009.12.009

Malz, P., Meier, W., Casassa, G., Jaña, R., Skvarca, P., and Braun, M. H. (2018). Elevation and mass changes of the southern patagonia icefield derived from tandem-x and srtm data. *Rem. Sens.* 10:188. doi: 10.3390/rs10020188

Maniak, U. (2010). *Hydrologie und Wasserwirtschaft: Eine Einführung für Ingenieure*. Verlag; Heidelberg: Springer.

Meier, W., Hochreuther, P., Grießinger, J., and Braun, M. (2018). An updated multi-temporal glacier inventory for the patagonian andes with changes between the little ice age and 2016. *Front. Earth Sci.* 6:62. doi: 10.3389/feart.2018.00062

Mernild, S. H., Liston, G. E., Hiemstra, C., and Wilson, R. (2016). The andes cordillera. Part III: glacier surface mass balance and contribution to sea level rise (1979–2014). *Int. J. Climatol.*. 37, 3154–3174. doi: 10.1002/joc.4907

Minowa, M., Sugiyama, S., Sakakibara, D., and Sawagaki, T. (2015). Contrasting glacier variations of glaciar perito moreno and glaciar ameghino, southern patagonia icefield. *Ann. Glaciol.* 56, 26–32. doi: 10.3189/2015AoG70A020

Möller, M., Finkelnburg, R., Braun, M., Hock, R., Jonsell, U., Pohjola, V. A., et al. (2011). Climatic mass balance of the ice cap vestfonna, svalbard: a spatially distributed assessment using era-interim and modis data. *J. Geophys. Res. Earth Surf.* 116, 1–14. doi: 10.1029/2010JF001905

Möller, M., Schneider, C., and Kilian, R. (2007). Glacier change and climate forcing in recent decades at gran campo nevado, southernmost patagonia. *Ann. Glaciol.y* 46, 136–144. doi: 10.3189/172756407782871530

Mouginot, J., and Rignot, E. (2015). Ice motion of the patagonian icefields of south america: 1984–2014. *Geophys. Res. Lett.* 42, 1441–1449. doi: 10.1002/2014GL062661

Muto, M., and Furuya, M. (2013). Surface velocities and ice-front positions of eight major glaciers in the southern patagonian ice field, south america, from 2002 to 2011. *Rem. Sens. Environ.* 139, 50–59. doi: 10.1016/j.rse.2013.07.034

Naruse, R., and Skvarca, P. (2000). Dynamic features of thinning and retreating glaciar upsala, a lacustrine calving glacier in southern patagonia. *Arctic Antarctic Alpine Res.* 32, 485–491. doi: 10.2307/1552398

Nishida, K., Satow, K., Aniya, M., Casassa, G., and Kadota, T. (1995). Thickness change and flow of glaciar tyndall, patagonia. *Bull. Glacier Res.* 13, 29–34.

Nuth, C., Schuler, T. V., Kohler, J., Altena, B., and Hagen, J. O. (2012). Estimating the long-term calving flux of kronebreen, svalbard, from geodetic elevation changes and mass-balance modeling. *J. Glaciol.* 58, 119–133. doi: 10.3189/2012JoG11J036

Oerlemans, J. (2001). *Glaciers and Climate Change*. Lisse: Swets and Zeitlinger.

Oerlemans, J., and Grisogono, B. (2002). Glacier winds and parametrisations of the related surface heat fluxes. *Tellus* 54, 440–452. doi: 10.3402/tellusa.v54i5.12164

Oerlemans, J., and Knap, W. (1998). A 1 year record of global radiation and albedo in the ablation zone of morteratschgletscher, switzerland. *J. Glaciol.* 44, 239–247.

Panofsky, H., and Brier, G. (1968). *Some Applications of Statistics to Meteorology*. Earth and Mineral Sciences Continuing Education, College of Earth and Mineral Sciences.

Rasmussen, L., Conway, H., and Raymond, C. (2007). Influence of upper air conditions on the patagonia icefields. *Global Planet. Change* 59, 203–216. doi: 10.1016/j.gloplacha.2006.11.025

Rignot, E., Rivera, A., and Casassa, G. (2003). Contribution of the patagonia icefields of south america to sea level rise. *Science* 302, 434–437. doi: 10.1126/science.1087393

Rivera, A., Benham, T., Casassa, G., Bamber, J., and Dowdeswell, J. A. (2007). Ice elevation and areal changes of glaciers from the northern patagonia icefield, chile. *Glob. Planet. Change* 59, 126–137. doi: 10.1016/j.gloplacha.2006.11.037

Rivera, A., and Casassa, G. (1999). Volume changes on pío xi glacier, patagonia: 1975–1995. *Glob. Planet. Change* 22, 233–244. doi: 10.1016/S0921-8181(99)00040-5

Rivera, A., Koppes, M., Bravo, C., and Aravena, J. C. (2012). Little ice age advance and retreat of glaciar jorge montt, chilean patagonia. *Clim. Past* 8, 403–414. doi: 10.5194/cp-8-403-2012

Rosenblüth, B., Casassa, G., and Fuenzalida, H. A. (1995). Recent climatic changes in western patagonia. *Bull. Glacier Res.* 13 127–132.

Sakakibara, D., and Sugiyama, S. (2014). Ice-front variations and speed changes of calving glaciers in the southern patagonia icefield from 1984 to 2011. *J. Geophys. Res. Earth Surf.* 119, 2541–2554. doi: 10.1002/2014JF003148

Schaefer, M., Machguth, H., Falvey, M., and Casassa, G. (2013). Modeling past and future surface mass balance of the northern patagonia icefield. *J. Geophys. Res. Earth Surf.* 118, 571–588. doi: 10.1002/jgrf.20038

Schaefer, M., Machguth, H., Falvey, M., Casassa, G., and Rignot, E. (2015). Quantifying mass balance processes on the southern patagonia icefield. *Cryosphere* 9, 25–35. doi: 10.5194/tc-9-25-2015

Schuler, T. V., Crochet, P., Hock, R., Jackson, M., Barstad, I., and Jóhannesson, T. (2008). Distribution of snow accumulation on the svartisen ice cap, norway, assessed by a model of orographic precipitation. *Hydrol. Process.* 22, 3998–4008. doi: 10.1002/hyp.7073

Schwalbe, E., Kröhnert, M., Koschitzki, R., Cárdenas, C., and Maas, H. (2017). "Determination of spatio-temporal velocity fields at grey glacier using terrestrial image sequences and optical satellite imagery," in *LFirst IEEE International Symposium of Geoscience and Remote Sensing (GRSS-CHILE)* (Valdivia).

Schwikowski, M., Schläppi, M., Santibañez, P., Rivera, A., and Casassa, G. (2013). Net accumulation rates derived from ice core stable isotope records of pío xi glacier, southern patagonia icefield. *Cryosphere* 7, 1635–1644. doi: 10.5194/tc-7-1635-2013

Shiraiwa, T., Kohshima, S., Uemura, R., Yoshida, N., Matoba, S., Uetake, J., et al. (2002). High net accumulation rates at the campo de hielo patagonico sur, south america, revealed by analyses of a 45.97m long ice core. *Ann. Glaciol* 35, 84–90. doi: 10.3189/172756402781816942

Smith, R. B., and Barstad, I. (2004). A linear theory of orographic precipitation. *J. Atmos. Sci.* 61, 1377–1391. doi: 10.1175/1520-0469(2004)061<1377:ALTOOP>2.0.CO;2

Spiess, M., Schneider, C., and Maussion, F. (2016). Modis-derived interannual variability of the equilibrium-line altitude across the tibetan plateau. *Ann. Glaciol.* 57, 140–154. doi: 10.3189/2016AoG71A014

Weidemann, S., Sauter, T., Schneider, L., and Schneider, C. (2013). Impact of two conceptual precipitation downscaling schemes on mass-balance modeling of gran campo nevado ice cap, patagonia. *J. Glaciol.* 59, 1106–1116. doi: 10.3189/2013JoG13J046

Willis, M. J., Melkonian, A. K., Pritchard, M. E., and Ramage, J. M. (2012a). Ice loss rates at the northern patagonian icefield derived using a decade of satellite remote sensing. *Rem. Sens. Environ.* 117, 184–198. doi: 10.1016/j.rse.2011.09.017

Willis, M. J., Melkonian, A. K., Pritchard, M. E., and Rivera, A. (2012b). Ice loss from the southern patagonian ice field, south america, between 2000 and 2012. *Geophys. Res. Lett.* 39, 1–6. doi: 10.1029/2012GL053136

Conflict of Interest Statement: The authors declare that the research was conducted in the absence of any commercial or financial relationships that could be construed as a potential conflict of interest.

frontiers in Earth Science

ORIGINAL RESEARCH
published: 13 September 2018
doi: 10.3389/feart.2018.00130

Snow Cover Change as a Climate Indicator in Brunswick Peninsula, Patagonia

Francisco Aguirre[1,2], Jorge Carrasco[2], Tobias Sauter[3], Christoph Schneider[4], Katherine Gaete[1,2], Enrique Garín[5], Rodrigo Adaros[5], Nicolas Butorovic[6], Ricardo Jaña[1] and Gino Casassa[2,7]*

[1] Scientific Department, Chilean Antarctic Institute, Punta Arenas, Chile, [2] Centro de Investigación Gaia Antártica (CIGA), Universidad de Magallanes, Punta Arenas, Chile, [3] Climate System Research Group, Institute of Geography, Friedrich-Alexander University Erlangen-Nürnberg (FAU), Erlangen, Germany, [4] Geography Department, Humboldt University, Berlin, Germany, [5] Club Andino, Punta Arenas, Chile, [6] Laboratorio de Climatologia, Instituto de la Patagonia, Universidad de Magallanes, Punta Arenas, Chile, [7] Dirección General de Aguas, Ministerio de Obras Públicas, Santiago, Chile

Snow cover changes are assessed for the Brunswick Peninsula in southern Patagonia (52.9°S to 53.5°S), located on the transition between the wet Pacific Ocean area and the drier leeward side of the Andes. We use the Normalized Difference Snow Index (NDSI) and a new index which we call $Snow_{power}$, combining the NDSI and the Melt Area Detection Index (MADI), to reconstruct the snow cover extent and its temporal distribution for the period 2000–2016, based on Moderate Resolution Imaging Spectroradiometer Sensor (MODIS) MOD09GA products. Comparison of these satellite-derived products with available snow duration and snow height data for 2010-2016 at the local Club Andino ski center of Punta Arenas shows that the NDSI exhibits the best agreement. A reasonable and significant linear correlation is found between the MODIS NDSI snow cover extent and the mean monthly temperature at Punta Arenas Airport combined with the monthly snow accumulation at Jorge Schythe station at Punta Arenas city for the extended winter period (April to September) from 2000 to 2016. Snow cover changes within this time series are extended to 1972 and 1958 based on historical climate data of Jorge Schythe and Punta Arenas airport, repectively. The results show a significant decreasing trend of snow extent of 19% for Brunswick Peninsula for the 45-year period (1972–2016), which can be attributed to a statistically significant long-term warming of 0.71°C at Punta Arenas during the extended winter (April–September) in the same period. Multiple correlation with different climate variables indicates that solid precipitation has a relevant role on short-term snow cover variability, but is not related to the observed long-term snow cover decrease.

Keywords: snow cover, climate change, remote sensing, MODIS, Patagonia

OPEN ACCESS

Edited by:
Michael Lehning,
École Polytechnique Fédérale de Lausanne, Switzerland

Reviewed by:
Christoph Marty,
WSL-Institut für Schnee- und Lawinenforschung SLF, Switzerland
Florian Hanzer,
Universität Innsbruck, Austria

****Correspondence:***
Francisco Aguirre
francisco.aguirre@umag.cl

Specialty section:
This article was submitted to Cryospheric Sciences, a section of the journal Frontiers in Earth Science

Received: *14 February 2018*
Accepted: *13 August 2018*
Published: *13 September 2018*

Citation:
Aguirre F, Carrasco J, Sauter T, Schneider C, Gaete K, Garín E, Adaros R, Butorovic N, Jaña R and Casassa G (2018) Snow Cover Change as a Climate Indicator in Brunswick Peninsula, Patagonia. Front. Earth Sci. 6:130. doi: 10.3389/feart.2018.00130

INTRODUCTION AND REGIONAL SETTING

Climate change particularly affects snow-covered areas (Hughes, 2003; IPCC, 2013), since even small changes in the surface–atmospheric energy balance may cause significant decreases in snow cover, affecting the local hydrology, associated ecosystems, hydroelectric power generation, and tourism activities (Gobiet et al., 2014; McGowan et al., 2018). Therefore, if climate trends can be detected, valuable information can be provided to decision makers and stakeholeders.

Snow cover is a critical component of the cryosphere and climate system at both local and global scales (Chen et al., 2018). Snow also affects other components of the Earth system at different scales by its radiative and thermal properties which modulate transfer of energy and mass at the surface-atmosphere interface (Frei et al., 2012). Snow cover can affect glaciers through changes in albedo and mass balance and also affects permafrost through its thermal insulation properties and meltwater input (Beniston et al., 2018). Additionally, snow is critical for water resources during the melt season, especially in areas lacking glaciers. Snow occurrence is also relevant for regional planning, including vehicle traffic, pasture and livestock management, its retarding effect on flash floods and slope erosion during extreme precipitation events and winter tourism and sports. In fact, snow-based tourism and sport was identified as particularly vulnerable to climate change. This climate dependency together with its economic impact on ski tourism (Steiger and Abegg, 2018), has prompted the authorities and private sector of the Magallanes Region in austral Chile to re-think the future of the current ski resort "Club Andino" located at Cerro Mirador, close to Punta Arenas city, which has barely operated for 10 days in the last two snow seasons (2016–2017). A possible alternative is a new ski resort planned to be located at Tres Morros, 25 km southwest and 200 m higher than Cerro Mirador.

The climate along the west coast of southern South America, including southern Patagonia, is determined by the permanent high pressure anticyclonic circulation (the subtropical South Pacific High, SPH) located in the south-eastern Pacific Ocean centered around 30°S, the circumpolar low pressure belt that surrounds the Antarctic continent around 60°S, and the resulting westerly wind regime that prevails in mid-latitudes (40–55°S). The seasonal north-south displacement of the SPH and the circumpolar trough modulate the westerly flow, and therefore, defines the eastward trajectory of the low-pressure frontal systems that cross southern South America. In particular, the west side of southernmost Patagonia is frequently affected by passing fronts and low-pressure systems that results in a high number of cloudy (77–86%) and precipitation days (81–88%) throughout the year (Carrasco et al., 2002). In addition, the complex topography defines a distinct climate regime at both sides of the Andes, with a relatively warmer and moister environment on the western side in comparison with the eastern side (Schneider et al., 2003; Weidemann et al., 2018). The precipitation is much higher and increases with altitude on the western slope due to orographically induced upward motion, and rapidly decreases toward the east due to the foehn mechanism (Weidemann et al., 2013).

The scarcity of rain-gauge stations precludes exhaustive regional and temporal analysis. The last IPCC report (Hartmann et al., 2013) reveals this difficulty. Their assessment indicates a negative trend of the annual precipitation ranging between 5 and 10 (2.5 – 5) mm per decade around Punta Arenas for the 1901–2010 (1951–2010) period using the GHCN (Global Historical Climatology Network of NOAA) dataset on the western coast of Patagonia (see their Figure 2.29). Earlier, Carrasco et al. (2008), analyzing the 1958–2006 period, showed an overall increase of the precipitation registered at the Punta Arenas airport from around 1967 to 1991, but no trend thereafter. Later, González-Reyes et al. (2017) with data updated to 2014, indicated that large interannual and inter-decadal precipitation variability has been observed for the last 100 years at Punta Arenas. Although a long-term trend is not evident from this record, a significant precipitation reduction has been observed after 1990, especially in spring and summer, while the winter precipitation has shown a significant increase.

Furthermore, an overall temperature increase has been detected in southern South America. Early work by Ibarzábal et al. (1996) and Rosenblüth et al. (1997) suggested that the warming has been higher in the eastern side of the Andes than on its western side. Falvey and Garreaud (2009) showed a strong temperature contrast in central and northern Chile (17° – 37°S) for the 1979-2006 period, with a coastal cooling of −0.2°C/decade and warming of +0.25°C/decade only 100–200 kilometers further inland. This cooling could be linked to an intensification of the South Pacific Anticyclone during recent decades, that enhances ocean upwelling off the coast of Chile. However, a recent study suggests that this recent period of coastal cooling has ended, modulated by a phase change of the Interdecadal Pacific Oscillation (Burger et al., 2018).

Therefore, there is a need for systematic studies to characterize the spatial and temporal distribution of snow cover in the Southern Hemisphere, and particularly in southernmost Patagonia, since all of the scarce long-term *in-situ* records from South America are from the central Andes (Vaughan et al., 2013). Here, we reduce this gap by using a remote sensing approach based on MODIS satellite data to reconstruct a snow cover time series and to relate snow conditions to present and past climate variations. This study is framed within a broader science programme that aims at contributing snow and climate information for regional planning in the Magallanes Region in southernmost Chile. The main problem we wish to target is whether snow cover has shown significant changes during the last few decades at Brunswick Peninsula, and if so, which are the main forcing factors. As such, this article will contribute to predict the future snow evolution in the area of Punta Arenas, the largest Chilean city in southern Patagonia.

STUDY AREA

The study area is located on Brunswick Peninsula in southern Patagonia between 52.9° and 53.9°S and 73.0° and 70.4°W. This peninsula is part of the southern extension of the Patagonian Andes where Punta Arenas is the largest city and capital of the Magallanes Region, the southernmost region of Chile. It is surrounded by the Strait of Magellan to the east, and by Seno Otway to the west. Most of the southwestern part is dominated by small mountains of the southern Andes, with many summits between 500 and 1,000 m, but all lower than 1,200 m a.s.l. Contrastingly, the northeastern part exhibits mostly a flat topography below 200 m a.s.l., which is part of the Patagonian steppe ("pampa"). The first mountains to the south are located west of Punta Arenas, with a maximum altitude of 590 m a.s.l. at Cerro Mirador. On the eastern slope

of this summit the skiing resort "Club Andino" is located at 53.15°S, 71.05°W. A future skiing resort is planned at "Tres Morros" at 53.31°S, 71.29°W, 866 m a.s.l., located 25 km SW of Cerro Mirador. The area has a strong Pacific Ocean influence, through the prevailing westerly circulation regime. This in combination with the unique topographic distribution of the Patagonian Andes creates one of the most pronounced precipitation gradients on earth (Carrasco et al., 2002; Schneider et al., 2003; Smith and Evans, 2007; Garreaud et al., 2013; Weidemann et al., 2018). Due to the north-south orientation of the Andes almost perpendicular to the westerly airflow, the regional west-to-east variation along the 53°S latitude and across the southern Andes shows an annual precipitation of about 6,000 mm on the western slopes of the mountain range decreasing to <1,000 mm on the eastern slope (Schneider et al., 2003) and to 416 mm at Punta Arenas (González-Reyes et al., 2017).

Figure 1 shows the geographical location and the three different specific study areas where the snow-cover variability has been reconstructed. The first chosen area is the "Macro zone" of 1,637 km^2 covering a large part of the Brunswick Peninsula, used here as representative of the snow cover distribution on the entire peninsula. Two smaller embeded zones are respectively centered on the existing ski resort "Cerro Mirador" (302 km^2) and the projected ski resort "Tres Morros" (291 km^2). These two locations, during the time frame of the analysis, proved to have less cloud coverage than the southern Macro zone area, allowing adequate snow sensing by visible and near-infrared MODIS imagery.

DATA AND METHOD

In this section we describe the different data and methods used to reconstruct the inter-annual snow cover variability and the spatial and temporal evolution. Data include MODIS satellite information, ground stations, radiosonde, and MERRA-2 reanalysis. Calculations including snow reconstruction and statistical applications were made using the open source programing language Python v._3.5 (http://www.python.org). Maps (**Figures 1**, **2**) were depicted using the open source QGIS v_2.18[1] A couple of figures (9 and 13B) were made using Matplotlib Python graphic package (Hunter, 2007).

MODIS Data and Snow Cover Detection

To reconstruct the extent of the seasonal snow cover at Brunswick Peninsula, we take advantage of the snow spectral reflectance properties given by the Moderate Resolution Imaging Spectroradiometer (MODIS) satellite data at 500 meters spatial resolution. The high temporal resolution (<2 days) of MODIS data facilitates selection of cloud-free imagery at the latitude of Brunswick Peninsula. Additionally, its multispectral capabilities make it one of the most advanced optical sensors available for large-scale terrestrial applications (Salomonson et al., 1989).

[1]QGIS Geographic Information System. QGIS Team (2017). *QGIS Geographic Information System*. Open Source Geospatial Foundation Project. Available Online at: https://qgis.org

Several MODIS products are available, including the MOD10 snow cover data in its version MOD10A1 (daily) and MOD10A2 (8-day composite). Both products use the Normalized Difference Snow Index (NDSI) algorithm based on MODIS reflectance data of bands 4 and 6 to discriminate snow from other targets (Winther and Hall, 1999; Sirguey et al., 2009). This method is usually preferred instead of other classification methods such as the supervised classification (Wang and Li, 2003).

The MODIS cloud product (MOD35) is also incorporated into the algorithm to construct the snow products. Nevertheless, inaccurate detection of clouds show some problems in high elevation regions such as the Southern Alps of New Zealand (Hall et al., 2002; Sirguey et al., 2009) and the Northern Patagonia Icefield (Lopez et al., 2008; Sirguey et al., 2009). Some corrections have been implemented in updated versions of the snow cover product but snow and cloud discrimination problems persist (Hall and Riggs, 2007). Recurrent misclassifications limit the suitability of the MOD10 snow product for detecting the snow cover in frequently cloud-covered regions, such as southernmost Patagonia.

Therefore in this study we use the MODIS land product MOD09GA from the Terra satellite in its version 6 (Vermote and Wolfe, 2015) at daily temporal resolution. We did not include the MODIS land product derived from the Aqua satellite due to malfunctioning of one of the spectral bands (Saavedra et al., 2018). The product MOD09GA includes corrected reflectance with a spatial resolution of 500 m (available from the Land Processes Distributed Active Archive Center, http://lpdaac.usgs.gov/) for the period 2000–2016. To optimize the download process, we used the script "*order_MWS.pl*" (available from https://ladsweb.modaps.eosdis.nasa.gov/tools-and-services/), downloading a total of 6079 images. We downloaded the satellite data covering approximately an area of 31,500 km^2, in order to obtain a general view and select image subsets.

To better discriminate potential cloud cover we conducted a visual inspection of the all images, which resulted in a selection of 484 could-free images. Sixty percent of the selected images (290) correspond to the period between April to September, temporal frame that we name "extended winter". At least, there is one cloud-free image for each extended winter month between 2000 and 2016, except for May and August 2000. **Figure 2** shows an example as a comparison between true-color (RGB: spectral MODIS bands B1, B4, B3) and false-color (RGB: spectral MODIS bands B3, B6, B7) compositions to help selecting cloud-free imagery.

A water mask was generated using the coastal margin of the Regional Government of Magallanes (http://www.goremagallanes.cl) and the information of lakes from the Dirección General de Aguas, (DGA, General Water Management of Chile, http://www.dga.cl/productosyservicios/mapas/Paginas/default.aspx#nueve) to exclude any possible interference between the snow detection and water bodies during in the analysis.

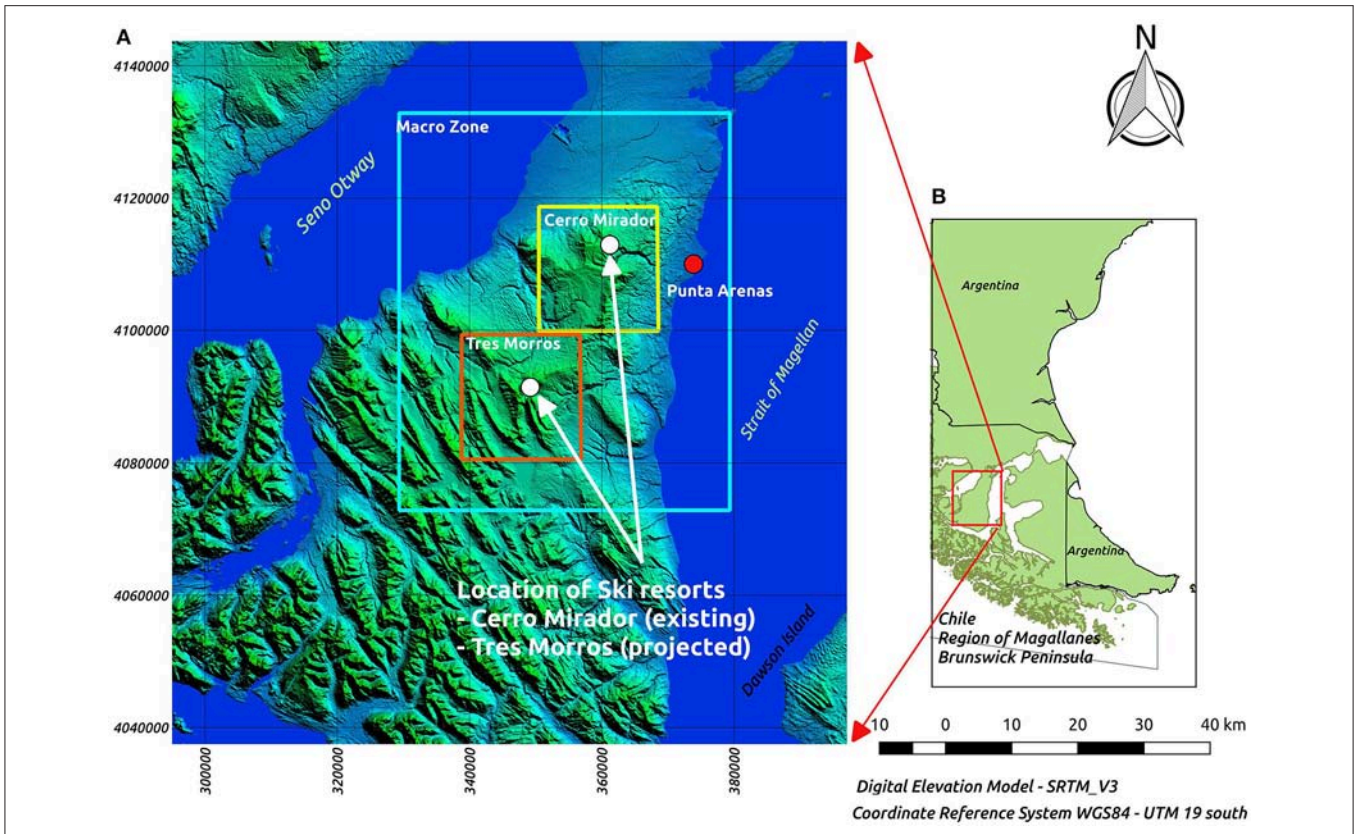

FIGURE 1 | General view of the study area. **(A)** shows the Brunswick Peninsula with the three study zones: Macro zone of 1637 km^2 (cyan), Cerro Mirador of 302 km^2 (yellow), and Tres Morros of 291 km^2 (red). The terrain elevation is shown with a DEM from SRTM_V3 data. **(B)** presents the general location of the study area.

Snow Detection Indices

There are several alternative methods for snow detection using different sensors and wavelengths. In this work, we computed two different indices from MOD09GA bands 1, 4, 6 and 7 (specified below): the NDSI and the Melt Area Detection Index (MADI). Both indices plus the calculation of the new proposed Index (Snow$_{power}$ index), were applied to each selected image and subsequently grouped to monthly means to obtain a monthly representation of the snow cover.

Normalized Difference Snow Index

NDSI is the most common method used for detection of the snow cover (Frei and Lee, 2010). It uses the contrast between the high reflectance (ρ) of snow in the green part of the visible spectrum (MODIS band 4, 545–565 nm) and the low reflectance in the short-wave infrared part of the spectrum (MODIS band 6, 1,628–16,52 nm). We used the threshold value NDSI ≥ 0.4 (Hall et al., 2002) for identification of snow pixels based on:

$$NDSI = \frac{\rho_{B4} - \rho_{B6}}{\rho_{B4} + \rho_{B6}}. \quad (1)$$

Melt Area Detection Index

The MADI approach uses the reflectance ratio between the red portion of the visible spectrum (MODIS spectral band 1, 0.62–0.67 μm) and the near-infrared (MODIS spectral band 7, 2.105–2.155 μm). Its principle is based on identifying liquid water layers that coat snow and ice when melt occurs to discriminate between frozen and liquid water (Chylek et al., 2007) according to:

$$MADI = \frac{\rho_{B1}}{\rho_{B7}} \quad (2)$$

MADI has been usually used to detect wet and dry snow over regions of known snow cover only. A study carried out by Bormann et al. (2012) in Australia considered a suitable threshold for snow cover detection similar to the NDSI method. This method establishes ranges for the MADI values using *in-situ* observations for snow detection. If the MADI value exceeds 6, then the pixel is characterized as snow. Additionally, Bormann et al. (2012) used the MADI values to infer snow depth validated with *in-situ* observations.

We combine the MADI and NDSI according to the following two steps procedure (see **Figure 2**):

1. We detect snow cover area (km^2) inside of each study zone. For this purpose, the NDSI is used as a binary snow cover detector representing snow-cover extent.

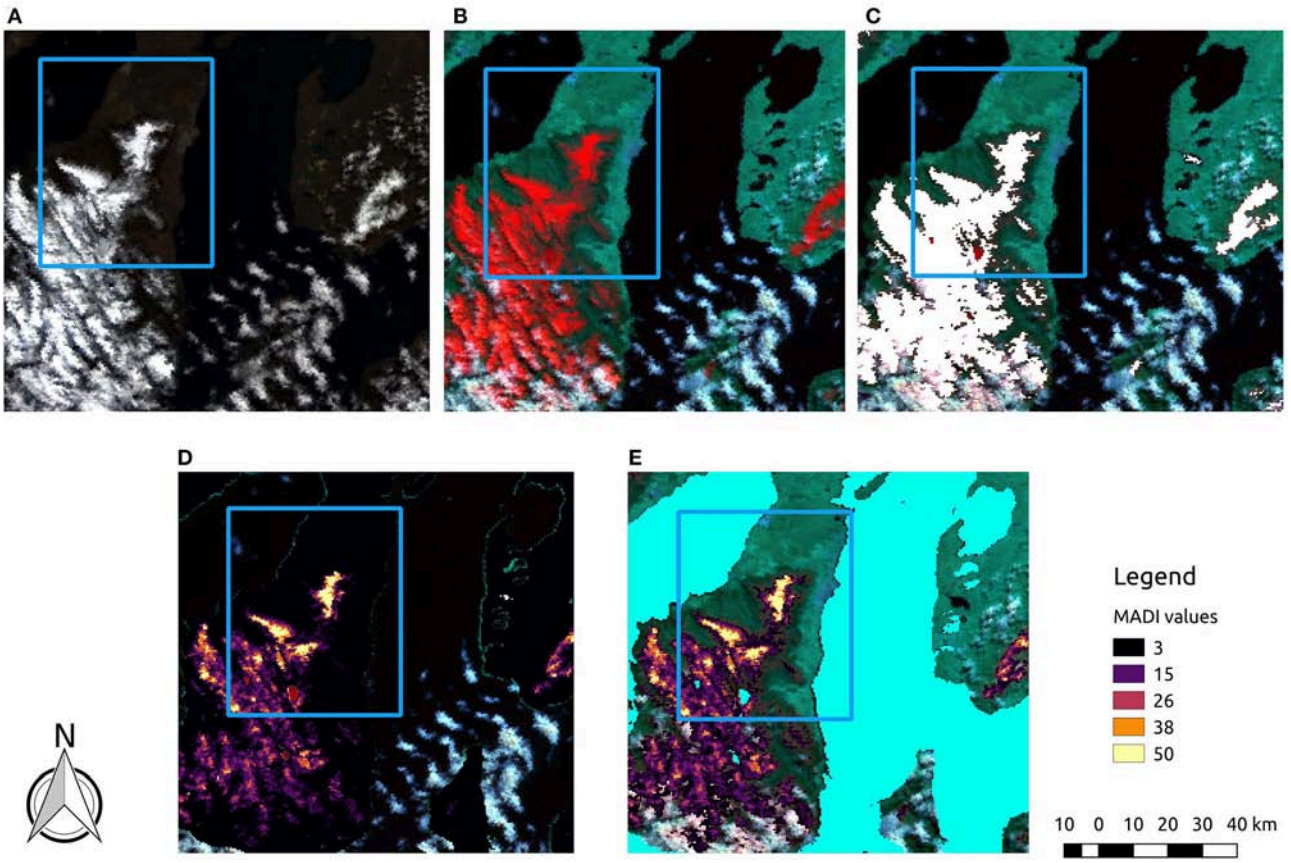

FIGURE 2 | MODIS-derived snow cover for the 26th of August 2015. **(A)** True color composition (1-4-3 MODIS bands), snow and clouds are both represented in white color. **(B)** False-color composite (MODIS bands 3-6-7) with snow in red and clouds in white. **(C)** NDSI mask, snow in white color. **(D)** MADI index, purple to light yellow colors show smaller to larger values, and clouds in white color. **(E)** Overlay of MADI values over the false color composite on snow covered areas as inferred from the NDSI mask, and the water mask in cyan. The macro zone limits are shown as a blue rectangle.

2. For the area detected above, we apply the MADI to each pixel classified as snow. Using a zonal mean we obtain a zonal representation expressed as a weight indicator of snow depth, according to Bormann et al. (2012).

With these two different indices we reconstruct and compare the inter-annual variability of snow cover for the period 2000–2016. Therefore, the NDSI is used to detect snow pixels and MADI is incorporated in a newly proposed index, called $\text{Snow}_{\text{power}}$, that incorporates the performance of both indices. We used the following equation for computing $\text{Snow}_{\text{power}}$ index:

$$SNOW_{power}(i) = \frac{\overline{\sum NDSI_{mask}}\,(i) \times \overline{MADI}_{zonal\ average}\,(i)}{\max(\overline{\sum NDSI_{mask}})} \quad (3)$$

Where $\overline{\sum NDSI_{mask}}\,(i)$ is the monthly average of the snow cover extension (pixels) for month (i), $\overline{MADI}_{zonal\ average}\,(i)$ is the zonal average MADI value for all snow-covered areas for the month (i), and $\max\left(\overline{\sum NDSI_{mask}}\right)$ is the maximum snow cover monthly NDSI value for all months considered.

Thus, this index is the result of the percentage of snow cover presence (NDSI) in a given area scaled by the zonal average MADI values for all the snow cover extent, divided by the present snow cover and its maximum monthly value for all months considered. We postulate that this relationship represents better the snow cover since it incorporates both snow cover fraction, in each zone of interest, and a weight linking it to snow depth obtained by MADI so that we derive the variability of the entire snowpack. In this study, we use both the snow cover extent using only NDSI, and the $\text{Snow}_{\text{power}}$ index as a combination of NDSI and MADI indices.

Meteorological Data and Climate Indices

Weather Station Data

A major difficulty in Patagonia is the scarcity of locally observed meteorological data, since weather stations are restricted to the main settlements and many stations have significant data gaps. A main weather station is Carlos Ibáñez Airport (53.00°S, 70.53°W, 38 m a.s.l), 18 km to the north of Punta Arenas city center. It has permanent atmospheric observations since 1958 and belongs to the Dirección Meteorológica de Chile (DMC, the

National Chilean Weather Service). In 1970 the Instituto de la Patagonia deployed the weather station "Jorge Schythe" (Santana et al., 2009) at 53.07°S and 70.52°W at 5 m a.s.l, within the city of Punta Arenas, 14 km south of the Punta Arenas Airport. In 1973 DGA (Dirección General de Aguas) installed at Jorge Schythe station a pluviometer, a thermometer and a relative humidity sensor. Data are available for Jorge Schythe station at a monthly level since 1972, and at a daily level since 1980. Another long-term meteorological record (more than 100 years) is also available from the Navy station Evangelistas Lighthouse (52.24°S, 75.06°W, 55 m a.s.l.) located at the western entrance of the Strait of Magellan.

The available station data allow studying the inter-annual and decadal pattern of air temperature and precipitation in relation to forcing mechanisms such as the El Niño Southern Oscillation (ENSO), the Antarctic Oscillation (AAO) or the Southern Annular Mode (SAM), and the Pacific Decadal Oscillation (PDO). Other stations have been deployed in recent decades in southern South America by DGA (e.g., Teniente Merino, San Gregorio, Pampa Huanaco and Bahía San Felipe), by DMC (Porvenir station) and by specific research projects such as Bahamondes station (Schneider et al., 2003; Weidemann et al., 2018). **Table 1** lists the above stations used in this study.

Radiosonde Data Punta Arenas

At Punta Arenas airport, radiosonde balloons are launched every day at 12 UTC (Universal Time Coordinated) since April 1975. This upper-air station measures a daily vertical profile of air temperature, relative humidity, wind direction and wind speed at different standard levels of the atmosphere. The zero-isotherm altitude (ZIA) can be determined from the air temperature profile. Monthly radiosonde data can be obtained from the Anuario Climatológico (Climatological Yearbook) available online from www.meteochile.gob.cl. Here, monthly averages of surface air temperature and 850 hPa (hectopascal) levels were used to determine the monthly altitudinal lapse rate which along with the geopotential height at the 850 hPa allowed to calculate the monthly and annual ZIA.

Reanalysis Data

The monthly snow cover product from MERRA-2 reanalysis data ("fractional snow-covered area FRSNO") for April–September (Gelaro et al., 2017) period were used for comparison with the MODIS snow cover reconstruction from 1980 to 2016. MERRA-2 data were downloaded from https://giovanni.gsfc.nasa.gov. MERRA-2 has a resolution of $0.5^\circ \times 0.625^\circ$ latitude-longitud grid with 72 model layers interpolated to 42 standard pressure levels (Bosilovich et al., 2015). It uses the modified three-layer snow model of Lynch-Stieglitz (1994). This snow hydrology model resolves for snow melting and refreezing, as well as dynamic changes in snow density, snow insulating properties, and other physics relevant to the growth and ablation of the snowpack (Stieglitz et al., 2001). The snow model component of the Land Surface Model (LSM) uses the minimum snow water equivalent (WEMIN) before it considers the surface to be snow covered (Reichle, 2012). In this sense, if the amount of snow (SNOMAS) on a given model-surface area is insufficient to cover the entire area with at least an amount of WEMIN, the snow cover fraction (FRSNO) will be the fraction of the area that is covered by an amount equal to WEMIN, that is expressed as, FRSNO = min(1, SNOMAS/WEMIN) (Reichle, 2012; Reichle et al., 2017). No studies have so far been conducted on how well the MERRA-2 can simulate snow cover in Patagonia.

The MERRA-2 snow cover values were extracted for the grid point 53.3°S, 71.1°W within the Macro zone. The values are expressed as a monthly snow cover fraction, with a value of 1 representing 100% of snow cover. For example, the maximum monthly FRSNO value for the period 2000–2016 was 0.38 for June 2002, when the NDSI snow cover extent indicated an area of 1,443 km^2 for the Macro zone, equivalent to 88% of the total domain area of 1,637 km^2.

Climate Indices

ENSO is the most significant mode of inter-annual climate variability in the Southern Hemisphere with world-wide impacts. El Niño (La Niña) corresponds to the warm (cold) phase which is characterized by weaker (stronger) trade winds and above (below) normal sea surface temperatures (SST) in the equatorial Pacific Ocean. Also, a weaker (stronger) SPH is encountered

TABLE 1 | Weather stations used in this research.

Station	Lat (S)	Lon (W)	Altitude (m a.s.l.)	Parameter	Period	Annual average precipitation (2000–2016) mm	Owner
Evangelistas	52°24′	75°06′	55	P,T	1899–2016	3,900	SERVIMET
Jorge Schythe	53°07′	70°52′	5	P,T,S	1970–2016	562	INST-PAT
Punta arenas (Airport)	53°00′	70°53′	38	P,T,RS	1958–2016	380	DMC
Teniente Merino	52°02′	70°44′	160	P	1984–2016	250	DGA
Bahamondes	52°48′	72°56′	26	P	1999–2016	4,535	UT_FAU_HU
San Gregorio	52°33′	70°04′	3	P	1992–2016	272	DGA
Porvenir	53°11′	70°19′	27	P	1970–2016	269	DMC
Pampa Huanaco	54°02′	68°47′	150	P	1994–2016	400	DGA
Bahía San Felipe	52°52′	69°55′	10	P	1970–2016	462	DGA

P, total precipitation; T, temperature; S, snow accumulations; RS, radiosonde data; Servimet, Servicio Meteorológico de la Armada; DMC, Dirección Meteorológica de Chile; INST-PAT, Instituto de la Patagonia; UT_FAU_HU_, Universities of Trier, Erlangen-Nürnberg and Humboldt, Germany.

during El Niño (La Niña) with stronger (weaker) subtropical and weaker (stronger) polar jet-streams (Chen et al., 1996). In southernmost South America, a weak correlation between ENSO and precipitation occurs to the west of the Patagonian Andes between 45° and 55°S (Schneider and Gies, 2004), i.e., with below (above) normal precipitation during El Niño (La Niña) (Montecinos and Aceituno, 2003).

The PDO, also called Interdecadal Pacific Oscillation (IPO) has a cycle of 15–30 years that shows similar SST and sea-level pressure anomaly patterns as ENSO (Garreaud and Battisti, 1999; Mantua and Hare, 2002). During the warm (or positive) PDO phase, El Niño events prevail in frequency and intensity. On the contrary, during the cool (or negative) phase, the opposite pattern occurs and La Niña episodes are more frequent and last longer (Andreoli and Kayano, 2005). In southern Patagonia the prevailing large-scale pattern associated with a positive PDO is an anticyclonic circulation centered in the southeastern Pacific Ocean to the west of the Antarctic Peninsula (Garreaud and Battisti, 1999). This pattern might reduce precipitation along the southern tip of South America, so that the storm systems may be steered northwards (Garreaud and Battisti, 1999).

Another natural internal mechanism for interannual variability is related to the SAM (also known as the Antarctic Annular Oscillation AAO) a large-scale alternation of atmospheric pressure between the mid-latitudes and high latitudes at the surface pressure level (Gong and Wang, 1999). These changes are linked with changes in the strength of the Southern Hemisphere westerly winds due to the latitudinal shift in the area of maximum zonal flow (∼45°S) or in its intensity (surface wind speed) (Moreno et al., 2010). Positive correlations between the westerlies and precipitation prevail along the western margin of the southern South America between 40° and 55°S, while correlations tend to be negative at similar latitudes along the Atlantic margin (Moreno et al., 2010). Thus positive (negative) AAO means southward (northward) displacement of the westerlies, and therefore, of the storm track in the Pacific Ocean. This can also favor (inhibit) precipitation events in the western coast of southern South America, although it depends how far the southward (northward) displacement extends and whether the area of interest is governed by orographic rain or rather by foehn effects on the east side of the Cordillera.

These different mechanisms are expressed by their respective indices. The interannual variability of ENSO can be studied by using SOI, a normalized sea-level pressure difference between Tahiti and Darwin stations (Chen, 1982; Trenberth, 1997). Alternatively, among other indices, the SST monthly anomalies in the central-equatorial sector of the Pacific Ocean, known as Niño 3.4 can be employed as an ENSO index (Trenberth, 1997). The PDO index is calculated by the leading principal component applied to the spatial monthly averaged SST of the North Pacific Ocean north of 20°N, using mainly the October to March period so that the interannual fluctuation mostly takes place in winter (Mantua and Hare, 2002). The AAO is calculated by principal component analysis so that the first three modes explain 33, 11 and 9% of the variance, respectively, and it can be constructed using the 700 hPa height anomalies poleward of 20°S (Gong and Wang, 1999). The above indices were downloaded from the Earth System Research Laboratory www.esrl.noaa.gov/psd/data/climateindices/list/, specifically, the SOI from www.cpc.ncep.noaa.gov/data/indices/soi, the PDO from www.esrl.noaa.gov/psd/ data/correlation/pdo.data and the AAO from www.esrl.noaa.gov/psd/data/correlation/aao.data.

Statistical Analysis

In order to analyse the variability of snow cover extent, statistical correlations were performed with different climate variables. We use the Pearson correlation quantified by the coefficient of determination (R^2), the Durbin-Watson statistics for detecting autocorrelation between variables, and significance tests with t-statistic using a p-value at 5% significance. The structure of the residuals is also analyzed to detect any biases. Based on the best relationship we express the satellite-derived snow cover as a function of climate variables, which allows to reconstruct the snow cover to 1965. In order to detect long-term trends we use an exponential filter (Rosenblüth et al., 1997) to reduce the interannual variability and apply a linear regression. Python Statsmodels statistic package was used (Seabold and Perktold, 2010).

RESULTS

Climate Variability and Trends

Precipitation and Temperature From Surface Stations

The average monthly precipitation 2000–2016 for 8 weather stations aligned from west to east around 53°S is shown in **Figure 3**. Precipitation is much higher (around one order of magnitude) in the western stations Evangelistas and Bahamondes located in the windward side of the Andes than the stations located in the leeward side (for example Punta Arenas). Precipitation occurs year-round with only little seasonality, although the minimum (maximum) tends to occur at the end of winter (summer)—beginning of spring (autumn). In general, precipitation increases from north to south although Bahía San Felipe station shows higher accumulation than Pampa Huanaco located further south. The annual variability during the 2000–2016 period is displayed in **Figure 4**. There are no correlations among different stations except between the two nearby ones located in Punta Arenas (airport and city). This reveals the large spatial variability of precipitation in southernmost South America. Also, no common and significant trends can be observed in the analyzed stations. Thus, while Evangelistas suggests an increase, Punta Arenas city and Bahía San Felipe suggest instead a decrease in precipitation in the last 17 years. This finding was already mentioned by González-Reyes et al. (2017) who analyzed the long-term behavior for the 1900-2014 period using precipitation data from Observatorio Meteorológico Monseñor Fagnano located in Punta Arenas city center (where the Salesian mission began measurements in 1887) and Punta Arenas Airport where observations started in 1930. The Airport station was first located in Bahía Catalina until 1958, 4 km north of the city center, and then moved 14 km north to Punta Arenas Airport (Presidente Carlos Ibáñez del Campo) where DMC continues the measurements at present.

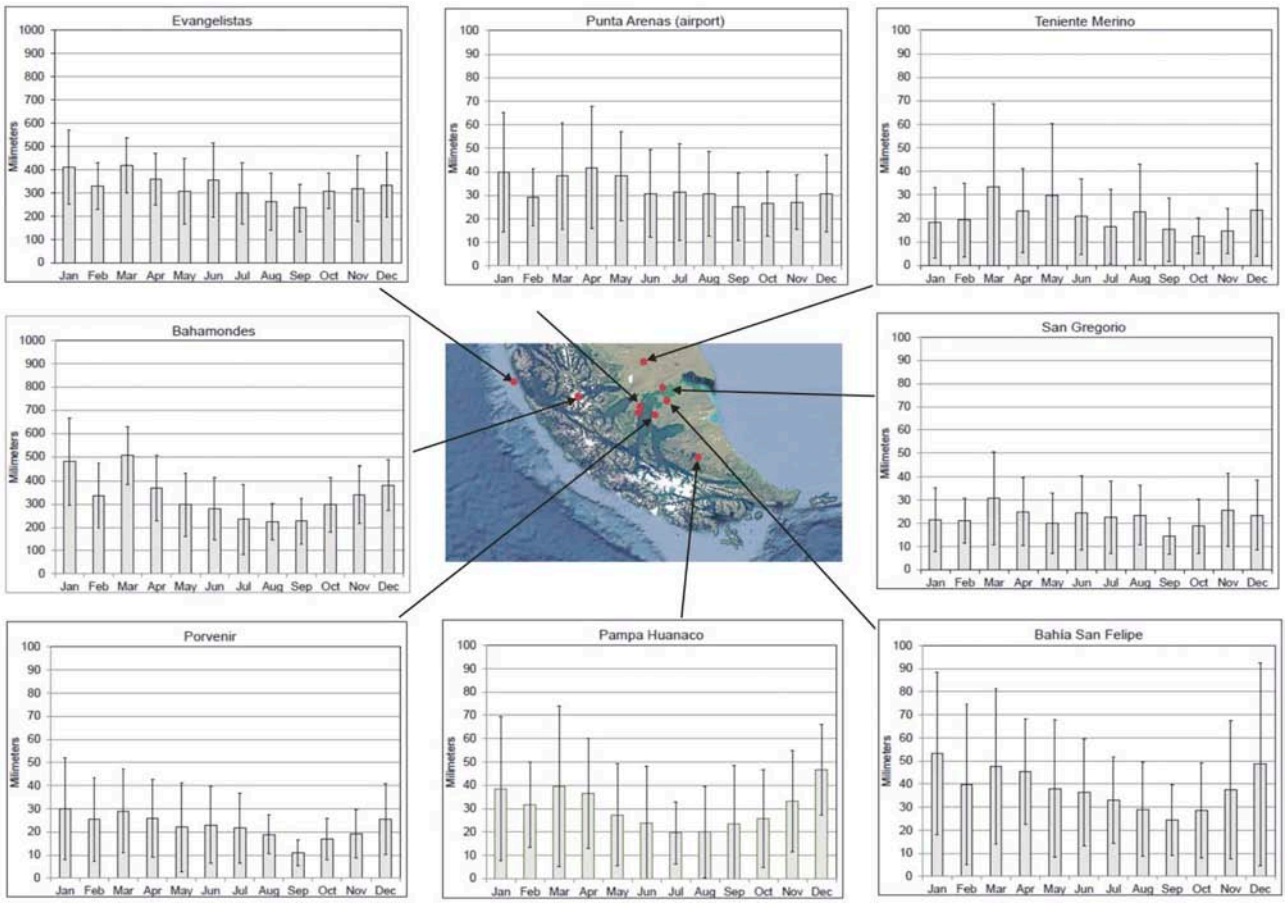

FIGURE 3 | Monthly precipitation averages over the period 2000–2016. Vertical lines are the 1st standard deviation. The red dot immediately south of Punta Arenas corresponds to Jorge Schythe station at Instituto de la Patagonia located in Punta Arenas city, shown in **Figure 4**. Note that the vertical scale at Evangelistas and Bahamondes stations (the two western locations) have a range of 1,000 mm, while the range for all the other stations is 100 mm.

González-Reyes et al. (2017) found a significant reduction in the annual precipitation sums after 1990, especially in spring and summer, while the winter precipitation showed a significant increase during that period.

The other long-term precipitation record is from Evangelistas with data available from 1899 onward, operated by the Chilean Navy. Monthly data and some complete years are missing which preclude exhaustive analysis. Nevertheless, 80% of the data are available and only 8 years have more than 6 months missing, with 3 complete years missing. **Figure 5** shows the annual and extended winter (April–September) annual variability and longterm trend of precipitation. It was constructed using the Evangelistas data, the missing monthly averages were replaced by the respective long-term monthly averages to facilitate data management. The vertical lines on the annual data are the sum of the 1st standard deviation of the missing months which assigns an upper and lower boundary for the most probable annual precipitation. The solid curve results by applying an exponential filter to the data to eliminate the inter-annual variability and highlighting the interdecadal variability (Essenwanger, 1986; Rosenblüth et al., 1997). This filter is similar to a moving mean, but it has the advantage of keeping the complete series for analyzing relatively short periods.

The annual data show an overall decrease in precipitation from 1899 until 1980, after which a significant increase took place between 1984 and 1998. The precipitation decline observed by González-Reyes et al. (2017) during 1990–2014 at Punta Arenas is not completely captured by the Evangelistas data, although an overall decrease could have taken place during 1997–2007. The significant precipitation increase from around 1984–1998 has been a matter of discussion of whether it is a real signal or rather a result of an instrument change or relocation of instrument or change in staff and operation mode (Carrasco et al., 2002; Aravena and Luckman, 2009). According to the Servicio Meteorológico de la Armada (Navy Weather Service) the weather station has not been changed in location, nor the instrument type or operation mode, only the staff is replaced every one or 2 years (personal communication Ismael Escobar, Chilean Navy). The insert in **Figure 5** shows an enlargement of

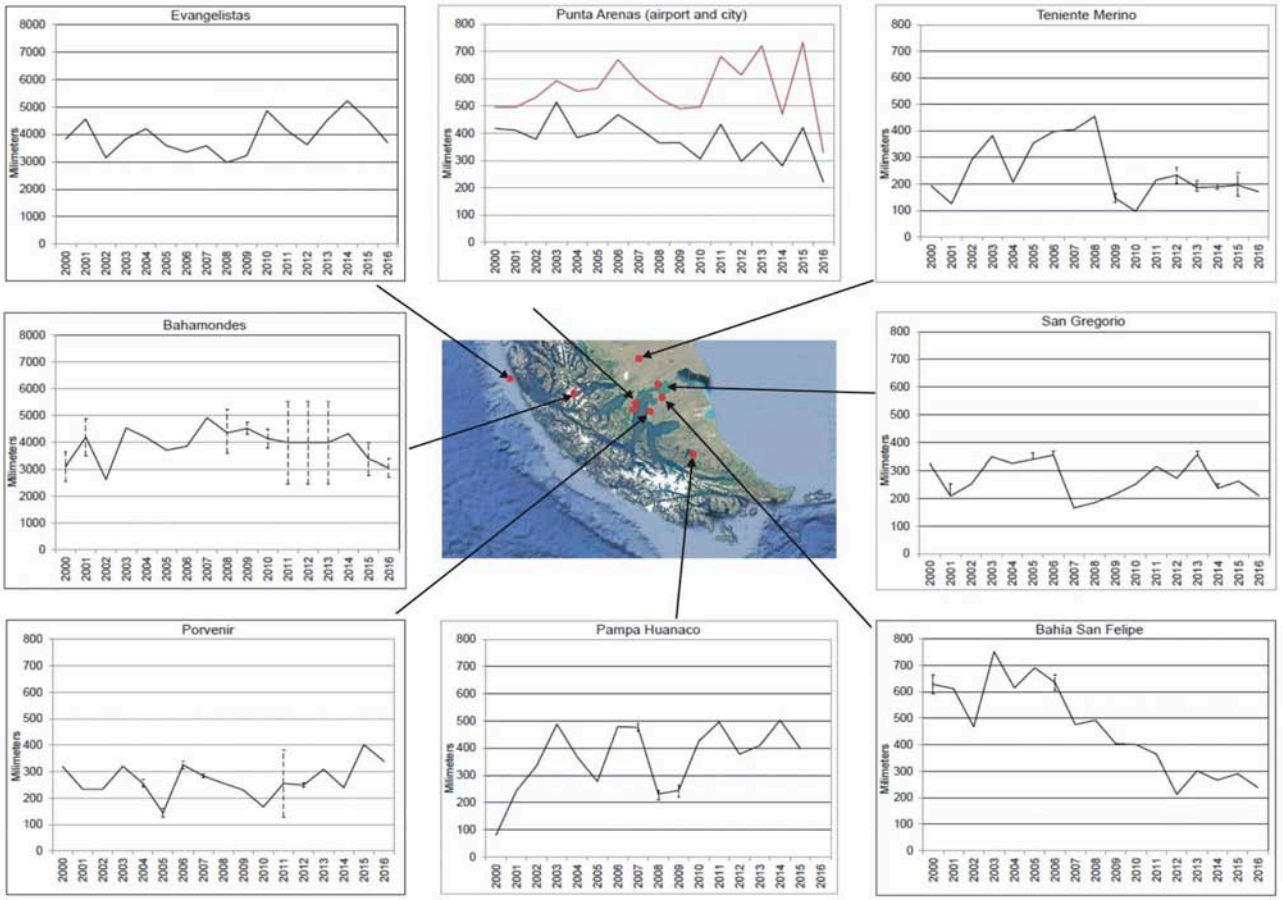

FIGURE 4 | Annual precipitation time series for the 2000–2016 period. Vertical lines in some graphs are the sum of the 1st standard deviation of the missing months, which were replaced by their respective monthly averages. Note that the vertical range at Evangelistas and Bahamondes stations (the two western locations) is 8,000 mm, while all other stations have a range of 800 mm.

the 1975–2000 period, suggesting a rapid but gradual increase of precipitation. However, the magnitude of the increment (of about 70% between 1984 and 1998) should be taken with caution, even though Evangelistas is located just to the south of the maximum precipitation region (Miller, 1976) and a slight southward displacement of the westerlies could indeed trigger such profound change in overall precipitation.

Figure 6A shows the monthly average of the mean air temperature at Evangelistas, Bahamondes and Punta Arenas Airport over the 2000–2016 period. The ocean and continental influences are clearly seen by comparing the annual cycle at each station located in the latitudinal transect around 53°S. The average winter (summer) air temperature at Punta Arenas Airport is about 3 (2)°C colder (warmer) than at Evangelistas. The inter-annual variability and the long-term trend (solid lines) of the extended winter (April–September) mean temperatures for Evangelistas and Punta Arenas are shown in **Figure 6B** for the available 1965–2016 and 1958–2016 periods, respectively. The temperature trends within both periods show a significant warming in all seasons (especially in the winter) including the montly mean and minimum temperatures. A total warming of 0.54°C (0.11°C/decade) and 0.72°C (0.12°C/decade) is found at Evangelistas and Punta Arenas Airport over the 1965–2016 and 1958–2016 periods, respectively, computed using the interannual extended winter data (smoothed data).

Upper Air Sounding

The analysis of upper air data from Punta Arenas Airport is restricted for the lower half troposphere given by the standard levels at 850, 700, and 500 hPa which respectively correspond to the annual (January-December) mean altitudes of 1,338, 2,856, and 5,377 m. This corresponds to an annual mean air temperature of −1.5, −9.7, and −26.1°C, respectively. The chosen levels show positive linear trends of +0.01, +0.25, and +0.45°C (non-statistically significant) over the 1976–2016 period at 850, 700, and 500 hPa, respectively, revealing a moderate warming trend in the mid-troposphere. Also, the zonal component of the wind (u-wind) at surface, 850, 700, and 500 hPa shows positive linear trends of 0.81, 1.73, 2.39, and 2.45 ms^{-1} for the 1976–2016 period, respectively (**Figure 7**). The increase in wind speeds is not statistically significant. However, this finding might be indicative of southernmost South America

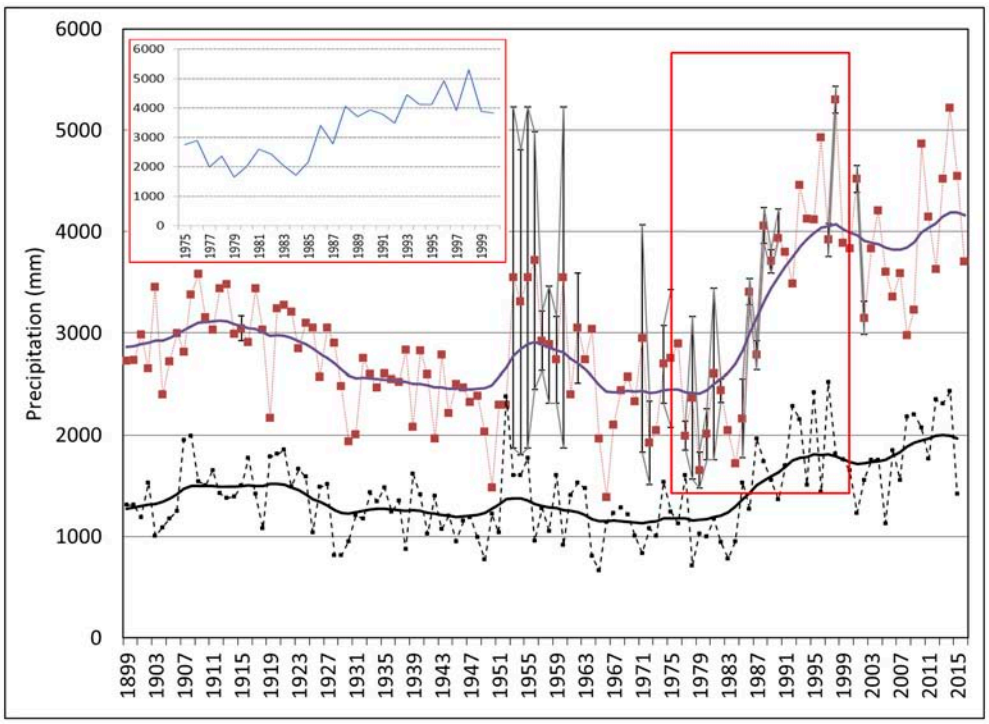

FIGURE 5 | Annual precipitation (red squares) at Evangelistas station over the period 1989–2016. The purple curve is the result of an exponential filter applied to smooth the original annual data (squares). Vertical lines in some years are the sum of the 1st standard deviation of the missing months, which were replaced by their respective monthly averages. The upper left inset shows a zoom of the 1975–2000 period. Lower curves (black) are the extended-winter (April-September) precipitation at Evangelistas station.

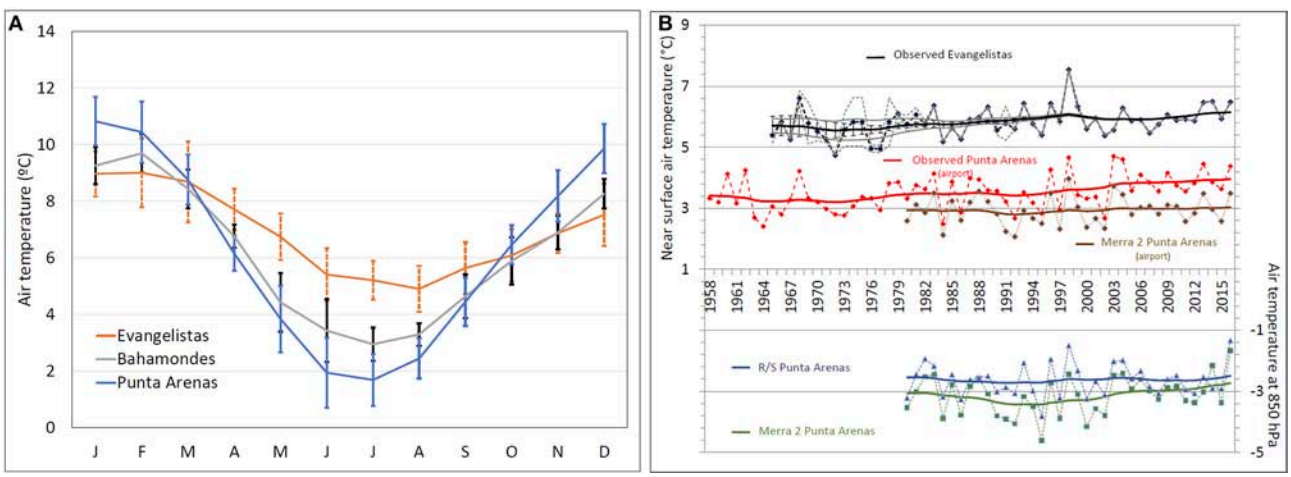

FIGURE 6 | (A) Annual cycle of mean air temperature at Punta Arenas Airport, Evangelistas and Bahamondes stations for the 2000–2016 period. Vertical lines are the 1st standard deviation. **(B)** Extended winter (April–September) mean air temperatures (dashed lines) at Evangelistas (upper curve, black) and Punta Arenas airport (lower curve, red) over the period 1958–2016. Thick lines are the result of an exponential filter applied to smooth the annual data (squares). Dashed (solid) gray curves in the annual (filtered) Evangelistas data are the lower and upper boundary of the sum of the 1st standard deviation of the missing months which were replaced by their respective monthly averages. Brown solid and dashed lines are the near surface air temperature as simulated by the MERRA-2 model at the nearest gridpoint from Punta Areans. **(C)** Winter mean air temperature at 850 hPa measured by the radiosonde (R/S) at Punta Arenas (blue lines) and simulated by the MERRA-2 model for the nearest gridpoint from Punta Arenas (green lines). Solid lines are the smooth behavior after applying the exponential filter, while dashed lines are the interannual variability. MERRA-2 data are available from 1980 onward.

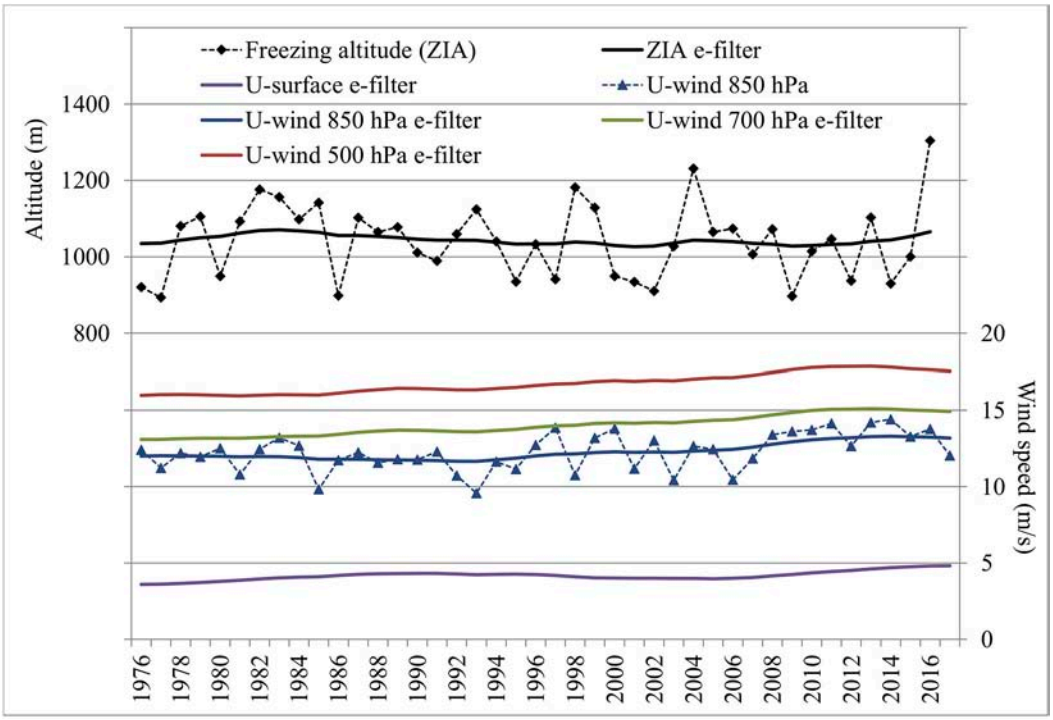

FIGURE 7 | Annual and long-term (using an exponential filter) Zero Isotherm Altitude (ZIA) (black) and zonal wind component at surface (purple), 850 hPa (blue), 700 hPa (green) and 500 hPa (red) from Punta Arenas Airport radiosonde data.

becoming more and more affected by a windier environment due possibly to the enhancement and southward displacement of the westerly winds associated with positive SAM during recent decades (Marshall, 2003). Following the analysis of Schneider and Gies (2004) and Garreaud et al. (2013), the correlation between precipitation and u-wind at 850 hPa reveals that with stronger zonal wind there is an increase in precipitation westward from the Patagonian Andes and a decrease over the eastern side. The overall different behavior of the precipitation observed at Evangelistas and Punta Arenas may be the result of the overall increase in the u-wind component.

The mean annual freezing level calculated from the radiosonde data shows a 49 m non-statistically significant increase during the 1976–2016 period. The highest freezing level recorded in the period occurred in 2016 with an altitude of 1,304 m, 263 m higher than the average in the whole period (see **Figure 7**). The year 2016 also showed the lowest annual precipitation since 1970 according to the Punta Arenas Airport station record.

Snow Cover Reconstruction and Variability

In **Figure 8**, we show the monthly average of the snow cover area using the NDSI and the MADI indices for each domain namely the Macro zone, Cerro Mirador, and Tres Morros (**Figure 1**). We assume that the beginning and the end of the snow season occur when the monthly snow cover extent rises or drops below 20% of the multi-year maximum montly snow extent, that is 327 km^2 for the Macro zone, 58 km^2 for Cerro Mirador and 60 km^2 for Tres Morros.

With this approach, we can identify the annual duration of the snow season which usually begins in May and ends in September for Cerro Mirador and in October for Tres Morros. The relation between the snow cover area and MADI values is shown in **Figure 8**. The monthly averaged snow cover duration is 4 weeks longer at Tres Morros compared to Cerro Mirador due to higher altitudes. Similar $Snow_{power}$ index values can be observed between Macro and Cerro Mirador zones, while Tres Morros shows higher values due to its higher altitude.

Figure 9 shows scatter plots between the $Snow_{power}$ index and the snow cover extent derived from the NDSI and MADI indices. Coefficient of determination (R^2-values) higher than 0.86 are obtained for the $Snow_{power}$ index between each pair of zones especially between the Macro zone and Cerro Mirador ($R^2 = 0.96$, **Figure 9A**). This is reasonable considering that the Macro zone includes the other two zones and considers a more varied topography. A slightly smaller $Snow_{power}$ index $R^2 = 0.86$ is obtained between Cerro Mirador and Tres Morros (**Figure 9C**), which can be attributed to its higher altitude which results in a larger and more permanent snow cover extent, unlike to the case of Cerro Mirador.

At Cerro Mirador the ski club "Club Andino" has recorded information of the ski season duration based on the opening and closing dates of the ski lifts and the snow height average during the ski season from a stake located close to the main hut. There is no artificial snow production at the ski club so

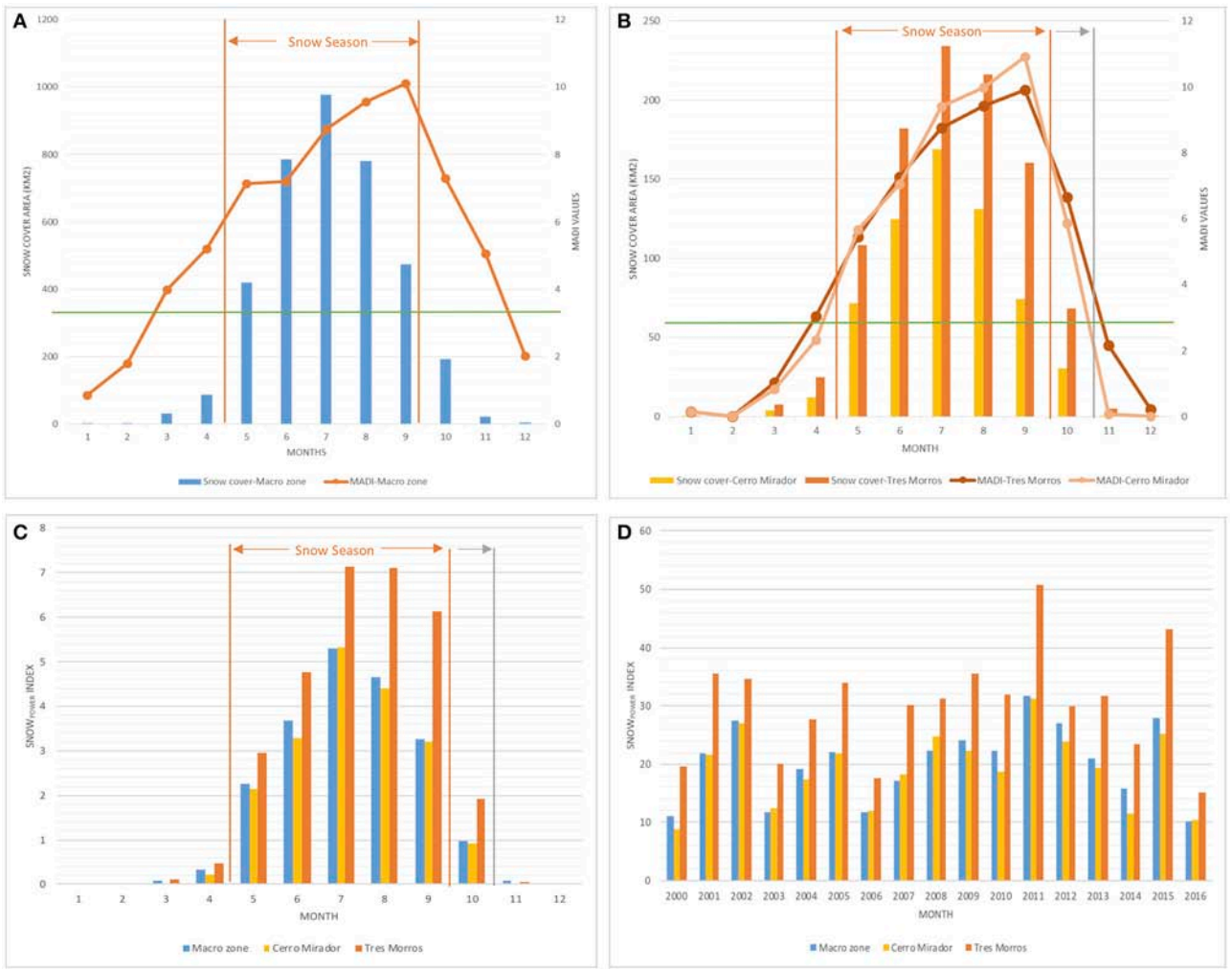

FIGURE 8 | Monthly average representation of the snow cover area and the $Snow_{power}$ index for 2000–2016. **(A)** shows the mean monthly snow cover area, the MADI index and the duration of the snow season in the Macro zone. **(B)** Represents the same snow properties for the sub-regions Cerro Mirador and Tres Morros. **(C)** Provides monthly averages of the $Snow_{power}$ index for the period 2000–2016, and **(D)** shows the monthly $Snow_{power}$ index sums for 2000–2016 for each zone. The green line on **(A,B)** represents 20% of the multi-year maximum monthly snow extent on each zone, which is used for inferring the beginning and the end of the snow season. The gray line on **(B,C)** represents the extent of the snow season on Tres Morros in comparison to Cerro Mirador.

the start and end of the ski season depends largely on snow precipitation and air temperature, with a minimum natural snow height requirement of about 20 cm without compaction to start the skiing operation. Since 2010 the longest season occurred in 2015 with 95 snow-days (representing the duration of the skiing season) and an average snow height of 140 cm. **Figure 10A** displays the relation between the duration of the ski season for the Macro zone and Cerro Mirador and its reconstructed snow cover extent from the NDSI index. We use the June-August period for the ski season, when most of the skiing activity is concentrated. The linear correlation between the ski season duration (days) and the Cerro Mirador snow cover (**Figure 10B**) is $R^2 = 0.94$, and $R^2 = 0.87$ for Macro Zone (**Figure 10C**). The correlation of the ski season duration with the $Snow_{power}$ index is also good but somewhat smaller, with $R^2 = 0.77$ for Cerro Mirador and $R^2 = 0.83$ for the Macro Zone, respectively. The correlation between of the average snow height from Club Andino with the NDSI snow cover extent ($Snow_{power}$ index) is not as good as the correlation with the ski season duration, with $R^2 = 0.72$ (0.80) and $R^2 = 0.75$ (0.67) for the Macro Zone and Cerro Mirador, respectively. Based on these results, hereafter we consider the NDSI snow cover extent as a better indicator of snow cover variability than the $Snow_{power}$ index.

Figure 11 shows the climate indices and snow cover of the Macro zone at Brunswick Peninsula after smoothing the interannual variability using the exponential filter (Rosenblüth et al., 1997) over the 2000–2016 period. It reveals the overall positive trend of the AAO, i.e., the southward displacement of the westerly winds, which could be linked with the decrease of

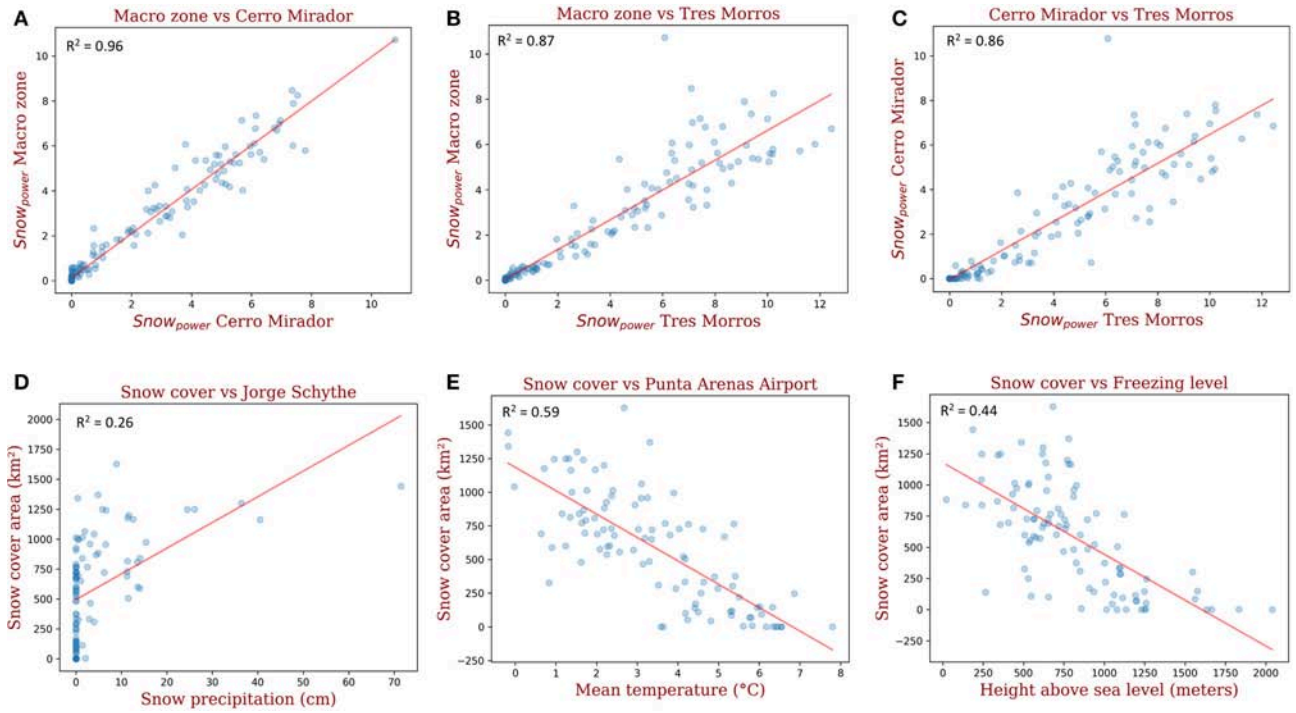

FIGURE 9 | Scatter plots. **(A–C)** show the correlation of the $Snow_{power}$ index between each study zones and the coefficient of determination (R^2). **(D–F)** show the correlations of the MODIS reconstructed snow cover on the Macro zone between the most relevant climatic variables at a monthly level during the extended winter: snow precipitation at Jorge Schythe station, mean temperatute at Punta Arenas Airport, and freezing level at Punta Arenas Airport.

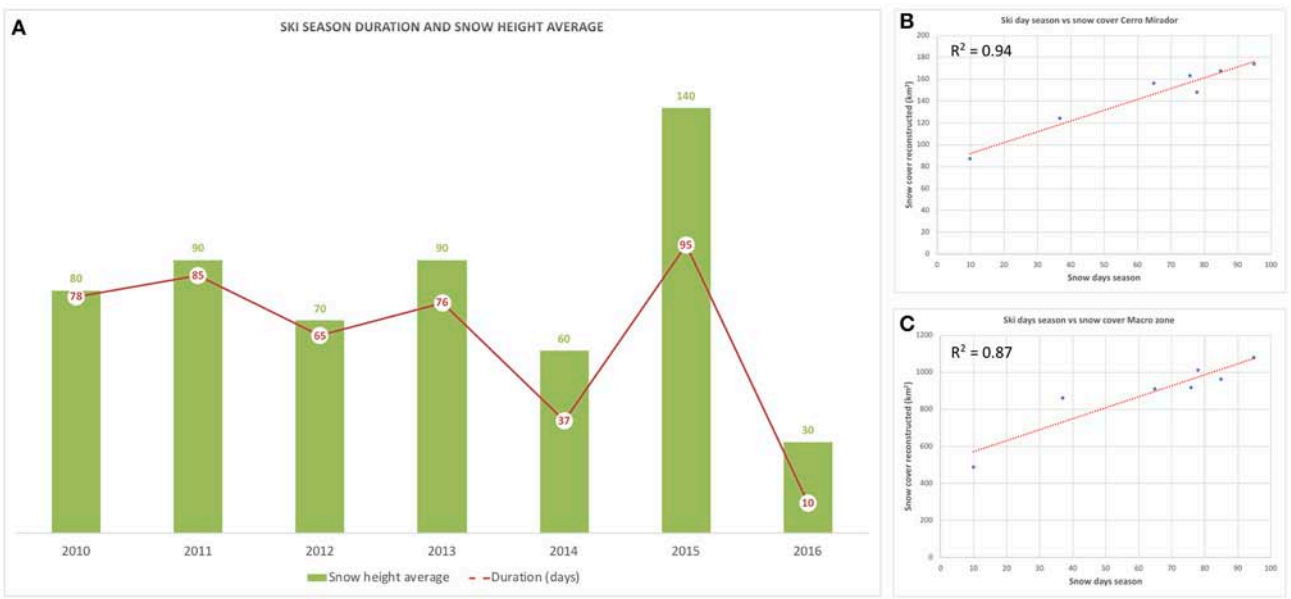

FIGURE 10 | Ski season duration and snow height average. **(A)** shows the relationship between the ski season duration and the average snow height measured at Club Andino. **(B,C)** display the correlation between the duration of the ski season and the monthly averaged NDSI-reconstructed snow cover from June-August (average of of the ski season period), for the Cerro Mirador and Macro zone, respectively. Both correlations are significant at the 95% confidence level.

the snow cover shown within the Macro zone. On the other hand, the PDO almost concurs with the decadal behavior of the snow cover. Thus, it seems that periods with positive (negative) PDO result in lower (higher) snow cover in the Brunswick Peninsula. Individual year-to-year variability given by El Niño and La Niña phases does not show a direct relation with snow

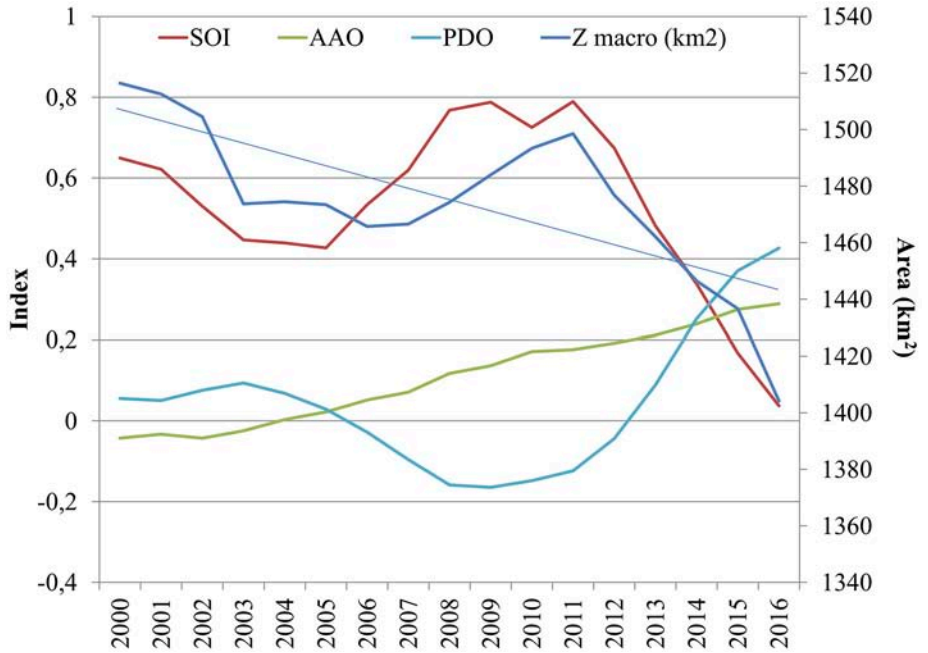

FIGURE 11 | Climate indices and snow cover at Brunswick Peninsula after smoothing the interannual variability using an exponential filter. The straight light blue line is the linear trend of the snow cover. SOI: Southern Oscillation Index (red), AAO: Antarctic Oscillation Index (green), PDO: Pacific Decadal Oscillation Index (black). Z macro (blue) is the snow cover extent (km2) on the study area (Brunswick Peninsula).

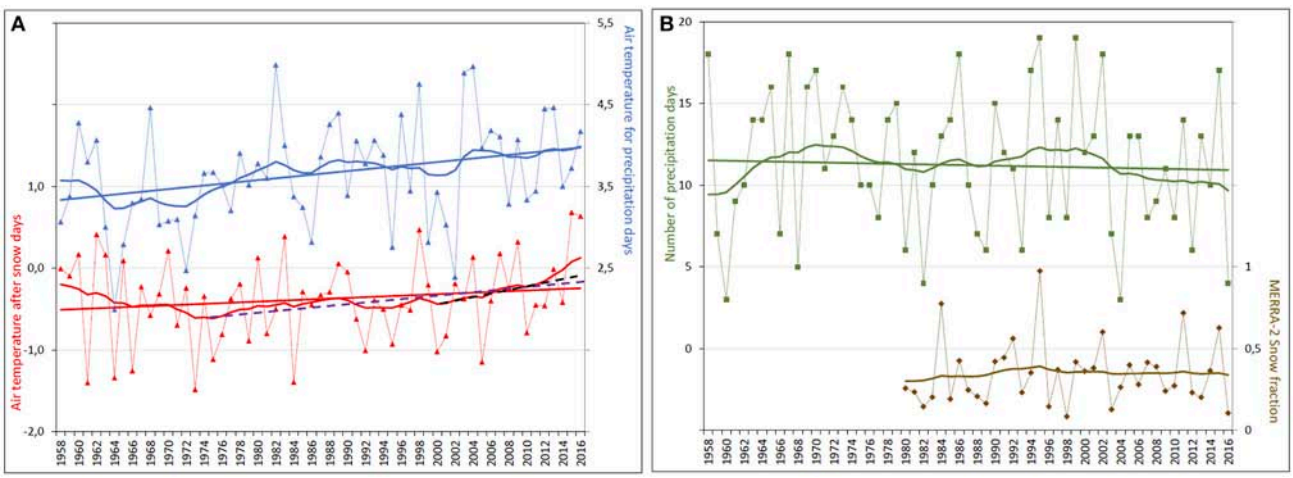

FIGURE 12 | Interannual variability, long-term behavior (after applying the exponential filter) and linear trend of: **(A)** mean air temperature for precipitation days (rain and snow) (blue, upper section) and for days after snow events (red, lower section). The dashed purple and black lines (lower section) are the linear trends for the 1973–2016 and 2000–2016 periods, respectively**. (B)** Number of precipitation days with air temperature <2°C for each year (green, upper section). The brown curve (lower section) is the snow fraction obtained from the MERRA-2 simulation. All variables are expressed as annual data calculated for the extended winter April to September.

cover behavior, although strong El Niño (La Niña) events tend to concur with less (more) snow cover and precipitation in the study area. This could be due to the interannual AAO that can also suppress or favor precipitation in the southern tip of South America.

Figure 12 shows the number of precipitation days with air temperature <2°C during April and September (extended winter) for each year for the 1958–2016 period at Punta Arenas Airport, along with the average of air temperature for these days. Also displayed is the air temperature average during days following a snow event. Results indicate a warming of 0.65°C ($p < 0.05$) for precipitation days over the 1958–2016 period. On average, 11.3 ± 4.4 (±1 standard deviation) of precipitation days with air temperature <2°C occur during the extended winter

in the period 1958–2016. These days are regarded as "snow days", revealing a decline of 11% (1.2 "snow days," $p < 0.05$) over the 1958–2016 period. The long-term behavior obtained after applying the exponential filter to the interannual variability shows an increase from 1958 to 1971 and from 1982 to 1999, as well as a decrease from 1972 to 1981 and also from 2000 to 2016. During 2000-2016 the linear trend indicates a decrease of 18% (2 "snow days," $p < 0.05$). The mean air temperature for days following the snow events reveals a slight positive trend of 0.27°C ($p < 0.05$) over the 1958–2016 period, of 0.52°C ($p < 0.05$) over the 1973–2016 period and of 0.55°C ($p < 0.05$) over the 2000–2016 period. In summary, this analysis indicates an overall decrease of snow precipitation days along with an overall increase of the air temperature, mostly concentrated in recent decades (**Figure 12**).

Figure 12 includes as well the snow fraction obtained from the MERRA-2 reanalysis data. Correlations of $R^2 = 0.16$ ($p < 0.05$) are obtained between the snow fraction and air temperature after snow events; $R^2 = 0.41$ ($p < 0.05$) between the snow fraction and air temperature during precipitation days; and $R^2 = 0.42$ ($p < 0.05$) between snow fraction and air temperature during "snow days."

DISCUSSION

The snow cover reconstruction can be analyzed in relation to climate variables at a montly and annual level, such as freezing level (upper air sounding at Punta Arenas Airport), snow accumulation (measured daily at Jorge Schythe and modeled at Punta Arenas Airport), and minimum and average temperatures

TABLE 2 | Result of the different linear regressions between $Snow_{power}$ index and NDSI snow cover (km^2) for the Macro zone, with the Punta Arenas Airport freezing level from radiosonde data, precipitation (mm), minimum, and mean temperature (monthly averages) from Punta Arenas Aiport and Jorge Schythe stations, for two different periods in 2000–2016: April–September (monthly and annual values) and June–August (annual).

	April–September (Monthly values)		April–September (Annual values)		June–August (Annual values)	
	$Snow_{power}$	**NDSI Snow cover**	**$Snow_{power}$**	**NDSI Snow cover**	**$Snow_{power}$**	**NDSI Snow-Cover**
Freezing level (mean)	Corr = −0.63 R^2 =0.40 *P*-value =0.000	Corr = −0.66 R^2 =0.44 *P*-value =0.000	Corr = −0.455 R^2 = 0.207 *P*-value = 0.067	Corr = −0.555 R^2 = 0.308 *P*-value = 0.021	Corr = −0.277 R^2 = 0.077 *P*-value = 0.281	Corr = −0.38 R^2 = 0.144 *P*-value =0.133
Precipitation Airport (sum)	Corr =0.002 R^2 =0.000 *P*-value =0.017	Corr = 0.043 R^2 = 0.002 *P*-value = 0.672	Corr = 0.465 R^2 = 0.216 *P*-value = 0.060	Corr = 0.389 R^2 = 0.151 *P*-value = 0.123	Corr = 0.603 R^2 = 0.363 *P*-value = 0.010	Corr = 0.564 R^2 = 0.318 *P*-value = 0.018
Precipitation Schythe (sum)	Corr = 0.048 R^2 = 0.002 *P*-value = 0.472	Corr = 0.087 R^2 = 0.008 *P*-value = 0.389	Corr = 0.572 R^2 = 0.327 *P*-value = 0.016	Corr = 0.512 R^2 = 0.262 *P*-value = 0.036	Corr = 0.56 R^2 = 0.313 *P*-value = 0.019	Corr = 0.507 R^2 = 0.257 *P*-value = 0.038
T° Average Airport (mean)	Corr = −0.67 R^2 = 0.45 *P*-value = 0.000	Corr = −0.767 R^2 = 0.588 *P*-value = 0.000	Corr = −0.318 R^2 = 0.101 *P*-value = 0.213	Corr = −0.226 R^2 = 0.051 *P*-value = 0.383	Corr = −0.23 R^2 = 0.05 *P*-value = 0.372	Corr = −0.119 R^2 = 0.014 *P*-value = 0.650
T° Average Schythe (mean)	Corr = −0.644 R^2 = 0. 415 *P*-value = 0.000	Corr = −0.742 R^2 = 0.551 *P*-value = 0.000	Corr = −0.251 R^2 = 0.063 *P*-value = 0.332	Corr = −0.294 R^2 = 0.087 *P*-value = 0.251	Corr = −0.09 R^2 = 0.008 *P*-value = 0.732	Corr = − 0.157 R^2 = 0.025 *P*-value = 0.548
Snow accum. Schythe (sum)	Corr = 0.459 R^2 = 0.210 *P*-value = 0.000	Corr = 0.51 R^2 = 0.26 *P*-value = 0.000	Corr = 0.468 R^2 = 0.219 *P*-value = 0.058	Corr = 0.46 R^2 = 0.212 *P*-value = 0.063	Corr = 0.405 R^2 = 0.164 *P*-value = 0.107	Corr = 0.374 R^2 = 0.14 *P*-value = 0.139
Snow accum. Airport M (sum)	Corr = 0.508 R^2 = 0.258 *P*-value = 0.000	Corr = 0.565 R^2 = 0.319 *P*-value = 0.000	Corr = 0.577 R^2 = 0.333 *P*-value = 0.015	Corr = 0.506 R^2 = 0.256 *P*-value = 0.038	Corr = 0.623 R^2 = 0.388 *P*-value = 0.008	Corr = 0.523 R^2 = 0.273 *P*-value = 0.031
T° Minimum Schythe (mean)	Corr = −0.558 R^2 = 0.312 *P*-value = 0.000	Corr = −0.664 R^2 = 0.441 *P*-value = 0.000	Corr = −0.08 R^2 = 0.006 *P*-value = 0.760	Corr = −0.125 R^2 = 0.016 *P*-value =0.631	Corr = 0.066 R^2 = 0.004 *P*-value = 0.802	Corr = −0.005 R^2 = 0.000 *P*-value = 0.985
T° Minimum Airport (mean)	Corr =-0.67 R^2 =0.45 *P*-value = 0.000	Corr = −0.75 R^2 = 0.56 *P*-value = 0.000	Corr = −0.172 R^2 = 0.03 *P*-value = 0.677	Corr = −0.226 R^2 = 0.051 *P*-value = 0.383	Corr = 0.018 R^2 = 0.000 *P*-value = 0.946	Corr = −0.045 R^2 = 0.02 *P*-value = 0.864

Corr, Pearson correlation; R^2, Coefficient of determination and p-value significance. The best correlations are highlighted in gray.

(at Jorge Schythe and Punta Arenas Airport). These variables were chosen because of the better correlation with the snow cover (summary shown in **Table 2**). The measured daily snow accumulation data are limited to the Jorge Schythe station only, published here for the first time. We use a threshold relation with air temperature to derive the solid/liquid precipitation fraction to infer snow accumulation [c(i)] at Punta Arenas Airport, as indicated by Schaefer et al. (2013), as follows:

$$c\,(i) = q\,(i) \times P(i) \tag{4}$$

Where q(i) is the solid part of the total precipitation, prescribed by temperature as:

$$q(i) = \begin{cases} if\ T\,(i) > Ut\ then\ q(I) = 0 \\ if\ Lt \leq T\,(i) \leq Ut\ then\ q\,(i) = \frac{Ut - T(i)}{1^{\circ}C} \\ if\ T\,(i) < Lt\ then\ q(i) = 1 \end{cases} \tag{5}$$

Where T(i) is the mean air temperature (°C), calculated as the average between the daily maximum and minimum air temperatures, P(i) is the daily total (liquid and solid) precipitation accumulation (mm), Ut and Lt are upper and lower temperature thresholds (°C).

Ut and Lt were estimated as 1.6 and 0.9°C, respectively. These values were determined through a sensitivity analysis using the daily snow accumulation and mean air temperature at Jorge Schythe for 1980–2016. In our case Ut and Lt are slightly larger than the values of 1.5 and 0.5°C assumed by Schaefer et al. (2013) for the Northern Patagonia Icefield. The modeled precipitated snow has a correlation of $R^2 = 0.48$ with the measured snow values at a daily level, $R^2 = 0.76$ for monthly values, and $R^2 = 0.88$ for annual values. Equation (5), based on daily values, was applied at Punta Arenas Airport to infer its monthly snow accumulation.

In this analysis we only used the Macro zone indices due to the high level of correlation with the other two study zones (**Figure 9**). This allows to extend back the period of analysis earlier than the year 2000 in order to identify long-term trends of snow cover behavior. Based on these results, to find a better relationship for explaining snow cover variability, we tested both simple and multiple linear regressions.

The multiple regressions with the best significant correlation for the MODIS snow cover reconstructed for the Macro zone in the period 2000–2016 was found using the monthly snow accumulation and the mean monthly temperature, with $R^2 = 0.62$ (Equation 6, which allows to model the snow cover for the period 1972–2016), and $R^2 = 0.62$ (Equation 7, which allows to model the snow cover for 1958–2016 period), both statistically significant at 95% (**Figure 13**). Temperatures were chosen at the Airport station to avoid possible urban effects at Jorge Schythe station located within the city of Punta Arenas. Correlations for the "extended winter" period from April to September were better than the annual (January–December) and the winter (June–July–August) correlations.

Inspection of **Table 2** shows that the snow cover extent reconstructed from the NDSI index derived from MODIS satellite data shows better correlations with temperatures (minimum and average) and freezing level than the snow cover derived from the $\text{Snow}_{\text{power}}$ index at monthly level. However, the $\text{Snow}_{\text{power}}$ index shows a slightly better correlation with total precipitation (at Jorge Schythe and Punta Arenas Airport stations) and snow accumulation (at Punta Arenas Airport), at seasonal level, compared with the NDSI index. This suggests that temperature may have a greater impact in the snow cover extent, while the winter precipitation may cause a more direct influence on the snow depth as reflected in the $\text{Snow}_{\text{power}}$ index. *In-situ* measurements are needed to verify these relations.

- Modeled Snow cover (SNC_1) in km^2 for 1972–2016:

$$SNC_1 = 1078.23 + 8.26 \cdot SN_{Sch} - 153.05 \cdot \overline{T^{\circ}}_{Apt} \tag{6}$$

- Modeled Snow cover (SNC_2) in km^2 for 1958–2016:

$$SNC_2 = 1049.45 + 12.97 \cdot SN_{Apt} - 148.34 \cdot \overline{T^{\circ}}_{Apt} \tag{7}$$

Where $\overline{T^{\circ}}_{Apt}$ $(^{\circ}C)$ is the monthly mean air temperature measured at Punta Arenas Airport during April to September.
SN_{Sch} (cm) is the monthly snow accumulation at Jorge Schythe during April to September.
SN_{Apt} (cm) is the monthly snow accumulation modeled at Punta Arenas Airport during April to September.

When we correlate the NDSI snow cover extent for the Macro zone for 2000–2016 with the monthly snow accumulation at Jorge Schythe station a correlation of $R^2 = 0.26$ is obtained, which increases to $R^2 = 0.59$ when correlated with the monthly mean temperature at Punta Arenas Airport. This means that the snow precipitation alone accounts for 26% of the variance of the NDSI snow cover extent, while the air temperature by itself accounts for 59% of the variance of the NDSI snow cover extent. Therefore, temperature is the main driver of snow cover changes, while the snow precipitation has a less relevant influence. The air temperature acts both as a forcing factor for solid/liquid precipitation, and also for melting the snow cover after precipitation events. As mentioned earlier, a clear warming trend of 0.52°C can be detected in the air temperature immediately after snow events at Punta Arenas Airport station in the period 1973–2016 (**Figure 12A**).

The modeled snow cover (Modeled Snow cover-1, Equation 6), shows a decreasing trend for the Macro zone of 19% between 1972 and 2016, from 4,162 to 3,360 km^2, with a 95% significance (**Figure 13**). This long-term snow decrease is attributed mainly to the significant long-term warming of 0.71°C at Punta Arenas for the same period (**Figures 6**, **12**).

When reconstructing the snow cover with the Modeled Snow cover-2 (Equation 7) for the period 1958–2016, the curve for the period 1972–2016 (**Figure 13**) turns out to be very similar to the Modeled Snow cover-1 (Equation 6). Expanding the period to 1958 allows seeing a slope change at the beginning of the 1970's, showing a snow cover increase from 1958 to 1973. Interestingly, this snow extent increase coincides with a Southern Hemisphere cooling of 0.2°C (annual average temperature) as reported by Bindoff et al. (2013) and Harris et al. (2014) for the same period.

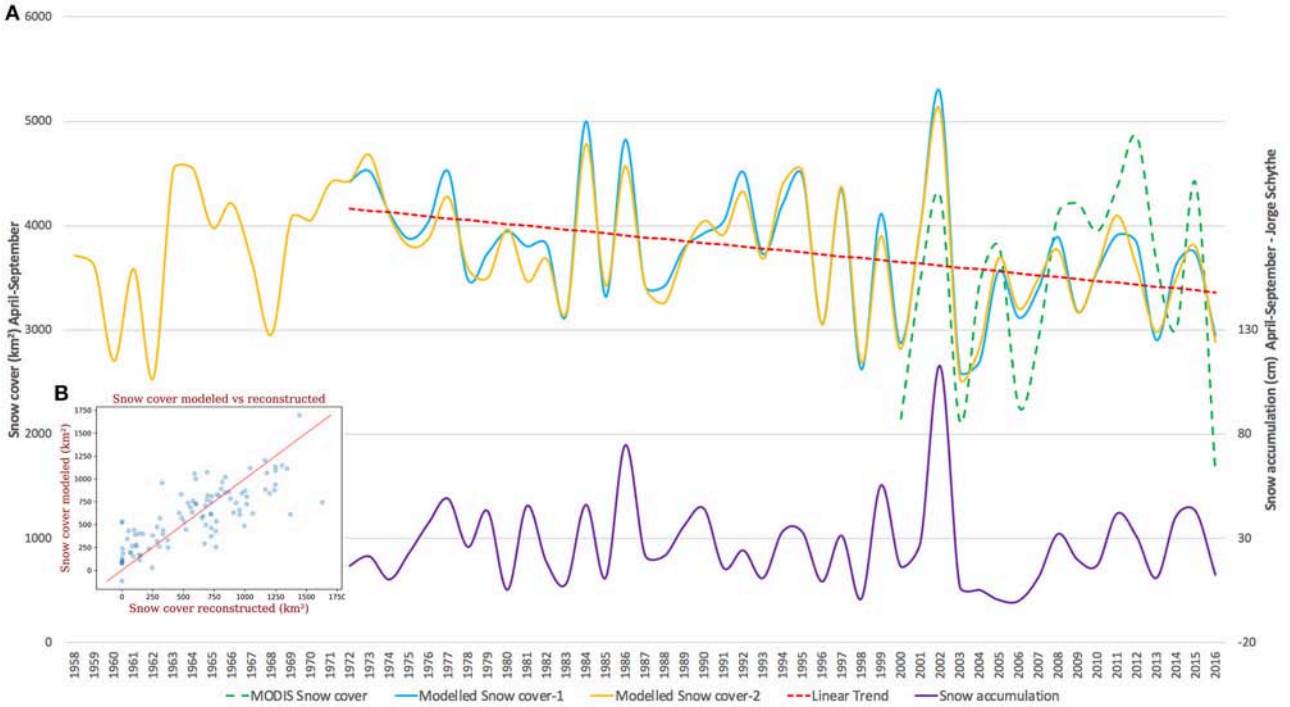

FIGURE 13 | (A) Upper section. Annual (April–September sums) of NDSI snow cover reconstructed for the Macro zone from MODIS data (dashed green) for the period 2000–2016. The annual (April–September sums) of snow cover modeled with Equation (6) (snow cover as a function of monthly mean temperature at Punta Arenas Airport and snow accumulation at Schythe station) is shown in light blue for the 1972–2016 period, while the red dashed line represents its linear trend. The annual (April–September sums) of snow cover modeled with Equation (7) (snow cover as a function of monthly mean temperature and snow accumulation modeled at Punta Arenas Airport) is shown in orange for the 1958–2016 period. The trend of the modeled snow cover is −19% for the period 1972–2016 ($p < 0.05$). Lower section. The annual (April–September) snow accumulation at Jorge Schythe station is shown as a purple curve. The inset **(B)** shows a scatter plot between the monthly values of modeled snow cover area on the Macro zone and the reconstructed snow cover from MODIS data for the 2000–2016 period, with $R^2 = 0.62$ and $p < 0.05$.

This is also evident at Punta Arenas Airport, which shows a cooling of 0.4°C for 1958–1973 (extended winter). Santana et al. (2009) reported that the annual average of the air temperature at Punta Arenas city decreased around 1°C from 1932 to 1971. This negative trend is part of the global cooling that took place from mid-40s to mid-70s (Jones and Moberg, 2002).

Furthermore, the Modeled Snow cover-1 for 1972–2016 is compared with the monthly snow fraction obtained from MERRA-2 reanalysis data for the period 1980–2016, resulting in a significant correlation of $R^2 = 0.48$ and $p < 0.05$. In spite of the significant correlation between the modeled snow cover and the MERRA-2 reanalisys data, the MERRA-2 data show no trend within the 36-year period (**Figure 12B**). In order to check the temperature trends within the MERRA-2 reanalysis dataset, the mean temperatures of the extended winter period (April–September) were analyzed for the same grid point 53.3°S, 71.1°W within the Macro zone at the near-surface and 850-hPa levels.

Figure 6B displays the observed and the MERRA-2 simulated air temperatures for both near-surface and 850-hPa levels. It shows the overall good agreement in the interannual variability, although the MERRA-2 data show a cold bias. The long-term behaviors given by the exponential filter show positive trends for both the near-surface and 850-hPa and for the observed and MERRA-2 data during the 1980–2016 period. All curves reveal a slight cooling during the 1980–1993 period and a slight warming during the 1994–2016 period. The results show a significant correlation of $R^2 = 0.83$ ($p < 0.05$) between the observed near-surface air temperature at Punta Arenas Airport and the temperature obtained at the nearest gridpoint of MERRA-2 reanalysis data for the 1980–2016 period. Also a significant correlation of $R^2 = 0.71$ ($p < 0.05$) is found between the observed 850-hPa monthly mean air temperature obtained from the radiosonde data (12 UTC) from Punta Arenas Airport and the 850-hPa MERRA-2 data for the same period (**Figure 6C**). However, there are some differences between the observed and reanalysis data. The observed near-surface warming is 0.60°C (0.52°C), larger than the 0.13°C (0.17°C) MERRA-2 warming for the1980–2016 (1994–2016) period, while the MERRA-2 warming of 0.40°C at 850-hPa level is larger than the 0.05°C given by the radiosonde data. Although the MERRA-2 data show good general correlations with the surface and radisonde data, its use for trend analysis is limited, as shown above. The main reason being that only few surface and upper air data are available in Patagonia for computing the reanalysis data.

Interannual precipitation changes affect the short-term snow cover variability as occurred in 2016, the year with the smallest winter precipitation for the last 50 years at Punta Arenas Airport and also at Punta Arenas city (90 mm and 165 mm, respectively, during April–September). The negative SOI phase that prevailed between 2008 and 2015 allowed the predominance of La Niña

events. Therefore, the large-scale atmospheric circulation favored an increase in precipitation in the region (**Figure 5**). This period ended with the development of a strong El Niño 2015–2016. The year 2016 presented some extreme climate events in Patagonia and the southern ocean which has been explained through climatecouplings. Garreaud (2018) reported for 2016 a significant precipitation deficit larger than 50% in western Patagonia while at the same time the lowest Southern Hemisphere (SH) sea ice extent of the satellite record occurred around Antarctica (Stuecker et al., 2017). Both studies agree that the coupling between the ENSO and AAO was the main causative factor of the 2016 event. This shows the sensitive response of the local and regional climate to wider-scale climate conditions.

The AAO index has been increasing in recent decades (Marshall, 2003), which points to windier conditions in southern South America, this as a result of the southward displacement of the westerly winds and the associated trajectory of the frontal systems that are the main contributor of precipitation in the region. The behavior of the AAO coincides with a non-significant wind increase at Punta Arenas Airport, and with the precipitation increase at Evangelistas. The precipitation increase at Evangelistas is probably an evidence of the increase of the intensity of the westerlies, while the precipitation decrease at Punta Arenas Airport, particularly in spring and summer, could be an evidence of the enhanced leeward effect of the wind increase which results in drier conditions (Schneider and Gies, 2004; Moreno et al., 2010; Garreaud et al., 2013).

A recent study of snow cover variability in Aysén basin, northern Patagonia, using MODIS data for period 2000–2016 period (Pérez et al., 2018), shows a decreasing but non-significant trend of 20 km^2 $year^{-1}$ in snow covered area. Similar trends have been detected in the Australian Alps where the maximum snow depth has declined by up to 15% since the 1960s, particularly in spring (McGowan et al., 2018). Model predictions suggest this trend will continue along with a reduction in length of the snow season in response to global warming (Hennessy et al., 2008; McGowan et al., 2018). In the European Alps, long-term observations show negative trends in snow depth and snow duration over the past decades (Beniston et al., 2018). The changes are typically elevation dependent, with more (less) pronounced changes at low (high) elevations due to changes in snowline altitude driven by warmer temperature. In Canada, the Canadian Sea Ice and Snow Evolution (CanSISE) Network has made an assessment of snow cover trends (Mudryk et al., 2018). The results show a decrease in terrestrial snow cover fraction in fall (delayed snow cover onset) and spring (earlier snow melt), generating a shortening of the snow season. These changes are driven by warmer temperatures and an associated modification of the elevation-dependent rainfall vs. snowfall ratios (Mudryk et al., 2018). These studies, as well as those published for other mountain regions of the world (Vaughan et al., 2013), agree that temperature increase is the main variable that drives the snow cover reduction.

By the end of this century, our study area in southern South America is predicted to warm by about 1°C (Representative Concentration Pathway RCP2.6) to 2.5°C (RCP8.5) (Magrin et al., 2014). An increase in westerly winds due intensification of the AAO and therefore of precipitation is expected to occur in western Patagonia in the future. However, the warming trend should result in a decrease of snow precipitation and therefore snow cover reduction at low elevation sectors of the Patagonian Andes (less than ca. 1,500 m a.s.l.) such as Brunswick Peninsula.

CONCLUSION

In this paper, we assess the snow cover changes for Brunswick Peninsula in southern Patagonia (53°S), where the Andes attain maximum elevations of about 1,100 m. The NDSI index applied to the MODIS satellite data at 500 m resolution provides an adequate estimation of the snow cover extent for the period 2000–2016. The MODIS snow cover data were compared with MERRA-2 reanalysis data and the snow data from the Andino ski center close to Punta Arenas city. The MODIS-derived snow cover extent compares well with the snow duration and snow height recorded at Club Andino in 2010–2016, which helps to validate the satellite data.

Two significant correlations between the MODIS NDSI snow cover extent and climate variables are found for the 17-year period 2000–2016. The first is a linear relation between the monthly mean temperature at Punta Arenas Airport station and monthly snow accumulation at Jorge Schythe station (Modeled snow cover-1, Equation 6), and the second is a similar correlation between the monthly mean temperature and monthly modeled snow accumulation at Punta Arenas Airport (Modeled snow cover-2, Equation 7). The snow cover series is extended with these linear models to 1972 and 1958, respectively. The first regression (Equation 6) shows a significant 19% snow extent reduction in the 45-year period 1972–2016 of 4.2% per decade, while the second regression (Equation 7) shows two different slopes, a significant 32% snow extent increase for the 1958–1973 (20% per decade) and a significant 16% snow extent reduction for the 1973–2016 period (3.6% per decade). The slope change in 1973 coincides with a cooling observed before mid-70's in Patagonia and in Southern Hemisphere temperatures. According to Equations. (6) and (7), the 1972–2016 snow cover reduction can be attributed mainly to a long-term atmospheric warming during the winter season.

AUTHOR CONTRIBUTIONS

RJ, FA, GC, TS, and CS jointly designed the study. FA and JC processed and analyzed the climatological data. FA, RJ, and GC processed and analysed MODIS satellite data. NB provided and analyzed the Jorge Schythe station meteorological data. EG, RA, and KG compiled snow depth and meteorological data. TS and CS among others designed, installed, and maintain the measurement network at Bahamondes station. All authors discussed the results and jointly worked on the manuscript.

ACKNOWLEDGMENTS

This study has been funded by the FNDR GORE Magallanes 2048 Programme Transferencia Científico Tecnológica Modelamiento Climático Planificación, XII Región, Código BIP Nº 30462410,

and by the Chilean Antarctic Institute MoCliM Programme. Partial funding has been contributed by the CONICYT-BMBF project GABY-VASA grant N° BMBF20140052 (Chile) and Nº 01DN15007 (Germany); by the German Research Foundation project Gran Campo Nevado grant N○ SCHN 680/1-1; by the German Research Foundation project MANAU grant No SA 2339/3-1; and Conicyt-Anillo ACT-1410. Data from Evangelistas station were kindly provided by Servicio Meteorológico de la Armada de Chile (SERVIMET). Data from Punta Arenas airport and Porvenir were downloaded from the institutional webpage of the Dirección Meteorológica de Chile, while data from San Gregorio, Pampa Huanaco, Bahía San Felipe, and Teniente Merino are from Dirección General de Aguas. The authors gratefully acknowledge the valuable comments and suggestions from both reviewers and the editor that helped improving the manuscript.

REFERENCES

Andreoli, R. V., and Kayano, M. T. (2005). ENSO-related rainfall anomalies in South America and associated circulation features during warm and cold Pacific decadal oscillation regimes. *Int. J. Climatol.* 25, 2017–2030. doi: 10.1002/joc.1222

Aravena, J. C., and Luckman, B. H. (2009). Spatio- temporal rainfall patterns in Southern South America. *Int. J. Climatol.* 29, 2106–2120. doi: 10.1002/joc.1761

Beniston, M., Farinotti, D., Stoffel, M., Andreassen, L. M., Coppola, E., Eckert, N., et al. (2018). The European mountain cryosphere: a review of its current state, trends, and future challenges. *Cryosphere* 12, 759–794. doi: 10.5194/tc-12-759-2018

Bindoff, N. L., Stott, P. A., AchutaRao, K. M., Allen, M. R., Gillett, N., Gutzler, D., et al. (2013). "Detection and attribution of climate change: from global to regional," in *Climate Change 2013: The Physical Science Basis*. Contribution of Working Group I to the *Fifth Assessment Report of the Intergovernmental Panel on Climate Change,* eds T. F. Stocker, D. Qin, G.-K. Plattner, M. Tignor, S. K. Allen, J. Boschung, A. Nauels, Y. Xia, J. Bamber, P. Huybrechts, and P. Lemke (Cambridge; New York, NY: Cambridge University Press), 1217–1308.

Bormann, K. J., McCabe, M. F., and Evans, J. P. (2012). Satellite based observations for seasonal snow cover detection and characterisation in Australia. *Remote Sens. Environ.* 123, 57–71. doi: 10.1016/j.rse.2012.03.003

Bosilovich, M. G., Lucchesi, R., and Suarez, M. (2015). *MERRA-2: File Specification*. GMAO Office Note No. 9 (Version 1.0), 73 pp, Available Online at: https://gmao.gsfc.nasa.gov/pubs/docs/Bosilovich785.pdf

Burger, F., Brock, B., and Montecinos, A. (2018). Seasonal and elevational contrasts in temperature trends in Central Chile between 1979 and 2015. *Glob. Planet. Change* 162, 136–147. doi: 10.1016/J.GLOPLACHA.2018.01.005

Carrasco, J. F., Casassa, G., and Rivera, A. (2002). "Meteorological and climatological aspects of the Southern Patagonia Icefield," in *The Patagonian Icefields: A Unique Natural Laboratory for Environmental and Climate Change Studies*, eds G. Casassa, F. V. Sepùlveda, and R. M. Sinclair (New York, NY: Kruwer Academic; Plenum Publishers), 29–41. doi: 10.1007/978-1-4615-0645-4_4

Carrasco, J. F., Osorio, R., and Casassa, G. (2008). Secular trend of the equilibrium line altitude in the western side of the southern Andes derived from radiosonde and surface observations. *J. Glaciol.* 54, 538–550. doi: 10.3189/002214308785837002

Chen, B., Smith, S. R., and Bromwich, D. H. (1996). Evolution of the tropospheric split jet over the South Pacific Ocean during the 1986–89 ENSO cycle. *Mon. Weather Rev.* 124, 1711–1731. doi: 10.1175/1520-0493(1996)124<1711:EOTTSJ>2.0.CO;2

Chen, W. Y. (1982). Assessment of Southern Oscillation sea level pressure indices. *Mon. Weather Rev.* 110, 800–807. doi: 10.1175/1520-0493(1982)110<0800:AOSOSL>2.0.CO;2

Chen, X., Long, D., Liang, S., He, L., Zeng, C., Hao, X., et al. (2018). Developing a composite daily snow cover extent record over the Tibetan Plateau from 1981 to 2016 using multisource data. *Remote Sens. Environ.* 215, 284–299. doi: 10.1016/j.rse.2018.06.021

Chylek, P., McCabe, M., Dubey, M. K., and Dozier, J. (2007). Remote sensing of Greenland ice sheet using multispectral near-infrared and visible radiances. *J. Geophys. Res.* 112:D24S20. doi: 10.1029/2007JD008742

Essenwanger, O. M. (1986). *General Climatology 1B, Elements of Statistical Analysis*. Amsterdam: Elsevier.

Falvey, M., and Garreaud, R. D. (2009). Regional cooling in a warming world: Recent temperature trends in the southeast Pacific and along the west coast of subtropical South America (1979–2006). *J. Geophys. Res.* 114:D04102. doi: 10.1029/2008JD010519

Frei, A., and Lee, S. (2010). A comparison of optical-band based snow extent products during spring over North America. *Remote Sens. Environ.* 114, 1940–1948. doi: 10.1016/j.rse.2010.03.015

Frei, A., Tedesco, M., Lee, S., Foster, J., Hall, D. K., Kelly, R., et al. (2012). A review of global satellite-derived snow products. *Adv. Sp. Res.* 50, 1007–1029. doi: 10.1016/j.asr.2011.12.021

Garreaud, R. (2018). Record-breaking climate anomalies lead to severe drought and environmental disruption in western Patagonia in 2016. *Clim. Res.* 74, 217–229. doi: 10.3354/cr01505

Garreaud, R., and Battisti, D. S. (1999). Interannual (ENSO) and Interdecadal (ENSO-like) variability in the Southern Hemisphere tropospheric circulation. *J. Clim.* 12, 2113–2123. doi: 10.1175/1520-0442(1999)012<2113:IEAIEL>2.0.CO;2

Garreaud, R., Lopez, P., Minvielle, M., Rojas, M., Garreaud, R., Lopez, P., et al. (2013). Large-scale control on the patagonian climate. *J. Clim.* 26, 215–230. doi: 10.1175/JCLI-D-12-00001.1

Gelaro, R., McCarty, W., Suárez, M. J., Todling, R., Molod, A., Takacs, L., et al. (2017). The Modern-Era retrospective analysis for research and applications, Version 2 (MERRA-2). *J. Clim.* 30, 5419–5454. doi: 10.1175/JCLI-D-16-0758.1

Gobiet, A., Kotlarski, S., Beniston, M., Heinrich, G., Rajczak, J., and Stoffel, M. (2014). 21st century climate change in the European Alps—a review. *Sci. Total Environ.* 493, 1138–1151. doi: 10.1016/j.scitotenv.2013.07.050

Gong, D., and Wang, S. (1999). Definition of Antarctic Oscillation index. *Geophys. Res. Lett.* 26, 459–462. doi: 10.1029/1999GL900003

González-Reyes, A., Aravena, J. C., Muñoz, A. A., Soto-Rogel, P., Aguilera-Betti, I., and Toledo-Guerrero, I. (2017). Variabilidad de la precipitación en la ciudad de Punta Arenas, Chile, desde principios del siglo XX. *An. Inst. Patagon.* 45, 31–44. doi: 10.4067/S0718-686X2017000100031

Hall, D. K., and Riggs, G. A. (2007). Accuracy assessment of the MODIS snow products. *Hydrol. Process.* 21, 1534–1547. doi: 10.1002/hyp.6715

Hall, D. K., Riggs, G. A., Salomonson, V. V., DiGirolamo, N. E., and Bayr, K. J. (2002). MODIS snow-cover products. *Remote Sens. Environ.* 83, 181–194. doi: 10.1016/S0034-4257(02)00095-0

Harris, I., Jones, P. D., Osborn, T. J., and Lister, D. H. (2014). Updated high-resolution grids of monthly climatic observations - the CRU TS3.10 Dataset. *Int. J. Climatol.* 34, 623–642. doi: 10.1002/joc.3711

Hartmann, D. L., Klein, A. M. G., Tank, M., Rusticucci, L. V., Alexander, S., Brönnimann, Y., et al. (2013). "Observations: atmosphere and surface," in *Climate Change 2013: The Physical Science Basis. Contribution of Working Group I to the Fifth Assessment Report of the Intergovernmental Panel on Climate Change,* eds T. F. Stocker, D. Qin, G. K. Plattner, M. Tignor, S. K. Allen, J. Boschung, A. Nauels, Y. Xia, V. Bex, and P. M. Midgley (Cambridge; New York, NY: Cambridge University Press), 159–254.

Hennessy, K., Whetton, P., Walsh, K., Smith, I., Bathols, J., Hutchinson, M., et al. (2008). Climate change effects on snow conditions in mainland Australia and adaptation at ski resorts through snowmaking. *Clim. Res.* 35, 255–270. doi: 10.3354/cr00706

Hughes, L. (2003). Climate change and Australia: trends, projections and impacts. *Austral Ecol.* 28, 423–443. doi: 10.1046/j.1442-9993.2003.01300.x

Hunter, J. D. (2007). Matplotlib: a 2D graphics environment. *Comput. Sci. Eng.* 9, 90–95. doi: 10.1109/MCSE.2007.55

Ibarzábal, Y., Donángelo, T., Hoffmann, J. A. J., and Naruse, R. (1996). Recent climate changes in southern Patagonia. *Bull. Glacier Res.* 14, 29–36.

IPCC (2013). *Summary of Policy Makers*. Available Online at: http://www.ipcc.ch/pdf/assessment-report/ar5/wg1/WG1AR5_SPM_FINAL.pdf (Accessed August 20, 2018), 27.

Jones, P. D., and Moberg, A. (2002). Hemispheric and large-scale surface air temperature variations: an extensive revision and an update to 2001. *J. Clim.* 16, 206–223. doi: 10.1175/1520-0442(2003)016<0206:HALSSA>2.0.CO;2

Lopez, P., Sirguey, P., Arnaud, Y., Pouyaud, B., and Chevallier, P. (2008). Snow cover monitoring in the Northern Patagonia Icefield using MODIS satellite images (2000–2006). *Glob. Planet. Change* 61, 103–116. doi: 10.1016/j.gloplacha.2007.07.005

Lynch-Stieglitz, M. (1994). The development and validation of a simple snow model for the GISS GCM. *J. Climate* 7, 1842–1855. doi: 10.1175/1520-0442(1994)007<1842:TDAVOA>2.0.CO;2

Magrin, G. O., Marengo, J. A., Boulanger, J.-P., Buckeridge, M. S., Castellanos, E., Vicuña, G., et al. (2014): "Central and South America," in: *Climate Change 2014: Impacts, Adaptation, and Vulnerability. Part B: Regional Aspects. Contribution of Working Group II to the* Fifth Assessment Report of the Intergovernmental Panel on Climate Change, eds V. R Barros, C. B. Field, D. J. Dokken, M. D. Mastrandrea, K. J. Mach, T. E. Bilir, M. Chatterjee, K. L. Ebi, Y. O. Estrada, R. C. Genova, B. Girma, E. S. Kissel, A. N. Levy, S. MacCracken, P. R. Mastrandrea, and L. L.White (Cambridge; New York, NY: Cambridge University Press), 1499–1566.

Mantua, N. J., and Hare, S. R. (2002). The pacific decadal oscillation. *J. Oceanogr.* 58, 35–44. doi: 10.1023/A:1015820616384

Marshall, G. J. (2003). Trends in the Southern annular mode from observations and reanalyses. *J. Clim.* 16, 4134–4143. doi: 10.1175/1520-0442(2003)016<4134:TITSAM>2.0.CO;2

McGowan, H., Callow, J. N., Soderholm, J., McGrath, G., Campbell, M., and Zhao, J. (2018). Global warming in the context of 2000 years of Australian alpine temperature and snow cover. *Sci. Rep.* 8:4394. doi: 10.1038/s41598-018-22766-z

Miller, A. (1976). "The climate of Chile," in *World Survey of Climatology*, ed Schwerdtfeger (Amsterdam: Climate of Central and South America), 113–131.

Montecinos, A., and Aceituno, P. (2003). Seasonality of the ENSO-related rainfall variability in central Chile and associated circulation anomalies. *J. Clim.* 16, 281–296. doi: 10.1175/1520-0442(2003)016<0281:SOTERR>2.0.CO;2

Moreno, P. I., Francois, J. P., Moy, C. M., and Villa-Martínez, R. (2010). Covariability of the Southern Westerlies and atmospheric CO_2 during the Holocene. *Geology* 38, 727–730. doi: 10.1130/G30962.1

Mudryk, L. R., Derksen, C., Howell, S., Laliberté, F., Thackeray, C., Sospedra-Alfonso, R., et al. (2018). Canadian snow and sea ice: historical trends and projections. *Cryosphere* 12, 1157–1176. doi: 10.5194/tc-12-1157-2018

Pérez, T., Mattar, C., and Fuster, R. (2018). Decrease in snow cover over the aysén river catchment in Patagonia, Chile. *Water* 10:619. doi: 10.3390/w10050619

Reichle, R. H. (2012). *The MERRA-Land Data Product*. GMAO Office Note No. 3 (Version 1.2), 38. Available Online at: http://gmao.gsfc.nasa.gov/pubs/office_notes

Reichle, R. H., Draper, C. S., Liu, Q., Girotto, M., Mahanama, S. P. P., Koster, R. D., et al. (2017). Assessment of MERRA-2 land surface hydrology estimates. *J.Clim.* 30, 2937–2960. doi: 10.1175/JCLI-D-16-0720.1

Rosenblüth, B. N., Fuenzalida, H. A., and Aceituno, P. (1997). Recent temperature variations in southern South America. *Int. J. Climatol.* 17, 67–85.

Saavedra, F. A., Kampt, S. K., Fassnacht, S. R., and Sibold, J. S. (2018). Changes in Andes Mountains snow cover from MODIS data 2000-2014. *Cryosphere* 12, 1027–1046, doi: 10.5194/tc-12-1027-2018

Salomonson, V. V., Barnes, W. L., Maymon, P. W., Montgomery, H. E., and Ostrow, H. (1989). MODIS: advanced facility instrument for studies of the Earth as a system. *IEEE Trans. Geosci. Remote Sens.* 27, 145–153. doi: 10.1109/36.20292

Santana, A., Butorovic, N., and Olave, C. (2009). Variación de la temperatura en Punta Arenas (Chile) en los ñltimos 120 años. *Anales Inst. Patagonia* 37, 85–96. doi: 10.4067/S0718-686X2009000100008

Schaefer, M., Machgut, H., Falvey, M., and Casassa, G. (2013). Modeling the mass balance of the Northern Patagonia Icefield. *J. Geophys. Res., Earth Surf.* 118, 571–588. doi: 10.1002/jgrf.20038

Schneider, C., and Gies, D. (2004). Effects of El Niño–southern oscillation on southernmost South America precipitation at 53°S revealed from NCEP–NCAR reanalyses and weather station data. *Int. J. Climatol.* 24, 1057–1076. doi: 10.1002/joc.1057

Schneider, C., Glaser, M., Kilian, R., Santana, A., Butorovic, N., and Casassa, G. (2003). Weather observations across the Southern Andes at 53°S. *Phys. Geogr.* 24, 97–119. doi: 10.2747/0272-3646.24.2.97

Seabold, S., and Perktold, J. (2010). "Statsmodels: econometric and statistical modeling with python," *9th Python in Science Conference*. Available Online at: http://conference.scipy.org/proceedings/scipy2010/pdfs/seabold.pdf (Accessed February 15, 2018).

Sirguey, P., Mathieu, R., and Arnaud, Y. (2009). Subpixel monitoring of the seasonal snow cover with MODIS at 250 m spatial resolution in the Southern Alps of New Zealand: methodology and accuracy assessment. *Remote Sens. Environ.* 113, 160–181. doi: 10.1016/j.rse.2008.09.008

Smith, R. B., and Evans, J. P. (2007). Orographic precipitation and water vapor fractionation over the Southern Andes. *J. Hydrometeorol.* 8, 3–19. doi: 10.1175/JHM555.1

Steiger, R., and Abegg, B. (2018). "Chapter 11: ski areas' competitiveness in the light of climate change: comparative analysis in the Eastern Alps," in *Tourism in Transitions*, eds D. Müller and M. Wiechowski (Cham: Springer), 187–199.

Stieglitz, M., Ducharne, A., Koster, R. D., and Suárez, M. J. (2001). The impact of detailed snow physics on the simulation of snow cover and subsurface thermodynamics at continental scales. *J. Hydrometeor.* 2, 228–242. doi: 10.1175/1525-7541(2001)002<0228:TIODSP>2.0.CO;2

Stuecker, M. F., Bitz, C. M., and Armour, K. C. (2017). Conditions leading to the unprecedented low Antarctic sea ice extent during the 2016 austral spring season. *Geophys. Res. Lett.* 44, 9008–9019. doi: 10.1002/2017GL074691

Trenberth, K. E. (1997). The Definition of El Niño. *Bull. Am. Meteorol. Soc.* 78, 2771–2777. doi: 10.1175/1520-0477(1997)078<2771:TDOENO>2.0.CO;2

Vaughan, D. G., Comiso, J. C., Allison, I., Carrasco, J., Kaser, G., Kwok, R., et al. (2013). "Observations: cryosphere in climate change 2013," in *The Physical Science Basis. Contribution of Working Group I to the Fifth Assessment Report of the Intergovernmental Panel on Climate Change*, eds T. F. Stocker, D. Qin, G. K. Plattner, M. Tignor, S. K. Allen, J. Boschung, A. Nauels, and Y. Xia (Cambridge; New York, NY: Cambridge University Press), 317–382.

Vermote, E., and Wolfe, R. (2015). *MOD09GA MODIS/Terra Surface Reflectance Daily L2G Global 1kmand 500m SIN Grid V006 [Data set]*. NASA EOSDIS LP DAAC.

Wang, J., and Li, W. (2003). Comparison of methods of snow cover mapping by analysing the solar spectrum of satellite remote sensing data in China. *Int. J. Remote Sens.* 24, 4129–4136. doi: 10.1080/0143116031000070409

Weidemann, S., Sauter, T., Schneider, L., and Schneider, C. (2013). Impact of two conceptual precipitation downscaling schemes on mass-balance modeling of Gran Campo Nevado ice cap, Patagonia. *J. Glaciol.* 59, 1106–1116. doi: 10.3189/2013JoG13J046

Weidemann, S. S., Sauter, T., Kilian, R., Steger, D., Butorovic, N., and Schneider, C. (2018). A 17-year record of meteorological observations across the Gran Campo Nevado Ice Cap in Southern Patagonia, Chile, related to synoptic weather types and climate modes. *Front. Earth Sci.* 6:53. doi: 10.3389/feart.2018.00053

Winther, J.-G., and Hall, D. K. (1999). Satellite-derived snow coverage related to hydropower production in Norway: present and future. *Int. J. Remote Sens.* 20, 2991–3008. doi: 10.1080/014311699211570

Conflict of Interest Statement: The authors declare that the research was conducted in the absence of any commercial or financial relationships that could be construed as a potential conflict of interest.

frontiers in Ecology and Evolution

ORIGINAL RESEARCH
published: 09 October 2018
doi: 10.3389/fevo.2018.00152

Genetic Structure and Gene Flow of Moss *Sanionia uncinata* (Hedw.) Loeske in Maritime Antarctica and Southern-Patagonia

Ingrid Hebel[1]*, *Maria Carmen Dacasa Rüdinger*[2], *Ricardo A. Jaña*[3] and *Joaquin Bastias*[4,5]

[1] Plant Biotechnology Lab, Department of Agriculture and Aquiculture, University of Magallanes, Punta Arenas, Chile, [2] Wood and Forestry Competence Centre, Forest Genetics and Forest Plant Breeding, Public Enterprise Sachsenforst, Pirna, Germany, [3] Scientific Department, Chilean Antarctic Institute, Punta Arenas, Chile, [4] Departamento de Geologia, Universidad de Chile, Santiago, Chile, [5] Department of Earth Sciences, University of Geneva, Geneva, Switzerland

Bryophytes are a major component of vegetation in ice-free coastal regions of Antarctica. *Sanionia uncinata* (Hedw.) Loeske is distributed from northern and central Maritime Antarctica to Marguerite Bay in the southern part of this biome where it occurs sparsely. Production of sporophytes is rare for *S. uncinata* in Antarctica, thus a high level of genetic uniformity among populations is expected (Lewis Smith, 1984). Several ice advances and retreats events in last thousands of years in Patagonia and Antarctica could have driven different processes of speciation at fine scale or triggered genetic differentiation among populations, leading to unique genetic populations. A few studies have analyzed the genetic structure of mosses in Antarctica, but none in Maritime Antarctica or in the nearby zones such as southern Patagonia. Based on Amplified Fragment Length Polymorphism (AFLP) and grouping analysis, we determined levels of intra/and inter-population genetic diversity of *S. uncinata* in sites of this region. The results revealed that gene diversity within populations was low and that populations did not have significant genetic differentiation. Also, no correlation was found between genetic variability and geographic distance ($R^2 = 0.031$). However, we distinguished two groups of populations. One of them clustered populations with low values of genetic diversity. The other one was made out of populations showing much higher genetic diversity. Cluster 1 was the most geographically widely distributed covering populations from northern part of southern Patagonia to southern part of studied populations in Maritime Antarctica. Cluster 2 had the highest level of polymorphism, but spatially is very restricted to four populations in the Maritime Antarctica and southern Patagonia. We found substructures in some populations of the Maritime Antarctica such as in the Coppermine, Byers and Suffield populations. The underlying causes of this subdivision could be the asexual reproduction and significant abiotic factor affecting the presence of this moss species, but also the autoecious condition of this species. The importance of results is the concept of genetic connectivity among bioregions of South Patagonia and Antarctica suggesting additionally this interaction may have occurred repeatedly after the LGM, resulting in the vegetation that grows in Antarctica today.

Keywords: gametophytes, ancestral origin, genetic diversity, fine-scale, HYSPLIT

OPEN ACCESS

Edited by:
Su Wang,
Beijing Academy of Agricultural and Forestry Sciences, China

Reviewed by:
Heinjo During,
Utrecht University, Netherlands
Lin Wang,
University of Hong Kong, Hong Kong

***Correspondence:**
Ingrid Hebel
ingrid.hebel@umag.cl

Specialty section:
This article was submitted to Population and Evolutionary Dynamics, a section of the journal Frontiers in Ecology and Evolution

Received: *13 April 2018*
Accepted: *12 September 2018*
Published: *09 October 2018*

Citation:
Hebel I, Dacasa Rüdinger MC, Jaña RA and Bastias J (2018) Genetic Structure and Gene Flow of Moss Sanionia uncinata (Hedw.) Loeske in Maritime Antarctica and Southern-Patagonia. Front. Ecol. Evol. 6:152. doi: 10.3389/fevo.2018.00152

INTRODUCTION

Bryophytes are a major component of the vegetation in ice-free coastal regions of Antarctica such as the South Shetland Islands (SSI) and in sites in the western sector of the Antarctic Peninsula (AP). A total of 117 species of mosses have been identified in these regions (Ochyra et al., 2008; Ellis et al., 2013a,b; Sollman, 2015). A large number of bryophyte species have also been identified in sectors of Patagonia, the sub-Antarctic region of South America. *Sanionia uncinata* (Hedw.) Loeske is widely distributed in the northern and central maritime Antarctic, with some isolated occurrences in Marguerite Bay in the southern part of this biome (Ochyra et al., 2008). *S. uncinata* has also been found in peri-Antarctic islands and archipelagoes, as well as in the west and east ice-free areas of the Antarctic Peninsula. In Chile, *S. uncinata* is found from Regions IX to XII, this last region belonging to Patagonia (Larraín, 2007). In many cases *S. uncinata* covers large extensions in valleys and beaches, alone or in association with other bryophyte species (Torres-Mellado et al., 2011). It grows also in free ice areas such as moraines, peri-glacier geoforms and on newly exposed areas at glacier fronts, tolerating relatively unstable conditions, severe dehydration and minimum nutrient concentrations.

The oldest evidence of this species in the Antarctic after the last glacial maximum (LGM) was found in subfossil peat on King George Island, which has been dated by radiocarbon method to be 4,950 ± 140 years old (Birkenmajer et al., 1985). Hedenas (2012), suggested that *Sanionia* became extinct during the LGM, based on the low number of haplotypes found in most of the sub-Antarctic islands outside the region from southernmost South America to the Antarctic Peninsula. The results of that study indicated that the presence of *Sanionia* is relatively young, so that it had little time to diversify; its distribution is best explained by dispersal of clonal gametophytes, the germination of diaspores dispersed by the rain and predominant western winds in the Southern Hemisphere, which has been also shown for other mosses such as *Leptobryum wilsonii* (Kato et al., 2013). In spite of this, several previous molecular genetic studies on moss species in Antarctica have demonstrated high or moderate genetic variability within clumps with some spatial relationships on meter to kilometer scales indicating that there is some clustering of populations (Selkirk et al., 1997, 1998; Skotnicki et al., 1998a,b,c, 1999a,b; Dale et al., 1999; Clarke et al., 2009).

It is known that spore germination and establishment of mosses are limited by local environmental conditions, such as edaphic conditions and light intensity (Caners et al., 2009).The production of sporophytes for some bryophyte species in Antarctica is rare, as is the case of *S. uncinata*, so that high levels of genetic uniformity among populations are expected (Lewis Smith, 1984). However, repeated cycles of advances and retreats of ice coverage in Patagonia and Antarctica during the last thousands years could have led to processes of speciation at a fine scale and genetic differentiation among populations, resulting in unique populations from a genetic point of view in these areas. To date there have been few studies on the genetic structure of mosses and that few have focused mainly on mosses in the Ross Sea region (west Antarctica), rather than on Maritime Antarctica or related zones such as southern Patagonia. In this study we analyzed the fine-scale genetic diversity, population differentiation and population subdivision of *S. uncinata* in populations in Maritime Antarctica and southern Patagonia. We discuss possible causes of the genetic structure and patterns of gene flow and (re)colonization in these regions and link these events to the reproductive dynamics of the species.

MATERIALS AND METHODS

Sampling Areas

A total of 17 populations in maritime Antarctica and southern-Patagonia were sampled (**Table 1**). The sampled sites are shown in **Figure 1**.

The geomorphology of both Antarctica and Patagonia is largely dominated by the effects of glaciers on the landscape. During the LGM, the Antarctic Peninsula, the South Shetland Island and Patagonia were covered by an extensive ice sheet. Several authors have suggested that soil generation began in these regions after the LGM, ca. 16–9 thousand years ago (Navas et al., 2008; Pfeiffer et al., 2010). The weathered bedrock that formed the soil at the *S. uncinata* sampling sites had different geological origins, depending on the location. The soils had a volcanic and volcaniclastic origin at several sites in King George Island (Smellie et al., 1984), Coppermine on Robert Island (Smellie et al., 1984), and Crooker Lake on Deception Island (Martí et al., 1996). The geology of Patagonia broadly consists of a volcanic to volcaniclastic and sedimentary succession assigned to the early to mid-Mesozoic (Fildani et al., 2008).

As described previously in other studies (Skotnicki et al., 1999b; Bijlsma et al., 2000; Van Der Velde and Bijlsma, 2000), samples were separated by 20 m, and consisted of several shoots, collected from moss pads close to streams, roads, Antarctic stations and glacier boundaries, both in the Antarctic Specially Protected Area (ASPA) and open access areas. A total of 281 samples of the studied species are stored at the Instituto de la Patagonia Herbarium (Access code HIP 15068–HIP15349).

DNA Extraction and AFLP Protocol

One shoot from each sample was washed repeatedly with distilled water. Then, DNA was extracted using an E.Z.N.A® High Performance DNA Kit (OMEGA bio-tek®, Doraville, GA, USA) and observed after separation on 1% agarose gels after staining with Gel Red (Biotium Inc. Fremont, CA, USA). The AFLP fingerprinting was performed according to the original protocol (Vos et al., 1995). Extracted DNA (50–500 ng) was digested with EcoRI and Tru9I for 2 h at 37°C and ligated with two adaptors for 3 h. Preamplification is usually done with +2,+1, or +0 primers or combination thereof. Most studies use +1/+1, but +0/+2 worked also well in plants (Weising et al., 2005). For small genomes it is recommended to use shorter selective primers, taking into account if they are "rare" cutters or "frequent" cutters (Paun and Schönswetter, 2012). Preamplification was carried out in a Maxygene thermal cycler (Axygen, Tewksbury, MA, USA) using primers for EcoRI+0 (E, 5′-GACTGCGTACCAATTC-3′) and MseI+1 (M, 5′-GATGAGTCCTGAGTAAA-3′). The quality

TABLE 1 | Results of genetic diversity analyses.

Region	Island or place	Population	Number of samples	N°ASPA or protected area	%PLP	Hj	% of samples assigned to clusters	
							Cluster 1	Cluster 2
Maritime Antarctica	King George	Ardley Peninsula	24	150	0	0.00033	100	
	King George	Barton Peninsula	16	171	11.2	0.02909	Mixed ancestry	
	King George	Collins	21	125	4.2	0.03406	90	10
	King George	Elephant Beach	17	No	1.5	0.00175	100	
	King George	Potter Peninsula	11	132	9.9	0.01778	100	
	King George	Suffield Point	30	No	38	0.07454	66	34
	King George	Lions Rump	10	151	0	0	100	
Maritime Antarctica	Livingston	Hannah Point	12	No	0.8	0.00237	100	
	Livingston	Hurd	11	No	0	0	100	
	Livingston	Byers	24	126	47.2	0.11880	50	50
Maritime Antarctica	Nelson	Pereira Point	11	No	2.8	0.00661	100	
Maritime Antarctica	Deception	Site B - Crater Lake	10	140	0	0	100	
Maritime Antarctica	Robert	Coppermine Peninsula	24	112	60.6	0.20420	42	58
Southern-Patagonia	Karukinka	Karukinka	30	Yes	11.3	0.04674	87	13
	Paine	Paine	11	Yes	0	0	100	
	Parrillar Lake	Parrillar	9	Yes	19	0.11268		100
	Riesco Island	Otway Bay	10	No	13.4	0.05152	100	

ASPA, Antarctic Specially Protected Area; %PLP, proportion of polymorphic loci at 5% level; Hj, expected heterozygosity under H-W proportion. Clusters 1 and 2 are the cluster defined by STRUCTURE.

and quantity of the pre-amplified products were determined by separation on 1% agarose gels after dilution (1:9) with ddH_2O. Fifteen selective primer combinations were checked to determine whether they produced polymorphic bands with sufficient reproducibility and clarity. We finally selected three primer combinations for selective amplification: EcoRI+AAGG and MseI+ACGG; EcoRI+ACA and MseI+AGC; EcoRI+ACA and MseI+CAG. Each PCR was performed in a 20-μL reaction mixture containing 3 μL diluted pre-amplification product, 0.25 μM E-primer, 0.3 μM M-primer, 10 mM Tris-HCl (pH 8.0), 1.5 mM $MgCl_2$, 0.2 mM dNTP, and 0.5 U Kapa Taq DNA polymerase (Kapa Biosystems, Boston, MA, USA). Amplification was performed with a touch-down cycling process. Each set of 96 reactions included a positive control and a blind sample (without DNA). The PCR products were resolved on 8% denaturing polyacrylamide gels (Sambrook and Russell, 2001). The multilocus AFLP profiles were scored as present (1), absent (0) or ambiguous (?) to create binary matrices using MyImageAnalysis Software (Thermo Scientific, Rockford, IL, USA). Two samples were included in all polyacrylamide gels to ensure comparability among gels. Furthermore, 36 samples were twice amplified and run in polyacrylamide gels to calculate the error rate of the AFLP analysis (Bonin et al., 2004), considering the ratio between observed and total number of phenotypic differences between replicates.

Genetic Diversity Analysis

A binary matrix of 1 and 0 values was generated based on the presence (1) or absence (0) of AFLP fragments in every sample for each selected pair of primers. The AFLP fragment presence/absence matrix was used to calculate descriptive statistics indices, including number of alleles, allele frequencies and percentage of polymorphic loci at the 5% level based on the Lynch and Milligan method implemented in AFLP SURV software version 1.0 (Vekemans et al., 2002). The numbers of private alleles and fixed alleles were calculated with FAMD (Schlueter and Harris, 2006). Estimates of expected heterozygosity (Hj), mean gene diversity (*Hw*) within populations (analogous to Nei's gene diversity within populations Hs), total gene diversity (Ht), and differentiation among populations (F_{ST}) in Antarctica and South Patagonia were analyzed using fragment frequency data, by comparing the levels of polymorphism. The genetic differentiation considered three hierarchical levels; genetic differentiation among populations, among islands and among regions (southern Patagonia and Antarctica). Given that samples were gametophytes [i.e., haploid (*n*) individuals], we followed the recommendation of the author for computing fragment frequency which reserves one option for haploid organisms and fixed homozygosity at each locus because of complete self-fertilization (Vekemans et al., 2002). The significance of the genetic differentiation among populations was

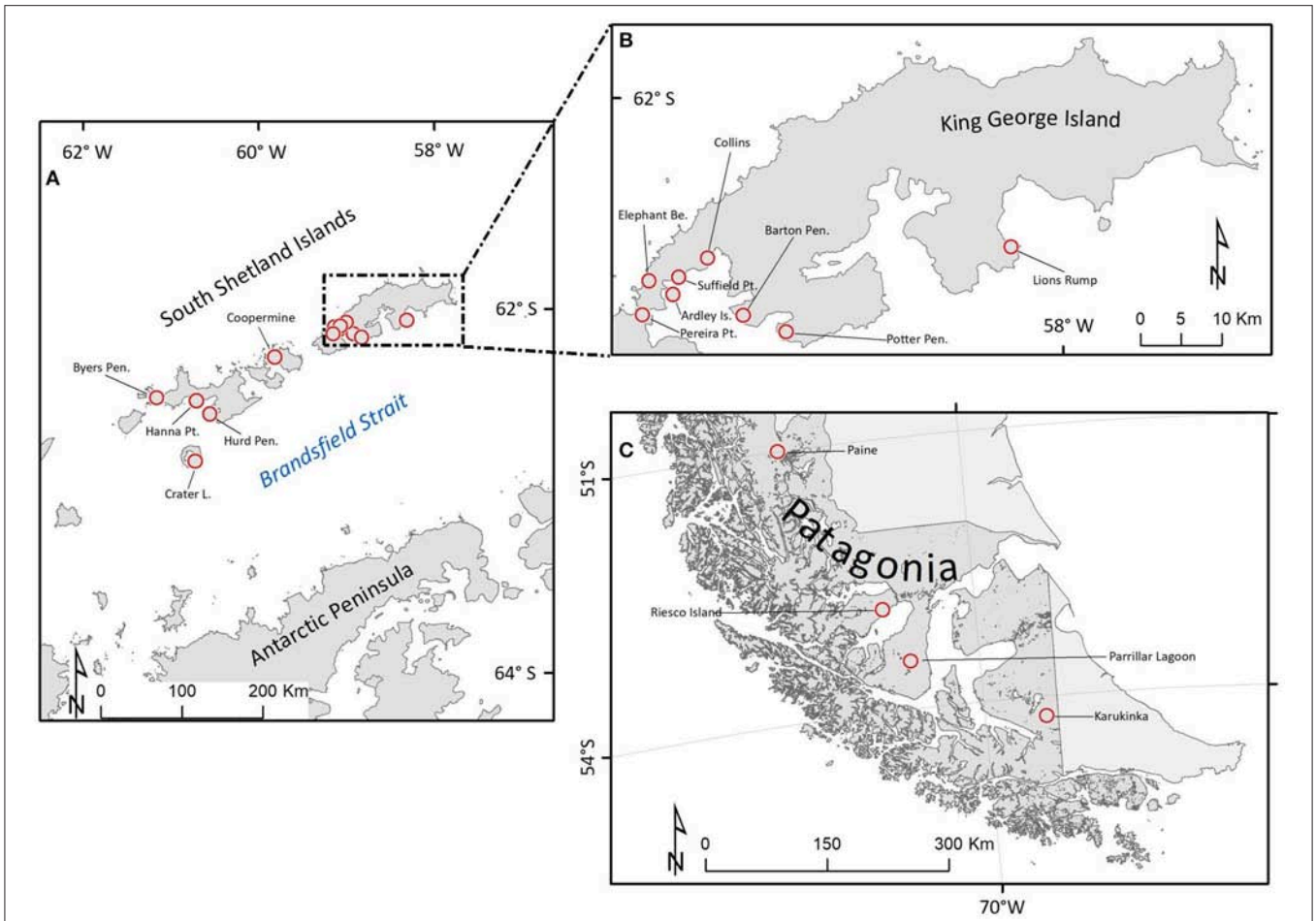

FIGURE 1 | Sampling locations of *Sanionia uncinata* populations in Maritime Antarctica and southern Patagonia (Chile). **(A)** Populations belonging to the South Shetland Islands: Byers Peninsula, Hurd Peninsula, and Hanna Point on Livingston Island (LI); Crater Lake on Decepcion Island (DI); Coppermine Peninsula on Robert Island (RI). **(B)** Inset detail for Pereira Point on Nelson Island (NI) and for populations on King George Island (KGI): Ardley Island, Elephant Beach, Suffield Point, Collins, Barton Peninsula, Potter Peninsula, and Lions Rump; **(C)** Populations along a latitudinal gradient in Southern Patagonia: Paine, Riesco, Parrillar Lagoon, and Karukinka (Chile).

tested under the hypothesis of no genetic structure, obtained by 10,000 random permutations of individuals among populations using AFLP-SURV 1.0 software (Vekemans et al., 2002).

A model-based clustering method implemented in the program STRUCTURE version 2.3.4 (Pritchard et al., 2000) was used first under a non-admixture model, as suggested by the authors for dominant markers, to infer population structure without considering sampling locations or allele frequencies correlated within populations. The burn-in was set to 10,000 and Markov chain Monte Carlo (MCMC) was set to 50.000, simulating number of clusters from K = 1 to K = 17 and 100 iteration for each cluster. We calculated ΔK, suggested by Evanno et al. (2005), which detects the true K as the maximum value of 'Ln P(D) implemented in Structure Harvester (Earl and Vonholdt, 2012) to assign individuals to the clusters probabilistically. We used the admixture model using prior population information with burn-in rate of 500,000 and MCMC of 10^6 runs simulating cluster numbers from 1 to 5. Under the admixture model, STRUCTURE was used to identify individuals in each population that formed subpopulations or that had recent immigrant ancestry. Then the samples were grouped according to the probability of belonging to the subpopulations recorded by STRUCTURE and checked the level of polymorphic alleles and the level of expected heterozygosity based on the Lynch and Milligan method within subpopulations. To detect if the apparent reduction of heterozygosity in a population is caused by a subpopulation structure, we compared the level of expected heterozygosity under Hardy-Weinberg genotypic proportions for each populations.

To test for isolation by distance, pairwise genetic and spatial distances were correlated using the Mantel test (Mantel, 1967). Also, genetic differentiation of population pairs was estimated with Φ_{PT} (a statistic analogous to F_{ST}) for AFLPs with their significance level (obtained by 9999 permutations). A principal coordinate analysis (PCoA) was performed to observe the distribution and ordering of the individuals on a

multidimensional axis system. The principal coordinates were calculated from pairwise Euclidian distance estimates between individual genotypes. Analyses were performed in GenAlEx6.5 (Peakall and Smouse, 2006, 2012).

The clustering analysis calculated a population distance matrix from the allele frequency data of all defined groups using the default option (Bayesian from a non-uniform among-populations prior) implemented in FAMD software (Schlueter and Harris, 2006). The bootstrap population tree option was used to generate multiple UPGMA or NJ trees from a distance matrix or Jaccard similarity index. Statistical support for the branches was assessed by 10,000 bootstrap replicates. The dendrogram was viewed using Treeview X 1.6.6 software (Page, 1996).

RESULTS

Genetic Diversity Within and Among Populations

In total, 142 alleles were scored in the 281 studied samples. The average proportion of polymorphic alleles was 12.9%. The mean scoring error calculated from 36 duplicate samples was 2.47%. The largest proportion of polymorphic loci was on the Shetland Islands population at Coppermine (RI) (60.6%) followed by the populations at Byers (LI) (47.2%) and Suffield (KGI) (38%) (**Table 1**). The lowest *Hj* value was found in the Lions Rump, Hurd, Deception and Paine populations and the highest value was in the Coppermine population (0.20). The mean gene diversity within populations of *S. uncinata* was *Hw*: 0.04. Total gene diversity (Ht) was 0.0550 and genetic differentiation among populations was not significant ($F_{ST} = 0.2426$, $P = 0.1867$). We found private alleles in only one population (Karukinka). The Mantel test indicated that genetic variability was not correlated with geographic distance ($R^2 = 0.031$). The AMOVA analysis indicated that 41% of genetic variability was within populations and 59% was among populations ($\Phi_{PT} = 0.592$).

The PCoA found three main groups (**Figure 2**). The distribution of the samples of group 1, formed by populations of Coppermine, Parrillar, Suffield, Karukinka, Collins, Byers, and Lions Rump was homogeneous, as was the distribution of group 2, formed by the populations Barton, Riesco, Paine, Pereira, and Elephant. In contrast, group 3 was not homogeneous, because it mixed samples from group 1 and 2 with the remaining samples of the Potter, Hanna, Hurd, Ardley, Deception populations.

The first principal coordinate explained 47.10% of the total variability, and the second and third axes explained much smaller proportions of total variability (12.35 and 7.10%, respectively). Thus 59.45% of the variability was visualized by the bi-dimensional coordinates system.

In accordance with the results of the Mantel test, which inferred absence of geographic relationships among the studied populations, the populations cluster in the dendrogram partially accordingly to their geographic position (**Figure 3**). For example, populations situated along the west–east orientation in King George Island, Elephant Bay and Barton populations clustered together. However, they did not cluster with nearer populations such as Suffield, Collins, or Ardley in KGI. Elephant Bay and Barton clustered with the Riesco population in southern Patagonia. We note clustering in Livingston Island for Hanna Point and Hurd, but the Byers population was in another branch.

Coppermine, Suffield, Byers from the maritime Antarctica and Parrillar from Southern-Patagonia shared the same lineage and diverged from the rest of the populations.

Genetic Analysis Among Islands

Robert Island had the highest number of polymorphic loci (60.6%) and the highest expected heterozygosity per island (0.20), followed by Livingston Island (47.2%), and southern Patagonia (21.1%). The lowest levels of polymorphism were found in King George Island (6.3%), Nelson Island (2.8%), Ardley Peninsula (0%), and Deception Island (0%). The *Hw* was 0.05 and Ht was 0.0648. The genetic differentiation among islands ($F_{ST} = 0.11$,) was not significant. The AMOVA analysis indicated that 58% of the genetic variability was within populations and 42% was among island ($\Phi_{PT} = 0.42$). The Mantel test indicated that genetic variability was not correlated with geographic distance ($R^2 = 0.0006$).

STRUCTURE Analysis

Bayesian analysis with STRUCTURE showed that samples are best grouped into two clusters with both the non-admixture model and admixture models. The highest value was found for $\Delta K = 2$ (Cluster 1 and Cluster 2). Each cluster includes populations from maritime Antarctica and southern Patagonia (**Figure 4**). We detected lower gene diversity for subpopulations of cluster 1, and higher gene diversity for subpopulations belonging to cluster 2. The mean within-population expected heterozygosity under Hardy–Weinberg genotypic proportions (Nei's gene diversity) within clusters of *S. uncinata* was higher in comparison with the same analysis considering each population (*Hw*: 0.10). The analyses of genetic structure among clusters showed that the Ht was 0.1129 and that there was a significant genetic differentiation among them ($F_{ST} = 0.06$, $^{***}P < 0.001$).

Analysis Under Admixture Model

The STRUCTURE analysis allowed us to identify subpopulations under the admixture model. Due to the clearly geographically limited subpopulations of *S. uncinata* in some populations, we decided to analyze the level of polymorphic alleles and the level of gene diversity within subpopulations to compare it with the previous analysis to know if the subpopulation have some influence in the final interpretation of the results. We did the analysis by grouping the samples in the subpopulations registered by STRUCTURE, symbolized by A for samples belonging to cluster 1 and B for samples belonging to cluster 2.

This new genetic analysis showed that the average proportion of polymorphic alleles was 16.4%. The largest proportion of polymorphic loci was found in Coppermine B (RI) and Suffield Point B (KGI) (each 65.5%) followed by Byers B (LI) (60.5). It was revealed that some differences in the level of polymorphic loci exist compared to the previous analysis that we have done without grouping the samples according to STRUCTURE. For example, individuals from Coppermine Peninsula (RI), grouped into two subpopulations. The analysis revealed a high level of

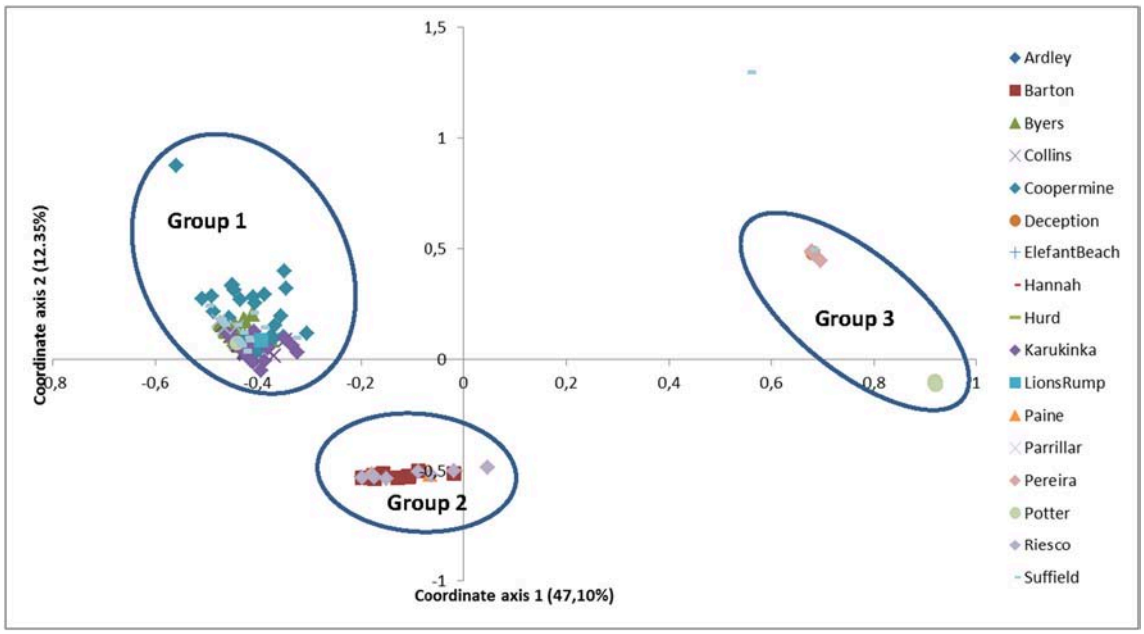

FIGURE 2 | Results of the principal coordinate analysis for 17 populations of *Sanionia uncinata*. The first principal coordinate explained 47.10% of the total variability and the second coordinate explained 12.35%.

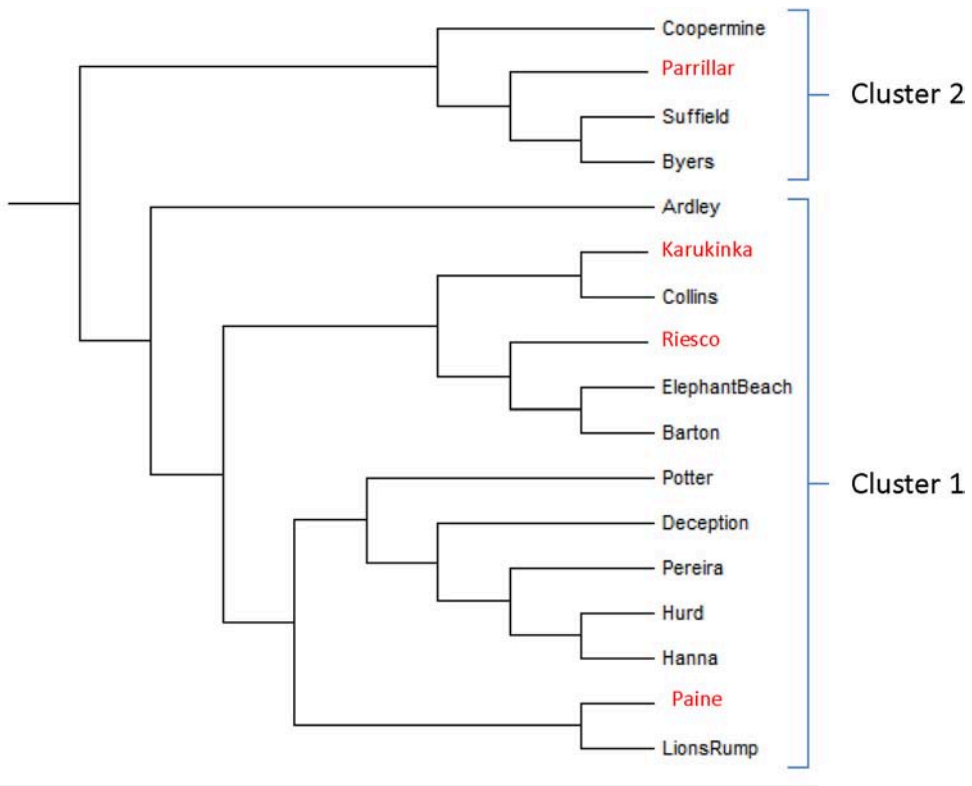

FIGURE 3 | Neighbor-joining tree showing clustering among studied *Sanionia uncinata* populations from Antarctica and southern Patagonia. Clusters 1 and 2 are the same groups of populations defined by the software STRUCTURE. Populations from southern Patagonia are red marked.

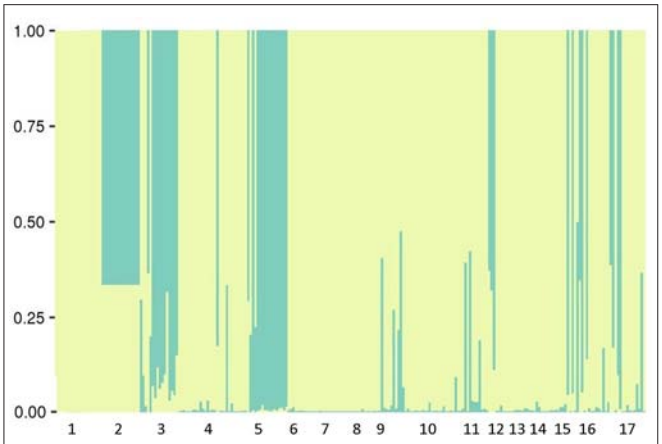

FIGURE 4 | Bayesian clustering of 281 individuals resulting from Structure analysis in 17 populations with an assumed number of K = 2.

polymorphism for Coppermine B shown with the blue line and a lower level in the samples shown with the red line, Coppermine A. (**Table 2** and **Figure 5**).

Other geographically delimited subpopulations were observed in Byers Peninsula (LI) (**Figure 6**) and Suffield Point (KGI) (**Figure 7**). All samples from Barton Peninsula (KGI) revealed a mixed ancestry. Isolated samples were found to have mixed ancestry or to belong totally to cluster 2 in populations such as Collins (KGI) and Karukinka in southern Patagonia.

The mean within-population expected heterozygosity under Hardy–Weinberg genotypic proportions (Nei's gene diversity) within populations of *S. uncinata* was similar to that calculated in the first analysis (Hw: 0.055). The highest scores of expected heterozygosity (Hj) were observed in Coppermine B (0.25), Byers B (0.187), and Suffield B (0.185) subpopulations in maritime Antarctica and Parrillar Lagoon (0.11) in Southern Patagonia (**Table 2**).

The analyses of population genetic structure found Ht = 0.072 and a significant genetic differentiation among (sub)populations ($F_{ST} = 0.237$, $^*P < 0.05$).

TABLE 2 | Results of genetic diversity analyses in each population and subpopulation.

Population	*n*	%PLP	Hj
Ardley	24	0.0	0.00033
Barton	16	11.2	0.02874
Byers_A	12	19.0	0.03242
Byers_B	12	60.6	0.18797
Collins_A	19	16.9	0.02267
Collins_B	2	14.1	0.10563
Coppermine_A	10	14.1	0.04351
Coppermine_B	14	65.5	0.25186
Deception	10	0.0	0.00000
Elephant Beach	17	1.5	0.00175
Hannah	12	0.8	0.00237
Hurd	11	0.0	0.00000
Karukinka_A	26	14.8	0.03645
Karukinka_B	4	26.8	0.09950
LionsRump	10	0.0	0.00000
Paine	11	0.0	0.00000
Parrillar	9	19.0	0.11268
Pereira	11	2.8	0.00661
Potter	11	9.9	0.01778
Riesco	10	13.4	0.05152
Suffield_A	20	6.3	0.02362
Suffield_B	10	65.5	0.18564

%PLP, proportion of polymorphic loci at 5% level; Hj, expected heterozygosity under H-W proportion.

DISCUSSION

Compared to other studied moss species, our populations of *S. uncinata* have shown similar or lower mean values for within-population gene diversity at populations and islands levels. Van Der Velde and Bijlsma (2000) reported low levels of microsatellite variability with gene diversity Hs ranging from 0,243 to 0,281 along with high genotypic diversity concluding that sexual reproduction in their studied populations of *Polytrichum formosum* had to have a stronger influence on the genetic structure of the species than clonal reproduction. In a study of the widespread Mediterranean moss *Pleurochaete squarrosa* (Grundmann et al., 2007) also described low within-population values of gene diversity with a mean value over thirty populations of Hs of 0,034 for nuclear DNA ITS markers. These authors found high levels of linkage among loci and explained their results with the model of Kimmerer (1991) who suggested that extensive vegetative propagation was responsible in her study for population growth, while the function of spores was to establish new populations.

We could distinguish two groups of populations. One of them clustered populations with either non-polymorphism or with low to very low values of genetic diversity. The other one was made out of populations showing much higher genetic diversity. We found that cluster 1, with lower levels of polymorphism and a low average of expected heterozygosity (0.03), was the most widely distributed, including populations from the northern part of southern Patagonia to the southern part of maritime Antarctica. Regarding cluster 2, it was formed by populations with the highest level of polymorphism and heterozygosity (0.17) restricted to 4 studied populations on the maritime Antarctica and Southern-Patagonia such as Parrillar Lagoon in Southern-Patagonia, Coppermine Peninsula (RI), Suffield (KGI), and Byers Peninsula (LI) in maritime Antarctica.

This dichotomy may also be partly explained by the model of Kimmerer. Vegetative propagation could be happening in some populations through gametophyte settlement with diaspores advancing with predominant western winds in the Southern Hemisphere (Muñoz et al., 2004), or being transported by birds (Parnikoza et al., 2018) or carried by snow and streams (McDaniel and Miller, 2000), while sexual reproduction could occur in Antarctica under appropriate environmental conditions

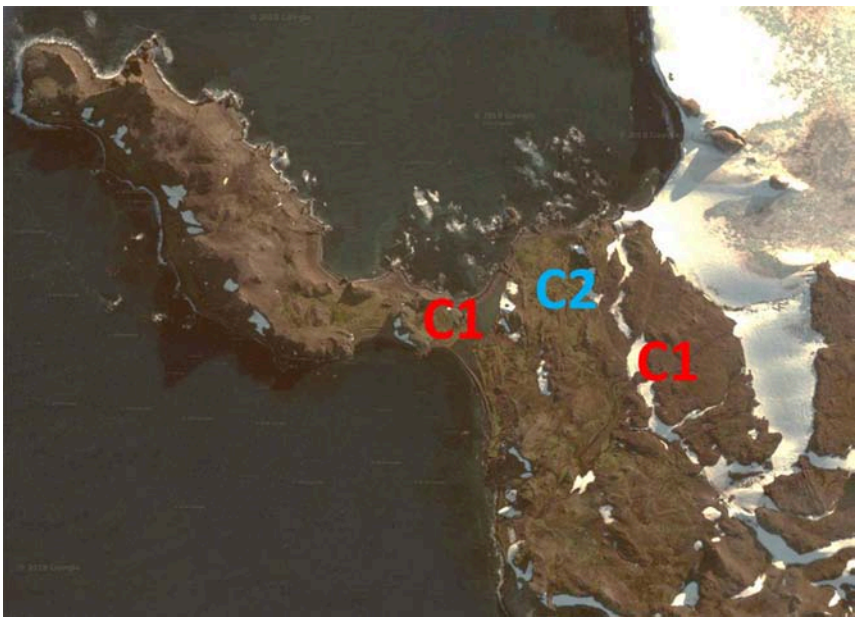

FIGURE 5 | Samples of Coppermine Peninsula (RI) populations grouped into two subpopulations. C1 indicate samples assigned to cluster 1 (Coppermine A). C2 group individuals assigned to cluster 2 (Coppermine B). Image capture from GoogleEarth.

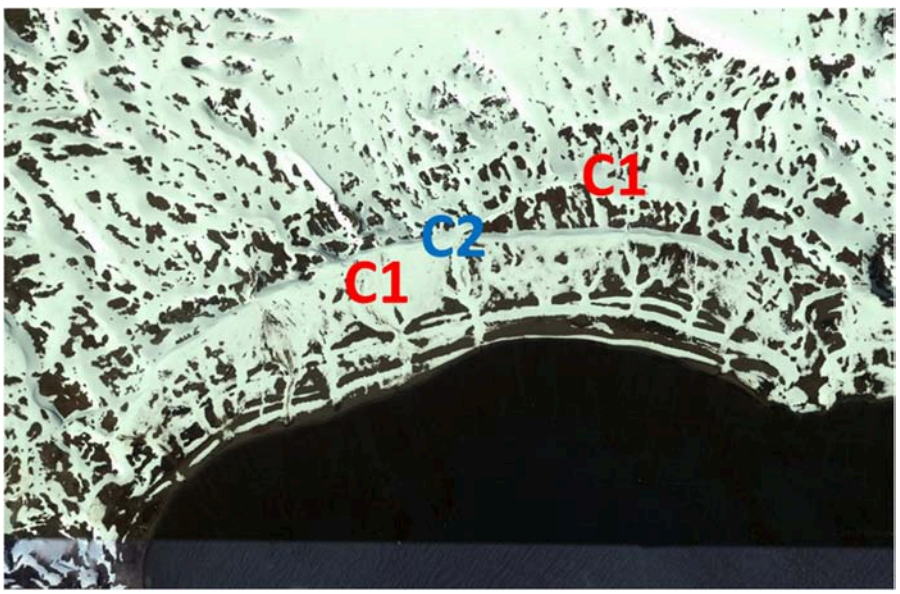

FIGURE 6 | Samples of Byers Peninsula (LI) population grouped into two subpopulations. C1 indicate samples assigned to cluster 1 which conform the population Byers A. C2 groups individuals assigned to cluster 2 conformed by Byers B. Image capture from GoogleEarth.

such as temperature and elevation conditions- which are the most significant abiotic factor affecting the presence of this moss species (Gonzalez et al., 2013). Microclimatic differences may explain why populations in the same area do not show the same levels of genetic diversity, although they are also under the influence of western winds. Ground surface temperatures have an important influence on biota biology, composition and distribution, such as in the case of the South Orkney Island-South Shetland Islands and south to Marguerite Bay (Smith and Convey, 2002), the Walker Glacier in Alaska (Dickson and Johnson, 2014), and in wind-protected sites with higher soil temperatures in the frontal moraine of the Bellingshausen glacial dome located north of Fildes Peninsula (Hebel et al., 2012). Convey et al. (2018) have shown that for Antarctic regions

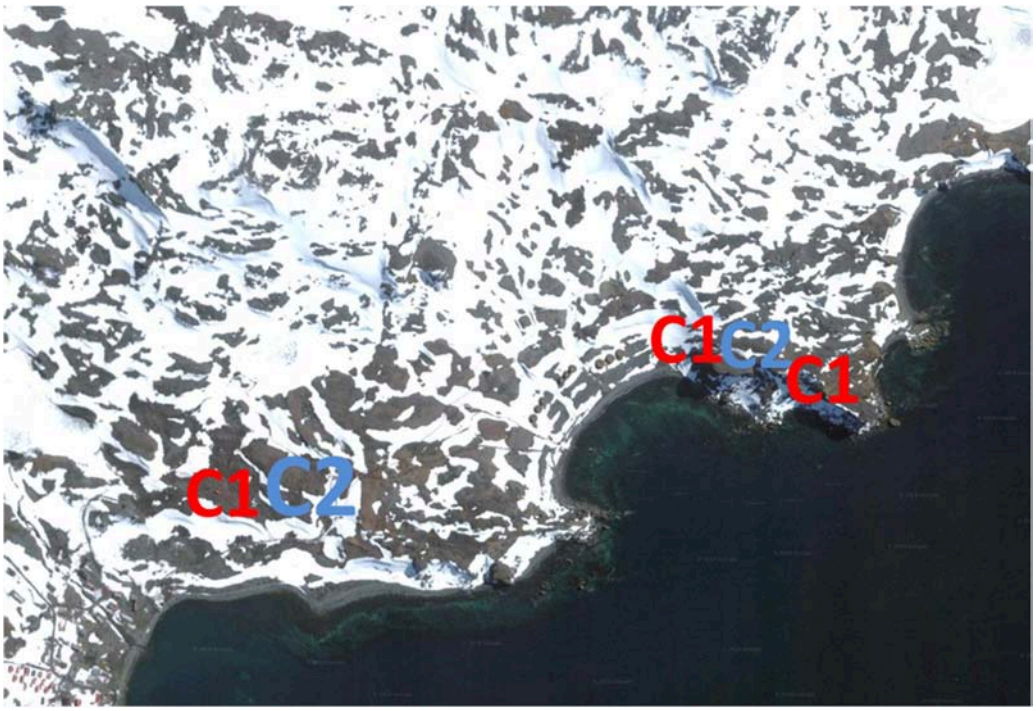

FIGURE 7 | Samples of Suffield Point population and surroundings areas (KGI). C1 indicate samples assigned to cluster 1, Suffield A. C2 group individuals assigned to cluster 2, Suffield B. Image capture from GoogleEarth.

"thermal environment is site-specific and can differ greatly over a landscape scale." In our case, unfavorable ground temperatures at some places could be preventing wind dispersed spores to establish counteracting the potential positive effects of wind on gene dispersal. Moreover, unfavorable ground temperatures could hinder the production of sporophytes leading also to reduced gene diversity and population substructuring. In this case, asexual reproduction could take the leading role in maintaining the populations as has been shown for other moss species growing under harsh environments (Frey and Kurschner, 2011).

But the low level of gene diversity could be also linked to the autoecious condition of *S. uncinata* since the level of heterozygosity depends both on the potential of self-crossing and on the haploid or diploid condition of an organism (McDaniel and Miller, 2000; Eppley et al., 2007). As a result, the frequent presence of gametophytes [i.e., haploid (*n*) individuals] of *S. uncinata* in Antarctica could bring the population to complete homozygosis in one generation. Another reason for low values of genetic diversity could be seen after a genetic drift in the influence of colonization events at the distribution edges and events of adaptation (Daniels et al., 2018). This may be of special importance on those areas where ice is retreating. Our results did not provide enough information to distinguish among all these different factors.

As suggested by Hedenas (2012) and supported also by other independent evidence like pollen rain studies (Marshall and Convey, 1997; Hebel and Rojas, 1999), it seems possible that the levels of gene flow during post-glacial colonization were sufficient to prevent a higher level of genetic differentiation among the studied populations. The applied Mantel test did not find correlation between genetic variability and geographic distance. This is also confirmed by the phylogenetic tree, which did not reveal geographically limited areas linked to genetic similarities.

Differentiation among populations becomes significant with the analysis of the substructure of populations for the Coppermine, Suffield and Byers populations (**Figures 5**–**7**) where the underlying causes of this subdivision could be the monoecious condition of the species, the typical asexual state, the low formation of sporophyte, and geographical or ecological barriers (isolation) to gene flow. However, it could be also possible that the high level of gene diversity in these three populations represents a new and recent colonization event after the ice retreat, because otherwise it is expected that autoecious species having mostly haploids states show lower levels of genetic diversity in each generation, which is not evident in our results.

Karukinka was the only site that had private alleles, indicating they have been genetically isolated for some time. On the other hand, it could be the origin of most of the samples in Antarctica linked to cluster 1, consistent with the dispersal via the western winds predominant from southern South America to Antarctica, and may have been acting as a refuge during the LGM, as described for *Buellia frigida* (Jones et al., 2015). However, our results indicated that gene flow is not limited to the route from South America to Antarctica, and evidently it

could also travel from Antarctica to southern Patagonia. Thus some samples in southern Patagonia have shown their ancestral origin in Antarctic populations. For example, in Karukinka four samples belong to cluster 2, which could be explained by gene flow from Antarctica to southern Patagonia (**Table 1**). The same relation was observed in Parrillar Lagoon in southern Patagonia, where most of the samples trace their ancestry to the Coppermine or Byers populations. This means that even with a low level of sporophyte development, the level of gene flow does not imply geographic restriction to gene flow and has occurred among Antarctica and southern Patagonia. This fact could increase the genetic diversity of the species within Antarctica and from Antarctica to other parts. The backward air trajectories detected using the HYSPLIT (HYbrid Single-Particle Lagrangian Integrated Trajectory) model (Stein et al., 2015) depict the transport of air masses in both directions between Patagonia and the SSI (**Figure 8**). This suggests that either spores or gametophytes have been responsible for migration within Antarctica, and from Antarctica to South America and *vice versa*. The dispersal model was not linked to predominant winds and fluctuated during the year and among years. The frequency of dispersal from Antarctica to South America is unpredictable, but based on the frequency of individuals that trace their ancestry to southern Patagonia, dispersal from Antarctica to Southern-Patagonia has been less frequent than in the opposite direction.

Present landscapes found in southern Patagonia and Antarctica offer a unique habitat for plant species establishment due to their particular environmental characteristics. In particular, they can provide new ground areas for moss colonization where the ice retreats. In some areas it is even possible that sediments and rocks are deposited on the glacier by the wind or through shearing from peripheral areas, also resulting in new areas for moss colonization. Furthermore, moss spore banks can act as accumulative genetic variation and colonize temporary microsites such as moraines as well as in high areas where the snow melts more quickly.

Consistent with the results of Hedenas (2012), our results suggest that the distribution of *Sanionia* in Antarctica and southern Patagonia is not linked to spatially limited refuges. The importance of geothermal sites as a refugium for genetic diversity has been highlighted in Fraser et al. (2014). Contrastingly, allele diversity on Deception Island was fixed although it is a geothermal site. One possible explanation for the lack of genetic diversity could be the highly active and recent volcanic dynamism since the nineteenth century on the island (Geyer et al., 2017).

All these places can be of special interest for researchers working on succession events who need to study variables such as exposure, height, roughness, and other factors related to substrate that could provide advantages for new settlers. Linked to molecular analyses the genetic diversity within species, helps to attribute if these characteristics are caused by natural processes associated with climatic or tectonic events, environmental variables at present or in the past or anthropogenic activities. This information allows us to identify links between species' colonization and glacial refuges and/or routes of dispersion.

The results of our genetic analyses, suggest that there is a gene flow route not only in the direction from South America to Antarctica but also from Antarctica to South America and within Antarctica. This means that our results support the concept of genetic connectivity among bioregions located on terrestrial areas of southern Patagonia and Antarctica and this interaction

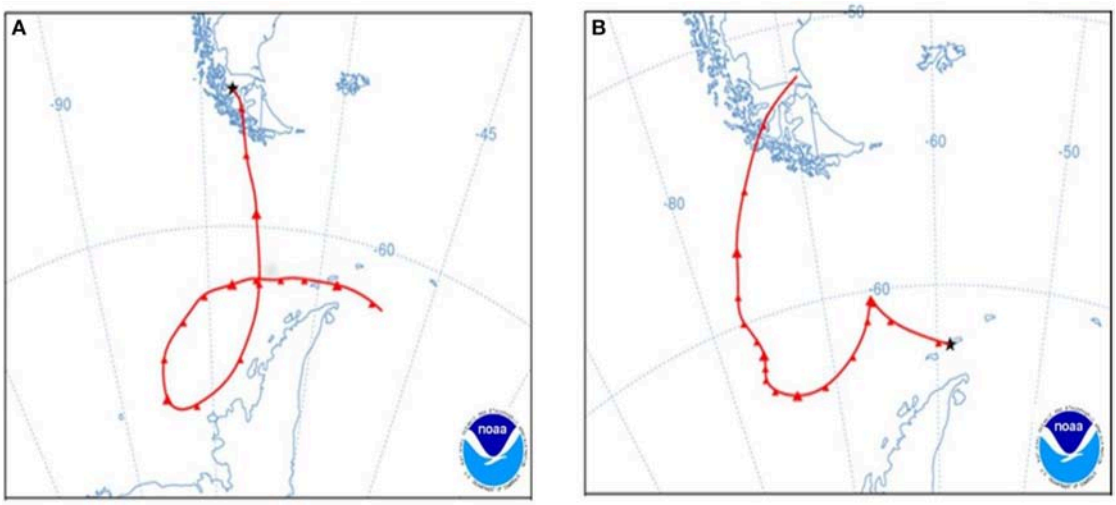

FIGURE 8 | Air mass transportation supported by forward a trajectory model using NOAA HYSPLIT (HYbrid Single-Particle Lagrangian Integrated Trajectory) (Stein et al., 2015; Rolph et al., 2017). **(A)**. Air masses moving southwards and passing over South Shetland Islands after 96 h of transport starting from a source location at Riesco Island (52.78° S, 71.70° W, 100 m above ground level) in Chilean Patagonia. Trajectory initiated at 08:00 UTC on 29 October 2006, using archived meteorological data from Global Data Assimilation System (GDAS) [NOAA HYSPLIT Job ID:187887]. **(B)** Air masses moving northwards after 108 h of transport starting from a source location at Barton Peninsula (62.23° S, 58.76° W, 100 m above ground level) on King George Island, South Shetland Islands. Trajectory initiated at 05:00 UTC on 02 February 2007, using archived meteorological data from NCEP/NCAR Global Reanalysis [NOAA HYSPLIT Job ID:187267].

may have occurred repeatedly after the LGM, resulting in the vegetation that grows in Antarctica today.

Considering the consequences of inbreeding depression in mosses (Eppley et al., 2007) and that our species is autoecious found mostly in haploid state, the recognition of geographically well-defined subpopulations with high levels of polymorphism would be important in studies applied to climate change, resilience and conservation of the species in Antarctica because the relatively recent colonization which should be a relevant target zone to manage.

DATA AVAILABILITY STATEMENT

- Datasets are available on request:

The raw data supporting the conclusions of this manuscript will be made available by the authors, without undue reservation, to any qualified researcher.

AUTHOR CONTRIBUTIONS

IH conceived the ideas, designed study, performed research, analyzed data, led the writing. MD and JB performed research. RJ performed research, analyzed data. All authors discussed the results and jointly worked on the manuscript.

FUNDING

Project T_17-09 (INACH). Project ACT-105, CONICYT-Programa de Investigación Asociativa, PIA (Anillos Antárticos). Project BMBF-Conicyt Responses of Glaciers, Biosphere and Hydrology to climate variability across the Southern Andes (GABY-VASA). Programa de Mejoramiento Institucional PMI MAG 1203 Gaia-Antártica.

ACKNOWLEDGMENTS

We thank the Chilean Antarctic Institute (INACH) for supporting this work. We thank the Wildlife Conservation Society to support our sampling and research in Karukinka. The authors gratefully acknowledge the NOAA Air Resources Laboratory (ARL) for the provision of the HYSPLIT transport and dispersion model and/or READY website (http://www.ready.noaa.gov) used in this publication. We also thank the anonymous referees for their comments.

REFERENCES

Bijlsma, R., van der Velde, M., van de Zande, L., Boerema, A. C., and van Zanten, B. O. (2000). Molecular markers reveal cryptic species within *Polytrichum commune* (common hair-cap moss). *Plant Biol.* 2, 408–414. doi: 10.1055/s-2000-5952

Birkenmajer, K., Ochyra, R., Olsson, I. U., and Stuchlik, L. (1985). Mid-holocene radiocarbon-dated peat at Admiralty Bay, King-George-Island (South-Shetland-Islands, West Antarctica). *Bull. Polish Acad. Sci. Earth Sci.* 33, 7–13.

Bonin, A., Bellemain, E., Eidesen, P. B., Pompanon, F., Brochmann, C., and Taberlet, P. (2004). How to track and assess genotyping errors in population genetics studies. *Mole. Ecol.* 13, 3261–3273. doi: 10.1111/j.1365-294X.2004.02346.x

Caners, R. T., Ellen Macdonald, S., and Belland, R. J. (2009). Recolonization potential of bryophyte diaspore banks in harvested boreal mixed-wood forest. *Plant Ecol.* 204, 55–68. doi: 10.1007/s11258-008-9565-0

Clarke, L. J., Ayre, D. J., and Robinson, S. A. (2009). Genetic structure of East Antarctic populations of the moss *Ceratodon purpureus*. *Antarct. Sci.* 21, 51–58. doi: 10.1017/S0954102008001466

Convey, P., Coulson, S. J., Worland, M. R., and Sjoblom, A. (2018). The importance of understanding annual and shorter-term temperature patterns and variation in the surface levels of polar soils for terrestrial biota. *Polar Biol.* 41, 1587–1605. doi: 10.1007/s00300-018-2299-0

Dale, T. M., Skotnicki, M. L., Adam, K. D., and Selkirk, P. M. (1999). Genetic diversity in the moss *Hennediella heimii* in Miers Valley, southern Victoria Land, Antarctica. *Polar Biol.* 21, 228–233. doi: 10.1007/s003000050357

Daniels, R. R., Taylor, R. S., Serra-Varela, M. J., Vendramin, G. G., Gonzalez-Martinez, S. C., and Grivet, D. (2018). Inferring selection in instances of long-range colonization: the Aleppo pine (*Pinus halepensis*) in the Mediterranean Basin. *Mole. Ecol.* 27, 3331–3345. doi: 10.1111/mec.14786

Dickson, J. H., and Johnson, R. E. (2014). Mosses and the beginnings of plant succession on Walker Glacier, southeastern Alaska. *Lindbergia* 37, 60–65. doi: 10.25227/linbg.01052

Earl, D. A., and Vonholdt, B. M. (2012). Structure Harvester: a website and program for visualizing Structure output and implementing the Evanno method. *Conserv. Genet. Res.* 4, 359–361. doi: 10.1007/s12686-011-9548-7

Ellis, L. T., Asthana, A. K., Gupta, R., Nath, V., Sahu, V., Bednarek-Ochyra, H., et al. (2013a). New national and regional bryophyte records, 34. *J. Bryol.* 35, 62–70. doi: 10.1179/1743282012Y.0000000042

Ellis, L. T., Bednarek-Ochyra, H., Ochyra, R., Benjumea, M. J., Sais, L. V., Caparros, R., et al. (2013b). New national and regional bryophyte records, 35. *J. Bryol.* 35, 129–139. doi: 10.1179/1743282013Y.0000000049

Eppley, S. M., Taylor, P. T., and Jesson, L. K. (2007). Self-fertilization in mosses: a comparison of heterozygote deficiency between species with combined versus separate sexes. *Heredity* 98, 38–44. doi: 10.1038/sj.hdy.6800900

Evanno, G., Regnaut, S., and Goudet, J. (2005). Detecting the number of clusters of individuals using the software structure: a simulation study. *Mole. Ecol.* 14, 2611–2620. doi: 10.1111/j.1365-294X.2005.02553.x

Fildani, A., Romans, B. W., Fosdick, J. C., Crane, W. H., and Hubbard, S. M. (2008). "Orogenesis of the Patagonian Andes as reflected by basin evolution in southernmost South America," in *Ores and Orogenesis: Circum-Pacific Tectonics, Geologic Evolution, and Ore Deposits*, Vol. 22, eds J. E. Spencer and S. R. Titley (Tucson, AZ: Arizona Geological Society Digest), 259–268.

Fraser, C. I., Terauds, A., Smellie, J., Convey, P., and Chown, S. L. (2014). Geothermal activity helps life survive glacial cycles. *Proc. Nat. Acad. Sci. U.S.A.* 111, 5634–5639. doi: 10.1073/pnas.1321437111

Frey, W., and Kurschner, H. (2011). Asexual reproduction, habitat colonization and habitat maintenance in bryophytes. *Flora* 206, 173–184. doi: 10.1016/j.flora.2010.04.020

Geyer, A., Marti, A., Giralt, S., and Folch, A. (2017). Potential ash impact from Antarctic volcanoes: insights from deception Island's most recent eruption. *Sci. Rep.* 7:16534. doi: 10.1038/s41598-017-16630-9

Gonzalez, I., Hebel, I., and Jaña, R. (2013). "Ice-free areas and distribution *Sanionia uncinata (Loeske)* on places of South Shetland Islands, Antarctica," in *Paper presented to the VII Congreso Latinoamericano de Ciencia Antártica* (La Serena).

Grundmann, M., Ansell, S. W., Russell, S. J., Koch, M. A., and Vogel, J. C. (2007). Genetic structure of the widespread and common Mediterranean bryophyte *Pleurochaete squarrosa* (Brid.) Lindb. (Pottiaceae) - evidence from nuclear and plastidic DNA sequence variation and allozymes. *Mole. Ecol.* 16, 709–722. doi: 10.1111/j.1365-294X.2007.03181.x

Hebel, I., Galleguillos, C., Jana, R., and Dacasa-Rudinger, M. D. C. (2012). Early knowledge of Antarctica's vegetation: expanding past and current evidence. *Rev. Chil. Hist. Nat.* 85, 409–418. doi: 10.4067/S0716-078X2012000400004

Hebel, I., and Rojas, G. (1999). "Estudio preliminar del contenido aerobiológico de la atmósfera de la Península Antártica y su relación con el ecosistema," in *Paper presented to the Reunión Chilena de Investigación Antártica,* Santiago, 12-13 Agosto 1999.

Hedenas, L. (2012). Global phylogeography in *Sanionia uncinata* (Amblystegiaceae: Bryophyta). *Bot. J. Linn. Soc.* 168, 19–42. doi: 10.1111/j.1095-8339.2011.01189.x

Jones, T. C., Hogg, I. D., Wilkins, R. J., Green, T. G. A. (2015). Microsatellite analyses of the Antarctic endemic lichen *Buellia frigida* Darb. (Physciaceae) suggest limited dispersal and the presence of glacial refugia in the Ross Sea region. *Polar Biol.* 38, 941–949. doi: 10.1007/s00300-015-1652-9

Kato, K., Arikawa, T., Imura, S., and Kanda, H. (2013). Molecular identification and phylogeny of an aquatic moss species in Antarctic lakes. *Polar Biol.* 36, 1557–1568. doi: 10.1007/s00300-013-1373-x

Kimmerer, R. W. (1991). Reproductive ecology of *Tetraphis pellucida*. II. Differential success of sexual and asexual propagules. *Bryologist* 94, 284–288. doi: 10.2307/3243966

Larraín, J. (2007). Adiciones a la flora de musgos de la isla grande de chiloe, chile. Gayana. *Botánica* 64, 7–23. doi: 10.4067/S0717-66432007000100002

Lewis Smith, R. I. (1984). Colonization and recovery by cryptogams following recent volcanic activity on Deception Island, South Shetland Islands. *Br. Antarct. Surv. Bull.* 62, 25–51.

Mantel, N. (1967). The detection of disease clustering and a generalized regression approach. *Cancer Res.* 27, 209–220.

Marshall, W. A., and Convey, P. (1997). Dispersal of moss propagules on Signy Island, maritime Antarctic. *Polar Biol.* 18, 376–383. doi: 10.1007/s003000050203

Martí, J., Vila, J., and Rey, J. (1996). *Deception Island (Bransfield Strait, Antarctica): An Example of a Volcanic Caldera Developed by Extensional Tectonics*. London: Geological Society, Special Publications, 253–65.

McDaniel, S. F., and Miller, N. G. (2000). Winter dispersal of bryophyte fragments in the Adirondack Mountains, New York. *Bryologist* 103, 592–600. doi: 10.1639/0007-2745(2000)103[0592:WDOBFI]2.0.CO;2

Muñoz, J., Felicísimo, A. M., Cabezas, F., Burgaz, A. R., Martinez, I. (2004). Wind as a long-distance dispersal vehicle in the Southern Hemisphere. *Science* 304, 1144–1147. doi: 10.1126/science.1095210

Navas, A., Lopez-Martinez, J., Casas, J., Machin, J., Jose Duran, J., Serrano, E., et al. (2008). Soil characteristics on varying lithological substrates in the South Shetland Islands, maritime Antarctica. *Geoderma* 144, 123–139. doi: 10.1016/j.geoderma.2007.10.011

Ochyra, R., Lewis Smith, R. I., and Bednarek-Ochyra, H. (2008). *The Illustrated Moss Flora of Antarctica*. Cambridge: Cambridge University Press.

Page, R. D. M. (1996). TreeView: an application to display phylogenetic trees on personal computers. *Comput. Appl. Biosci.* 12, 357–358.

Parnikoza, I., Rozhok, A., Convey, P., Veselski, M., Esefeld, J., Ochyra, R., et al. (2018). Spread of Antarctic vegetation by the kelp gull: comparison of two maritime Antarctic regions. *Polar Biol.* 41, 1143–1155. doi: 10.1007/s00300-018-2274-9

Paun, O., and Schönswetter, P. (2012). Amplified fragment length polymorphism (AFLP) - an invaluable fingerprinting technique for genomic, transcriptomic and epigenetic studies. *Methods Mol. Biol.* 862, 75–87. doi: 10.1007/978-1-61779-609-8_7

Peakall, R., and Smouse, P. E. (2006). GENALEX 6: genetic analysis in Excel. Population genetic software for teaching and research. *Mole. Ecol. Notes* 6, 288–295. doi: 10.1111/j.1471-8286.2005.01155.x

Peakall, R., and Smouse, P. E. (2012). GenAlEx 6.5: genetic analysis in Excel. Population genetic software for teaching and research-an update. *Bioinformatics* 28, 2537–2539. doi: 10.1093/bioinformatics/bts460

Pfeiffer, M., Mascayano, C., and Aburto, F. (2010). Soils of Chilean Patagonia in Glacial and periglacial environments. *Eurasian Soil Sci.* 43, 1430–1438. doi: 10.1134/S106422931013003X

Pritchard, J. K., Stephens, M., and Donnelly, P. (2000). Inference of population structure using multilocus genotype data. *Genetics* 155, 945–959.

Rolph, G., Stein, A., and Stunder, B. (2017). Real-time environmental applications and display sYstem: READY. *Environ. Model. Softw.* 95, 210–228. doi: 10.1016/j.envsoft.2017.06.025

Sambrook, J., and Russell, D. W. (2001). *Molecular Cloning: A Laboratory Manual, 3rd Edn*. New York, NY: Cold Spring Harbor Laboratory Press.

Schlueter, P. M., and Harris, S. A. (2006). Analysis of multilocus fingerprinting data sets containing missing data. *Mole. Ecol. Notes* 6, 569–572. doi: 10.1111/j.1471-8286.2006.01225.x

Selkirk, P. M., Skotnicki, M., Adam, K. D., Connett, M. B., Dale, T., Joe, J. W., et al. (1997). Genetic variation in Antarctic populations of the moss *Sarconeurum glaciale*. *Polar Biol.* 18, 344–350. doi: 10.1007/s003000050198

Selkirk, P. M., Skotnicki, M. L., Ninham, J., Connett, M. B., and Armstrong, J. (1998). Genetic variation and dispersal of *Bryum argenteum* and *Hennediella heimii* populations in the Garwood Valley, southern Victoria Land, Antarctica. *Antarct. Sci.* 10, 423–430. doi: 10.1017/S0954102098000510

Skotnicki, M. L., Ninham, J. A., and Selkirk, P. M. (1998a). High levels of RAPD diversity in the moss *Bryum argenteum* in Australia, New Zealand, and Antarctica. *Bryologist* 101, 412–421.

Skotnicki, M. L., Ninham, J. A., and Selkirk, P. M. (1999a). Genetic diversity and dispersal of the moss *Sarconeurum glaciale* on Ross Island, East Antarctica. *Mole. Ecol.* 8, 753–762.

Skotnicki, M. L., Selkirk, P. M., and Beard, C. (1998b). RAPD profiling of genetic diversity in two populations of the moss *Ceratodon purpureus* in Victoria Land, Antarctica. *Polar Biol.* 19, 172–176.

Skotnicki, M. L., Selkirk, P. M., and Ninham, J. A. (1998c). RAPD analysis of genetic variation and dispersal of the moss *Bryum pseudotriquetrum* from Southern Victoria Land, Antarctica. *Polar Biol.* 20.121–126.

Skotnicki, M. L., Selkirk, P. M., and Ninham, J. A. (1999b). RAPD analysis of genetic variation and dispersal of the moss *Bryum argenteum* in Ross Island and Victoria Land, Antarctica. *Polar Biol.* 21.417–422.

Smellie, J. L., Pankhurst, R. J., Thomson, M. R., and Davies, R. E. (1984). *The Geology of the South Shetland Island: IV. Stratigraphy, Geochemistry and Evolution*. British Antarctic Survey Reports 87, Cambridge. p. 84.

Smith, R. I. L., and Convey, P. (2002). Enhanced sexual reproduction in bryophytes at high latitudes in the maritime Antarctic. *J. Bryol.* 24, 107–117. doi: 10.1179/037366802125000962

Sollman, P. (2015). The genus *Bryoerythrophyllum* (Musci, Pottiaceae) in Antarctica. *Polish Bot. J.* 60, 19–25. doi: 10.1515/pbj-2015-0004

Stein, A. F., Draxler, R. R., Rolph, G. D., Stunder, B. J. B., Cohen, M. D., and Ngan, F. (2015). Noaa's hysplit atmospheric transport and dispersion modeling system. *Bull. Am. Meteorol. Soc.* 96, 2059–2077. doi: 10.1175/BAMS-D-14-00110.1

Torres-Mellado, G. A., Jana, R., and Casanova-Katny, M. A. (2011). Antarctic hairgrass expansion in the South Shetland archipelago and Antarctic Peninsula revisited. *Polar Biol.* 34, 1679–1688. doi: 10.1007/s00300-011-1099-6

Van Der Velde, M., and Bijlsma, R. (2000). Amount and structure of intra- and interspecific genetic variation in the moss genus Polytrichum. *Heredity* 85, 328–337. doi: 10.1046/j.1365-2540.2000.00762.x

Vekemans, X., Beauwens, T., Lemaire, M., and Roldan-Ruiz, I. (2002). Data from amplified fragment length polymorphism (AFLP) markers show indication of size homoplasy and of a relationship between degree of homoplasy and fragment size. *Mole. Ecol.* 11, 139–151. doi: 10.1046/j.0962-1083.2001.01415.x

Vos, P., Hogers, R., Bleeker, M., Reijans, M., Vandelee, T., Hornes, M., et al. (1995). AFLP - a new technique for dna-fingerprinting. *Nucleic Acids Res.* 23, 4407–4414. doi: 10.1093/nar/23.21.4407

Weising, K., Nybom, H., Wolff, K., and Kahl, G. (2005). *DNA Fingerprinting in Plants Principles, Methods, and Applications Boca*. Raton: Taylor & Francis Group.

Conflict of Interest Statement: The authors declare that the research was conducted in the absence of any commercial or financial relationships that could be construed as a potential conflict of interest.

frontiers in Earth Science

ORIGINAL RESEARCH
published: 30 November 2018
doi: 10.3389/feart.2018.00219

Lagrangian Detection of Moisture Sources for the Southern Patagonia Icefield (1979–2017)

Lukas Langhamer[1]*, *Tobias Sauter*[2] *and Georg J. Mayr*[1]

[1] *Institute of Atmospheric and Cryospheric Sciences Innsbruck, University of Innsbruck, Innsbruck, Austria,* [2] *Institute of Geography, Friedrich-Alexander-Universität Erlangen-Nürnberg, Erlangen, Germany*

The origin of moisture for the Southern Patagonia Icefield and the transport of moisture toward it are not yet fully understood. These quantities have a large impact on the stable isotope composition of the icefield, adjacent lakes, and nearby vegetation, and is hard to quantify from observations. Clearly identified moisture sources help to interpret anomalies in the stable isotope compositions and contribute to paleoclimatological records from the icefield and the close surrounding. This study detects the moisture sources of the icefield with a Lagrangian moisture source method. The kinematic 18-day backward trajectory calculations use reanalysis data from the European Centre for Medium-Range Weather Forecasts (ERA-Interim) from January 1979 to January 2017. The dominant moisture sources are found in the South Pacific Ocean from 80 to 160°W and 30 to 60°S. A persistent anticyclone in the subtropics and advection of moist air by the prevailing westerlies are the principal flow patterns. Most of the moisture travels less than 10 days to reach the icefield. The majority of the trajectories originate from above the planetary boundary layer but enter the Pacific boundary layer to reach the maximum moisture uptake 2 days before arrival. During the last day trajectories rise as they encounter topography. The location of the moisture sources are influenced by seasons, Antarctic Oscillation, El-Niño Southern Oscillation, and the amount of monthly precipitation, which can be explained by variations in the location and strength of the westerly wind belt."

Keywords: Southern Patagonia Icefield, moisture sources, moisture origin, moisture transport, El-Niño Southern Oscillation, Antarctic Oscillation, ERA-Interim, trajectories

OPEN ACCESS

Edited by:
Marius Schaefer,
Southern University of Chile, Chile

Reviewed by:
Lukas Arenson,
BGC Engineering, Canada
Martín Jacques-Coper,
Departamento de Geofísica, Facultad de Ciencias Físicas y Matemáticas, Universidad de Concepción, Chile

***Correspondence:**
Lukas Langhamer
lukas@langhamer.de

Specialty section:
This article was submitted to Cryospheric Sciences, a section of the journal Frontiers in Earth Science

Received: *06 January 2018*
Accepted: *14 November 2018*
Published: *30 November 2018*

Citation:
Langhamer L, Sauter T and Mayr GJ (2018) Lagrangian Detection of Moisture Sources for the Southern Patagonia Icefield (1979–2017). Front. Earth Sci. 6:219. doi: 10.3389/feart.2018.00219

1. INTRODUCTION

The Southern Patagonia Icefield is the biggest temperate ice mass in the Southern Hemisphere, and thus an important fresh water storage for southern South America. It is located at the southern end of the Andes cordillera between 48.3 and 51.0°S along 73.0°W with an average width of 30–40 km and the narrowest section being 8 km wide (**Figure 1**) (Aniya et al., 1996). The icefield consists of 48 major outlet glaciers and over 100 small cirque and valley glaciers and has an average elevation of 1,600 m above mean sea level (m msl), while the icefield extends from the sea level with the highest peaks reaching above 3.000 m msl. Overall the climate can be summarized as temperate, very humid with freezing levels generally above 1 km msl, with a modest annual cycle and high annual precipitation rates (Miller, 1976; Weischet, 1996; Garreaud et al., 2013). Extreme environmental conditions and inaccessibility of the icefield pose a challenge for scientists to acquire records of meteorological conditions.

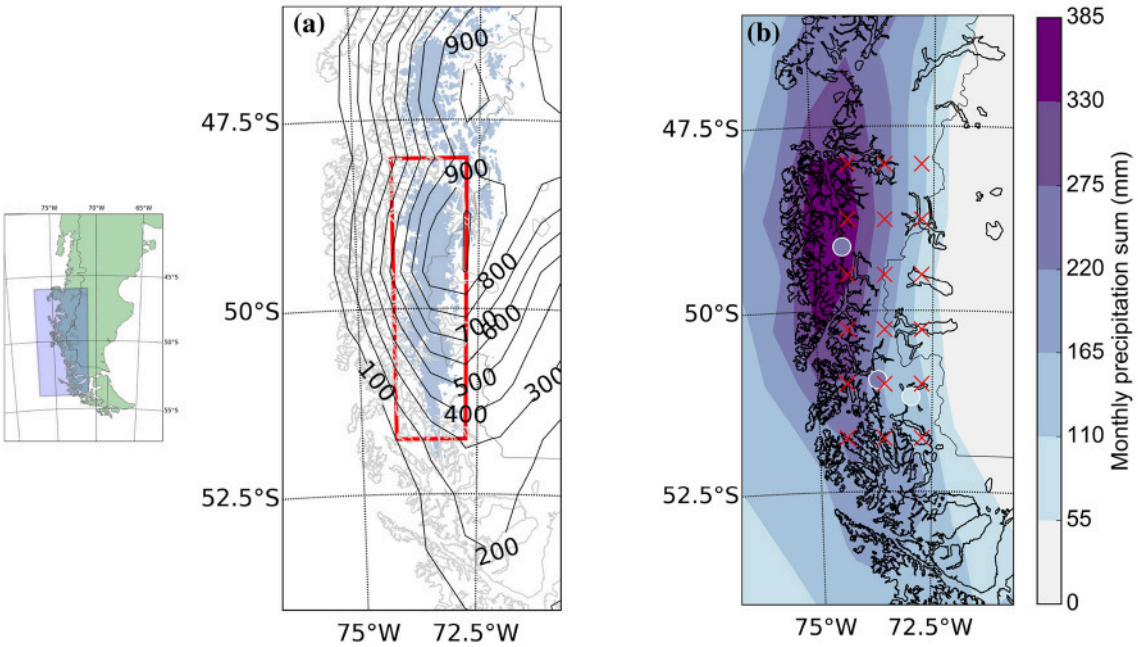

FIGURE 1 | (a) ERA-Interim model topography in meters (contour lines) and the Patagonian icefields (light blue). The red rectangle illustrates the target area. **(b)** ERA-Interim total monthly mean precipitation and raw measurements of automatic weather stations from north to south: Puerto Eden, Amalia, Torres del Paine. The red crosses illustrate the trajectory starting positions.

The reconstruction of past climate behavior is essential to predict accurate the development of the icefield. Appropriate climate proxies are the stable isotopes of hydrogen and oxygen contained in firn and ice cores, adjacent lakes (sediments), and nearby vegetation. The isotope composition is mainly dependent on the moisture source, the sea surface temperature of marine moisture sources, ambient air temperature and the saturation vapor pressure (Merlivat and Jouzel, 1979). Thus the stable isotope composition is a natural tracer for changes in the global hydrological cycle (Gat, 1996). The knowledge of moisture origin and transport is important to interpret stable isotope data (Mayr et al., 2007; Steen-Larsen et al., 2013). Anomalies in the isotope composition not only result from changes in the environmental surrounding, but can be an effect of anomalies in the moisture sources and/or different moisture transport pathways (Berkelhammer and Stott, 2008; Wernicke et al., 2017). Thus clearly identified moisture sources contribute to paleoclimatological studies and help to reconstruct past climate conditions. A better understanding of the general atmospheric circulation in context with the hydrological cycle is one principal component to make accurate climate projection. But where does the moisture come from?

We currently know that the cyclones embedded in the circumpolar vortex and orographic enhancement are responsible for the high precipitation sum at the icefield (Schneider et al., 2003; Schneider and Gies, 2004; Smith and Evans, 2007; Barrett et al., 2009; Garreaud et al., 2013; Viale et al., 2013). *In-situ* measurements show that over 90 % of the moisture is advected from southwesterly to northwesterly direction (Rivadeneira, 2011). Prevailing westerlies advect moist air masses from the Pacific Ocean, which makes the Pacific as major moisture contributor very likely. But so far studies, which indicate the moisture sources of the icefield, have been missing. Filament structures of tropospheric water vapor, so called "atmospheric rivers" (Newell et al., 1992), transport moist air masses from the subtropics polewards, and are responsible for heavy winter precipitation events upstream the central Andes (Viale and Nuñez, 2011). Another case study indicated that atmospheric rivers are the principal moisture source for narrow cold-frontal rainbands approaching the Andes (Viale et al., 2013). But the significance of moisture transported by atmospheric rivers from the subtropics and its contribution to the precipitation of the icefield is vague. Also the role of Antarctic Cold Air Outbreaks (Papritz et al., 2015) as a trigger of a moisture uptake region remains uncertain.

This study presents a diagnostic picture of the moisture source regions from the icefield, the average transport time of moisture and favored pathways. Backward trajectories in combination with an established moisture source diagnostic technique are used to reach these objectives.

2. METHODOLOGY

Trajectories allow to trace the moisture contributions to air parcels. Various models for computing trajectories based on output of numerical prediction models exists. Stohl et al.

(2001) carried out a survey of the Lagrangian analysis tool (LAGRANTO) (Wernli and Davies, 1997), the KNMI (Koninklijk Nederlands Meteorologisch Instituut) trajectory tool TRAJKS (Scheele et al., 1996), and the hybrid single-particle Lagrangian integrated trajectory model (HYSPLIT). Trajectories differ by <2 % between the average distance of the starting and ending position within the free atmosphere during a 48 h time interval. This paper uses LAGRANTO, which Sprenger and Wernli (2015) describe in detail.

2.1. Lagrangian Moisture Diagnostic

Trajectories describe the motion of air particles through space and time. By neglecting the impact of mixing with adjacent air parcels and ignoring the presence of liquid water and ice in the atmosphere, evaporation E and precipitation P along a trajectory during the time interval Δt_0 control the change in specific humidity q (Stohl and James, 2004),

$$\frac{\mathrm{D}q}{\mathrm{D}t} \approx \frac{\Delta q}{\Delta t_0} = E - P. \tag{1}$$

The atmosphere is assumed to be well mixed in the planetary boundary layer (PBL) where turbulent fluxes can change moisture of an air parcel (trajectory). Therefore, the moisture content can increase where air parcels entrain PBL air. If a moisture uptake happens above the PBL, moisture changes are detached from the surface and attributed to other physical or numerical processes, such as convection, evaporation of precipitating hydro-meteors, change of liquid water content or ice water content, subgrid-scale turbulent fluxes or to numerical diffusion, numerical errors associated with the trajectory calculation, or physical inconsistence between two analysis time steps (Sodemann et al., 2008).

The present study applies the moisture source diagnostic of Sodemann et al. (2008). Along the trajectories moisture uptake inside the PBL is weighted by the contribution to the total precipitation in the target area. En route precipitation is considered. Winschall et al. (2014) show that the approach yields similar moisture source regions as the more complex Eulerian tagging approach for a case study in Europe and recommend using the Lagrangian approach of Sodemann et al. (2008) for climatological studies due to lower computational cost.

Since numerical weather prediction models underestimate the marine PBL (Zeng et al., 2004), a somewhat arbitrary factor of 1.5 counteracts the underestimation (Sodemann et al., 2008). A moisture uptake within the PBL, and thus a moisture source is defined if the following condition holds,

$$p_{\mathrm{traj}} \geq p_0 \left(1 - \frac{1.5\gamma h_{\mathrm{PBL}}}{T_0}\right)^{5.2561}, \tag{2}$$

where p_0 and T_0 are pressure (in hPa) and temperature (in K) at the surface respectively, p_{traj} is the pressure height of the trajectory (in hPa), h_{PBL} the planetary boundary layer height (in meters above ground level) of the point x at the time t. The conversion of the h_{PBL} into pressure height ensued by a constant lapse rate $\gamma = 0.0065\,\mathrm{K\,m^{-1}}$. These assumptions allow a conversion into pressure height more precisely than using a US standard atmosphere as originally suggested.

2.2. Implementation

The trajectory calculation is based on the global atmosphere reanalysis product ERA-Interim (Berrisford et al., 2011; Dee et al., 2011; Persson, 2015). ERA-Interim is a numerical weather prediction model which assimilates the most accurate initial conditions (reanalysis) based on *in-situ* measurements and remote sensing. Due to a lack of data in high southern latitudes, the accuracy of reanalyzed products is likely less than in other regions. Bromwich et al. (2011) evaluate the temporal variability of the Antarctic surface mass balance. The authors conclude that ERA-Interim offers the most accurate and reliable depiction of precipitation changes in high southern latitudes during 1989–2009. Bracegirdle and Marshall (2012) compared the Antarctic tropospheric pressure and temperature of common reanalysis products with observations. One of their findings was that ERA-Interim has the most reliable mean sea level pressure and 500 hPa geopotential height trends. Nicolas and Bromwich (2011) investigated the precipitation changes in high southern latitudes from different global reanalysis products. The authors achieved the most realistic depiction with ERA-Interim. Bracegirdle (2013) emphasize the accuracy of ERA-Interim to capture individual weather systems over the Bellingshausen Sea. On these grounds ERA-Interim is particularly suitable for the study presented here.

Fields from ERA-Interim have a horizontal resolution of 0.75°, are vertically subdivided in 60 model levels (from the surface to 0.1 hPa), and are available every 6 hours (Δt_0). The dataset consisting of the 3-D wind field $\vec{u} = (u, v, w)$, the logarithm of surface pressure, the PBL height, the 2 m-temperature, and q, is taken from 10°N to 90°S latitudes and all longitudes and covers the period from January 1979 to January 2017.

The starting position of the backward trajectory calculation are the nodes of a 0.75° regular grid, extending from 74.25 to 72.75°W and 48.0 to 51.75°S at levels equally spaced ($\Delta p = 49.9$ hPa) from the surface to 500 hPa (red crosses **Figure 1**). A starting grid thus defined leads to 198 trajectories ($3 \times 6 \times 11$ starting points). To clarify the nomenclature of backward trajectory modeling, the trajectory starting position is the starting point of the backward trajectory calculation above the icefield, and the trajectory ending position is the position where an air parcel is located after a particular time of backward trajectory calculation. Since the fraction of moisture already included at the trajectory ending position, hereinafter called total unknown moisture uptake fraction, goes to zero for an infinitely long backward calculation time, the interval is chosen to have the best efficiency. Longer backward trajectory calculation increase the computational cost and have no notable improvements on the results. Shorter backward trajectory calculation increases the total unknown moisture uptake fraction significantly. A backward calculation time of 18-day was found to have the best relation between computational cost and detection efficiency. Every 6 h an 18-day backward trajectory calculation is started from the predefined grid points. Only trajectories responsible for the precipitation in the target region are considered (red

rectangle). They have to satisfy at their starting point: (i) the relative humidity has to exceed a threshold of 80 % and (ii) q has to decrease during the last Δt_0, as in Sodemann et al. (2008). Whenever a trajectory would cross the lower boundary, LAGRANTO artificially lifts trajectories to 10 hPa above the model surface.

3. THE LARGE SCALE FLOW

The trajectory calculations are based on the ERA-Interim Re-Analysis meteorological fields. Before we examine the Lagrangian perspective this section illustrates a selection of the corresponding Eulerian fields to highlight the main characteristics of the large scale atmospheric circulation, and surface conditions in South America and surrounding.

The Hadley circulation at ∼30°S and the circumpolar band of low pressure around Antarctica at ∼60°S are the main drivers of the climate in southern South America. The two regions generate a strong north-south pressure gradient. As a consequence a strong circumpolar vortex exists around Antarctica (**Figure 2**). There are small seasonal variations. Austral winter months show an equatorwards displacement of the subtropical high-pressure belt of about 5° in comparison to the summer months. The northern shift and the weakening of the anticyclone during austral winter cause a geopotential height gradient decrease at 800 hPa from ∼15 m to ∼11 m per degree around 50°S over the South Pacific. Thus, the austral winter months exhibit the lowest wind velocities on average over the South Pacific.

The Pacific Ocean is free from topographic disturbances. High wind velocities are present even in lower levels and the westerly wind belt almost coincides with the jet axis at approximately 50°S (**Figure 3**). The highest 10 m mean wind velocities (∼15 m s^{-1}) occur at the Antarctic coast. Strong Antarctic outflow is present at the Bellingshausen and Amundsen Sea with its minimum in the austral summer months. Only on extreme rare occasions does a meridional circulation cause blocking of the west wind drift (Trenberth and Mo, 1985). Hence, the prevailing westerlies permanently advect moist air from the Pacific Ocean toward the southern tip of South America. This makes the southern Andes cordillera the only obstacle for the embedded baroclinic waves.

The north-south oriented Andes mountain ridge intersects the westerlies forming a pronounced climatic wall with very moist conditions on its upstream side and very dry conditions on the lee-side (Weischet, 1996; Schneider and Gies, 2004; Smith and Evans, 2007; Garreaud et al., 2009, 2013). Upstream of the mountain ridge orographic enhanced uplift leads to high accumulation rates of precipitation. The orography enhances the precipitation at the icefield. The amount of orographic precipitation in a stable flow depends, among other factors, on the strength of the crossbarrier flow U, the terrain height H, and the thermodynamic stability of the oncoming flow quantified by the Brunt-Väisälä Frequency N, and can be summarized in a non-dimensional ratio $U(NH)^{-1}$. It is often referred to as Froude number (or the inverse non-dimensional mountain height), which determines the flow regime (Houze, 2012). Past studies findings show a correlation between u and precipitation in west Patagonia (Schneider et al., 2003; Garreaud et al., 2013). The crossbarrier flow is one of three main drivers to describe the flow over a terrain and thus reasonable to correlate with the orographic precipitation.

Estimates of annual mean precipitation at the icefield range from 5,000 to 10,000 mm (Miller, 1976; DGA, 1987; Carrasco et al., 2002; Garreaud et al., 2013). Firn core measurements indicate extremely high accumulation rates. For example, net annual accumulation at glacier Tyndall, located at the southernmost part of the icefield, is 11,000–17,800 mm water equivalent (Shiraiwa et al., 2002). By contrast, only a few dozen kilometers downstream, the annular mean precipitation decreases to 300 mm (Garreaud et al., 2013). This west-east precipitation gradient is the most intense one worldwide (Schneider et al., 2003; Garreaud et al., 2013) and can be quantified with the drying ratio. The drying ratio describes the fraction of water vapor which rains out while passing a mountainous barrier. Smith and Evans (2007) estimated drying ration $\approx$ 0.56 in the southern Andes (40 to 48°S), the highest value yet found to date in a mountain range.

The precipitation accumulated over the target region amounts 220 mm per month on median obtained from ERA-Interim. The monthly variation of the amount of precipitation hardly shows any seasonality (**Figure 4**). Warmer austral summer (DJF) and autumn (MAM) months indicate slightly more precipitation ($P_{DJF,median}$ = 233 mm per month and $P_{MAM,median}$ = 232 mm per month) than colder winter (JJA) months ($P_{JJA,median}$ = 198 mm per month). But austral winter months show the highest variation of the monthly mean precipitation in the target region indicated by the inner-quartile range of 96 mm per month. During spring (SON) the median of the monthly mean precipitation accounts 213 mm per month. Note, the monthly resolved precipitation accumulated over the target area shows only the absolute amount, and is not a measurement for the intensity and frequency of individual precipitation events.

The ERA-Interim model topography reaches from the sea surface to 1.011 m msl with an average of 595 m msl (**Figure 1a**). Only a few long term precipitation records are present in the vicinity of the icefield (**Figure 1b**). The automatic weather stations (AWS) "Amalia" and "Puerto Eden" are situated upstream of the icefield. The mean precipitation amounts significantly (p-value $<$ 0.002) correlate with the ERA-Interim reanalysis (r_{Pearson} = 0.65 to 0.70) after the annual cycle is removed. They register a monthly mean sum of 255 mm at Amalia and 249 mm of Eden, respectively. Downstream of the icefield the AWS "Torres del Paine" provides 14 years of measurements. The monthly mean observations, obtained from http://explorador.cr2.cl/, correlate positively with the ERA-Interim data (r_{Pearson} = 0.68, p-value = 3.5e-26). The averaged monthly mean amounts to 64 mm, about a quarter of the upstream values. The AWS report a strong decreasing precipitation amount going from west to east across the cordillera. The ERA-Interim re-analysis data reproduces the precipitation features of southernmost South America in a temporal and spatial sense but a validation of the amounts of precipitation is impossible in absence of reliable observations. Extreme high wind velocities, with 10 m s^{-1} on average, and

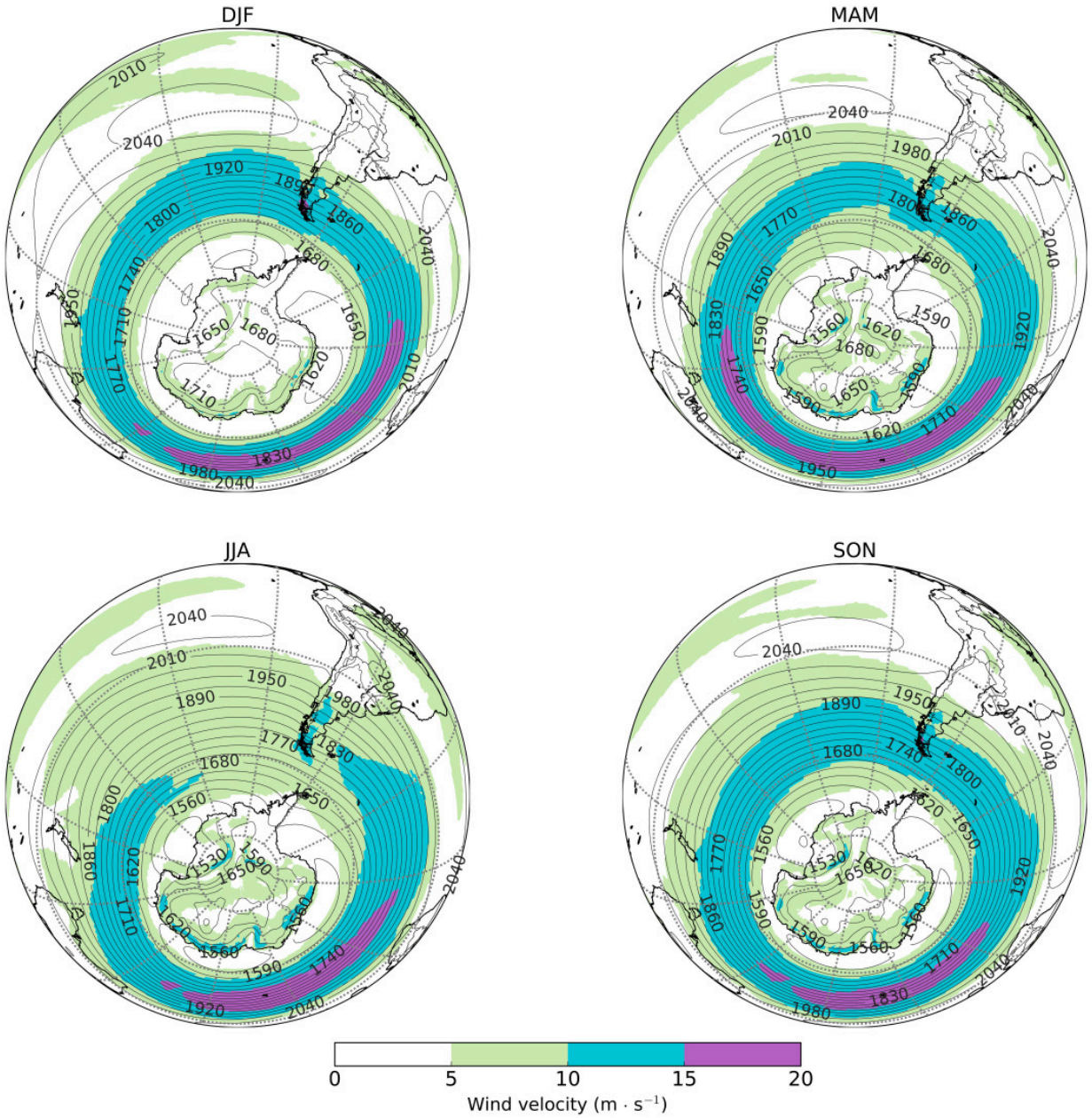

FIGURE 2 | Mean wind velocity (colored areas) and geopotential height (contour lines) of 800 hPa from 1979 to 2017 obtained from ERA-Interim subdivided into seasons. An isohypse is plotted every 30 m. The interval of the meridians and parallels is 30°.

snow events cause an under-catch of the rain gauges especially upstream of the cordillera e.g. AWS Puerto Eden, where the monthly mean observations are lower than the ERA-Interim data (**Figure 1b**) and the root-mean-square error indicate a deviation of $RMSE_{Puerto\ Eden} = 154$ mm. In general, global re-analysis data tends to underestimate the amount of precipitation in southern South America (Ward et al., 2011; Lenaerts et al., 2014). This feature is also observed by the station Amalia ($RMSE_{Amalia} = 80$ mm) and Puerto Eden ($RMSE_{Torres\ del\ Paine} = 48$ mm).

4. RESULTS

4.1. Moisture Sources for the Southern Patagonia Icefield From 1979 to 2017

The mean moisture sources are derived from the Lagrangian methodology and represent the mean moisture uptake (in mm per month) within the scaled PBL, which contributes to the monthly precipitation in the icefield averaged over the time period from February 1979 to January 2017 (**Figure 5**). This plot contains 2,972,903 18-day backward trajectory calculations. The

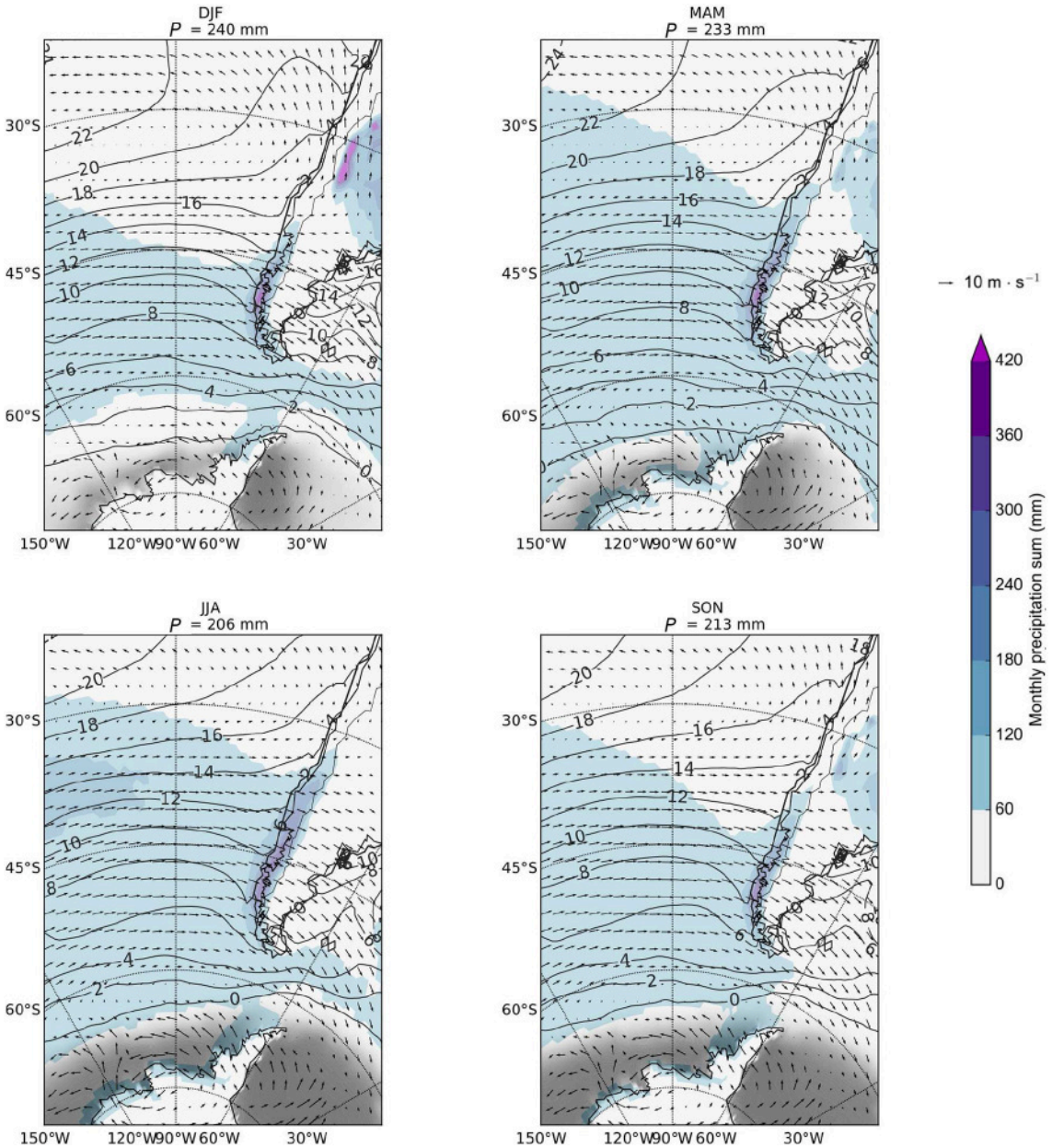

FIGURE 3 | Seasonal precipitation (blue contours in mm per month), 10 m wind field (arrows with reference arrow), sea surface temperature (contour lines, 2 K interval) and sea ice cover (gray shaded area) from ERA-Interim (1979–2017). The corresponding monthly mean precipitation sum *P* accumulated over the target area is written in the header.

identified moisture sources are interpolated on a regular 1.5° grid.

The majority of the moisture uptake originates from the South Pacific Ocean. The absolute maximum of 3.16 mm per month is close to the coast line of West Patagonia from where it takes about 1 day to reach the icefield. In that region the moisture transport time is about 1 day. Moisture source regions, which contribute more than 1 mm per month, reach to the subtropics. Within this region the transport of moisture takes up to 6 days from the source to the precipitation at the icefield. Significant moisture source regions southward of 60°S and in the Atlantic Ocean are absent. The contribution of moisture to the precipitation at the icefield from within the scaled PBL (evaporation from the surface) is 71 %. At the trajectory ending position is already 4 % of moisture included and 25 % originate above the scaled PBL (see also **Table S1** in Supplementary Material). The origin of this moisture is unknown and excluded in **Figure 5**.

At the trajectory ending position ($t = -18$ d) 75 % of the trajectories are above the median of the scaled h_{PBL} (**Figure 6a**).

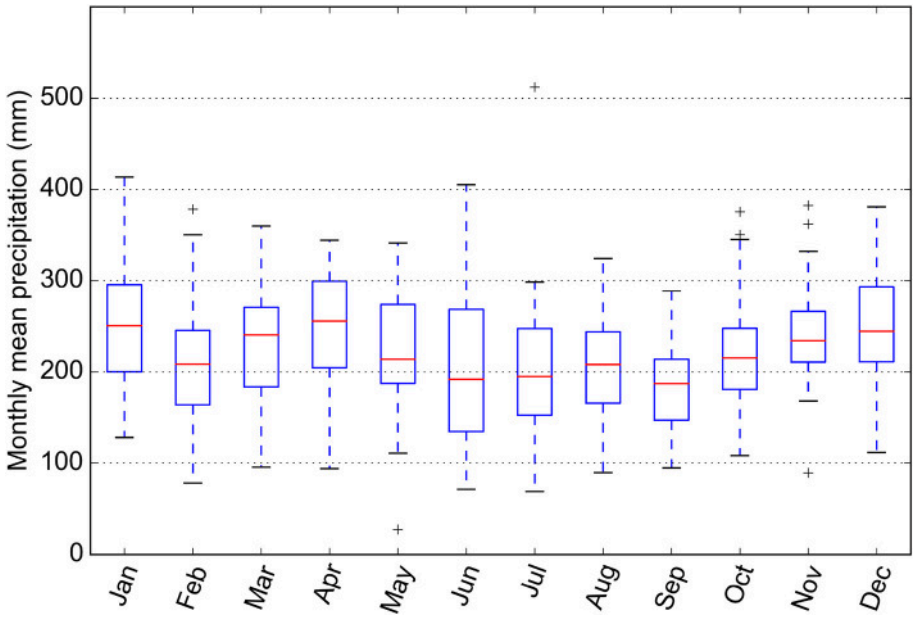

FIGURE 4 | Monthly precipitation accumulated over the target area obtained from ERA-Interim (1979–2017).

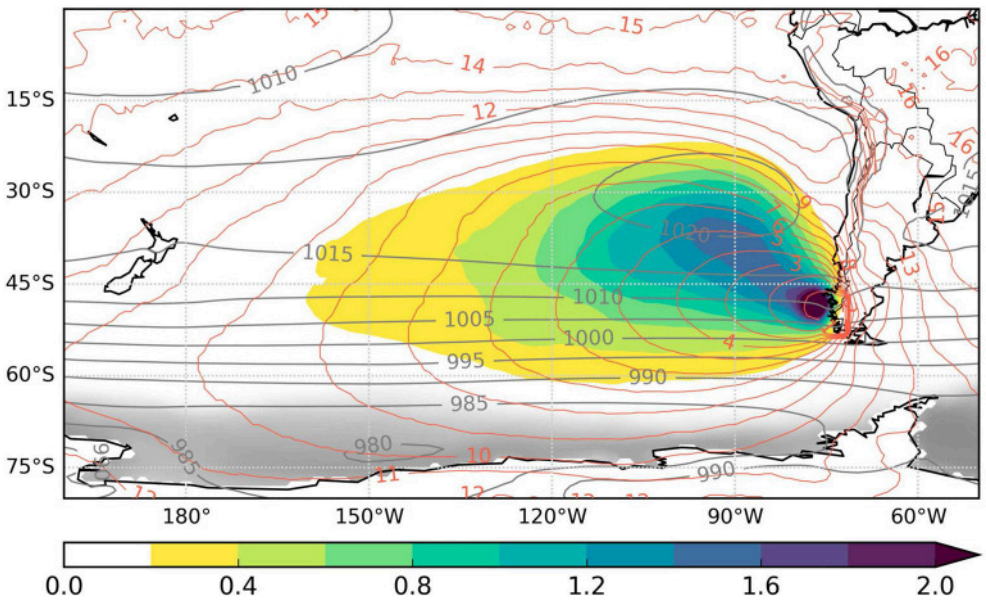

FIGURE 5 | Mean moisture sources of the Southern Patagonia Icefield (colored area) in mm per month. Only moisture sources within the scaled PBL are considered. The maximal moisture uptake is 3.16 mm per month. The red lines indicate the mean travel time of the trajectories toward the icefield in days before arrival. The averaged mean sea level pressure (gray lines) and sea ice cover (gray shaded area) are depicted as well.

From −18 days to −2 days, the median trajectory pressure level decreases from 703 hPa to 905 hPa. The moisture content within the trajectory increases from 2.0 g kg^{-1} at −18 days to 4.8 g kg^{-1} at $t = -12$ h (blue line, **Figure 6b**). Most of the trajectories are located within the scaled h_{PBL} from $t = -4$ d to arrival. During that time interval the largest six-hourly moisture uptake within the PBL contributes with $\Delta q_{\mathrm{median}} = 0.024$ g kg^{-1} to the precipitation at the icefield. The moisture change along the trajectory above the scaled PBL is about 1/3 of the moisture change within the scaled PBL. From $t = -1$ d to arrival we see an overall lifting of the trajectories to 835 hPa (on median). Since moisture decrease for all trajectories in the last 6 hours before reaching the icefield the moisture uptake is 0 g kg^{-1} at −6 h to 0 h. Note that only the trajectories were selected, for

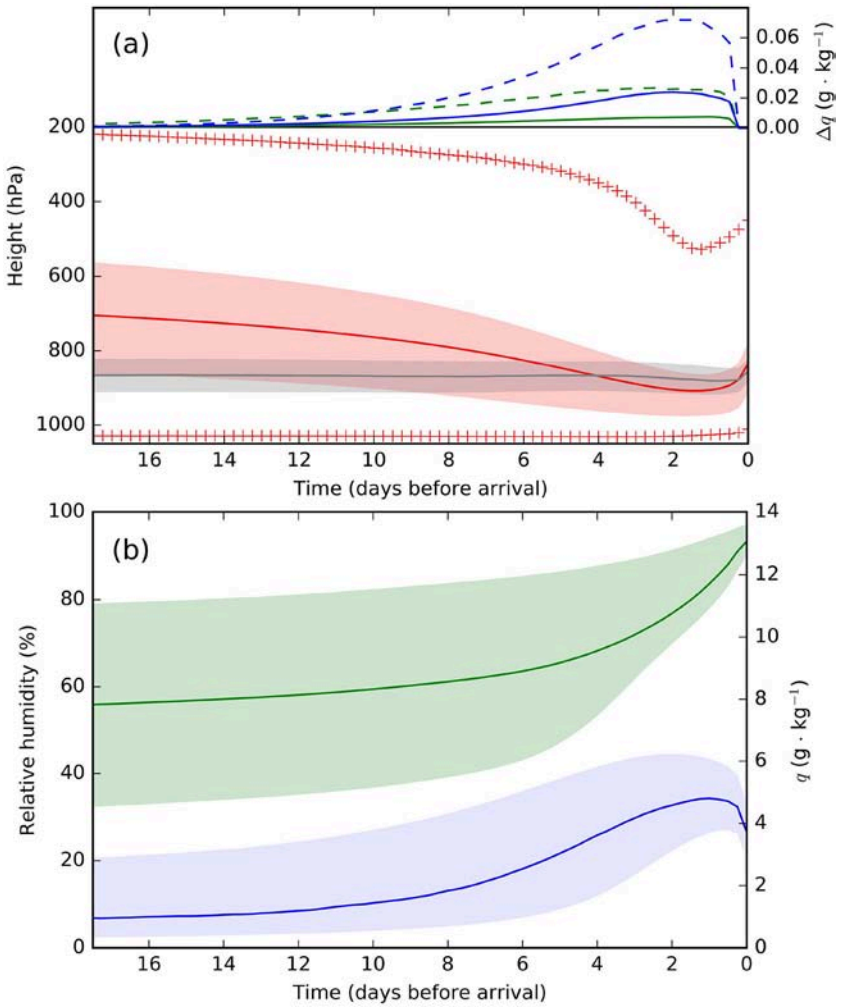

FIGURE 6 | Vertical cross section of the trajectories. **(a)** (Bottom) Mean pressure height, quartiles and extremes (red), and the scaled boundary layer height (gray). (Top) Changes of the weighted specific humidity of moisture uptake within the scaled planetary boundary layer (PBL) (blue) and above the scaled PBL (green), which contribute to the precipitation at the icefield. Dashed lines show the corresponding upper quartile. **(b)** Quartiles and mean of relative humidity (green) and specific humidity (blue) of the trajectories.

which $RH > 80\,\%$ and $\Delta q < 0$ during $t = -6\,\text{h}$ to $0\,\text{h}$. Trajectories above the Antarctic continent originate from higher levels [$p_{\text{traj}}(t > 13\,\text{d}) \leq 600\,\text{hPa}$] (**Figure 7**). Above the central Andes they reach mean heights of up to 500 hPa. Over the South Pacific Ocean a west-east gradient is visible with higher mean trajectory elevations in the west.

The trajectories are very dry ($RH < 20\,\%$) at the subtropical west coast of South America and Africa (**Figure 8**) due to subsidence. Very humid parts of the trajectories ($RH > 80\,\%$) are present in the tropics and in the southeastern Pacific Ocean. The trajectories naturally cluster in the vicinity of the starting location of the icefield. The gradient of the number of trajectories per grid point is stronger in north-south than in west-east direction. Some regions show an absence of trajectories (white areas). During the whole calculation period not even one trajectory reached central Africa for instance.

4.2. Moisture Source Anomalies

4.2.1. Seasonal Variation

Seasons influence the moisture sources of the icefield (**Figures 9a–d**). Orange areas highlight a loss and green areas a surplus of the moisture source relative to the long-term annual climatological mean (1979–2017, **Figure 5**). A dipole like pattern is visible comparing the moisture source anomalies of JJA with DJF months, and MAM with SON months. The moisture uptake is reduced by 0.55 mm per month in the eastern South Pacific in the months DJF (**Figure 9a**). There is a moisture source deficit northwards and southwards of the icefield. By contrast there are positive anomalies along the 45°S parallel (0.5–0.25 mm per month). The 800 hPa geopotential height rises about 30 m in the central South Pacific which enhances the westerlies from 45 to 60°S parallel. Enhanced anticyclonic flow occurs in the subtropics. The geopotential height anomaly over the Ross

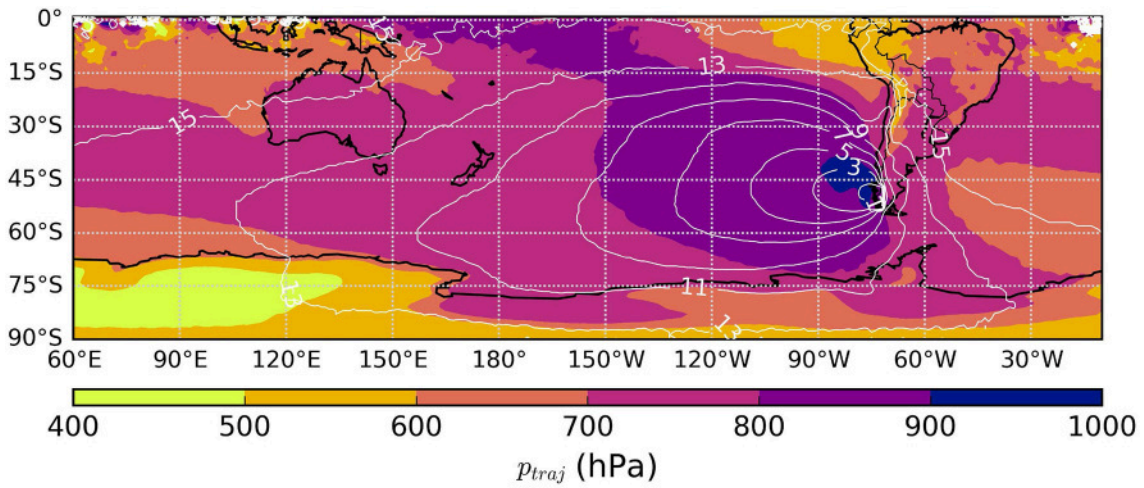

FIGURE 7 | Mean pressure height of the trajectories interpolated on a 1.5° regular grid. White lines indicate the mean transport time of the moisture toward the Southern Patagonia Icefield in days before arrival.

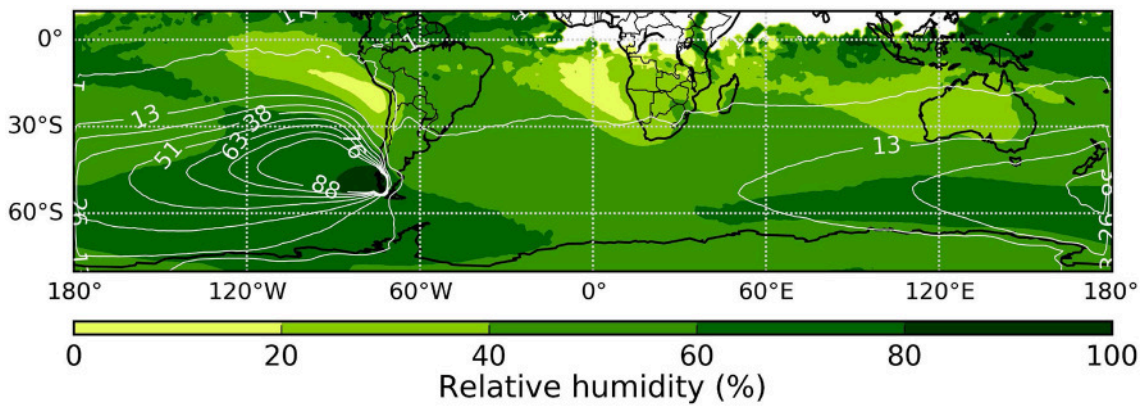

FIGURE 8 | Mean relative humidity *RH* of the trajectories interpolated on a 1.5° regular grid. White contour lines present the averaged number of trajectories per grid point. White areas indicate a lack of information due to absence of trajectories.

Sea is 80 m, concomitant with a weakening of the westerlies in the proximity of Antarctica.

The austral winter months (**Figure 9c**) show an inverted situation of the moisture source and geopotential height anomalies. In the eastern South Pacific northward of the icefield the monthly mean moisture sources increases to up to 0.55 mm per month. There is a deficit along the 45°S parallel, with the most pronounced region in the eastern South Pacific Ocean (up to −0.25 mm per month). An up to 40 m lower geopotential height decreases the negative poleward oriented gradient. In fact lower wind velocities occur upstream of the icefield at 800 hPa. The south-western part of the South Atlantic Ocean contributes up to 0.15 mm per month more to the precipitation at the icefield. MAM and SON months show small wind field anomalies ($\leq$ 1.6 m s^{-1}) (**Figures 9b,d**). Despite small wind field anomalies those seasons show contrary moisture source anomalies. The MAM months show a positive evaporative moisture source anomaly in the eastern South Pacific of up to 0.55 mm per month. SON months show moisture source anomalies from −0.35 to 0.15 mm per month.

4.2.2. El-Niño Southern Oscillation and Antarctic Oscillation Teleconnections

Beside seasons, determine large scale flow anomalies in the atmosphere the moisture sources of the icefield. A period of at least five consecutive overlapping 3-month seasons must exceed (deceed) an Ocean Niño Index (ONI) threshold of 0.5 (−0.5) in order to be classified as a full-fledge El-Niño (La-Niña) episode (National Oceanic and Atmospheric Administration, 2017). Considering these definitions, the time period from February 1979 to January 2017 contains 126 El-Niño and 90 La-Niña months (also see **Figures S1**, **S2** in Supplementary Material). Both phenomenas have a similar seasonal distribution (**Figure 10**). Nevertheless, the annual cycle is considered in **Figures 9e–h** by subtracting the monthly climatology for each month respectively.

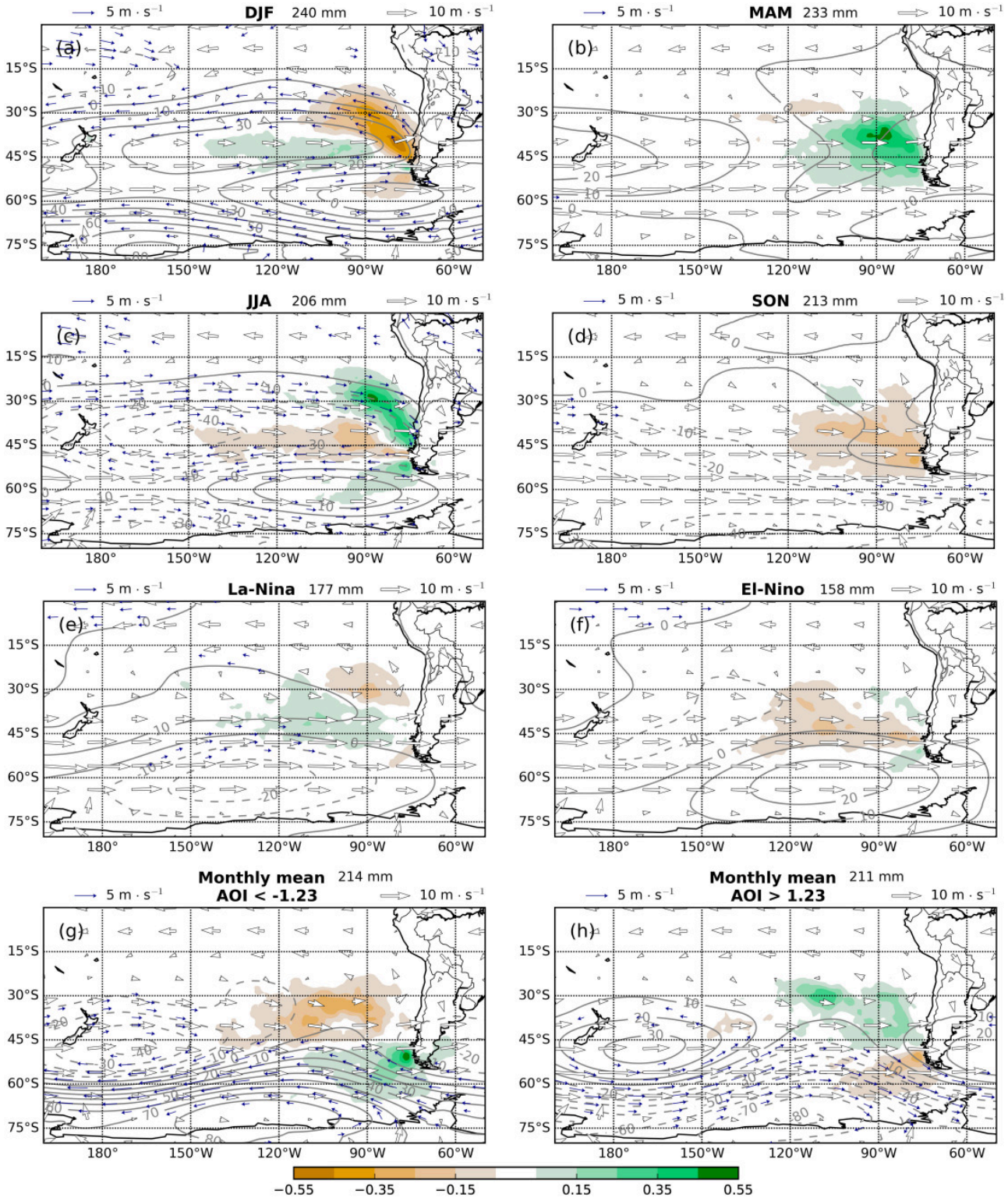

FIGURE 9 | Significant ($p < 0.05$) moisture source anomalies (shaded areas in mm per month) derived from the climatological mean (1979–2017, **Figure 5**). Also shown are the geopotential height field anomalies at 800 hPa level in m (solid and dashed lines), wind field anomalies ($> 1.5\,\mathrm{m\,s^{-1}}$, blue arrows), and the mean wind field at 800 hPa level (white arrows with reference arrow). The anomalies are given for different seasons **(a–d)**, La-Niña **(e)**, El-Niño **(f)**, strong negative **(g)**, and positive **(h)** Antarctic oscillation index (AOI). Orange areas highlight lower, green areas a higher than average contribution to icefield precipitation from the evaporative moisture sources within the scaled PBL. The header includes the monthly mean precipitation in the target region.

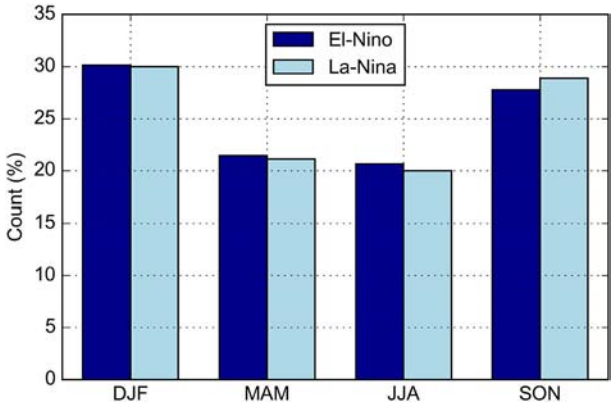

FIGURE 10 | Seasonal distribution of El-Niño and La-Niña months relative to their respective totals.

El-Niño Southern Oscillation (ENSO) periods have moisture source anomalies of up to 0.35 mm per month (**Figures 9e,f**). La-Niña related positive anomalies of up to 0.25 mm per month occur in the central South Pacific Ocean between 30 and 45°S (**Figure 9e**). Up to 0.25 mm per month lower contributions appear in the subtropics at 30°S, 90°W. During El-Niño events, the moisture source decreases by 0.25 mm per month in the east South Pacific along the 45°S parallel (**Figure 9f**). Slightly more moisture of up to 0.15 mm per month originates from the east South Pacific Ocean northward and southward of the icefield. La-Niña (El-Niño) months indicate a lower (higher) geopotential height of up to 20 m at the South Pacific Ocean around 60°S, 120°W. The largest 800 hPa wind field anomalies appear in the tropical west Pacific. La-Niña (El-Niño) months show 2 m s^{-1} stronger (weaker) easterlies, and depict the typical ENSO feature in the equatorial band.

A subset of months with standardized monthly mean Antarctic Oscillation index (AOI) falling the 10 percentile (AOI < -1.27) and exceeding the 90 percentile (AOI > 1.27) during the time period from February 1979 to January 2017 is taken to investigate Antarctic Oscillation dependent moisture source variations. Strong negative AOI months have up to 0.35 mm per month lower moisture uptake between 30 and 45°S in the east South Pacific, whereas moisture uptake from the ocean PBL in the proximity of the southern tip of South America is enhanced. Geopotential height anomalies weakens the westerly wind belt between 45 and 65°S in the South Pacific. Strong positive AOI months show stronger westerlies. Up to 0.35 mm per month more moisture originates from the mid-latitudes to the subtropics. The moisture sources in between 45 and 65°S show a deficit.

4.2.3. Extreme Events

The moisture source variability with respect to climatic extreme precipitation events is investigated. For purpose, we selected months with precipitation above the 90 percentile and below the 10 percentile, respectively, accumulated over the icefield obtained from the whole ERA-Interim data set. These selection represents dry (P_{median} = 343 mm) and humid (P_{median} = 111 mm) months.

Dry months are characterized by a 60 m increase of the geopotential height in the Drake Passage and 30 m lower geopotential heights over the South Pacific Ocean between 30 and 45°S. The lower meridional geopotential height gradient leads to weaker westerlies, an enhanced northerly flow at the west Patagonian coast, and have a deficit in the major moisture source region (**Figure 11a**). They contribute 0.15 mm per month less moisture just off the coastline of the icefield. A shift of the moisture source toward the south-west South Atlantic Ocean is apparent. This moisture source contributes up to 0.15 mm per month to the precipitation at the icefield. Dry months show up to 0.3 mm per month more moisture uptake over the South American continent where trajectories need on average less time (approximately 4 days; not shown) to reach the icefield.

During humid months the Drake Passage shows a 40 m decrease and in the subtropics a 10 m increase of the geopotential height in 800 hPa. The stronger poleward decreasing gradient of the 800 hPa geopotential height strengthens the westerlies. Trajectories which originate from southern South America, parts of the subtropical east South Pacific and the south-west South Atlantic in vicinity of the South American continent, need longer (approximately 12–15 days; not shown) to reach the icefield. There are negative anomalies (−0.15 mm per month) just off the coast line of South America. In the major moisture source region an overall increase of moisture uptake (up to 0.90 mm per month) is visible (**Figure 11b**).

An almost contrary pattern show the geopotential height anomaly of 800 hPa and the moisture source anomaly. The indicated anomalies in between the climatic extreme precipitation months have a dipole-like character. As before the annual cycle is taken into account.

The sea surface temperature and the mean sea level pressure anomaly are shown in **Figure S3**. The 800 hPa geopotential height and wind velocity (**Figure S4**), and the moisture sources (**Figures S5–S8**) are depicted as well.

5. DISCUSSION

5.1. Major Evaporative Sources

The South Pacific Ocean is the major moisture source of the icefield in the 38 year climatology (**Figure 5**). The main moisture sources are located around 45°S and extend from 160°W to the west coast of South America. Those uptake regions appear a few degrees northward of the circumpolar vortex. There is a region of cyclogenesis at approximately 170°W in the proximity of New Zealand (Taljaard, 1968). In addition, along 45°S baroclinic instabilities exist due to the polar front. These features explain the longitudinal extent of the moisture sources close to New Zealand at 45°S and their location a few degrees northward of the westerly wind belt.

The prevailing westerlies in the high southern latitudes cause a high trajectory density, count of trajectories per grid point, upstream of the target region (**Figure 8**), which is responsible for the moisture uptake maximum in a small region just off the coast line of west Patagonia. On the

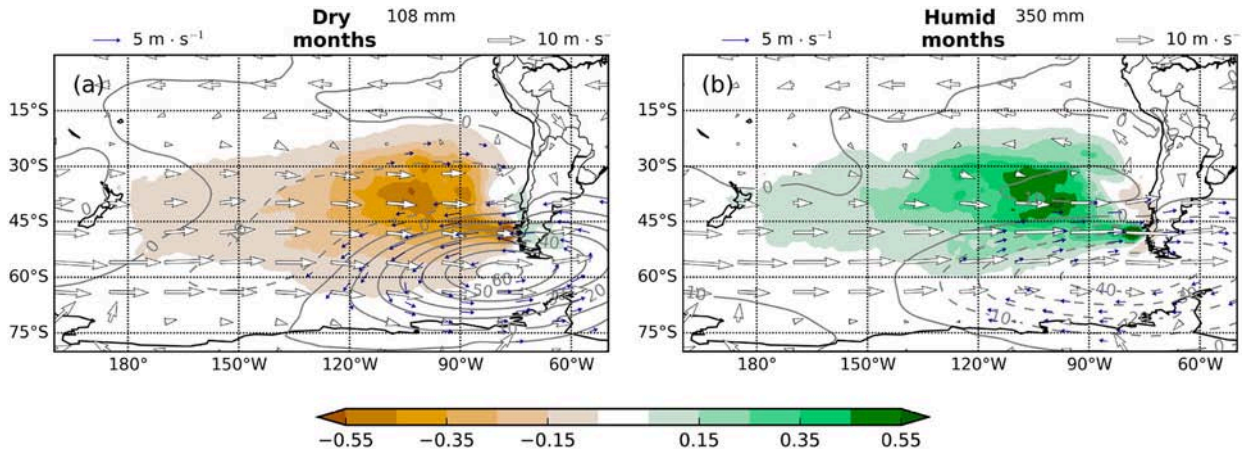

FIGURE 11 | Significant ($p < 0.05$) moisture source anomalies (shaded areas in mm per month). Also shown are the geopotential height field anomalies at 800 hPa (in m; solid and dashed lines), wind field anomalies ($> 1.5\,\mathrm{m\,s^{-1}}$, blue arrows), and the mean wind field at 800 hPa level (white arrows). The anomalies are given for extremely **(a)** dry (10 percentile) and **(b)** humid (90 percentile) months. The minimum of the moisture uptake is -1.07 mm per month and maximum 0.90 mm per month respectively. The header includes the monthly mean precipitation in the target region.

one hand the moisture uptake of each trajectory add up at the same grid point. On the other hand, uptake regions closer to the target have greater influence. They achieve a higher contribution due to less en route precipitation in comparison with identified uptake regions several days before arrival.

Moisture uptake regions extend to the subtropics and make an important contribution to the precipitation at the icefield. This highlights the role of the subtropical high pressure system in terms of the moisture origin of the icefield. In the Subtropics downstream of the Andes relatively dry air masses descend. Under the influence of the anticyclonical flow the air masses reach low heights (**Figure 7**) and moisten with the Pacific PBL (**Figure 8**). The air masses travel polwards into the mid-latitudes, where they come into the influence of the strong westerly storm track and finally reach the icefield. Pfahl et al. (2014) identified a moisture source in the subtropical South Pacific of warm conveyor belts. The importance of the warm conveyor belts in association with the regional precipitation at the icefield remains unknown in the present results.

The stationary high pressure region in the middle of Antarctica characterizes the circulation features at the coast of the continent (**Figure 2**). A closer examination of the 10 m wind shows the characteristics of the katabatic outflow (**Figure 3**). High offshore wind velocities occur close to the surface at Bellingshausen Sea, Amundsen Sea, and Ross Sea. Trajectories from those regions originate from the lower troposphere and indicate a subsidence at the transition from the continent to the South Pacific Ocean (**Figure 7**). The dominant mechanism for the offshore air flow in the Bellingshausen and Amundsen Sea is the persistent low pressure system in the Ross Sea (Papritz et al., 2015). This location is characterized by having the lowest mean sea level pressure of the South Pacific (**Figure 5**). If the cold and dry air masses from the inner Antarctic Continent are advected equatorwards across the sea ice shelfs over the relatively warm and moist ocean (cold air outbreaks), they can trigger convection and PBL fronts (Drüe and Heinemann, 2001). Thus the Ross, Amundsen and Bellingshausen Sea have a high density of mesocyclones (Irving et al., 2010). Seasonal trends of mesoscale cyclone activity over the ice-free southern ocean from 1999 to 2008 show an agreement with the examined seasonal moisture source anomaly. For instance, the ERA-Interim reanalysis data shows the strongest mean outflow off Antarctica during MAM and JJA (**Figure 3**) when Irving et al. (2010) indicate the highest density of mesocyclones in the Amundsen and Bellingshausen Sea. The moisture sources during this time period display positive anomalies south of 50°S (**Figures 9b,c**). Specially during JJA the positive moisture source anomalies reach close to the Amundsen and Bellingshausen Sea. This could be an evidence for cold air outbreaks, which moisten inside the Pacific PBL and contribute to the precipitation at the icefield. The identified source regions in the southernmost South Pacific might be the result of polar lows and their strengthening of the storm track.

5.2. Transport Time of Moisture

A substantial amount of moisture needs <10 days from its origin to the icefield (**Figure 5**). The zonal moisture exchange is faster than the meridional due to the westerly wind belt. Trajectories have the highest density (**Figure 8**) and reach on average the highest velocities in vicinity of the jet axis. The highest moisture uptake occurs 2 days before arrival (**Figure 6**). At this point, the majority of the trajectories are located inside the scaled PBL. The day before arrival the trajectories show an overall lifting due to the orography. Beyond 10 days before arrival, backward trajectories originate from higher levels, and hence indicate higher moisture uptake rates above the scaled PBL. This contribution is negligible. The highest moisture loss of the trajectories is due to precipitation at icefield. The absence of obstacles

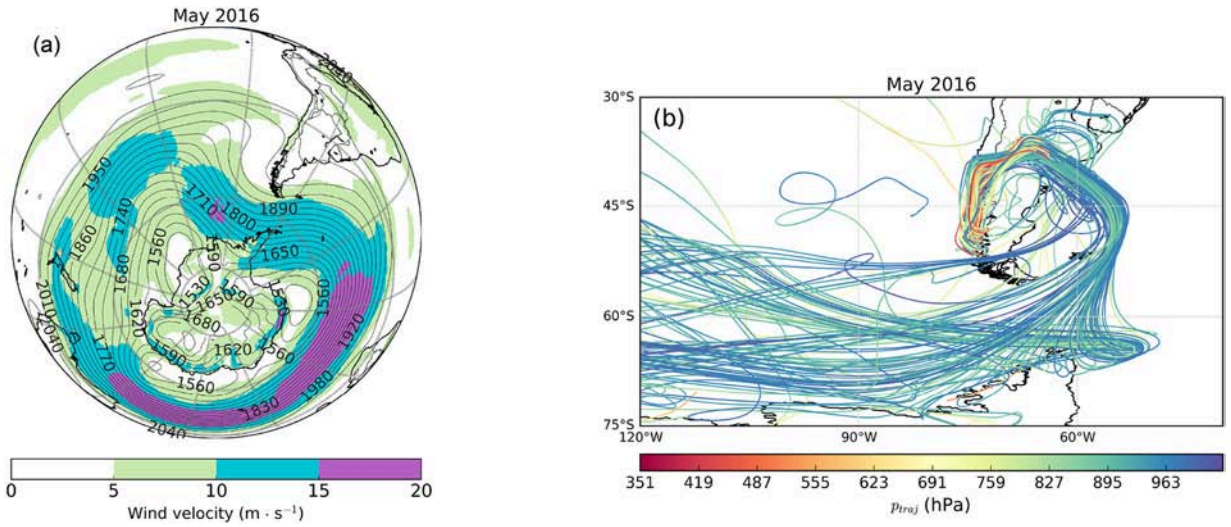

FIGURE 12 | (a) ERA-Interim 800 hPa geopotential height and wind velocity from May 2016. **(b)** Sample of trajectories with moisture uptake in the south-west South Atlantic during May 2016. The color indicate their pressure height.

in the Pacific Ocean leads to only small amounts of en route precipitation (compare averaged precipitation amounts in **Figure 3**).

5.3. Moisture Source Variabilities

Disturbances of the westerly wind belt, caused by baroclinic instabilities in the mid-latitudes, inject moist air masses from the tropics into the westerly wind belt. Thus, the westerlies are the dominant transport mechanism of moist air toward the icefield. A dislocation of the westerly wind belt leads to anomalies of precipitation (Garreaud et al., 2013), changes transport pathways of moisture toward the icefield and the location of moisture sources concerning the icefield. The contribution from the south-west South Atlantic Ocean is negligible. A substantial amount of moisture originates in the South Atlantic only in particular situations. One of the requirements is a positive geopotential height anomaly close to the Drake Passage (**Figure 11**). As a consequence, anticyclonic flow occurs over southern South America accompanied by a shift of the moisture sources to the south-east South Atlantic. The moisture uptake decreases in the major moisture source region between 40 and 50°S. Positive moisture source anomalies appear only in the vicinity of the southern South American coast. This phenomenon is more likely during El-Niño (**Figure 9f**) and JJA months (**Figure 9c**), and characterizes dry months (**Figure 11a**). Dry months are the most frequent during El-Niño and JJA (**Figure 13**), and thus they exhibit similar anomaly patterns. May 2016 shows the lowest accumulation rate of precipitation at the icefield in the whole ERA-Interim data and is used to point out those circulation features (**Figure 12**).

For May 2016 the averaged 800 hPa geopotential height indicates strongly meridional flow upstream of southern South America (**Figure 12a**). The high pressure ridge above southern South America causes an anticyclonic flow with the center at the southern South American continent. The polewards displacement of the storm track (positive geopotential height anomaly in the Drake Passage) forces the trajectories to travel through the Drake passage (**Figure 12b**). Anticyclonic curvature above the south-eastern South Atlantic Ocean moves the trajectories equatorwards. The air masses moisten inside the PBL of the Atlantic and the anticyclonic flow controls their westward flow over the continent. En route precipitation above the continent, with the maximum upstream of the Andes cordillera (see Supplementary Material **Figure S9**) due to orographic lifting, decreases the moisture source contribution of the South Atlantic but increases the intercontinental moisture recycling also visible in **Figure 11a**. Finally, meridional flow occurs along the coast line of west Patagonia. Trajectories within the Pacific PBL increase their moisture content and contribute to the positive moisture source anomaly along the western Patagonia coast. The strongly meridional flow at high southern latitudes in vicinity of the South American continent causes a low monthly precipitation sum at the icefield. This phenomenon is twice as frequent during austral winter compared to summer months (**Figure 13** and Trenberth and Mo, 1985).

By contrast, a strengthening of the zonal westerly flow in the south-east South Pacific increases the moisture uptake in the major moisture source region. During humid months (**Figure 11b**), DJF (**Figure 9a**), and La-Niña months (**Figure 9e**) the zonal flow around 50°S is most intense. Those months show a poleward shift of the subtropical anticyclone accompanied by a poleward shift of moisture sources from the subtropics to the mid-latitudes. In addition, a lower geopotential height at around 60°S increases the north-south pressure gradient between 45 and 60°S and results in a strengthening of the westerlies. As a consequence, long-range transport of moisture

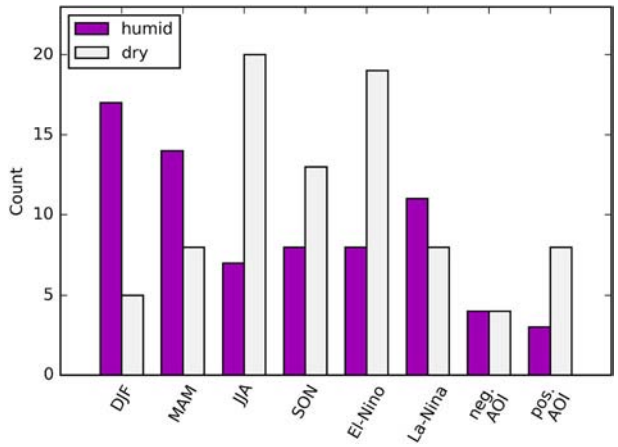

FIGURE 13 | The count of humid (90 percentile) and dry (10 percentile) months grouped by seasons, El-Niño, La-Niña , negative and positive antarctic oscillation index (AOI).

occurs with its maximal extent close to 180°W during humid months.

5.4. Variations of the Moisture Sources

Extreme precipitation events coincide with the strongest north-south pressure gradient anomaly between 45 and 60°S. Past studies emphasize a correlation between wind velocity and precipitation in west Patagonia (Schneider et al., 2003; Garreaud et al., 2013). The strength and location of the westerly wind belt controls the orographic precipitation at the icefield. The crossbarrier flow is one of three main drivers to describe the flow over a terrain and thus reasonable to correlate with the orographic precipitation. The main drivers can be summarized in a nondimensional ratio $U(NH)^{-1}$, which is often referred to as Froude number (or the inverse nondimensional mountain height), and determines the flow regime (Houze, 2012). Whenever the upstream Froude number is high (fast flow velocity, low stability, and/or a small mountain height), the airflow rises over the terrain. If the upstream Froude number is low (slow flow velocity, high stability and/or high mountains) the upcoming air is blocked and the flow is deflected laterally. In case of a narrow mountain ridge, high wind velocities and atmospheric conditions as observed in southernmost South America, the maximum of precipitation shifts from the hill top to the windward slope (Smith and Evans, 2007). Enhanced upstream precipitation at the icefield is also indicated by ERA-Interim and shown in **Figure 3**.

ERA-Interim reanalysis data indicate no significant monthly correlation between the ENSO phenomenon and the precipitation at the icefield ($r_{\text{Pearson}} = -0.06$, p-value $= 0.34$). The moisture source variability during ENSO months is half of the magnitude in comparison to the seasonal variation. El-Niño monthly evaporative moisture source anomalies show similarities to the austral winter months. La-Niña months show similarities to summer months. But both events show similar seasonal occurrence and thus only mirror the ENSO related anomalies. A direct link between SST anomalies in the South Pacific and moisture source anomalies does not exist.

The monthly mean precipitation at the icefield is independent of the AOI ($r_{\text{Pearson}} = -0.06$, p-value $= 0.19$). Strong negative AOI months show less moisture contribution from the subtropics and enhanced moisture uptake in the mid-latitudes (**Figure 9g**). A reduction of the westerly wind in the South Pacific decreases the moisture transport from the subtropics toward the icefield. Enhanced Antarctic outflow in the Bellingshausen and Amundsen Sea increases the moisture sources in the south-east South Pacific. Strong positive AOI months indicate an opposite pattern (**Figure 9h**). They show stronger westerly winds around 60°S. Less katabatic outflow from the Bellingshausen and Amundsen Sea results in a moisture source deficit in the south-east South Pacific. The north-westerly wind field anomalies in vicinity of the icefield increase the moisture uptake regions from the subtropics to 45°S.

5.5. Uncertainties

Evaporation or precipitation affect the net moisture change along a trajectory (Equation 1). We have omitted formation and dissolution of clouds and the amount of evaporative moisture source. Considering the specific cloud ice water content and the specific cloud liquid water content the whole amount of moisture sources decreases by approximately 5 % (not shown). It has a negligible effect on the evaporation pattern. Furthermore, the applied moisture source detection technique neglects moisture changes due to convection. Especially in warmer regions, such as the tropics and subtropics, or due to cold air outbreaks in high southern latitudes, convection plays a major role. In those regions we expect lower accuracy of the detected moisture sources. Transport errors increase significantly for trajectory calculations beyond 10 days (Stohl and Seibert, 1998). We applied 18-day backward trajectory calculations and have to consider inaccurate trajectory ending positions. However, a longer backward trajectory calculation time period than 10 days is not necessary to examine the moisture sources of the icefield (**Figure 5**). This is in accordance with the average residence time of water in the atmosphere (Van Der Ent and Tuinenburg, 2017). Shorter backward calculation periods are recommended for upcoming studies.

6. CONCLUSION

An established moisture source detection technique (Sodemann et al., 2008) was applied to identify moisture sources for precipitation at the Southern Patagonia Icefield. The three-dimensional kinematic 18-day backward trajectories are based on ERA-Interim reanalysis data from January 1979 to January 2017. This method is able to quantify the water vapor origin, the transport time and the favored transport paths, and presents a diagnostic picture of moisture source regions of the icefield.

The major moisture source of the icefield is found in the South Pacific between 80 to 160°W and 30 to 60°S (**Figure 5**). We detected 71 % of the moisture sources responsible for the precipitation at the icefield. The cause for the moisture

uptake above the PBL (25 %) and the moisture content already included at the trajectory ending position (4 %) have not been investigated.

The maximum moisture uptake is located just off the coastline of west Patagonia. The largest contribution of moisture sources extends north up to the subtropics, where a persistent anticyclone centered around 100°W and 30°S exists. Moisture uptake regions in the subpolar regions have a smaller contribution. In the high southern latitudes, cold air outbreaks are likely the dominant mechanism for moisture uptake. Relatively cold and dry descending air masses become moistened in the relatively warm planetary boundary layer over the ice-free Southern Pacific. The rather instable situation of relatively cold air masses above the relatively warm sea surface initialize convection and enhance the baroclinity of the westerly storm track. Furthermore, moisture sources which coincide with the prevailing westerlies have the biggest westward extent to 160°W. This region shows the highest trajectory density and indicates the favored pathways of moist air masses (**Figure 8**).

In addition controlling the transport pathways, the location of the westerly wind belt determines the amount of precipitation and the moisture origin of the icefield (**Figure 3** and **Figure 11**). In general, stronger westerly winds around 50°S lead to more long-range transport and enhanced moisture uptake from subtropics to mid-latitudes, and characterize climatic humid months (**Figure 11b**). By contrast, a weakening of the westerlies, and/or a poleward shift of the jet axis, is accompanied by enhanced moisture uptake along the southern tip of South America and less moisture supply from the subtropics and mid-latitudes in the central South Pacific (**Figure 9g** and **Figure 11a**). An appropriate proxy is an anomaly of the 800 hPa geopotential height extending from the Ross Sea to the Drake Passage. An extraordinarily strong positive anomaly of the geopotential height in the Drake Passage results in an anticyclonic flow over the southern tip of South America (**Figure 12a**). The high pressure ridge transports moisture from the south-western Atlantic above the Andes along the west Patagonians coast toward the icefield (**Figure 12b**). The north-westerly advection of moisture enhances the moisture source contribution from the subtropics only along the coast line. These events occur during climatologically drier months (**Figure 11a**).

Seasonal variation of moisture source regions exist. During MAM (**Figure 9b**) and JJA (**Figure 9c**) up to ∼40 % more moisture originates from the subtropics. Austral summer months have enhanced moisture uptake in the mid-latitudes and less contribution from the subtropics (**Figure 9a**). The ENSO related moisture source anomalies are half as large as the seasonal anomalies. During La-Niña more moisture originates from the mid-latitude region of South Pacific due to enhanced westerlies (**Figure 9e**). Opposite behavior is exhibited by El-Niño months (**Figure 9f**). The Antarctic Oscillation related moisture source anomalies show a similar strength of anomalies as the seasonal anomalies. Months with a strong negative Antarctic Oscillation Index show less moisture sources between subtropics and mid-latitudes (**Figure 9g**). More moisture originates from high southern latitudes due to increased outflow from Bellingshausen and Amundsen Sea. By contrast, months with a strong positive Antarctic Oscillation Index show an opposite pattern in moisture source and geopotential height anomalies, due to the anomalous meandering geopotential pattern (**Figure 9h**).

The Lagrangian analysis of precipitation origins for the icefield considers en route precipitation. A large part of the moisture uptake in remote regions such as the Indian Ocean or the tropics does not reach the icefield since it is rained out during transport. Identified moisture sources outside the 10-day backward calculation time period have a negligible impact as expected due to the average residence time of water in the atmosphere (Van Der Ent and Tuinenburg, 2017). The moisture uptake is at its maximum 2 days before arrival, when the majority of air masses are inside the PBL (**Figure 6a**).

The Lagrangian perspective highlights the interplay between the large scale climate modes and moisture sources of the icefield. These findings may help to interpret anomalies of paleo-climatological records of isotopic composition obtained from lake sediments (e.g. Mayr et al., 2005), lakes or precipitation samples (e.g. Mayr et al., 2007), ice cores (e.g. Schwikowski et al., 2013), or vegetation (e.g. Grießinger et al., 2018), in Fuego-Patagonia where a direct link to ambient environmental changes is absent. Thus, the identified moisture sources are one more building block to interpret climate proxies at the icefield from 1979 to 2017. A companion paper compares the findings of the Lagrangian moisture source detection with tree-ring records from Perito Moreno (Grießinger et al., 2018). The comparison shows, that variations in the moisture sources influence the $\delta^{18}O$ Tree-ring chronology of *Nothofagus pumilio* located in the vicinity of the Perito Moreno Glacier. A simultaneous study compares findings of the stable hydrogen and oxygen isotope composition of precipitation, and lake and river systems from different sites in southern South America with results of the moisture source detection method presented in this manuscript. They found that identified moisture sources and major transport pathways of moist air masses can clarify isotopic fractionation processes.

AUTHOR CONTRIBUTIONS

LL implemented the trajectory model, prepared the figures and wrote the manuscript. TS initialized the idea of this study and supported the research with in-depth knowledge of the Southern Patagonia Icefield. GM was the supervisor at the University of Innsbruck and he provided all the necessary resources to deal with a comprehensive climatological study. All authors discussed the findings and participated in preparing the final manuscript.

ACKNOWLEDGMENTS

We have to acknowledge the support of Michael Sprenger. His fundamental knowledge of technical details and willingness to help contributed to a successful application of LAGRANTO.

We gratefully acknowledge financial support by the Deutsche Forschungsgemeinschaft (DFG), no. SA 2339/4-1. The study was conducted in the frame of the research area Alpiner Raum of the University of Innsbruck. The publication fund of the University of Innsbruck supported its publication.

SUPPLEMENTARY MATERIAL

The Supplementary Material for this article can be found online at: https://www.frontiersin.org/articles/10.3389/feart.2018.00219/full#supplementary-material

REFERENCES

Aniya, M., Sato, H., Naruse, R., Skvarca, P., and Casassa, G. (1996). The use of satellite and airborne imagery to inventory outlet glaciers of the Southern Patagonia Icefield, South America. *Photogr. Eng. Remote Sens.* 62, 1361–1369. doi: 10.1175/2009MWR2881.1

Barrett, B. S., Garreaud, R., and Falvey, M. (2009). Effect of the Andes cordillera on precipitation from a midlatitude cold front. *Mon. Weather Rev.* 137, 3092–3109.

Berkelhammer, M. B., and Stott, L. D. (2008). Recent and dramatic changes in Pacific storm trajectories recorded in δ^{18}O from Bristlecone Pine tree ring cellulose. *Geochem. Geophys. Geosyst.* 9:Q04008. doi: 10.1029/2007GC001803

Berrisford, P., Dee, D., Poli, P., Brugge, R., Fielding, K., Fuentes, M., et al. (2011). *The ERA-Interim archive Version 2.0*. Reading: Shinfield Park.

Bracegirdle, T. J. (2013). Climatology and recent increase of westerly winds over the Amundsen Sea derived from six reanalyses. *Int. J. Climatol.* 33, 843–851. doi: 10.1002/joc.3473

Bracegirdle, T. J., and Marshall, G. J. (2012). The reliability of Antarctic tropospheric pressure and temperature in the latest global reanalyses. *J. Clim.* 25, 7138–7146. doi: 10.1175/JCLI-D-11-00685.1

Bromwich, D. H., Nicolas, J. P., and Monaghan, A. J. (2011). An assessment of precipitation changes over Antarctica and the Southern Ocean since 1989 in contemporary global reanalyses. *J. Clim.* 24, 4189–4209. doi: 10.1175/2011JCLI4074.1

Carrasco, J. F., Casassa, G., and Rivera, A. (2002). "Meteorological and climatological aspects of the Southern Patagonia Icefield," in *The Patagonian Icefields*. Series of the Centro de Estudios Científicos (Boston, MA: Springer), 29–41.

Dee, D., Uppala, S., Simmons, A., Berrisford, P., Poli, P., Kobayashi, S., et al. (2011). The ERA-Interim reanalysis: configuration and performance of the data assimilation system. *Q. J. R. Meteorol. Soc.* 137, 553–597. doi: 10.1002/qj.828

DGA (1987). *Balance Hídrico de Chile*. Santiago: Dirección General de Aguas, 34.

Drüe, C., and Heinemann, G. (2001). Airborne investigation of arctic boundary-layer fronts over the marginal ice zone of the Davis Strait. *Bound. -Layer Meteorol.* 101, 261–292. doi: 10.1023/A:1019223513815

Garreaud, R., Lopez, P., Minvielle, M., and Rojas, M. (2013). Large-scale control on the Patagonian climate. *J. Clim.* 26, 215–230. doi: 10.1175/JCLI-D-12-00001.1

Garreaud, R. D., Vuille, M., Compagnucci, R., and Marengo, J. (2009). Present-day South American Climate. *Palaeogeogr. Palaeoclimatol. Palaeoecol.* 281, 180–195. doi: 10.1016/j.palaeo.2007.10.032

Gat, J. R. (1996). Oxygen and hydrogen isotopes in the hydrologic cycle. *Annu. Rev. Earth Planet. Sci.* 24, 225–262. doi: 10.1146/annurev.earth.24.1.225

Grießinger, J., Langhamer, L., Schneider, C., Saß, B.-L., Steger, D., Skvarca, P., et al. (2018). Imprints of climate signals in a 204 year δ^{18}O tree-ring record of Nothofagus pumilio from Perito Moreno Glacier, Southern Patagonia (50°S). *Front. Earth Sci.* 6:27. doi: 10.3389/feart.2018.00027

Houze, R. A. (2012). Orographic effects on precipitating clouds. *Rev. Geophys.* 50:RG1001. doi: 10.1029/2011RG000365

Irving, D., Simmonds, I., and Keay, K. (2010). Mesoscale cyclone activity over the ice-free Southern Ocean: 1999–2008. *J. Clim.* 23, 5404–5420. doi: 10.1175/2010JCLI3628.1

Lenaerts, J. T., Van Den Broeke, M. R., van Wessem, J. M., van de Berg, W. J., van Meijgaard, E., van Ulft, L. H., et al. (2014). Extreme precipitation and climate gradients in Patagonia revealed by high-resolution regional atmospheric climate modeling. *J. Clim.* 27, 4607–4621. doi: 10.1175/JCLI-D-13-00579.1

Mayr, C., Fey, M., Haberzettl, T., Janssen, S., Lücke, A., Maidana, N. I., et al. (2005). Palaeoenvironmental changes in southern Patagonia during the last millennium recorded in lake sediments from Laguna Azul (Argentina). *Palaeogeogr. Palaeoclimatol. Palaeoecol.* 228, 203–227. doi: 10.1016/j.palaeo.2005.06.001

Mayr, C., Lücke, A., Stichler, W., Trimborn, P., Ercolano, B., Oliva, G., et al. (2007). Precipitation origin and evaporation of lakes in semi-arid Patagonia (Argentina) inferred from stable isotopes (δ 18 O, δ 2 H). *J. Hydrol.* 334, 53–63. doi: 10.1016/j.jhydrol.2006.09.025

Merlivat, L., and Jouzel, J. (1979). Global climatic interpretation of the deuterium-oxygen 18 relationship for precipitation. *J. Geophys. Res.* 84, 5029–5033. doi: 10.1029/JC084iC08p05029

Miller, A. (1976). The climate of Chile. *World Survey Climatol.* 12, 113–145.

National Oceanic and Atmospheric Administration (2017). *ENSO: Recent Evolution, Current Status and Predictions*. Avaialble online at: http://www.cpc.ncep.noaa.gov/products/analysis_monitoring/lanina/enso_evolution-status-fcsts-web.pdf (Accessed March 10, 2017).

Newell, R. E., Newell, N. E., Zhu, Y., and Scott, C. (1992). Tropospheric rivers?–A pilot study. *Geophys. Res. Lett.* 19, 2401–2404. doi: 10.1029/92GL02916

Nicolas, J. P., and Bromwich, D. H. (2011). Precipitation changes in high southern latitudes from global reanalyses: a cautionary tale. *Surveys Geophys.* 32, 475–494. doi: 10.1007/s10712-011-9114-6

Papritz, L., Pfahl, S., Sodemann, H., and Wernli, H. (2015). A climatology of cold air outbreaks and their impact on air–sea heat fluxes in the high-latitude South Pacific. *J. Clim.* 28, 342–364. doi: 10.1175/JCLI-D-14-00482.1

Persson, A. (2015). *User Guide to ECMWF Forecast Products*. Reading: ECMWF.

Pfahl, S., Madonna, E., Boettcher, M., Joos, H., and Wernli, H. (2014). Warm conveyor belts in the ERA-Interim dataset (1979–2010). Part II: Moisture origin and relevance for precipitation. *J. Clim.* 27, 27–40. doi: 10.1175/JCLI-D-13-00223.1

Rivadeneira, M. C. (2011). *Natural Variability of the Atmospheric Composition and Anthropogenic Influence in Patagonia : Contribution to the Understanding of Transport Pathways Along the Equator - Mid latitudes - Pole Transect*. Ph.D. dissertation, Université de Grenoble, Montpellier.

Scheele, M., Siegmund, P., and Van Velthoven, P. (1996). Sensitivity of trajectories to data resolution and its dependence on the starting point: in or outside a tropopause fold. *Meteorol. Appl.* 3, 267–273. doi: 10.1002/met.5060030308

Schneider, C., and Gies, D. (2004). Effects of El Niño–southern oscillation on southernmost South America precipitation at 53 S revealed from NCEP–NCAR reanalyses and weather station data. *Int. J. Climatol.* 24, 1057–1076. doi: 10.1002/joc.1057

Schneider, C., Glaser, M., Kilian, R., Santana, A., Butorovic, N., and Casassa, G. (2003). Weather observations across the southern Andes at 53 S. *Phys. Geogr.* 24, 97–119. doi: 10.2747/0272-3646.24.2.97

Schwikowski, M., Schläppi, M., Santibañez, P., Rivera, A., and Casassa, G. (2013). Net accumulation rates derived from ice core stable isotope records of Pío XI glacier, Southern Patagonia Icefield. *Cryosphere* 7, 1635–1644. doi: 10.5194/tc-7-1635-2013

Shiraiwa, T., Kohshima, S., Uemura, R., Yoshida, N., Matoba, S., Uetake, J., et al. (2002). High net accumulation rates at Campo de Hielo Patago´ nico Sur, South America, revealed by analysis of a 45.97 m long ice core. *Ann. Glaciol.* 35, 84–90. doi: 10.3189/172756402781816942

Smith, R. B., and Evans, J. P. (2007). Orographic precipitation and water vapor fractionation over the southern Andes. *J. Hydrometeorol.* 8, 3–19. doi: 10.1175/JHM555.1

Sodemann, H., Schwierz, C., and Wernli, H. (2008). Interannual variability of Greenland winter precipitation sources: Lagrangian moisture diagnostic

and North Atlantic Oscillation influence. *J. Geophys. Res.* 113:D03107. doi: 10.1029/2007JD008503

Sprenger, M., and Wernli, H. (2015). The LAGRANTO Lagrangian analysis tool–version 2.0. *Geosci. Model Dev.* 8, 2569–2586. doi: 10.5194/gmd-8-2569-2015

Steen-Larsen, H. C., Johnsen, S. J., Masson-Delmotte, V., Stenni, B., Risi, C., Sodemann, H., et al. (2013). Continuous monitoring of summer surface water vapor isotopic composition above the Greenland Ice Sheet. *Atmos. Chem. Phys.* 13, 4815–4828. doi: 10.5194/acp-13-4815-2013

Stohl, A., Haimberger, L., Scheele, M., and Wernli, H. (2001). An intercomparison of results from three trajectory models. *Meteorol. Appl.* 8, 127–135. doi: 10.1017/S1350482701002018

Stohl, A., and James, P. (2004). A Lagrangian analysis of the atmospheric branch of the global water cycle. Part I: Method description, validation, and demonstration for the August 2002 flooding in central Europe. *J. Hydrometeorol.* 5, 656–678. doi: 10.1175/1525-7541(2004)005<0656:ALAOTA>2.0.CO;2

Stohl, A., and Seibert, P. (1998). Accuracy of trajectories as determined from the conservation of meteorological tracers. *Q. J. R. Meteorol. Soc.* 124, 1465–1484. doi: 10.1002/qj.49712454907

Taljaard, J. (1968). Climatic frontal zones of the Southern Hemisphere. *Notos* 17, 23–39.

Trenberth, K. F., and Mo, K. C. (1985). Blocking in the southern hemisphere. *Mon. Weath. Rev.* 113, 3–21. doi: 10.1175/1520-0493(1985)113<0003:BITSH>2.0.CO;2

Van Der Ent, R. J., and Tuinenburg, O. A. (2017). The residence time of water in the atmosphere revisited. *Hydrol. Earth Syst. Sci.* 21:779. doi: 10.5194/hess-21-779-2017

Viale, M., Houze R. A. Jr, and Rasmussen, K. L. (2013). Upstream orographic enhancement of a narrow cold-frontal rainband approaching the Andes. *Mon. Weath. Rev.* 141, 1708–1730. doi: 10.1175/MWR-D-12-00138.1

Viale, M., and Nuñez, M. N. (2011). Climatology of winter orographic precipitation over the subtropical central Andes and associated synoptic and regional characteristics. *J. Hydrometeorol.* 12, 481–507. doi: 10.1175/2010JHM1284.1

Ward, E., Buytaert, W., Peaver, L., and Wheater, H. (2011). Evaluation of precipitation products over complex mountainous terrain: a water resources perspective. *Adv. Water Resour.* 34, 1222–1231. doi: 10.1016/j.advwatres.2011.05.007

Weischet, W. (1996). *Regionale Klimatologie Teil 1*. Stuttgart: Schweizerbart Science Publishers.

Wernicke, J., Hochreuther, P., Grießinger, J., Zhu, H., Wang, L., and Bräuning, A. (2017). Air mass origin signals in $\delta^{18}O$ of tree-ring cellulose revealed by back-trajectory modeling at the monsoonal Tibetan plateau. *Int. J. Biometeorol.* 61, 1109–1124. doi: 10.1007/s00484-016-1292-y

Wernli, B. H., and Davies, H. C. (1997). A Lagrangian-based analysis of extratropical cyclones. I: the method and some applications. *Q. J. R. Meteorol. Soc.* 123, 467–489. doi: 10.1002/qj.49712353811

Winschall, A., Pfahl, S., Sodemann, H., and Wernli, H. (2014). Comparison of Eulerian and Lagrangian moisture source diagnostics–the flood event in eastern Europe in May 2010. *Atmos. Chem. Phys.* 14, 6605–6619. doi: 10.5194/acp-14-6605-2014

Zeng, X., Brunke, M. A., Zhou, M., Fairall, C., Bond, N. A., and Lenschow, D. H. (2004). Marine atmospheric boundary layer height over the eastern Pacific: data analysis and model evaluation. *J. Clim.* 17, 4159–4170. doi: 10.1175/JCLI3190.1

Conflict of Interest Statement: The authors declare that the research was conducted in the absence of any commercial or financial relationships that could be construed as a potential conflict of interest.

Advantages of publishing in Frontiers

OPEN ACCESS
Articles are free to read for greatest visibility and readership

FAST PUBLICATION
Around 90 days from submission to decision

HIGH QUALITY PEER-REVIEW
Rigorous, collaborative, and constructive peer-review

TRANSPARENT PEER-REVIEW
Editors and reviewers acknowledged by name on published articles

Frontiers
Avenue du Tribunal-Fédéral 34
1005 Lausanne | Switzerland

Visit us: www.frontiersin.org
Contact us: info@frontiersin.org | +41 21 510 17 00

REPRODUCIBILITY OF RESEARCH
Support open data and methods to enhance research reproducibility

DIGITAL PUBLISHING
Articles designed for optimal readership across devices

FOLLOW US
@frontiersin

IMPACT METRICS
Advanced article metrics track visibility across digital media

EXTENSIVE PROMOTION
Marketing and promotion of impactful research

LOOP RESEARCH NETWORK
Our network increases your article's readership